frontiers | Research Topics

Experimental and analytical investigations on nuclear reactor safety, severe accident phenomena and severe accident mitigation of nuclear power plants

Edited by
Yapei Zhang, Luteng Zhang and Jun Wang

Published in
Frontiers in Energy Research

ISSN 1664-8714
ISBN 978-2-83251-312-5
DOI 10.3389/978-2-83251-312-5

About Frontiers

Frontiers is more than just an open access publisher of scholarly articles: it is a pioneering approach to the world of academia, radically improving the way scholarly research is managed. The grand vision of Frontiers is a world where all people have an equal opportunity to seek, share and generate knowledge. Frontiers provides immediate and permanent online open access to all its publications, but this alone is not enough to realize our grand goals.

Frontiers journal series

The Frontiers journal series is a multi-tier and interdisciplinary set of open-access, online journals, promising a paradigm shift from the current review, selection and dissemination processes in academic publishing. All Frontiers journals are driven by researchers for researchers; therefore, they constitute a service to the scholarly community. At the same time, the *Frontiers journal series* operates on a revolutionary invention, the tiered publishing system, initially addressing specific communities of scholars, and gradually climbing up to broader public understanding, thus serving the interests of the lay society, too.

Dedication to quality

Each Frontiers article is a landmark of the highest quality, thanks to genuinely collaborative interactions between authors and review editors, who include some of the world's best academicians. Research must be certified by peers before entering a stream of knowledge that may eventually reach the public - and shape society; therefore, Frontiers only applies the most rigorous and unbiased reviews. Frontiers revolutionizes research publishing by freely delivering the most outstanding research, evaluated with no bias from both the academic and social point of view. By applying the most advanced information technologies, Frontiers is catapulting scholarly publishing into a new generation.

What are Frontiers Research Topics?

Frontiers Research Topics are very popular trademarks of the *Frontiers journals series*: they are collections of at least ten articles, all centered on a particular subject. With their unique mix of varied contributions from Original Research to Review Articles, Frontiers Research Topics unify the most influential researchers, the latest key findings and historical advances in a hot research area.

Find out more on how to host your own Frontiers Research Topic or contribute to one as an author by contacting the Frontiers editorial office: frontiersin.org/about/contact

Experimental and analytical investigations on nuclear reactor safety, severe accident phenomena and severe accident mitigation of nuclear power plants

Topic editors

Yapei Zhang — Xi'an Jiaotong University, China

Luteng Zhang — Chongqing University, China

Jun Wang — University of Wisconsin-Madison, United States

Citation

Zhang, Y., Zhang, L., Wang, J., eds. (2023). *Experimental and analytical investigations on nuclear reactor safety, severe accident phenomena and severe accident mitigation of nuclear power plants*. Lausanne: Frontiers Media SA. doi: 10.3389/978-2-83251-312-5

Table of contents

frontiers in Energy Research

ORIGINAL RESEARCH
published: 03 December 2021
doi: 10.3389/fenrg.2021.782086

Assessment of CHF and Post-CHF Heat Transfer Models for High-Pressure Condition

Meiqi Song[1] *and Xiaojing Liu*[2]*

[1]Institute of Applied Thermofluidics, Karlsruhe Institute of Technology, Karlsruhe, Germany, [2]School of Nuclear Science and Engineering, Shanghai Jiao Tong University, Shanghai, China

Supercritical heat transfer systems may undergo trans-critical procedures and work at subcritical conditions during startup, shutdown, or some accidents. However, well-validated heat transfer models for the high-pressure condition ($P/P_c > 0.7$) are still missing. In the present work, with exhaustive literature review, extensive experimental databanks of CHF and post-dryout heat transfer under high-pressure condition are established, respectively. Existing prediction models for the high-pressure condition are also summarized from all over the world. Thereby, with the aid of the high-pressure experimental databank, prediction models get evaluated. It has been demonstrated that CHF correlation developed by Song et al. shows good predictive capability. Post-dryout heat transfer could get well predicted by the Song correlation. These recommended prediction models could be implemented to upgrade safety analysis codes for simulation of trans-critical transients.

Keywords: trans-critical transient, high-pressure condition, CHF, post-CHF heat transfer, SCWR

OPEN ACCESS

Edited by:
Luteng Zhang,
Chongqing University, China

Reviewed by:
Yuan Yuan,
Sichuan University, China
Haochun Zhang,
Harbin Institute of Technology, China

***Correspondence:**
Xiaojing Liu
xiaojingliu@sjtu.edu.cn

Specialty section:
This article was submitted to Nuclear Energy, a section of the journal Frontiers in Energy Research

Received: *23 September 2021*
Accepted: *01 November 2021*
Published: *03 December 2021*

Citation:
Song M and Liu X (2021) Assessment of CHF and Post-CHF Heat Transfer Models for High-Pressure Condition. Front. Energy Res. 9:782086. doi: 10.3389/fenrg.2021.782086

INTRODUCTION

A substance above its critical temperature T_c and critical pressure P_c is referred as a supercritical fluid (SCF). As can be seen from **Figure 1**, the vapor–liquid phase change in the supercritical region disappears, and the fluid is always single phase. With its unique properties, SCFs have been widely used in a variety of fields such as chemical engineering, power generation, refrigeration, and food engineering (Eggers, 2012).

Supercritical power cycles, working with SCFs, are of great interest for their higher thermal efficiency. Currently, supercritical water (SCW) and supercritical carbon dioxide (sCO_2) are actively considered as a coolant for power cycles throughout the world. For instance, it has been reported by Marion et al. (2019) that the STEP 10 MWe sCO_2 Pilot Plant Demonstration would achieve a net efficiency over 50%. Particularly, supercritical power cycles have a great potential in waste heat recovery and application of clean energy (such as nuclear energy, solar energy, geothermal energy, and bioenergy) (Ahn et al., 2015; Sarkar, 2015; Crespi et al., 2017).

(A) Waste heat

The application market of the industrial waste is extraordinarily large, such as waste heat from metal mines, chemical plants, cement plants, gas turbines, and reciprocating engines. However, the development of the utilization of low temperature waste heat is still limited. The critical temperature of CO_2 is about 30.98°C, which allows the sCO_2 power cycles to be applied for various temperature ranges and therefore for low-temperature heat sources (Sarkar, 2015; Musgrove et al., 2017). Currently, organic Rankine cycle (ORC), with the flammable hydrocarbon-based organic as

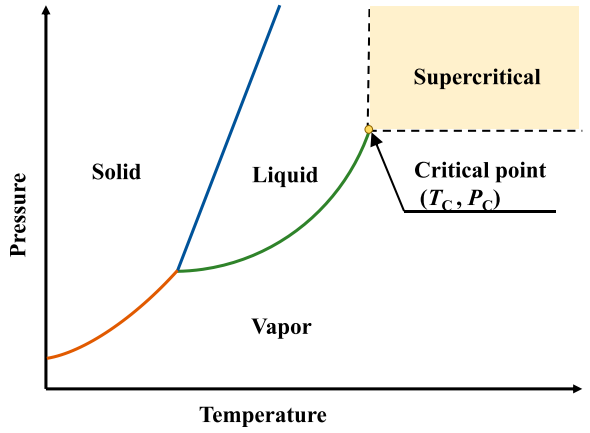

FIGURE 1 | Phase diagram (pressure–temperature) of substance (Debenedetti et al., 1994).

working fluid, is applied to use the low-temperature heat sources. For safety measures, an intermediate loop is used to transfer heat from the heat source to the organic fluid. Obviously, when applying sCO_2 power cycle to waste heat recovery, the safety measures are not required further, since CO_2 is nontoxic and nonflammable. Moreover, compared to ORC plants, the equipment size of sCO_2 power cycles would be smaller, and it could work with even lower heat source temperature (Li et al., 2017; Poerner et al., 2017).

(B) Nuclear energy

The supercritical water-cooled reactor (SCWR), as the only reactor concept with supercritical water as working fluid, was recommended as one of the six most promising Generation IV reactor systems by the Generation IV International Forum (GIF) (uclear Energy R, 2002). Designed to be operated at 25 MPa and outlet temperature over 500°C, the net efficiency of SCWR can reach up to 45%. In addition, due to a direct-cycle design with single-phase coolant, expensive plant components utilized in conventional nuclear power plants such as steam generators in pressurized water reactor (PWR) or moisture separator and steam dryer in boiling water reactor (BWR) are eliminated in SCWR. Hence, SCWR achieves a considerable reduction in capital costs (Oka et al., 2010; Cheng et al., 2016; Pioro et al., 2016; Pioro and Pioro, 2016; Schulenberg et al., 2016).

Concepts of cooling system with sCO_2 power cycles have been proposed for various kinds of Generation IV reactors, such as direct cycle and indirect cycle (Qi et al., 2018). Compared to the most often considered gas cycles for gas cooled fast reactor (GFR), i.e., Helium cycles, the sCO_2 cycles eliminate the leakage problem practically, as CO_2 is a triatomic gas with a much higher molecular weight (Dostal et al., 2002; Hejzlar et al., 2006). The high-density sCO_2 enables the cycle layout to be more compact and provides an acceptable size of heat exchangers. Taking place of the traditional Rankine superheated steam cycle, the application of sCO_2 Brayton cycle to the sodium-cooled fast reactor (SFR) could avoid considering the sodium–water reaction since sCO_2 is stable and relative inert in the working range (Sienicki et al., 2014).

For fusion reactors, a simple but high-efficiency sCO_2 Brayton cycle could realize the integration of all three main heat sources (i.e., blanket, divertor, and vacuum vessel) taking the advantage of the wide working range of sCO_2 Brayton cycle (Linares et al., 2015; Vesely et al., 2017; Syblik et al., 2019).

(C) Solar energy, geothermal energy, and bioenergy

sCO_2 power cycle is appealing to be utilized in renewable energy systems, not only taking the advantage of its higher efficiency, good power scalability (~10–150 MWe), smaller size, and simpler layout but also because CO_2 is environment-friendly. Moreover, it allows concentrating solar power (CSP) plants to be applied in the desert places where water is scarce while solar energy is abundant (Osorio et al., 2016; Binotti et al., 2017; Yin et al., 2020). Similar for dry geothermal reservoirs, in which water is inadequate, the energy resource could be captured by injecting cold sCO_2 through wells into the thermal plume (Frank et al., 2012; Wang et al., 2019). As indicated, another benefit is that 2% of the CO_2 flowing through the geothermal heat source would be captured in the well (Musgrove et al., 2017).

As seen, supercritical power cycles have been designed to utilize various energy sources. Studies of heat transfer characteristics for supercritical condition are thereby carried out. Since supercritical fluid is single phase, the two-phase boiling crisis phenomena, which is a crucial limitation to conventional subcritical systems, are eliminated and regarded as an advantage of the supercritical power cycle (Oka et al., 2010). However, trans-critical processes in which the system pressure transfers between supercritical condition and subcritical condition could happen during startup, shutdown, and abnormal transients such as the loss-of-coolant accidents (LOCA) (Liu et al., 2016). Obviously, the boiling crisis problem cannot be avoided when taking these trans-critical transients into consideration.

Moreover, as can be seen from **Figure 2**, differences in thermal property between the saturated vapor and saturated liquid phase will be smaller when the pressure increases, and in the high-pressure region, thermal properties change drastically, which may lead to the difference in heat transfer characteristic compared to conventional pressure condition. It is noted that the evaporation heat decreases to zero at the critical point, which could enhance the vaporization process. Thus, in the high-pressure region, the boiling crisis could occur even with a low heat flux, and post-CHF heat transfer region will be encountered, which could even cause burnout of the heated wall. Therefore, the heat transfer behavior not only at supercritical pressure but also at high-pressure subcritical condition is of great significance for the supercritical systems.

In subcritical condition, with the development of conventional steam generators, the great majority of previous heat transfer research are usually at pressure lower than the PWR working pressure (15.5 MPa, with reduced pressure at 0.7, $P/P_c = 0.7$), while well-validated prediction methods for higher pressure condition ($P/P_c > 0.7$) are still missing. The present work will evaluate existing prediction models of CHF and post-CHF heat transfer for the high-pressure subcritical condition, since CHF and post-CHF heat transfer are usually the most important phenomena under subcritical condition.

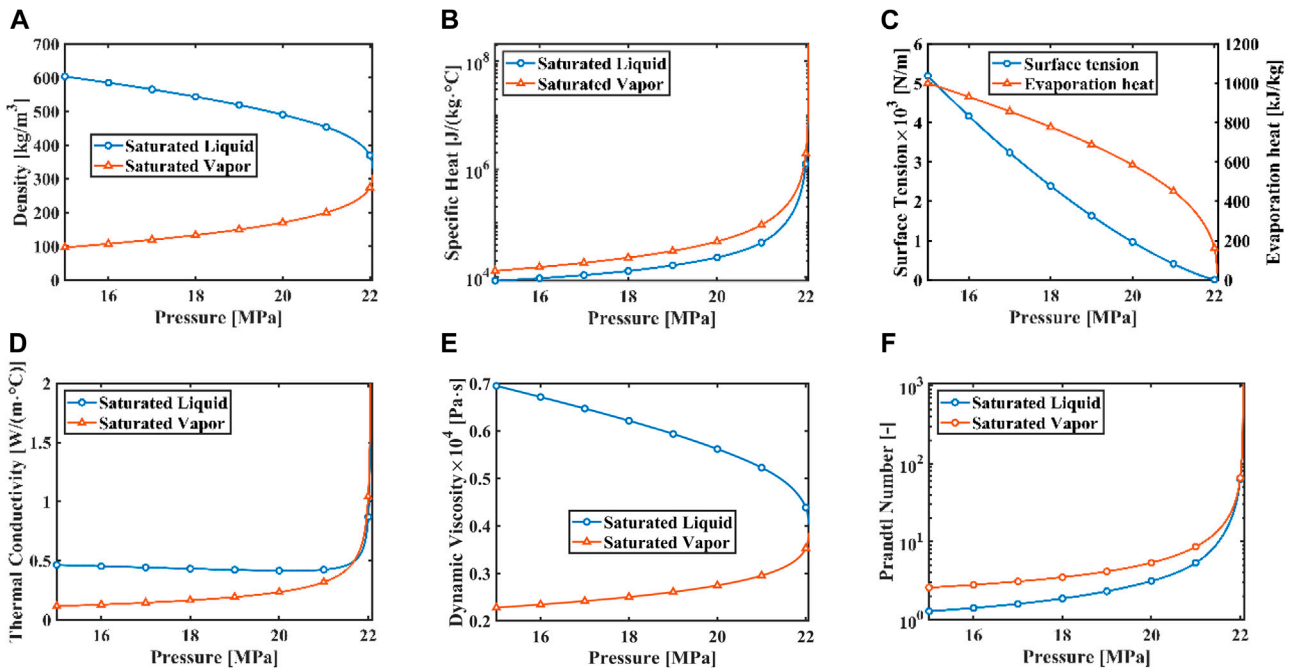

FIGURE 2 | Variation of saturated properties for water (Lemmon et al., 2007). **(A)** Density. **(B)** Specific heat. **(C)** Surface tension and evaporation heat. **(D)** Thermal conductivity. **(E)** Dynamic viscosity.

In the present work, experimental databank of CHF and post-CHF heat transfer for the high-pressure condition will be established, and existing prediction methods will be collected based on literatures all over the world and previous research by the authors. Thereby, prediction methods could be examined with the aid of the new developed experimental databank. Besides, the influence of pressure on CHF and post-CHF heat transfer will be analyzed.

ASSESSMENT OF CHF PREDICTION METHOD FOR HIGH-PRESSURE REGION

Boiling crisis occurs when the heat flux raises up to a high level that the heated surface can no longer support the continuous liquid-wall contact (Thermohydrau, 2001). The heat flux at the boiling crisis point is usually referred as critical heat flux (CHF). Because of the poor heat transfer capability of vapor, the boiling crisis could lead to failure of the heated surface. Therefore, CHF is a significant safety limitation.

Regarding flow boiling in a pressure duct, two boiling crisis mechanisms are supposed to be considered (Tong and Tang, 2018). The first is referred as "departure from nucleate boiling (DNB)," as shown in **Figure 3A**, occurring in a subcooled or low-quality condition. The upstream of the DNB point is the so-called "nucleate boiling" (bubbly flow). After the DNB point, the flow pattern transfers to inverted annular flow, where the liquid phase forms as a continuous core with dispersed vapor bubbles, while the vapor phase flows along the wall. Since vapor flows faster, it causes instabilities in the liquid core and leads to break up of the liquid core. The flow will transfer to dispersed droplet flow in which the liquid droplets dispersed in the vapor phase (Tong and Tang, 2018). **Figure 3B** exhibits another kind of boiling crisis, "dryout (DO)." The upstream of the DO point is an annular flow, where the liquid film flows along the heated wall. Then, the dryout of the liquid film leads to dispersed droplet flow where the liquid droplets dispersed in vapor phase, and the heated wall lost the cooling through continuous liquid phase. Normally, the dryout type boiling crisis occurs under higher quality (Tong and Tang, 2018).

CHF Databank for High-Pressure Condition

CHF experiments are usually carried out with constant mass flux, pressure, and inlet subcooling, whereas the supplied heat flux is increased stepwise until boiling crisis occurs. In the present work, experiments in uniformly heated round tubes are collected from literatures and previous experiments carried out in the Institute for Applied Thermofluidic (IATF) (Song et al., 2021a; Katto and Yokoya, 1984; (2019). Unpublished, 2019). Accordingly, a CHF databank with water, R12, CO_2, or helium as coolant is obtained for reduced pressure (P/P_c) above 0.7. For each experiment record, the information contains the system pressure P, mass fluxtube diameter D_h, critical quality x_c (equilibrium quality at the CHF location), and critical heat flux q_c. Parameter range of current high-pressure CHF databank is listed in **Table 1**. Since inlet quality x_{in}(x_{in}) and the distance from the start of the heated section to the boiling crisis point (L_c) might be unavailable in some cases, they are not listed in **Table 1**. As seen, the CHF databank covers an extensive range of x_c, which implies that the present databank contains both DNB and DO experiments.

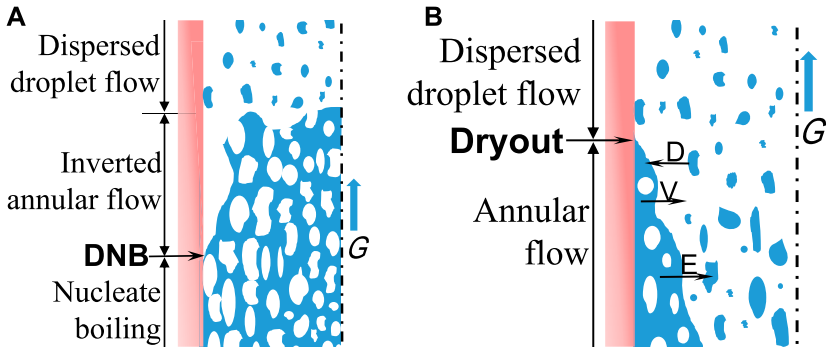

FIGURE 3 | Sketch of flow patterns near the CHF point for flow boiling (Tong and Tang, 2018). **(A)** DNB. **(B)** Dryout.

TABLE 1 | Parameter range of high-pressure CHF databank.

Parameters	Water		R12		CO_2		Helium	
	Min	Max	Min	Max	Min	Max	Min	Max
P MPa	15.5	21.5	2.9	3.5	6.2	7.1	0.2	0.2
P_r	0.703	0.974	0.700	0.846	0.839	0.956	0.875	0.875
G, kg/(m^2·s)	156	6,907	121	10,440	494	2041	10.47	89.51
D_h, m	1.9	24.7	3.0	15.8	8.0	8.0	1.0	1.0
x_c	−1.768	0.955	−0.745	0.902	−0.771	0.294	−0.191	0.681
q_c, kW/m^2	135.0	7,770.0	18.0	991.0	53.6	225.2	0.6	3.5
N	1,484	–	1,140	–	28	–	43	–

Especially, the Song correlation (Song et al., 2021a) was developed by the authors based on water experiments listed in **Table 1**.

Existing CHF Prediction Method for High-Pressure Condition

Up to now, numerous prediction methods for CHF have been proposed (Hall and Mudawar, 2000). For example, the W-3 correlation (Tong, 1967), which could evaluate the value of critical heat flux as a function of pressure, mass flux, quality, hydraulic diameter, and inlet subcooled, has been widely applied for the safety analysis of PWR. However, prediction methods for the high-pressure region ($P/P_c > 0.7$) are relatively rare.

In the present work, CHF prediction methods that are applicable to high-pressure condition are collected from the literature and summarized in **Table 2**. Most of these prediction methods were derived from water experiments. Nevertheless, Kariya et al. (2013) developed a CHF correlation from experiments with R22, R134a, or water as coolant. Vijayarangan correlation (Vijayarangan et al., 2006) is derived from their R134a measurements. Shah correlation (Mohammed Shah, 1987) is developed from 23 different fluids including water, halocarbon refrigerants, chemicals, liquid metals, helium, and other cryogens. Chen correlation (Chen et al., 2017), Becker correlation (Becker et al., 1972), Lombardi correlation (Lombardi, 1995), Vijayarangan correlation (Vijayarangan et al., 2006), and Shah correlation (Mohammed Shah, 1987) require known inlet quality x_{in} or the distance from the start of heated section to the boiling crisis point L_c, which cannot be provided in some experimental tests. Katto (1992) developed a semitheoretical model based on sublayer dryout mechanism. The Hall correlation (Hall and Mudawar, 2000) and Katto's model (Katto, 1992) can only be applied for test cases with negative quality. The 2006 CHF LUT (Groeneveld et al., 2007) gives a tabular form of critical heat flux values as a function of pressure, mass flux, and quality. Furthermore, validity range of these CHF prediction methods could be found in **Table 3**.

Assessment of High-Pressure CHF Prediction Method

In order to evaluate predictive capability of CHF models with the aid of CHF databank, for each experimental data point, the error parameter is defined by,

$$\varepsilon_i = \frac{q_{c,cal}(i) - q_{c,m}(i)}{q_{c,m}(i)} \tag{1}$$

with $q_{c,cal}(i)$ for the calculated CHF and $q_{c,m}(i)$ for CHF measured by experiment. Mean value (μ) and root-mean-square value (RMS) of the error parameter are calculated by **Eqs. 2** and **3**, respectively.

$$\mu = \frac{1}{N}\sum_{i=1}^{N}\varepsilon_i \tag{2}$$

$$RMS = \sqrt{\frac{1}{N}\sum_{i=1}^{N}\varepsilon_i^2} \tag{3}$$

TABLE 2 | CHF prediction models for high-pressure condition.

References	CHF model
(Song et al., 2021a)	$Bo_c = f(We_V) \cdot f(x_c)$ where $f(We_V) = \max(A_1, A_2)$ $f(x_c) = (B_1 + B_2 + B_3) - \max(B_1, B_2, B_3) - \min(B_1, B_2, B_3)$ and $A_1 = 7.796 \times 10^{-2} \cdot We_V^{-0.439}$ $A_2 = 1.530 \times 10^{-3} \cdot We_V^{-0.0803}$ $B_1 = 2.156 \cdot (1 - x_c)^{0.688}$, $B_2 = 1.841 \cdot (1 - x_c)^{2.137}$, $B_3 = 0.672 \cdot (1 - x_c)^{0.219}$
(Miropol'skii and Shitsman, 1962)	$\frac{q_c \mu_L}{\sigma \rho_L H_{VL}} = \begin{cases} \frac{0.174}{3600}\left(\frac{c_{p,L} T_{sat}}{H_{VL}}\right)^{0.8} K^{0.4}\left[1 - 0.45\left(\frac{\rho_L}{\rho_V}\right)^{0.8} x_c\right], x_c < 0 \\ \frac{0.174}{3600}\left(\frac{c_{p,L} T_{sat}}{H_{VL}}\right)^{0.8} K^{0.4}(1 - x_c)^n, x_c \geq 0 \end{cases}$ Where $K = (\frac{G\mu_L}{\sigma \rho_L})(\frac{\rho_L}{\rho_V})^{0.2}$ $n = \begin{cases} 0.8, K \leq 0.016 \\ 50K, 0.016 < K \leq 0.06 \\ 3, K > 0.06 \end{cases}$
(Levitan and Lantsman, 1975)	$q_c = 10^6 (10.3 - 17.5P_r + 8.0P_r^2)(\frac{G}{1000})^{0.68P_r - 1.2x_c - 0.3} \exp(-1.5x_c)(\frac{0.008}{D})^{0.5}$
(Chernobai, 1980)	$\frac{8D_*}{Re_L Pr_L}\left(1 + \frac{1.8H_L}{H_{VL}}\right)\left(1 + \frac{D_*}{Nu_L}\right) = \begin{cases} \left(Bo + \frac{x_c Nu_L}{Re_L Pr_L}\right)^2, x_c < 0 \\ Bo + \frac{2x_c Nu_L}{Re_L Pr_L}, x_c \geq 0 \end{cases}$ where $D_* = 10(\frac{D_*}{0.004})^{0.5}$ $Nu_L = \frac{(\frac{f}{2})Re_D Pr_L}{1.07 + 12.7(\frac{f}{2})^{0.5}(Pr_L^{\frac{2}{3}} - 1)}$ $f = [1.58 \ln(Re_L) - 3.28]^{-2}$
(Chen et al., 2017)	$q_c = \frac{[1 - 0.00216(GH_{VL})^{0.25}](1 - x_c)GD_h H_{VL}}{4L}$
(Becker et al., 1972)	$q_c = \frac{G(450 + \Delta H_{in})}{40\frac{L}{D_h} + 156G^{0.45}}[1.02 - (\frac{P}{P_r} - 0.54)^2]$
(Hall and Mudawar, 2000)	$Bo = 0.0722 We_L^{-0.312}(\frac{\rho_L}{\rho_V})^{-0.644}[1 - 0.9(\frac{\rho_L}{\rho_V})^{0.724} x_c]$
(Lombardi, 1995)	$q_c = \frac{G\Delta H_{in}}{4[\frac{L}{D_h} + 2(\frac{0.5G^2}{\rho_L})^{0.5} D_h^{0.4}]}$
2006 CHF LUT (Groeneveld et al., 2007) (Katto, 1992)	Look-up table, see reference (Groeneveld et al., 2007) Sublayer dryout model, see reference (Katto, 1992)
(Kariya et al., 2013)	$Bo = \begin{cases} Bo_{F1}, Bo_{F1} > Bo_{F2} \\ Bo_{D2}, Bo_{F1} \leq Bo_{F2} \text{ and } Bo_{F2} \geq Bo_{D1} \text{ and } Bo_{F2} \geq Bo_{D2} \\ Bo_{F2}, Bo_{F1} \leq Bo_{F2} \text{ and } Bo_{F2} \geq Bo_{D1} \text{ and } Bo_{F2} < Bo_{D2} \\ Bo_{D2}, Bo_{F1} \leq Bo_{F2} \text{ and } Bo_{F2} < Bo_{D1} \text{ and } Bo_{D1} \geq Bo_{D2} \\ Bo_{D1}, Bo_{F1} \leq Bo_{F2} \text{ and } Bo_{F2} < Bo_{D1} \text{ and } Bo_{D1} < Bo_{D2} \end{cases}$ Where $Bo_{F1} \times 10^4 = \begin{cases} -10.6(x_c - 0.1), \text{ for R22 and R134A} \\ -18.1(x_c - 0.1), \text{ for water} \end{cases}$ $Bo_{F2} \times 10^4 = -5.43(\frac{\rho_L}{\rho_V})^{-0.47}(\frac{\rho_L \sigma}{G^2 D_h})^{0.082}(\frac{GD}{\mu_L})^{0.08} x_c + 5.17(\frac{\rho_L}{\rho_V})^{-1.87}(\frac{\rho_L \sigma}{G^2 D_h})^{0.35}(\frac{GD_h}{\mu_L})^{0.3}$

(Continued on following page)

TABLE 2 | (*Continued*) CHF prediction models for high-pressure condition.

References	CHF model
	$Bo_{D1} \times 10^4 = -1.62x_c + 5.13\left(\frac{\rho_L}{\rho_V}\right)^{-0.64}\left(\frac{\rho_L \sigma}{G^2 D_h}\right)^{0.39}\left(\frac{GD_h}{\mu_L}\right)^{0.36}$
	$Bo_{D2} \times 10^4 = 4.74\left(\frac{\rho_L}{\rho_V}\right)^{0.83} x_c \left(\frac{1}{x_c} - 1\right)^{2.5}$
(Vijayarangan et al., 2006)	$Bo = 0.0051\left(\frac{\rho_L}{\rho_V}\right)^{-0.133}\left(\frac{\rho_L \sigma}{G^2 L}\right)^{1/3} \times \left(\frac{1}{1+0.0031\frac{L}{D_h}}\right) P_r^{0.147} Re_L^{0.25}$
(Mohammed Shah, 1987)	$Bo = F_E \cdot F_x \cdot Bo_0$
	Where
	$F_E = \max(1.54 - 0.032\frac{L_c}{D_h}, 1)$
	$Bo_0 = \max(15Y^{-0.612}, 0.082Y^{-0.3}(1 + 1.45P_r^{4.03}), 0.0024Y^{-0.105}(1 + 1.15P_r^{3.39}))$
	$Y = G^{1.8} D_h^{0.6}\left(\frac{c_p}{\lambda_L \rho_L^{0.8} g^{0.4}}\right)\left(\frac{\mu_L}{\mu_V}\right)^{0.6}$
	$\begin{cases} x_c \le 0, F_x = F_3\left[1 + \frac{(F_3^{-0.29} - 1)(P_r - 0.6)}{0.35}\right]^c \\ x_c > 0, F_x = F_1\left[1 - \frac{(1 - F_2)(P_r - 0.6)}{0.35}\right]^b \end{cases}$
	$c = \begin{cases} 0, P_r \le 0.6 \\ 1, P_r > 0.6 \end{cases}$
	$F_3 = (1.25 \times \frac{10^5}{Y})^{0.833 x_c}$
	$b = \begin{cases} 0, P_r \le 0.6 \\ 1, P_r > 0.6 \end{cases}$
	$F_1 = \begin{cases} 1 + 0.0052(-x_c^{0.88})Y^{0.41}, Y \le 1.4 \times 10^7 \\ 1 + 0.0052(-x_c^{0.88})(1.4 \times 10^7)^{0.41}, Y > 1.4 \times 10^7 \end{cases}$
	$F_2 = \begin{cases} F_1^{-0.42}, F_1 \le 4 \\ 0.55, F_1 > 4 \end{cases}$

Applied to high-pressure CHF databank for water as listed in **Table 1**, the mean error and RMS error of CHF prediction models are summarized in **Table 4**. As exhibited, mean error of Levitan correlation (Levitan and Lantsman, 1975), Chernobai correlation (Chernobai, 1980), Becker correlation (Becker et al., 1972), Vijayarangan correlation (Vijayarangan et al., 2006), and Shah correlation (Mohammed Shah, 1987) are above ±50%. Although only applied to 414 subcooled data points, the RMS error of Hall correlation (Hall and Mudawar, 2000) and Katto's sublayer dryout model (Katto, 1992) is still up to 42.4% and 89.1%, respectively. The Song correlation (Song et al., 2021a) proposed by the author obtains mean error of 2% and RMS error of 37.4%, which seems better than other prediction models.

Since some prediction models in **Table 2** developed from water experiments are not dimensionless, they could not be applied to non-aqueous fluids. Thereby, **Table 4** only gives prediction accuracy of dimensionless models when compared with experiments using non-aqueous fluids (R12, CO_2, or helium) as coolant. It is indicated that when applied to different fluids, the prediction capability of CHF prediction model is also different. In general, RMS error of Miropol'skii correlation (Miropol'skii and Shitsman, 1962), Vijayarangan correlation (Vijayarangan et al., 2006), and Shah correlation (Mohammed Shah, 1987) exceeds 50%. When applied to 356 subcooled experimental data points for R12, Hall correlation (Hall and Mudawar, 2000) and Katto's sublayer dryout model (Katto, 1992) obtain RMS error of 23.6% and 31.9%, respectively. Besides, Katto's sublayer dryout model (Katto, 1992) gives a good prediction to subcooled CO_2 experiments with mean error of 0.2% and RMS error of 37.6%.

Furthermore, the prediction capability of these eight dimensionless models is evaluated with experiments carried out with four different fluids (water, R12, CO_2, and helium) together. The variations in error parameters versus the reduced pressure are shown in **Figure 4**. Besides, the mean error and RMS error in different ranges of reduced pressure are displayed in **Figure 5**. Apparent systematic deviation of Miropol'skii correlation (Miropol'skii and Shitsman, 1962), Lombardi correlation (Lombardi, 1995), Katto's sublayer dryout model (Katto, 1992), Kariya correlation (Kariya et al., 2013), Vijayarangan correlation (Vijayarangan et al., 2006), and Shah correlation (Mohammed Shah, 1987) can be observed.

TABLE 3 | Validity range of high-pressure CHF prediction models.

CHF model	–	Reduced pressure	Mass flux, kg/(m^2·s)	Diameter, mm	Critical quality
(Song et al., 2021a)	Min	0.7	156	1.9	−1.768
	Max	0.97	6,907	24.7	0.955
(Miropol'skii and Shitsman, 1962)	Min	0.155	400	4.0	-0.5
	Max	0.889	10,000	8.0	0.8
(Levitan and Lantsman, 1975)	Min	0.133	750	4.0	0.0
	Max	0.889	5,000	16.0	0.5
(Chernobai, 1980)	Min	0.227	400	0.4	−1.75
	Max	0.888	30,000	37.0	0.7
(Chen et al., 2017)	Min	0.389	1,157	8.2	−0.97
	Max	0.943	3,776	–	0.53
(Becker et al., 1972)	Min	0.45	156	10.0	−0.3
	Max	0.906	7,560	–	0.6
(Hall and Mudawar, 2000)	Min	0.004	340	0.25	−1.0
	Max	0.906	30,000	15.0	0.0
(Lombardi, 1995)	Min	0.005	100	0.3	13.0
	Max	0.974	9,000	37.5	338.0
2006 CHF LUT (Groeneveld et al., 2007)	Min	0.004	0	8.0	−0.5
	Max	0.952	8,000	8.0	0.9
(Katto, 1992)	Min	0.004	350	2.5	0.0
	Max	0.906	40,600	11.07	117.5
(Kariya et al., 2013)	Min	0.961	400	4.4	N/A
	Max	0.992	1,000	4.4	
(Vijayarangan et al., 2006)	Min	0.24	200	12.7	017
	Max	0.99	2000	12.7	0.94
(Mohammed Shah, 1987)	Min	0.0014	3.9	0.315	−2.6
	Max	0.96	29,051	37.5	1.0

TABLE 4 | Predictive capability of CHF models for water experiments.

CHF model	H_2O			R12			CO_2			Helium			Total		
	μ	RMS	*n*	μ	RMS	*n*	μ	RMS	*n*	μ	RMS	*n*	μ	RMS	*n*
(Song et al., 2021a)	0.020	0.373	1,484	−0.020	0.333	1,140	0.068	0.304	28	−0.156	0.284	43	0.001	0.355	2,695
(Miropol'skii and Shitsman, 1962)	0.206	0.736	1,484	−0.440	0.476	1,140	0.332	0.743	28	−0.725	0.732	43	−0.081	0.639	2,659
(Levitan and Lantsman, 1975)	0.548	3.223	1,484	–	–	–	–	–	—	–	–	–	–	–	–
(Chernobai, 1980)	0.958	2.069	1,484	–	–	–	–	–	–	–	–	–	–	–	–
(Chen et al., 2017)	−0.380	0.706	1,254	–	–	–	–	—	–	–	–	–	–	–	–
(Becker et al., 1972)	−0.952	0.953	1,188	–	–	–	–	–	–	–	–	–	–	–	–
(Hall and Mudawar, 2000)	0.133	0.424	414	−0.162	0.236	356	0.785	0.886	9	0.150	0.218	11	0.008	0.359	790
(Lombardi, 1995)	−0.125	0.881	1,188	−0.349	0.487	1,140	−0.607	0.620	28	−0.227	0.496	32	−0.239	0.712	2,388
2006 CHF LUT (Groeneveld et al., 2007)	0.116	0.537	1,387	–	–	–	–	–	–	–	–	–	–	–	–
(Katto, 1992)	0.225	0.891	414	0.113	0.319	356	0.002	0.376	9	0.217	0.282	11	0.171	0.682	790
(Kariya et al., 2013)	0.148	0.960	1,484	0.434	0.879	1,140	0.093	0.304	28	−0.598	0.640	43	0.257	0.918	2,695
(Vijayarangan et al., 2006)	−0.593	0.793	1,316	−0.674	0.686	1,140	−0.765	0.767	28	−0.551	0.563	43	−0.630	0.743	2,527
(Mohammed Shah, 1987)	1.181	2.020	1,316	0.368	1.169	1,140	1.277	1.526	28	6.376	10.199	43	0.904	2.130	2,527

As discussed above, with respect to general prediction accuracy and predictive capability under different pressures, the Song correlation (Song et al., 2021a) will be recommended, since it shows the best prediction accuracy for different fluids and performs good at different pressure conditions even when reduced pressure is up to 0.974.

In addition, since conditions of low mass flux achieves more interest in safety analysis, the performance of Song correlation (Song et al., 2021a) at different mass flux conditions gets evaluated. As **Figure 6** shows, it is demonstrated that there is no apparent systematic error at low mass flux conditions. Therefore, the CHF prediction model proposed by Song et al. (2021a) can be applied to safety analysis.

Effect of Pressure on CHF

As shown in **Figure 7**, the discrete dots are experimental results, while the solid lines stand for the corresponding calculation results with the Song correlation (Song et al., 2021a). **Figure 7A** is the comparison of CHF for pressure at 16.0 and 20.0 MPa, with mass flux at 1,000 kg/(m^2·s) and tube diameter at 10 mm. **Figure 7B** shows the results with constant mass flux at 1,500 kg/(m^2·s) and tube diameter at 10 mm, while the pressures

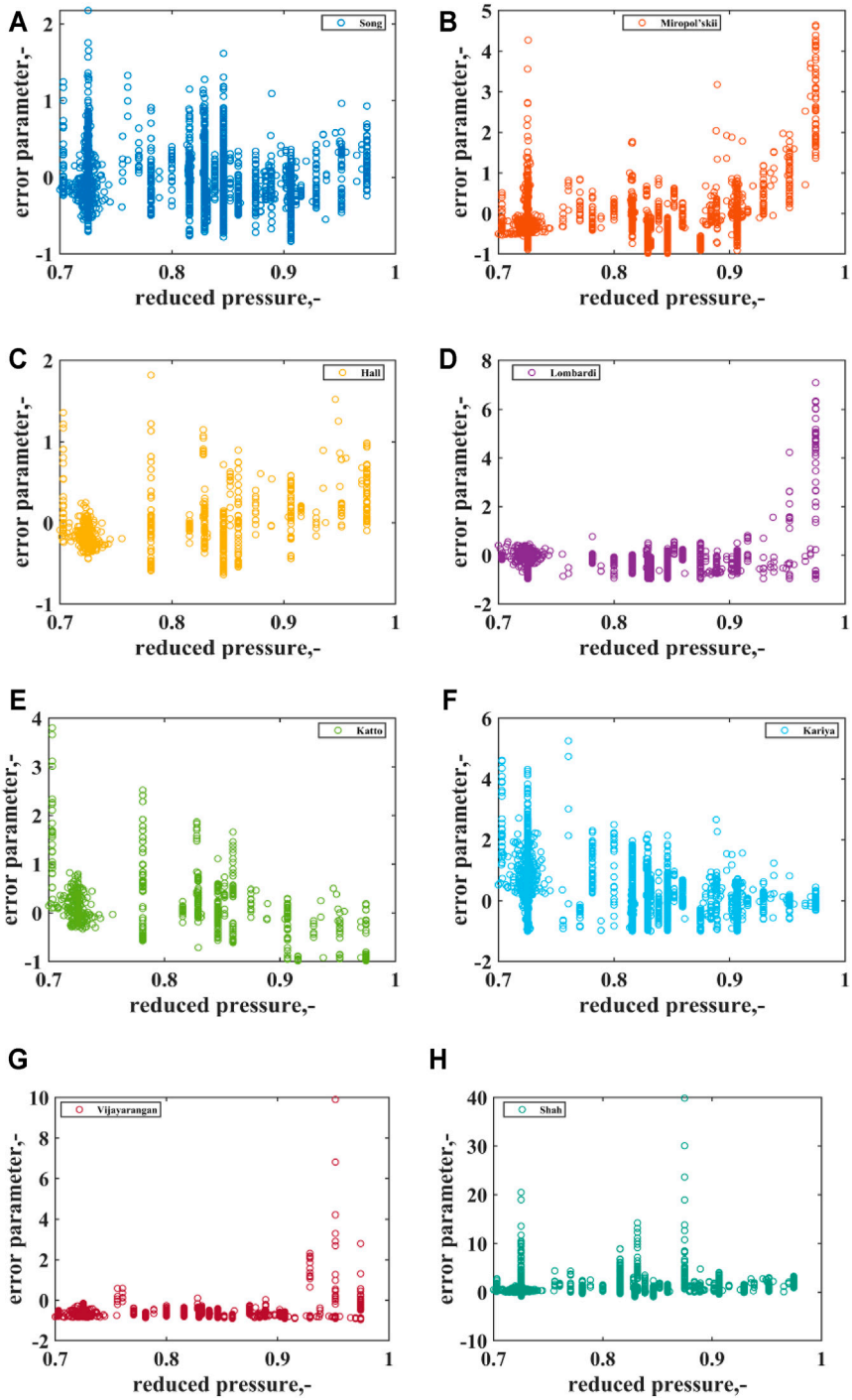

FIGURE 4 | Distribution of error parameters versus reduced pressure. **(A)** Song correlation (Song et al., 2021a). **(B)** Miropol'skii correlation (Miropol'skii and Shitsman, 1962). **(C)** Hall correlation (Hall and Mudawar, 2000). **(D)** Lombardi correlation (Lombardi, 1995). **(E)** Katto's sublayer dryout model (Katto, 1992). **(F)** Kariya correlation Kariya et al., 2013). **(G)** Vijayarangan correlation (Vijayarangan et al., 2006). **(H)** Shah correlation (Vijayarangan et al., 2006).

are at 16, 18.5, and 21.5 MPa, respectively. Obviously, the higher pressure results in a lower CHF. As shown by **Figure 2**, the increase in pressure leads to a reduction in evaporation heat, which promotes the vaporization process. Thereby, the heat flux leading to dryout of liquid sublayer [DNB-type boiling crisis, if considering the sublayer dryout model (Lee and Mudawwar, 1988; Katto, 1990; Celata et al., 1994; Liu et al., 2000)] or liquid film (dryout-type boiling crisis) will decrease. Hence, the value of CHF both for DNB and dryout drops when the pressure increases.

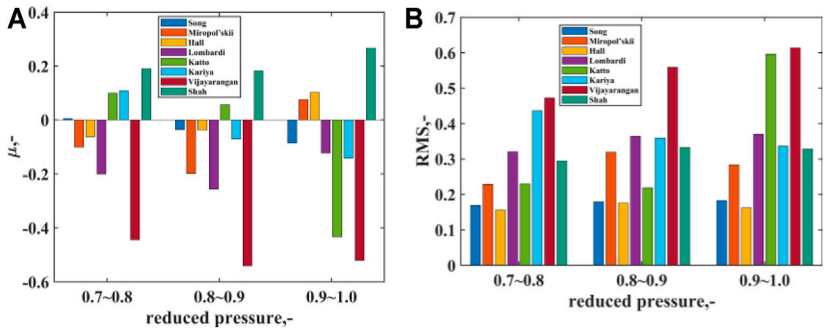

FIGURE 5 | Mean error and RMS error in different reduced pressure ranges. **(A)** Mean error. **(B)** RMS.

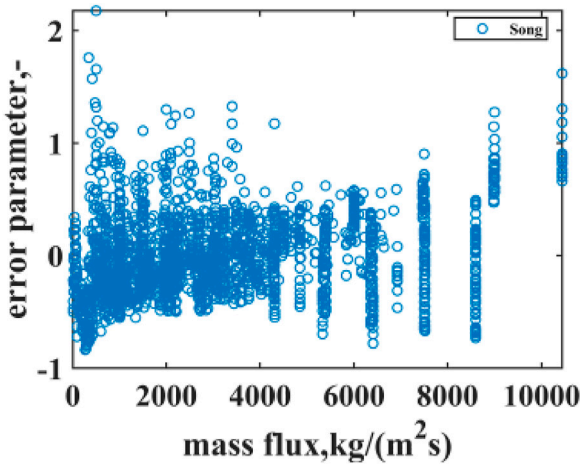

FIGURE 6 | Prediction accuracy of Song correlation (Song et al., 2021a) varied with mass flux.

ASSESSMENT OF POST-CHF HEAT TRANSFER PREDICTION METHODS FOR HIGH-PRESSURE CONDITION

As discussed before, post-CHF heat transfer will be encountered after the occurrence of boiling crisis. In this region, due to loss of cooling through continuous liquid phase, the heated wall may undergo drastic temperature increase.

After the boiling crisis takes place, the post-CHF heat transfer is initiated subsequently. As mentioned in the last section, for flow convection, the DNB-type boiling crisis, associated with subcooled and low-quality condition, leads to the inverted annular flow in the downstream. While for the dryout-type boiling crisis related to higher quality, the dispersed droplet flow is encountered after the dryout of the liquid film. Since different flow patterns would result in different heat transfer characteristics, in addition, post-DNB and post-dryout (PDO) are termed, and their heat transfer will be discussed, respectively.

Post-DNB Heat Transfer

Concerning post-DNB, the heat transfer in the inverted annular flow regime is of interest. Since the heated wall is covered by continuous vapor blanket and the liquid core is in the tube center with dispersed vapor bubbles, the following three significant heat transfer processes are taken into account:

1) convective heat transfer from the wall to the vapor blanket;
2) radiation heat transfer from the wall to the liquid core; and
3) heat transfer from vapor blanket to the liquid core at the vapor–liquid interface.

Post-Dryout Heat Transfer

As **Figure 3B** shows, after the disappearance of the annular liquid film, in the post-dryout regime, the saturated droplets disperse in the vapor bulk. Among the droplets, the vapor phase and the heating wall, the main heat transfer mechanisms are as follows:

1) convective heat transfer from the wall to the vapor $q_{c,w-V}$;
2) convective heat transfer from the wall to the droplets $q_{c,w-d}$;
3) heat transfer from the vapor to the droplets at the vapor–liquid interface $q_{c,V-d}$; and
4) radiation heat transfer from the wall to vapor $q_{r,w-V}$, from the wall to droplets $q_{r,w-d}$, and from vapor to droplet $q_{r,V-d}$.

As reviewed by Hammouda (1996), Nakla et al. (2011), Groeneveld (1993), etc., due to the high CHF value, the large temperature rise in the inverted annular regime would lead to the burnout of the heated surface easily. Thereby, it is nearly impossible to perform related heat transfer experiments with a heat-flux controlled water–steam system. The invention of the "hot-patch" technique makes it feasible to obtain inverted annular flow heat transfer measurements. However, as a result of the complicated experiment design, the range of available experiments is very limited so far (Groeneveld, 1993). Hence, research about post-DNB heat transfer in inverted annular flow regime is not as common as PDO. As a result, research in this region has focused more on avoiding the occurrence of boiling crisis. As reviewed by Nakla et al. (2011) and Liu and Sun (2020), the existing measurement with water for inverted annular heat transfer is only up to 9 MPa (reduced pressure at 0.4), from the experiment performed by Stewart and Groeneveld (1982). Even though taking scaling fluids (e.g., R12 and R134a) into consideration, the maximum pressure is 2.39 MPa with R134a (13 MPa for water at the same reduced pressure 0.59) from the

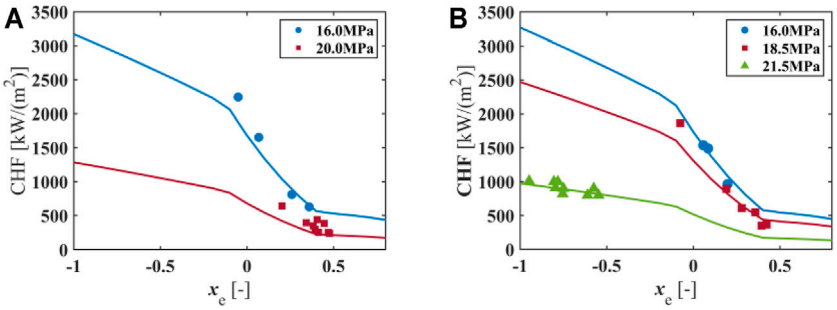

FIGURE 7 | Variation in CHF with quality at different pressures for water. **(A)** G = 1,000 kg/(m^2·s), D = 10 mm. **(B)** G = 1,500 kg/(m^2·s), D = 10 mm.

TABLE 5 | Parameter ranges of high-pressure post-CHF heat transfer experiments.

Coolant	–	P (MPa)	P_r [-]	G [kg/(m^2·s)]	D_h (mm)	q (kW/m^2)	x_e(-)]
Water	Min	15.92	0.722	497.8	2.5	147.0	0.001
	Max	21.51	0.975	3,500.0	24.7	1923.0	0.999
CO_2	Min	6.49	0.88	497	8	59.8	0.003
	Max	7.01	0.95	1991	8	225.2	0.965

experiment carried out by Nakla et al. (2011). Due to shortage of experiments, a prediction approach for the high-pressure post-DNB heat transfer is missing. Thereby, further discussion about post-DNB heat transfer in the high-pressure region could not be carried out. The present work will only focus on the evaluation of post-dryout heat transfer models.

Post-Dryout Heat Transfer Databank for High-Pressure Condition

As summarized in **Table 5**, an experiment databank of post-CHF heat transfer for high-pressure condition ($P/P_c > 0.7$) is compiled from the literature (Swenson et al., 1962; Bishop et al., 1964; Herkenrath, 1967; Becker, 1983; Eter et al., 2017). These experiments were carried out in uniformly heated round tubes with water or CO_2 as coolant. The water database covers the range of reduced pressure from 0.722 to 0.975 and contains 5,391 data points. For the CO_2 database, which is made up of 497 data points, the reduced pressure ranges from 0.88 to 0.95.

Existing Post-Dryout Heat Transfer Model for High-Pressure Condition

Concerning post-dryout heat transfer, some prediction approaches with reduced pressure above 0.7 for water in uniformly heated tubes are collected and summarized in **Table 6**. These correlations are developed from water experiments carried out in vertical round tubes. The Groeneveld-3 correlation (Groeneveld and Delorme, 1976) developed by Groeneveld and Delorme (1976) includes an extra correlation to calculate the actual quality. The 2003 FB LUT (Groeneveld et al., 2003) is a look-up table giving post-CHF heat transfer coefficient as a function of pressure, mass flux, quality, and wall temperature.

The validity range of these post-dryout heat transfer correlations can be found in **Table 7**. Some of these correlations are only validated for the high-pressure condition, e.g., the Herkenrath correlation (Herkenrath, 1967) with pressure range from 17 to 21.5 MPa, Bishop-3 correlation (Bishop et al., 1964) with pressure range from 16.8 to 21.9 MPa, and the Swenson correlation (Swenson et al., 1962) only for pressure at 20.68 MPa.

Assessment of Existing Post-Dryout Heat Transfer Prediction Models

By comparing heat transfer models as shown in **Table 6** with the experimental databank listed in **Table 5**, the error parameter of every data point will be computed by,

$$\varepsilon_i = \frac{h_{c,cal}(i) - h_{c,m}(i)}{h_{c,m}(i)} \tag{4}$$

Furthermore, the mean error and RMS error of each prediction model could be evaluated with **Eqs. 2**, **3**, respectively.

Accordingly, error information of these post-dryout heat transfer models are exhibited in **Table 8**. When applied to high-pressure water database, the Song correlation (Song et al., 2021b) obtains mean error of 2.3% and RMS error of 17.6%, respectively. The mean error of Bishop-1 correlation (Bishop et al., 1964) is 1.6%, and the RMS error is 23.8%. Miropol'skii correlation (Miropol'skii, 1963) and Swenson correlation (Swenson et al., 1962) achieve mean error above 40%. Regarding experiments with CO_2 as coolant, since Herkenrath correlation (Herkenrath, 1967) and Slaughterbeck correlation (Slaughterbeck et al., 1973) are not dimensionless, and the 2003 FB LUT (Groeneveld et al., 2003) cannot be utilized to nonaqueous fluids without scaling, their error information for CO_2 experiments is not displayed in

TABLE 6 | Prediction models of post-CHF heat transfer for high-pressure condition.

References	Correlations
Song (Song et al., 2021b)	$h = \frac{\lambda_V}{D_h} \cdot F_1 \cdot F_2 \cdot F_3 \cdot (0.023 Re_{TP}^{0.8} Pr_w^{0.4})$ with $F_1 = 8.346 \times 10^{-03} Re_{TP}^{0.319}$ $F_2 = \max(0.795 Pr_W^{-1.752}, 0.809 Pr_W^{1.287})$ $F_3 = \begin{cases} 0.715(1-x_e)^{-0.678}, x_e < 0.4 \\ 1.0,\ x_e \geq 0.4 \end{cases}$ $Re_{TP} = \frac{GD_h}{\mu_V}[x_m + \frac{\mu_V}{\mu_L}(1-x_m)]$
Bishop-1 (Bishop et al., 1964)	$h = 0.0193 \frac{\lambda_f}{D_h} Re_f^{0.8} Pr_f^{1.23} (\frac{\rho_V}{\rho_L})^{0.068} [x_m + \frac{\rho_V}{\rho_L}(1-x_m)]^{0.68}$
Bishop-2 (Bishop et al., 1964)	$h = 0.033 \frac{\lambda_f}{D_h} Re_w^{0.8} Pr_w^{1.25} (\frac{\rho_V}{\rho_L})^{0.197} [x_m + \frac{\rho_V}{\rho_L}(1-x_m)]^{0.738}$
Bishop-3 (Bishop et al., 1964)	$h = 0.098 \frac{\lambda_w}{D_h} [Re_w (\frac{\rho_w}{\rho_V})(x_m + \frac{\rho_V}{\rho_L}(1-x_m))]^{0.8} Pr_w^{0.83} (\frac{\rho_V}{\rho_L})^{0.5}$
Miropol'skii (Miropol'skii, 1963)	$h = 0.023 \frac{\lambda_V}{D_h} [Re_V (x_m + \frac{\rho_V}{\rho_L}(1-x_m))]^{0.8} Pr_w^{0.8} Y$ with
Swenson (Swenson et al., 1962)	$Y = 1 - 0.1(\frac{\rho_L}{\rho_V} - 1)^{0.4}(1-x_m)^{0.4}$
Groeneveld-1 (Groeneveld, 1975)	$h = 0.076 \frac{\lambda_w}{D_h} [Re_w (\frac{\rho_w}{\rho_V})(x_m + \frac{\rho_V}{\rho_L}(1-x_m))]^{0.8} Pr_w^{0.4}$
Groeneveld-2 (Groeneveld, 1975)	$h = 0.00109 \frac{\lambda_V}{D_h} [Re_V (x_m + \frac{\rho_V}{\rho_L}(1-x_m))]^{0.989} Pr_w^{1.41} Y^{-1.15}$ $h = 0.00327 \frac{\lambda_V}{D_h} [Re_V (x_m + \frac{\rho_V}{\rho_L}(1-x_m))]^{0.901} Pr_w^{1.32} Y^{-1.5}$ $Y = 1 - 0.1(\frac{\rho_L}{\rho_V} - 1)^{0.4}(1-x_m)^{0.4}$
Groeneveld-3 (Groeneveld and Delorme, 1976)	$h = 0.008348 \frac{\lambda_f}{D_h} [Re_f (x_a + \frac{\rho_V}{\rho_L}(1-x_a))]^{0.8774} Pr_f^{0.6112}$, with, $x_a = \frac{x_e H_{VL}}{H_{V,a} - H_L}$, $\frac{H_{V,a} - H_{V,e}}{H_{VL}} = \exp(-\tan\psi)\exp[-(3\alpha)^{-4}]$, $\psi = 0.13864 Pr_V^{0.2031} (\frac{GD_h x_m}{\mu_V \alpha})^{0.20006} (\frac{qD_h c_{p,V}}{\lambda_V H_{VL}})^{-0.09232} \cdot (1.3072 - 1.0833 x_e + 0.8455 x_e^2)$, $\begin{cases} x_m = 0, x_e < 0 \\ x_m = x_e, 0 \leq x_e \leq 1 \\ x_m = 1, x_e > 1 \end{cases}$, $\alpha = \frac{x_m}{x_m + \frac{\rho_V}{\rho_L}(1-x_m)}$
Herkenrath (Herkenrath, 1967)	$h = 0.06 \frac{\lambda_w}{D_h} [Re_w (\frac{\rho_w}{\rho_V})(x_m + \frac{\rho_V}{\rho_L}(1-x_m))]^{0.8} Pr_w^{0.8} (\frac{G}{G_0})^{0.4} (\frac{P}{P_c})^{2.7}$
Slaughterbeck (Slaughterbeck et al., 1973)	$h = 0.0001604 \frac{\lambda_V}{D_h} [Re_V (x_m + \frac{\rho_V}{\rho_L}(1-x_m))]^{0.838} Pr_w^{1.81} (q \times 0.317)^{0.278} (\frac{\lambda_V}{\lambda_c})^{-0.508}$ $G_0 = 1000\ \mathrm{kg/(m^2 \cdot s)}$
2003 FB LUT (Groeneveld et al., 2003)	Look-up table, see reference (Groeneveld et al., 2003)

1. $\begin{cases} x_m = 0, x_e < 0 \\ x_m = x_e, 0 \leq x_e \leq 1 \\ x_m = 1, x_e > 1 \end{cases}$

2. Properties with the subscript "V," "L," and "w," stand for saturated vapor properties, saturated liquid phase properties, and vapor properties evaluated at wall temperature, respectively. Properties with the subscript "f" are evaluated at the average temperature of the saturation temperature and the wall temperature.

TABLE 7 | Validity range of post-CHF heat transfer models.

Author	P (MPa)		G [kg/(m^2·s)]		x_e(-)		Dh (mm)	
	Min	Max	Min	Max	Min	Max	Min	Max
Song (Song et al., 2021b)	2.98	21.51	469.3	3,500	0.001	0.999	2.5	24.7
Bishop-1 (Bishop et al., 1964)	4.08	21.9	700	3,400	0.07	1.0	N/A	–
Bishop-2 (Bishop et al., 1964)	4.08	21.9	700	3,400	0.07	1.0	N/A	–
Bishop-3 (Bishop et al., 1964)	16.8	21.9	1,350	3,400	0.1	1.0	N/A	–
Miropol'skii (Miropol'skii, 1963)	4.05	22	700	2000	0.06	1.0	8	24
Swenson (Swenson et al., 1962)	20.68	20.68	949.4	1,356.2	0.08	0.98	10.4	10.4
Groeneveld-1 (Groeneveld, 1975)	6.88	21.5	700	5,300	0.1	0.9	1.5	25.0
Groeneveld-2 (Groeneveld, 1975)	3.4	21.5	700	5,300	0.1	0.9	1.5	25.0
Groeneveld-3 (Groeneveld and Delorme, 1976)	0.69	21.5	130	5,200	-0.12	3.09	2.54	12.8
Herkenrath (Herkenrath, 1967)	17	21.5	700	3,500	0.1	1.0	5	20
Slaughterbeck (Slaughterbeck et al., 1973)	6.8	20	1,050	5,300	0.0	1.0	13.4	17.0
2003 FB LUT (Groeneveld et al., 2003)	0.1	20	0	7,000	-0.2	2.0	8	8

TABLE 8 | Predictive capability of post-CHF prediction models.

References	Water			CO_2			Total		
	μ	RMS	*n*	μ	RMS	*n*	μ	RMS	*n*
Song (Song et al., 2021b)	0.023	0.176	5,391	–0.079	0.289	497	0.023	0.176	5,391
Bishop-1 (Bishop et al., 1964)	0.016	0.238	5,391	0.130	0.230	497	0.016	0.238	5,391
Bishop-2 (Bishop et al., 1964)	0.100	0.267	5,391	0.268	0.341	497	0.100	0.267	5,391
Bishop-3 (Bishop et al., 1964)	0.065	0.250	5,391	0.464	0.520	497	0.065	0.250	5,391
Miropol'skii (Miropol'skii, 1963)	0.487	0.742	5,391	1.035	1.117	497	0.487	0.742	5,391
Swenson (Swenson et al., 1962)	0.432	0.642	5,391	0.954	1.020	497	0.432	0.642	5,391
Groeneveld-1 (Groeneveld, 1975)	0.243	0.370	5,391	0.059	0.216	497	0.243	0.370	5,391
Groeneveld-2 (Groeneveld, 1975)	0.193	0.371	5,391	0.159	0.275	497	0.193	0.371	5,391
Groeneveld-3 (Groeneveld and Delorme, 1976)	–0.061	0.316	5,391	0.132	0.283	497	–0.061	0.316	5,391
Herkenrath (Herkenrath, 1967)	–0.097	0.183	5,391	–	–	–	–	–	–
Slaughterbeck (Slaughterbeck et al., 1973)	–0.205	0.252	5,391	–	–	–	–	–	–
2003 FB LUT (Groeneveld et al., 2003)	–0.151	0.256	5,391	–	–	–	–	–	–

Table 8. Additionally, the mean error and RMS error of Groeneveld-1 correlation (Groeneveld, 1975) is 5.9% and 21.6%, respectively.

More details about the distribution of error parameters could be found in **Figure 8**, which displays prediction results of both water and CO_2 experiments together. Generally, extreme prediction deviation is not observed in Song correlation (Song et al., 2021b), Bishop-1 correlation (Bishop et al., 1964), Bishop-2 correlation (Bishop et al., 1964), Bishop-3 correlation (Bishop et al., 1964), and Groeneveld-3 correlation (Groeneveld and Delorme, 1976), of which the error parameters are distributed within −0.5 and 1.0. However, in contrast, for example, the error parameter of the Miropol'skii correlation (Miropol'skii, 1963) could even reach up to nearly 500% at a reduced pressure of approximately 0.95. Besides, the distribution of mean error and RMS error at different pressure ranges is exhibited in **Figure 9**. It can be seen that mean error and RMS error of the Groeneveld-3 correlation (Groeneveld and Delorme, 1976) become higher while the reduced pressure is above 0.9.

Considering the value of mean error and RMS error listed in **Table 8** and the distribution of error information shown in **Figures 8**, **9** together, Song correlation (Song et al., 2021b) and Bishop-1 correlation (Bishop et al., 1964) are the best for the prediction of post-dryout heat transfer in the high-pressure condition. Even when pressure is near to the critical point with reduced pressure at 0.975, both of these two correlations can give good prediction accuracy.

Besides, the error parameter at different mass flux condition is shown in **Figure 10**. As illustrated, there is no systematic prediction error of Song correlation (Song et al., 2021b). However, the value of error parameter given by Bishop-1 correlation (Bishop et al., 1964) tends to reduce as the mass flux increases. Hence, only Song correlation (Song et al., 2021b) will be recommended for safety analysis.

Effect of Pressure on PDO Heat Transfer

A comparison of PDO heat transfer under different pressure conditions could be found in **Figure 11**. The parameters for selected test cases are summarized in **Table 9**. **Figure 11A** shows the variation of heat transfer coefficient versus the equilibrium quality, when the pressure increases from 16 to 20 MPa for water experiments. **Figure 11B** compares the PDO heat transfer for

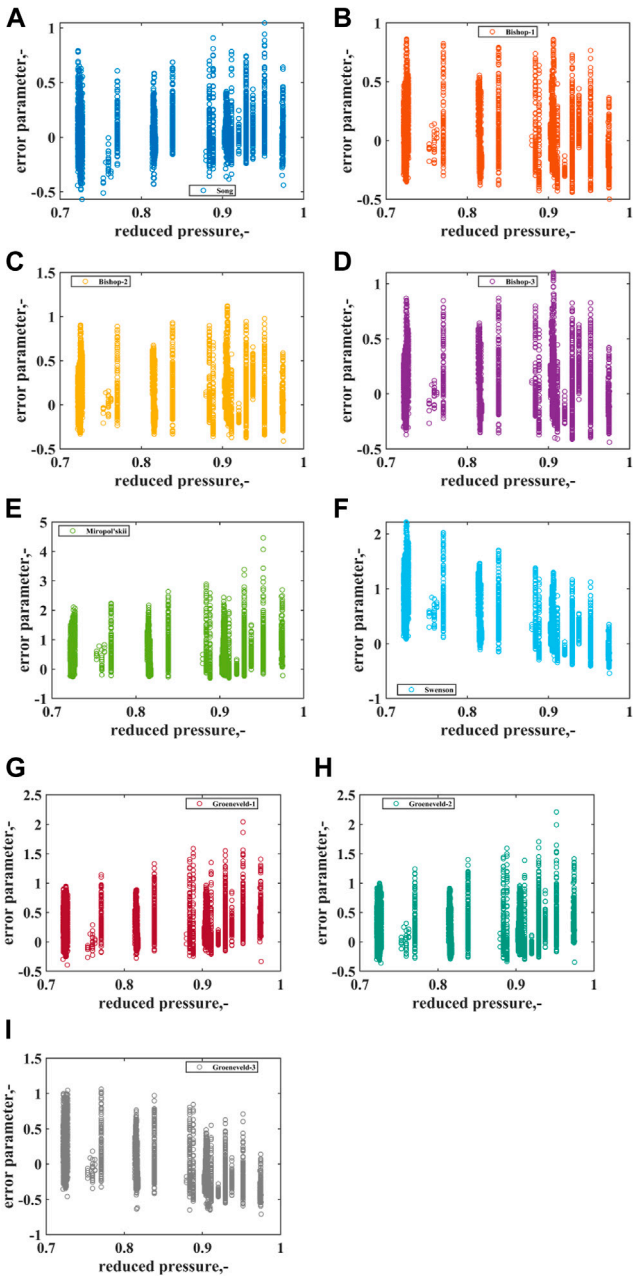

FIGURE 8 | Distribution of error parameters versus reduced pressure for different post-dryout correlation. **(A)** Song correlation (Song et al., 2021b). **(B)** Bishop-1 correlation (Bishop et al., 1964). **(C)** Bishop-2 correlation (Bishop et al., 1964). **(D)** Bishop-3 correlation (Bishop et al., 1964). **(E)** Miropol'skii correlation (Miropol'skii, 1963). **(F)** Swenson correlation (Swenson et al., 1962). **(G)** Groeneveld-1 correlation (Groeneveld, 1975). **(H)** Groeneveld-2 correlation (Groeneveld, 1975). **(I)** Groeneveld-3 correlation (Groeneveld and Delorme, 1976).

uniformly heated round tubes with CO_2 at pressure of 6.49 and 7.0 MPa, respectively. Moreover, the prediction results with Song correlation (Song et al., 2021b) for each test case are plotted in **Figure 11** as well. In general, the predicted heat transfer coefficient gets a good agreement with the experiment.

As observed, PDO heat transfer coefficient increases with increasing pressure. As the pressure increases, according to the research of Kataoka et al. (1983), the droplet diameter will be smaller with a lower surface tension; therefore, the number of droplets will increase, and the total interfacial area will be larger at the same equilibrium quality. It facilitates the interfacial heat transfer from the vapor phase to liquid droplets. In consequence, a better total heat transfer could be obtained at a higher pressure.

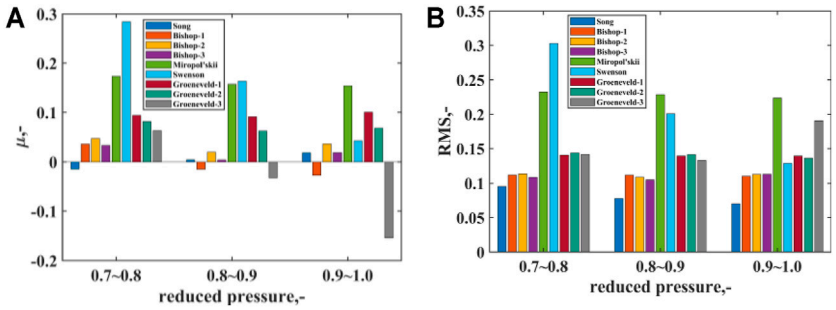

FIGURE 9 | Mean error and RMS error at different reduced pressure range. **(A)** Mean error. **(B)** RMS error.

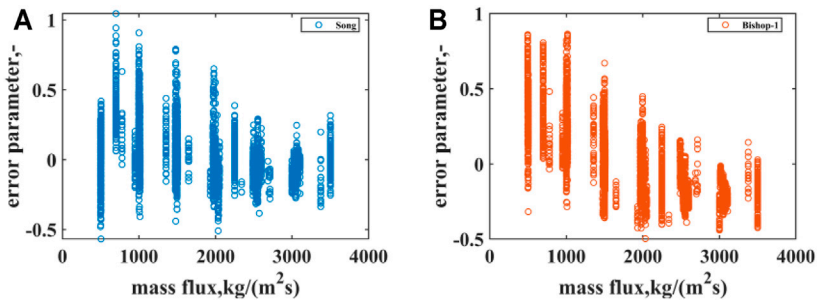

FIGURE 10 | Variation of error parameter with mass flux. **(A)** Song correlation (Song et al., 2021b). **(B)** Bishop-1 correlation (Bishop et al., 1964).

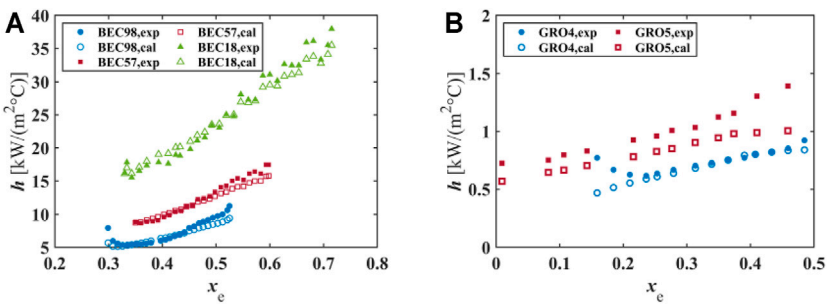

FIGURE 11 | Effect of pressure on PDO heat transfer. **(A)** Water experiments: G = 2000 kg/(m^2·s) , q = 600 kW/m^2. **(B)** CO_2 experiment: G = 703 kg/(m^2 s) , q = 79.9 kW/m^2

TABLE 9 | Test cases for PDO heat transfer under different pressure.

Case No	Fluid	P (MPa)	P_r (–)	G [kg/(m^2·s)]	D_h (mm)	q (kW/m^2)
BEC98	Water	15.99	0.72	1,970.10	14.9	608.0
BEC57	Water	17.99	0.82	1,974.40	14.9	608.0
BEC18	Water	19.92	0.90	1,979.50	14.9	603.0
GRO4	CO_2	6.49	0.88	703	8	79.9
GRO5	CO_2	7.00	0.95	703	8	79.9

SUMMARY

Supercritical power cycles may experience subcritical condition during some trans-critical transients. However, it is found that research about heat transfer in the high-pressure subcritical condition is still rare so far. Thereby, two significant heat transfer phenomena, i.e., boiling crisis and post-CHF heat transfer, are discussed in the present work. Existing prediction approaches of CHF and post-dryout heat transfer for high-pressure condition are collected and evaluated. In the present

work, prediction models of CHF and post-dryout heat transfer at the high-pressure condition are recommended for safety analysis.

Main achievements can be summarized as follows:

About CHF:

1) A databank of high-pressure CHF experiment with water, R12, CO_2, or helium as coolant are established containing 2,695 data points in total.
2) Thirteen prediction models for high-pressure condition are collected and assessed by comparing with the high-pressure CHF experimental databank. It is demonstrated that the CHF correlation developed by Song et al. (2021a) gives good prediction accuracy to different fluids at the high-pressure condition.
3) The value of CHF decreases as the pressure rises, which implies that boiling crisis occurs easier at a higher pressure.

About post-dryout heat transfer:

1) A post-dryout heat transfer experimental databank for high-pressure condition is compiled, including tests for water and CO_2 experiments and 5,888 data points.
2) By comparing prediction of 12 post-CHF heat transfer models with the high-pressure post-dryout heat transfer experimental databank, it can be concluded that Song correlation (Song et al., 2021b) obtains the best predictive capability.
3) With the increase in pressure, post-dryout heat transfer becomes better.

DATA AVAILABILITY STATEMENT

The original contributions presented in the study are included in the article/supplementary material. Further inquiries can be directed to the corresponding author.

AUTHOR CONTRIBUTIONS

MS: Simulation, Original draft; XL: Conceptualization, supervision.

ACKNOWLEDGMENTS

The authors would like to thank the German Federal Ministry for Economic Affairs and Energy (BMWi, MOPOW II Project, No. 1501544) for providing the financial support for this study.

REFERENCES

Ahn, Y., Bae, S. J., Kim, M., Cho, S. K., Baik, S., Lee, J. I., et al. (2015). Review of Supercritical CO2 Power Cycle Technology and Current Status of Research and Development. *Nucl. Eng. Tech.* 47 (6), 647–661. doi:10.1016/j.net.2015.06.009

Becker, K. M. (1983). *An Experimental Investigation of post Dryout Heat Transfer*. Stocholm, Sweden: KTH-NEL-33, Department of nuclear reactor engineering, Royal Institute of Technology.

Becker, K. M., Djursing, D., Lindberg, K., Eklind, O., and Österdahl, C. (1972). "Burnout Conditions for Round Tubes at Elevated Pressures," in *Proceedings of the International Symposium on Two-phase Systems*. Editors G. Hetsroni, S. Sideman, and J. P. Hartnett (Pergamon), 55–73. doi:10.1016/b978-0-08-017035-0.50009-4

Binotti, M., Astolfi, M., Campanari, S., Manzolini, G., and Silva, P. (2017). Preliminary Assessment of sCO2 Cycles for Power Generation in CSP Solar tower Plants. *Appl. Energ.* 204, 1007–1017. doi:10.1016/j.apenergy.2017.05.121

Bishop, A. A., Sandberg, R. O., and Tong, L. S. (1964). *Forced-convection Heat Transfer to Water at Near-Critical Temperatures and Supercritical pressures WCAP-5449*. United States: Westinghouse Electric Corporation.

Celata, G. P., Cumo, M., Mariani, A., Simoncini, M., and Zummo, G. (1994). Rationalization of Existing Mechanistic Models for the Prediction of Water Subcooled Flow Boiling Critical Heat Flux. *Int. J. Heat Mass Transfer* 37, 347–360. doi:10.1016/0017-9310(94)90035-3

Chen, Y., Zhao, M., Bi, K., Yang, B., Zhang, D., and Du, K. (2017). Critical Heat Flux of Flowing Water in Tube for Pressure up to Near Critical Point—Experiment and Prediction. *J. Nucl. Eng. Radiat. Sci.* 4 (1), 011006. doi:10.1115/1.4038215

Cheng, X., Yang, Y. H., and Liu, X. J. (2016). *Super-critical Water Cooled Reactor with Mixed Spectrum: Design and Key Technologies*. Shanghai: Shanghai Jiao Tong University Press.

Chernobai, V. (1980). Model for Heat-Transfer Crisis for Water Bolling in Pipes. *Teplofizika vysokikh temperatur* 18 (5), 1046–1050.

Crespi, F., Gavagnin, G., Sánchez, D., and Martínez, G. S. (2017). Supercritical Carbon Dioxide Cycles for Power Generation: A Review. *Appl. Energ.* 195, 152–183. doi:10.1016/j.apenergy.2017.02.048

Debenedetti, P. G. (1994). "Supercritical Fluids: Fundamentals and Applications," in *Developments in Food Engineering: Proceedings of the 6th International Congress on Engineering and Food*. Editors T. Yano, R. Matsuno, and K. Nakamura (Boston, MA: Springer US), 30–35. doi:10.1007/978-1-4615-2674-2_6

Dostal, V., Driscoll, M. J., Hejzlar, P., and Todreas, N. E. (2002). "A Supercritical CO_2 Gas Turbine Power Cycle for Next-Generation Nuclear Reactors," in 10th International Conference on Nuclear Engineering, Arlington, Virginia, USA, April 14–18, 2002 (ASME), 567–574.

Eggers, R. (2012). *Industrial High Pressure Applications: Processes, Equipment, and Safety*. John Wiley & Sons.

Eter, A., Groeneveld, D., and Tavoularis, S. (2017). Convective Heat Transfer at High Subcritical Pressures in Tubes with and without Flow Obstacles. *Nucl. Eng. Des.* 318, 1–23. doi:10.1016/j.nucengdes.2017.04.013

Frank, E. D., Sullivan, J. L., and Wang, M. Q. (2012). Life Cycle Analysis of Geothermal Power Generation with Supercritical Carbon Dioxide. *Environ. Res. Lett.* 7 (3), 034030. doi:10.1088/1748-9326/7/3/034030

Groeneveld, D. C. (1993). A Review of Inverted Annular and Low Quality Film Boiling. *Multiphase Sci. Tech.* 7 (1-4), 327–365. doi:10.1615/multscientechn.v7.i1-4.60

Groeneveld, D. C., and Delorme, G. G. J. (1976). Prediction of thermal Non-equilibrium in the post-dryout Regime. *Nucl. Eng. Des.* 36 (1), 17–26. doi:10.1016/0029-5493(76)90138-2

Groeneveld, D. C., Leung, L. K. H., Vasic', A. Z., Guo, Y. J., and Cheng, S. C. (2003). A Look-Up Table for Fully Developed Film-Boiling Heat Transfer. *Nucl. Eng. Des.* 225 (1), 83–97. doi:10.1016/s0029-5493(03)00149-3

Groeneveld, D. C. (1975). Post-dryout Heat Transfer: Physical Mechanisms and a Survey of Prediction Methods. *Nucl. Eng. Des.* 32 (3), 283–294. doi:10.1016/0029-5493(75)90099-0

Groeneveld, D., Shan, J., and Vasić, A. (2007). The 2006 CHF Look-Up Table. *Nucl. Eng. Des.* 237 (15-17), 1909–1922. doi:10.1016/j.nucengdes.2007.02.014

Hall, D. D., and Mudawar, I. (2000). Critical Heat Flux (CHF) for Water Flow in Tubes-II. *Int. J. Heat Mass Transfer* 43 (14), 2605–2640. doi:10.1016/s0017-9310(99)00192-1

Hammouda, N. (1996). *Subcooled film boiling in non-aqueous fluids*. Dissertation, Ottawa-Carleton Institute for Mechanical and Aeronautical Engineering, University of Ottawa.

Hejzlar, P., Dostal, V., and Driscoll, M. J. (2006). Assessment of Gas Cooled Fast Reactor with Indirect Supercritical CO_2 Cycle. *Nucl. Eng. Tech.* 38 (2), 109–118.

Herkenrath, H. (1967). *Heat Transfer in Water with Forced Circulation in the 140 to 250 Bar Pressure Range: Results of Investigations*. German: No. EUR-3658, Europ. Atomgemeinschaft-Euroatom.

IAEA (2001). *Thermohydraulic Relationships for Advanced Water Cooled Reactors*. Vienna, Austria: IAEA-TECDOC-1203, International Atomic Energy Agency.

IATF (2019). *Unpublished CHF data bank in Institute of Angewandte Thermofluidik (IATF)*. Karlsruhe, Germany: Institut für Angewandte Thermofluidik (IATF), KIT.

Kariya, K., Yoshizumi, K., and Mori, H., (2013). "Correlation for Critical Heat Flux at Near-Critical Pressure in Tubes," in The 6th International Symposium on Supercritical Water-Cooled Reactors. Shenzhen, Guangdong, China, March 03-07, 2013, 1–12.

Kataoka, I., Ishii, M., and Mishima, K. (1983). Generation and Size Distribution of Droplet in Annular Two-phase Flow. *J. Fluids Eng.* 105 (2), 230–238. doi:10.1115/1.3240969

Katto, Y. (1990). A Physical Approach to Critical Heat Flux of Subcooled Flow Boiling in Round Tubes. *Int. J. Heat Mass Transfer* 33 (4), 611–620. doi:10.1016/0017-9310(90)90160-v

Katto, Y. (1992). A Prediction Model of Subcooled Water Flow Boiling CHF for Pressure in the Range 0.1-20 MPa. *Int. J. Heat Mass Transfer* 35 (5), 1115–1123. doi:10.1016/0017-9310(92)90172-o

Katto, Y., and Yokoya, S. (1984). Critical Heat Flux of Liquid Helium (I) in Forced Convective Boiling. *Int. J. Multiphase Flow* 10 (4), 401–413. doi:10.1016/0301-9322(84)90052-1

Lee, C. H., and Mudawwar, I. (1988). A Mechanistic Critical Heat Flux Model for Subcooled Flow Boiling Based on Local Bulk Flow Conditions. *Int. J. Multiphase Flow* 14 (6), 711–728. doi:10.1016/0301-9322(88)90070-5

Lemmon, E. W., Huber, M. L., and McLinden, M. O. (2007). *NIST Standard Reference Database 23: Reference Fluid Thermodynamic and Transport Properties-REFPROP, Version 8.0: Standard Reference Data Program*.

Levitan, L., and Lantsman, F. (1975). Investigating Burnout with Flow of a Steam-Wwater Mixture in a Round Tube. *Therm. Eng. (Ussr) (Engl. Transl.)* 22 (1), 102–105.

Li, M.-J., Zhu, H.-H., Guo, J.-Q., Wang, K., and Tao, W.-Q. (2017). The Development Technology and Applications of Supercritical CO2 Power Cycle in Nuclear Energy, Solar Energy and Other Energy Industries. *Appl. Therm. Eng.* 126, 255–275. doi:10.1016/j.applthermaleng.2017.07.173

Linares, J. I., Herranz, L. E., Fernández, I., Cantizano, A., and Moratilla, B. Y. (2015). Supercritical CO2 Brayton Power Cycles for DEMO Fusion Reactor Based on Helium Cooled Lithium Lead Blanket. *Appl. Therm. Eng.* 76, 123–133. doi:10.1016/j.applthermaleng.2014.10.093

Liu, Q., and Sun, X. (2020). Wall Heat Transfer in the Inverted Annular Film Boiling Regime. *Nucl. Eng. Des.* 363, 110660. doi:10.1016/j.nucengdes.2020.110660

Liu, W., Nariai, H., and Inasaka, F. (2000). Prediction of Critical Heat Flux for Subcooled Flow Boiling. *Int. J. Heat Mass Transfer* 43 (18), 3371–3390. doi:10.1016/s0017-9310(99)00373-7

Liu, X. J., Sun, C., Wang, Z. D., Chai, X., Xiong, J. B., Yang, Y. H., et al. (2016). Preliminary Study to Improve the Performance of SCWR-M during Loss-Of-Flow Accident. *Nucl. Eng. Des.* 307, 431–444. doi:10.1016/j.nucengdes.2016.07.030

Lombardi, C. (1995). "A Formal Approach for the Prediction of the Critical Heat Flux in Subcooled Water," in 7th international topical meeting on nuclear reactor thermal-hydraulics, Saratoga Springs, NY (United States), September, 10-15, 1995.

Marion, J., Kutin, M., McClung, A., Mortzheim, J., and Ames, R. (2019). "The STEP 10 MWe sCO_2 Pilot Plant Demonstration," in Turbo Expo: Power for Land, Sea, and Air, Phoenix, Arizona, USA, June 17–21, 2019 (American Society of Mechanical Engineers (ASME)).

Miropol'skii, Z. L. (1963). Heat Transfer in Film Boiling of a Steam-Water Mixture in Steam-Generator Tubes. *Teplonergetika* 10, 49–52.

Miropol'skii, Z. L., and Shitsman, M. E. (1962). The Critical Heat Flux for Boiling Water in Tubes. *Soviet J. At. Energ.* 11 (6), 1166–1173. doi:10.1007/bf01591377

Mohammed Shah, M. (1987). Improved General Correlation for Critical Heat Flux during Upflow in Uniformly Heated Vertical Tubes. *Int. J. Heat Fluid Flow* 8 (4), 326–335. doi:10.1016/0142-727x(87)90069-5

Musgrove, G., and Wright, S. (2017). "Introduction and Background," in *Fundamentals and Applications of Supercritical Carbon Dioxide (sCO_2) Based Power Cycles*. Editors K. Brun, P. Friedman, and R. Dennis (Cambridgeshire, England: Woodhead Publishing), 1–22. doi:10.1016/b978-0-08-100804-1.00001-3

Nakla, M. E., Groeneveld, D. C., and Cheng, S. C. (2011). Experimental Study of Inverted Annular Film Boiling in a Vertical Tube Cooled by R-134a. *Int. J. Multiphase Flow* 37 (1), 67–75. doi:10.1016/j.ijmultiphaseflow.2010.08.006

Oka, Y., Koshizuka, S., Ishiwatari, Y., and Yamaji, A. (2010). *Super Light Water Reactors and Super Fast Reactors: Supercritical-Pressure Light Water Cooled Reactors*. Springer Science & Business Media.

Osorio, J. D., Hovsapian, R., and Ordonez, J. C. (2016). Effect of Multi-Tank thermal Energy Storage, Recuperator Effectiveness, and Solar Receiver Conductance on the Performance of a Concentrated Solar Supercritical CO2-based Power Plant Operating under Different Seasonal Conditions. *Energy* 115, 353–368. doi:10.1016/j.energy.2016.08.074

Pioro, I. L., Duffey, R. B., Kirillov, P. L., and Panchal, R. (2016). "Introduction: A survey of the status of electricity generation in the world," in *Handbook of Generation IV Nuclear Reactors*. Editor I. L. Pioro (Cambridge, UK: Woodhead Publishing), 1–34. doi:10.1016/b978-0-08-100149-3.00001-x

Pioro, I. L. (2016). "Introduction," in *Handbook of Generation IV Nuclear Reactors*. Editor I. L. Pioro (Cambridge, UK: Woodhead Publishing), 37–54. doi:10.1016/b978-0-08-100149-3.00002-1

Poerner, M., and Rimpel, A. (2017). "Waste Heat Recovery," in *Fundamentals and Applications of Supercritical Carbon Dioxide (sCO_2) Based Power Cycles*. Editors K. Brun, P. Friedman, and R. Dennis (Cambridge, UK: Woodhead Publishing), 255–267. doi:10.1016/b978-0-08-100804-1.00010-4

Qi, H., Gui, N., Yang, X., Tu, J., and Jiang, S. (2018). The Application of Supercritical CO2 in Nuclear Engineering: A Review. *The J. Comput. Multiphase Flows* 10 (4), 149–158. doi:10.1177/1757482x18765377

Sarkar, J. (2015). Review and Future Trends of Supercritical CO2 Rankine Cycle for Low-Grade Heat Conversion. *Renew. Sust. Energ. Rev.* 48, 434–451. doi:10.1016/j.rser.2015.04.039

Schulenberg, T., and Leung, L. (2016). "Super-critical Water-Cooled Reactors," in *Handbook of Generation IV Nuclear Reactors*. Editor I. L. Pioro (Schulenberg: Woodhead Publishing), 189–220. doi:10.1016/b978-0-08-100149-3.00008-2

Sienicki, J. J., Moisseytsev, A., and Krajtl, L. (2014). "Utilization of the Supercritical CO_2 Brayton Cycle with Sodium-Cooled Fast Reactors," in The 4th Internation Symposium-Supercritical CO2 Power Cycles, Pittsburgh, Pennsylvania, USA, September 9-10, 2014 (Pittsburgh, Pennsylvania: Citeseer), 9–10.

Slaughterbeck, D., Ybarrondo, L., and Obenchain, C. (1973). *Flow Film Boiling Heat Transfer Correlations: A Parametric Study with Data comparisonsCONF-730803-5*. Idaho Falls, Idaho (USA): Aerojet Nuclear Co.

Song, M., Liu, X., and Cheng, X. (2021). Prediction of Critical Heat Flux (CHF) for the High-Pressure Region in Uniformly Heated Vertical Round Tubes. *Ann. Nucl. Energ.* 158, 108303. doi:10.1016/j.anucene.2021.108303

Song, M. Q., Liu, X. J., and Cheng, X. (2021). *A New Correlation of post-dryout Heat Transfer for Upward Vertical Flow in Round Tubes*. Under review.

Stewart, J. C., and Groeneveld, D. C. (1982). Low-quality and Subcooled Film Boiling of Water at Elevated Pressures. *Nucl. Eng. Des.* 67 (2), 259–272. doi:10.1016/0029-5493(82)90145-5

Swenson, H. S., Carver, J. R., and Szoeke, G. (1962). The Effects of Nucleate Boiling versus Film Boiling on Heat Transfer in Power Boiler Tubes. *J. Eng. Power* 84 (4), 365–371. doi:10.1115/1.3675052

Syblik, J., Vesely, L., Entler, S., Stepanek, J., and Dostal, V. (2019). Analysis of Supercritical CO2 Brayton Power Cycles in Nuclear and Fusion Energy. *Fusion Eng. Des.* 146, 1520–1523. doi:10.1016/j.fusengdes.2019.02.119

Tong, L. S. (1967). Prediction of Departure from Nucleate Boiling for an Axially Non-uniform Heat Flux Distribution. *J. Nucl. Energ.* 21 (3), 241–248. doi:10.1016/s0022-3107(67)90054-8

Tong, L. S., and Tang, Y. S. (2018). *Boiling Heat Transfer and Two-phase Flow*. 2 ed. Oxfordshire, England: Routledge.

U.S. DOE Nuclear Energy Research Advisory Committee, Generation IV International Forum (2002). *A Technology Roadmap for Generation IV*

Nuclear Energy Systems. GIF-002-00. U.S. DOE Nuclear Energy Research Advisory Committee and the Generation IV International Forum.

Vesely, L., Dostal, V., and Entler, S. (2017). Study of the Cooling Systems with S-CO 2 for the DEMO Fusion Power Reactor. *Fusion Eng. Des.* 124, 244–247. doi:10.1016/j.fusengdes.2017.05.029

Vijayarangan, B. R., Jayanti, S., and Balakrishnan, A. R. (2006). Studies on Critical Heat Flux in Flow Boiling at Near Critical Pressures. *Int. J. Heat Mass Transfer* 49 (1), 259–268. doi:10.1016/j.ijheatmasstransfer.2005.06.029

Wang, X., Levy, E. K., Pan, C., Romero, C. E., Banerjee, A., Rubio-Maya, C., et al. (2019). Working Fluid Selection for Organic Rankine Cycle Power Generation Using Hot Produced Supercritical CO2 from a Geothermal Reservoir. *Appl. Therm. Eng.* 149, 1287–1304. doi:10.1016/j.applthermaleng.2018.12.112

Yin, J. M., Zheng, Q. Y., Peng, Z. R., and Zhang, X. R. (2020). Review of Supercritical CO 2 Power Cycles Integrated with CSP. *Int. J. Energ. Res* 44 (3), 1337–1369. doi:10.1002/er.4909

Conflict of Interest: The authors declare that the research was conducted in the absence of any commercial or financial relationships that could be construed as a potential conflict of interest.

Publisher's Note: All claims expressed in this article are solely those of the authors and do not necessarily represent those of their affiliated organizations, or those of the publisher, the editors and the reviewers. Any product that may be evaluated in this article, or claim that may be made by its manufacturer, is not guaranteed or endorsed by the publisher.

NOMENCLATURE

General

Bo boiling number

c_p specific heat, J/(kg·°C)

D_h tube diameter, m

f friction factor

G mass flux, kg/(m^2·s)

h heat transfer coefficient, W/(m^2·°C)

H_{VL} evaporation heat, J/kg

L length, m

ME mean value

N number of data point

Nu Nusselt number

P pressure, Pa

P_r reduced pressure

Pr Prandtl number

q heat flux, W/m^2

q_c critical heat flux, W/m^2

Re Reynolds number

RMS root-mean-square value

T temperature, °C

x_m mass quality ($0 \le x_m \le 1$)

x_a Actual quality

x_e equilibrium quality

z elevation, m

Greek

λ thermal conductivity, W/(m·°C)

μ dynamic viscosity, Pa·s; or mean error

ρ density, kg/m^3

σ surface tension, N/m

α void fraction

ε error parameter

Subscripts

c critical

L liquid phase

V vapor phase

f flim

w wall

s saturated

Abbreviations

BWR boiling water reactor

DNB departure from nucleate boiling

DO dryout

GFR gas cooled fast reactor

GIF generation IV international forum

IATF institute for applied thermofluidics

LOCA loss-of-coolant accident

LUT look-up table

PWR pressurized water reactor

sCO$_2$ supercritical carbon dioxide

SCW supercritical water

SCWR supercritical water-cooled reactor

SCF supercritical fluid

SFR sodium-cooled fast reactor

frontiers in Energy Research

POLICY AND PRACTICE REVIEWS
published: 24 December 2021
doi: 10.3389/fenrg.2021.785494

Status and Assessment Method of Nuclear Safety Analysis Software in China

Xinli Gao[1,2]*, *Jianping Jing*[1,2], *Xiangzhen Han*[1,2], *Bin Jia*[1,2], *Xinlu Tian*[1,2], *Fudong Liu*[1,2] *and Chunming Zhang*[1]*

[1]*Nuclear and Radiation Safety Center, Ministry of Environmental Protection, Beijing, China,* [2]*State Environmental Protection Key Laboratory of Nuclear and Radiation Safety Regulatory Simulation and Validation, Beijing, China*

In recent years, China's nuclear power industry has enjoyed a good momentum of development, and related companies have also developed many nuclear analysis software applications. However, as the National Nuclear Safety Administration (NNSA, Chinese nuclear regulatory institution) did not approve any software before 2018, all these software applications were not evaluated formally, so they have not yet been used in reactor safety analysis. In order to solve this problem, in 2018, the National Nuclear Safety Administration started to carry out an engineering applicability evaluation for software developed by Chinese companies. After several years of review, as the first approved Chinese domestic software, core physics analysis software PCM developed by the China General Nuclear Power Group officially passed the software safety evaluation of the China Nuclear Safety Administration. This study will present the basic situation of the development of China's nuclear power engineering software and introduce the framework, methods, procedures, requirements, and other aspects of China's software safety evaluation work. The evaluation process and evaluation key issues of PCM software will also be illustrated.

Keywords: software assessment, Chinese domestic software, code review procedure, software development progress, PCM

OPEN ACCESS

Edited by:
Jun Wang,
University of Wisconsin-Madison, United States

Reviewed by:
Muhammad Saeed,
East China University of Technology, China
Luteng Zhang,
Chongqing University, China
Chenglong Wang,
Xi'an Jiaotong University, China
Yuhao Zhang,
North China Electric Power University, China

***Correspondence:**
Xinli Gao
laborforce@163.com
Chunming Zhang
zhangchunming@chinansc.cn

Specialty section:
This article was submitted to Nuclear Energy, a section of the journal Frontiers in Energy Research

Received: *29 September 2021*
Accepted: *16 November 2021*
Published: *24 December 2021*

Citation:
Gao X, Jing J, Han X, Jia B, Tian X, Liu F and Zhang C (2021) Status and Assessment Method of Nuclear Safety Analysis Software in China. Front. Energy Res. 9:785494. doi: 10.3389/fenrg.2021.785494

1 INTRODUCTION

As of September 2021, there are 62 nuclear reactors in China in total, and 51 of them are under operation. Before Hualong One was built, with the exception of Qinshan unit 2#, all operating power plants housed imported reactors designed by Canada, Russia, or France. Because of this, the safety analysis software for nuclear power plants used in China was also developed by Canada, Russia, or France, simultaneously. Since such software was reviewed by foreign nuclear safety authorities, NNSA's position was to approve the evaluation opinions of foreign safety review agencies and allow the use of these supporting software applications in the safety analysis and design of domestic nuclear power plants. For example, safety analysis codes WCOBRA/TRAC used in AP1000 safety analysis have been used in AP600, and they have passed NRC's licensing review (USNRC, 2021). Therefore, NNSA has directly approved using WCOBRA/TRAC in AP1000 safety analysis.

As the designs of CAP1400 and AP1000 have similar characteristics in many aspects, the safety analysis software of AP1000 is also used in the design and safety analysis of CAP1400. When NNSA was carrying out the license review of CAP1400, in addition to the ordinary safety analysis report

review, a review of the applicability of the Westinghouse codes (LOFTRAN, NOTRUMP, WCOBRA/TRAC, and WGOTHIC) to CAP1400 was added.

Nowadays, more and more Chinese nuclear energy companies have independently researched and developed third-generation pressurized water reactors. Since 2011, China General Nuclear Power and the China National Nuclear Corporation have developed two types of third-generation reactors, CPR1000 (Brief, 2006) and ACP1000, respectively. Both are three-loop designs, but the core design is different. These two reactors were both designed with a 60-year lifespan, with 1150 MWe power output, and used a combination of passive and active safety systems. The first constructed units of Hualong One were Fuqing 5 and 6, followed by Fangjiashan 3 and 4 and Fangchenggang 3 and 4. Other than the pressurized water reactor, the Shidaowan high-temperature gas-cooled reactor (HTGR) (Zhang et al., 2006); (Zhang et al., 2016) reached the critical stage of success in 2021, and the Xiapu fast reactor demonstration project started construction in 2020 (Zhang, 2016).

For this new reactor design, although various companies have developed a large number of codes to meet the needs of related reactor-type safety analysis, these software applications have not been evaluated and licensed for engineering applications by authoritative organizations, so they cannot be formally applied in in-progress autonomous reactor-type designs. Therefore, evaluating these autonomous safety analysis software applications has become an urgent problem for NNSA to solve.

2 SOFTWARE DEVELOPMENT PROGRESS IN CHINA

Now, in China, there are a number of software applications under development, and also, many software applications have been developed and published, such as a software package called COSINE (COre and System Integrated Engine for design and analysis) (Ge et al., 2016); (Hu et al., 2017); (Yu et al., 2013); (Hao, 2015); (Jun et al., 2017); (Aning et al., 2019), published by the State Power Investment Corporation and NESTOR published by the Nuclear Power Institute of China (NPIC) (Dong et al., 2017). Different software applications have been developed for different reactors, for example, the Shanghai Nuclear Engineering Design and Research Institute has developed a series of codes to evaluate the performance of CAP1400, and the China General Nuclear Power Corporation (CGN) has developed specialized safety analysis software for Hualong One safety analysis (Ning et al., 2011). In addition, the China Institute of Atomic Energy (CIAE) has developed its own safety analysis software for sodium-cooled reactor safety analysis (Yang, 2010) (Zhang, 1997).

The NESTOR package includes design, manufacturing, installation, testing, and operation of a nuclear power project based on our Hualong One design (Liu, 2017). It will pave the way for China to export entire nuclear power projects and technologies. The software package consists of 68 pieces of software which will help with more efficient reactor design, safety analysis, live tests, nuclear refueling, and emergency response systems for a plant based on the Hualong One design.

COSINE is the software series for NPP design and analysis. COSINE covers a wide range of engineering functions, including nuclear reactor core physical design, thermal hydraulics design, deterministic accident analysis, radiation-shielding design, fuel design, severe accident analysis, probabilistic safety analysis, and neutron group-constant. COSINE includes 15 programs sorted in 8 software categories, which cover over 80 traditional nuclear power software functions.

The China General Nuclear Power Corporation has developed a series of software applications, including a nuclear fuel assembly calculation code known as PINE (Wang et al., 2018), a 3D core calculation code called COCO (Cai et al., 2016), a system thermal-hydraulic analysis code known as GINKGO, and a sub-channel analysis code called LINDEN, and so on (Ke et al., 2019).

Universities in China have also developed many software applications. For example, the research group NuThel from Xi'an Jiaotong University has developed a series of thermal-hydraulic analysis software programs (Jie et al., 2013); (Shiying et al., 2018); (Tian et al., 2007); (Xiao et al., 2014), and the NECP team, also from Xi'an Jiaotong University, has developed a complete set of physical safety analysis software programs (Xu et al., 2017); (Hongchun et al., 2019); however, these pieces of software have not been developed for safety analysis of nuclear power plants, are short of complete quality assurance, and have not been certified and validated sufficiently. Therefore, at this stage, NNSA will not evaluate these programs.

3 SOFTWARE ASSESSMENT HISTORY IN CHINA

As mentioned in the first paragraph, in the past, nuclear reactor safety analysis software did not need to be reviewed in China because the reactors which were built here in the past were designed by other countries. These reactors had already been built in other countries, and the safety analysis software had already been reviewed by the authority in other countries, so NNSA's position was not to do any other additional independent reviews of the codes. For instance, as AP1000 was designed by Westinghouse and the Nuclear Regulatory Commission (NRC) approved the final design certification for AP1000, the analysis software W-TRAC for AP1000 accident analysis was approved in China.

In 2014, NNSA reviewed an application of using a newly developed fuel management software system for the Qinshan nuclear power plant. This code was developed by the Shanghai Nustar Company independently, and it was the first autonomous software used in Chinese nuclear power plant safety analysis.

In 2015, the Nuclear and Radiation Safety Center began to conduct research on the evaluation methods of autonomous software and conducted detailed research and planning on the licensing conditions, autonomous software evaluation procedures, and document requirements for the application of the software in reactor safety analysis work. The Nuclear and

Radiation Safety Center also wrote the "safety analysis software assessment methods research report (draft)," which initially determined the implementation plan for autonomous software evaluation.

In 2016, under the framework of the NESTOR software preliminary validation stage, the Nuclear and Radiation Safety Center carried out a series of verification, validation, and third-party testing of the NESTOR software. By deeply participating in the software development process as a third party, the Nuclear and Radiation Safety Center had a full understanding of the NESTOR's theoretical model, software framework, and verification status, which laid the foundation for further software safety evaluation.

At the beginning of 2017, NNSA developed a preliminary software evaluation action plan by drawing on the experience of international mature software engineering application certification, and extensively solicited opinions from various domestic nuclear power safety software-developing companies in China on the contents of the plan. In November 2017, NNSA officially published the guidelines "Development and Application of Computer Software for Safety Analysis of Nuclear Power Plant" (China National Nuclear Safety Administration, 2017) and "Implementation measures of Nuclear power plant safety analysis software evaluation." The assessment of safety analysis software for nuclear power plants was officially launched. As of October 2021, 25 pieces of software have been submitted to NNSA.

4 ASSESSMENT METHOD

4.1 Scope

NNSA only accepts software licensing applications from Chinese companies so far, and the code must be developed for new generation reactors. The software which NNSA accepts can be categorized as follows:

1) Nuclear reactor design code;

The nuclear reactor design code includes fuel assembly analysis code, reactor core physics analysis code, and space-time neutron kinetics analysis code. An example of this kind of code is the neurotic cross-section calculation code known as PINE carried out by CGN.

2) Thermal-hydraulics code;

The thermal-hydraulics code is designed to carry out both steady-state and transient analysis, including LOCA analysis codes and sub-channel calculation codes, such as subchannel code CosSub-C developed by SPIC.

3) Containment thermo-hydraulic analysis code;

The containment thermo-hydraulic analysis code is designed to calculate the pressure and temperature behavior of the containment after a LOCA accident.

4) Fuel performance analysis code;

The fuel performance analysis code is designed to simulate the behavior of nuclear fuel during normal operation and an accident situation, such as FUPAC, a fuel performance analysis code developed by NPIC.

5) Radioactive safety analysis code;

The radioactive safety analysis code can simulate radioactive material and radiation, such as the radioactive source term analysis code, radiation-shielding analysis code, and radioactive consequence analysis code.

The severe accident code is not on the list because NNSA holds the opinion that the theory of serious accidents has still not been clarified. Utilizing different calculation models may result in completely opposite calculation results. In addition, there are not enough verification tests that can be used to confirm software for severe accidents.

Table 1 displays the list of software under review and the stage of the review.

4.2 Evaluation Model

The evaluation model (EM) is a concept proposed in NRC's regulatory guideline (U.S., 2005). An evaluation model is the calculational framework for evaluating the behavior of the reactor system during a postulated transient or design-based accident. The EM may include one or more computer programs, special models, and all further information needed to apply the calculation framework to a specific event.

China's software evaluation implementation measure has adopted the EM concept. To be more precise, the software evaluation work carried out by NNSA is not only for the software coding itself, but also includes the review of input parameters, model selection, meshing, and other factors. Therefore, software evaluation will only be carried out for the "frozen version" of the software. Applicants are not allowed to make any changes to the software during the code review stage.

4.3 Procedure

The software safety evaluation workflow is shown in **Figure 1**. First, the applicant needs to submit the relevant materials required for the application to NNSA, and then, NNSA will conduct a preliminary review of the software. This preliminary review focuses on whether the format and content of the submitted materials meet the requirements in the "Implementation Measures". After passing the preliminary review, NNSA will officially begin to review the submitted software. After the review, NNSA will formulate a review plan for different pieces of software and initially draw up the evaluation time; however, it should be noted that this evaluation time is not limited for completion but limits the shortest time for evaluation. Generally speaking, for an autonomous piece of software, the shortest evaluation time is 18 months.

After the formal acceptance of the review, the reviewer will begin to review the document report and question the applicant

TABLE 1 | Software under review and the stage of the review.

Stage of review	Name	Type
First round of questioning	Rope	Fuel rod analysis software
First round of dialogue	PALM	Fuel consumption calculation software
	POPLAR	One-dimensional Neutronics Program
	SuperMC	Monte Carlo calculation simulation software
	WILLOW	Core inlet temperature distribution calculation software
	GINKGO	System transient analysis software
	BIRCH	Fuel rod temperature analysis software
	CPDS	Radioactive system–derived source term calculation program
	CPCP	The calculation program of the source term of the primary circuit activation corrosion products
	JMCT	3D Monte Carlo particle transport simulation software
	JSNT	Three-dimensional discrete ordinate neutron photon transport software
Second round of questioning	LINDEN	Sub-channel analysis software
	CATALPA	Containment Analysis Software
Second round of dialogue	JASMINE	Fuel rod analysis software
	CORTH	Sub-channel analysis software
	cosSub-C	Sub-channel analysis software
Finished	PCM	Core physics analysis software

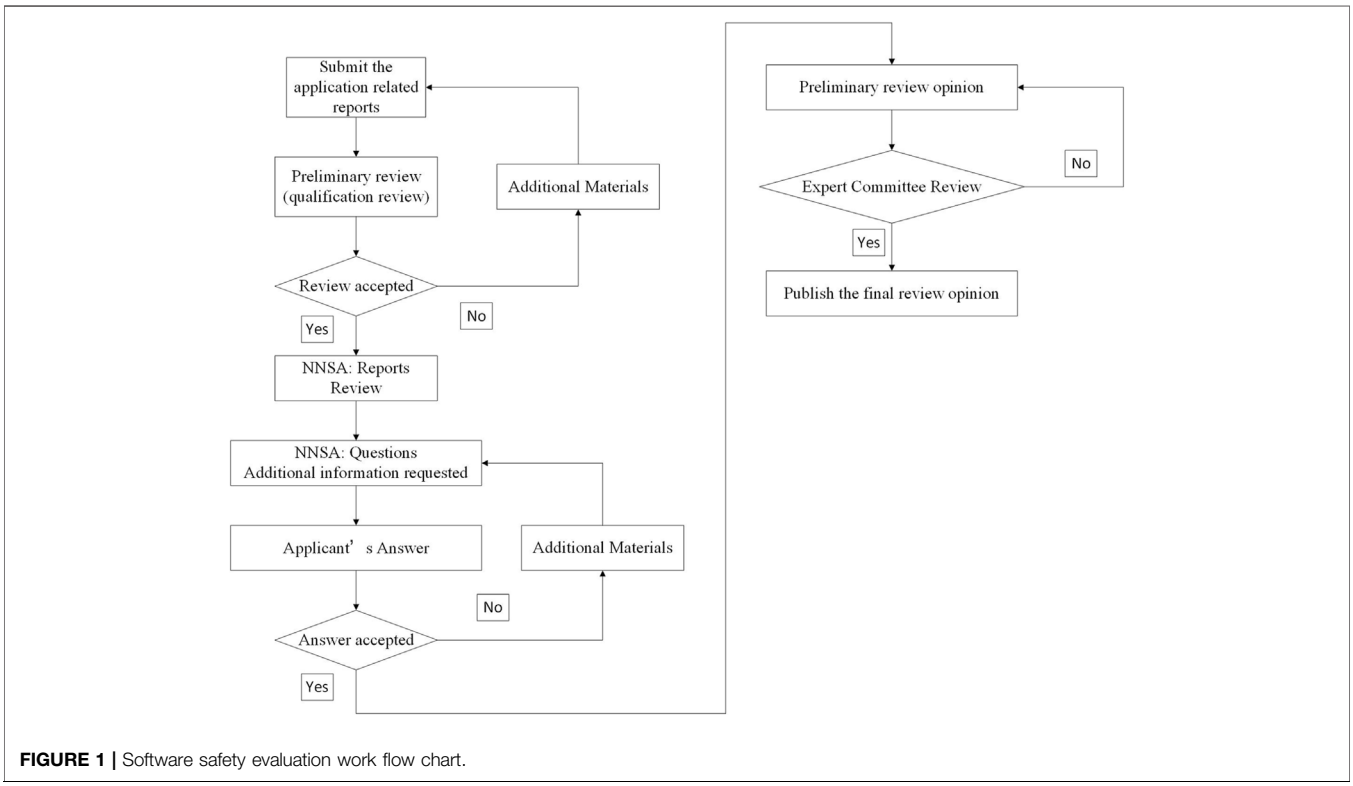

FIGURE 1 | Software safety evaluation work flow chart.

for the problems found in the report, or request that the applicant provide additional information. Generally, there will be at least two rounds of questioning, and after receiving written responses from applicants, a dialogue will be organized to discuss the key issues. Not all issues can be addressed at the dialogue session. On some key issues, where the reviewer and the applicant cannot reach an agreement, this kind of problem will be resolved through more in-depth communication and discussion on the issue by holding a separate thematic meeting.

When all the reviewers' questions are closed, NNSA will ask them to write a software evaluation report. The final report will be submitted to the expert committee, which is composed of software-related experts from various Chinese nuclear research institutions. And those experts with software development experience or software verification experience will be given priority consideration. After being approved by the expert committee, the evaluation report will be published and sent to the applicant.

Depending on the requirements, applicants should submit six reports, including the software requirement report, V&V report, software theory report, software quality assurance report, software application object report, and software self-evaluation report. The first four reports have no specific format requirements, but they must include relevant content. The latter two reports, the software self-assessment report and the software application object report, need to be written in the format required by NNSA. The report should contain complete and detailed information about the software. Conceptual or incomplete preliminary information will not be reviewed by NNSA.

Similar to the review of the nuclear power plant document safety analysis report, the software safety evaluation is mainly conducted in the form of a document review. In addition, some audit calculations and check calculations will also be carried out to ensure the authenticity of materials submitted. Check calculation refers to the use of the original input card and program provided by the applicant to reproduce the calculation results of the selected phenomenon and model and to confirm the correctness of the results in the report. Audit calculation means by using the applicant's program, the reviewer chooses some cases or scenarios, builds a new model independently, and then compares the calculation result with the test result. During the process of Audit calculation, the reviewer also often does some sensitivity analyses of the results to deepen their understanding of the software and models. Audit calculation will select models that have a greater impact on the calculation results for verification, and check calculation will randomly select from the calculation examples provided by the applicant.

4.4 Focus Points of Software Evaluation

Software evaluation mainly focuses on five aspects.

1) Functional integrity

The applicator needs to be able to prove that their software has the function of calculating related working conditions. The application scope of different professional software programs is different, and their functions are not completely the same, but the functions of the software must meet all the application requirements.

2) Empirical correlation applicability

NNSA will focus on whether the theoretical model is correct, whether the source of the theoretical model is reliable, whether the form and coefficients of the theoretical model are suitable for the object calculated by the program, whether the theoretical model has been fully verified, and whether the verification scope covers the parameter range of the simulation object.

Since the evaluation object is the EM, the reviewers will also pay attention to the selection of key parameters of the model, correctness of nodelization, and whether the time step setting is reasonable.

3) Adequacy of validation

Verification and validation are very important to nuclear safety analysis software, but due to the lack of test data and insufficient validation, validation is often the weakest part in nuclear safety analysis software. Therefore, NNSA will focus on the verification of autonomous software during the review process.

According to the requirements of the software development and application guidelines, the reviewers need to determine whether the validation of the software is sufficient, and they will focus on the process, methods, and logic of the establishment of the confirmation matrix. A complete validation matrix should include the phenomenon to be confirmed, the experiment data used, and the types of experiment data. When identifying the phenomena contained in the validation matrix, each transient/accident that needs to be calculated by the software should be analyzed, so as to evaluate the integrity of the confirmation matrix.

When evaluating the completeness of the phenomena in the confirmation matrix, it is important to sort out models and phenomena which need to be validated completely. It should be noted that code, models, and phenomena which need to be validated should be sorted out from transients or accidents calculated by the program. To validate all the models which the code has is not only unnecessary but also may result in an incomplete validation.

Confirmation data include test data, power plant operation data, domestic and international benchmark questions, analytical solutions, etc., and comparison with similar software is generally not an acceptable basis for confirmation. The reviewer will pay attention to the credibility of the test data and should make a comprehensive judgment based on factors such as the qualifications of the test developer, the year of test development, the completeness of the test report, and the test quality assurance situation.

For the confirmed data from the published article, it should be comprehensively judged based on factors such as the authority of the source of the literature, the year of publication, the completeness of the experimental information in the literature, and the application of other similar pieces of software.

In order to judge whether the test data are available, the reviewer will pay attention to the following aspects:

a) Whether the test objectives and research content are clear, and the test plan is reasonable and feasible;
b) Whether the test party has established a complete quality assurance system and ensured that the test implementation process meets the quality assurance requirements;
c) There should be a similar relationship in physical phenomena between the verification test and the software application target nuclear power plant, and whether the proportional analysis of the test can ensure the correspondence between the test facility and the prototype power plant;
d) The confirmation data in the test should include measurement method information, error information, test conditions, test results, and all relevant parameters necessary for modeling and analysis;

4) Conservatism, sensitivity, and uncertainty

The reviewer will pay attention to the rationality of conservative argumentation, the uncertainty analysis methods, the rationality of the selection of parameters and sensitivity factors, and the uncertainty and the correctness of the sensitivity analysis results.

Sensitivity analysis can be used as an auxiliary means to evaluate the impact of key parameters on the results. Sensitivity analysis cannot replace uncertainty analysis. The impact of key models, grids, and time steps can be judged by combining the results of sensitivity analysis.

The uncertainty of best estimate software must be evaluated. The applicant can choose different methods to analyze the uncertainty of the software, but the correctness of the method must pass the review.

5) Quality assurance

According to the requirements of software development and application guidelines, the reviewer evaluates the integrity of the quality assurance system, the completeness of the documentation, the compliance of personnel qualifications, etc.

4.5 Copyrights

Applicants should have the copyright of the submitted safety analysis software or the certificate of authorization and should also promise to have the legitimate right to use the experimental data used in the validation activity.

5 ASSESSMENT OF PCM

The assessment of PCM (Jun and Hao-Liang, 2014) is the first official code assessment project accepted by NNSA, and PCM is the first safety analysis computer code that passed the assessment of NNSA.

NNSA officially accepted the application of assessment of PCM, the nuclear design code package developed by CGN, on February 5, 2018. The PCM code package comprises the neurotic cross-section calculation code PINE and the 3-D nuclear design code COCO. The complete assessment process took 37 months and ended in March 2021. NNSA has issued the accepted application range of the code.

NNSA organized three rounds of questioning (containing 119, 50, and 29 questions, respectively), two dialogue conferences, two consulting conferences, and one workshop for the assessment of PCM.

The important issues identified during the assessment process are divided into three categories: the correctness of the physical models, the sufficiency of verification and validation, and the rationality of uncertainty analysis. No important issues on physical models were found during the assessment process.

NNSA and the Nuclear and Radiation Safety Center performed an assessment on PCM, which includes physical models, verification and validation, uncertainty analysis, and quality assurance. Several important issues were raised by experts in the process, and the applicant has made substantial supplements and modifications according to the queries of the Nuclear and Radiation Safety Center.

In March 2021, NNSA approved the conclusions of the assessment on PCM, thus finishing the first safety analysis computer code assessment project of China.

6 CONCLUSION

This article introduces the safety evaluation work of nuclear power plant analysis software carried out in China, including the scope of software evaluation, evaluation process, and key issues of evaluation concern.

At present, after several years of effort, NNSA's reviewers have accumulated a lot of experience in software validation and confirmation, models, calculation methods, etc., and at the same time have a clearer understanding of the difficulties in software evaluation work. Now in the software evaluation work, there are the following key issues that need to be solved in the application of software engineering in China:

1) Lack of software validation data

Although China has carried out many experiments in the past 10 years and obtained a lot of data, and at the same time, through international cooperation, many international classic data have been obtained as software support. There are still many engineering verification tests that need to be carried out, which is caused by the many unique designs of China's Hualong One and CAP1400.

2) Uncertainty and conservativeness analysis

The uncertainty analysis or conservativeness analysis of the software needs to be fully proved, which requires a rigorous methodology and a lot of confirmation work.

3) Long software evaluation work cycle

Due to lack of experience and technical accumulation, the safety evaluation of PCM software took 3 years. It can be predicted that the evaluation time of thermal hydraulic analysis software will greatly exceed this time.

In order to solve the current lack of data, China is collecting and sorting out power plant data and test data and establishing its own software verification and confirmation database. In the future, new data will be developed and shared, and the credibility of Chinese software will be further enhanced through international cooperation.

AUTHOR CONTRIBUTIONS

XG contributed to the conception of the paper and wrote the manuscript; JJ, XH, BJ, XT, and FL contributed significantly to the code assessment project; ChZh contributed significantly to the code assessment methods.

FUNDING

This research is supported by the National Science and Technology Major Project of China (2019ZX06005001).

REFERENCES

Aning, Y., Su, W., Lin, M., Li, Y., and Xu, W. (2019). Typical Benchmarks Verification of Neutron Kinetic Code cosKIND for the Simulation Application of Nuclear Power Plant. *Nucl. Sci. Eng.* 39 (2), 7.

Brief, C. G. N. (2006). Introduction of China's Improved Pressurized Water Reactor Nuclear Power Plant CPR1000. *Mod. Electric Power* 023 (005), 36–38. doi:10.3969/j.issn.1007-2322.2006.05.006

Cai, L., Chen, J., and Gao, S. (2016). *Development of a 3D Core Calculation Code: COCO[J]*. Singapore: Springer.

China National Nuclear Safety Administration (2017). *Nuclear Safety Guideline, Development and Application of Computer Software for Safety Analysis of Nuclear Power Plant*. Available at: http://www.mee.gov.cn/gkml/sthjbgw/haq/201712/t20171222_428460.htm

Dong, L., Qing, L., and Zongjian, L. (2017). Development of Nuclear Power Design and Analysis Package NESTOR. *China Nucl. Power* 010 (004), 532–536. doi:10.12058/zghd.2017.04.532

Ge, W., Yanhua, Y., and Sa, L. (2016). Autonomy of Key Design Software for Large-Scale Advanced Pressurized Water Reactor Nuclear Power Plants and Development of COSINE Software Package. *China Energy* 38 (7), 39–44.

Hao, R. (2015). *Breadth First Search Based COSINE Software Code Framework Automation Algorithm*.

Hongchun, W. U., Cao, L., Zheng, Y., Li, Y, Zu, T, Liu, Z, et al. (2019). Development and Application of NECP Code Package of Deterministic Nuclear Reactor Physics Code System[J]. *Atomic Energy Science and Technology*. doi:10.7538/yzk.2019.53.10.1833

Hu, Y., Chen, Y., Zhang, B., Sun, Y., and Yu, H. (2017). Development and Preliminary Verification of Reactor Shielding Design Code cosSHIELD of COSINE Code Package. *Energ. Proced.* 127, 87–95. doi:10.1016/j.egypro.2017.08.113

Jie, W., Tian, W., Su, G., and Qiu, S. Z (2013). Development of TSACO and Application to Chinese HCCB TBM Cooling System[J]. *Fusion Eng. Des.* 88 (11), 2983–2990. doi:10.1016/j.fusengdes.2013.06.011

Jun, C., Bin, L., Zhaoguo, L., and Liangzhi, C (2017). Development of Homogeneous Subchannel Code of COSINE. *Nucl. Sci. Eng.* 037 (004), 684–690. 10.1016/j.egypro.2017.08.121 .

Jun, C., and Hao-Liang, L. (2014). *Verification of Domestic Core Physical Calculation Software Package PCM in Unit 1 of Ningde Nuclear Power Plant*. Chengdu: COPRHY Chengdu, Chinese Nuclear Society.

Ke, W., Jie, J., and Zhihao, R. (2019). Study of CPR1000 Complete Loss of Coolant Flow Accident Based on Sampling Statistical Method. *Nucl. Sci. Eng.* 039 (004), 581–587. CNKI:SUN:HKXY.0.2019-04-013. doi:10.3969/j.issn.0258-0918.2019.04.013

Liu, D. (2017). Development of Nuclear Power Design and Analysis Package NESTOR. *China Nucl. Power* 10 (4). doi:10.12058/zghd.2017.04.532

Ning, B., Zhihao, R., and Mingan, C. (2011). "Research and Development of CGN Thermal-hydraulic Series Software", in Proceedings of the The Fifth Symposium on Reactor Physics and Nuclear Materials and the Second Symposium, Chongqing, China, October 31–November 5, 2021. Nuclear Energy Software Autonomy.

Shiying, W., Chenglong, W., and Guanghui, S. (2018). Development of Analysis Code for Pb-Bi Cooled Direct-Contact-Boiling Water Fast Reactor System[J]. *Hedongli Gongcheng/Nuclear Power Eng.* 39 (4), 067–070.

Tian, W., Qiu, S., Guo, Y., Su, G, Jia, D, Liu, T, et al. (2007). Development of a Steady thermal-hydraulic Analysis Code for the China Advanced Research Reactor[J]. *Front. Energ. Power Eng. China* 1 (002), 189–194. doi:10.1007/s00000-007-0024-8

USNRC (2021). Final Safety Evaluation Report Related to Certification of the AP600 Standard Design. Available at: https://www.nrc.gov/docs/ML9935/ML993550127.pdf (Accessed 9 Aug 1998).

U.S. (2005). *Nuclear Regulatory Commission, REGULATORY GUIDE 1.203, Transient and Accident Analysis Methods*.

Wang, C., Yang, S, Peng, S, and Li, G (2018). Automated Validation of CGN Nuclear Software Package PCM. *Hedongli Gongcheng/Nuclear Power Eng.* 39, 43–46.

Xiao, Y., Hu, L. W., Qiu, S., Zhang, D, Su, G, Tian, W, et al. (2014). *Development of a thermal-hydraulic Analysis Code and Transient Analysis for a FHTR[J]. International Conference on Nuclear Engineering*. Proceedings: ICONE.

Xu, L, Cao, L, Zheng, Y, and Wu, H (2017). Development of a New Parallel S-N Code for Neutron-Photon Transport Calculation in 3-D Cylindrical Geometry [J]. *Prog. Nucl. engergy* 94 (Jan.), 1–21.

Yang, H. Y. (2010). *GenerationⅣInternational Forum(GIF) R&D Progress for Sodium Cooled Fast Reactor*.

Yu, H., Wang, S, Liu, Z. Q, Wang, C. H, and Chen, Y. X. (2013). Design and Development of Neutron Kinetics Code KIND in COSINE Code Package[J]. *Atomic Energy Science and Technology* 47(B06), 318–322. doi:10.7538/yzk.2013.47.S0.0318

Zhang, D. (2016). *Generation IV Concepts Handbook of Generation IV Nuclear Reactors*, 373–411. doi:10.1016/b978-0-08-100149-3.00014-8

Zhang (1997). *SUNF Code for Fast Neutron Data Calculations. China Nuclear Technology Report S3*, 24–26.

Zhang, Z., Wu, Z, Sun, Y, and Li, F (2006). Design Aspects of the Chinese Modular High-Temperature Gas-Cooled Reactor HTR-PM. *Nucl. Eng. Des.* 236, 5485–6490. doi:10.1016/j.nucengdes.2005.11.024

Zhang, Z, Dong, Y, Li, F, Wang, F, Hunag, X, Li, H, et al. (2016). The Shandong Shidao Bay 200 MWe High-Temperature Gas-Cooled Reactor Pebble-Bed Module (HTR-PM) Demonstration Power Plant: An Engineering and Technological Innovation. *Engineering*. 2(1). doi:10.1016/J.ENG.2016.01.020

Conflict of Interest: The authors declare that the research was conducted in the absence of any commercial or financial relationships that could be construed as a potential conflict of interest.

Publisher's Note: All claims expressed in this article are solely those of the authors and do not necessarily represent those of their affiliated organizations, or those of the publisher, the editors, and the reviewers. Any product that may be evaluated in this article, or claim that may be made by its manufacturer, is not guaranteed or endorsed by the publisher.

frontiers in Energy Research

POLICY AND PRACTICE REVIEWS
published: 03 January 2022
doi: 10.3389/fenrg.2021.819634

Status and Perspective of China's Nuclear Safety Philosophy and Requirements in the Post-Fukushima Era

Zhiyi Yang[1], *Fengchen Li*[2] *and Guohan Chai*[1]*

[1]Nuclear and Radiation Safety Center, MEE, Beijing, China, [2]Key Laboratory of Efficient Utilization of Low and Medium Grade Energy (Tianjin University), MOE, School of Mechanical Engineering, Tianjin University, Tianjin, China

The significant impact brought by a severe nuclear accident at the Fukushima Daiichi Nuclear Power Plant (NPP) in Japan in March 2011 has made global regulators to review the requirements against severe accidents. In China, comprehensive safety inspection and external hazard safety margin assessment on NPPs were carried out, regulatory requirements on improvement measures for NPPs based on the inspection were given, the nuclear safety 5-year plan was made and executed, and the safety requirements on the new NPP design were drafted. The Nuclear Safety Law came into effect in 2018. The "Code on the Safety of Nuclear Power Plant Design" (HAF102) was revised in 2016, and relevant safety guides were developed. In this article, improvement actions and requirements about NPP safety in China over the past 10 years were reviewed, and the nuclear safety philosophy and requirements including practical elimination, classification of accident conditions, and defense in depth portable equipment were elaborated. In summary, some suggestions of NPP safety in China in the future were provided.

Keywords: Fukushima nuclear accident, nuclear safety, practical elimination, defense in depth, severe accident, portable equipment

OPEN ACCESS

Edited by:
Yapei Zhang,
Xi'an Jiaotong University, China

Reviewed by:
Penghui Chai,
Japan Atomic Energy Agency, Japan
Shanshan Bu,
Chongqing University of Technology, China
Yidan Yuan,
China Nuclear Power Engineering Co. Ltd., China

***Correspondence:**
Guohan Chai
chaiguohan@chinansc.cn

Specialty section:
This article was submitted to Nuclear Energy, a section of the journal Frontiers in Energy Research

Received: *22 November 2021*
Accepted: *07 December 2021*
Published: *03 January 2022*

Citation:
Yang Z, Li F and Chai G (2022) Status and Perspective of China's Nuclear Safety Philosophy and Requirements in the Post-Fukushima Era. Front. Energy Res. 9:819634. doi: 10.3389/fenrg.2021.819634

INTRODUCTION

As of October 2021, there were 51 Nuclear Power Plant (NPP) units in operation and 14 units under construction in China (IAEA, 2021). In order to improve the industrial structure and energy mix and promote toward the goals of achieving peak carbon emissions and carbon neutrality, the Chinese government would take active and well-ordered steps to develop nuclear power under the premise of ensuring its safe use (State Council of China, 2021). China has been adhering to a rational, coordinated, and balanced nuclear safety strategy and taking nuclear safety as an important element of China's overall national security framework. Under the effective regulation of nuclear safety, China had maintained a good nuclear safety record for a long time, and the performance indicators of NPPs are generally good. There were no incidents or accidents at or above Level 2 under the International Nuclear and Radiological Event Scale (INES). China has established a nuclear safety regulatory system and regulatory standards in line with international specifications. In 2000, 2004, 2010, and 2016, the International Atomic Energy Agency (IAEA) conducted four comprehensive reviews of China's nuclear and radiation safety regulation, giving fully positive recognition to China's good practices and experiences (State Council Information Office of China, 2019).

TABLE 1 | Percentage changes in positive opinion toward nuclear power pre- and post-Fukushima (Hayashi and Hughes (2013)).

Country		Pre-Fukushima	Post-Fukushima
OECD countries	Canada	51	43
	The United States	53	47
	Austria	13	9
	France	66	58
	Germany	34	26
	Italy	28	24
	Switzerland	40	34
	Japan	62	39
	South Korea	65	64
Non-OECD countries	China	83	70
	India	58	49
	Russia	63	52
Global average		57	49

On 11 March 2011, the Great East Japan Earthquake at magnitude 9 happened off the Pacific coast of Japan and resulted in 14- to 15-m-high tsunami waves which overwhelmed the tsunami barriers of the Fukushima Daiichi NPP site. Systems and equipment of the primary and backup powers as well as the ultimate heat sink of all six units on the site were flooded. Loss of the off-site power occurred due to the earthquake before the tsunami. Units 1–5 of the Fukushima Daiichi NPP experienced extended station blackout (SBO) events, and severe accident occurred in Units 1, 2, and 3. The radioactive material escaped from the reactors and further released directly to the environment either in a controlled manner or in an uncontrolled manner due to hydrogen explosion. The Fukushima Daiichi Nuclear Accident (FDNA) caused serious consequence and brought deep effect to the nuclear industry (IAEA, 2015).

However, with more than 440 NPP units in operation around the world, it seems unlikely to give up nuclear energy completely (**Table 1**), which is an inevitable option for some countries to secure energy supplies, optimize their energy mix, and contribute to reducing carbon emissions (Hayashi and Hughes, 2013). Re-examination and reflection on nuclear safety to ensure and improve the nuclear safety became an urgent issue in the peaceful use of nuclear energy once again. A series of actions, including safety inspections, re-evaluation, and update of nuclear safety requirement and standard, were implemented to improve the nuclear safety level among the main nuclear organizations such as IAEA and Western European Nuclear Regulators' Association (WENRA), and countries such as the United States and United Kingdom (US NRC, 2011; WENRA, 2013; UK ONR, 2014; IAEA, 2016a).

In this study, the post-Fukushima nuclear safety improvement actions in China were reviewed, the nuclear safety philosophy and requirements were introduced and elaborated, the future development of nuclear safety in China was discussed, and some suggestions were put forward. Several inspections, such as nuclear safety considerations, emergency preparedness and response, radiological consequence, and post-accident recovery (IAEA, 2015), are relevant to FDNA experience and lessons, and only part of nuclear safety considerations are referred to in this article. Note that the research on FDNA is still ongoing, and the technical positions may be changed along with lessons learned in the future.

POST-FUKUSHIMA NUCLEAR SAFETY IMPROVEMENT ACTIONS IN CHINA

A series of nuclear safety improvement actions were taken in China after the FDNA, mainly including:

1) Comprehensive Safety Inspections (CSIs) were carried out.
2) General Technical Requirements (GTRs) on post-Fukushima improvement actions (trial version) were published.
3) Safety margin evaluation for beyond design-basis external events was performed.
4) The Nuclear Safety Plan (NSP) was made and executed.
5) Safety requirements on new NPP designs were drafted, and "Code on the Safety of Nuclear Power Plant Design" (HAF102) was revised.
6) Relevant safety guides and technical documents of HAF102 were developed.

The FDNA also prompted the establishment of the Nuclear Safety Law, which had come into effect in 2018. This is the first law in the nuclear safety field in China which was launched to strengthen publicity on the rule of law and to improve the system, to reinforce the strict regulation by law, and to implement the nuclear safety responsibility.

Comprehensive Safety Inspections

The CSIs (NNSA NEA CEA, 2012) were conducted from March 2011 to December 2011 to find out potential safety weaknesses according to laws, rules, standards in force, and latest IAEA documents. Eleven aspects were focused on, including external events taken into account in siting based on recent developments, review and reassessment of the flood prevention design basis, and prevention and mitigation of severe accidents. The main general conclusions of the CSI are as follows:

1) The design, construction, and operation of NPPs satisfy requirements of Chinese safety regulations and reach the

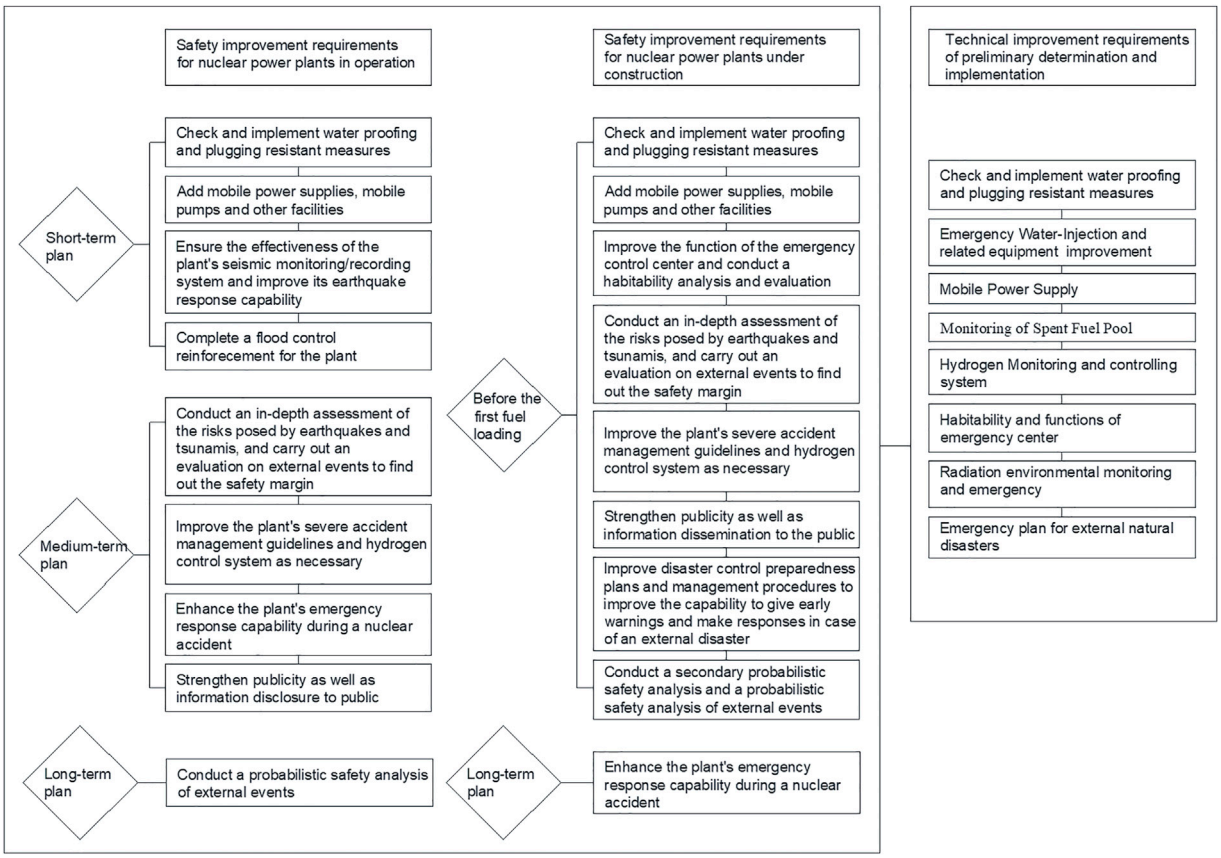

FIGURE 1 | Improvement actions and technical measures for China (2012).

safety level in IAEA new requirements. The NPPs have fully ability to prevent design-basis accident (DBA) and have basic ability to prevent and mitigate severe accidents, and risk is under control.

2) A number of specific issues have been identified. Qinshan NPP's flood prevention capacity is not fully adequate according to the latest regulation requirements, some NPPs have not established and conducted severe accident management guideline (SAMG), and effects of tsunami triggered by earthquake need further investigations and assessment.

In order to enhance the safety level of the NPPs further, some improvement actions were put forth, including short-, medium- and long-term improvements (**Figure 1**) (Zhang and Li, 2014).

General Technical Requirements on Post-Fukushima Improvement Actions (Trial Version)

In order to provide guidance for the NPPs to carry out post-Fukushima improvement measures, the common improvements were standardized, and technical integrity was reached during the implementation, the GTRs on post-Fukushima improvement actions (trial version) were compiled (NNSA, 2012a). It can also coordinate the depth and broadness of safety improvement strategies and set definite improvement acceptance criteria. Eight specific technical requirements are given, which can be seen in **Figure 2**.

The GTR specified some conditions and requirements in implementation of the improvements, such as the flood considered (design-basis flood plus superimpose once in 1,000 years' precipitation), portable equipment sets, capacity and preparation time (6 h after reactor trip), hydrogen amount considered, emergency center seismic class, and habitability criteria. The requirements were issued as a trial version because it took into account the preliminary experience feedback from the FDNA and would be amended and improved while more progress is made and more knowledge is acquired through domestic and international research and studies on the FDNA.

Safety Margin Evaluation for Beyond Design-Basis External Events

In February 2012, the National Nuclear Safety Administration (NNSA) requested operating NPPs to carry out comprehensive assessments of the plants' safety margin to beyond design-basis

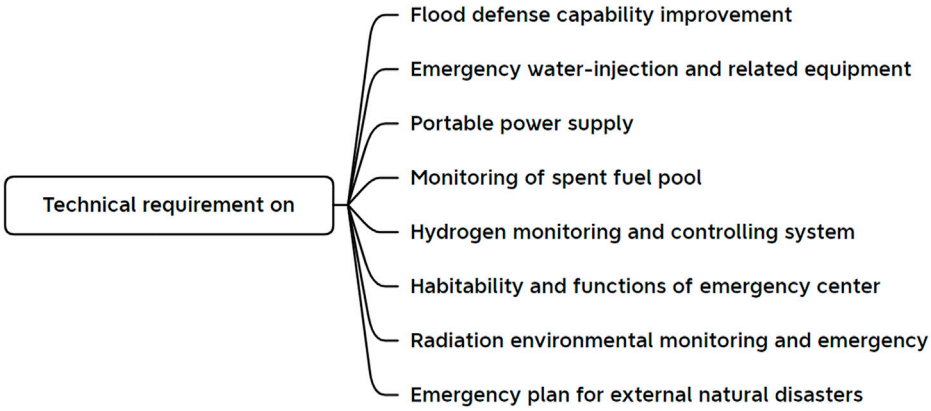

FIGURE 2 | Technical requirements on improvement actions.

TABLE 2 | General conclusions of safety margin evaluation for BDBEE.

	Evaluation event	Conclusion
1	Anti-seismic margin	NPPs in operation have a seismic safety margin not less than 1.5 times of the design-basis earthquake
2	Flood safety margin	NPPs in operation have the safety margin to cope with BDF. For Qinshan NPP on a wet site, it will have the safety margin against BDF after improvement action completion
3	SBO	NPPs in operation have taken measures to keep at least 8 h of battery power in case of loss of AC power

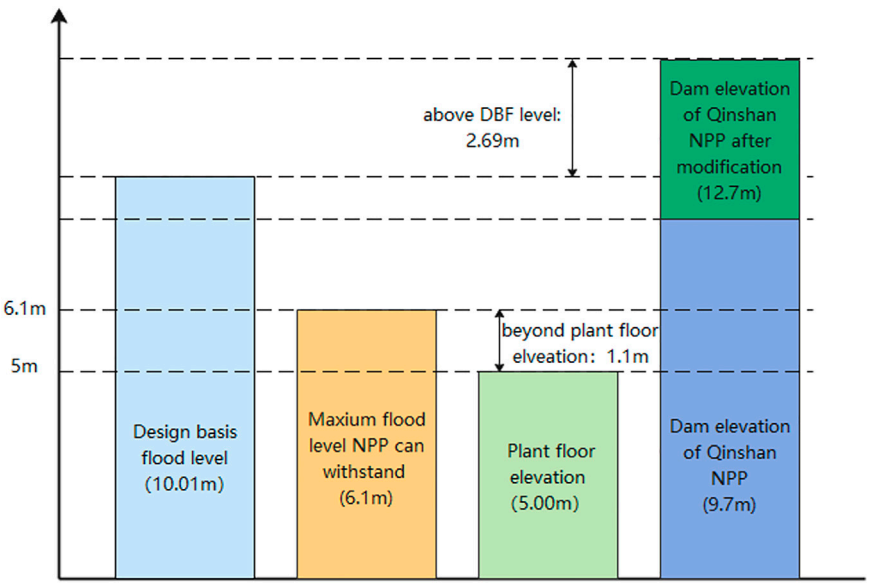

FIGURE 3 | Flood safety margin assessment and improvement of Qinshan NPP.

external events (BDBEEs) and to optimize and implement improvement measures proposed in CSI. The external events selected in the evaluation covered earthquake (initiating event), flood (initiating event), and SBO (with subsequent safety system failures). The general conclusions are shown in **Table 2**. In Qinshan NPP, plant floor elevation is 5.00 m, the design-basis flood (DBF) level is 10.01 m, and the dam elevation of Qinshan NPP is 9.70 m, which means that flood can occur. When flood occurs, the maximum flood level that an NPP can withstand is 1.1 m higher than plant floor elevation. After modification, the dam elevation of Qinshan is 12.7 m, and compared with DBF, there is a 2.69-m safety margin for the

external flood. Now, the modification has been completed (**Figure 3**).

Nuclear Safety Plan

China makes medium- and long-term development plans for nuclear safety every 5 years under the framework of the Five-Year Plan for National Economic and Social Development. The NNSA has released the 12th Five-Year Plan for Nuclear Safety and Radioactive Pollution Prevention and Control and Vision for 2020 (NNSA, 2012b) and the 13th Five-Year Plan for Nuclear Safety and Radioactive Pollution Prevention and Control and Vision for 2025, analyzing the situation, clarifying guidelines and principles, and defining goal indicators, key tasks and projects, and supportive measures for nuclear safety. These plans have helped effectively improve our nuclear safety and regulatory capacity.

The 12th Five-Year NSP and another plan developed by the National Energy Administration (NEA), named the Chinese Nuclear Power Safety Plan, set the safety goal for new NPP designs in China for a period in the future; the important ones are as follows:

— During the 12th five-year plan period (before 2015), the new NPP designs should have comprehensive measures to prevent and mitigate severe accidents, the core damage frequency (CDF) should be lower than 10^{-5}/yr, and the large release frequency (LRF) should be lower than 10^{-6}/yr.
— For NPPs built in and after the 13th five-year plan period (after 2015), efforts should be made to practically eliminate the possibility of large radioactive release in the design.
— Adopting the highest nuclear safety requirements in the world, new NPP designs should comply with the third-generation safety standards.

According to the 13th Five-Year NSP, the lessons learned from the FDNA should be continually studied and the "Code on the Safety of Nuclear Power Plant Design" (HAF102-2004) should be further revised.

Safety Requirements on New NPP Designs and Code on the Safety of the Nuclear Power Plant Design

The safety requirements on new NPP designs were compiled by the NNSA to implement the high-level safety goal given in the 12th Five-Year NSP and Nuclear Power Safety Plan. The safety requirements on new NPP designs were based on laws, rules, standards in force, and latest IAEA safety standards. The preliminary experience feedback from the FDNA and the results of CSI, as well as the improved actions adopted around the world, were also reflected. The design, construction, and operation experience in China were fully taken into account.

In 2016, No SSR-2/1 (Rev. 1), Safety of Nuclear Power Plant: Design was issued by the IAEA, which incorporated the lessons and experiences learned from the FDNA (IAEA, 2016a). The NNSA decided to take No. SSR-2/1 as a reference, in conjunction with the draft version of safety requirements on new NPP designs, and revise the HAF102-2004 Code on the Safety of Nuclear Power Plant Design. And the new version, HAF102-2016, was published by the NNSA in October 2016 (NNSA, 2016).

Safety Guides and Technical Documents of HAF102-2016

Many new nuclear safety concepts and requirements were put forward in HAF102-2016 Code on the Safety of Nuclear Power Plant Design. And the IAEA has been already or is developing safety guides and technical documents to give specific methodologies on how to implement these new concepts and requirements, such as IAEA TECDOC-1791 (IAEA, 2016b), SSG-2 (IAEA, 2019), and SSG-30 (IAEA, 2014). Also, in China, a safety guide, namely, HAD, of HAF102-2016 should be revised. On the other hand, the number of new NPPs under construction in China is the largest around the world, so it is a necessary work to give the specific criteria for these requirements, which will be a basis for the design and safety review.

Until now, the NNSA has already completed some of the HAD documents, such as HAD102-01 Deterministic Safety Analysis for Nuclear Power Plants, HAD102-07 Design of the Reactor Core for Nuclear Power Plants, and HAD 102–13 Design of Electrical Power Systems for Nuclear Power Plants. Meanwhile, some technical policy documents were also developed by the NNSA to provide the technical position. The Nuclear Safety Review Guideline of NPPs adopting the HPR1000 gives the review methodology on practical elimination of large or early radioactive release, design extension condition analysis and criteria, and portable equipment configuration. Several technical policies, such as the technical policy on cyber security and the technical policy on configuration risk management, put forward technical positions on some specific safety issues. Some safety guides and technical documents are still under development.

STUDY OF NEW SAFETY PHILOSOPHY IN THE POST-FUKUSHIMA ERA

In conjunction with the safety review practice, the technical position and application of new safety goals, philosophy, and concepts were elaborated and discussed.

New Safety Goal

Although no loss of life and no significant increase in cancer risk due to radiological releases from the FDNA were found, the radioactive releases resulted in radiological exposure to the workers at the site and the general public residing in the surrounding communities and caused radiological contamination of the environment in those areas, which caused huge social and economic impacts in Japan and around the world. So, the consequence of the FDNA was definitely unacceptable. Some current safety goals, such as the two 0.1 percent related to CDF and LRF, may not be enough to protect the people and public (Bier et al., 2014). In China, the IAEA safety goal, practical elimination of large or early radioactive releases, is adopted in the Nuclear Safety Plan and HAF102-2016 as a new safety goal.

TABLE 3 | Enhanced defense in depth level structure.

Level of DID	Safety goals	Basic measures	Plant states
1	Prevention of abnormal operation and failure	Conservative design and high-quality construction and operation	Normal operation
2	Control of abnormal operation and detection of failures	Control, limiting, and protection system and other surveillance features	Anticipated operational occurrence
3	Control of accidents within design basis	Engineered safety features and emergency operating procedures	DBA, single failure postulated initial event
4	Control of severe accident, including prevention of severe accident (4a) and mitigation of consequence (4b)	Additional safety systems and severe accident management	DEC, including multiple failures (4a) and severe accident (4b)
5	Emergency rescue work on extremely condition, mitigation of off-site radioactive release	Safety margins, supplementary safety measures, DID measures, extensive damage mitigation, off-site emergency response	Residual risks, that is, extensive damage state

In the Nuclear Safety Review Guidelines of NPPs, adopting the HPR1000, the scope, methodology, and supporting probabilistic judgment value (10^{-7}/yr) for "practical elimination" was provided. Practical elimination of large or early radioactive releases is a high-level and overall safety goal, and it is related to defense in depth, DBA, design extension condition (DEC), and corresponding design safety features. Complete design and safety analyses are mandatory to demonstrate this goal, which include deterministic safety analysis as well as probabilistic safety assessment (PSA). When the specific scenarios should be practically eliminated, first, corresponding design features should be incorporated and reliable, and PSA should be used to support the demonstration (low probability less than 10^{-7}/yr).

Safety Philosophy

Enhancement of Defense in Depth

The defense in depth (DID) principle was re-examined, and its importance was confirmed by the FDNA. In China, two enhancement approaches of the DID principle have been studied, emphasizing the effectiveness of DID and the independence between all DID levels.

A proposed enhanced DID-level structure is summarized in **Table 3**. First, the DID levels were enhanced. The fourth level, which addresses the DEC, was divided into two parts. The fifth level was improved to address the residual risk. For the DBA, engineered safety features were used, and effectiveness should be demonstrated *via* conservative analysis. For the DEC, additional safety systems were used, and the best estimate and realistic analysis can be used. For the fifth level, supplemental safety measures were used to minimize the consequences of residual risk as far as possible. In the new DID approach, the multi-failure accident and severe accident conditions should be emphasized in the NPP design process, and the design features should be reliable and effective. The prevention and mitigation of accident should be equally addressed.

Second, the independence between all levels should be taken into account. In HAF102-2016, the levels of DID must be as independent as practicable, and safety features for DECs (especially features for mitigating the consequences of accidents involving the melting of fuel) should be independent of safety systems as far as practicable. How to realize this requirement as far as practicable has been discussed widely in the regulatory and design sides. The independence between all DID levels would be beneficial for the enhancement of nuclear safety. Some systems used in severe accident, such as the heat removal system from the reactor core or containment, and the electric power system for the important equipment and instrument, should be independent as far as possible. For example, in-vessel retention (IVR) is adopted in HPR1000 to perform heat removal function in severe accident, which is independent with the emergency core cooling system (ECCS) in DBA. On the other hand, it is impossible to guarantee all systems and equipment to be independent, such as some passive barriers, including the reactor pressure vessel (RPV) and the containment itself. In China, specific requirement on the independence between each DID level is not the same if the design philosophy is different, and should be addressed specifically.

The Application of Risk-Informed Approach

China always attaches importance to the application of PSA in the nuclear safety regulation. The technical policy on the application of PSA in the nuclear safety was issued by the NNSA in 2010. The PSA can be a useful tool in conjunction with the deterministic method to assess the overall safety level and guide improvement *via* identifying the weakness. On the other hand, the limited human resources are used to improve the efficiency, depth, and breadth of nuclear safety regulation based on performance-based and risk-informed approaches. The safety and economy of the NPP design are also balanced. A typical example in the design process is the risk-informed safety classification of structure, system, and components (SSCs). In terms of operation, China is also trying to strengthen the risk-informed approach application in technical specifications, maintenance rules, and so on. The risk-informed design and regulation approach is under discussion and is prepared to reflect in a high-level requirement document.

Advocating as High as Reasonably Achievable

Safety priority philosophy should be carried out since it is the premise and lifeline of nuclear energy development. Economy is also important because it is the basis of nuclear power development. The balance between safety and development has been discussed widely in the nuclear industry. Due to the limitations of human cognition, the severity of consequences, nuclear safety as high as reasonably achievable (AHARA) is

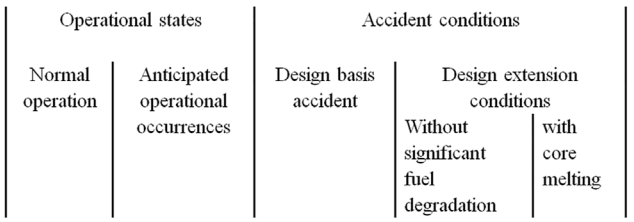

FIGURE 4 | Plant states considered in the design.

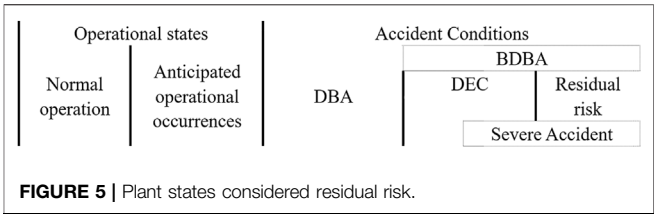

FIGURE 5 | Plant states considered residual risk.

suggested to be considered in the design of NPPs. The AHARA philosophy is with reference to AHARA principles of radiation protection and risk AHARA requirements of the United Kingdom. Actually, this philosophy is always used, though not mentioned in requirement up to now, in practice in China. For example, the IVR strategy was adopted actively by the designer in the Yangjiang NPP Units 3 and 4 before the FDNA occurred.

Safety and development are both considered in AHARA philosophy, which encourage adopting effective and reasonable achievable measures to improve the safety of the NPP design, even if the requirement is already met. AHARA philosophy can improve the nuclear safety continually with the up-to-date technology and research achievements, and update nuclear safety requirements through the summary of nuclear safety improvement practice and experience. Now, the AHARA philosophy is being studied, and relevant guidance is not established.

Safety Requirements

Categories of Plant States

Categories of plant states were optimized in HAF102, and the DEC concept was adopted. A part of beyond design-basis accidents (BDBAs) was considered as DECs, and relevant DEC safety features, as well as their design criteria, was identified, which was intended to enhance the plant's capability to withstand accidents that are more severe than DBAs. The plant states considered in design are shown in **Figure 4**. There are two categories of the DEC: DEC-A without significant fuel degradation and DEC-B with core melting. However, it must be noted that the DEC is only a part of the BDBA, and so there are conditions other than DECs which cannot be considered in the design of NPPs. These conditions should be practically eliminated, which are called conditions "practically eliminated" or "residual risk." It is not necessary to consider residual risk specifically in the design but can be treated through a safety margin in DID and accident management measures as far as possible. The plant states considering residual risk is shown in **Figure 5**.

Compared to the single failure postulated initial event considered in DBA, the multi-failures are considered in the DEC. The DEC is a postulated plant state, and for the same reasons that design-basis hazards are not considered in DBA, more severe hazards are not considered in DECs as well, although they might result in a DBA or a DEC. The Nuclear Safety Review Guidelines of NPPs adopting the HPR1000 and HAD102-01 provided the DEC identification principle and typical accident list. Best estimate and realistic analysis can be used in the DEC analysis. Technical acceptance criteria of DEC-A and DEC-B should be no fuel melting and containment integrity. And for radiological acceptance criteria, DEC-A should demonstrate that the effective dose received by any individual at the exclusion area boundary is below 10 mSv. However, some quantitative criteria are still not clear, such as the probabilistic cutoff value frequency of DEC, and the radiological acceptance criteria of DEC-B, which are related to radiation protection and other factors. In practice, relatively conservative methodology was used, and the results showed a considerable margin compared with domestic standards, which is considered an acceptable practice.

Safety Classification and Availability

In HAF102-2016, the safety features for the DEC are obviously items important to safety, and the reliability and availability should be guaranteed. However, there are still confusions and discussions. From the viewpoint of the deterministic approach, it is difficult to ensure the availability of safety features for the DEC when the safety system for DBA fails, if there is no high requirement. From the viewpoint of the probabilistic approach, the probability of the DEC is lower than DBA, so the requirement of safety features for the DEC should be comparatively low. In practice, the latter one seems preferred. Safety features for the DEC can be non-safety classification, but equipment availability under severe accident conditions should be demonstrated, and no higher seismic requirement is required.

Commercial Aircraft Impacts

9/11 events in 2001 brought the commercial aircraft impact issue to the nuclear safety. In HAF102-2016, the relevant requirement was given. The design should take into account the effects of malicious aircraft crash in the event that the NPP might suffer such crashes due to its topographical conditions. An appropriate type of commercial aircraft should be selected to evaluate the effects of the aircraft crash, and the aviation fuel loading should be calculated based on the relative distance between the NPP site and the take-off/landing airport of that type of aircraft. The angle and speed of the potential aircraft crash can be determined as per the topographical conditions and the layout of the NPP, and crash-proof measures for the plant should be assessed and determined using realistic analyses. The assessment results should demonstrate that the plant design is capable of maintaining reactor core cooling (or containment integrity) and spent fuel cooling (or spent fuel pool integrity).

The technical policy on NPPs withstanding commercial aircraft Impacts is being developed by the NNSA to give guidance on how to meet the requirement in HAF102-2016. For new NPP designs, the commercial aircraft impact should be included

in the design process. And for operating NPPs, accident mitigation measures should be considered as far as possible. The policy also clarified that some kind of information should be incorporated in the public safety analysis report, while others should be classified and not open to the public.

Portable Equipment Configuration

The importance of portable equipment was confirmed from the feedback of the FDNA. Specific requirement is being developed in some countries, such as the FLEX strategy of the United States (NEI, 2016). Portable equipment relevant requirement was put forward in HAF102-2016. Each unit of a multiple unit NPP must have its own safety systems and must have its own safety features for DECs. To further enhance safety, means allowing interconnections between units of a multiple unit NPP must be considered in the design. For multiple unit plant sites, the design must properly consider the potential for specific hazards to impact on several or even all units on the site simultaneously. According to GTR (trial version), NPPs may analyze and assess their emergency response capabilities based on the conditions of two reactors being in accident simultaneously. Arrangement of the portable pumps should be considered to meet the need of core cooling and spent fuel pool cooling simultaneously, and at least two sets of equipment should be equipped on one multiple unit plant site. At least two portable power supplies should be equipped, and no less than one of them should have the capability of carrying a low-pressure safety injection pump or an auxiliary feed-water pump, and the necessary monitoring, communication and ventilation loads, etc., should also be included. Other requirements on layout, location, distance, and preparation time are also mentioned.

There are some sites in China involving multiple units, that is, usually 4–6 units are built at one site. In the WANO assessment, relevant questions were put forward by assessment experts. This issue is also discussed widely in China. There are some specific features of Chinese NPPs. First, the site condition of the NPPs is relatively good, and the probability of the beyond design-basis external event is extremely low. Second, the design standard of NPPs in China is relatively new, most of which have the ability to cope with the SBO condition. After the Fukushima nuclear accident, the ability of prevention and mitigation of severe accident was also improved. Besides the portable equipment on site, other portable equipment in nearby NPPs, nuclear region rescue centers, and conventional region rescue centers can also be used. Therefore, it is a problem needed to be studied in China on how to configure portable equipment properly.

CONCLUSION AND PERSPECTIVE

The lessons and experience learned from the Fukushima nuclear accident can be a long process, and some further enhancement actions probably would be necessary in the future along with the additional research and study on the accident. A series of nuclear safety enhancement actions were taken in China in recent years after the Fukushima nuclear accident based on preliminary lessons and experiences. Higher safety requirements were put forward, and the safety level of NPPs in China has elevated, which obtained positive recognitions in domestic and international organizations (IAEA, 2016c; Lam et al., 2018). The post-Fukushima nuclear safety enhancement actions in China were summarized. Based on the application and discussion of nuclear safety philosophy and requirements in China, the future development of nuclear safety was discussed preliminarily, and the following suggestions were put forward.

New safety goal and high-level safety requirements were established in China, while some specific requirement and criteria are still being studied and discussed. Relevant safety guides and technical document should be improved, and a complete and logic nuclear safety regulation system should be established.

1) Detail innovation and assessment criteria of practical elimination of large or early radioactive release.
2) Assessment criteria of independence between all defense in depth levels.
3) Balance and combination of deterministic and probabilistic approaches, such as application of the risk-informed approach, AHARA philosophy, and the safety requirement on the design feature for design extension condition.
4) The establishment of probabilistic cutoff value frequency and radiological acceptance criteria of design extension condition with core melting.
5) Assessment criteria of the beyond design-basis external event in the design.
6) Number and configuration of portable equipment on the multiple unit plant site.

In addition, the requirement discussed in this article only refers to the large pressurized water reactor (PWR). Other types of reactors, such as small modular reactor (SMR), high-temperature gas-cooled reactor (HTGR), and molten salt reactor (MSR) are also in design or under construction in China. The safety goal may be the same, but specific requirement and criteria would be different for these new design reactors, some of which may be completely new and innovative around the world, and it is a challenge work for nuclear safety regulation.

AUTHOR CONTRIBUTIONS

ZY involved in investigation, discussion, and application of some safety requirements and wrote the article. FL involved in formal analysis and discussions. GC put forward some philosophy originally and involved in discussion and application of all safety requirements.

ACKNOWLEDGMENTS

The authors gratefully acknowledge the support of the National Key R&D Program of China (Grant No. 2018YFB1900100).

REFERENCES

Bier, V., Corradini, M., Youngblood, R., Roh, C., and Liu, S. (2014). "Development of an Updated Societal-Risk Goal for Nuclear Power Safety," in PSAM 2014-Probabilistic Safety Assessment and Management, Honolulu, Hawaii, USA, June 2014.

Hayashi, M., and Hughes, L. (2013). The Fukushima Nuclear Accident and its Effect on Global Energy Security. *Energy Policy* 59, 102–111. doi:10.1016/j.enpol.2012.11.046

IAEA (2014). *Safety Classification of Structures, Systems and Components in Nuclear Power Plants*. Specific Safety Guides. Vienna: IAEA Press.

IAEA (2015). *The Fukushima Daiichi Accident*. Vienna: IAEA Press.

IAEA (2016). *Safety of Nuclear Power Plants: Design*. IAEA Safety Standards Series No.SSR-2/1. Vienna: IAEA Press.

IAEA (2016). *Considerations on the Application of the IAEA Safety Requirements for the Design of Nuclear Power Plants*. TECDOC Series. Vienna: IAEA Press.

IAEA (2016). *Integrated Regulatory Review Service (IRRS) Follow-Up Mission to China*. Vienna: IAEA Press.

IAEA (2019). *Deterministic Safety Analysis for Nuclear Power Plants*. Specific Safety Guides. Vienna: IAEA Press.

IAEA (2021). Power Reactor Information. Available at: https://pris.iaea.org/PRIS/home.aspx (Accessed November 18, 2021).

Lam, J., Cheung, L., Han, Y., and Wang, S. (2018). China's Response to Nuclear Safety Post-Fukushima: Genuine or Rhetoric? Cambridge Working Papers in Economics 1866. Faculty of Economics, University of Cambridge.

NEI (2016). *Diverse and Flexible Coping Strategies (FLEX) Implementation Guide*. Washington, DC: NEI.

NNSA NEA CEA (2012). Report on the Comprehensive Safety Inspection of Civilian Nuclear Facilities in Mainland China. Available at: http://www.mee.gov.cn/gkml/hbb/bgth/201206/t20120626_232383.html (Accessed November 18, 2021).

NNSA (2012). General Technical Requirements on post-Fukushima Improvement Actions (Trial Version). Available at: https://www.mee.gov.cn/gkml/hbb/haq/201206/t20120615_231698.htm (Accessed November 18, 2021).

NNSA (2012). 12th Five-Year Plan for Nuclear Safety and Radioactive Pollution Prevention and Control and Vision for 2020. Available at: http://www.mee.gov.cn/gkml/hbb/bgth/201206/t20120626_232383.html (Accessed November 18, 2021).

NNSA (2016). *Safety of Nuclear Power Plants: Design, HAF102*. Beijing, China: NNSA.

State Council Information Office of China (2019). *Nuclear Safety in China*. Beijing: People's Publishing House.

State Council of China (2021). *Report on the Work of the Government*. Beijing: People's Publishing House.

UK ONR (2014). *Safety Assessment Principles for Nuclear Facilities*. London, United Kingdom: ONR.

US NRC (2011). *Recommendation on Enhancing Reactors Safety in the 21st Century*. Washington, DC: NRC.

WENRA (2013). *Report Safety of New NPP Designs*. Paris, France: WENRA.

Zhang, L., and Li, W. H. (2014). Analysis of Nuclear Power Plant Safety Improvement Action after Fukushima Daiichi NPP Accident. *At. Energ. Sci. Techn.* 48, 486–491. doi:10.7538/yzk.2014.48.03.0486

Conflict of Interest: The authors declare that the research was conducted in the absence of any commercial or financial relationships that could be construed as a potential conflict of interest.

frontiers in Energy Research

ORIGINAL RESEARCH
published: 27 January 2022
doi: 10.3389/fenrg.2022.819033

The Super Thermal Conductivity Model for High-Temperature Heat Pipe Applied to Heat Pipe Cooled Reactor

Yuchuan Guo, Zilin Su, Zeguang Li and Kan Wang*

Department of Engineering Physics, Tsinghua University, Beijing, China

Differing from the traditional Pressurized Water Reactor (PWR), heat pipe cooled reactor adopts the high-temperature heat pipes to transport fission heat generated in the reactor core. Therefore, the basis of coupling calculation on this type of reactor system is to have a suitable model for high-temperature heat pipe simulation. Not only is it required that this model can well describe the transient characteristics of heat pipe, but it should be simple enough to reduce the computational resource. In this paper, the super thermal conductivity model (STCM) for high-temperature heat pipe is proposed for this purpose. In this model, heat transport of vapor flow is simplified as high efficiency heat conductance. Combined with the network method, the evaporation rate, the condensation rate, and the flow rate in the wick region can be preliminarily obtained. Using recommended equations to calculate the heat transfer limitation, this model can realize the safety judgment of heat pipe. The heating system for high-temperature heat pipe is established to validate this model. The heating experiments with different heating powers is tested. Then, this model is applied on the numerical calculation of Kilowatt Reactor Using Stirling TechnologY (KRUSTY) reactor. In the steady state calculation, the results show that the temperature distribution on contact surface between fuel and heat pipe is nonuniform, which will lead to higher peak temperature and temperature difference for the reactor core. In the transient calculation, the load-following accident is chosen. Comparing with the experimental results, the applicability of the proposed model on heat pipe cooled reactor is verified. This model can be used for heat pipe cooled reactor simulation.

Keywords: heat pipe cooled reactor, high-temperature heat pipe, STCM, heating system, KRUSTY reactor

OPEN ACCESS

Edited by:
Luteng Zhang,
Chongqing University, China

Reviewed by:
Chenglong Wang,
Xi'an Jiaotong University, China
Roger Riehl,
National Institute of Space Research (INPE), Brazil

****Correspondence:***
Zeguang Li
lizeguang@mail.tsinghua.edu.cn

Specialty section:
This article was submitted to Nuclear Energy, a section of the journal Frontiers in Energy Research

Received: *20 November 2021*
Accepted: *06 January 2022*
Published: *27 January 2022*

Citation:
Guo Y, Su Z, Li Z and Wang K (2022) The Super Thermal Conductivity Model for High-Temperature Heat Pipe Applied to Heat Pipe Cooled Reactor. Front. Energy Res. 10:819033. doi: 10.3389/fenrg.2022.819033

1 INTRODUCTION

Alkali metal has the characteristics of having a high boiling point and large latent heat of vaporization. Heat pipes using alkali metal can realize efficient heat transport in special environments with high temperature (Faghri, 2014). Wicks with a porous structure can generate an effective pressure head at the vapor-liquid interface, maintaining the stable circulation of working medium (Reay et al., 2013). Due to these characteristics, high-temperature heat pipe is widely used for the design of heat pipe cooled reactor systems. So far, proposed conceptual designs of heat pipe cooled reactor systems include the kilopower reactor system (McClure et al., 2020a), the Heatpipe-Operated Mars Exploration Reactor (HOMER) system (Poston, 2001), and the Heat Pipe-segmented Thermoelectric Module Converters Space Reactor (HP-STMCs) system (El-Genk and Tournier,

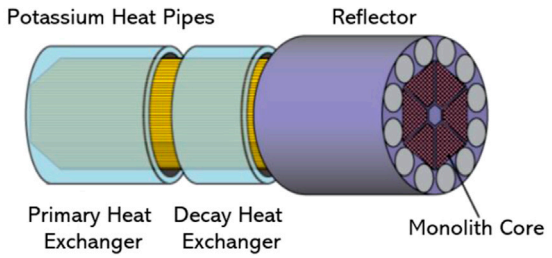

FIGURE 1 | Basic constitution of a heat pipe cooled reactor (Mcclure, 2015).

2004). This type of reactor system has the advantages of having a compact structure and high safety. It can be used as a mobile nuclear power system or space nuclear system for portable and efficient energy supply (Yan et al., 2020).

Figure 1 shows the basic constitution of a heat pipe cooled reactor (Mcclure, 2015). Heat generated in the reactor core is absorbed by high-temperature heat pipes. Then it is released in the primary heat exchanger through the heat convection between heat pipes and coolant in the secondary system. When the reactor shuts down, decay heat can be taken out of the reactor core through the decay heat exchanger. In general, due to the nonuniformity of reactor power distribution and the directionality of coolant flow in the heat exchanger, the actual heat transport and temperature distribution of each heat pipe are different. Meanwhile, to ensure the safety of heat transport, there are a large number of high-temperature heat pipes in the reactor core. The complex two-phase flow and heat transfer also brings challenges to the numerical calculation of heat pipe. For heat pipe models using the analysis on heat pipe cooled reactors, it is hoped that it can describe the transient behavior of heat pipes well, and it should be simple enough to reduce the computational resources as much as possible.

So far, there have been many studies on the numerical analysis of high-temperature heat pipe (Costello et al., 1986; Cao and Faghri, 1991; Cao and Faghri, 1992; Tournier and El-Genk, 1992; Vasiliev and Kanonchik, 1993). Before the 1990s, computing power was limited, so the complex physical phenomena that existed in heat pipe could not be simulated in detail. Therefore, the heat pipe models at this period were based on some reasonable assumptions. For example, the vapor flow in vapor space was assumed to be one-dimensional, while heat conductance in solid region was treated as two-dimensional. The backflow in wick subregion was ignored. During this period, several typical models for heat pipe were put forward successively, including the self-diffusion model (Cao and Faghri, 1993a), the plat-front model (Cao and Faghri, 1993b), the network model (Zuo and Faghri, 1998), and the improved network model (Ferrandi et al., 2013). These models were applied for the simulation of heat pipe cooled reactor (Yuan et al., 2016; Liu et al., 2020; Ma et al., 2020; Wang et al., 2020). However, there are limitations to using these models. For example, the network model cannot consider the nonuniform heat transfer between the heat pipe and the environment. Both the self-diffusion model and the plat-front model consider the two-phase flow and heat transfer in the pipe. During startup, the drastic variation of vapor density, pressure, and velocity may lead to numerical instability.

With the development of high-performance computers, there are more studies on heat pipe simulation using the CFD method (Annamalai and Ramalingam, 2011; Asmaie et al., 2013; Lin et al., 2013; Yue et al., 2018). Using commercial codes such as FLUENT and CFX, the modeling difficulty can be greatly simplified, and built-in advanced numerical algorithms can ensure the stability of numerical calculation as much as possible. The physical processes such as heat conduction, evaporation, condensation, and vapor flow in the heat pipe can be modeled and calculated. CFD modeling and calculation have gradually become the main method for heat pipe analysis. It should be noted that the two-phase flow simulation using CFD method requires large amounts of computing resources. Moreover, for the numerical analysis of heat pipe cooled reactor, more attention should be paid to the heat absorption capability, the temperature variation and distribution, and the operating safety of heat pipe. Phenomena such as vapor flow and vapor-liquid interface shape variation are not important for the safety analysis of heat pipe cooled reactor.

To meet the requirements of heat pipe cooled reactor simulation, the super thermal conductivity model (STCM) is proposed. The heat transport of vapor flow is simplified as high efficiency heat conductance. Combined with the network method, the evaporation, condensation, and backflow can be obtained (Ferrandi et al., 2013). The experimental system for high-temperature heat pipe is established to verify the proposed model. It is then used for the simulation on KRUSTY reactor to discuss the applicability of this model and the characteristics of this type of reactor system.

2 MODEL DESCRIPTION

The model proposed in this paper ignores the two-phase flow and capillary phenomenon in heat pipe, as it simplifies the heat

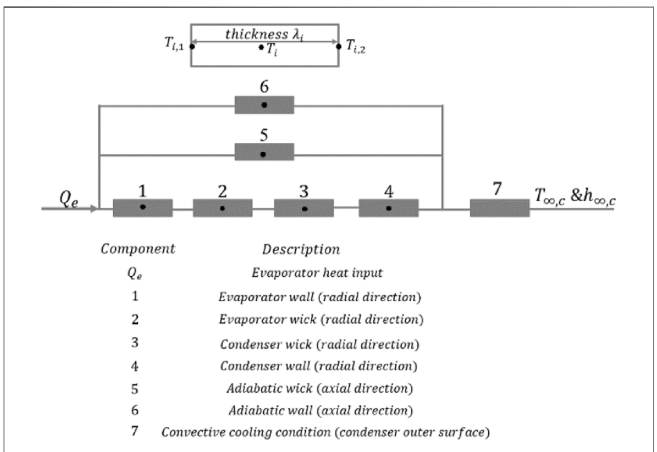

FIGURE 2 | The network system for heat pipe operation.

transport caused by vapor flow into high-efficiency heat conductance. Using the network method, the flow of working medium is approximately accounted for. Combined with the recommended heat transfer limitation model (Busse, 1973; Levy, 1968; Deverall et al., 1970; Tien and Chung, 1979), the fast calculation of heat pipe performance and the evaluation of heat pipe safety are realized.

2.1 Network Model

Network model was proposed by Zuo and Faghri (1998); the schematic diagram of this model is shown in **Figure 2**. Zuo ignored the temperature drop caused by the vapor flow and considered that the temperature drop of the heat pipe was mainly caused by the heat conduction in wall and wick. In addition, Zuo ignored the energy transport caused by the backflow of working medium in wick. Zuo divided the heat pipe into several subregions, and the lumped temperature was used to represent the real temperature of specific subregions. The three-dimensional temperature distribution in each subregion cannot be calculated.

2.2 Proposed Model

In this paper, the proposed model simplified the heat transport into multi-region heat conduction. The equation that needs to be solved is the differential equation of heat conduction (**Eq. 1**):

$$\rho_{(i)} C_{(i)} \frac{dT_{(i)}}{dt} = \nabla\left(\lambda_i \nabla T_{(i)}\right) + H_{(i)} \tag{1}$$

where ρ is the density, C is the specific heat capacity, T is the temperature, λ is the thermal conductivity coefficient, and H is the volumetric heating source.

For heat pipe, it includes the wall, the wick, and the vapor space. The key to the realization of this model is to determine the thermophysical parameters and heating source of each subregion.

2.2.1 Wall Subregion

Wall is usually a cylindrical closed shell made of metal. The thermophysical parameters required to solve **Eq. 1** are the physical parameters of the corresponding metal. Generally, there is no heat source in wall, and the heat transfer between heat pipe and environment can be described using suitable boundary conditions. Three boundary conditions (**Eqs 2–4**) can be selected for heat transfer:

$$T_{(i)} = T_0 \tag{2}$$

$$Q_{(i)} = -\lambda_i A_i \nabla T_i \tag{3}$$

$$h_i\left(T_i - T_\infty\right) = -\lambda_i \nabla T_i \tag{4}$$

where Q is the heating source, A is the surface area, h is the convective coefficient, $T_{(i)}$ is the surface temperature of wall, and T_∞ is the environment temperature.

2.2.2 Wick Subregion

Wick is composed of a porous structure and liquified working medium. Forms of it include channels, screen, and concentric annulus (Reay et al., 2013). This subregion is usually regarded as the compound material. The thermophysical properties are

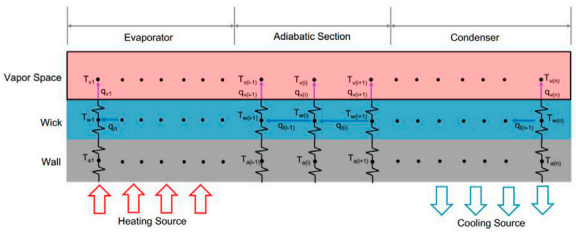

FIGURE 3 | Backflow calculation using network model.

determined by two materials. For example, for wick with a mesh type, the density, specific heat capacity, and thermal conductivity can be approximately described by **Eqs 5–7** (Chi, 1976).

$$\rho_{equ} = \varepsilon\rho_f + (1-\varepsilon)\rho_{wc} \tag{5}$$

$$C_{equ} = \varepsilon C_f + (1-\varepsilon)C_{wc} \tag{6}$$

$$\lambda_{equ} = \lambda_f \frac{\left(\lambda_f + \lambda_{wc}\right) - (1-\varepsilon)\left(\lambda_f - \lambda_{wc}\right)}{\left(\lambda_f + \lambda_{wc}\right) + (1-\varepsilon)\left(\lambda_f - \lambda_{wc}\right)} \tag{7}$$

ρ is the density, C is the heat capacity, λ is the thermal conductivity coefficient, ε is the porosity, the subscripts of *equ* means the equivalent value, f means the fluid value, and *wc* is the wick mesh value.

During the operation of heat pipe, liquified working medium in wick will return from condenser to the evaporator. The backflow of working medium is treated as a heating source in a differential equation of heat conduction. Based on the network method, Ferrandi et al. (2013) proposed a simplified method to consider the evaporation, condensation, and backflow (**Figure 3**). Based on the temperature field calculated at the latest time, the value of each temperature node can be obtained. Combined with the thermal resistance, the evaporation and condensation at vapor-liquid interface can be obtained:

$$q_{v(i)} = \frac{T_{w(i)} - T_{v(i)}}{R_{(i)} h_{v(i)}}, \quad \begin{cases} q_v(j) > 0 & evaporation \\ q_v(j) < 0 & condention \end{cases} \tag{8}$$

where q_v is the vapor mass flow rate at vapor-liquid interface, T_w is the temperature in wall subregion, T_v is the temperature in vapor space, R is the thermal resistance, and h_v is the vapor enthalpy.

Moreover, it is assumed that the fluid circulation is always constant, so backflow in wick can be obtained based on the mass conservation:

$$q_{l(i)} = \sum_{j=i+1}^{n} q_v(j) \tag{9}$$

Heating source in wick is:

$$H_{(i)} = \frac{\left(q_{l(i)} h_{l(i)} - q_{l(i-1)} h_{l(i-1)}\right)}{V_i} \tag{10}$$

q_l is the liquid mass flow rate in wick subregion, h_l is the liquid enthalpy, and V is the subregion volume. Once the mass flow rate

is known, the flow pressure drop in wick subregion can also be obtained:

$$\Delta P_l = \sum_{i=1}^{n} \Delta P_{l(i)} = \sum_{i=1}^{n} \frac{\mu L_{(i)}}{K\rho_l} \frac{1}{\varepsilon\pi\left(r_{out}^2 - r_{in}^2\right)} q_{l(i)} - \rho_l g L_{(i)} sin\theta \tag{11}$$

For permeability parameter K:

$$K = \frac{4r_g^2\varepsilon^2}{150(1-\varepsilon)^2} \tag{12}$$

μ is the dynamic viscosity, L is the length, ρ is the density, ε is the porosity, r_{out} is the outer radius of wick, r_{in} is the inner radius of wick, r_g is the capillary radius, g is the acceleration of gravity, and θ is the inclined angle.

2.2.3 Vapor Space Subregion

For vapor space, the density and specific heat capacity of vapor are the physical parameters of alkali metal (Fink and Leibowitz, 1995; Ohse, 1985; Lee et al., 1969). Therefore, for heat conduction calculation of vapor space, the key is to solve the equivalent thermal conductivity of this subregion.

Firstly, the pressure drops in the evaporator, adiabatic section, and condenser are calculated (Busse, 1967; Reid, 2002; Li et al., 2015).

$$\Delta P_v = \Delta P_{evap} + \Delta P_{adia} + \Delta P_{cond} \tag{13}$$

For evaporator:

$$\Delta P_{evap} = \left(\frac{Q_{in}}{h_{fg}}\right)^2 \frac{16 L_{evap} f}{\pi^2 \rho_v d_v^5} \left[1 + \psi\right] \tag{14}$$

The friction coefficient f can be divided into:

$$f = 16/Re_D \qquad for\ Re_D < 2000; \tag{15}$$

$$f = 0.079 Re_D^{-0.25} \qquad for\ 2000 < Re_D < 20000; \tag{16}$$

$$f = 0.046 Re_D^{-0.20} \qquad for\ 20000 < Re_D; \tag{17}$$

The axial Reynolds number is:

$$Re_D = \frac{4Q_{in}}{\pi d_v h_{fg} \mu_v} \tag{18}$$

The velocity profile correction factor ψ, is the function of the radial Reynolds number:

$$\psi = 0.61 Re_r \tag{19}$$

The radial Reynolds number is:

$$Re_r = -\frac{Q_{in}}{2\pi L_e h_{fg} \mu_v} \tag{20}$$

where Q_{in} is the heating power, h_{fg} is the latent heat of vaporization, d_v is the diameter of vapor space, μ_v is the dynamic viscosity, and L_{evap} is the length of evaporator.

For the adiabatic section:

$$\Delta P_{adia} = \frac{32\mu_v u_v L_{adia}}{d_v^2} \left[1 + \frac{1 + 0.106 Re_r}{18 + 5Re_r} \times \frac{1 - exp(-60 L_{adia}/Re_D d_v)}{2L_{adia}/Re_D d_v}\right] \tag{21}$$

For the condenser:

$$\Delta P_{cond} = -\frac{16\mu_v u_v L_{cond}}{d_v^2} \left[1 - Re_r\left(\frac{7}{9} - \frac{8\alpha}{27} + \frac{23\alpha^2}{405}\right)\right] \left(1 - \frac{x}{L_{cond}}\right)^2 \quad Re_r > -2.25 \tag{22}$$

$$\Delta P_{cond} = \frac{(-Re_r - 2)}{\rho_v\left(-1.23 Re_r + 2L_{evap}/L_{cond}\right)} \left(\frac{4Q_{in}}{\pi d_v^2 h_{fg}}\right)^2 \quad Re_r < -2.25 \tag{23}$$

The velocity profile correction α is:

$$\alpha = \frac{15}{22}\left\{5 + \frac{18}{Re_r} + \left[\left(5 + \frac{18}{Re_r}\right)^2 - \frac{44}{5}\right]^{0.5}\right\} \tag{24}$$

u_v is vapor velocity, L_{adia} is the length of adiabatic section, and L_{cond} is the length of condenser.

Combining **Eq. 14**, **Eqs 21–23**, the total pressure drop can be determined.

It is assumed that vapor in vapor space and liquified working medium in wick are homogeneous. The Clausius-Clapeyron equation is chosen to describe the relationship between temperature and pressure (Brown, 1951) :

$$\frac{dP}{dT} = \frac{\rho_v h_{fg}}{T} \tag{25}$$

Changing **Eq. 25** into the differential form:

$$\Delta T = \left(\frac{T}{\rho_v h_{fg}}\right)_{av} \Delta P \tag{26}$$

The heat transfer length along the axial direction is selected as the effective length of heat pipe (Reay et al., 2013):

$$L_{eff} = 0.5\left(L_{evap} + L_{cond}\right) + L_{adia} \tag{27}$$

Combining Fourier's Law, the equivalent thermal conductivity in vapor space can be obtained:

$$Q = -A_v \lambda \nabla T \approx A_v \lambda \frac{\Delta T}{L_{eff}} \tag{28}$$

2.3 Heat Transfer Limitations

During the operation of heat pipe, the possible heat transfer limitations include the viscosity limit, the sonic limit, the entrainment limit, and the capillary limit. When the heat transfer limitations occur, the heat transfer capacity of heat pipe will significantly reduce. In this model, the recommended equations for heat transfer limitations are adopted (Busse, 1973; Levy, 1968; Deverall et al., 1970; Tien and Chung, 1979):

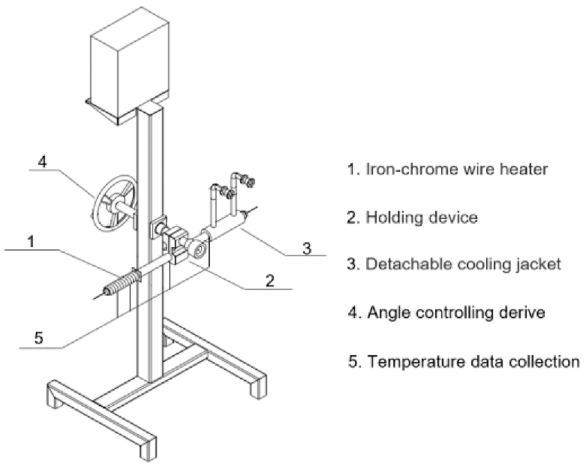

FIGURE 4 | Schematic diagram of heating system.

$$\text{viscosity limit}: \quad Q_v = \frac{d_v^2 h_{fg}}{64\mu_v L_{eff}} \rho_v P_v A_v \tag{29}$$

$$\text{sonic limit}: \quad Q_s = A_v \rho_v h_{fg} \left[\frac{\gamma R_v T}{2(\gamma+1)}\right]^{0.5} \tag{30}$$

$$\text{entrainment limit}: \quad Q_s = A_v \rho_v h_{fg} \left[\frac{\gamma R_v T}{2(\gamma+1)}\right]^{0.5} \quad Q_e = A_v h_{fg} \left[\frac{\rho_v \sigma}{2r_c}\right]^{1/2} \tag{31}$$

$$\text{capillary limit}: \quad Q_c = \frac{\frac{2\sigma}{r_c} - \rho_l g d_v \cos\phi + \rho_l g L \sin\phi}{(f_l + f_v) L_{eff}} \tag{32}$$

P_v is the vapor pressure, A_v is the cross-sectional area of vapor space, γ is the specific ratio, R_v is the gap constant, σ is the surface tension coefficient, r_c is the capillary radius, ϕ is the angle of inclination, f_l is the friction coefficient of liquified working medium, and f_v is the friction coefficient of vapor.

During the transient calculation, each limiting power will be calculated using **Eqs 29–32**. If the calculated value is less than the heating power, the heat transfer limitation will be deemed to occur, and it is assumed that the heat pipe will be damaged. In the future, further numerical analysis and experimental studies will be carried out to investigate the real characteristics of heat pipe when the heat transfer limitation occurs.

3 MODEL VALIDATION

3.1 Heating System for Heat Pipe

To verify the proposed model, a heating system for high-temperature heat pipe is built (**Figure 4**). It includes the iron-chrome wire heater, the holding device, the angle controlling derive, and the temperature data collection. The iron-chrome wire heater can provide a maximum heating power of 4000 W. To reduce heat leakage as much as possible, the evaporator and the adiabatic section are both wrapped by an insulating layer with aluminum silicate wool.

TABLE 1 | Parameter description of sodium heat pipe.

Description	Value
Length of evaporator (*mm*)	300.0
Length of adiabatic section (*mm*)	300.0
Length of condenser (*mm*)	400.0
Outer diameter of heat pipe (*mm*)	20.0
Inner diameter of vapor space (*mm*)	14.0
Wall thickness (*mm*)	2.0
Wick thickness (*mm*)	1.0
Mesh number	300
Wick structure	Screen wick
Wall material	316 L stainless steel
Wick material	316 L stainless steel

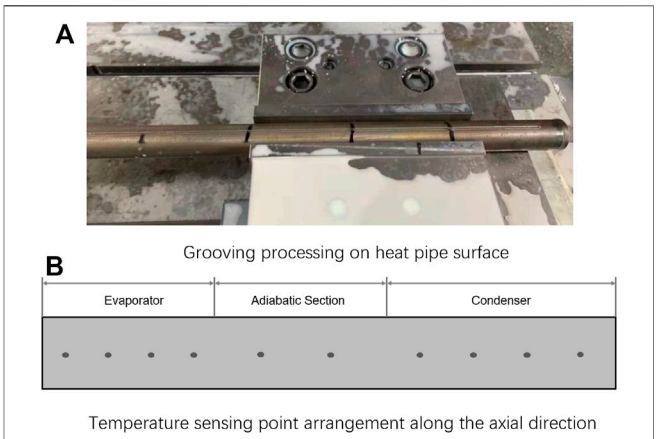

FIGURE 5 | Heat pipe processing for heating experiments. **(A)** Grooving processing on heat pipe surface. **(B)** Temperature sensing point arrangement along the axial direction.

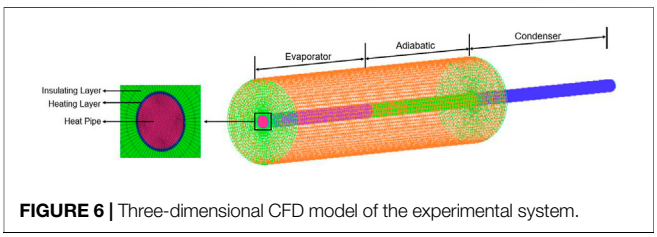

FIGURE 6 | Three-dimensional CFD model of the experimental system.

The sodium heat pipe with 1.0 m length is selected as the experiment object. The main parameters of this heat pipe are listed in **Table. 1**. To ensure the accuracy of temperature data, the groove with 1 mm depth is processed in wall. Using a high-temperature adhesive, all K-type armored thermocouples are fixed in the groove (**Figure 5A**). Then, they are fixed with the high-temperature adhesive tape. Particularly for the thermocouples in the evaporator, to reduce the effect of heating on temperature measurement, when winding the iron-chrome wire, all the measuring points are bypassed. Ten thermocouples are arranged along the axial direction; the layout position for each thermocouple is shown in **Figure 5B**.

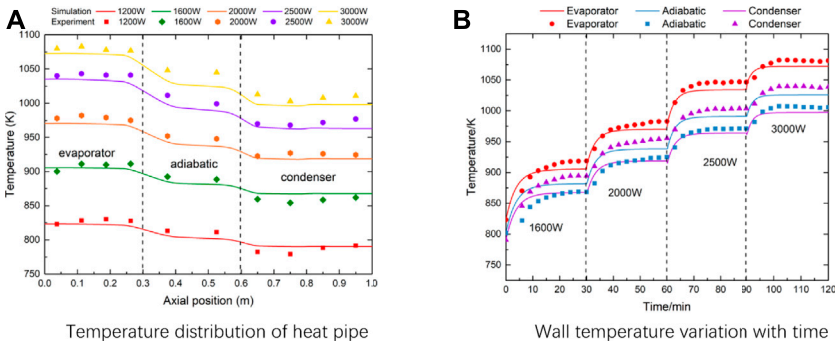

FIGURE 7 | Model verification with experimental results. **(A)** Temperature distribution of heat pipe **(B)** Wall temperature variation with time.

3.2 Validation of Propose Model

To simplify the experiment, the heat pipe is kept horizontal and is cooled by the natural convection of air. The three-dimensional CFD model of the experimental system is shown in **Figure 6**, which includes the sodium heat pipe, the electric heater, and the insulating layer. The electric heater is simplified as the thin layer with a thickness of 2 mm, and the heating source is set in this layer as equivalent to an electrical heating. The natural convection between the insulating layer and environment causes heat leakage, and the convective heat transfer coefficient can be determined by **Eqs 33, 34**. Considering the high temperature of the condenser section, not only the natural convection, but the radiation heat transfer also exist. For radiation of wall, it is treated as the radiant heat transfer to infinite space (**Eq. 35**).

$$Nu = C(Gr \cdot Pr)^n \quad \begin{cases} C = 0.85, n = 0.188 & 10^2 \le Gr \cdot Pr < 10^4 \\ C = 0.48, n = 1/4 & 10^4 \le Gr \cdot Pr < 10^7 \\ C = 0.125, n = 1/3 & 10^7 \le Gr \cdot Pr < 10^{12} \end{cases} \tag{33}$$

$$Nu = \frac{\lambda d}{h} \quad Gr = \frac{g\alpha(T_w - T_\infty)d^3}{\nu^2} \quad Pr = \frac{\nu}{a} \tag{34}$$

$$Q_{rad} = A\varepsilon\sigma T^4 \tag{35}$$

where Nu is the Nusselt number, Gr is Grashof number, Pr is the Prandtl number. ε is the emissivity of material, and σ is the Stefan-Boltzmann coefficient.

During the experiment, heat pipe is firstly heated to 1200 W to ensure the full startup of heat pipe. Then, the temperature is recorded with the increase of heating power. **Figure 7A** shows the surface temperature distribution with different heating powers, and **Figure 7B** shows the temperature variation of heat pipe with time. In these figures, the curve represents the calculated results using this model, and the scatter points represent the results measured by the experiment. According to the comparison, it is found that the temperature calculated by this model differs little from the experimental results. This model can well predict the transient characteristics of high-temperature heat pipe, and the correctness of the proposed model is verified. The difference between two results can be approximately considered to be caused by the uncertainty of parameters used in the model and the uncertainty of the experimental system. Generally, the convective heat transfer coefficient obtained from equation (**Eq. 33**) is not completely equal to the real value. The uncertainty of boundary conditions will directly lead to the deviation of calculated temperature. Meanwhile, the nonstandard operation during the experiment will also lead to uncertainty of the results. The uncertainty of an experimental system is inevitable. From **Figure 7B**, it can also be seen that with the continuous increase of heating power, operating temperature of heat pipe will be higher, resulting in the faster response of heat pipe. When heating power is 1600 W, it takes about 13 min to enter the quasi-steady state; when heating power is 3000 W, it takes only about 7 min.

Figure 8A shows the variation of total temperature difference of heat pipe under the different heating power conditions. When the heating power is low enough, more power leads to the larger temperature difference. This is because that both the temperature drop caused by vapor flow and the temperature gradient caused by heat conduction will increase with the increase of power (**Figures 8**, **9**). When the heating power is high enough, the increase of total temperature difference will become inconspicuous, which means heat pipe has entered the optimal working range. Even if the power is high enough, generated vapor can quickly transport heat to the condenser, meaning the heat pipe shows excellent isothermal property and efficient heat transfer capability.

This model does not directly calculate the vapor flow in the vapor space, however, the evaporation, the condensation, and vapor flow rate can be obtained using the simplified method mentioned in **Section 2.2.2**. The greater the power, the more evaporation and the greater vapor flow in vapor space. From **Figure 8B**, it can also be found that although there is an insulating layer wrapped outside the adiabatic section, the high-temperature vapor will still be partially condensed in this section, resulting in the reduction of vapor flow rate in vapor space. It can be predicted that if heat pipe is not well insulated, a considerable part of the heat will be transferred to the environment through the adiabatic section, leading to the decrease in heat transfer efficiency of the heat pipe.

4 APPLICATION OF PROPOSED MODEL

In this section, the proposed model will be used for numerical simulation of KRUSTY reactor. The applicability of this model

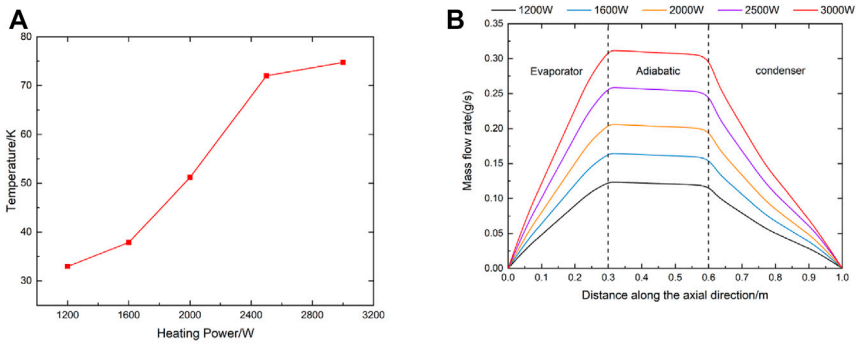

Temperature difference with different heating power

Mass flow rate with different heating power

FIGURE 8 | Calculated results using proposed model. **(A)** Temperature difference with different heating power. **(B)** Mass flow rate with different heating power.

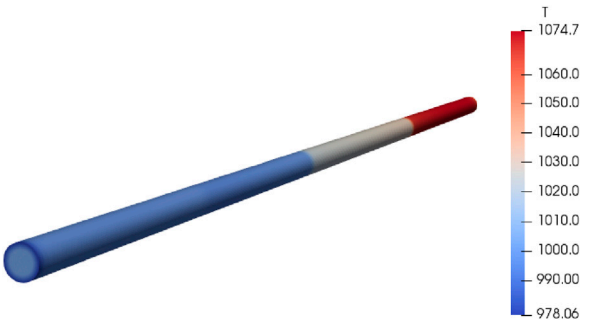

FIGURE 9 | Temperature distribution of heat pipe (3000 W).

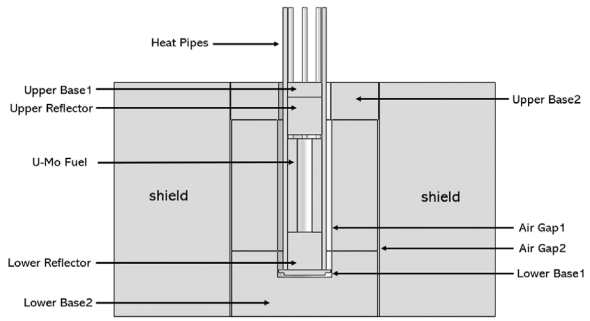

FIGURE 11 | Geometric model for KRUSTY reactor.

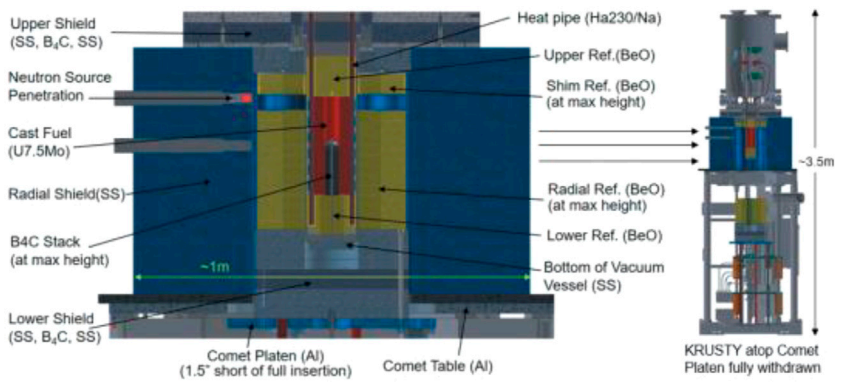

FIGURE 10 | Detailed view of the KRUSTY reactor system (Poston et al., 2020).

will be discussed. The characteristics of this reactor are also discussed.

4.1 Reactor Description

The typical heat pipe cooled reactor named KRUSTY is chosen as the research object. It is the prototype reactor to evaluate the performance of Kilopower reactor system (Poston et al., 2020; Sanchez et al., 2020; McClure et al., 2020b) The composition of KRUSTY reactor is shown in **Figure 10**. It includes the U-Mo fuel, the BeO reflector, the control rod, the shielding layer, the Na heat pipes, the vacuum vessel, the lift table, and the Stirling generators. The thermal power of the reactor is 5.0 kW. In total, eight sodium heat pipes are used to transport heat to the generators. The Stirling cycle is adopted to generate 1kW electric power. To simplify the modeling, the lift table and support structure are all ignored; only the reactor is

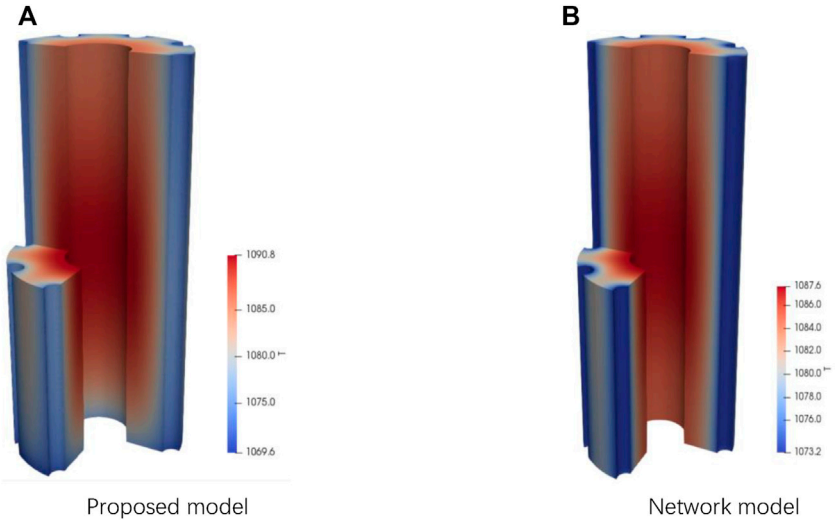

FIGURE 12 | Calculated temperature distribution of reactor core. **(A)** Proposed model. **(B)** Network model.

established (**Figure 11**). The Stirling generators are also ignored, the operation of generators is approximated by setting reasonable boundary conditions of the condenser section of heat pipes.

The outer surface of the reactor always maintains natural convection with the environment. During the steady state analysis (**section 4.2**), the boundary of the condenser section is set as the fixed temperature. During the load-following analysis (**section 4.3**), it is set as the fixed temperature gradient.

4.2 Steady State Analysis

In this section, the steady state of KRUSTY reactor system is investigated. Both the proposed model in this paper and the network model are adopted. The boundary temperature of the condenser of heat pipes is set as 1,052.0 K, and the fission power is set as 5.0 kW. **Figure 12** shows the fuel temperature distribution using the proposed model and network model. For network model, lumped temperature is used to represent the temperature distribution of a specific subregion. Temperature on the contact surface between fuel and heat pipe is always consistent. However, the proposed model can consider the nonuniformity of temperature on contact surface. Compared with the results using network model, the peak temperature of fuel increases from 1,087.6 k to 1,090.8 k, and the total temperature difference increases from 14.4 k to 21.2 k. For KRUSTY reactor, the operation is sensitive to fuel temperature, so the slight variation of temperature may cause an obvious change in fission power. Therefore, it is important for the numerical calculation of heat pipe cooled reactor to obtain the accurate temperature distribution as much as possible. Moreover, for reactor systems with higher power density and more complex heat pipe arrangement, it can be expected that the temperature non-uniform effect of the contact surface will have a more significant impact on the operation of the reactor.

The reason for this phenomenon is the uneven power distribution in space. **Figure 13** shows the axial distribution of

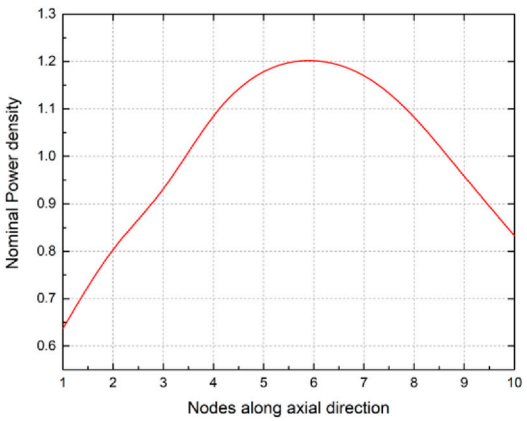

FIGURE 13 | Power density distribution along axial distribution.

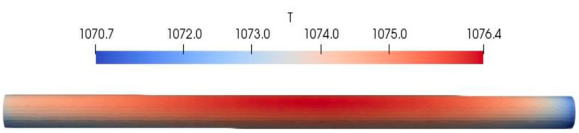

FIGURE 14 | Temperature distribution of contact surface between fuel and heat pipe.

power density obtained by Monte Carlo code RMC. Because of the large aspect ratio of this reactor, the power density presents the distribution of a large value in the middle and a small value on both sides. For reactor systems with a solid attribute, heat conductance is the only way for heat transfer. Based on Fourier's law, higher heat flux will lead to a larger temperature gradient, resulting in non-uniformity of temperature distribution

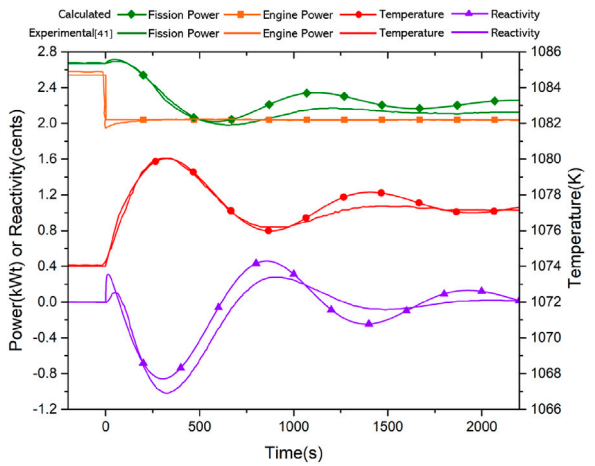

FIGURE 15 | The comparison of calculated results between experimental results (Poston, 2017).

on the contact surface. It directly affects the actual temperature distribution of the core (**Figure 13**). From **Figures 12–14**, it can be concluded that only the three-dimensional modeling of heat pipes and the coupling calculation between heat pipe and the reactor core can obtain the accurate results of heat transfer. The results obtained using the uniform temperature assumption will deviate from the reality.

4.3 Load-Following Analysis

In this section, the load-following transient is selected. At T = 0.0 s, the cooling power of the condenser of heat pipe is set as 2.54 kW to represent the decrease of engine power, and the initial fission power is set as 2.67 kW. The difference between the two values is the heat leakage through shield. The comparison between simulated results using the proposed model and experimental results shows in **Figure 15**. From that, it can be concluded that there is a slight difference between the two results, and proposed model is suitable for the analysis of heat pipe cooled reactor system. On the one hand, to realize the coupling calculation of the heat pipe cooled reactor, the proposed heat pipe model does not directly calculate the working fluid circulation, but adopts a simplified method, which may cause uncertainty to a certain extent. Meanwhile, the detailed information about this experiment is inadequate, and the three-dimensional modeling and the setting of boundary conditions may not be accurate enough.

During this accident, with the decrease of engine power, heat transport power of heat pipes also reduces, leading to the increase of fuel temperature. Benefiting from the reactivity feedback of fuel, fission power gradually decreases to slow the rate of temperature rise. At about T = 300.0 s, fuel reaches the peak temperature of about 1,080.3 K. At about T = 2,200.0 s, the reactor reaches the new steady state. In the early stage of this accident, the reactor will be briefly supercritical, resulting in the increase in reactor power. This is because heat pipes absorb less power, leading to the increase of Na inventory in the reactor (Poston, 2017). The proposed model can calculate the variation of absorbed power of heat pipes. Using the feedback coefficient, this important phenomenon can be preliminarily simulated (Guo et al., 2022). This model does not directly calculate the two-phase flow of working medium in heat pipe, and the difference is acceptable.

Figure 16 shows the temperature distribution of reactor T = 0.0 s and T = 2,200.0 s respectively. Due to the high thermal conductivity of material and the compactness of this reactor, the total temperature difference of the reactor is small enough, and the peak temperature locates at the inner surface of the fuel. After the load-following accident, reactor temperature rises slightly due to the reduction of the output power of the Stirling generators. During this accident, the control rod always remains stationary, and the reactor only relies on

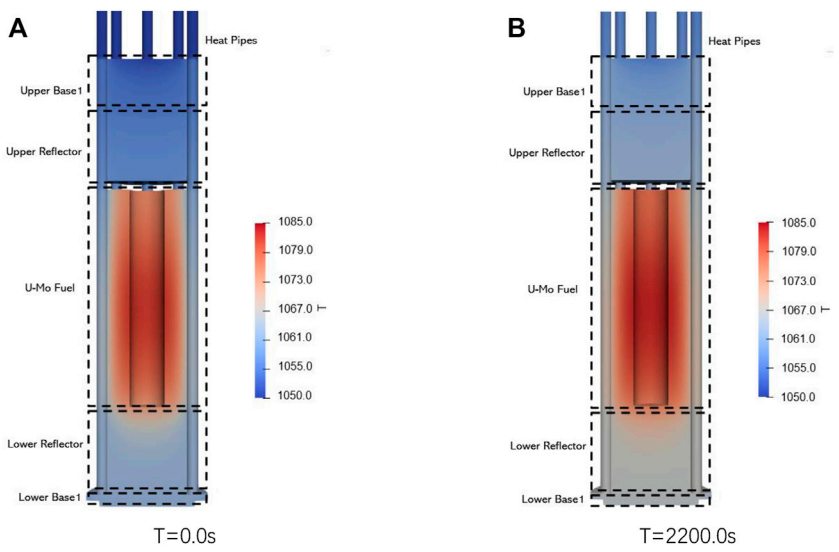

FIGURE 16 | Temperature distribution of reactor. **(A)** T = 0.0s. **(B)** T = 2,200.0s.

the reactivity feedback to achieve the power regulation, showing the automatic-stability-regulation ability of this reactor.

5 CONCLUSION

In this paper, the super thermal conductivity model (STCM) for high-temperature heat pipe is proposed, which simplifies the vapor flow and heat transport in vapor space into heat conductance. Combined with the network method, the proposed model can preliminarily calculate the evaporation, condensation, and flow rate of working medium. Adding the heat transfer limitation, it can realize the judgment of heat pipe safety. According to the comparison with the experimental results, the accuracy of the model is verified. It can well predict the temperature variation of high-temperature heat pipes under different conditions.

Using this model, the numerical simulation on KRUSTY reactor is executed. During the steady state calculation, it can be found that the proposed model can obtain a more realistic fuel temperature distribution. For load-following transient calculation, calculated results are in good agreement with the experimental results, showing the applicability of the proposed model to this type of reactor system. It can be a powerful tool for the design and simulation of heat pipe cooled reactor systems.

DATA AVAILABILITY STATEMENT

The raw data supporting the conclusion of this article will be made available by the authors, without undue reservation.

AUTHOR CONTRIBUTIONS

YG, ZL, and ZS contributed to conception and design of the study. YG wrote the first draft of the manuscript. All authors contributed to manuscript revision, read, and approved the submitted version.

FUNDING

This study was funded by the National Key Research and Development Project of China, No. 2020YFB1901700, Science Challenge Project (TZ2018001), Project 11775126/11775127 by National Natural Science Foundation of China, and Tsinghua University Initiative Scientific Research Program.

REFERENCES

Annamalai, S., and Ramalingam, V. (2011). Experimental Investigation and CFD Analysis of a Air Cooled Condenser Heat Pipe. *Therm. Sci.* 15 (3), 759–772. doi:10.2298/tsci100331023a

Asmaie, L., Haghshenasfard, M., Mehrabani-Zeinabad, A., and Nasr Esfahany, M. (2013). Thermal Performance Analysis of Nanofluids in a Thermosyphon Heat Pipe Using CFD Modeling. *Heat Mass. Transfer* 49 (5), 667–678. doi:10.1007/s00231-013-1110-6

Brown, O. L. I. (1951). The Clausius-Clapeyron Equation. *J. Chem. Educ.* 28 (8), 428. doi:10.1021/ed028p428

Busse, C. A. (1967). "Pressure Drop in the Vapor Phase of Long Heat Pipes," in Proc. Thermionic Conversion Specialist Conference, United States, November 1-2, 1967, 391–398.

Busse, C. A. (1973). Theory of the Ultimate Heat Transfer Limit of Cylindrical Heat Pipes. *Int. J. Heat Mass Transfer* 16 (1), 169–186. doi:10.1016/0017-9310(73)90260-3

Cao, Y., and Faghri, A. (1993). Simulation of the Early Startup Period of High-Temperature Heat Pipes from the Frozen State by a Rarefied Vapor Self-Diffusion Model[J]. *J. Heat Transfer* 114 (4), 1028–1035. doi:10.1115/1.2910655

Cao, Y., and Faghri, A. (1993). A Numerical Analysis of High-Temperature Heat Pipe Startup from the Frozen State. *J. Heat Transfer* 115 (1), 247–254. doi:10.1115/1.2910657

Cao, Y., and Faghri, A. (1991). Transient Two-Dimensional Compressible Analysis for High-Temperature Heat Pipes with Pulsed Heat Input. *Numer. Heat Transfer, A: Appl.* 18 (4), 483–502. doi:10.1080/10407789008944804

Cao, Y., and Faghri, A. (1992). Closed-form Analytical Solutions of High-Temperature Heat Pipe Startup and Frozen Startup Limitation. *[J] J. Heat Transfer* 114 (Nov), 1028–1035. doi:10.1115/1.2911873

Chi, S. W. (1976). *Heat Pipe Theory and Practice [M]*. Washington, DC: Hemispere Publishing Corporation.

Costello, F. A., Montague, A. F., and Merrigan, M. A. (1986). *Detailed Transient Model of a Liquid-Metal Heat Pipe. Costello (FA), Inc* NM (USA): Los Alamos National Lab

Deverall, J. E., Kemme, J. E., and Florschuetz, L. W. (1970). *Sonic Limitations and Startup Problems of Heat Pipes*. Los Alamos, NM (United States): Los Alamos National Lab.

El-Genk, M. S., and Tournier, J. M. (2004). Conceptual Design of HP-STMCs Space Reactor Power System for 110 kWe. *AIP Conf. Proc. Am. Inst. Phys.* 699 (1), 658–672.

Faghri, A. (2014). Heat Pipes: Review, Opportunities and Challenges. *Front. Heat Pipes* 5 (1). doi:10.5098/fhp.5.1

Ferrandi, C., Iorizzo, F., Mameli, M., Zinna, S., and Marengo, M. (2013). Lumped Parameter Model of Sintered Heat Pipe: Transient Numerical Analysis and Validation. *Appl. Therm. Eng.* 50 (1), 1280–1290. doi:10.1016/j.applthermaleng.2012.07.022

Fink, J. K., and Leibowitz, L. (1995). *Thermodynamic and Transport Properties of Sodium Liquid and Vapor*. Lemont, IL, United States: Argonne National Lab

Guo, Y. C., Li, Z. G., Wang, K., and Su, Z. (2022). A Transient Multiphysics Coupling Method Based on OpenFOAM for Heat Pipe Cooled Reactors[J]. *Sci. China Technol. Sci.* 65, 102–114. doi:10.1007/s11431-021-1874-0

Lee, C. S., Lee, D. I., and Bonilla, C. F. (1969). Calculation of the Thermodynamic and Transport Properties of Sodium, Potassium, Rubidium and Cesium Vapors to 3000°K. *Nucl. Eng. Des.* 10 (1), 83–114. doi:10.1016/0029-5493(69)90008-9

Levy, E. K. (1968). Theoretical Investigation of Heat Pipes Operating at Low Vapor Pressures. *ASME J. Eng. Industry.* 90, 547–552. doi:10.1115/1.3604687

Li, H., Jiang, X., Chen, L., Ning, Y., Pan, H., and Tengyue, M. (2015). Heat Transfer Capacity Analysis of Heat Pipe for Space Reactor[J]. *At. Energ. Sci. Tech.* 49 (1), 7. doi:10.7538/yzk.2015.49.01.0089

Lin, Z., Wang, S., Shirakashi, R., and Winston Zhang, L. (2013). Simulation of a Miniature Oscillating Heat Pipe in Bottom Heating Mode Using CFD with Unsteady Modeling. *Int. J. Heat Mass Transfer* 57 (2), 642–656. doi:10.1016/j.ijheatmasstransfer.2012.09.007

Liu, X., Zhang, R., Liang, Y., Tang, S., Wang, C., Tian, W., et al. (2020). Core thermal-hydraulic Evaluation of a Heat Pipe Cooled Nuclear Reactor. *Ann. Nucl. Energ.* 142, 107412. doi:10.1016/j.anucene.2020.107412

Ma, Y., Chen, E., Yu, H., Zhong, R., Deng, J., Chai, X., et al. (2020). Heat Pipe Failure Accident Analysis in Megawatt Heat Pipe Cooled Reactor. *Ann. Nucl. Energ.* 149, 107755. doi:10.1016/j.anucene.2020.107755

Mcclure, P. R. (2015). *Design of Megawatt Power Level Heat Pipe Reactors*. Los Alamos, NM (United States): Los Alamos National Lab

McClure, P. R., Poston, D. I., Clement, S. D., Restrepo, L., Miller, R., and Negrete, M. (2020). KRUSTY Experiment: Reactivity Insertion Accident Analysis. *Nucl. Tech.* 206 (Suppl. 1), S43–S55. doi:10.1080/00295450.2020.1722544

McClure, P. R., Poston, D. I., Gibson, M. A., Mason, L. S., and Robinson, R. C. (2020). Kilopower Project: The KRUSTY Fission Power Experiment and Potential Missions. *Nucl. Tech.* 206 (Suppl. 1), S1–S12. doi:10.1080/00295450.2020.1722554

Ohse, R. W. (1985). *Handbook of Thermodynamic and Transport Properties of Alkali Metals*. Oxford: Blackwell.

Poston, D. I. (2017). *Space Nuclear Reactor Engineering*. Los Alamos, NM (United States): Los Alamos National Lab

Poston, D. I. (2001). The Heatpipe-Operated Mars Exploration Reactor (HOMER). *AIP Conf. Proc. Am. Inst. Phys.* 552 (1), 797–804. doi:10.1063/1.1358010

Poston, D. I., Gibson, M. A., Godfroy, T., and McClure, P. R. (2020). KRUSTY Reactor Design. *Nucl. Tech.* 206 (Suppl. 1), S13–S30. doi:10.1080/00295450.2020.1725382

Reay, D., McGlen, R., and Kew, P. (2013). *Heat Pipes: Theory, Design and Applications*. Oxford, United Kingdom: Butterworth-Heinemann.

Reid, R. S. (2002). Heat Pipe Transient Response Approximation. *AIP Conf. Proc. Am. Inst. Phys.* 608 (1), 156–162. doi:10.1063/1.1449720

Sanchez, R., Grove, T., Hayes, D., Goda, J., McKenzie, G., Hutchinson, J., et al. (2020). Kilowatt Reactor Using Stirling TechnologY (KRUSTY) Component-Critical Experiments. *Nucl. Tech.* 206 (Suppl. 1), S56–S67. doi:10.1080/00295450.2020.1722553

Tien, C. L., and Chung, K. S. (1979). Entrainment Limits in Heat Pipes. *Aiaa J.* 17 (6), 643–646. doi:10.2514/3.61190

Tournier, J. M., and El-Genk, M. S. (1992). "HPTAM"heat-pipe Transient Analysis Model: an Analysis of Water Heat Pipes. *AIP Conf. Proc. Am. Inst. Phys.* 246 (1), 1023–1037. doi:10.1063/1.41777

Vasiliev, L. L., and Kanonchik, L. E. (1993). *Dynamics of Heat Pipe Start-Up from a Frozen State. AV Luikov Heat and Mass Transfer Institute, Byelorussian Academy of Sciences*. Minsk, Belarus: CIS. unpublished data.

Wang, C., Sun, H., Tang, S., Tian, W., Qiu, S., and Su, G. (2020). Thermal-hydraulic Analysis of a New Conceptual Heat Pipe Cooled Small Nuclear Reactor System. *Nucl. Eng. Tech.* 52 (1), 19–26. doi:10.1016/j.net.2019.06.021

Yan, B. H., Wang, C., and Li, L. G. (2020). The Technology of Micro Heat Pipe Cooled Reactor: A Review. *Ann. Nucl. Energ.* 135, 106948. doi:10.1016/j.anucene.2019.106948

Yuan, Y., Shan, J., Zhang, B., Gou, J., Zhang, B., Lu, T., et al. (2016). Study on Startup Characteristics of Heat Pipe Cooled and AMTEC Conversion Space Reactor System. *Prog. Nucl. Energ.* 86, 18–30. doi:10.1016/j.pnucene.2015.10.002

Yue, C., Zhang, Q., Zhai, Z., and Ling, L. (2018). CFD Simulation on the Heat Transfer and Flow Characteristics of a Microchannel Separate Heat Pipe under Different Filling Ratios. *Appl. Therm. Eng.* 139, 25–34. doi:10.1016/j.applthermaleng.2018.01.011

Zuo, Z. J., and Faghri, A. (1998). A Network Thermodynamic Analysis of the Heat Pipe. *Int. J. Heat Mass Transfer* 41 (11), 1473–1484. doi:10.1016/s0017-9310(97)00220-2

Conflict of Interest: The authors declare that the research was conducted in the absence of any commercial or financial relationships that could be construed as a potential conflict of interest.

frontiers in Energy Research

ORIGINAL RESEARCH
published: 14 February 2022
doi: 10.3389/fenrg.2022.841998

Uncertainty Analysis of Reactor Structure Material Activation Calculation Induced From Nuclear Data

Wu Jiebo[1,2], *Yang Chao*[1,2]*, *Yu Tao*[1,2]* *and Chen Zhenping*[1,2]

[1]School of Nuclear Science and Technology, University of South China, Hengyang, China, [2]Research Center for Digital Nuclear Reactor Engineering and Technology of Hunan Province, University of South China, Hengyang, China

Highly accurate activation calculations are the basis of radiation protection optimization design, and the accuracy of activation calculations depends on nuclear data. Based on the ENDF/B-VIII.0 and JEFF3.3 decay evaluation libraries, the influence of different nuclear data on the reactor structural material activation calculation is analyzed, and the nuclear data-related sensitivity and uncertainty quantification of radioactivity, decay heat and photon sources are carried out by the global sensitivity analysis method and the Latin Hypercube Sampling method. Based on uncertainty data in ENDF/B-VIII.0 and JEFF3.3, quantifying the uncertainty of radioactivity, decay heat and photon source in the shutdown dose calculation of reactor structural materials, the maximum uncertainty of radioactivity and decay heat reach 4.54 and 1.45%, respectively. The half-life and decay energy of ^{55}Fe are the main sources of uncertainty.

Keywords: nuclear data, activation calculation, uncertainty quantification, sensitivity analysis, evaluation library

OPEN ACCESS

Edited by:
Yapei Zhang,
Xi'an Jiaotong University, China

Reviewed by:
Liangzhi Cao,
Xi'an Jiaotong University, China
Kan Wang,
Tsinghua University, China

***Correspondence:**
Yang Chao
yangc066@163.com
Yu Tao
yutao29@sina.com

Specialty section:
This article was submitted to Nuclear Energy, a section of the journal Frontiers in Energy Research

Received: *23 December 2021*
Accepted: *27 January 2022*
Published: *14 February 2022*

Citation:
Jiebo W, Chao Y, Tao Y and Zhenping C (2022) Uncertainty Analysis of Reactor Structure Material Activation Calculation Induced From Nuclear Data. Front. Energy Res. 10:841998. doi: 10.3389/fenrg.2022.841998

INTRODUCTION

Nuclear data are the basic input parameters of activation calculations, and their accuracy directly affects the activation calculation results (Liem and Sembiring, 2013; Tsilanizara and Huynh, 2021). Uncertainties are unavoidable when nuclear data are obtained through experimental measurements (Awan et al., 2012; Katakura, 2013), and nuclear data uncertainties are propagated in activation calculations, which eventually affect the accuracy of activation calculation results. Therefore, it is necessary to quantify the uncertainty in the activation calculation results caused by nuclear data. ORIGEN2 is a typical depletion and decay code widely used in the design of nuclear power plants and reprocessing plants (Croff, 1980; Croff, 1983). The code uses the matrix exponential method to solve the fuel inventory equation, which is a well-developed theoretical method, so its calculation accuracy depends mainly on the accuracy of the activation library (Mehboob et al., 2013; Foudil et al., 2017). The current activation library that comes with the ORIGEN2 code is processed based on the ENDF/B-VI.8 basic evaluation data library, which inevitably influences the activation calculation results. Therefore, the activation library for the ORIGEN2 code is obtained by processing nuclear data based on the latest version of the JEFF3.3 and ENDF/B-VIII.0 decay evaluation libraries (McLane, 1996; Herman, 2009; Brown

TABLE 1 | Minimum samples with different confidence levels and tolerance intervals.

	Single-side limit distribution			Bilateral limit distribution		
Confidence	0.9	0.95	0.99	0.9	0.95	0.99
0.9	22	45	239	38	77	388
0.95	29	59	299	46	93	473
0.99	44	90	459	64	130	663

TABLE 2 | Nuclide composition of 6,115 structural materials.

Nuclide components									
nuclide	C	^{28}Si	^{50}Cr	^{52}Cr	^{53}Cr	^{54}Cr	^{55}Mn	^{54}Fe	^{56}Fe
mass fraction	0.01%	0.02%	0.83%	15.92%	1.81%	0.45%	1.98%	4.07%	63.29%
nuclide	^{57}Fe	^{58}Fe	^{58}Ni	^{60}Ni	^{61}Ni	^{62}Ni	^{64}Ni	^{94}Mo	
mass fraction	1.45%	0.21%	6.77%	2.59%	0.11%	0.36%	0.09%	0.03%	

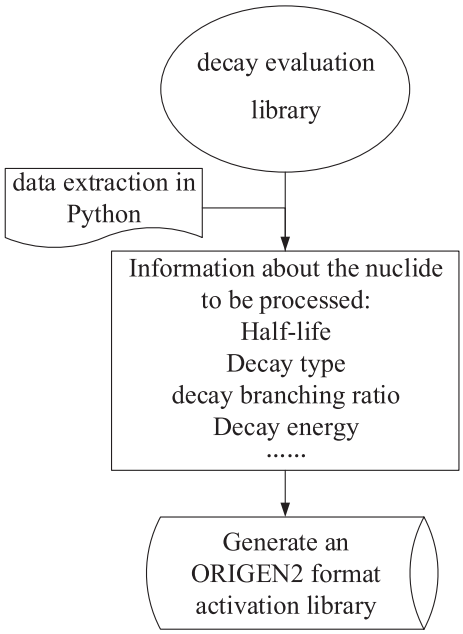

FIGURE 1 | ORIGEN2 activation library processing flowchart.

TABLE 3 | The nuclides with large contributions to radioactivity, decay heat and photon source.

Fraction of radioactivity contribution					
Nuclides	0–0.5 h	Nuclides	0.5 h-30 d	Nuclides	30days-48a
^{56}Mn	50–54%	^{54}Mn	1–5%	^{55}Fe	15–80%
^{55}Fe	15–17%	^{55}Fe	14–47%		
^{58}Co	2–3%	^{58}Co	2–6%		
^{64}Cu	0–1%				
^{66}Cu	0–1%				

Fraction of decay heat contribution					
Nuclides	0–0.5 h	Nuclides	0.5 h-30 d	Nuclides	30days-48a
^{56}Mn	95–96%	^{54}Mn	1–29%	^{60}Co	2–25%
^{58}Co	1–2%	^{55}Fe	0–3%	^{55}Fe	1–16%
		^{58}Co	1–45%		

Fraction of photon source contribution			
Nuclides	0–0.5 h	Nuclides	0.5 h-30 d
^{56}Mn	50–87%	^{58}Co	1–83%

et al., 2018; Trkov et al., 2018; Plompen et al., 2020). The two new versions of the decay evaluation libraries are compared to the ENDF/B-VI.8. First, the improvement of the experimental method making the measured nuclear data closer to the real values. Second, the new version of the evaluation libraries gives the variance information that can evaluate the uncertainty of the nuclear data, which is the basis for the uncertainty analysis performed in the paper. Therefore, based on uncertainty data in ENDF/B-VIII.0 and JEFF3.3, the uncertainty analysis program SIMLAB is used to carry out uncertainty quantification analysis and sensitivity analysis of the activation source term radioactivity, decay heat and photon source of the reactor structural materials after shutdown.

THEORETICAL FOUNDATION

Activation Library Processing

The processing flow of the ORIGEN2 activation library is shown in **Figure 1**. Based on ENDF/B-VIII.0 and JEFF3.3 decay evaluation libraries, the half-life, decay energy, decay type, decay branching ratio and abundance of nuclides to be processed are read, and then the data are stored according to activation product group, fission product group and actinide

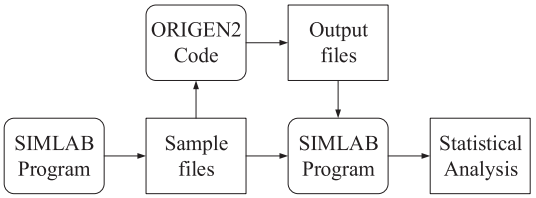

FIGURE 2 | SIMLAB and ORIGEN2 coupling method.

group like the format of the ORIGEN2 activation library. Finally, the card image format library is generated.

Uncertainty Analysis Theory

Uncertainty quantification refers to determining the effect of input uncertainty on the model output. The main data-driven algorithms for uncertainty quantification include: the sampling statistics method, the alternative model method, the UMAE method (uncertainty methodology based on accuracy extrapolation), and the deterministic approach (Briggs, 2009).

The Latin Hypercube Sampling method was chosen as the sampling method due to its widespread use in reactor physics. For the number of samples, a nonparametric statistical method (Wilks formula) was used to determine the minimum number of n that samples required, based on the confidence level b of the distribution interval and the probability of the output parameter a. The Wilks formula is (Wilks, 1942):

$$1 - a^n \geq b \tag{1}$$

$$(1 - a^n) - n(1 - a)a^{n-1} \geq b \tag{2}$$

Eq. 1 applies to the single-side limit distribution, and **Eq. 2** applies to the bilateral limit distribution.

The minimum sample size n satisfying different confidence levels and tolerance intervals calculated by the Wilks formula are shown in **Table 1**. Based on nonparametric statistical theory, when the minimum sample size is 59, the upper tolerance limit value of the target parameter takes the maximum value; when the minimum sample size is 93, the upper tolerance limit value of the target parameter takes the next largest value (Mui and Kozlowski, 2018).

Uncertainty Analysis Program SIMLAB

Based on the above approach, this paper uses the SIMLAB program developed by the JRC (Joint Research Center) in Europe to perform uncertainty analysis (Bieda, 2012), which applies the LHS method, and has been carried out for uncertainty and sensitivity analysis in the fields of economics as well as fuzzy inference systems. The SIMLAB program includes a statistical preprocessing module, an execution module, and a statistical postprocessing module. The statistical preprocessing module of the SIMLAB program provides parameter distribution types and sampling methods, and users can choose different parameter distributions in SIMLAB, including normal, uniform, and discrete distributions. You can also create a new functional relationship and visualize the parameter distributions in the statistical preprocessing module of SIMLAB. The execution

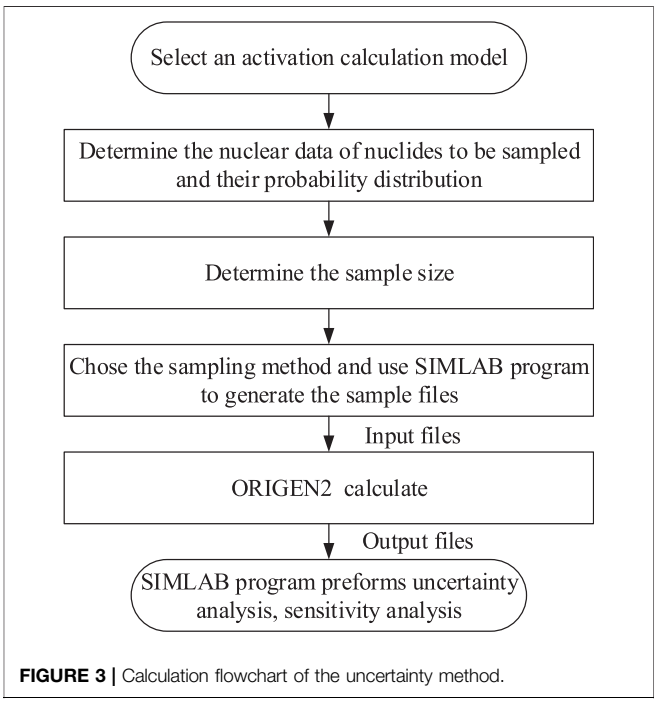

FIGURE 3 | Calculation flowchart of the uncertainty method.

TABLE 4 | Uncertainty input parameter information.

Serial number	Nuclides	Parameter	Unit	Distribution	Uncertainty	Base value
n1	^{54}Mn	Half-life	s	Normal	±0.11%	2.696×10^{7}
n2	^{54}Mn	Decay energy	MeV	Uniform	±0.05%	8.401×10^{-1}
n3	^{56}Mn	Half-life	s	Normal	±0.10%	9.284×10^{3}
n4	^{56}Mn	Decay energy	MeV	Uniform	±1.14%	2.523×10^{0}
n5	^{55}Fe	Half-life	s	Normal	±5.25%	8.653×10^{7}
n6	^{55}Fe	Decay energy	MeV	Uniform	±6.56%	5.843×10^{-3}
n7	^{58}Co	Half-life	s	Normal	±0.11%	6.122×10^{6}
n8	^{58}Co	Decay energy	MeV	Uniform	±0.25%	9.788×10^{-1}
n9	^{64}Cu	Half-life	s	Normal	±0.30%	4.572×10^{4}
n10	^{64}Cu	Decay energy	MeV	Uniform	±0.20%	2.629×10^{-1}
n11	^{66}Cu	Half-life	s	Normal	±0.39%	3.072×10^{2}
n12	^{66}Cu	Decay energy	MeV	Uniform	±0.17%	1.165×10^{0}

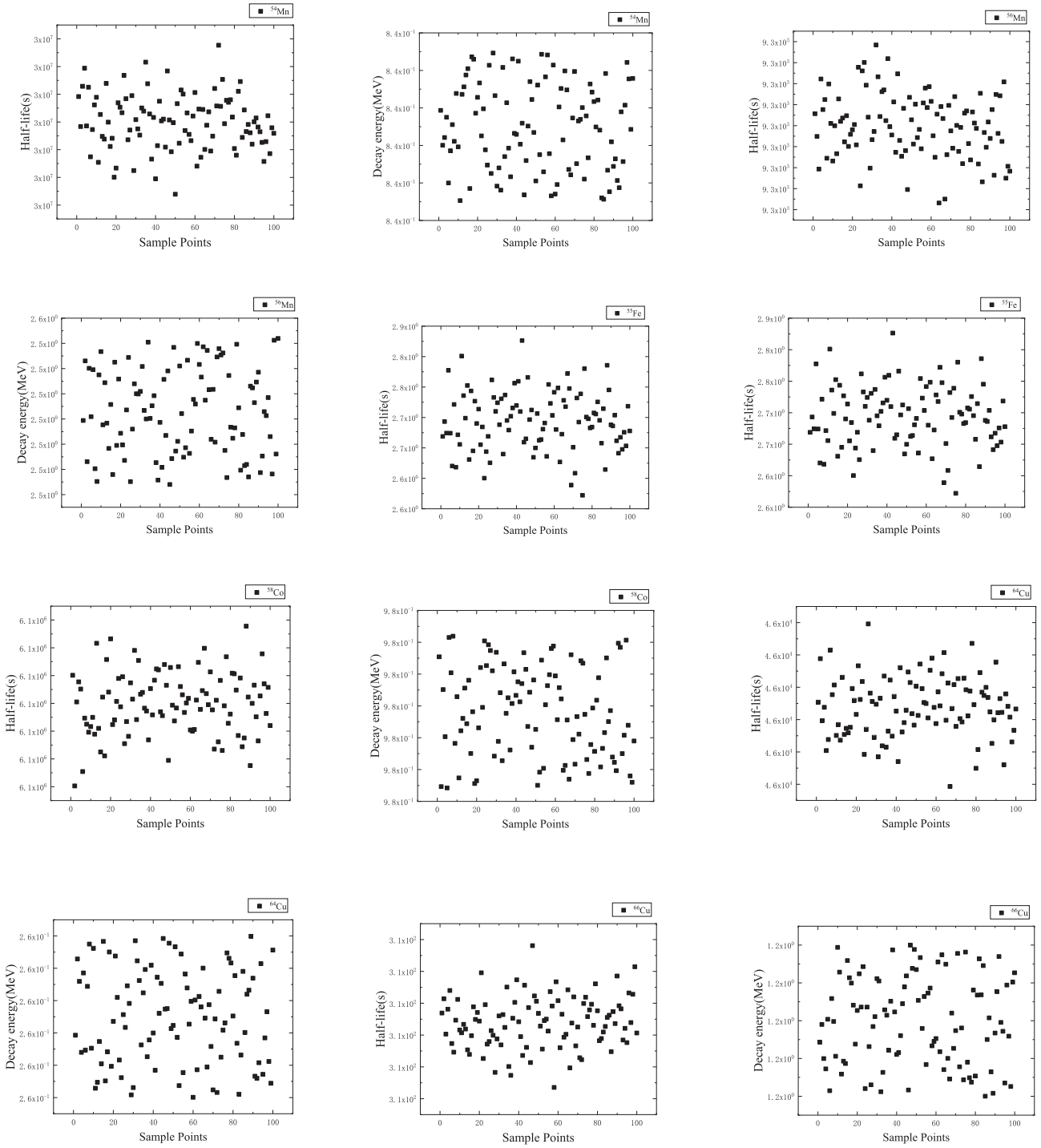

FIGURE 4 | Distribution of half-lives and decay energies of nuclides.

module needs a seed number (usually with more than a five-digit number) and then samples to generate the required number of samples. The statistical postprocessing module of the SIMLAB program is used for uncertainty analysis and sensitivity assessment. Uncertainty analysis can visualize the probability distribution of parameters and give statistical results such as the mean value, variance, standard deviations and maximum and minimum values of parameters. Sensitivity assessment gives the correlation coefficient or sensitivity index of input and output parameters.

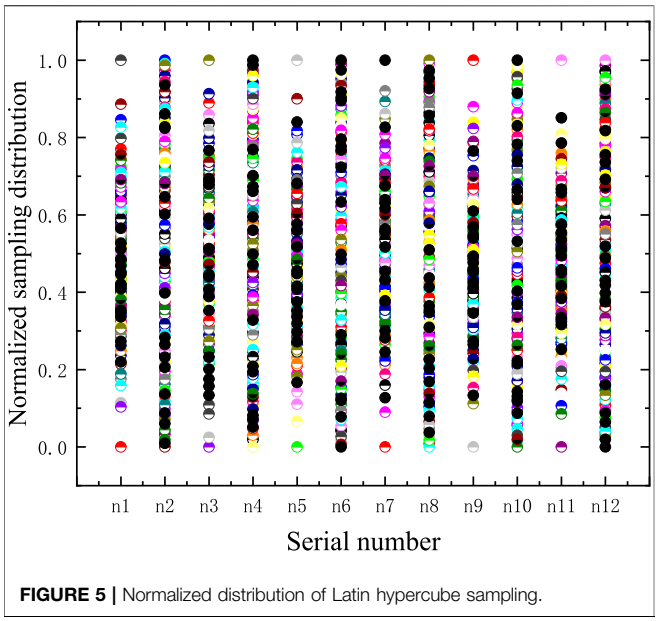

FIGURE 5 | Normalized distribution of Latin hypercube sampling.

Activation Calculation Uncertainty Analysis

As in **Figure 2**, the uncertain input parameters in the activation calculation are randomly sampled through the model import module interface in the SIMLAB program to generate the sample files. First, the sample files are passed to the ORIGEN2 code, and the output files are obtained by calculation. Second, the output files are passed back to the SIMLAB program through the external interface of the execution module, and the SIMLAB program is applied to statistically analyze the correlation coefficients of the sample input parameters and the output parameters. Finally, a sensitivity analysis of the output parameters is performed. The calculation process is shown in **Figure 3**: 1) Determine the nuclides that have important effects on the radioactivity, decay heat and photon source in the activation calculation model; 2) Specify the range of values and probability distribution of nuclear data of nuclides, select the sampling method and obtain different sample combinations; 3) Pass the sample combinations obtained by sampling to the ORIGEN2 code for calculation and obtain the output file; 4) Pass the output file to the SIMLAB program and use the program to perform sensitivity analysis on the results and obtain the correlation coefficients of the input and output values.

REACTOR STRUCTURAL MATERIAL ACTIVATION CALCULATION UNCERTAINTY ANALYSIS

Based on the above analysis, different nuclear data have a great impact on the activation calculation. Therefore, it is necessary to quantify the uncertainties in activation calculations introduced by the differences in nuclear data, and to clarify the important influencing nuclides in activation calculations for reactor structural materials.

NUREG/CR-6115 Reactor Structural Material Model

The important structural components in a pressurized water reactor are covered in the NUREG/CR-6115 reactor model. The reactor core has a total of 204 boxes of 21.485 × 21.485 × 335.28 cm^3 fuel assemblies (Carew, 2001). The top and bottom of the core are reactor reflectors, and the radial periphery of the core is an envelope with a thickness of 1.5875 cm. The nuclide composition of the structural materials of the pressurized water reactor model is shown in **Table 2**.

Selection of Uncertainty Parameters

First, the NUREG/CR-6115 reactor structure material model was irradiated for 50 years with a neutron injection rate of 1×10^{13} cm^{-2} s^{-1} and a shutdown time of 48 years. Using ORIGEN2 to output the nuclides with large contributions to radioactivity, decay heat and photon source during the 48-years time period after reactor shutdown.

We can see in **Table 3**, that dividing the time after reactor shutdown into three phases, the nuclides that have a large influence on the radioactivity, decay heat and photon source are ^{54}Mn, ^{56}Mn, ^{55}Fe, ^{58}Co, ^{64}Cu and ^{66}Cu, so after comprehensive consideration, these six nuclides are finally selected as uncertainty input parameters.

The six nuclides were finally determined as uncertainty input parameters with normal distribution of half-life and uniform distribution of decay energy, where the uncertainty variance information of decay energy is given by the evaluation data library of ENDF/B-VIII.0, and the uncertainty variance information of half-life is not provided by the evaluation data library, so the uncertainty information is obtained by the differences of ENDF/B-VI.8, ENDF/B-VIII.0 and JEFF3.3, with a more conservative uncertainty range taken as shown in **Table 4**. It should be pointed out that the uncertainty given in **Table 4** is only part of the uncertainty sources, in which only six radionuclides that have a clear influence on radioactivity and decay heat in the reactor structure material are considered.

Finally, the important characteristic parameters of radioactivity, decay heat and photon source are used as uncertainty output parameters in the analysis of NUREG/CR-6115 reactor structural material activation calculations.

Uncertainty Analysis

The Latin hypercube method was selected to sample the input parameters, and according to **Table 1**, the minimum sample size to satisfy the two 95% bilaterally limited distributions was 93. For conservative estimation, 100 samples were taken as inputs (Zhao et al., 2021), and the 12 input parameters were sampled with the distribution shown in **Figure 4**.

To detect the distribution of the input parameters intuitively, the input parameters are normalized. Assuming that the upper limit value of the ith parameter is U_{ij}, the lower limit value is L_{ij}, and the parameter value of the jth sample is K_{ij}, the normalized result X_{ij} as **Eq. 3**:

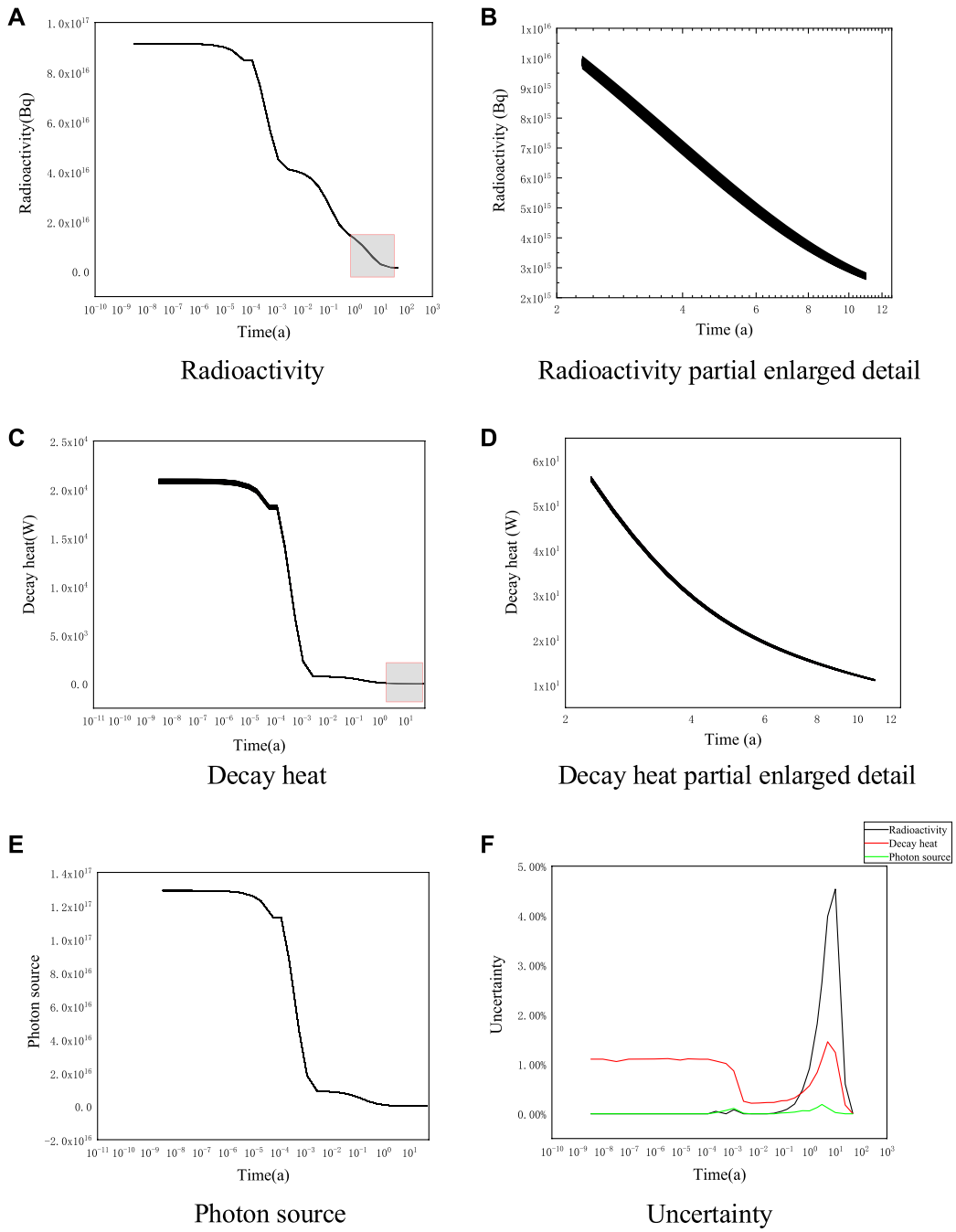

FIGURE 6 | NUREG/CR-6115 structural material radioactivity, decay heat and photon uncertainty. **(A)** Radioactivity **(B)** Radioactivity partial enlarged detail **(C)** Decay heat **(D)** Decay heat partial enlarged detail **(E)**. Photon source **(F)** Uncertainty.

$$X_{ij} = \frac{K_{ij} - L_{ij}}{U_{ij} - L_{ij}} \tag{3}$$

It can be seen that the value of X_{ij} is between 0 and 1. The distribution state of the sample in the interval reflects the kind of distribution to which it belongs. The normalized distribution of hypercube sampling samples is shown in **Figure 5**. It is evident that the normalized half-life parameter sample points are clustered in the middle and sparse on both sides, obeying a normal distribution; the decay energy sample points are distributed with equal probability in the interval, so the input parameters obey a uniform distribution, which verifies the rationality of the input parameter sampling.

Figure 6A, **Figure 6C**, and **Figure 6E** show the changes in radioactivity, decay heat, and photon source over time for 100 different nuclear data samples from the NUREG/CR-6115

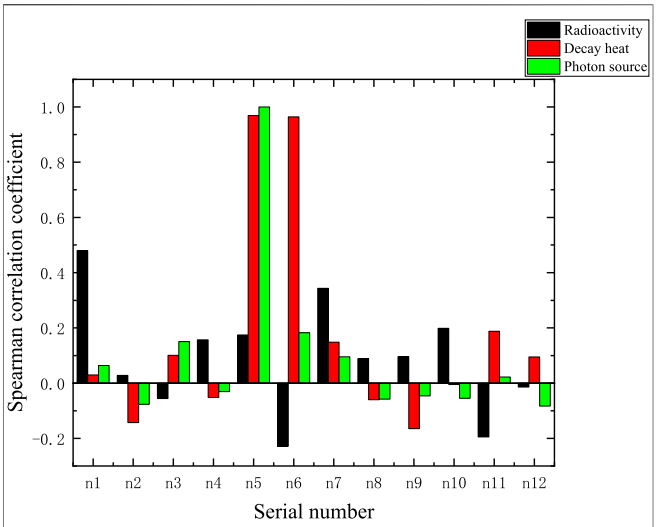

FIGURE 7 | Spearman's correlation coefficient of input and output parameters at 10th year.

reactor structural material activation calculations. **Figure 6B** and **Figure 6D** show partially enlarged details from 2 to 11 years for radioactivity and decay heat (within the gray rectangle in **Figure 6A** and **Figure 6C**), respectively. **Figure 6F** shows the uncertainty variation of the calculated results for radioactivity, decay heat, and photon source for 48 years after reactor shutdown.

The perturbation of nuclear data has a small effect on the photon source, and the uncertainty will reach a maximum of 4.54% at the 10th year of shutdown for radioactivity. The reason is that the half-life of ^{55}Fe has great uncertainty, and ^{55}Fe is the main contributor to radioactivity. From **Table 4**, it can be seen that ^{55}Fe has the longest half-life of 2.774 years among the six nuclides, and from **Table 3**, it can be seen that the reactor structure material has the largest proportion of Fe by mass. These two reasons lead to the fact that ^{55}Fe will have the largest impact on the inventory and radioactivity at this time. The uncertainty introduced by the half-life of ^{55}Fe as a main contributing nuclide will be shown during this time. The uncertainty of the decay heat is approximately 1% within 1 day of the shutdown, and the decay heat is mainly produced by ^{56}Mn and ^{58}Co. From **Table 4**, the half-lives of ^{56}Mn and ^{58}Co were 2.579 h and 70.856 days, respectively, so the uncertainty is introduced by ^{56}Mn and ^{58}Co during this time. The uncertainty of the decay heat starts to rise to the maximum value of 1.45% at 5 years, because the ^{55}Fe decay heat contribution is increasing (15.52%) at this time, which also introduces uncertainty to the decay heat. The maximum value of 0.19% uncertainty in the photon source occurs in the third year, which is the main photon source emitted by ^{54}Mn. From **Table 4**, the half-life of ^{54}Mn is 312.037 days. Additionally, the uncertainty is introduced by ^{54}Mn.

Sensitivity Analysis

The Spearman correlation coefficient is one of the commonly used global sensitivity analysis methods to test the sensitivity of multiple input parameters to the response parameters (Sedgwick, 2014). The Spearman correlation coefficient was used as an output parameter for the analysis of radioactivity, decay heat and photon source sensitivity, and the correlation coefficient takes values in the range of [-1,1]. The magnitude of the absolute value indicates the strength of the sensitivity; the positive sign of the value indicates a positive correlation, the negative sign indicates a negative correlation, and 0 indicates no correlation, and its expression is shown in **Eq. 4**.

$$y = \frac{\sum_{i=1}^{n} R_{X_i} R_{Y_i} - n\left(\frac{n+1}{2}\right)^2}{\sqrt{\sum_{i=1}^{n} R_{X_i}^2 - n\left(\frac{n+1}{2}\right)^2}\sqrt{\sum_{i=1}^{n} R_{Y_i}^2 - n\left(\frac{n+1}{2}\right)^2}} \tag{4}$$

Where, R_{X_i} is the size ranking of X_i in X; R_{Y_i} is the size ranking of Y_i in Y; y is the correlation coefficient; and n is the number of samples.

As shown in **Figure 7**, in the field of statistics, the correlation coefficient is defined as extremely strong correlation from 0.8 to 1, strong correlation from 0.6 to 0.8, moderate correlation from 0.4 to 0.6, weak correlation from 0.2 to 0.4, and extremely weak correlation from 0 to 0.2. Since the uncertainty in radioactivity is highest at the 10th year after reactor shutdown, the correlation between the input and output values (the half-life and decay energy of the nucleus are input values, and the radioactivity, decay heat and photon source are output values) at that moment is calculated in **Figure 7**. Therefore, the half-life of ^{55}Fe is extremely strongly correlated with the decay heat and photon source, and the decay energy of ^{55}Fe is extremely strongly correlated with the decay heat; it can also support the fact that the uncertainty introduced by ^{55}Fe in the previous section is the largest. The half-life of ^{54}Mn is moderately correlated with radioactivity, and the half-life and decay energy of other nuclides are weakly and extremely weakly correlated with the response of the three output parameters.

CONCLUSION

In this paper, the activation library of the depletion and decay code ORIGEN2 was updated based on ENDF/B-VIII.0 and JEFF3.3 decay evaluation libraries, and uncertainty quantification analysis of activation calculations and global sensitivity analysis of nuclear data were carried out. The conclusions are as follows.

(1) The uncertainties of radioactivity, decay heat and photon source of the reactor structure material within 48 years of reactor shutdown due to nuclear data perturbation are obtained by uncertainty analysis, and the radioactivity will reach the maximum uncertainty of 4.54% at 10 years and the maximum uncertainty of 1.45% for decay heat at 5 years.
(2) The Spearman correlation coefficient shows that the changes in its half-life and decay energy have the greatest influence on the radioactivity, decay heat and photon source of the

structural material after the reactor is deactivated. Therefore, for the design of the scheme of radiation shielding of the reactor structural material, the half-life and decay energy of ^{55}Fe should be determined more precisely to improve the accuracy of the activation calculation.

DATA AVAILABILITY STATEMENT

The original contributions presented in the study are included in the article/supplementary material, further inquiries can be directed to the corresponding authors.

AUTHOR CONTRIBUTIONS

YC:Conceptualization, Methodology, Software WJ:Data curation, Writing Original draft preparation YT:Visualization, Investigation CZ:Supervision.

FUNDING

This work is supported by the National Natural Science Foundation of China (approved number: 12105136), the Hunan Province Natural Science Foundation of China (approved number: 2021JJ40449), and the Doctoral Research Fund of University of South China.

REFERENCES

Awan, S. E., Mirza, N. M., and Mirza, S. M. (2012). Kinetic Study of Fission Product Activity Released inside Containment under Loss of Coolant Transients in a Typical MTR System. *Appl. Radiat. Isot.* 70 (12), 2711–2719. doi:10.1016/j.apradiso.2012.08.002

Bieda, B. (2012). "Risk Analysis of the Waste to Energy Pyrolysis Facility Designs for City of Konin, in Poland, Using SimLab® Toolpack," in *Novel Approaches and Their Applications in Risk Assessment* (London, UK: intechopen), 245.

Briggs, L. L. (2009). *Uncertainty Quantification Approaches for Advanced Reactor Analyses*. Lemont: Argonne National Laboratory.

Brown, D. A., Chadwick, M. B., Capote, R., Kahler, A. C., Trkov, A., Herman, M. W., et al. (2018). ENDF/B-VIII.0: The 8 Th Major Release of the Nuclear Reaction Data Library with CIELO-Project Cross Sections, New Standards and Thermal Scattering Data. *Nucl. Data Sheets* 148, 1–142. doi:10.1016/j.nds.2018.02.001

Carew, J. F. (2001). *PWR and BWR Pressure Vessel Fluence Calculation Benchmark Problems and Solutions*. North Bethesda: Division of Engineering Technology, Office of Nuclear Regulatory Research, US Nuclear Regulatory Commission.

Croff, A. G. (1983). ORIGEN2: a Versatile Computer Code for Calculating the Nuclide Compositions and Characteristics of Nuclear Materials. *Nucl. Tech.* 62 (3), 335–352. doi:10.13182/NT83-1

Croff, A. G. (1980). *User's Manual for the ORIGEN2 Computer Code (No. ORNL/TM–7175)*. Oak Ridge: Oak Ridge National Lab.

Foudil, Z., Mohamed, B., and Tahar, Z. (2017). Estimating of Core Inventory, Source Term and Doses Results for the NUR Research Reactor under a Hypothetical Severe Accident. *Prog. Nucl. Energ.* 100, 365–372. doi:10.1016/j.pnucene.2017.07.013

Herman, M.Cross Sections Evaluation Working Group (2009). *ENDF-6 Formats Manual Data Formats and Procedures for the Evaluated Nuclear Data File ENDF/B-VI and ENDF/B-VII (No. BNL-90365-2009). Brookhaven National Lab. (BNL), Upton, NY (United States)*. Upton, New York: National Nuclear Data Center.

Katakura, J.-i. (2013). Uncertainty Analyses of Decay Heat Summation Calculations Using JENDL, JEFF, and ENDF Files. *J. Nucl. Sci. Tech.* 50 (8), 799–807. doi:10.1080/00223131.2013.808004

Liem, P. H., and Sembiring, T. M. (2013). Development of New ORIGEN2 Data Library Sets for Research Reactors with Light Water Cooled Oxide and Silicide LEU (20w/o) Fuels Based on JENDL-3.3 Nuclear Data. *Nucl. Eng. Des.* 262, 52–62. doi:10.1016/j.nucengdes.2013.03.049

McLane, V. (1996). *ENDF-201, ENDF/B-VI Summary Documentation Supplement 1, ENDF/HE-VI Summary Documentation (No. BNL-NCS–17541-ED. 4-SUPPL. 1)*. Upton, New York: Brookhaven National Lab.

Mehboob, K., Xinrong, C., Ahmed, R., and Ali, M. (2013). Numerical Simulation of Radioisotope's Dependency on Containment Performance for Large Dry PWR Containment under Severe Accidents. *Nucl. Eng. Des.* 262, 435–451. doi:10.1016/j.nucengdes.2013.05.021

Mui, T., and Kozlowski, T. (2018). Confirmation of Wilks' Method Applied to TRACE Model of Boiling Water Reactor spray Cooling experiment. *Ann. Nucl. Energ.* 117, 53–59. doi:10.1016/j.anucene.2018.03.011

Plompen, A. J. M., Cabellos, O., De Saint Jean, C., Fleming, M., Algora, A., Angelone, M., et al. (2020). The Joint Evaluated Fission and Fusion Nuclear Data Library, JEFF-3.3. *The Eur. Phys. J. A* 56 (7), 181. doi:10.1140/epja/s10050-020-00141-9

Sedgwick, P. (2014). Spearman's Rank Correlation Coefficient. *Bmj* 349, g7327. doi:10.1136/bmj.g7327

Trkov, A., Brown, D. A., and Brown, D. A. (2018). *ENDF-6 Formats Manual: Data Formats and Procedures for the Evaluated Nuclear Data Files (No. BNL-203218-2018-INRE)*. Upton, NY: Brookhaven National Lab. doi:10.2172/1425114

Tsilanizara, A., and Huynh, T. D. (2021). New Feature of DARWIN/PEPIN2 Inventory Code: Propagation of Nuclear Data Uncertainties to Decay Heat and Nuclide Density. *Ann. Nucl. Energ.* 164, 108579. doi:10.1016/j.anucene.2021.108579

Wilks, S. S. (1942). Statistical Prediction with Special Reference to the Problem of Tolerance Limits. *Ann. Math. Statist.* 13 (4), 400–409. doi:10.1214/aoms/1177731537

Zhao, P., Lei, Z., Yu, T., Zhao, Y., Qin, Z., Li, Q., et al. (2021). Uncertainty Analysis in Coupled neutronic/thermal-hydraulic Calculations Based on Computational Fluid Dynamics. *Ann. Nucl. Energ.* 156, 108215. doi:10.1016/j.anucene.2021.108215

Conflict of Interest: The authors declare that the research was conducted in the absence of any commercial or financial relationships that could be construed as a potential conflict of interest.

Publisher's Note: All claims expressed in this article are solely those of the authors and do not necessarily represent those of their affiliated organizations, or those of the publisher, the editors, and the reviewers. Any product that may be evaluated in this article, or claim that may be made by its manufacturer, is not guaranteed or endorsed by the publisher.

frontiers in Energy Research

ORIGINAL RESEARCH
published: 24 February 2022
doi: 10.3389/fenrg.2021.785513

Research on Optimized Design of In-Vessel Retention–External Reactor Vessel Cooling Strategy and Negative Effect Assessment

*Peng Chen, Zijie Wu, Dekui Zhan, Shaoxiong Xia and Xinhai Zhao**

China Nuclear Power Technology Research Institute, Shenzhen, China

Due to large uncertainty, the effectiveness of in-vessel retention (IVR) with external reactor vessel cooling (ERVC) for high-power reactors cannot be fully demonstrated during the transient process. To optimize the current IVR-ERVC strategy, the concept of IVR-ERVC with in-vessel injection (IVI) is studied. Two feasible IVI designs are proposed: 1) using the passive IVR water tank to implement simultaneous water injection in-vessel and ex-vessel and 2) using the passive severe accident dedicated in-vessel injection tanks (SADITs) to implement water injection in-vessel. The research on the feasibility and effectiveness of IVI is performed, and the corresponding negative effects are analyzed. The calculation results by using MIDAC show that the two proposed IVI concepts can greatly delay the accident progression in the core and reduce the decay heat peak of the molten pool in the lower head, thereby improving the effectiveness of the current IVR-ERVC strategy. And the negative effects are within acceptable ranges.

Keywords: severe accidents, IVR-ERVC, in-vessel injection, optimized design, negative effect assessment

OPEN ACCESS

Edited by:
Yapei Zhang,
Xi'an Jiaotong University, China

Reviewed by:
Shanshan Bu,
Chongqing University of Technology, China
Ivo Kljenak,
Institut Jožef Stefan (IJS), Slovenia

****Correspondence:***
Xinhai Zhao
zhaoxinhai2@cgnpc.com.cn

Specialty section:
This article was submitted to Nuclear Energy, a section of the journal Frontiers in Energy Research

Received: *29 September 2021*
Accepted: *06 December 2021*
Published: *24 February 2022*

Citation:
Chen P, Wu Z, Zhan D, Xia S and Zhao X (2022) Research on Optimized Design of In-Vessel Retention–External Reactor Vessel Cooling Strategy and Negative Effect Assessment. Front. Energy Res. 9:785513. doi: 10.3389/fenrg.2021.785513

INTRODUCTION

After the Fukushima nuclear accident, nuclear regulatory authorities of various countries put forward more stringent requirements for nuclear safety. The Chinese National Nuclear Safety Administration (NNSA) requires new nuclear reactors to achieve "practical elimination of large radioactive release" (Ma et al., 2016). As the last safety barrier, the integrity of the containment is essential to prevent large-scale leakage of radioactive materials. To avoid the occurrence of molen corium concrete interaction (MCCI) and direct containment heating (DCH) which threatens the integrity of containment, the in-vessel retention (IVR) with external reactor vessel cooling (ERVC) strategy is adopted in Chinese HPR1000 (Xing et al., 2016).

Due to high reliability and low construction difficulty, the concept of IVR-ERVC is widely employed in the GEN-III and GEN-II+ pressurized water reactors (PWRs), including AP600/1000 (Zhang et al., 2010), APR1400 (Oh and Kim, 2005), VVER1000/320 (Sangiorgi and Ezzidi, 2015), and CAP1400 (Shi et al., 2019). The key principle of the IVR-ERVC strategy lies in that the external cooling water is quickly injected into the reactor pit through active or passive means after severe accidents, forming a natural circulation in the annular flow channel. The heat generated by corium is taken away by means of external cooling of the reactor pressure vessel (RPV), and other safety functions are simultaneously implemented (such as primary circuit

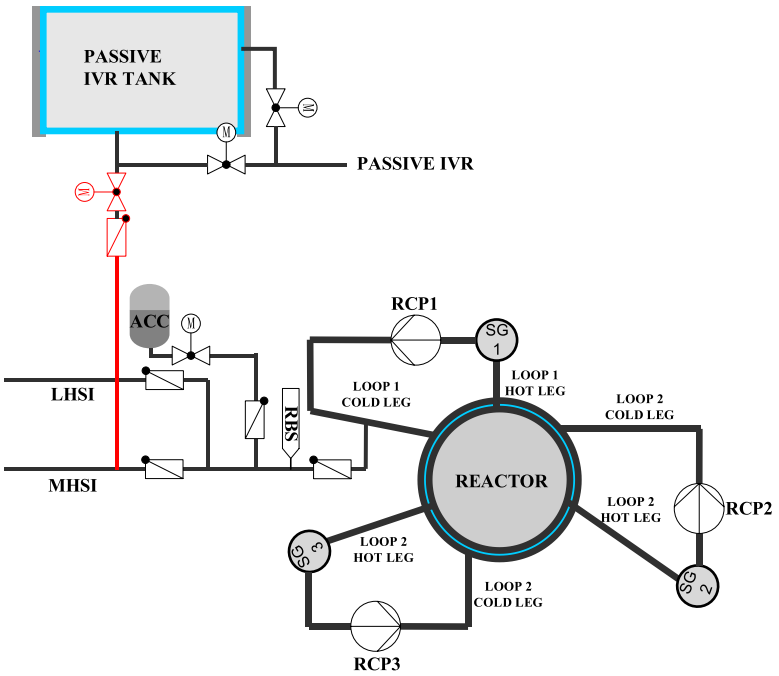

FIGURE 1 | Schematic of the IVI strategy with a passive IVR tank.

pressure relief) to maintain the integrity of the pressure vessel. The successful implementation of the IVR-ERVC strategy needs to meet the following criteria (Fichot et al., 2018):

1) The local heat flux density on the inner wall surface of the lower head is less than the critical heat flux (CHF) profiles.
2) The minimum vessel thickness reached after ablation by corium can withstand the maximum load that is applied to the vessel during the transient process.

For low-power reactors such as VVER440 and AP600, the effectiveness of the IVR-ERVC strategy has enough margin due to low decay heat of corium (Kymäläinen et al., 1997; Theofanous et al., 1997). But for reactors with higher power, such as AP1000 and APR1400, the effectiveness of the IVR-ERVC strategy cannot be fully guaranteed (Fichot et al., 2018). It is firstly due to the large uncertainty of accident progression in the core. In some transient processes, the focusing effect is significant due to a thin metallic layer, in which the local heat flux density of the lower head may be greater than the CHF profiles (Carénini and Fichot, 2016). It is secondly due to the uncertainty of physical models used in integral codes for severe accident analysis. The calculation results of integral codes (including ASTEC, ATHLET-CD, and MAAP_EDF) for the minimum vessel thickness show a large variability (about ±80%) (Carénini et al., 2019). The significant discrepancy leads to a great uncertainty in the reasonable assessment of IVR-ERVC effectiveness.

Although there is uncertainty in the analysis of the IVR-ERVC strategy for high-power reactors, it is certain that the decay heat of the core decreases with time after shutdown. It can be deduced that as long as the core melt relocates to the lower head late enough, the maximum decay heat in the corium pool can be greatly reduced, thereby increasing the successful possibility of the IVR-ERVC strategy.

One of the most effective ways to delay or even terminate the accident process in the reactor is to perform the injection of water into the vessel. In severe accidents, more than 80% of core damage can be mitigated by implementing additional core cooling (Nuclear Regulatory Commission, 1989). But the in-vessel injection (IVI) is always accompanied by negative risks. And the effectiveness and negative effects of IVI are highly correlated with the time of water injection (Jun et al., 2011). The key negative effects include the following (Dorsselaere et al., 2006):

1) *Hydrogen risk*: After the injected cooling water comes into contact with the exposed fuel bundle or debris bed at high temperature, a large amount of steam will be generated instantly, which enhances the oxidation of zirconium cladding. It is found from the CORA13 experiment that 48% of the total hydrogen was generated during the flooding phase (Hagen et al., 1993). The oxidation heat accelerates the core damage, and the massive hydrogen generated increases the risk of hydrogen explosion inside the containment.
2) *Primary System (PS) overpressure*: The overpressure risk in the primary system induced by massive steam generated may result in yield failure of the lower head and creep failure of the steam generator heat transfer tubes, which penalizes the integrity of RPV and increases the leakage risk of fission products to the secondary circuit.

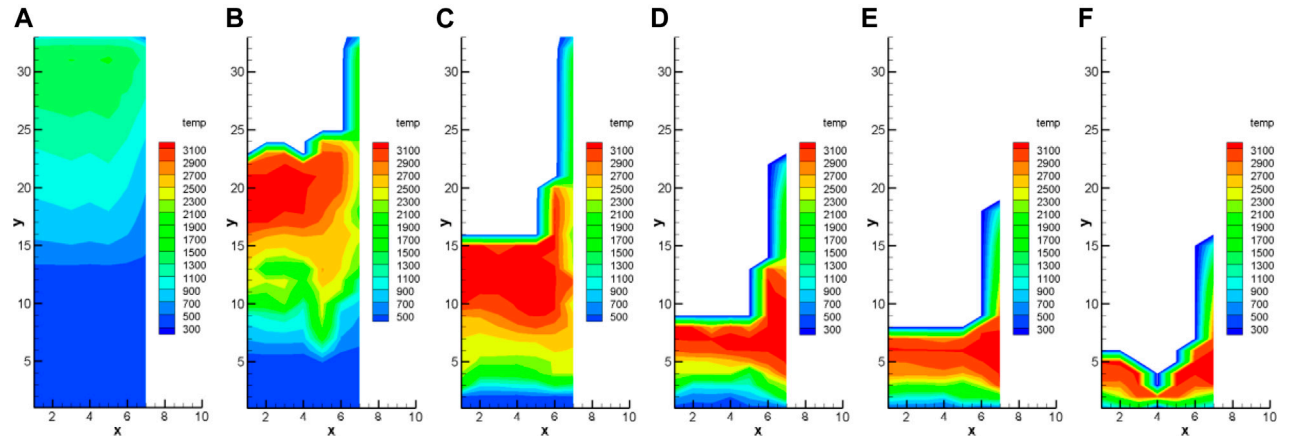

FIGURE 2 | Temperature distribution at different implementation moments of IVI: **(A)** 20 min; **(B)** 40 min; **(C)** 60 min; **(D)** 80 min; **(E)** 100 min; **(F)** 120 min.

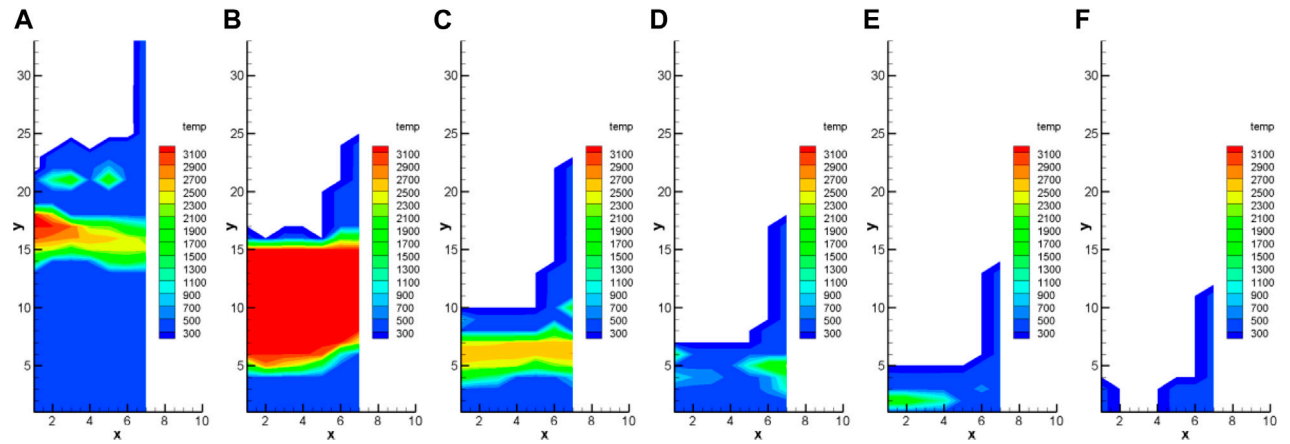

FIGURE 3 | Temperature distribution at 5 h for different implementation moments of IVI: **(A)** 20 min; **(B)** 40 min; **(C)** 60 min; **(D)** 80 min; **(E)** 100 min; **(F)** 120 min.

3) *Fission Product (FP) release*: A large number of cracks are produced between or within the grains in the high-temperature fuel pellets during the reflooding phase, and the injected coolant crushes the embrittled fuel rods, causing the increase in the amount of fission products released from the core. The LOFT-LP-FP2 experiment data show that 80% of the initial storage of fission products was released during the reflooding process (Coryell and April, 1994). The PBF SFD-ST experiment also presents that most of the fission products were released during and after water injection (Wright, 1994).

To delay the accident progression in the core and reduce the decay heat of the molten pool in the lower head, the research on the feasibility and effectiveness of in-vessel injection is performed in this paper, and the corresponding negative effects are analyzed. The concept of IVR-ERVC with IVI is studied to optimize the current IVR-ERVC strategy, thereby improving the IVR effectiveness for high-power reactors and enhancing their ability to deal with severe accidents.

OPTIMIZED DESIGN OF IN-VESSEL RETENTION–EXTERNAL REACTOR VESSEL COOLING STRATEGY

For typical advanced Chinese 1000MWe PWRs using the IVR-ERVC strategy, the severe accident management strategies include the following: 1) Once the temperature of the core outlet exceeds 650°C, the severe accident dedicated valve is opened to prevent the occurrence of high-pressure melt ejection (HPME). 2) Then, the passive IVR tank is activated by the operator, in which water is injected into the pit through a large flow line to quickly flood the lower head of the pressure vessel. 3) When the

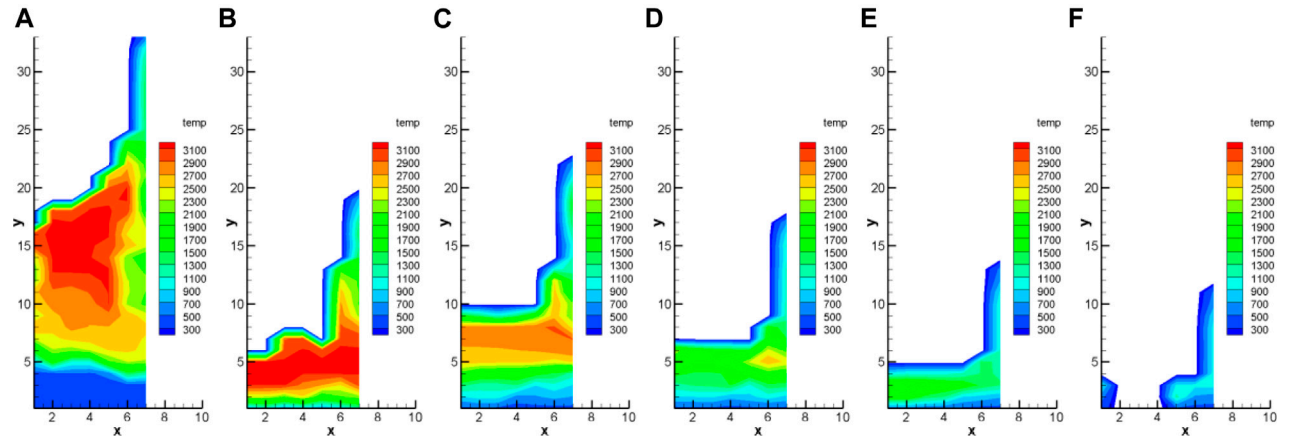

FIGURE 4 | Temperature distribution at 10 h for different implementation moments of IVI: **(A)** 20 min; **(B)** 40 min; **(C)** 60 min; **(D)** 80 min; **(E)** 100 min; **(F)** 120 min.

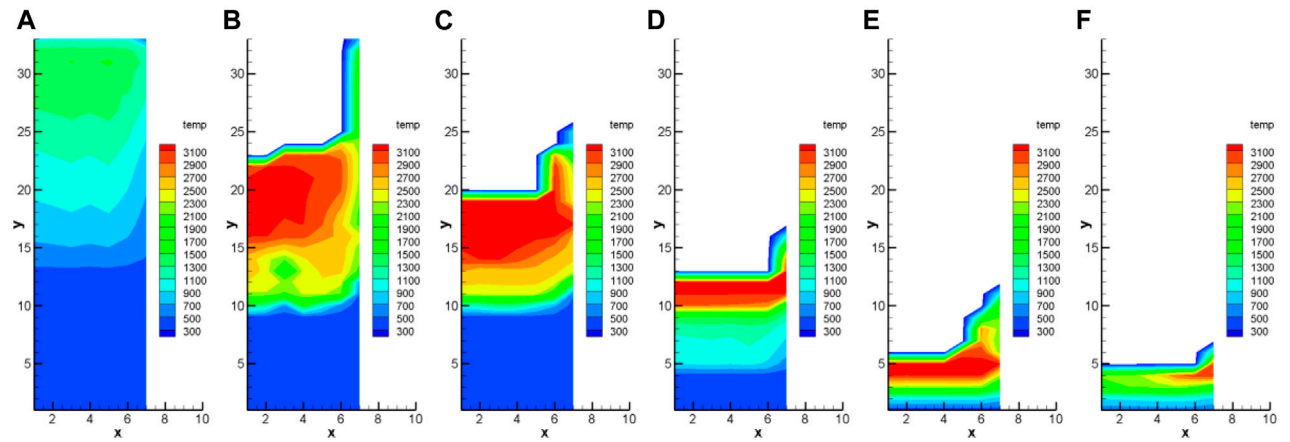

FIGURE 5 | Temperature distribution at different time with 40 mm of IVI pipeline diameter: **(A)** 20 min; **(B)** 40 min; **(C)** 60 min; **(D)** 3 h; **(E)** 5 h; **(F)** 10 h.

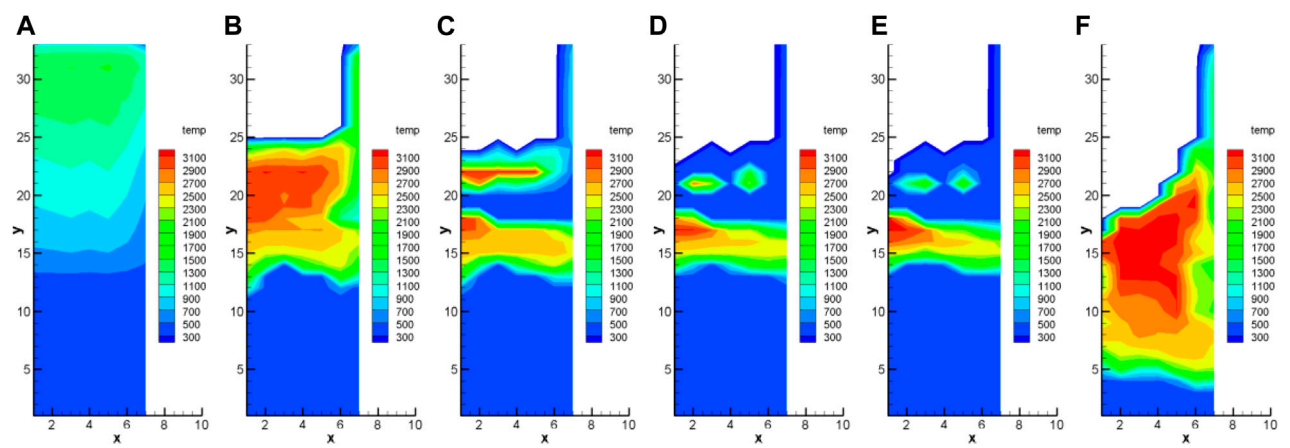

FIGURE 6 | Temperature distribution at different time with 60 mm of IVI pipeline diameter: **(A)** 20 min; **(B)** 40 min; **(C)** 60 min; **(D)** 3 h; **(E)** 5 h; **(F)** 10 h.

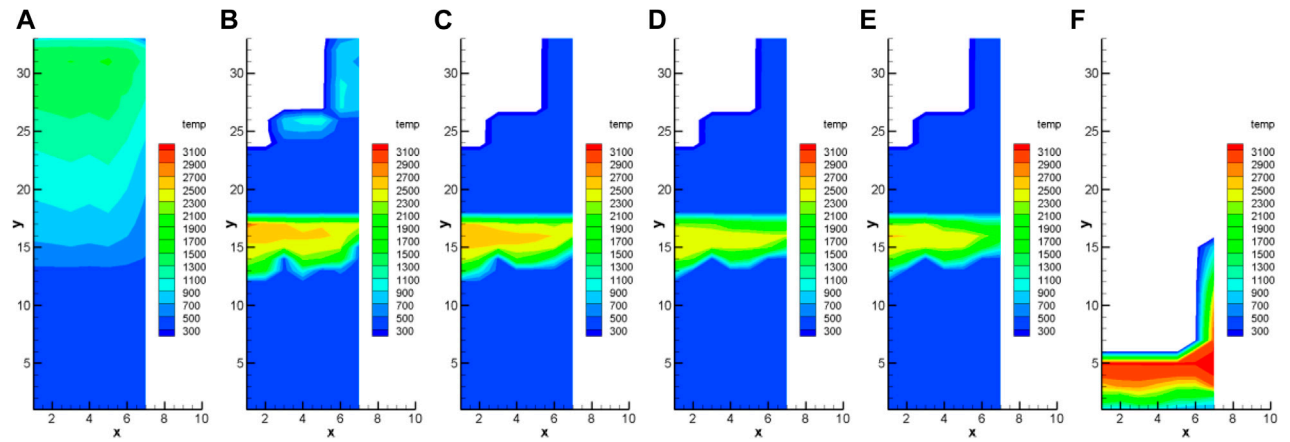

FIGURE 7 | Temperature distribution at different time with 80 mm of IVI pipeline diameter: **(A)** 20 min; **(B)** 40 min; **(C)** 60 min; **(D)** 3 h; **(E)** 5 h; **(F)** 10 h.

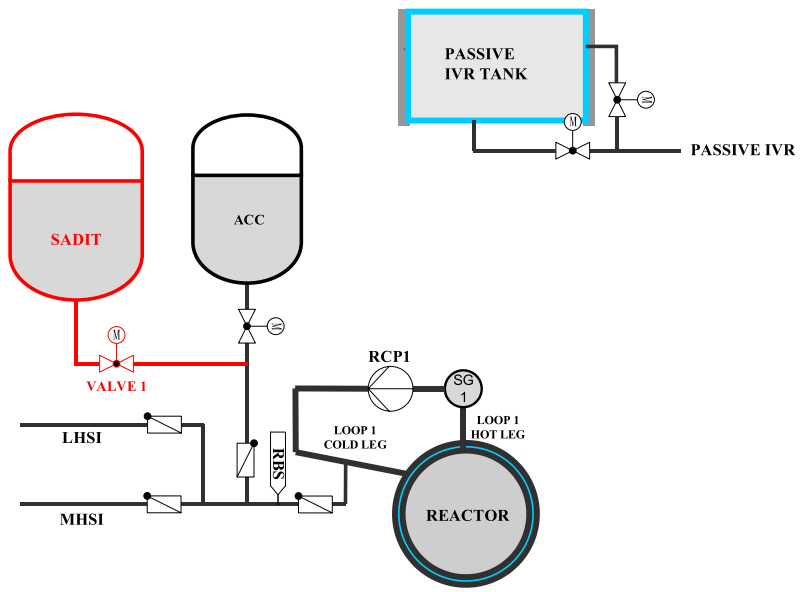

FIGURE 8 | Schematic of the IVI strategy with the passive SADIT.

water in the IVR tank is nearly depleted, the active water injection from the in-containment refueling water storage tank (IRWST) into the pit with small flow lines is carried out, to compensate for the loss of evaporated water and realize the long-term cooling.

The research on the concept of IVR-ERVC with IVI is performed to optimize the current IVR-ERVC strategy. Considering not challenging the current severe accident mitigation strategies and not significantly increasing the pressure boundary of the primary circuit, the following two IVI strategies are proposed:

1) Using the passive IVR water tank to implement simultaneous water injection in-vessel and ex-vessel
2) Using passive severe accident dedicated in-vessel injection tanks (SADITs) to implement water injection in-vessel

To verify the effectiveness of IVI strategies and evaluate negative effects, MIDAC (Module In-vessel Degraded severe accident Analysis Code) (Wang et al., 2014a) is used to calculate and analyze the impact of IVI on core degradation, corium relocation, and heat transfer in the molten pool under severe accidents. MIDAC is developed by Xi'an Jiaotong University, which can analyze the processes of in-vessel severe accident thoroughly (Wang et al., 2014b). Through the verification of FROMA, QUENCH06&16, TMI-2, and other experiments (Wu et al., 2021; Wang et al., 2019), MIDAC

TABLE 1 | Key events in the core damage progression.

Event	Without IVI	40 min 60 mm	Optimization 1.1	Optimization 1.2	Optimization 1.3	Optimization 2
First core uncovery	200.34s	200.34s	200.34s	200.34s	200.34s	200.34s
IVI start-up	—	2,618.6s	1,419.1s	1,419.1s	1,419.1s	251.5s
Second core uncovery	—	28,278.9s	28,676.1s	36,680.3s	—	11,752.4s
Melt relocation to the lower head	4,060.8s	29,790.9s	37,366.9s	42,846.1s	—	19,082.2s
Core completely exposed	2,779.5s	30,649.9s	37,587.3s	42,887.1s	—	19,124.3s
RPV dryout	4,850.6s	31,941.5s	38,551.7s	44,479.6s	—	20,285.3s

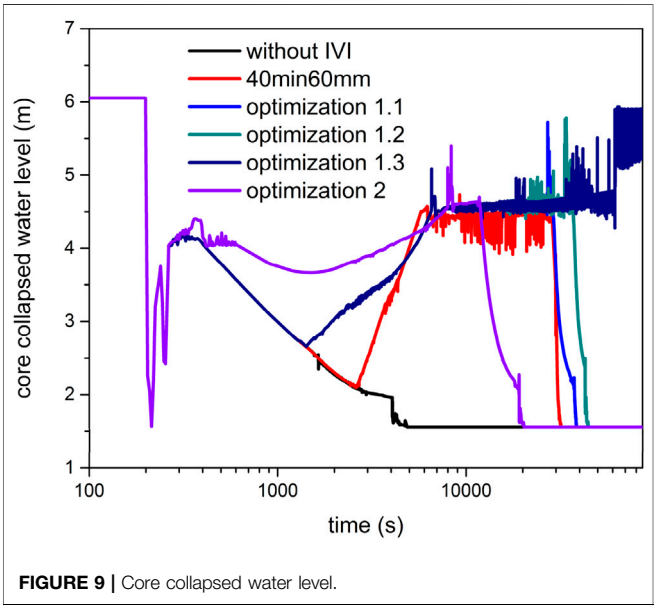

FIGURE 9 | Core collapsed water level.

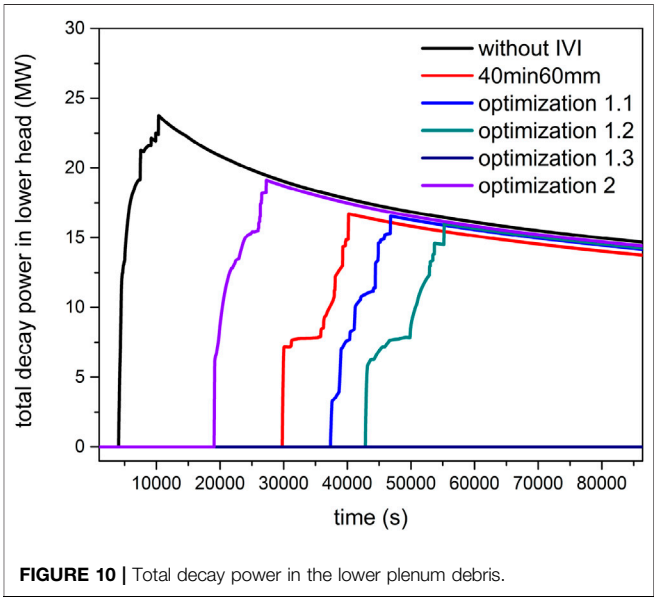

FIGURE 10 | Total decay power in the lower plenum debris.

proved to be able to provide the relevant analyzing result of each course accurately.

The accident scenario of large break-loss of coolant accident (LB-LOCA) is the fastest, and the consequences are the worst. Therefore, LB-LOCA is selected as the bounding case for other accident sequences to perform the effectiveness analysis. The main assumptions include the following:

1) Occurrence of double-ended guillotine break at a cold leg in loop 1 at 200 s
2) Failure of medium head safety injection (MHSI), low head safety injection, and containment spray system
3) Accumulators (ACCs), passive IVR, and active injection of the IRWST available

As for the boundary conditions, the calculation object includes all the components inside the containment of HPR1000. The boundary conditions include the boundaries of RPV, the primary circuit, and the containment. In the scenario of IVR, the cavity is flooded with water. The code calculates the boiling heat flux at the RPV outer surface boundary. For the rest of the primary circuit, according to HPR1000 reactor design, a layer of rock wool insulation is implemented in the model, providing an extra thermal resistance. For the containment wall, an adiabatic boundary is used for the conservative consideration of containment pressure and temperature.

In-Vessel Injection With Passive In-Vessel Retention Tank

The schematic of the first IVI strategy with a passive IVR tank is shown in **Figure 1**, in which the red line shows the additional pipelines and equipment. When the primary system is fully depressurized under severe accidents, the water from the passive IVR tank is simultaneously injected into the cold leg in loop 1 and the reactor pit by gravity.

The effectiveness and negative effects of IVI strongly depend on the implementation moment and the amount of water injection in-vessel. In case of a small part of core exposed and the fuel bundle is at low temperature, the core is quickly reflooded after in-vessel injection which can greatly prevent the core degradation from further deterioration. When most part of the core area has been exposed, the temperature of fuel rods rises rapidly due to lack of effective cooling. After the implementation of in-vessel injection, the large amount of steam generated enhances the oxidation of cladding, resulting in a further increase of temperature in fuel rods and aggravating

TABLE 2 | Maximum decay heat and composition in the molten pool.

Parameter	Without IVI	40 min 60 mm	Optimization 1.1	Optimization 1.2	Optimization 1.3	Optimization 2
Max. decay heat (MW)	23.8	16.7	16.5	15.9	—	19.1
Mass of Zr (t)	13.718	13.045	13.617	16.683	—	12.057
Mass of ZrO_2 (t)	11.91	13.27	11.97	7.747	—	14.078
Mass of UO_2 (t)	92.312	92.292	92.503	92.727	—	92.378
Mass of steel (t)	38.395	30.744	30.893	29.350	—	35.052

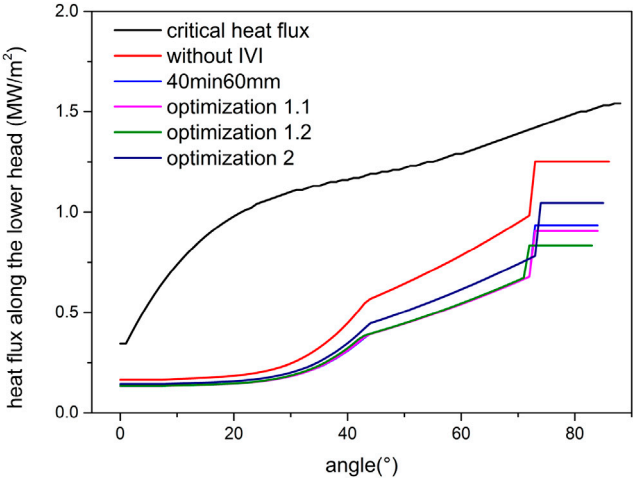

FIGURE 11 | Heat flux along the lower head compared with the CHF.

the core damage process. When performing the in-vessel injection in the late phase of core degradation, a solidified crust is formed on the periphery of molten pool in the core region or lower head, which hinders the cooling of the central area in the molten pool, causing the melt to present uncoolability.

In addition, due to the limited amount of water in the passive IVR tank, the implementation of IVI will inevitably affect the volume of injected water in the pit. In order to reduce the impact on ex-vessel injection, and also to select the most effective measures for water injection in the vessel, the sensitivity analysis on the IVI implementation moment and water injection flow is performed.

Sensitivity Analysis of Injection Time

To perform the sensitivity analysis on the implementation moment of IVI, 20, 40, 60, 80, 100, and 120 min after the core outlet temperature exceeds 650°C are considered in the calculation by MIDAC. Namely, if the core outlet temperature exceeds 650°C at 0 s, the water injection in the reactor shall be carried out at 1200 s/2400 s/3600 s/4800 s/6000 s/7200 s, respectively, for different sensitivity analysis cases.

Figures 2–4, respectively, show the distribution of core node temperature at different time for the various selected implementation moments of IVI, from which the core damage fraction can be clearly observed. The core node temperature in MIDAC represents the average temperature of core components such as fuel, cladding, and control rods in each computational cell. It can be found that the implementation moment of IVI is earlier, and the core damage fraction at 5 and 10 h after LB-LOCA is lower, which indicates that the water injection in-vessel in the early core degradation phase can reduce the melt mass relocated into the lower head and then decrease the decay heat of the molten pool. It can be explained by the fact that the earlier the IVI is implemented, the longer the water injection in-vessel is maintained before the IVR tank is depleted, which can provide more long-term cooling in the core.

Sensitivity Analysis of Injection Tube Diameter

Without additional water supply, the core is in a pool boiling state before being dried out. The purpose of water injection in the reactor is to compensate for the loss of coolant due to evaporation. The water injection flow rate is actually determined by the pipeline diameter. Through comparing the evaporation rate of the coolant, 40, 60, and 80 mm of IVI pipeline diameter are selected to perform sensitivity analysis.

Figures 5–7 present the temperature distribution at different time with 40, 60, and 80 mm of IVI pipeline diameter, respectively. It can be found that the water injection with 20 mm of pipe diameter cannot significantly alleviate the damage process in the core due to the small injection flow. Within 5 h after the accident, the mitigation effect for core damage with 80 mm pipe diameter is better than that of 60 mm. But the core damage fraction with 80 mm pipe diameter at 10 h is significantly greater than that of 60 mm, which is due to the fact that the IVR water tank is depleted earlier in the case of 80 mm pipe diameter, resulting in a shorter period to maintain the water injection in-vessel. After the IVR tank is depleted, the water injection in the core is ceased, causing the core damage process to be restarted.

Optimized In-Vessel Injection Strategy With Passive In-Vessel Retention Tank

According to the sensitivity analysis on the IVI implementation moment and injection pipeline diameter, it can be concluded that the best IVI strategy is to implement the water injection in-vessel at 20 min after the core outlet temperature exceeds 650°C and with 60 mm of injection pipeline diameter. However, the calculation results of this strategy show that the amount of water injected into the reactor pit within half an hour after the implementation of passive IVR is less than the design value. In order to meet this requirement, the implementation of IVI at 40 min after the core outlet temperature exceeds 650°C and with 60 mm of pipeline diameter is selected as the first IVI strategy with a passive IVR tank (referred to as the ***40 min 60 mm strategy***).

TABLE 3 | IVR margin for various IVI strategies.

Parameter	Without IVI	40 min 60 mm	Optimization 1.1	Optimization 1.2	Optimization 1.3	Optimization 2
Max. heat flux (MW/m^2)	1.252	0.934	0.906	0.834	—	1.045
CHF (MW/m^2)	1.42	1.42	1.42	1.41	—	1.43
IVR margin (%)	11.8	34.2	36.2	40.9	—	26.9

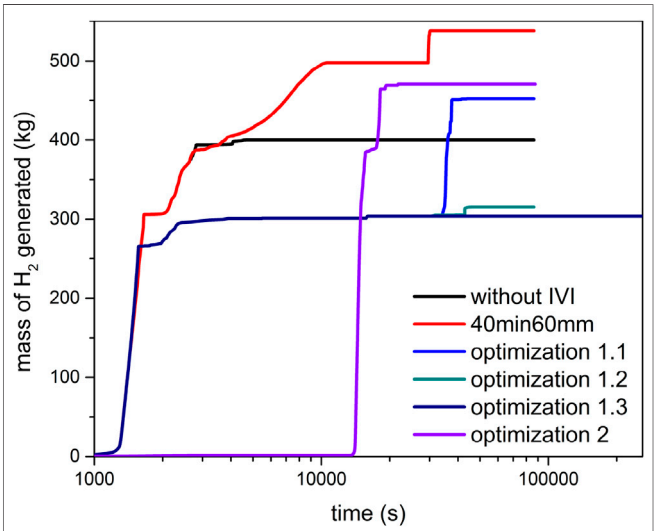

FIGURE 12 | Integrated mass of H_2 generated in the core and lower plenum.

Nevertheless, **Figures 2–4** show that the mitigation effect for core damage with the 20 min 60 mm strategy is much better than that of 40 min 60 mm. In order to satisfy the requirement on the quantity of water injection ex-vessel, it is necessary to increase the initial water capacity in the passive IVR tank under the premise of available space. Based on the sensitivity analysis on the initial water level in the IVR tank, the following optimized strategy is proposed.

***Optimization strategy 1.1*:** 1) Increase the initial water level in the IVR tank to 8.01 m. 2) Implement the simultaneous water injection in-vessel and ex-vessel at 20 min after the core outlet temperature exceeds 650°C and with 60 mm of IVI pipeline diameter. 3) When the water level in the IVR tank is nearly depleted, carry out the active water injection from the IRWST into the pit.

After the passive IVR tank is depleted, the core meltdown process is restarted. To delay the time for the IVR tank to be empty, the initial water capacity in the IVR tank can be continued to be increased. However, the containment space is limited. The IVR tank with too large volume will inevitably affect the space availability of other equipment. The redistribution of equipment in the containment will bring too much work. Therefore, the method of continuously increasing the water volume in the IVR tank is not operable in the engineering practice. Instead, it may be considered to carry out the active pit injection system in advance, to increase the water injection volume in-vessel while reducing the water injection ex-vessel from the IVR tank. Through sensitivity analysis, the second selected IVI optimization strategy with a passive IVR tank is presented.

***Optimization strategy 1.2*:** 1) Increase the initial water level in the IVR tank to 8.01 m. 2) Implement the simultaneous water injection in-vessel and ex-vessel at 20 min after the core outlet temperature exceeds 650°C and with 60 mm of IVI pipeline diameter. 3) When the water level in the IVR tank is less than 2 m, carry out the active water injection from the IRWST into the pit and cease the passive water injection into the pit.

The water capacity of the IVR tank is much smaller than that in the IRWST. Therefore, for further optimization of the IVI strategy, it can be considered to continue the in-vessel injection through the IRWST after the passive IVR tank is depleted (referred to as optimization strategy 1.3). The detailed description is as follows.

***Optimization strategy 1.3*:** 1) Increase the initial water level in the IVR tank to 8.01 m. 2) Implement the simultaneous water injection in-vessel and ex-vessel at 20 min after the core outlet temperature exceeds 650°C and with 60 mm of IVI pipeline diameter. 3) When the water level in the IVR tank is nearly depleted, inject water into the IVR tank through the active pipeline from the IRWST, to continue the simultaneous water injection in-vessel and ex-vessel.

In-Vessel Injection With Additional Passive Severe Accident Dedicated In-Vessel Injection Tanks

In the process of water injection in-vessel, a large amount of steam will be generated after the contact between the coolant and fuel rods at high temperature, which may cause the pressure in the primary circuit to increase significantly. The passive IVR water tank injects water into the reactor through gravity. In this condition, the in-vessel injection by a passive IVR tank may be ceased due to the overpressure in the primary circuit. In order to ensure the successful implementation of water injection in-vessel, the concept of passive SADITs is proposed (referred to as ***optimization strategy 2***).

The schematic of the IVI strategy with passive SADITs is shown in **Figure 8**, in which the passive IVR tank is only used for ex-vessel injection. The key equipment added contains three trains of passive dedicated in-vessel injection tanks as well as related valves and pipelines, the principle of which is consistent with that of ACCs, including a compressed gas zone and a water zone. The process of water injection into the reactor is divided into two stages:

1) When the primary circuit pressure is lower than the setting value, the ACCs are triggered, in which the water is quickly injected into the pressure vessel through a large flow pipeline.
2) When the primary circuit pressure is lower than 0.5 MPa and the core outlet temperature exceeds 650°C, the passive SADITs are activated by the operator. The in-vessel injection is carried

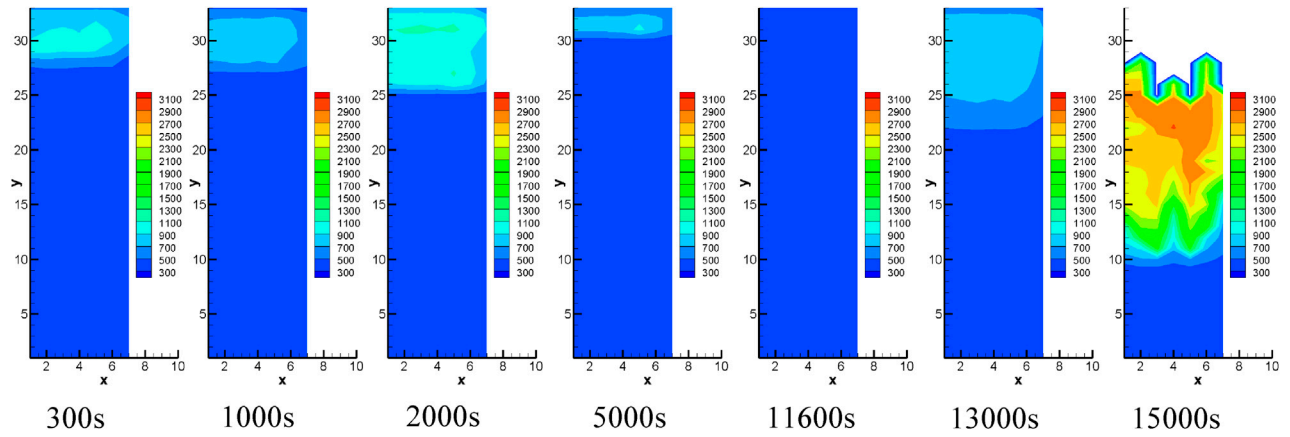

FIGURE 13 | Temperature distribution of cladding for optimization strategy 2.

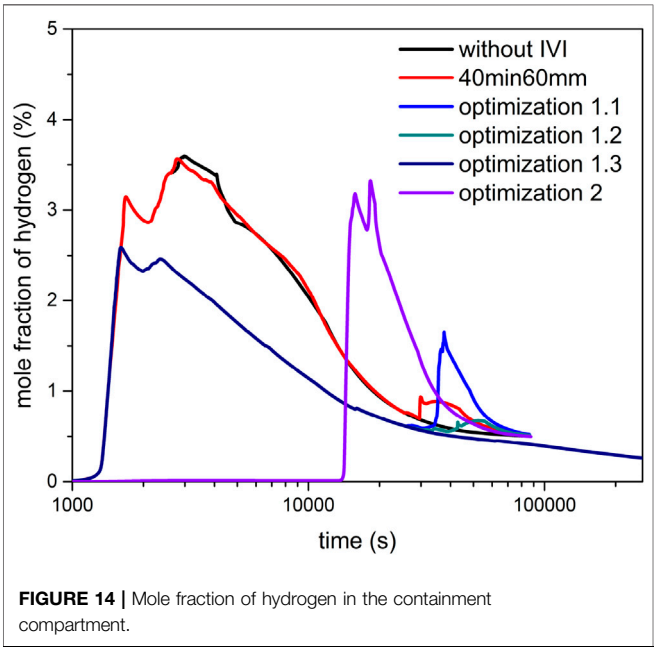

FIGURE 14 | Mole fraction of hydrogen in the containment compartment.

out with a small pipeline (60 mm diameter). Each train of SADIT injects 60 m^3 of water into the pressure vessel. The initial pressure of compressed gas in the SADIT is 1 MPa.

EFFECTIVENESS ASSESSMENT OF IN-VESSEL INJECTION

In this section, the effectiveness assessment for various IVI strategies mentioned above is performed compared with the design without IVI.

Effect on Core Damage Progression

The key events in the core damage progression after LB-LOCA for various IVI strategies are shown in **Table 1**. Compared with the design without the water injection in-vessel, the various IVI strategies can significantly delay the moment at which the core is completely exposed and the corium relocates into the lower head. **Figure 9** presents the core collapsed water level. It could be found that optimization strategy 2 implements earliest the water injection in-vessel, in which most of the core area is not exposed during the water injection process. In optimization strategy 1.3, the IRWST maintains the in-vessel injection for more than 72 h, which ensures that the core is always submerged and prevents the core melt from relocating into the lower head. Compared with the design without IVI, the 40 min 60 mm strategy, optimization strategy 1.1, optimization strategy 1.2, and optimization strategy 2 delay the relocation moment of corium to the lower head for 7.15, 9.25, 10.77, and 4.17 h, respectively. And the following can be summarized:

1) Optimization strategy 1.1 can maintain the core in the submerged state for at least 6 h.
2) Optimization strategy 1.2 can maintain the core in the submerged state for at least 10 h.
3) Optimization strategy 1.3 can maintain the core in the submerged state for at least 72 h.

Effect on Molten Pool in Lower Head

Figure 10 shows total decay power in the lower plenum debris, from which it could be found the moment of corium relocated into the lower head and there is the maximum decay power in the molten pool. The maximum decay heat and the composition in the molten pool are presented in **Table 2**. Since the decay heat power decreases with time after shutdown, the delay on the moment of corium relocation can greatly reduce the maximum decay heat in the molten pool. Compared with the design without the water injection in-vessel, the peaks of decay heat for the 40 min 60 mm strategy, optimization strategy 1.1, optimization strategy 1.2, and optimization strategy 2 are decreased by 29.8, 30.7, 33.2, and 19.7%, respectively.

Effect on IVR Effectiveness

To assess the effectiveness of various IVI strategies, the local heat flux along the lower head is compared with CHF profiles in the external surface of lower head, in which the CHF profiles are determined by the REVECT (REactor Vessel External Cooling Test) facility (Zhan

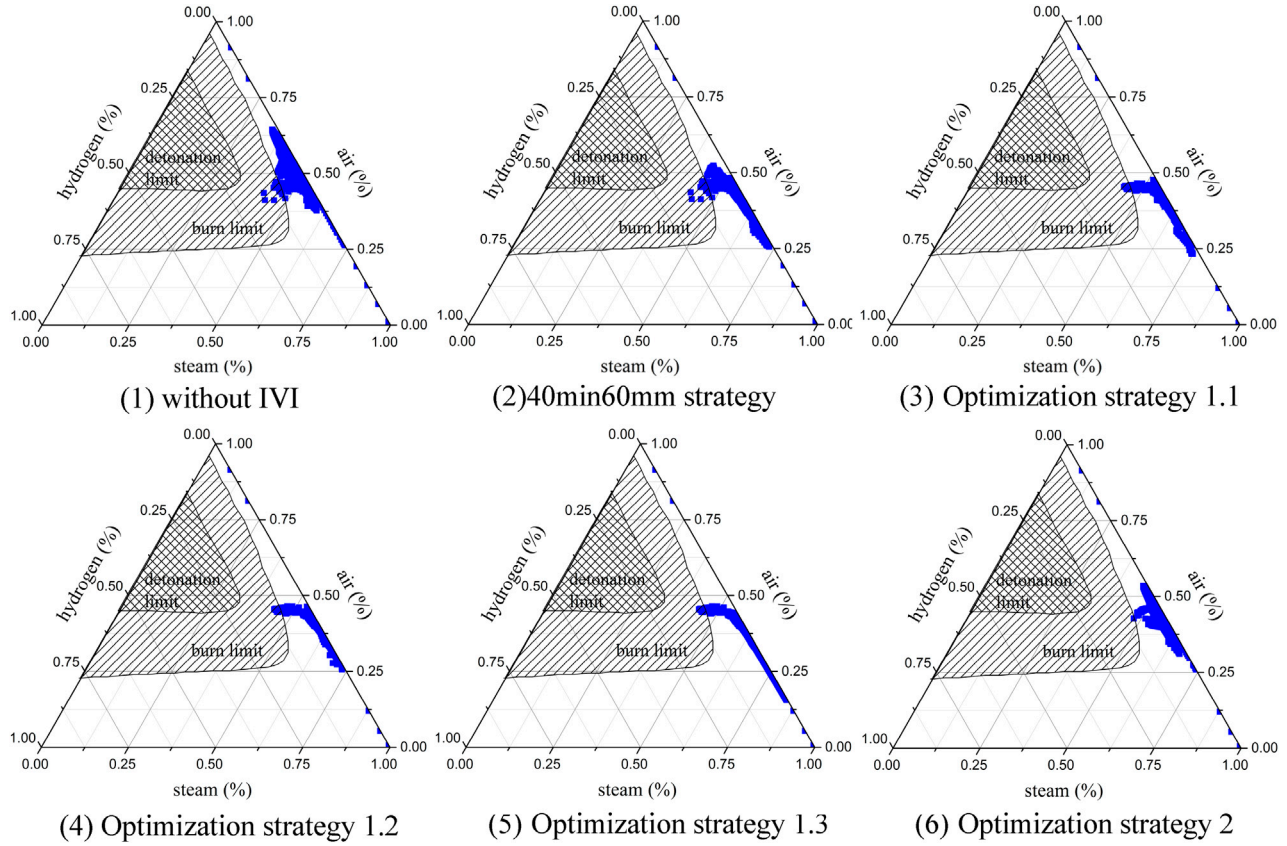

FIGURE 15 | Hydrogen deflagration diagram for the cold leg compartment.

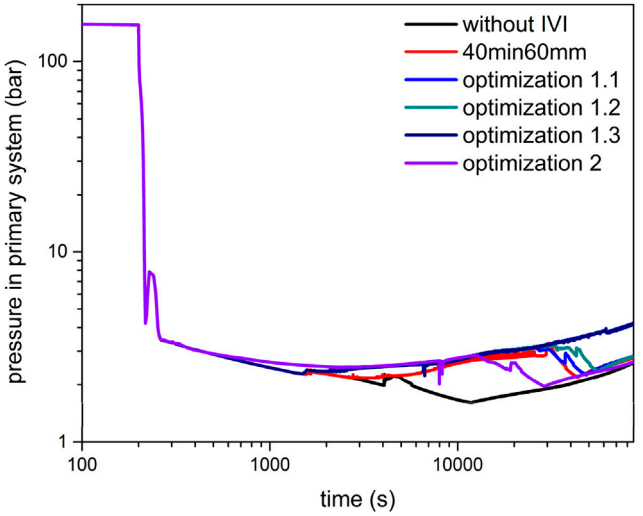

FIGURE 16 | Pressure in the primary system.

et al., 2020). **Figure 11** presents the comparison between the local heat flux and the CHF profiles. Due to the focusing effect in the molten pool, the local heat flux in the metallic layer is maximum. Since the decay heat in the molten pool is reduced by delaying the relocation of corium in the lower head in various IVI strategies, the margin for the effectiveness of IVR can be greatly increased, as shown in **Table 3**. It can be concluded that the implementation of early in-vessel injection after severe accidents has a significant positive effect on delaying the accident progression in the core and increasing the margin of IVR effectiveness.

ASSESSMENT OF NEGATIVE EFFECTS

The key risks of water injection in-vessel are concentrated in 1) hydrogen explosion, 2) PS and containment overpressure, 3) FP release, and 4) steam explosion in-vessel. Severe experiments have been carried out to analyze the mechanism of steam explosion, including KROTOS (Huhtiniemi and Magallon, 2001) and FARO (Magallon et al., 1999). It is found that, without external triggering, the spontaneous occurrence of steam explosion in-vessel is very hard (Fletcher, 1994). The SERG (Steam Explosion Review Group) project points out that the conditions for triggering the in-vessel explosion are very rigorous, and the possibility is concluded to be unlikely (Basu and Ginsberg, 1996). And the SERENA (Steam Explosion Resolution for Nuclear Application) program demonstrates the safety margin for in-vessel steam explosion could be considered sufficient (Magallon and Bang, 2007). Therefore, the negative effect for steam explosion in-vessel is not considered in this paper.

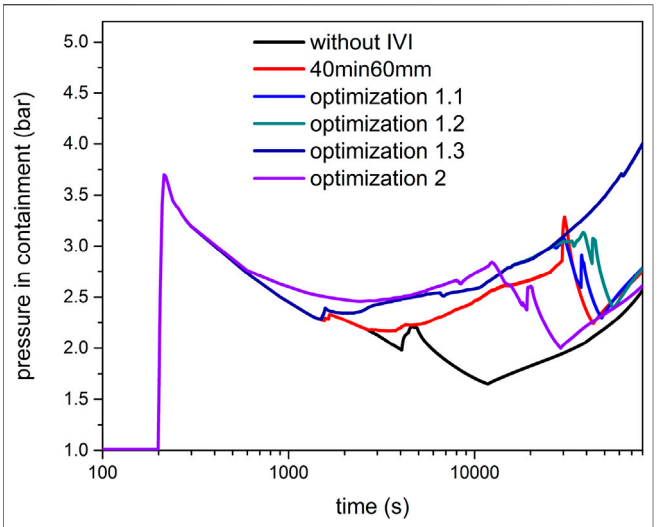

FIGURE 17 | Pressure in the containment.

Risk Analysis of Hydrogen Explosion

Integrated Mass of Hydrogen

Figure 12 presents the integrated mass of H_2 generated in the core and lower plenum. Before the implementation of in-vessel injection, the hydrogen mass in 40 min 60 mm, optimization 1.1, optimization 1.2, and optimization 1.3 is consistent with the design without IVI. After the first core uncovery, the temperature of the fuel rods rises rapidly and the cladding is oxidized to generate a large amount of hydrogen.

As shown in **Figure 2**, most of the core temperature has exceeded 1000 K when the IVI is carried out in the 40 min 60 mm strategy. Once the cladding temperature exceeds 1000 K, the zirconium alloy begins to undergo intense oxidation. After the water injection in-vessel is implemented, the generated steam greatly increases the oxidation rate, thereby significantly increasing the hydrogen production in the core.

The water injection in-vessel in optimization strategies 1.1–1.3 is carried out earlier, at which about 1/3 of the core area has not been exposed. During the water injection process, this part of core is not oxidized then reducing the mass of hydrogen generated compared with the strategy without IVI. **Figure 13** presents the temperature distribution of cladding for optimization strategy 2. It can be found the temperature of the entire core cladding is lower than 1500 K during the water injection stage, which penalizes the cladding oxidation, resulting in hydrogen production close to zero. After the water injection in-vessel is ceased, the core degradation is restarted, causing an increase in hydrogen production. Compared with the design without IVI, optimization

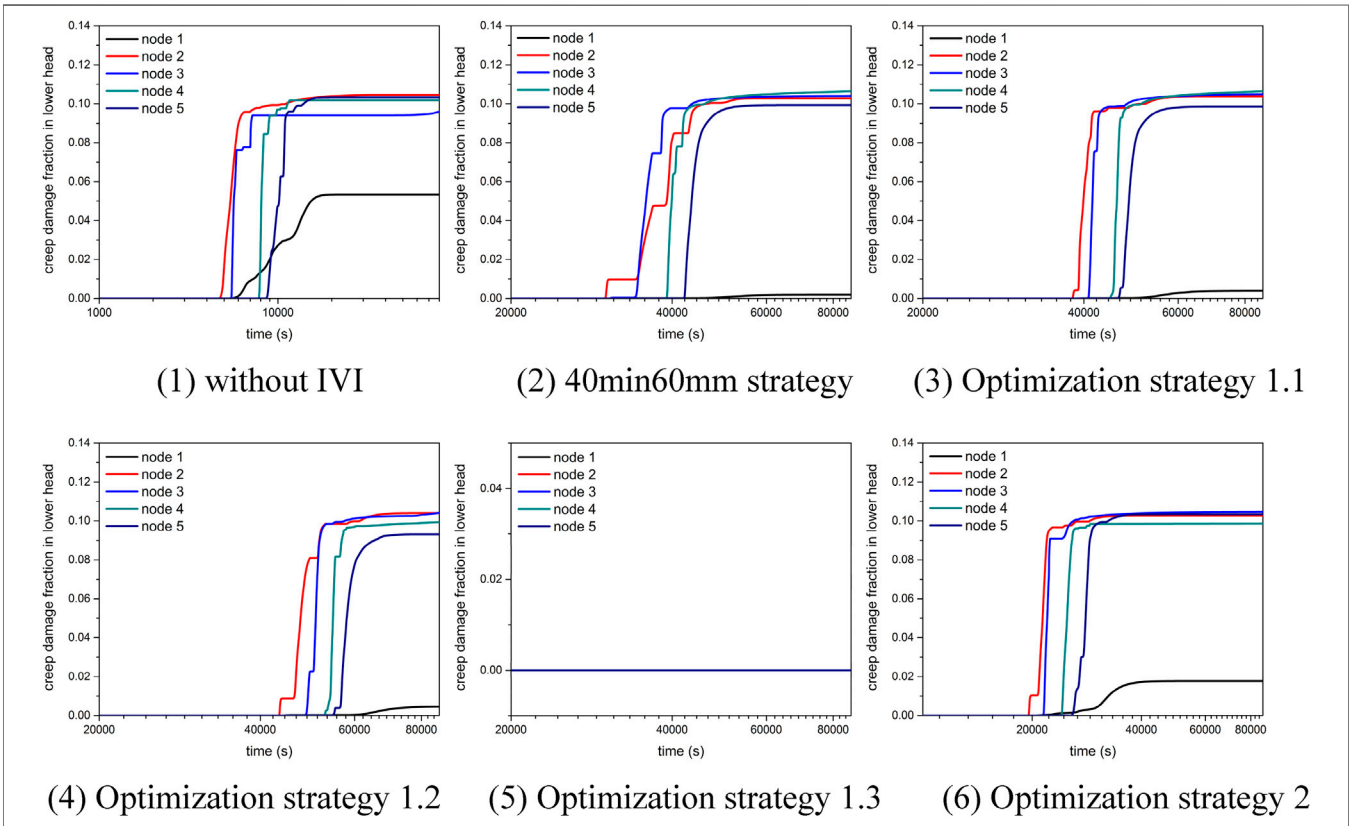

FIGURE 18 | Creep damage fraction.

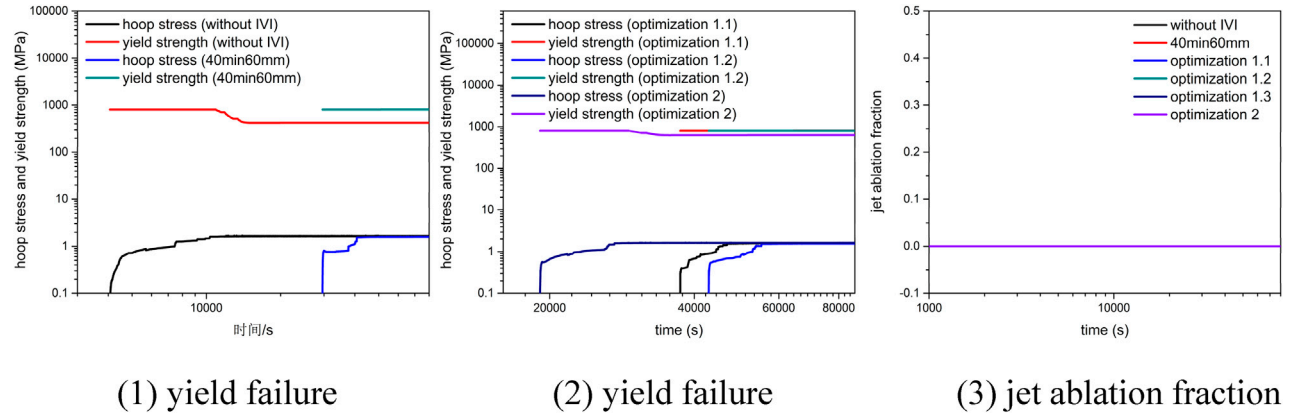

FIGURE 19 | Yield failure and jet ablation fraction.

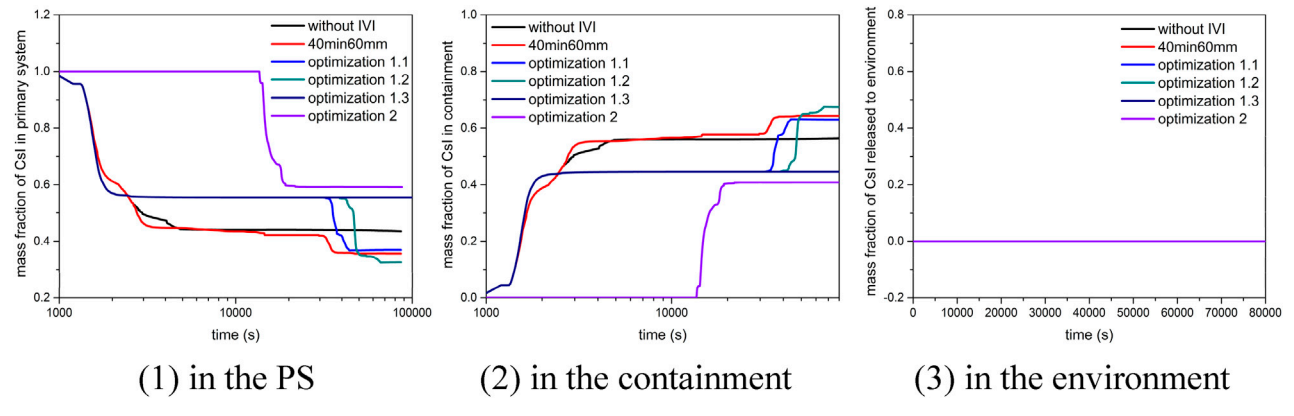

FIGURE 20 | Mass fraction of CsI.

strategy 2 can significantly reduce the amount of hydrogen produced within 3.6 h after severe accidents, providing valuable response time for external emergency measures to be put into operation.

Hydrogen Risk in Cold Leg and Containment Compartments

The hydrogen generated in the core and lower plenum is released into the containment through the break position in the primary circuit, which is at the cold leg in loop 1. Hydrogen is most likely to accumulate in the cold leg compartment and the containment compartment. Therefore, the risk of hydrogen explosion in the cold leg compartment and containment compartment is given priority. **Figure 14** presents the average mole fraction of uniformly distributed hydrogen in the containment compartment.

For the analysis of hydrogen risk in the containment, the flame accelerated to sound velocity and the deflagration to detonation transition (DDT) can be excluded if the average mole fraction of uniformly distributed hydrogen is less than 10% (IAEA, 2011). It can be seen from **Figure 14** that the average hydrogen mole fraction in containment for various strategies is much lower than 10%. Consequently, the risk of global detonation in the containment can be eliminated.

For the analysis of hydrogen risk in the cold leg compartment, the ternary characteristic curve for hydrogen deflagration proposed by Shapiro and Moffette (Shapiro and Moffette T, 1957) is used to determine whether hydrogen combustion or explosion occurs. The hydrogen deflagration diagram for various strategies is presented in **Figure 15**. It can be found that, in all strategies, only the hydrogen combustion zone is reached, which indicates that there is no risk of a violent explosion of hydrogen in the cold leg compartment.

It can be concluded that the risk of hydrogen detonation in both the containment and the cold leg compartment is at a low level. The failure of containment integrity due to hydrogen flame acceleration can be excluded.

Primary System and Containment Overpressure

The risk analysis of overpressure is used to assess the impact of steam generated due to in-vessel injection on the primary system and the containment.

Pressure Evolution in Primary System and Containment

In the calculation, the double-ended guillotine break occurs at the cold leg in loop 1 at 200 s. The failure of pressure boundary makes the primary circuit pressure drop rapidly from 155 bar (as shown in **Figure 16**). At the same time, a large amount of primary coolant enters the containment, causing the containment pressure to rise rapidly (as presented in **Figure 17**). When the pressure of the primary circuit drops below the setting value, the ACCs are triggered to quickly inject water into the RPV with a large flow rate, causing the primary circuit pressure to rise briefly. Afterward, due to the continuous evaporation of water in the pressure vessel, the water inventory in the core is gradually reduced. Therefore, the pressure in the primary circuit decreases. The high-temperature steam entering the containment condenses after contacting the cold containment wall surface, causing the pressure in the containment to be reduced. After the water injection in-vessel is implemented, the pressure in the primary circuit and the containment rises again. Meanwhile, the water in the pit continuously evaporates, causing the pressure in the containment to rise continuously.

Owing to using a small tube diameter to implement the in-vessel injection, the water injection flow rate is limited. Therefore, there is not significant pressure increase in the primary circuit and the containment during the water injection process. Compared with the design without IVI, the pressure increase in the PS and containment does not exceed 2 bar. And the maximum pressure in the containment within 24 h after LB-LOCA does not exceed the design limit of 5.2 bar. Consequently, the integrity of the containment within 24 h after the accident can be guaranteed.

Effect on Lower Head

In MIDAC, five mechanisms are considered to analyze the failure risk of a reactor vessel lower head. Ignoring the influence of lower head penetrations, three failure mechanisms of the lower head are analyzed in this paper, including the following:

1) *Creep failure*: The internal pressure in the vessel and the weight of the molten pool with high temperature may induce the creep failure of the lower head. Once the cumulative creep damage fraction reaches 1.0, the creep failure occurs.
2) *Yield failure*: The metallic layer may thermally attack and weaken the vessel wall. When the hoop stress load on the RPV lower head exceeds the yield stress, the integrity of the lower head will be lost due to yield failure.
3) *Jet ablation failure*: The corium jet may cause localized ablation of the lower head. When the ratio between the eroded depth and the lower head wall thickness reaches 1.0, the jet ablation failure occurs.

Figures 18, **19** present, respectively, the creep damage fraction and the comparison between the hoop stress and the yield strength as well as the jet ablation fraction for various strategies. It can be found that the creep damage fraction and the jet ablation fraction are far less than 1.0, and the hoop stress is much smaller than the yield strength. It can be concluded that the integrity of the lower head can be guaranteed after the implementation of IVI.

Effect on SG Tubes

In the case of overpressure in the primary circuit, the heat transfer tubes of the steam generator may be broken, resulting in an increased risk of fission products from the primary circuit being released into the secondary circuit. The failure of SG tubes in MIDAC is determined by the creep damage fraction. The calculation results show that the creep damage fractions in SG tubes for various strategies are close to 0 during the accidents. It may be explained by the fact that the calculation condition is LB-LOCA, in which the pressure in the primary circuit remains at a low level after the implementation of IVI. Therefore, the temperature and pressure of the saturated steam flowing through the steam generator are low, which has little effect on the creep failure of the heat transfer tubes.

Risk Analysis of Fission Product Release

Fission products are divided into 12 groups according to chemical properties in MIDAC, in which the isotope nuclides of Kr, Xe, I, and Cs elements contribute 95.48 and 90.17% to the external radiation dose within 2 h and 30 days after severe accidents. Therefore, the distribution characteristics of nobles and CsI are given priority for the risk analysis of fission product release. **Figure 20** presents the mass fraction of CsI in the primary system, containment, and environment, respectively. The variation tendencies of nobles are consistent with those of CsI. Compared with CsI, nobles are more volatile, causing all the nobles in the core to be transported to the containment.

During the IVI process in the 40 min 60 mm strategy and optimization strategies 1.1 and 1.2, massive cracks are generated between and within the grains in the fuel pellets with high temperature due to quenching, which is favorable to the release of fission products. Since the core remains submerged in optimization strategy 1.3, the zirconium cladding in the bottom region is not oxidized and damaged. Therefore, the integrity of the zirconium cladding hinders the release of CsI and nobles. The implementation of IVI is earliest in optimization strategy 2, in which the temperature of the entire core is at a low level which prevents the fuel pellets from shattering due to quenching. The release quantities of CsI and nobles are the lowest after the core is exposed again.

The maximum pressure in the containment does not exceed the design limit of 5.2 bar within 24 h after the severe accidents for various strategies. Therefore, the integrity of the containment can be guaranteed. When the containment is intact, the amount of fission products released into the environment through the natural leakage channel of the containment can be neglected. Therefore, the risk of fission products being released into the environment can be eliminated.

CONCLUSION

In order to improve the margin of the current IVR-ERVC strategy for high-power reactors, two feasible IVI designs are proposed: 1) using the passive IVR water tank to implement simultaneous water injection in-vessel and ex-vessel and 2) using passive SADITs to implement water injection in-vessel. The effectiveness of IVI is performed, and the negative effects after water injection are analyzed by using MIDAC. It can be found that compared with

the design without IVI, the early water injection in-vessel can significantly delay the accident process in the core, reducing the maximum decay heat of the molten pool in the lower head and increasing the effectiveness margin of IVR-ERVC; especially, the following can be found:

1) The three optimization strategies in the first IVI design can realize, respectively, that the core is submerged within 6/10/72 h after severe accidents.
2) The second design can significantly reduce the hydrogen production in 3.6 h after severe accidents, providing valuable response time for external emergency measures to be put into operation.

In addition, when the IVI is implemented, the risk of violent explosion of hydrogen in the cold leg compartment and the containment is at a low level. And compared with the design without IVI, the pressure increase in the primary circuit and the containment does not exceed 2 bar after water injection in-vessel. The risk of yield failure, creep failure, and jet ablation failure of the lower head can be eliminated. And the maximum pressure in the containment does not reach the design limit of 5.2 bar within 24 h after severe accidents. Therefore, the integrity of the containment can be guaranteed, and the amount of fission products released into the environment through the natural leakage channel of the containment can be neglected.

Except for HPR1000, the sensitivity analysis conclusions in the paper are also applicable to the Severe Accident Management Guidelines (SAMG) of other reactor types, including AP1000 and CAP1400. Namely, compared with late water injection, early in-vessel water injection has a more obvious effect on delaying the process of accidents in the reactor and increases the safety margin of the current IVR-ERVC strategy for high-power reactors. In the late phase of water injection, it is possible that the debris bed and molten pool present uncoolability, resulting in an insignificant effect of water injection in the reactor, and serious negative risks such as steam explosion may occur. In contrast, in the case of early in-vessel water injection, the uncertainties of the phenomenon and the calculation models of severe accident codes are limited. Meanwhile, the negative risk after water injection is in an acceptable state.

DATA AVAILABILITY STATEMENT

The original contributions presented in the study are included in the article/**Supplementary Material**, and further inquiries can be directed to the corresponding author.

AUTHOR CONTRIBUTIONS

The authors listed in this article have all made important contributions to the completion of this paper. Among them, PC and XZ completed the main writing of this article. ZW completed the modeling of MIDAC calculation. DZ and SX provided the main ideas for creation.

FUNDING

This work was supported by the National Key R&D Program of China (Grant No. 2019YFB1900702).

SUPPLEMENTARY MATERIAL

The Supplementary Material for this article can be found online at: https://www.frontiersin.org/articles/10.3389/fenrg.2021.785513/full#supplementary-material

REFERENCES

Basu, S., and Ginsberg, T. (1996). A Reassessment of the Potential for an Alpha-Mode Containment Failure and a Review of the Current Understanding of Broader Fuel-Coolant Interaction Issues. Second Steam Explosion Review Group Workshop. *Antimicrob. Agents Chemother.* 52 (8), 2937–2939.

Carénini, L., Fichot, F., Bakouta, N., Le Tellier, R., Viot, L., Melnikov, I., and Filippov, A. (2019). "Main Outcomes from the IVR Code Benchmark Performed in the IVMR Project," in *Proc. Of the 9th European Review Meeting on Severe Accident Research (ERMSAR2019)*, 18–20.

Carénini, L., and Fichot, F. (2016). "The Impact of Transient Behavior of Corium in the Lower Head of a Reactor Vessel for In-Vessel Melt Retention Strategies," in International Conference on Nuclear Engineering, Charlotte, North Carolina, June 26-30, 2016 (American Society of Mechanical Engineers (ASME)), V004T13A009.

Coryell, W., and April (1994). *Summary of Important Results and SCDAP/RELAP5 Analysis for OECD LOFT Experiment LP-FP-2*. Idaho Falls: EG&G Idaho. Inc.

Dorsselaere, J. P. V., Fichot, F., and Seiler, J. M. (2006). Views on R&d Needs about In-Vessel Reflooding Issues, with a Focus on Debris Coolability. *Nucl. Eng. Des.* 236 (19-21), 1976–1990. doi:10.1016/j.nucengdes.2006.03.039

Fichot, F., Carénini, L., Sangiorgi, M., Hermsmeyer, S., Miassoedov, A., Bechta, S., et al. (2018). Some Considerations to Improve the Methodology to Assess In-Vessel Retention Strategy for High-Power Reactors. *Ann. Nucl. Energ.* 119, 36–45. doi:10.1016/j.anucene.2018.03.040

Fletcher, D. F. (1994). A Review of the Available Information on the Triggering Stage of a Steam Explosion. *Nucl. Saf.* 35, 1.

Hagen, S., Hofmann, P., Noack, V., Schanz, G., Schumacher, G., and Sepold, L. (1993). *Results of SFD Experiment CORA-13 (OECD International Standard Problem 31)*. Karlsruhe, Germany: No. KFK–5054 Kernforschungszentrum Karlsruhe GmbH (Germany). Hauptabteilung Ingenieurtechnik.

Huhtiniemi, I., and Magallon, D. (2001). Insight into Steam Explosions with Corium Melts in KROTOS. *Nucl. Eng. Des.* 204 (1-3), 391–400. doi:10.1016/s0029-5493(00)00319-8

IAEA (2011). *Mitigation of Hydrogen Hazards in Severe Accidents in Nuclear Power Plants*. IAEA-TECDOC-1661.

Jun, T., Jingxi, L. I., Lili, T., and Xuewu, C. (2011). Core Cooling in Pressurized-Water Reactor during Water Injection. *Nucl. Sci. Tech.* (01), 62–66. doi:10.13538/j.1001-8042/nst.22.60-64

Kymäläinen, O., Tuomisto, H., and Theofanous, T. G. (1997). In-vessel Retention of Corium at the Loviisa Plant. *Nucl. Eng. Des.* 169 (1-3), 109–130. doi:10.1016/s0029-5493(96)01280-0

Ma, W., Yuan, Y., and Sehgal, B. R. (2016). In-vessel Melt Retention of Pressurized Water Reactors: Historical Review and Future Research Needs. *Engineering* 2 (1), 103–111. doi:10.1016/j.eng.2016.01.019

Magallon, D., and Bang, K. H. (2007). *FCI Phenomena Uncertainties Impacting Predictability of Dynamic Loading of Reactor Structures (Serena Programme)*. OECD (NEA) Committee on the Safety of Nuclear Installations.

Magallon, D., Huhtiniemi, I., and Hohmann, H. (1999). Lessons Learnt from Faro/termos Corium Melt Quenching Experiments. *Nucl. Eng. Des.* 189 (1/3), 223–238. doi:10.1016/s0029-5493(98)00274-x

Oh, S. J., and Kim, H. T. (2005). "Effectiveness of External Reactor Vessel Cooling (ERVC) Strategy for APR1400 and Issues of Phenomenological Uncertainties," in Workshop Proceedings: Evaluation of Uncertainties in Relation to Severe Accidents and Level-2 Probabilistic Safety Analysis, Aix-en-Provence (France), November 7-9, 2005, 7–9.

Sangiorgi, M., and Ezzidi, A. (2015). "In-vessel Melt Retention (IVMR) Analysis of a VVER-1000 NPP," in In 6th ASTEC user's club/2nd CESAM workshop.

Shapiro, Z. M., and Moffette T, R. (1957). *WAPD-SC-545*. Pittsburgh, PA: Atomic Energy Commission.

Shi, G., Gu, P., Lu, W., Wang, J., Cao, K., Zhang, K., et al. (2019). CAP1400 IVR Related Design Features and Assessment. *Nucl. Eng. Des.* 346, 35–45. doi:10.1016/j.nucengdes.2019.03.002

Theofanous, T. G., Liu, C., Additon, S., Angelini, S., Kymäläinen, O., and Salmassi, T. (1997). In-vessel Coolability and Retention of a Core Melt. *Nucl. Eng. Des.* 169 (1-3), P35–P42. doi:10.1016/s0029-5493(97)00009-5

Nuclear Regulatory Commission (1989). Severe Accident Risks: An Assessment of Five U.S. Nuclear Power Plant. *NUREG-1150, Revision* 1.

Wang, D., Zhang, Y., Chen, R., Su, G. H., Qiu, S., and Tian, W. (2019). Numerical Simulation of Zircaloy-Water Reaction Based on the Moving Particle Semi-implicit Method and Combined Analysis with the Midac Code for the Nuclear-Reactor Core Melting Process. *Prog. Nucl. Energ.* 118.

Wang, J., Tian, W., Fan, Y., Mao, K., Lu, J., Su, G., et al. (2014). The Development of a Zirconium Oxidation Calculating Program Module for Module In-Vessel Degraded Analysis Code Midac. *Prog. Nucl. Energ.* 73, 162–171. doi:10.1016/j.pnucene.2014.02.006

Wang, J., Tian, W., Zhang, Y., Chen, L., Li, L., Zhang, L., et al. (2014). The Development of Module In-Vessel Degraded Severe Accident Analysis Code Midac and the Relevant Research for Cpr1000 during the Station Blackout Scenario. *Prog. Nucl. Energ.* 76 (sep), 44–54. doi:10.1016/j.pnucene.2014.05.015

Wright, A. L. (1994). *Primary System Fission Product Release and Transport*. Oak Ridge, Tennessee, United States.

Wu, S., Zhang, Y., Wang, D., Tian, W., Qiu, S., and Su, G. H. (2021). *Assessment of the Severe Accident Code Midac Based on Froma, Quench-06&16 Experiments*. Xi'an, China: Nuclear Engineering and Technology.

Xing, J., Song, D., and Wu, Y. (2016). HPR1000: Advanced Pressurized Water Reactor with Active and Passive Safety. *Engineering* 2 (1), 79–87. doi:10.1016/j.eng.2016.01.017

Zhan, D., Zhao, X., Xia, S., Chen, P., and Chen, H. (2020). Studies on Key Effect Factors of Natural Circulation Characteristics for Advanced PWR Reactor Cavity Flooding System. *Sci. Techn. Nucl. Installations* 2020, 1–11. doi:10.1155/2020/4765046

Zhang, Y. P., Qiu, S. Z., Su, G. H., and Tian, W. X. (2010). Analysis of Safety Margin of In-Vessel Retention for AP1000. *Nucl. Eng. Des.* 240 (8), 2023–2033. doi:10.1016/j.nucengdes.2010.04.020

Conflict of Interest: Authors PC, ZW, DZ, SX, and XZ were employed by China Nuclear Power Technology Research Institute Co., Ltd.

frontiers in Energy Research

ORIGINAL RESEARCH
published: 15 March 2022
doi: 10.3389/fenrg.2022.868211

Experimental Analysis and Performance Evaluation of Spider Hydraulic Buffer for Rod Dropping in Reactor

Ti Yue, Pan Yuan, Shan Huang, Fawen Zhu, Yuanming Li, Chunlan Huang, Lele Zheng, Haoyu Wang and Menglong Liu*

Science and Technology on Reactor System Design Technology Laboratory, Nuclear Power Institute of China, Chengdu, China

Control rod drop is one of the key measures for the safe shutdown of the reactor. The two important evaluation indicators of the drop process are the drop time-length and the maximum impact force. By theoretical and experimental methods, this paper analyzes the influencing factors and evaluates the performance of a new type of spider hydraulic buffer with compact structure and ingenious design, which couples mechanical force and fluid resistance. First, through experiments, it is found that the real-time curve of the maximum impact force often has a bimodal structure. And the double peaks vary with the change of the internal structure of the hydraulic buffer. Secondly, since there are many variables about the structure (aperture, position, quantity, piston stroke et al.), in order to consider their influence on the maximum impact force, an equivalent ongoing flow area of the drain holes is introduced. It suggested that when the flow area of the working holes which can be covered by the stroke is close to the flow area of the remaining holes, the impact force tends to appear a minimum value. A relationship between the maximum impact force and the structure is proposed accordingly. Finally, this paper proposes a quantitative evaluation method for comprehensive buffering performance, in which the comprehensive performance evaluation factor η ($0<\eta<1$) takes into account both the maximum impact force and the drop time. The smaller the maximum impact force and the rod drop time-length, the closer the evaluation factor η is to 1, indicating that the buffering performance is better. The research in this paper will not only help to further understand the mechanism of the drop rod buffering process, but also contribute to the structural optimization of the subsequent spider hydraulic buffer.

Keywords: control rod drop, spider hydraulic buffer, maximum impact force, drop time-length, performance evaluation

OPEN ACCESS

Edited by:
Luteng Zhang,
Chongqing University, China

Reviewed by:
Kui Zhang,
Xi'an Jiaotong University, China
Wei Ding,
Helmholtz Association of German Research Centres (HZ), Germany

****Correspondence:***
Fawen Zhu
254085634@qq.com

Specialty section:
This article was submitted to Nuclear Energy, a section of the journal Frontiers in Energy Research

Received: *02 February 2022*
Accepted: *28 February 2022*
Published: *15 March 2022*

Citation:
Yue T, Yuan P, Huang S, Zhu F, Li Y, Huang C, Zheng L, Wang H and Liu M (2022) Experimental Analysis and Performance Evaluation of Spider Hydraulic Buffer for Rod Dropping in Reactor. Front. Energy Res. 10:868211. doi: 10.3389/fenrg.2022.868211

INTRODUCTION

In a reactor, the control rod assembly is one of the most important safety and security facilities. The control rod assembly is driven by the drive system to control the reactivity of the reactor, so as to realize the startup, normal shutdown, and power regulation of the reactor, and ensure the safety of the reactor under accident conditions. The two most concerned points in the process of dropping are the drop time-length and the maximum impact forcegenerally. If the rod drop time is too long, the

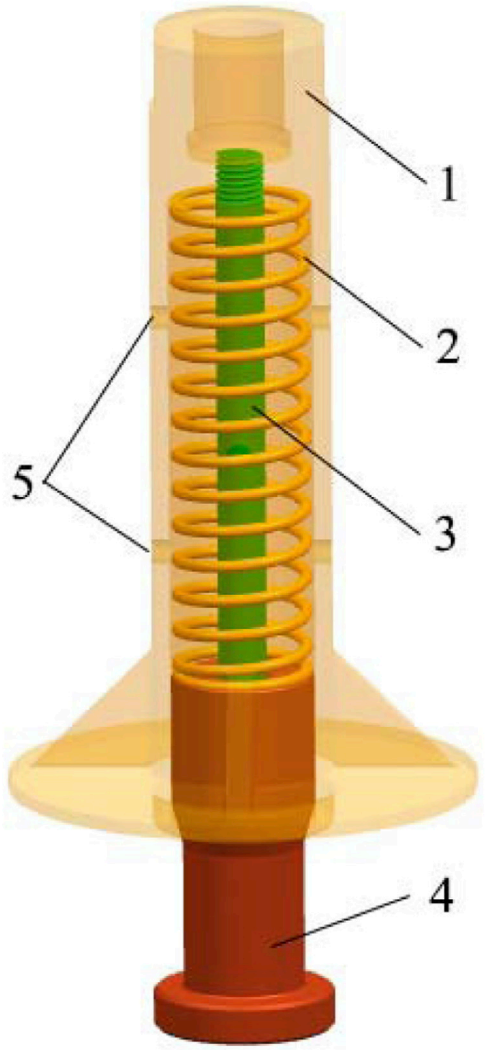

FIGURE 1 | Working principle diagram of the spider hydraulic buffer. (1-Spider body, 2-spring, 3-center pole, 4-piston body, 5-drain holes).

reactor will fail toshutdown in time. While if the maximum impact force is too large, the core equipment will be damaged. Therefore, the control rod drop process needs to be equipped with a suitable buffer mechanism, which can not only effectively buffer the impact force of the rod drop, but also affect the drop time as little as possible.

In the past, the buffering method of the control rod assembly mainly used the reduced diameter section at the bottom of the rod bundle and supplemented the reverse resistance provided by the top spring to complete the rod drop buffer (Rabiee and Alireza, 2016; Xiao et al., 2017a; Xiao et al., 2017b). However, the machining of the reduced diameter section of the guide tube is difficult, and it is easy to cause rod wear or stickingamong droppingbehavior (Fu and Pu, 1997; Andriambololona et al., 2007; Zhang, 2017).

To this end, this paper studies a new type of hydraulic buffer structure, as shown in **Figure 1**. In addition to the top spring, the buffer also has a liquid cavity inside the handle body of the connecting handle. When the piston is pressed into the spider body, the fluid in the cavity is squeezed out from the drain holes on the wall of the spider body. In this process, the drain holes will hinder the liquid and play the role of hydraulic buffer to a certain extent, so as to avoid the excessive impact force of the falling rod. Due to the coupling of the dual effects of mechanical force and fluid resistance, the hydraulic buffer has a compact structure and ingenious design, so its application potential is great (Qin et al., 2018; Mingmin and Claus, 2013). So far, several researches have analyzed the control rod dropping program by simulated or experimental method (Yoon et al., 2009; Lin et al., 2017; Zhang et al., 2020; Zhang et al., 2021). However, the analysis of the subsequent buffer program during rod dropping, especially the relationship between the buffer performance and structural parameters, has not been systematically studied yet.

In this paper, through theoretical analysis and experimental research, the sensitivity analysis of the maximum impact force and the drop time-length of the rod are carried out under different buffer structures such as drain holes and pistons respectively. The relationship between the maximum impact force and the structure is obtained, and a quantitative evaluation method for comprehensive buffering performance is proposed. Based on the above analysis methods, the potential optimal structural suggestionsfor the spider hydraulic buffer are finally given.

BUFFERING PROCESS

The process can be divided into two stagesfor the control rod drop—the free fall stage and the buffer stage. First, the entire control rod assembly is dropped as a whole with severe control rods. Then, when the bottom of the buffer hits the top plate of the reactor core, the entire control rod assembly is buffered by mechanically or hydraulically action. As follows, the two steps are modeled separately and the effects of mechanical and hydraulic buffering are considered, respectively.

The Free-Falling Process

The kinematic equation describing the vertical fall of the buffer is established using Newton's second law,

$$\left(m_1 + m_{1f} + m_2 + m_{2f}\right)\ddot{x} = \left(m_1 - m_{1f} + m_2 - m_{2f}\right)g - \frac{1}{2}\rho C^s S_{cup}|\dot{x}|\dot{x} \tag{1}$$

This can be simplified into

$$\ddot{x} = c_2 - c_1|\dot{x}|\dot{x} \tag{2}$$

Where the c_1 and c_2 can be described as

$$c_2 = \frac{\left(m_1 - m_{1f} + m_2 - m_{2f}\right)}{\left(m_1 + m_{1f} + m_2 + m_{2f}\right)}g \tag{3}$$

$$c_1 = \frac{1}{2}\rho\frac{C^s S_{cup}}{\left(m_1 + m_{1f} + m_2 + m_{2f}\right)} \tag{4}$$

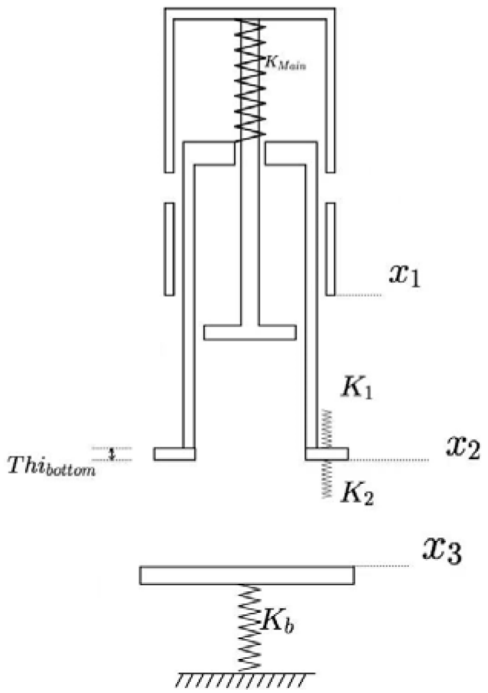

FIGURE 2 | Mechanical simplified model of buffer calculation.

Among them, the m_1, m_2 are the mass of the spider and the piston respectively. The m_{1f}, m_{2f} are the added fluid mass of the spider and the piston respectively. C^s is the overall shape drag coefficient of the buffer. The x is the vertical drop displacement of the buffer and the S_{cup} is the cross-sectional area of piston.

The Buffering Process

Since the hydraulic buffer couples both mechanical buffering and hydraulic buffering forces at the same time, its buffering effect is enhanced compared to other buffers. After the piston hits the bottom plate, on the one hand, the spring in the buffer chamber hinders the advancement of the piston. On the other hand, the fluid in the buffer chamber is pressed out by the piston, which also hinders the advancement of the piston, so that the impact kinetic energy is gradually dissipated. This coupling mechanism is also one of the advantages of spider hydraulic buffers. Therefore in recent years, the spider hydraulic buffers have begun to be favored in rod drop buffering process.

A simplified mechanical model is established to perform the effects caused directly by impacting behavior in the buffering process, as shown in **Figure 2**.

Impacting Behavior in the Buffering Process

According to the energy law, the vibration differential equation for buffering process can be expressed as **Eq. 5**,

$$M\ddot{x} + C\dot{x} + Kx = F_S + F_G + F_F \tag{5}$$

The F_S is the spring`s pretension force, the F_G is the gravity force, and the F_F is the fluid hydraulic force. Their calculation can be realized by **Eqs. 6–8** respectively,

$$F_S = \begin{bmatrix} K_{Main}L_{Main} - K_{Main}C_{L1} + \delta_1 K_1 Thi_{Bottom} \\ -K_{Main}L_{Main} + K_{Main}C_{L1} - \delta_1 K_1 Thi_{Bottom} \\ 0 \end{bmatrix} \tag{6}$$

$$F_G = \begin{bmatrix} -m_1 g \\ -m_2 g \\ -m_3 g \end{bmatrix} \tag{7}$$

$$F_F = \begin{bmatrix} Pressure_1 \\ Pressure_2 \\ 0 \end{bmatrix} \tag{8}$$

where the L_{Main} is the spring free height, and the Thi_{Bottom} is the thickness of piston base-plate. The C_{L1} is the pre-tightening height, defined as $Len_{CylInner} - Len_{Cup}$. The $Pressure_1$ and the $Pressure_2$ are the differential pressure resistance acted on the spider and the piston separately.

Hydraulic Effects in the Buffering Process

For a long time, the quantitative calculation of hydraulic action in the process of rod dropping has been a major problem for scholars. The fluid resistance is difficult to express because it is related to the relative fluid velocity who often changes with space and time. In the previous drop rod model, the following two methods are usually adopted to calculate the fluid resistance. One is to use the dynamic mesh technique to obtain the resistance effect of the fluid through the iteration of the flow field. The second is to obtain the empirical formula of hydraulic force through the fitting of test data, and finally form the dedicated rod drop program. The buffers involved in this paper have different drain holes structures, and correspondingly, their fluid resistances are different. To solve practical engineering problems, however, this paper does not plan to simulate the actual fluid resistance. Instead, the influence of different drain holes structures on the buffer performance was investigated directly through experiments.

EXPERIMENTAL SETUP

In this project, a hydrostatic buffer drop-rod test platform is built. The drop-weight testing machine was used as the subject of the experiment, and the connecting handle assembly with the control rod was placed in a transparent glass water tank. After the power is cut off, the buffer starts to fall from a certain height above the water tank with an initial velocity of zero and hits a flexible stainless steel bottom plate at the bottom of the test platform. After the impacting, the spider hydraulic buffer starts its process and finally ends when the entire spider body is stabilized.

During the experiments, two laser displacement sensors (Type: KEYENCE IL-600) were used to measure the displacement of the buffer during the dropping process and calculate its velocity and acceleration. A ring-shaped force sensor (Type: TH2IC) at the bottom of the water tank is used to measure the impact force on the bottom plate in real time. At

TABLE 1 | Key dimensions of spider hydraulic buffer.

Parts		Dimensions
Spider Body	Outer Diameter	φ45 mm
	Total Height	205 mm
	Inner Diameter,D_{si}	φ36 mm
	Height of Inner Cavity	160 mm
	Material	06Cr18Ni11Ti
Piston Body	#Stroke, L_0	50 mm
	#Outer Diameter, D_{po}	φ35.6 mm
	#(Gap between Piston and Spider)	(0.2 mm)
	Inner Diameter, D_{pi}	φ13 mm
	Material	05Cr17Ni4Cu4Nb
Center Pole	Outer Diameter, D_{ce}	φ12 mm
Stiffness of Resume Spring		1850 N/m
#Summary of Equivalent Weight		7.6 kg

Note: #These Dimensions can be varied in tests.

the same time, the experimental environment is strictly guaranteed by thermometers and voltmeters.

The schematic diagram of the buffer in this experiment is shown in **Figure 3**, and its key structural size parameters are shown in **Table 1**. As the equivalent weight, several rod-shaped structures which have been weighed precisely are fixed around the body of spider body before each test. The specific settings of the variable values in **Table 1** are shown in **Table 2**. The tests here are all univariate experiments. Each Experiment only changes one parameter on the basis of the benchmark case "A0".

RESULTS AND DISCUSSION

Effects of Piston Structure

The variable dimensions of the piston concerned in this paper mainly include the outer diameter and height, which correspond to the clearance between the piston and the connecting handle and the piston stroke, respectively.

The relationship between the maximum impact force and the piston clearance is shown in **Figure 4**. With the increase of the clearance, the maximum impact force will first decrease and then increase. By analyzing their real-time curves of the maximum impact force (as shown in **Figure 5**), it can be found that there are generally two large peaks during the buffering process. The first indicates the impact between the bottom surface of the piston and the bottom plate of the test bench, and the second is the collision between the crown of the piston and the spider body. For different cases, the peak distribution of the two shocks is also different. Taking the A0 case as an example, when the gap flow area is small, the maximum impact force appears at the first peak position. As the gap fluid flow area increases, the first peak decreases and the second peak increases gradually. When the unilateral clearance is increased to 0.30 mm, the maximum impact force will appear at the second peak.

This shows that as the flow area increases, part of the instantaneous impact energy can be converted into fluid kinetic energy, and the impact between the piston and the bottom plate is thus buffered. However, when the flow area is too large, the fluid flow rate is significantly reduced, and the original potential energy cannot be completely released in the first impact, so the impact force will be larger during the second impact.

The relationship between the maximum impact force and the piston stroke is shown in **Figure 6**. The maximum impact force decreases as the stroke increases. Analysis of the impact force real-time curve in **Figure 7** shows that when the stroke is only 30 mm, the kinetic energy of the entire system is not fully consumed by the buffering process due to the short buffering stroke. As a result, after the buffer stroke is completed, the spider body will continue to bounce up and down and generate multiple impact peaks. When the stroke of the piston increases to 70 mm, the buffer can completely consume the potential energy, and the piston will not collide with the spider body.

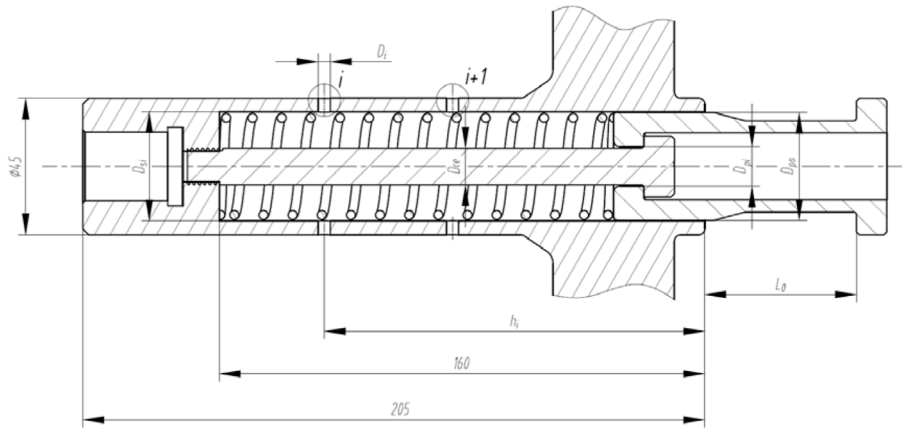

FIGURE 3 | Simplified schematic and key parameters of spider hydraulic buffer.

TABLE 2 | Settings for Changeable Structures in series of Univariate Experiments.

Changeable parameters		**Available values**									
Choice of Stroke (mm)		30 (*X1)			50 (A0)			70 (X2)			
Choice of Outer Diameter-or Gap (mm)		φ35.4–0.30 (J1)			φ35.6–0.20 (A0)			φ35.7–0.15 (J2)			
Choice of Drain Holes (mm)	a) Focus on Numbers	*N0		N1	N2	A0	N4		N5		
		[#](×)		[&](×)	(×)	(3)	(2.5)		(2)		
		[#](×)		(×)	(3.5)	(×)	(2.5)		(2)		
		[#](×)		[&](4)	(×)	(3)	(×)		(2)		
		[#](×)		(×)	(3.5)	(×)	(2.5)		(2)		
		[#](×)		(×)	(×)	(3)	(2.5)		(2)		
	b) Focus on Locations	W1	W2	W3	W4	A0	W5	W6	W7	W8	W9
		(3)	(3)	(3)	(3)	(3)	(3)	(×)	(×)	(×)	(×)
		(3)	(3)	(3)	(×)	(×)	(×)	(3)	(3)	(3)	(×)
		(3)	(×)	(×)	(3)	(3)	(×)	(3)	(3)	(×)	(3)
		(×)	(3)	(×)	(3)	(×)	(3)	(3)	(×)	(3)	(3)
		(×)	(×)	(3)	(×)	(3)	(3)	(×)	(3)	(3)	(3)
	c) Focus on Diameters	*K3-2	K3-3		A0	K3-4	K3-5		K4-1	K4-2	
		(2)	(2.5)		(3)	(3.5)	(4)		(3.5)	(2.5)	
		(×)	(×)		(×)	(×)	(×)		(×)	(×)	
		(2)	(2.5)		(3)	(3.5)	(4)		(3)	(3)	
		(×)	(×)		(×)	(×)	(×)		(×)	(×)	
		(2)	(2.5)		(3)	(3.5)	(4)		(2.5)	(3.5)	
Choice of Equivalent Weight (kg)		6.4 (M1)					7.4 (A0)			8.8 (M2)	
Choice of Dropping Height (mm)		340 (H1)					370 (A0)			400 (H2)	

Note.

**The "letter-number" or "letter-number-number" in this table are the case numbers of operating conditions.*

[#]*The five layers of brackets from top to bottom correspond to the heights (h_i) of five layers of drain holes respectively. (h_1 = 130 mm, h_2 = 110 mm, h_3 = 90 mm, h_4 = 70 mm, h_5 = 50 mm).*

[&]*The data in brackets are the aperture of drain holes in this height, and the "×" means that the two holes in this height are blocked.*

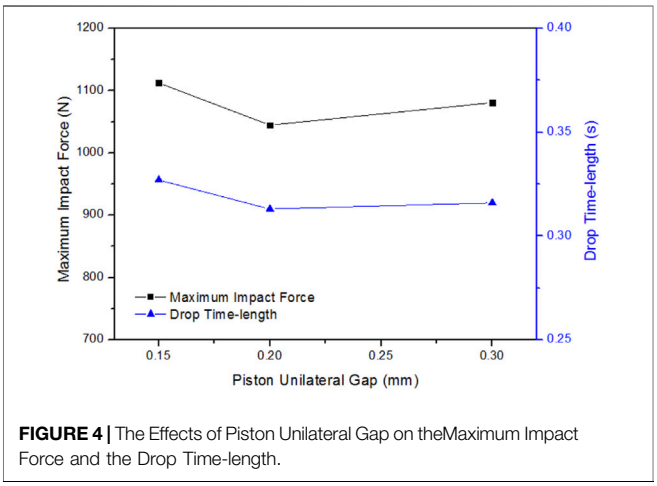

FIGURE 4 | The Effects of Piston Unilateral Gap on theMaximum Impact Force and the Drop Time-length.

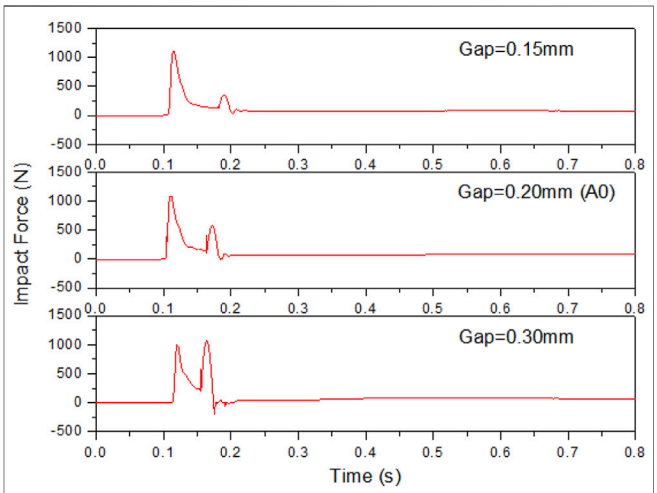

FIGURE 5 | The effects of piston unilateral gap on the real-time impact force.

Effects of Drain Holes

Experiments and numerical simulations show that there is a certain relationship between the maximum impact force and the number, diameter, and position of the drain holes, as shown in **Figures 8–10**. The maximum impact force seems to have a decreasing trend with the increase of the pore size and the number of holes. This may be due to the increase of the flow area with the increase of the pore diameter and the number of holes. Correspondingly, the fluid resistance decreases, so the resistance of the water to the piston decreases, and finally the impact force of the falling rod increases. Although the maximum impact force is somewhat related to the number, diameter, and position of holes, its regularity is still not obvious enough.

To explore the influence law of the drain holes on the maximum impact force more detailed, the real-time change curves of the impact force during the buffering process were compared in **Figure 11**. For the W1 condition with higher holes position, the values of the two peaks are very close. For the W9 condition with lower holes position, the first peak is obviously

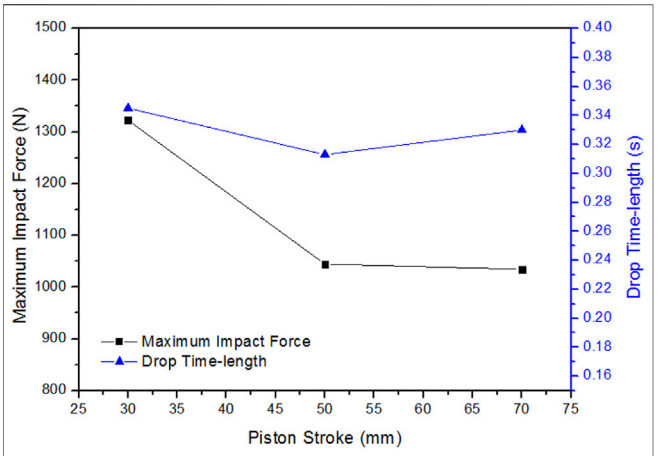

FIGURE 6 | The effects of piston stroke on the maximum impact force and the drop time-length.

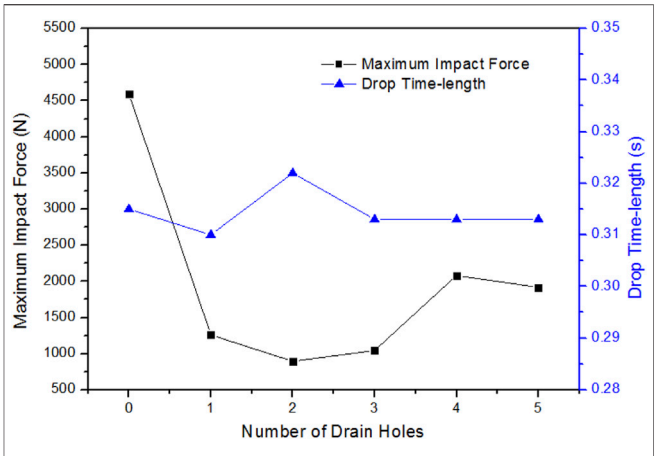

FIGURE 8 | The effects of HolesNumber on the maximum impact force and the drop time-length.

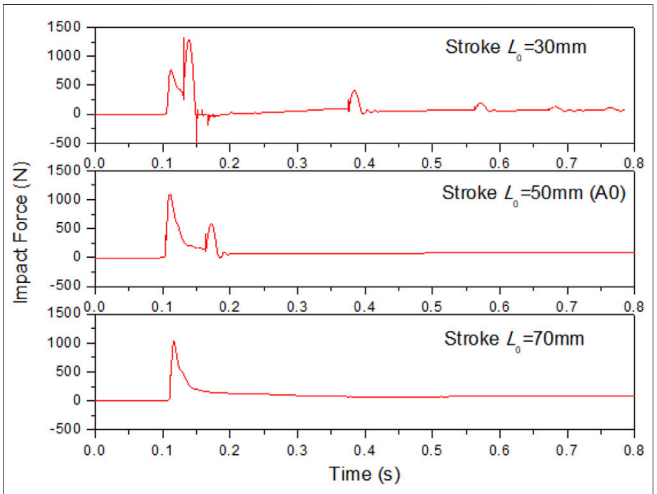

FIGURE 7 | The effects of piston stroke on the real-time impact force.

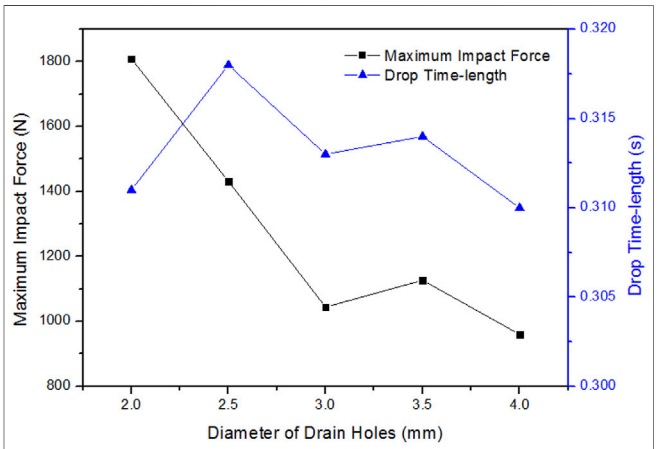

FIGURE 9 | The effects of HolesDiameter on the maximum impact force and the drop time-length.

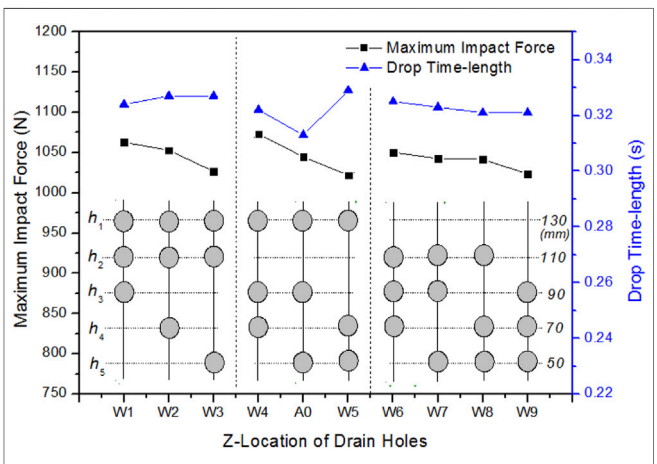

FIGURE 10 | The effects of hole location on the maximum impact force and the drop time-length.

higher than the second peak. That is, the impact between the piston and the bottom plate in W9 is more severe than the impact between the piston and the spider. This phenomenon shows that the maximum impact force is not only related to the total flow area but also to the relative position of the piston and the drain holes.

In order to consider the influence of structural parameters such as hole position and piston size on the buffer process while measuring the total flow area in the buffer cavity, the equivalent ongoing flow area of the drain holes S_{wh} is introduced here, which is expressed as

$$S_{wh} = \sum_{i=1}^{N}\left[\left(\frac{h_i}{L}\right)\cdot\pi\left(\frac{D_i}{2}\right)^2\sqrt{I}\right] \tag{9}$$

Where D_i is the diameter of each row of holes, h_i is the distance from each row of holes to the bottom edge of the spider body (as

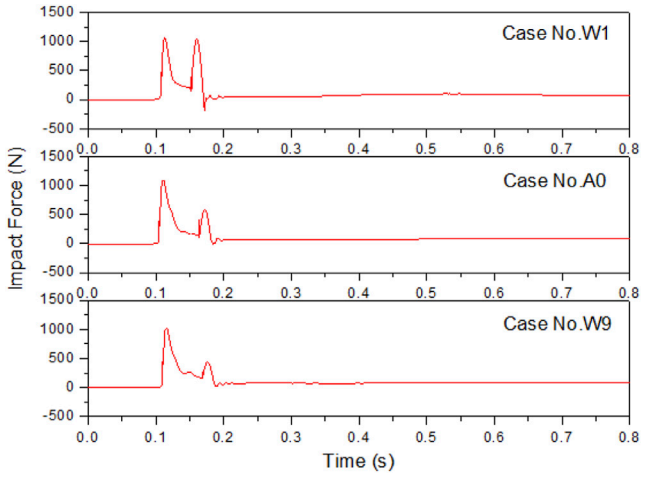

FIGURE 11 | The effects of holes location on the real-time impact force.

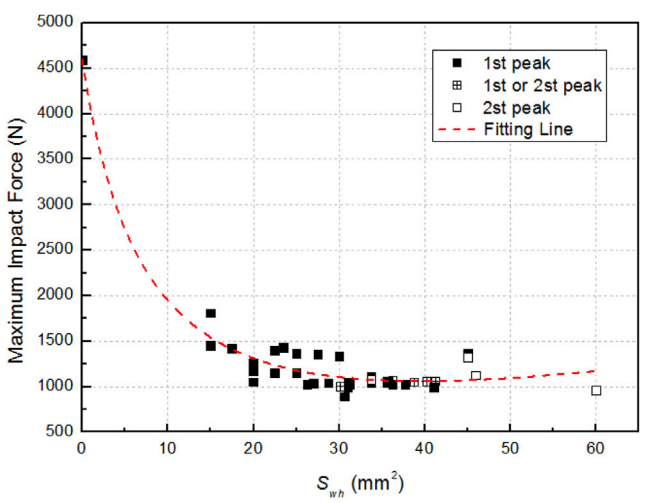

FIGURE 12 | The relationship between the maximum impact force and the equivalent ongoing flow area of the drain holes.

illustrated in **Table 2**), L is the penetration depth of the piston when it contacts the spider body ($L = L_0$+30), I is the number of holes in each row ($I = 2$), and N is the total number of rows.

The relationship between the maximum impact force and the equivalent ongoing flow area of the drain holes is shown in **Figure 12**. Within this range, the maximum impact force first decreased sharply and then increased slowly with the increase of the equivalent ongoing flow area of the drain holes. When the flow area increases to about 35 mm^2, the maximum impact force begins to appear at the second peak. This shows that when the flow area of the drain holes increases initially within the range of (0–60) mm^2, the maximum impact force caused by the first peak is slowly released, and when the flow area continues to increase, the effect of the second peak is gradually highlighted. It is speculated from the figure that when the flow area is between

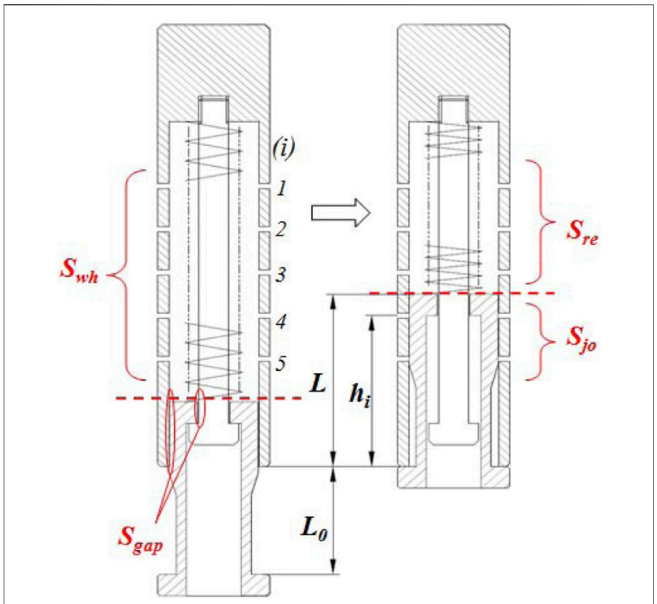

FIGURE 13 | Illustration of the Corresponding Definition of the Equivalent flow area.

13 and 40 mm^2, the impact force will be the smallest (about 1000N) and the buffering effect will be the best.

A formula for calculating the maximum impact force F and the equivalent ongoing flow area is recommended here, as follows:

$$F = 946.8\left[\frac{4S_{jo}}{S_{wh}+S_{gap}} + \frac{S_{wh}+S_{gap}}{S_{re}+S_{gap}}\right] \Big/ S_{wh} + 1071 \qquad (10)$$

Among them, S_{jo} is the equivalent flow area of the drain holes shielded by the piston when the piston is fully pressed in, which is called the equivalent flow area of the working hole. And S_{re} is the equivalent flow area of the drain holes that has not been shielded when the piston is completely pressed, which is called the equivalent flow area of the remaining hole. The corresponding definition of these equivalent flow area physical quantities has been illustrated in **Figure 13**. And they can be calculated respectively as

$$S_{re} = \sum_{i=1}^{n}\left[\left(\frac{h_i}{L}\right)\cdot\pi\left(\frac{D_i}{2}\right)^2\sqrt{I}\right] \quad (for\ 1\le n\le N,\ h_n > L) \qquad (11)$$

$$S_{jo} = \sum_{i=n}^{N}\left[\left(\frac{h_i}{L}\right)\cdot\pi\left(\frac{D_i}{2}\right)^2\sqrt{I}\right] \quad (for\ 1\le n\le N,\ h_n \le L) \qquad (12)$$

$$S_{wh} = S_{re} + S_{jo} \qquad (13)$$

The S_{gap} is the flow areas of other areas occupied by the gap between the piston and the spider, the gap between the piston and the tie pole, which is called the equivalent flow area of the gap, and can be expressed as

$$S_{gap} = S_{s-p} + S_{p-c} = \pi\left(\frac{D_{si}-D_{po}}{2}\right)^2 + \pi\left(\frac{D_{pi}-D_{ce}}{2}\right)^2 \qquad (14)$$

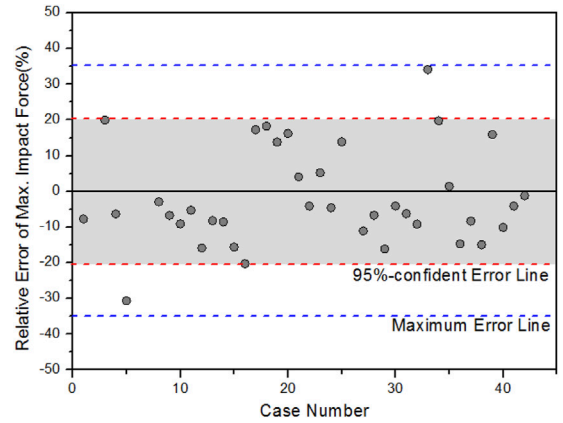

FIGURE 14 | The calculation relative error of the maximum impact force.

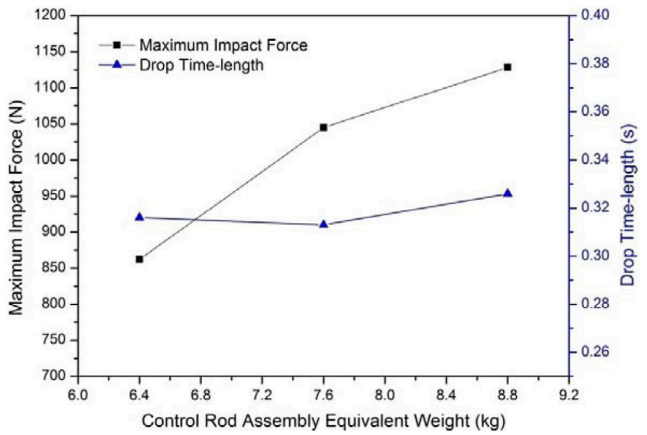

FIGURE 15 | The effects of equivalent weight on the maximum impact force and the drop time-length.

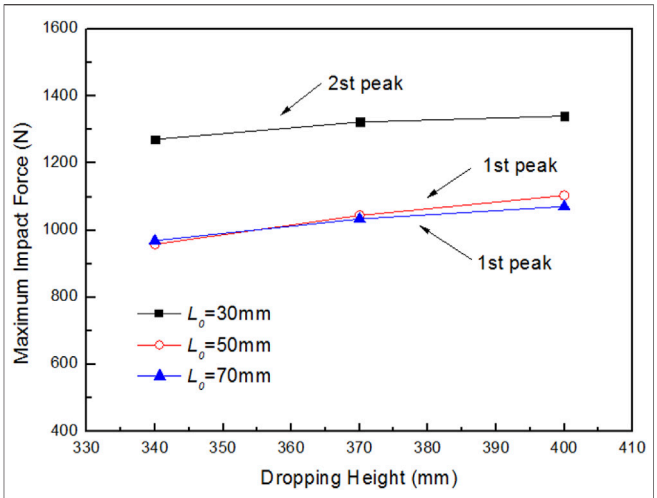

FIGURE 16 | The effects of dropping height on the maximum impact force under different piston stroke.

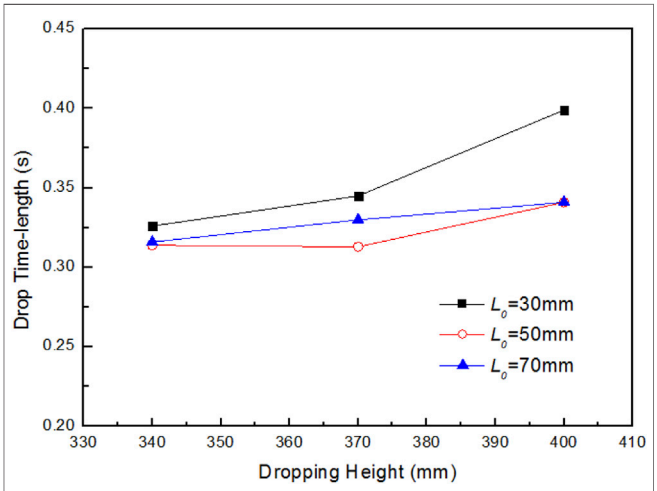

FIGURE 17 | The effects of dropping height on the drop time-length under different piston stroke.

For the cases involved in this paper, the relative error based on the 95% confidence for the above formula is 21%, and the maximum relative error is 35%, as shown in **Figure 14**.

Under the condition that the total flow area of the drain holes remains unchanged, the impact force F is most likely to have a minimum value when $S_{jo} = S_{re} + S_{gap} = (S_{wh} + S_{gap})/2$.That is to say, for two spider hydraulic buffers with the same total area of drain holes but different hole structures, if the flow area of the working holes is close to the flow area of the remaining holes and gaps, the impact force is more likely to be smaller.

Effects of Potential Energy

The relationship between the buffering performance, the equivalent weight and the falling height was investigated through experiments. In **Figures 15**, **16**, obviously, the relationship between the maximum impact force and the equivalent weight basically increases linearly. At the same time, the maximum impact force gradually increases with the increase of the drop height. However, in **Figure 17**, the change rule of the drop time is not obvious.

In the figure, noting that when the piston stroke is too short ($L_0 = 30$ mm), not only the impact force is significantly increased, but the buffering time-length is also longer. That is, the buffering performance becomes extremely poor. It can be seen from the previous analysis in **Figure 7** that due to the short stroke, the energy released during the pressing of the piston is obviously insufficient. After that, although the impact force reaches the maximum at the second impact, there is still some energy remaining. Thus, the piston will continue to bounce and collide multiple times until it stabilizes, which causes the buffer time-length to increase significantly.

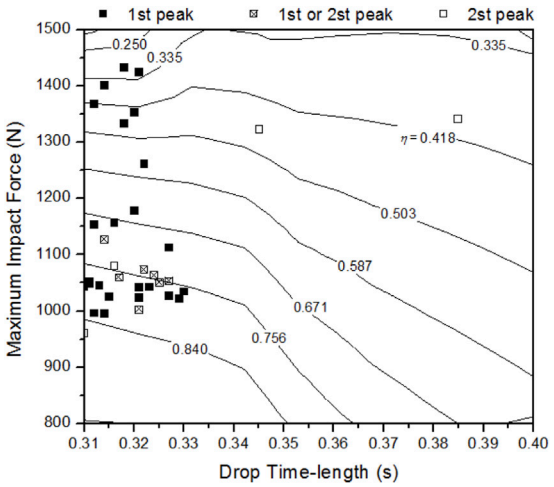

FIGURE 18 | The isogram of buffering performance evaluation factor and cases scatter in tests.

Comprehensive Performance Evaluation

In practical engineering applications, the buffer should not only ensure that the impact force is not too large, but also meet the requirement to keep the drop time-length as short as possible. Excessive impact force will cause damage to the core floor, and too long drop time-length will cause the reactor to fail to shut down in time, resulting in a major reactor shutdown accident. Therefore, the buffering performance needs to take into account both the maximum impact force and the drop time.

A comprehensive performance evaluation factor η is proposed here, defined as

$$\eta = -\left\{ \sqrt{1 - \frac{F}{F_{cr}}} \cdot \ln\left(\frac{t}{t_{cr}}\right) \right\} \tag{15}$$

Where the F is the maximum impact force during the buffering process, the t is the drop time-length. And the F_{cr} is the allowable maximum impact force on the upper plate of the core in the actual core (1500N here), and the t_{cr} is the limit drop time-length allowed in the actual rod drop process (1.3 s here). When the maximum impact force F is not greater than the allowable maximum impact force F_{cr}, if the drop time-length exceeds the limit drop time-length, the evaluation factor η is less than 0.

Accordingly, the relationship between the comprehensive performance evaluation factor and the maximum impact force and the drop time-length is shown in **Figure 18**. It can be seen that the smaller the maximum impact force and the drop time-length, the closer the comprehensive performance evaluation factor is to 1, and the better the buffering performance. Conversely, the closer the evaluation factor is to 0, the worse the buffer performance is. Overall, when the impact force values of the first peak and the second peak are closer, the comprehensive performance is better, as shown by the scattered points in **Figure 18**.

By the above evaluation method, under the same weight and drop height, several better performance conditions ($\eta > 0.78$) are A0/W9/K3-5/K4-2, and some typical poor performance conditions ($\eta < 0.46$) are N0/K3-2/X1. It indicates that for the drain hole structures involved in this paper, the buffering performance is better when: 1) the total flow area of the holes is larger, or 2) there are more holes that can be covered by the piston stroke. On the contrary, the buffering performance is poor when: 1) the total area of the drain holes is small, or 2) the piston stroke is too short. This information will make recommendations for the design optimization of the spider hydraulic buffer.

CONCLUSION

Aiming at a new type of spider hydraulic buffer adopted in the rod drop buffering, this paper studies the effects of different structural dimensions on the buffer performance, such as the distribution of drain holes, piston stroke and outer diameter, drop height and equivalent weight. The following conclusions are obtained.

(1) The real-time curve of the maximum impact force often has a bimodal structure. Generally, the first impact is the impact between the bottom of the piston and the test platform, and the second impact is the impact between the piston cap and the bottom of the spider body. The double peaks vary with the change of the internal structure of the hydraulic buffer.

(2) The experimental data show some evidently qualitative law when analyzing the maximum impact force. Most obviously, the maximum impact force is positively related to the weight and the dropping height. In addition, for the piston structure, an increase of stroke (30–70 mm) will bring a decrease of the maximum impact force. Meanwhile, an increase of outer diameter (clearance) will cause the maximum impact force to decrease first and then increase, the optimal size of clearance in these tests is 0.2 mm. For the drain holes, the influence of its parameters' changing (including hole diameter and hole locations) is more complicated. Therefore, it calls for several quantitative features that reflect equivalent flow area to characterize the hydraulic effects of these holes.

(3) In order to simultaneously consider the influence of the drain holes parameters on the maximum impact force, a new characteristic parameter—the equivalent ongoing flow area of the drain holes—is introduced in this paper. The analysis found that with the increase of the equivalent ongoing flow area of the drain holes, the first peak value of the maximum impact force gradually decreased, and the second peak value gradually increased. Under the conditions with the same total flow area of the drain holes, when the flow area of the working holes located within the stroke approximately equal to the flow area of the remaining holes, that is, when the first peak value is close to the second peak value, the impact force seems to have a minimum value. To calculate the impact force under different equivalent ongoing flow areas, a formula with a 95%-confidence

relative error of 21% are recommended here. It suggested that when the flow area locates in a range of (13–40) mm^2, the impact force will be the smallest (about 1000N) and the buffering effect will be the best.

(4) In order to take into account both the maximum impact force and the drop time-length when analyzing the buffering performance, a comprehensive performance evaluation factor η ($0<\eta<1$) is proposed. For the structures involved in this paper, when the total area of the drain holes is large enough or the holes are mostly located within the piston stroke, the comprehensive buffering performance is better ($\eta > 0.78$). While when the total area of the relief holes is small or the piston stroke is too short, the comprehensive buffering performance is poor ($\eta < 0.46$).

In summary, the maximum impact force and the comprehensive performance of spider hydraulic buffers are both closely related to their own structure. Designers can further optimize the buffer structure based on the above conclusions to obtain potential best buffer performance.

DATA AVAILABILITY STATEMENT

The raw data supporting the conclusions of this article will be made available by the authors, without undue reservation.

AUTHOR CONTRIBUTIONS

TY: Conceptualization, Formal analysis, Data curation, and Writing the original draft; PY: Methodology, Data collection and Data curation; SH: Methodology, Supervision; FZ: Conceptualization, Review and editing; YL: Conceptualization, Project administration; CH: Review and editing; LZ: Visualization; HW: Supervision; ML: Supervision.

FUNDING

This work presented in this paper is supported by the National Key R&D Program of China (2018YFE0116100).

REFERENCES

Andriambololona, H., Bosselut, D., and Massin, P. (2007). Methodology for a Numerical Simulation of an Insertion or a Drop of the Rod Cluster Control Assembly in a PWR. *Nucl. Eng. Des.* 237 (6), 600–606. doi:10.1016/j.nucengdes.2006.09.001

Fu, X. G., and Pu, J. L. (1997). Safety Analysis and Review of Control Rod Falling Time Out of Tolerance in Dayawan Nuclear Power Plant[J]. *Nucl. Power Eng.* 18 (03), 2–8. doi:10.1007/s00376-997-0061-6

Lin, Z., Zhai, L., Zhu, L., Wang, X., Zhang, X., Cao, Y., et al. (2017). Control Rod Drop Dynamic Analysis in the TMSR - SF1 Based on Numerical Simulation and experiment. *Nucl. Eng. Des.* 322 (322), 131–137. doi:10.1016/j.nucengdes.2017.06.031

Mingmin, R., and Claus, M. (2013). *Predictions of RCCA Drop Times under Consideration of Fuel Assembly Distortions[C]//the Structural Mechanics International Reactor Transactions*. San Francisco, California, USA: SMiRT-22.

Qin, B., Li, L., and Bo, H. (2018). Study on the Decelerating Mechanism of the New Control Rod Hydraulic Decelerator for the CRHDS Based on Numerical Simulation and experiment. *Ann. Nucl. Energ.* 120 (oct), 814–827. doi:10.1016/j.anucene.2018.06.044

Rabiee, A., and Alireza, A. (2016). Control Rod Drop Hydrodynamic Analysis for a Pressurized Water Reactor[J]. *Prog. Nucl. Energ.* 88, 191–197. doi:10.1016/j.pnucene.2015.12.007

Xiao, C., Luo, Y., Du, H., and Wang, L. (2017). Simulation and Analysis of Single Control Rod DroppingBehavior Based on Dynamic Grid Technique[J]. *Nucl. Power Eng.* 38 (02), 103–107. doi:10.13832/j.jnpe.2017.02.0103

Xiao, C., Luo, Y., Zhang, H. L., Liu, X., Du, H., Huang, k., et al. (2017). Analysis of Control Rod Dropping and Buffering Behavior ofSupercritical Water-Cooled Reactor Based onDynamic Grid Technology[J]. *Nucl. Power Eng.* 38 (S2), 79–83. doi:10.13832/j.jnpe.2017.S2.0079

Yoon, K. H., Kim, J. K., Lee, K. H., Lee, Y. H., and Kim, H. K. (2009). Control Rod Drop Analysis by Finite Element Method Using Fluid-Structure Interaction for A Pressurized Water Reactor Power Plant[J]. *Nucl. Eng. Des.* 239, 1857–1861. doi:10.1016/j.nucengdes.2009.05.023

Zhang, G. L. (2017). Reasons Analysis for Abnormal Control Rod Dropping Behavior in Pressurized Water Reactor Nuclear Power Plant[J]. *Nucl. Elect. Detect. Tech.* 37 (07), 683–687.

Zhang, J. B., Gao, X. L., and He, H. X. (2020). Dynamics Numerical Calculation for Control-Rod Drop[J]. *Nucl. Power Eng.* 41 (6), 218–223.

Zhang, J. B., Li, Y. M., and Huang, C. L. (2021). Study on the Buffer Design Method of the Control Rod Assembly Buffer Structure[J]. *Nucl. Power Res. Des.* 14 (1), 35–39. www.cnki.net

Conflict of Interest: The authors declare that the research was conducted in the absence of any commercial or financial relationships that could be construed as a potential conflict of interest.

Publisher's Note: All claims expressed in this article are solely those of the authors and do not necessarily represent those of their affiliated organizations, or those of the publisher, the editors, and the reviewers. Any product that may be evaluated in this article, or claim that may be made by its manufacturer, is not guaranteed or endorsed by the publisher.

frontiers in Energy Research

TECHNOLOGY AND CODE
published: 24 March 2022
doi: 10.3389/fenrg.2022.852501

Development and Application of an Aerosol Model Under a Severe Nuclear Accident

Xianbao Yuan [1,2], Jingyu Wei [1,2], Binhang Zhang [1,2], Yuefeng Guo [1,2], Qiang Shi [1,2], Pan Guo [1,2], Senquan Yang [3] and Chao Tan [3]*

[1]College of Mechanical and Power Engineering, China Three Gorges University, Yichang, China, [2]Hubei Key Laboratory of Hydroelectric Machinery Design and Maintenance, China Three Gorges University, Yichang, China, [3]China Nuclear Power Operation Technology Corporation, Ltd., Wuhan, China

Radioactive aerosol will transport in the containment and also will leak into the environment under a severe nuclear accident. Thus, it is of great significance for predicting the behavior of aerosol under a severe nuclear accident. In order to analyze the aerosol behavior, an improved multi-component sectional model is developed, which improves section numbers and updates the aerosol particle density at each time step. The model's dependability is confirmed to use benchmark and experimental values. An excellent agreement can be observed between simulation and benchmark. On this premise, the LBLOCA accident is chosen to explore the behavior of radioactive aerosol in the containment. The finding shows that the aerosol is mostly deposited on the structure's surface due to gravity in the LBLOCA accident. According to a comparison of the influence of aerosol natural deposition mechanisms on the distribution of diameter particles, Brownian diffusion, thermophoresis, diffusiophoresis, and gravity all have an effect on aerosol in the range of 0.01 μm–0.03 μm particles, and the deposition of 2 μm–20 μm particles is mainly due to gravity. After comparing and evaluating the influence of aerosol density in the containment, it can be inferred that changed aerosol particle density leads aerosol particles coagulate into larger particles.

Keywords: severe accident, radioactive aerosols, sectional model, LBLOCA, aerosol behavior

OPEN ACCESS

Edited by:
Yapei Zhang,
Xi'an Jiaotong University, China

Reviewed by:
Wei Peng,
Tsinghua University, China
Alexandra Ioannidou,
Aristotle University of Thessaloniki, Greece

****Correspondence:***
Jingyu Wei
numbwjy@163.com

Specialty section:
This article was submitted to Nuclear Energy, a section of the journal Frontiers in Energy Research

Received: *11 January 2022*
Accepted: *10 February 2022*
Published: *24 March 2022*

Citation:
Yuan X, Wei J, Zhang B, Guo Y, Shi Q, Guo P, Yang S and Tan C (2022) Development and Application of an Aerosol Model Under a Severe Nuclear Accident. Front. Energy Res. 10:852501. doi: 10.3389/fenrg.2022.852501

INTRODUCTION

After the Fukushima accident, the study of severe accidents (SA) has gained more international attention (Wittneben, 2012). In a hypothetical nuclear power plant severe accident, the release of radioactive fission products can occur from the core fuel, the fuel-cladding gap, and the material in the cavity. The fission product released by core melting will leak into the containment through the primary system break, and if the accident deteriorates further, it will lead to containment failure, resulting in radioactive fission products being released into the environment (Allelein et al., 2009; Lin, W. et al., 2014). Radioactive fission products exist as gases, aerosols, or deposited onto heat structure, and the most radioactive fission products within the containment are transported with the movement of the aerosol (Soffer et al., 1995). Aerosol particles released into the containment will change due to collisions between particles, and some of the aerosol particles will deposit onto the containment heat structure because of temperature, density, diffusion, and gravity (Raj Sehgal, 2012). Otherwise, the detailed aerosol property is necessary to calculate the radioactive aerosol removal efficiency of engineered safeguards, such as the spray system and the filtration system (Porcheron

et al., 2008; Rýdl et al., 2019; Wang et al., 2021). Therefore, it is significant to study the radioactive aerosol distribution and the radioactive aerosol behavior under a severe nuclear accident.

In the past research studies, many researchers have developed codes to study the behavior of the radioactive aerosol. For instance, Klinik et al. (2010) used the integrated program ASTEC to perform transient simulations of thermal-hydraulic phenomena and aerosol behavior in tests on containment systems of different sizes, such as the Phebus. The FP containment bench, the KAEVER containment bench, and the Battelle containment bench obtained good simulation results. For the deposition and coagulation behavior of aerosols in a nuclear reactor, Alipchenkov et al. (2009) have developed a code for calculating the behavior of aerosol-shaped fission products in the primary circuit of a nuclear reactor, which focuses on the development of models for predicting the deposition and coagulation rate of aerosols. There are also many numerical studies to solve the aerosol general dynamic equation, such as the sectional method (Gelbard and Seinfeld, 1980), the moment method (Wang et al., 2019), the discrete-sectional method (Li and Cai, 2020), and the Monte Carlo method (Bird, 1994; Liu and Chan, 2018). The sectional method is commonly used to describe the multicomponent aerosol dynamic behavior in the nuclear power plant. Because the sectional method requires the number of sections and the boundary of the section is fixed, this model also is called the fixed section model. MAEROS code developed based on the sectional method is widely used in the accident analysis program (Gelbard, 1982), such as MELCOR (Humphries et al., 2017) and CONTAIN (Murata et al., 1997). MAEROS is a multi-sectional, multi-component aerosol dynamic code that evaluates the size distribution of each type of aerosol mass, or component, as a function of time. MAEROS code also will deal with deposition processes of the radioactive aerosol. In the MAEROS code, the radioactive aerosol particles are allocated into fixed sections by particle volume, and the composition of the aerosol particles in the same section is considered uniform.

This sectional method discussed previously has fixed a section boundary and constant section number, and the aerosol particle density is constant by the input data. As known, when the reactor core begins melting in a severe accident, the radioactive aerosol source will continuously change along with the development of the accident, and the radioactive aerosol components released from the reactor core are also different. Moreover, the radioactive aerosol coagulation behavior and deposition behavior will change the components of radioactive aerosol. Thus, the radioactive aerosol density is closely associated with the deposition behavior and coagulation behavior. In the MAEROS code, in order to simplify the coefficients, it restricts the maximum section number. The geometric constraint is $v_{l+1}/v_l > 2$, where v_l is the radioactive aerosol particle volume at the lower boundary of section l. v_{l+1} is the radioactive aerosol particle volume at the upper boundary of section $l+1$. The fixed section model cannot improve the calculation accuracy and get more detailed radioactive aerosol distribution by increasing the section number. In a word, the traditional sectional method has some drawbacks which need to increase the section number and update the radioactive aerosol density to simulate multi-component radioactive aerosol behavior during severe accidents.

The objective of this research first proposes an improved multi-component sectional method to simulate aerosols under severe accident. Then, the improved model is verified and validated by the benchmark and experiment. Furthermore, this research investigates the distribution of CsI aerosol under the LBLOCA accident and the effect of the natural deposition mechanism and aerosol density on the aerosol distribution.

MATHEMATICAL METHOD

Aerosol Dynamic Models

The spatial and chemical composition of the particles are represented by the size distribution function $n(v,t)$, where $n(v,t)dv$ is the number of particles in the particle range $[v, v+dv]$ and the number of particles in the volume range v to $v+dv$. The collide and coagulate are described by the general particulate conservation (Gelbard and Seinfeld, 1978).

$$\frac{\partial n(v,t)}{\partial t} = -\frac{\partial}{\partial v}\left[I(v,t)n(v,t)\right] + \frac{1}{2}\int_0^v \beta(u, v-u)n(u,t)n(v-u,t)du - n(v,t)\int_0^\infty \beta(v,u)n(u,t)du + S(v,t) \tag{1}$$

where $I(v,t)$ is the rate of change of the particle volume due to mass exchange with the liquid phase. $\beta(v,u)$ is the coagulation coefficient for particles of volumes v and u. S is the net increase rate of particles flowing into the system.

By discretizing the aerosol particles into m sections and s components, the mass of the section l at a given time is defined as Q_l:

$$Q_l(t) = \sum_{k=1}^{s} Q_{l,k}(t) = \int_{v_{l-1}}^{v_l} v n(v,t)dv \tag{2}$$

where $Q_{l,k}(t)$ is the mass of the component k in the section l. v_l and v_{l-1} are the upper and lower boundaries of the section l, respectively. $n(v,t)$ is the distribution function of the section l; the mass concentration change rate for the component k of the aerosol particle in the section l can be written as the following equation (Gelbard and Seinfeld, 1980).

$$\frac{dQ_{l,k}(t)}{dt} = \frac{1}{2}\sum_{i=1}^{l-1}\sum_{j=1}^{l-1}\left[{}^{1a}\bar{\beta}_{i,j,l}Q_{j,k}Q_i + {}^{1b}\bar{\beta}_{i,j,l}Q_{i,k}Q_j\right] - \sum_{i=1}^{l-1}\left[{}^{2a}\bar{\beta}_{i,l}Q_iQ_{l,k} - {}^{2b}\bar{\beta}_{i,l}Q_lQ_{i,k}\right] - \frac{1}{2}{}^{3}\bar{\beta}_{l,l}Q_lQ_{l,k} - Q_{l,k}\sum_{i=l+1}^{m}{}^{4}\bar{\beta}_{i,l}Q_i + \bar{S}_{l,k} - \bar{\Psi}_{l,k}Q_{l,k} \tag{3}$$

where $dQ_{l,k}(t)/dt$ is the aerosol mass change rate of the component k in the section l at a time t, ${}^{1a}\bar{\beta}_{i,j,l}$, ${}^{1b}\bar{\beta}_{i,j,l}$ is agglomeration rata of particles in section i and section j to form a particles in section l, ${}^{2a}\bar{\beta}_{i,l}$ is agglomeration rata of particles in section i and section l to form a particle larger than section l, ${}^{2b}\bar{\beta}_{i,l}$ is agglomeration rata of particles in section i and section l to form a particle in section l, ${}^{3}\bar{\beta}_{l,l}$ is agglomeration rata of particles both in section l to form a particle

TABLE 1 | Coagulation coefficients (Gelbard and Seinfeld, 1980).

Symbol	Remarks	Coefficient
${}^{1a}\bar{\beta}_{i,j,l}$	${}^{1a}\bar{\beta}_{i,j,l} \neq {}^{1a}\bar{\beta}_{j,j,l}$ ${}^{1a}\bar{\beta}_{i,j,l} = {}^{1b}\bar{\beta}_{j,j,l}$ $1 < l \leq m$ $1 \leq i < l$ $1 \leq j < l$	$\int_{x_{i-1}}^{x_i}\int_{x_{j-1}}^{x_j} \frac{\theta(v_{l-1} < u+v < v_l)u\beta(u,v)}{uv(x_i-x_{i-1})(x_j-x_{j-1})}dydx$
${}^{1b}\bar{\beta}_{i,j,l}$	${}^{1b}\bar{\beta}_{i,j,l} \neq {}^{1b}\bar{\beta}_{j,j,l}$ ${}^{1b}\bar{\beta}_{i,j,l} = {}^{1a}\bar{\beta}_{j,j,l}$ $1 < l \leq m$ $1 \leq i < l$ $1 \leq j < l$	$\int_{x_{i-1}}^{x_i}\int_{x_{j-1}}^{x_j} \frac{\theta(v_{l-1} < u+v < v_l)v\beta(u,v)}{uv(x_i-x_{i-1})(x_j-x_{j-1})}dydx$
${}^{2a}\bar{\beta}_{i,j}$	${}^{2a}\bar{\beta}_{i,j} \neq {}^{2a}\bar{\beta}_{l,j}$ $1 < l \leq m$ $1 \leq i < l$	$\int_{x_{i-1}}^{x_i}\int_{x_{j-1}}^{x_j} \frac{\theta(u+v > v_j)u\beta(u,v)}{uv(x_i-x_{i-1})(x_j-x_{j-1})}dydx$
${}^{2b}\bar{\beta}_{i,j}$	${}^{2b}\bar{\beta}_{i,j} \neq {}^{2b}\bar{\beta}_{l,j}$ $1 < l \leq m$ $1 \leq i < l$	$\int_{x_{i-1}}^{x_i}\int_{x_{j-1}}^{x_j} \frac{\theta(u+v < v_j)v\beta(u,v)}{uv(x_i-x_{i-1})(x_j-x_{j-1})}dydx$
${}^{3}\bar{\beta}_{l,j}$	$1 \leq l \leq m$	$\int_{x_{i-1}}^{x_i}\int_{x_{j-1}}^{x_j} \frac{\theta(u+v > v_j)(u+v)\beta(u,v)}{uv(x_i-x_{i-1})^2}dydx$
${}^{4}\bar{\beta}_{i,j}$	${}^{4}\bar{\beta}_{i,j} \neq {}^{4}\bar{\beta}_{l,j}$ $1 \leq l < m$ $i < i \leq m$	$\int_{x_{i-1}}^{x_i}\int_{x_{i-1}}^{x_i} \frac{u\beta(u,v)}{uv(x_i-x_{i-1})(x_j-x_{j-1})}dydx$

in section l, ${}^{4}\bar{\beta}_{i,l}$ is agglomeration rata of particles in section l and section i $(i > l)$. The coagulation coefficient of the traditional sectional method is shown in **Table 1**. $\bar{S}_{l,k}$ is the source of the component k of the aerosol particle in section l. $\bar{\Psi}_{l,k}$ is the aerosol removal rate of component k of the aerosol particle in section l.

Moreover, the first and second terms in the right of **Eq. 3** indicate the flux of the radioactive aerosol component k into the size section l from the lower size sections by coagulating with each section. The third term represents the flux of the component k out of the section l due to the coagulation of particles within the section l. For $l < m$ in the fourth term, the flux of the component k leaves section l by coagulation of particles within the section l and those of higher sections. The fifth term represents the source term of the component k in the section l entering the containment. The sixth term is the removal flux of the component k in the section l by a natural settlement mechanism. The detailed theory of the natural settlement mechanism is as follows.

Aerosol Removal Models

For the calculation of the deposition term in this study, gravity, Brownian diffusion, thermophoresis, and diffusiophoresis are considered for each heat structure surface of the containment, and the removal rate of all heat structure surfaces is added up to the total removal rate (Murata et al., 1997; Humphries et al., 2017).

$$\bar{\Psi}_{l,k} = \sum_{j=1}^{N_{str}} \lambda_{j,l} Q_{l,k} \tag{4}$$

where N_{str} is the total number of heat structure surfaces for aerosol deposition in the control volume, and $\lambda_{j,l}$ is the deposition rate for the heat structure j for the aerosol section l. The natural deposition coefficients can be calculated by using the deposition velocity.

$$\lambda_{j,l} = \frac{A_j}{V}\left(v_s + v_{diff} + v_{therm} + v_{diffusio}\right) \tag{5}$$

where A_j is the area of the heat structure surface j, and V is the control volume atmosphere volume. The velocity of aerosol deposition on a heat structure surface is defined as follows.

Gravitational Deposition

$$v_s = \frac{d_p^2 \rho_p g C_m}{18\mu\chi} \tag{6}$$

where v_s is the gravitational deposition velocity, d_p is the particle diameter, ρ_p is the particle density, C_m is the Cunningham slip correction factor, μ is the viscosity of air, χ is the dynamic shape factor, and g is the acceleration of gravity.

The Cunningham slip correction factor in **Eq. 6** is expressed as follows.

$$C_m = 1 + N_{Kn}\left[1.257 + 0.4\exp\left(-\frac{1.1}{N_{Kn}}\right)\right] \tag{7}$$

Here, N_{Kn} is the Knudsen number $2\lambda/d_p$, and λ is the mean-free path of gas.

The gravitational deposition is effective for upward surfaces, such as the floor and pool. As for the downward surface, this mechanism will not act on it. Also, one basic hypothetical condition of this model is that the aerosol particle Reynolds number must be less than 1, which means that inertial effects of the flow may be neglected.

Brownian Diffusion

Brownian diffusion of aerosols refers to the deposition of aerosols due to mutual collision between the aerosol and the heat structure surface. The deposition velocity because of Brownian diffusion is defined as follows.

$$v_{diff} = \frac{\sigma T C_m}{3\pi\mu\chi d_p \Delta} \tag{8}$$

where v_{diff} is the diffusion deposition velocity, σ is Boltzmann constant, T is atmosphere temperature, and Δ is the diffusion boundary layer thickness.

Thermophoresis

Thermophoresis is caused by the temperature gradient between the aerosol particles and heat structure surface, and the aerosol particles will deposit on the object surface at a lower temperature. The thermophoretic deposition velocity is defined as follows.

$$v_{therm} = \frac{3\mu C_m\left(c_t N_{Kn} + \frac{k_{gas}}{k_p}\right)}{2\mu\rho_{gas} T\left(1 + 3F_{slip}N_{Kn}\right)\left(1 + 2c_t N_{Kn} + \frac{k_{gas}}{k_p}\right)}\nabla T \tag{9}$$

where k_{gas}/k_p is the ratio of the air thermal conductivity to aerosol thermal conductivity, ∇T is the structure surface temperature gradient, ρ_{gas} is the gas density, T is the wall temperature, F_{slip} is the slip factor, and c_t is the constant associated with the thermal accommodation coefficients.

Diffusiophoresis

The diffusiophoresis process is also as known as a vapor condensation process. When the vapor condenses on the surface of the heat structure surface, composition gradients will exist in the adjacent gas, which will affect aerosol deposition behavior on the surface. The aerosol particles will remove along with the concentration gradient, which is caused by vapor condensation on the heat structure surface.

$$v_{diffusio} = \left(\frac{\sqrt{M_s}}{X_s\sqrt{M_s} + X_{NC}\sqrt{M_{NC}}}\right)\left(\frac{W_{cond}}{\rho_s}\right) \tag{10}$$

where M_s is the molecular weight of water, M_{NC} is the molecular weight of non-condensable gases, W_{cond} is the condensation mass flux to the surface, ρ_s is the density of bulk gas, X_s is the mole fraction of water vapor in the bulk gas, and X_{NC} is the mole fraction of non-condensable gases in the bulk gas.

Improvement of the Multi-Component Sectional Method

The agglomeration kernels of the four mechanisms are proposed in the study by Humphries et al. (2017).

$$\beta_B = \frac{2\pi\left(D_i + D_j\right)\left(\gamma_i d_i + \gamma_j d_j\right)}{F} \tag{11}$$

$$\beta_S = \varepsilon_g \frac{\pi}{4} C_s \left(\gamma_i d_i + \gamma_j d_j\right)^2 \left|v_{s,i} - v_{s,j}\right| \tag{12}$$

$$\beta_{T1} = \sqrt{\frac{\pi^2 \varepsilon_t}{120 v_g}} C_s \left(\gamma_i d_i + \gamma_j d_j\right)^3 \tag{13}$$

$$\beta_{T2} = \frac{0.04029 \rho_g^{1/4} \varepsilon_t^{3/4}}{\mu_g^{5/4}} C_s \left(\gamma_i d_i + \gamma_j d_j\right)^2 \left|\frac{\rho_i C_i d_i^2}{\chi_i} - \frac{\rho_j C_j d_j^2}{\chi_j}\right| \tag{14}$$

where d is the aerosol particle diameter, γ is the agglomeration shape factor, F is the correction coefficient, C_s is the aerosol particle sticking coefficient, and ε_g is the collision efficiency, which is defined below.

$$\varepsilon_g = 1.5\left[\frac{\min\left(d_i, d_j\right)}{\left(d_i + d_j\right)}\right]^2 \tag{15}$$

where v_s is the settling velocity of the gravitational mechanism, which is defined as

$$v_s = \frac{\rho_i g d_i^2 C_i}{18 \mu_g \chi_i} \tag{16}$$

where ρ is the particle density, g is the acceleration of gravity, μ_g is the gas viscosity, χ_i is the dynamic shape factor, and C is the Cunningham slip correction factor in **Eq. 7**. D is the particle diffusivity, which is defined as

$$D = \frac{k T_g}{3\pi d \mu_g \chi} C \tag{17}$$

According to the traditional section method, if the coagulation coefficient is resolved at each time step, it will waste the computation time. Therefore, it is necessary to simplify the calculation process of the coagulation coefficient.

Such as ${}^{1a}\bar{\beta}_{i,j,l}$ in **Table 1**, it can be written as

$${}^{1a}\bar{\beta}_{i,j,l} = \sum_n \int_{x_{i-1}}^{x_j}\int_{x_{j-1}}^{x_j} \frac{\theta(v_{l-1} < u + v < v_l) u \beta_n(u,v)}{uv\left(x_i - x_{i-1}\right)\left(x_j - x_{j-1}\right)} dydx \tag{18}$$

where the subscript n represents the agglomeration mechanisms. According to **Eq. 11**, the variable related to the aerosol particle density is separated from the double integral sign in **Eq. 18**. The Brownian agglomeration can be further written as

$$\begin{aligned} {}^{1a}\bar{\beta}_{B,i,j,l} &= \frac{\rho_j^*}{\rho_j}\int_{x_{i-1}}^{x_j}\int_{x_{j-1}}^{x_j} \frac{\theta(v_{l-1} < u + v < v_l) u \beta_B^*(u,v)}{uv\left(x_i - x_{i-1}\right)\left(x_j - x_{j-1}\right)} dydx \\ &= k_B \int_{x_{i-1}}^{x_j}\int_{x_{j-1}}^{x_j} \frac{\theta(v_{l-1} < u + v < v_l) u \beta_B^*(u,v)}{uv\left(x_i - x_{i-1}\right)\left(x_j - x_{j-1}\right)} dydx \end{aligned} \tag{19}$$

where the superscript $*$ represents the standard agglomeration coefficients and density. By analogy, the gravitational agglomeration can be written as

$$\begin{aligned} {}^{1a}\bar{\beta}_{S,i,j,l} &= \left| \frac{\rho_i \rho_j^*}{\rho_i^* \rho_j}\int_{x_{i-1}}^{x_j}\int_{x_{j-1}}^{x_j} \frac{\theta(v_{l-1} < u + v < v_l) u \beta_{S(1)}^*(u,v)}{uv\left(x_i - x_{i-1}\right)\left(x_j - x_{j-1}\right)} dydx \right. \\ &\quad \left. + \frac{\rho_j \rho_j^*}{\rho_j^* \rho_j}\int_{x_{i-1}}^{x_j}\int_{x_{j-1}}^{x_j} \frac{\theta(v_{l-1} < u + v < v_l) u \beta_{S(2)}^*(u,v)}{uv\left(x_i - x_{i-1}\right)\left(x_j - x_{j-1}\right)} dydx \right| \\ &= \left| k_{s1}\int_{x_{i-1}}^{x_j}\int_{x_{j-1}}^{x_j} \frac{\theta(v_{l-1} < u + v < v_l) u \beta_{S(1)}^*(u,v)}{uv\left(x_i - x_{i-1}\right)\left(x_j - x_{j-1}\right)} dydx \right. \\ &\quad \left. + k_{s2}\int_{x_{i-1}}^{x_j}\int_{x_{j-1}}^{x_j} \frac{\theta(v_{l-1} < u + v < v_l) u \beta_{S(1)}^*(u,v)}{uv\left(x_i - x_{i-1}\right)\left(x_j - x_{j-1}\right)} dydx \right| \end{aligned} \tag{20}$$

The turbulent agglomeration can be written as

$$\begin{aligned} {}^{1a}\bar{\beta}_{T1,i,j,l} &= \left(\frac{\rho_g}{\rho_g^*}\right)^{0.5} \frac{\rho_j^*}{\rho_j}\int_{x_{i-1}}^{x_i}\int_{x_{j-1}}^{x_j} \frac{\theta(v_{l-1} < u + v < v_l) u \beta_{T1(1)}^*(u,v)}{uv\left(x_i - x_{i-1}\right)\left(x_j - x_{j-1}\right)} dydx \\ &= k_{t1}\int_{x_{i-1}}^{x_i}\int_{x_{j-1}}^{x_j} \frac{\theta(v_{l-1} < u + v < v_l) u \beta_{S(1)}^*(u,v)}{uv\left(x_i - x_{i-1}\right)\left(x_j - x_{j-1}\right)} dydx \end{aligned} \tag{21}$$

$$\begin{aligned} {}^{1a}\bar{\beta}_{T2,i,j,l} &= \left| \left(\frac{\rho_g}{\rho_g^*}\right)^{0.25} \frac{\rho_i \rho_j^*}{\rho_i^* \rho_j}\int_{x_{i-1}}^{x_i}\int_{x_{j-1}}^{x_j} \frac{\theta(v_{l-1} < u + v < v_l) u \beta_{T2(1)}^*(u,v)}{uv\left(x_i - x_{i-1}\right)\left(x_j - x_{j-1}\right)} dydx \right. \\ &\quad \left. + \left(\frac{\rho_g}{\rho_g^*}\right)^{0.25} \frac{\rho_j \rho_j^*}{\rho_j^* \rho_j}\int_{x_{i-1}}^{x_i}\int_{x_{j-1}}^{x_j} \frac{\theta(v_{l-1} < u + v < v_l) u \beta_{T2(1)}^*(u,v)}{uv\left(x_i - x_{i-1}\right)\left(x_j - x_{j-1}\right)} dydx \right| \\ &= \left| k_{t2(1)}\int_{x_{i-1}}^{x_i}\int_{x_{j-1}}^{x_j} \frac{\theta(v_{l-1} < u + v < v_l) u \beta_{S(1)}^*(u,v)}{uv\left(x_i - x_{i-1}\right)\left(x_j - x_{j-1}\right)} dydx \right. \\ &\quad \left. + k_{t2(2)}\int_{x_{i-1}}^{x_i}\int_{x_{j-1}}^{x_j} \frac{\theta(v_{l-1} < u + v < v_l) u \beta_{S(1)}^*(u,v)}{uv\left(x_i - x_{i-1}\right)\left(x_j - x_{j-1}\right)} dydx \right| \end{aligned} \tag{22}$$

According to the above equation, the standard agglomeration coefficients are only calculated before the iterative process.

The coefficients of k_B, k_{s1}, k_{s2}, k_{t1}, $k_{t2(1)}$, and $k_{t2(2)}$ need an update at every time step. Therefore, the aerosol model is developed based on the aforementioned work. The flow chart of the radioactive aerosol analysis is shown in **Figure 1**, where t is time, Δt is the time step, l is the section number, m is the total section number, ρ_p is the radioactive aerosol particle density, v_l is the lower boundary of the section l, and v_{l+1} is the upper boundary of the section l. Detailed information for calculating the coagulation coefficient is discussed in the study by Gelbard (1982). The radioactive aerosol density is updated at each time step. The Runge–Kutta integration methods are adopted to numerically solve the equation and update the radioactive aerosol conditions.

VERIFICATION AND VALIDATION OF THE MODEL

The aerosol model is validated by comparison with the benchmark, including two different coagulation problems and two different coagulation problems combined with deposition problems (Shaker et al., 2012). The aerosol model next is verified with the STORM experiment (Castelo et al., 1999), in which the main objective is to ensure the aerosol behaviors.

Validation With the Benchmark

Benchmark 1: Constant coagulation rate [$\beta(\mathbf{u},\mathbf{v})$ = constant, $\bar{\Psi} = 0$]

It is assumed that the coagulation rate is constant, and the deposition rate and source term are zero. The exact solution is as follows.

$$n(v,t) = \frac{4N_0}{v_{m0}(2+N_0\beta t)} exp - \frac{2}{v_{m0}(2+N_0\beta t)} v \tag{23}$$

where N_0 is the total initial number of particles per unit volume, and v_{m0} is the initial mean volume of particles present in the distribution.

Benchmark 2: Linear coagulation rate [$\beta(u,v) = \beta_1(u+v)$, $\bar{\Psi} = 0$]

$$n(v,t) = \frac{N_0(1-T_1)}{v\sqrt{T_1}} \exp\left(-(1+T_1)\left(\frac{v}{v_{m0}}\right)\right) I_1\left(2\left(\frac{v}{v_0}\right)\sqrt{T_1}\right) \tag{24}$$

$$T_1 = 1 - \exp(-\tau_2) \tag{25}$$

$$\tau_2 = N_0\beta v_0 t \tag{26}$$

Benchmark 3: Constant coagulation rate and a constant deposition rata [$\beta(\mathbf{u},\mathbf{v})$ = constant and $\bar{\Psi}$ = constant]

$$n(v,t) = \frac{GN_0}{v_{m0}} \exp\left(-G\frac{v}{v_{m0}}\right) \tag{27}$$

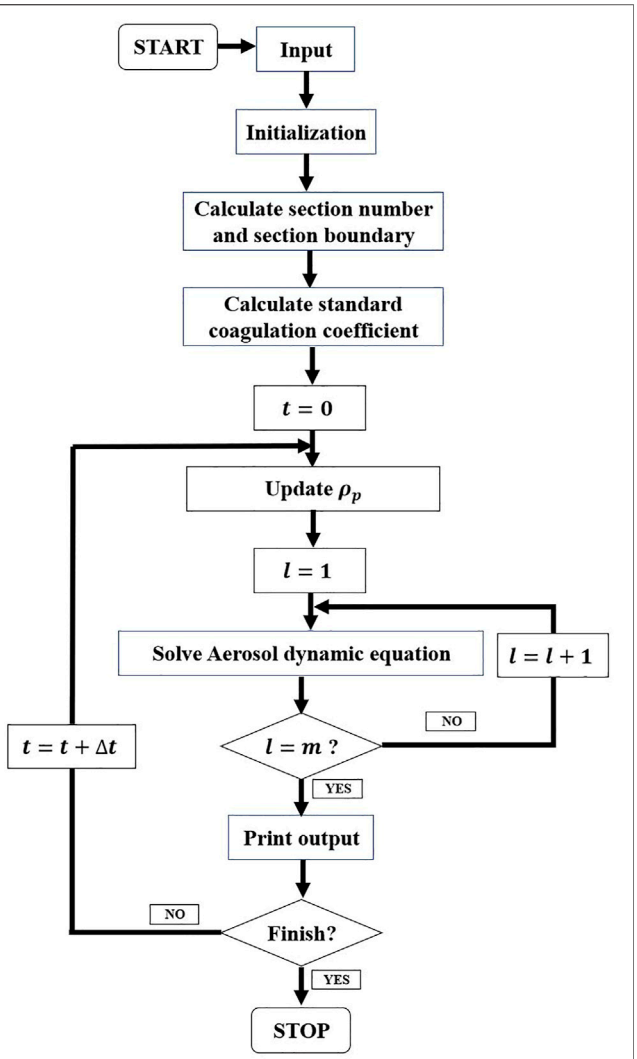

FIGURE 1 | Flow chart of the model.

$$G = \frac{N + \frac{2\lambda_0}{\beta}}{N_0 + \frac{2\lambda_0}{\beta}} \tag{28}$$

$$N = \frac{2\lambda_0}{\beta} \frac{\exp(-\lambda_0 t)}{\left(1 + \frac{2\lambda_0}{\beta N_0}\right) - \exp(-\lambda_0 t)} \tag{29}$$

Benchmark 4: Linear coagulation rate and a constant deposition rata [$\beta(u,v) = \beta_1(u+v)$ and $\bar{\Psi}$ = constant]

$$n(v,t) = \frac{N_0 T exp\left(\frac{T-1}{\theta}\right)}{v_0\left(\frac{v}{v_0}\right)\sqrt{g}} \exp\left(-(1+g)\left(\frac{v}{v_0}\right)\right) I_1\left(2\left(\frac{v}{v_0}\right)\sqrt{g}\right) \tag{30}$$

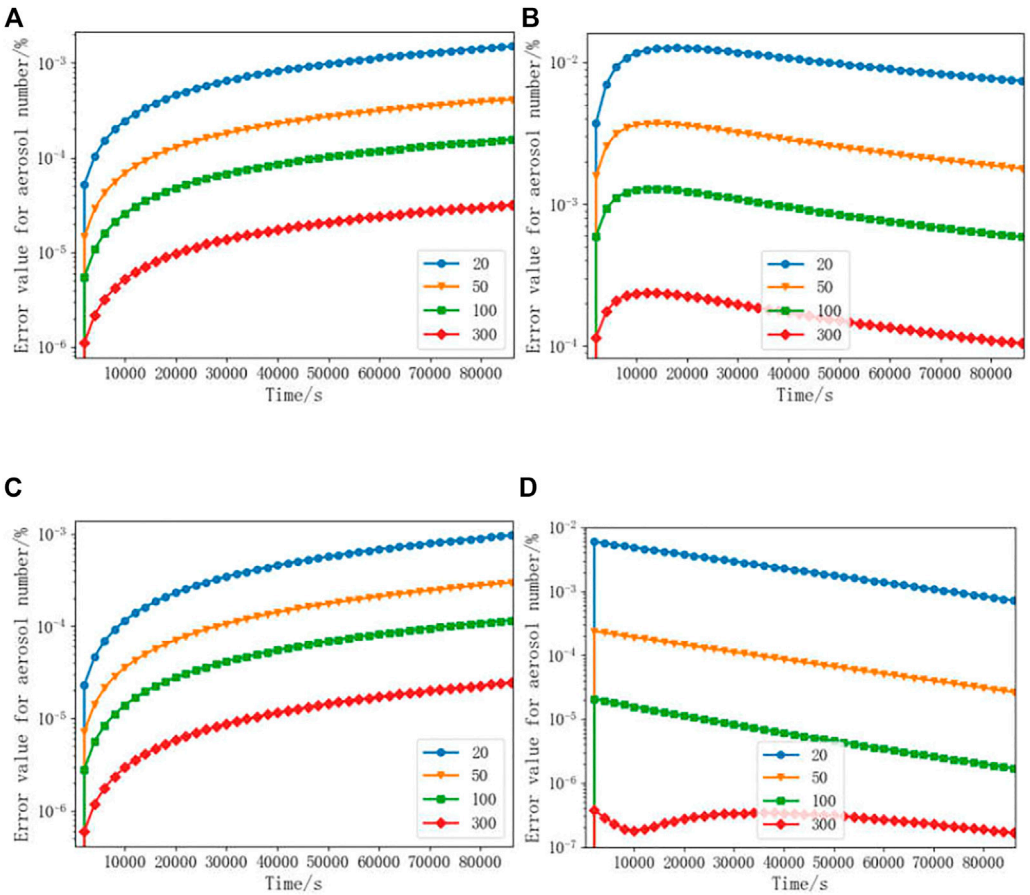

FIGURE 2 | Error value for the number of radioactive aerosols for the different sections. [**(A)**, Constant coagulation kernel; **(B)**, linear coagulation kernel; **(C)**, constant coagulation kernel and the constant deposition rate of particles; and **(D)**, linear coagulation kernel and the constant deposition rate of particles].

$$T = \exp(-\theta\tau) \tag{31}$$

$$g = 1 - \exp\left(\frac{T-1}{\theta}\right) \tag{32}$$

$$\theta = \frac{\lambda_0}{N_0 v_0 \beta} \tag{33}$$

The error value for the radioactive aerosol number of different section numbers between numerical and exact solutions to the equation GED is less than 10^{-3}, as shown in **Figure 2**. The number of sections is selected as 20, 50, 100, and 300. The initial number of the radioactive aerosol number is 1×10^{10}. By calculating the error value for chosen sections, the errors in the four selected sections gradually decreased. The error value is the least one when dividing the radioactive aerosol particle into 300 sections, as shown in **Figure 2**. It is mainly due to the effective reduction of the assumed initial distribution function when the number of sections increases. Therefore, the appropriate number of sections can be selected in the numerical simulation to reduce the error between the simulation values and the exact solution.

The error value for the radioactive aerosol number of different initial particles between the numerical and exact solutions to the equation GDE is less than 10^{-3}, as shown in **Figure 3**. The initial radioactive aerosol particle concentration is selected as $10^{10}/m^3$, $10^{11}/m^3$, and $10^{12}/m^3$. The section number of radioactive aerosol is 200 sections. By comparing the influence of different initial particles on the error, it appears that the error increases with the increasing initial radioactive aerosol particles, as shown in **Figure 3**.

The distribution of the radioactive aerosol particle number is presented in **Figure 4**. The initial radioactive aerosol particle number is $10^{10}/m^3$. The radioactive aerosol particles are divided into 200 sections. **Figures 4A,B** depict the radioactive aerosol particles distribution of different coagulation kernels at 0 and 24 h, respectively. This is because a smaller radioactive aerosol particle when coagulated with a larger radioactive aerosol particle will form a new bigger radioactive aerosol particle. This leads radioactive aerosol particles to move from a less section to a larger section. The radioactive aerosol particles move to the larger section obviously in benchmark 1. **Figures 4C,D** show the radioactive aerosol particle distribution with deposition at 0 and 24 h, respectively. It shows that radioactive aerosol particle deposition has a significant impact on the behavior of radioactive aerosol in nuclear power plants.

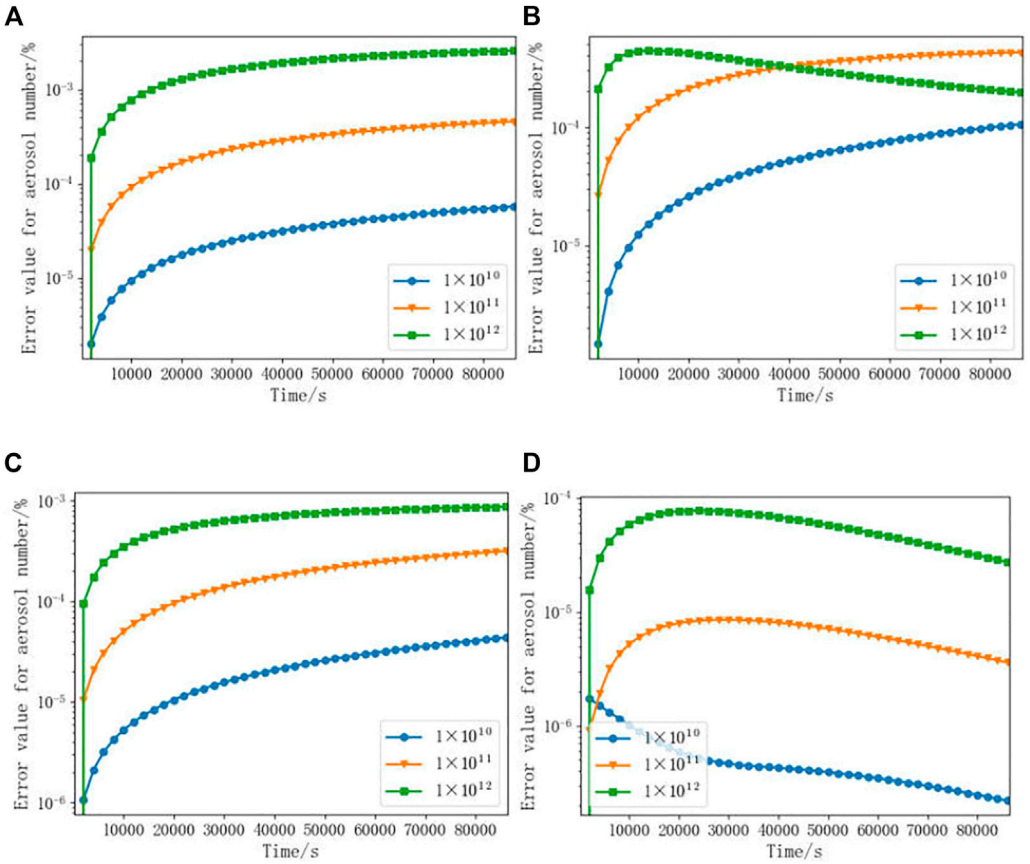

FIGURE 3 | Error value for the number of radioactive aerosols for different initial particle numbers. [**(A)**, Constant coagulation kernel; **(B)**, linear coagulation kernel; **(C)**, constant coagulation kernel and the constant deposition rate of particles; **(D)**, linear coagulation kernel and the constant deposition rate of particles].

Verification With the Experiment

The STORM-SR11 test from the International Standard Problem 40 (ISP-40) is selected for aerosol model validation. The experiment consisted of two phases: the first focusing on deposition due to natural deposition mechanisms and the second on the resuspension process of aerosols under conditions of increased airflow. This study focuses on the first phase for validation.

Figure 5 shows a schematic diagram of the STORM test facility. The test section is a 5.0055 m long straight tube with an internal diameter of 63 mm made of stainless steel. In the deposition test, the supplied carrier gas and aerosol are mixed in a mixing tank and flow into the test section, where the exhaust from the test section is connected to a cleaning and filtration system. The aerosol used is tin oxide (SnO_2), and the carrier gas is a mixture of nitrogen, steam, argon, helium, and air.

The constant mass flow rate of the aerosol in the test is 3.83 × 10–4 kg/s. Assuming that its initial distribution follows a log-normal distribution, the number distribution particle size f(d) is defined as follows.

$$f(d) = \frac{1}{d \ln \sigma_g \sqrt{2\pi}} exp\left[-\frac{1}{2}\left(\frac{\ln d - \ln d_g}{\ln \sigma_g} \right)^2 \right] \quad (34)$$

where $d_g = \overline{\ln d}$ is the geometric mean diameter. $\ln \sigma_g = [\overline{[\ln d - \ln d_g]^2}]^{1/2}$ is the standard geometric deviation. d is the particle diameter. The aerosol distribution in the initial state is shown in **Figure 6**.

The time of the numerical simulation is the same as the experiment time of 9,000 s. **Figure 7** shows the comparison between the simulated results and the experiment values. There are three distinct peaks, which are located at 1.02, 3.27, and 4.36 m. The maximum measured peak value is 0.292 kg/m^2. The peak of the measured values in the experiment is caused by the uneven surface of the test pipe joints. The simulated results and the measured values of the smooth pipes agree very well, and they all show a constant decrease in the aerosol mass along the pipe. **Table 2** depicts the deposition mass of the simulated and measured values. The deposition mass changes with the number of nodes. As the number of nodes increases, the error between the simulated value and the measured value also decreases, which gave the minimum error 6.19%.

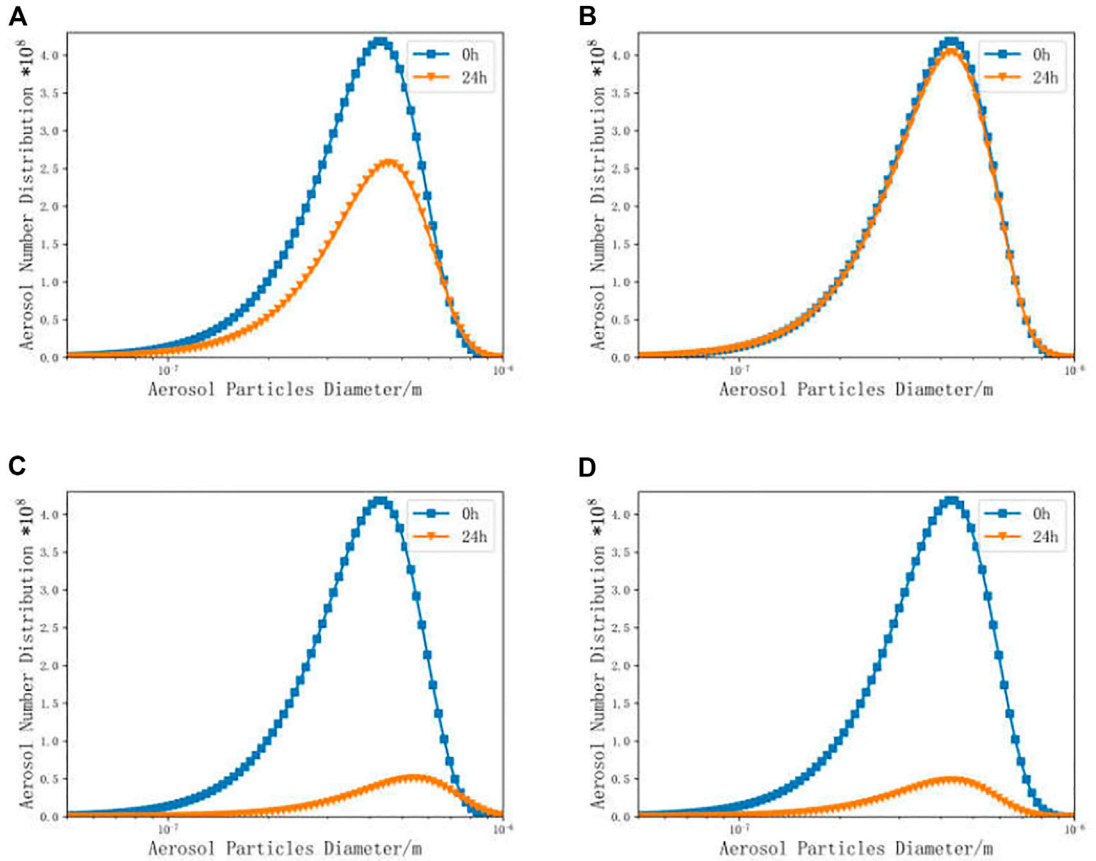

FIGURE 4 | Distribution of radioactive aerosol particles. [**(A)**, constant coagulation kernel; **(B)**, linear coagulation kernel; **(C)**, constant coagulation kernel and the constant deposition rate of particles; **(D)**, linear coagulation kernel and the constant deposition rate of particles].

APPLICATION OF THE AEROSOL MODEL UNDER SEVERE ACCIDENT

Accident Sequences

In this research, an LBLOCA accident is selected to study the particle distribution and behavior of aerosols, with a breach diameter of 50 cm and a breach location in the hot leg. To maximize the release rate of aerosols under accident conditions, all safe injection systems in the primary system are shut down. The sequence of events is shown in **Table 3**, the pressure vessel failing at 5,489 s.

According to the source term evaluation results after the Fukushima accident, when a serious accident occurs, the monitoring data for I^{131}, Cs^{134}, and Cs^{137} are the most nuclides, and they are also the widely important nuclides in the radiation evaluation. The air source term of I^{131} is 60–390 PBq, the air source term of Cs^{134} is 15–20 PBq, and the air source term of Cs^{137} is 5–50 PBq, after the accident (Bois et al., 2014; Cervone and Franzese, 2014; Koo et al., 2014). Therefore, this study focuses on the fission product CsI. **Figure 8** shows the variation of the mass of CsI aerosols with time for the accident sequence. The aerosol starts to increase at 8 s due to core exposure; when the temperature exceeds the melting temperature at 1,664 s, the core starts to melt and the aerosol release rate starts to increase dramatically and reaches a peak, with a small increase at 5,489 s due to pressure vessel failure.

As the accident proceeds, the aerosol mass will peak at 2,000 and 6,710 s. **Figure 9** shows the distribution of the aerosol mass at 2,000, 6,710, and 10,000 s. According to the mass distribution, the CsI aerosol particles mainly concentrated at 0.41 um. The mass of the CsI aerosol mass at 2,000 s is maximum in the containment, as shown in **Figure 8**, and the max aerosol mass in **Figure 9** is 2 kg. When the pressure vessel failure is at 5,489 s, the CsI aerosol mass rises again and reaches a maximum at 6,710 s, in which the max aerosol particle mass is 1.43 kg. At the end of the calculation, the CsI aerosol mass drops to 1.22 kg. It can also be seen that according to **Figure 9**, the distribution of the CsI aerosol mass is declining with the accident process.

Effect of the Natural Deposition on Aerosols

The natural deposition is the primary removal mechanism of aerosols. Thus, the effect of different natural deposition on aerosols is important. As shown in **Figure 10**, at the end of the simulation, gravity accounts for 54% of the total deposition mass, thermophoresis 28%, diffusion 3%, and Brownian diffusion 15%. Comparing the natural deposition mass of aerosols under

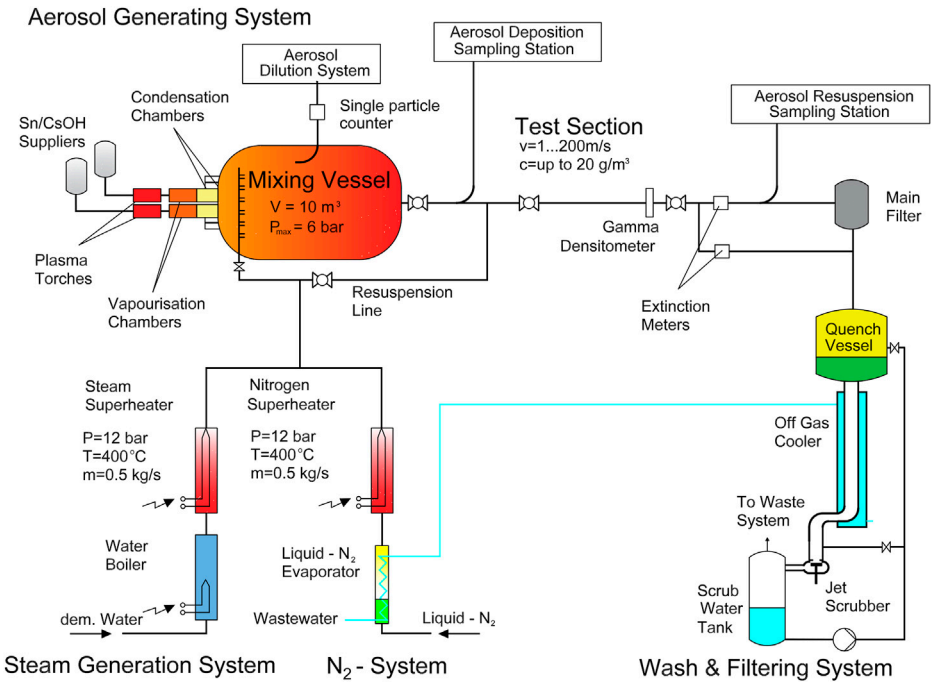

FIGURE 5 | STORM experimental facility (Castelo et al., 1999).

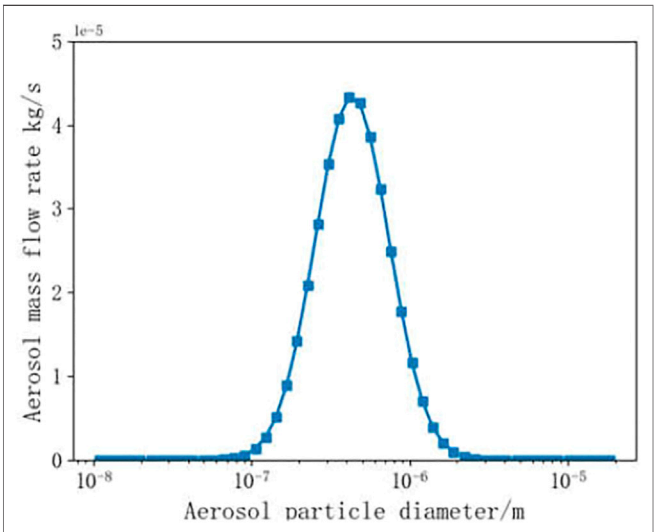

FIGURE 6 | Initial aerosol distribution.

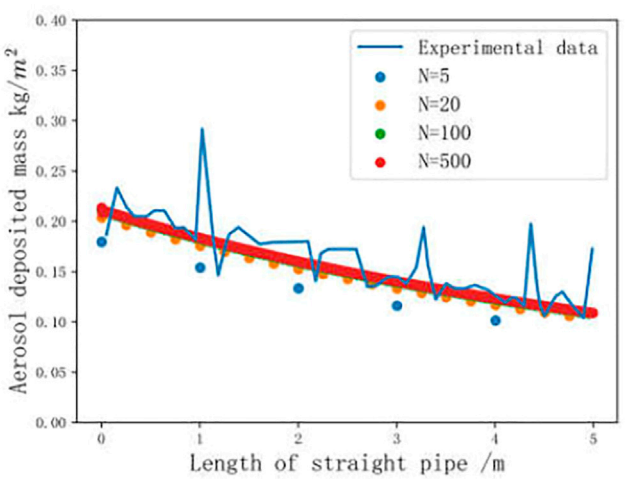

FIGURE 7 | Aerosol deposition along with the test pipe.

the accident conditions, gravitational effect is more than the other three deposition mechanisms.

Different deposition mechanisms can also have an impact on aerosol particle distribution. **Figure 11** shows the effect of the different mechanisms on the aerosol particle. As can be seen from the figure, the natural deposition mechanism has a certain impact on the particles between 0.01 μm and 0.03 μm and has an obvious effect on the particle gravity between 2 μm and 20 μm, especially

TABLE 2 | The deposited mass.

Number of nodes	Deposition mass (g)	Error (%)
5	135.74	16.21
20	147.22	9.12
100	151.13	6.71
500	151.97	6.19

TABLE 3 | Sequence of events.

Main events	Time/s
Reactor scram	0.4
Core uncover	8.4
Core begins to melt	1664.8
Relocation of core materials to the lower head started	2198.3
RV failed	5489.7
Program terminated	10000

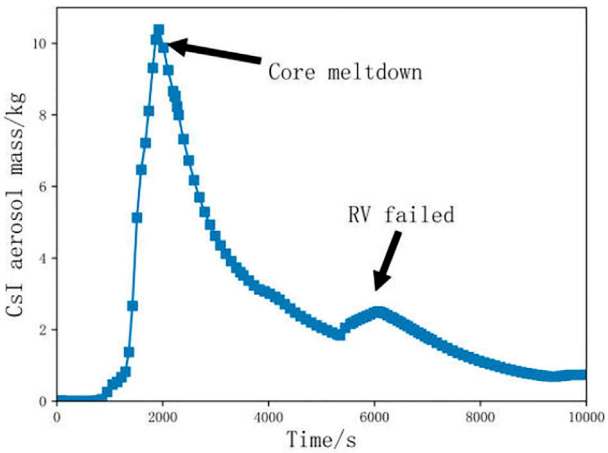

FIGURE 8 | Change of the CsI aerosol mass with time.

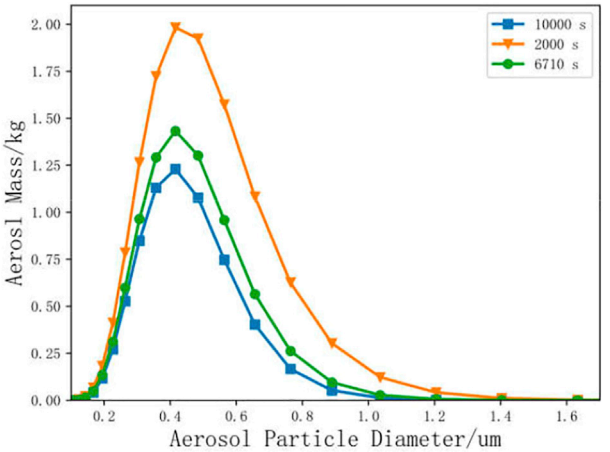

FIGURE 9 | Distribution of the CsI aerosol mass.

because the excessive gravity will increase, leading to the removal of large-diameter particles.

Influence of the Aerosol Particle Density

In this section, the influence of the radioactive aerosol particle density of a seven-component problem is discussed. The detailed density of the seven components is listed in **Table 4**. The initial components' mass concentration and the initial radioactive

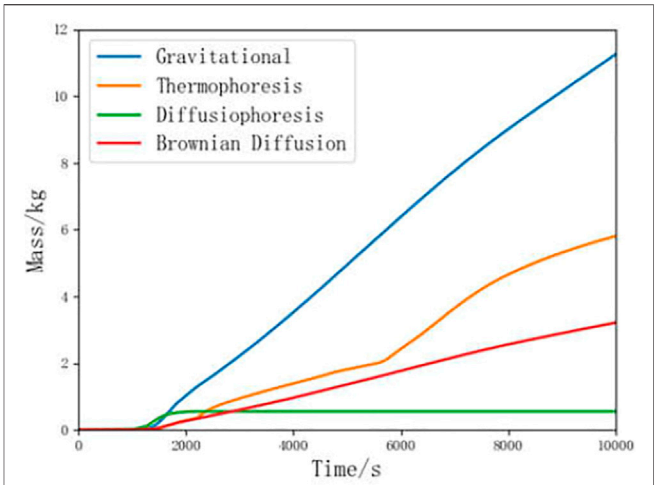

FIGURE 10 | Natural deposition of the CsI aerosol within the containment.

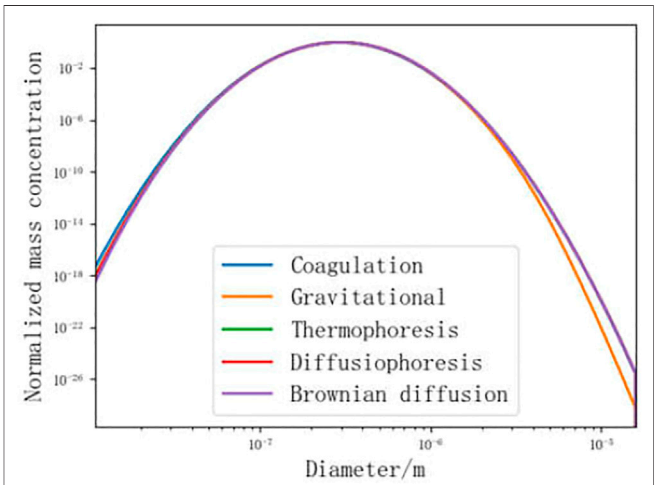

FIGURE 11 | Effect of the deposition mechanism on the distribution of aerosol diameter particles.

aerosol particle numbers are shown in **Figure 12**. The different line types represent different component mass distribution and the radioactive aerosol particle number distribution. CsI is defined as component 1, UO_2 as component 2, H_2O as component 3, Te as component 4, B_2O_3 as component 5, Cd as component 6, and Pb as component 7. Number distribution is the axis on the left. Other curves are the axis on the right.

The particle number and component mass distribution in the presence of the aerosol coagulation process have been tabulated in **Figures 13**, **14**. The difference in the radioactive aerosol particle number distribution can be seen in **Figure 13**. The aerosol particle number of the fixed density peaks at 0.45 μm, but the aerosol particle number of the changed density peaks at 0.65 μm. Therefore, the distribution of the changed density moves to larger particles, where the aerosol particle number decreases 16% relative to the fixed density. **Figure 14** depicts the effect

TABLE 4 | Component densities.

Component	Density (kg/m^3)
Uranium oxide (UO_2)	10970
Water (H_2O)	1000
Tellurium (Te)	6240
Cadmium (Cd)	8650
Lead (Pb)	11340
Cesium iodide (CsI)	4510
Boron oxide (B_2O_3)	2550

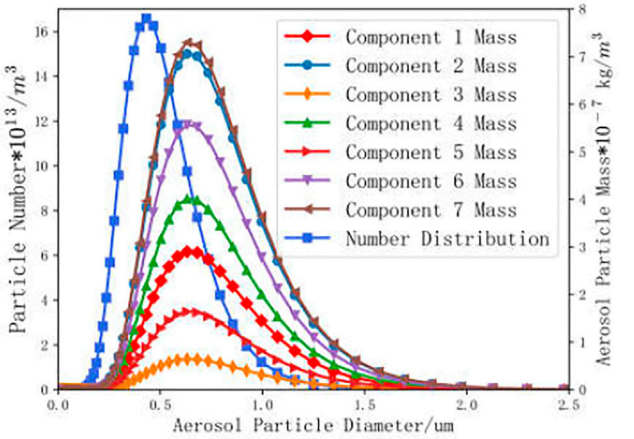

FIGURE 12 | Initial aerosol distribution.

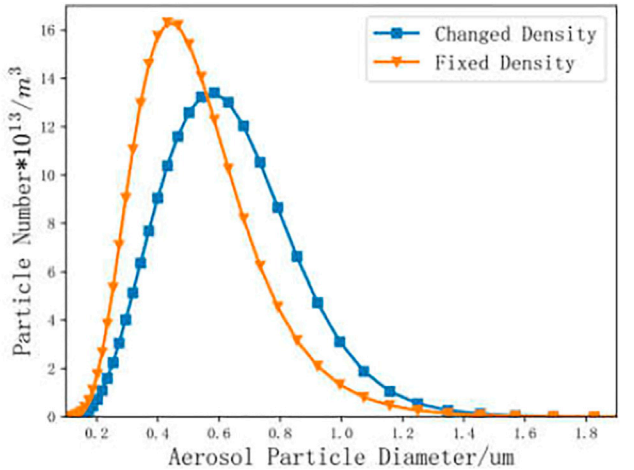

FIGURE 13 | Effect of different densities on the aerosol particle number distribution.

of different densities on the seven components', mass distribution. The mass distribution of seven components increases as the radioactive aerosol particles coagulate into bigger aerosol particles. The aerosol particle mass of the fixed density peaks at 0.63 μm, and the aerosol particle mass of the changed density peaks

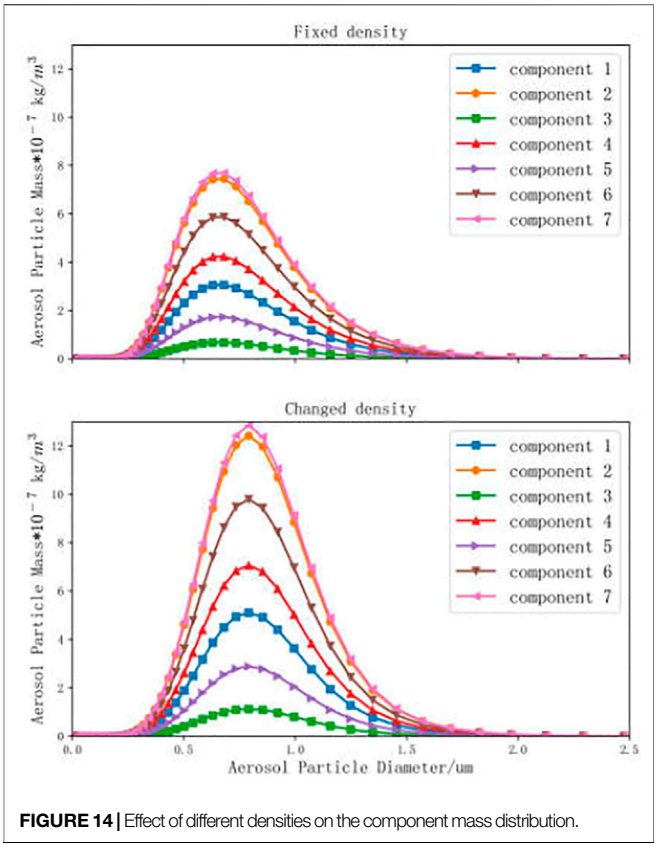

FIGURE 14 | Effect of different densities on the component mass distribution.

at 0.80 μm. So we can conclude that the density has a great influence on the multicomponent aerosol particle distribution.

CONCLUSION

This research adopts the improved multi-component aerosol sectional model to analyze the behavior of radioactive aerosol under severe accidents, which considers coagulation, deposition, and source term. The development model has demonstrated encouraging accuracy throughout the validation with the benchmark and experiment. The simulation result has a good agreement with the benchmark, where the error is less than 10^{-3}. The comparison with the STORM experiment also has a satisfied result. The sensitivity analysis of the section number shows that the appropriate number can effectively improve the simulation error.

Furthermore, according to the analysis under the LBLOCA accident, gravity deposition is the main deposition method in the aerosol deposition mechanism, accounting for 54% of the total deposition. The natural deposition mechanism affects the particles in the 0.01 μm–0.03 μm, and for the aerosol particles in the 2 μm–20 μm, gravity has a significant influence on it. Otherwise, compared to the influence of different densities on the aerosol distribution at the end of the study, it shows that the fixed density is significantly different from the changed density. The changed density will lead aerosol particles to move to bigger sections. The results of this study can be used to predict the behavior of radioactive aerosols in the

containment under severe nuclear accidents and provide a basis for emergency measures. Further optimization and improvement will be made for the problems existing in this model, containing the influence of the temperature on the aerosol behavior.

DATA AVAILABILITY STATEMENT

The original contributions presented in the study are included in the article/Supplementary Material, further inquiries can be directed to the corresponding author.

AUTHOR CONTRIBUTIONS

JW conceived and planned this work, wrote, and finalized the manuscript. XY and BZ provided constructive discussions. YG, QS, PG, SY, and CT contributed to review and revision.

FUNDING

This study is financially supported by the National Natural Science Foundation of China (Grant Nos. 12175116 and 11805112).

REFERENCES

Alipchenkov, V. M., Kiselev, A. E., Strizhov, V. F., Tsaun, S. V., and Zaichik, L. I. (2009). Advancement of Modeling Deposition and Coagulation of Aerosols in a Nuclear Reactor. *Nucl. Eng. Des.* 239 (4), 641–647. doi:10.1016/j.nucengdes.2008.12.025

Allelein, H. J., Auvinen, A., Ball, J. S. G., and Weber, G. (2009). *State of the Art Report on Nuclear Aerosols*. OECD Report NEA/CSNI/R(2009)5.

Bailly du Bois, P., Garreau, P., Laguionie, P., and Korsakissok, I. (2014). Comparison between Modelling and Measurement of marine Dispersion, Environmental Half-Time and 137cs Inventories after the Fukushima Daiichi Accident. *Ocean Dyn.* 64 (3), 361–383. doi:10.1007/s10236-013-0682-5

Bird, G. A. (1994). *Molecular Gas Dynamics and the Direct Simulation of Gas Flows. Oxford Engineering Science Series*. Oxford, New York: Clarendon Press, Oxford University Press.

Castelo, A. R., Capitao, J. A., and Santi, G. D. (1999). International Standard Problem 40 Aerosol Deposition and Resuspension. *Magn. Reson. Med.* 21 (2), 302–307.

Cervone, G., and Franzese, P. (2014). "Source Term Estimation for the 2011 Fukushima Nuclear Accident," in *Data Mining for Geoinformatics Methods and Applications*. Editors G. Cervone, J. Lin, and N. Waters (New York: Springer), 49–64. doi:10.1007/978-1-4614-7669-6_3

Gelbard, F. (1982). MAEROS User Manual. Sandia National Laboratories Report SAND80-0822, U. S. Nuclear Regulatory Commission Report NUREG/CR-1391. doi:10.2172/6459120

Gelbard, F., and Seinfeld, J. H. (1978). Numerical Solution of the Dynamic Equation for Particulate Systems. *J. Comput. Phys.* 28 (3), 357–375. doi:10.1016/0021-9991(78)90058-X

Gelbard, F., and Seinfeld, J. H. (1980). Simulation of Multicomponent Aerosol Dynamics. *J. Colloid Interf. Sci.* 78 (2), 485–501. doi:10.1016/0021-9797(80)90587-1

Humphries, L. L., Beeny, B. A., Gelbard, F., Louie, D. L., and Phillips, J. (2017). MELCOR Computer Code Manuals. In Reference Manual (Vol. 2). Sandia National Laboratories Report SAND2017-0876 O. doi:10.2172/1433918

Kljenak, I., Dapper, M., Dienstbier, J., Herranz, L. E., Koch, M. K., and Fontanet, J. (2010). Thermal-hydraulic and Aerosol Containment Phenomena Modelling in ASTEC Severe Accident Computer Code. *Nucl. Eng. Des.* 240 (3), 656–667. doi:10.1016/j.nucengdes.2009.12.002

Koo, Y.-H., Yang, Y.-S., and Song, K.-W. (2014). Radioactivity Release from the Fukushima Accident and its Consequences: a Review. *Prog. Nucl. Energ.* 74 (3), 61–70. doi:10.1016/j.pnucene.2014.02.013

Li, C., and Cai, R. (2020). Tutorial: the Discrete-Sectional Method to Simulate an Evolving Aerosol. *J. Aerosol Sci.* 150, 105615. doi:10.1016/j.jaerosci.2020.105615

Lin, W., Chen, L., Yu, W., Ma, H., Zeng, Z., Lin, J., et al. (2014). Radioactivity Impacts of the Fukushima Nuclear Accident on the Atmosphere. *Atmos. Environ.* 102, 311–322. doi:10.1016/j.atmosenv.2014.11.047

Liu, H. M., and Chan, T. L. (2018). Two-component Aerosol Dynamic Simulation Using Differentially Weighted Operator Splitting Monte Carlo Method. *Appl. Math. Model.* 62 (OCT), 237–253. doi:10.1016/j.apm.2018.05.033

Murata, K. K., Williams, D. C., Tills, J., Griffith, R. O., Gido, R. G., Tadios, E. L., et al. (1997). Code Manual for Contain 2.0: A Computer Code for Nuclear Reactor Containment Analysis. *Nuclear React. Tech.*7. doi:10.2172/569132

Porcheron, E., Lemaitre, P., Nuboer, A., and Vendel, J. (2008). Heat, Mass and Aerosol Transfers in spray Conditions for Containment Application. *Jpes* 2 (2), 633–647. doi:10.1299/jpes.2.633

Raj Sehgal, B. (2012). *Nuclear Safety in Light Water Reactors*, 426–509. doi:10.1016/C2010-0-67817-5

Rýdl, A., Fernandez-Moguel, L., and Lind, T. (2019). Modeling of Aerosol Fission Product Scrubbing in Experiments and in Integral Severe Accident Scenarios. *Nucl. Tech.* 205 (5), 655–670. doi:10.1080/00295450.2018.1511213

Shaker, M. O., Aziz, M., Ali, R., Sirwah, M., and Slama, M. (2012). Numerical and Analytical Solutions of the Aerosol Dynamic Equation in Reactor Containment. *Arab J. Nucl. Sci. Appl.* 45 (4), 96–108. http://www.esnsaeg.com/download/researchFiles/10_96-108.pdf.

Soffer, L., Burson, S. B., Ferrell, C. M., Lee, R. Y., and Ridgely, J. N. (1995). *Accident Source Terms for Light-Water Nuclear Power Plants*. Final Report. U.S. Nuclear Regulatory Commission. Washington, DC(United States): Division of Systems Technology. doi:10.2172/29438

Wang, F., Cheng, X., and Gupta, S. (2021). Cocosys Analysis on Aerosol Wash-Down of Thai-AW3 experiment and Generic Containment. *Ann. Nucl. Energ.* 153, 108076. doi:10.1016/j.anucene.2020.108076

Wang, K., Yu, S., and Peng, W. (2019). A Novel Moment Method Using the Log Skew normal Distribution for Particle Coagulation. *J. Aerosol Sci.* 134, 95–108. doi:10.1016/j.jaerosci.2019.04.013

Wittneben, B. B. F. (2012). The Impact of the Fukushima Nuclear Accident on European Energy Policy. *Environ. Sci. Pol.* 15 (1), 1–3. doi:10.1016/j.envsci.2011.09.002

Conflict of Interest: Authors SY and CT were employed by the China Nuclear Power Operation Technology Corporation, Ltd.

The remaining authors declare that the research was conducted in the absence of any commercial or financial relationships that could be construed as a potential conflict of interest.

Publisher's Note: All claims expressed in this article are solely those of the authors and do not necessarily represent those of their affiliated organizations, or those of the publisher, the editors, and the reviewers. Any product that may be evaluated in this article, or claim that may be made by its manufacturer, is not guaranteed or endorsed by the publisher.

frontiers | Frontiers in Energy Research

ORIGINAL RESEARCH
published: 01 April 2022
doi: 10.3389/fenrg.2022.869240

Study on the Effect of Jet Position and Size on Heat Transfer in a Small Containment

Wang Xiong[1], *Yuan Fang*[1], *Shengsheng Lin*[2] *and Shengfei Wang*[1]*

[1]*Beijing Key Laboratory of Passive Nuclear Power Safety and Technology, North China Electric Power University, Beijing, China,* [2]*China Nuclear Power Engineering Co., Ltd., Beijing, China*

In the main steam line break (MSLB) accident, the rise in temperature and pressure threatens the integrity of the containment, which is caused by a large amount of mixed gas injected into the containment rapidly. Due to the structural difference between small and large containment, it is necessary to study the heat transfer in the complex space of the small containment. Based on the research method, which is from simple to complex, in this study, a series of experiments and numerical simulations are carried out with different jet positions and sizes using hot air without phase change as the working medium. The results show that the temperature field above the jet is complex and affected by many factors such as buoyancy, initial kinetic energy, and internal structure. When the jet flow rate is constant, the jet size is smaller and the velocity is faster, which results in a large circulation and stronger heat exchange with the wall of containment. This means that the temperature above the jet is lower than the large jet size, and the temperature below the jet is slightly higher. The jet position mainly affects the relative position of the jet and the complex space in the containment. When the jet is located in a narrow space, the overall temperature in the containment is higher than the jet located in a large space. In addition, when it is close to the obstacle, the core region of the jet will shift slightly toward the obstacle.

Keywords: small steel containment, complex space, heat transfer, jet position, jet size

OPEN ACCESS

Edited by:
Yapei Zhang,
Xi'an Jiaotong University, China

Reviewed by:
Zhaoming Meng,
Harbin Engineering University, China
Luteng Zhang,
Chongqing University, China

***Correspondence:**
Shengfei Wang
zt970831@ncepu.edu.cn

Specialty section:
This article was submitted to Nuclear Energy, a section of the journal Frontiers in Energy Research

Received: *04 February 2022*
Accepted: *28 February 2022*
Published: *01 April 2022*

Citation:
Xiong W, Fang Y, Lin S and Wang S (2022) Study on the Effect of Jet Position and Size on Heat Transfer in a Small Containment. Front. Energy Res. 10:869240. doi: 10.3389/fenrg.2022.869240

INTRODUCTION

As the last barrier of the reactor, the containment must ensure its integrity by preventing over-temperature and over-pressure in it. When MSLB accidents or LOCAs occur, a large amount of high-temperature and high-pressure mixed gas will be released from the break into the containment and threatens the integrity of the containment. Therefore, the heat transfer in the containment is the key problem during the MSLB accident/LOCA. Currently, research on large-scale containment is nearly mature. However, the volume of small-scale containments is significantly smaller than that of large-scale containments, and the low heat capacity and rapid boost pressure after an accident are the main characteristics that distinguish them from large-scale containments. Therefore, the heat transfer mechanism and empirical formulas in the containment of large reactors are not suitable for small containment completely. Papini et al. (2011) implemented a simplified model of IRIS containment drywell with RELAP5 to investigate the effect of drywell temperature and pressure response, heat transfer coefficient (HTC) and steam volume fraction distribution, and internal recirculating mass flow rate on containment behavior prediction. Zhang et al. (2015) developed a new code, which is based on thermal stratification and is used to solve heat transfer problems in large enclosures, which can give good results in a short time without complex meshing. Niu et al. (2016) conducted the

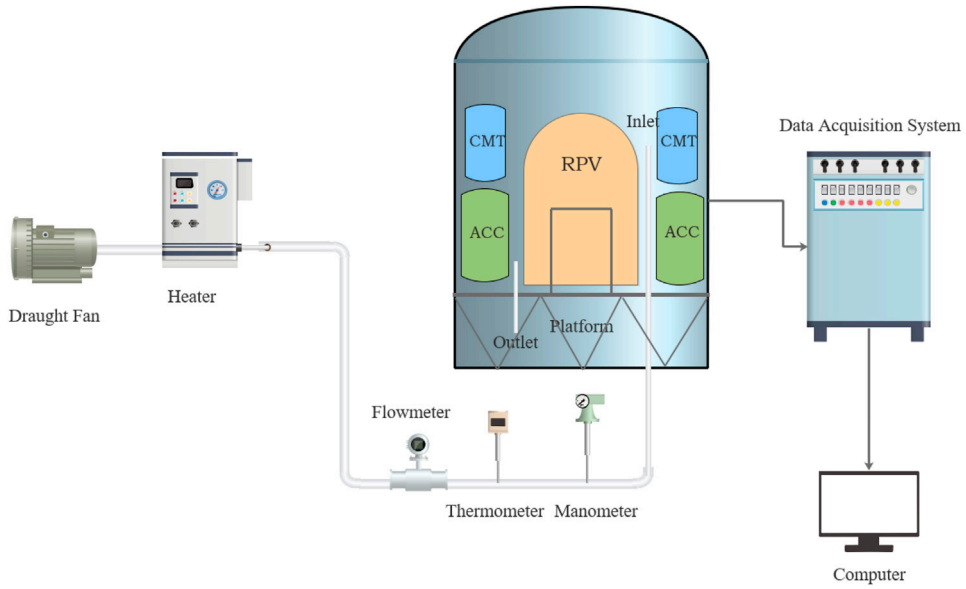

FIGURE 1 | Schematic of the experimental facility.

experiment with various jet inlet temperatures and flow rates to identify the influence of plumes or buoyant jets on thermal stratification phenomena. Wang et al. (2017) conducted the experiment with various jet inlet temperatures and spray water flow rates to identify their influence on the thermal stratification phenomena during the LOCA or MSLB accidents. Albadawi et al. (2018) explained the phenomenon of thermal stratification in SMR's reactor pool by comparing experimental data and simulation results. In Kim et al. (2020), the accident sequence during an SBO accident was simulated using the CINEMA-SMART (code for integrated severe accident management and analysis–SMART) code to evaluate the transient scenario inside the reactor vessel after an initiating event, core heating and melting by core uncovery, relocation of debris, reactor vessel failure, discharge of molten core, and pressurization of the containment. Liu et al. (2020) analyzed the steam mass and energy released from the break, in comparison with the prototype and the experimental facility modeled by MELCOR.

Due to the complex factors, the study is divided into 3 stages. Stage 1 used hot air without phase change as a working medium, and stages 2 and 3 used steam and mixed gas, respectively. In our previous work (Lin et al., 2021), we have studied the heat transfer phenomenon in the complex space of small steel containment using hot air as the working medium with various jet inlet temperatures, velocities, and heights. In this study, we studied the influence of different jet sizes and different jet positions on it, which are two other factors with air as the working medium. A series of experiments were carried out, and the experimental results were compared with the simulation results to analyze the heat transfer phenomenon.

EXPERIMENT

Experimental Facility

The previous experimental facility (Lin et al., 2021) was retrofitted to suit this research. As shown in **Figure 1**, the experimental facility mainly consists of six devices: high-pressure fan, heater, measuring system, containment, data acquisition system, and computer. The equipment and instruments used in the experiment have been calibrated. According to the calibration result, the measurement error and uncertainty are shown in **Table 1**. The height of the containment is 2.4 m, which has a platform with a height of 0.77 m at the bottom. The material of the containment shell is 304 stainless steel without coating. The containment consists of two accumulated tanks (ACC) and two core makeup tanks (CMT). The interval of each layer between A-1 and A-7 is 200 mm, and the interval of A-7 and A-8 is 1,000 mm. In addition, another temperature measurement point is set in the heater and near the jet. The size of the containment and the distribution of the measuring points are shown in **Figure 2** (units = mm).

Experimental Conditions

Air is used as the working medium to study the influence of different jet sizes and jet positions on temperature distribution. The specific experimental data are shown in **Table 2**. The jet position corresponding to the horizontal location of the jet at different angles is shown in **Figure 3**.

Experimental Steps

The experiment procedure is divided into 4 steps:

TABLE 1 | Measurement error and uncertainty.

Measurement parameter	Measurement tool	Range	Error	Relative error (%)
Volume flow rate	Vortex flowmeter	0–32 m^3/h	0.16 m^3/h (°C)	0.5
Temperature 1	Nail-type K thermocouple	0–150°C	0.8	0.4
Temperature 2	K-type thermocouple	0–120°C	0.6	0.5

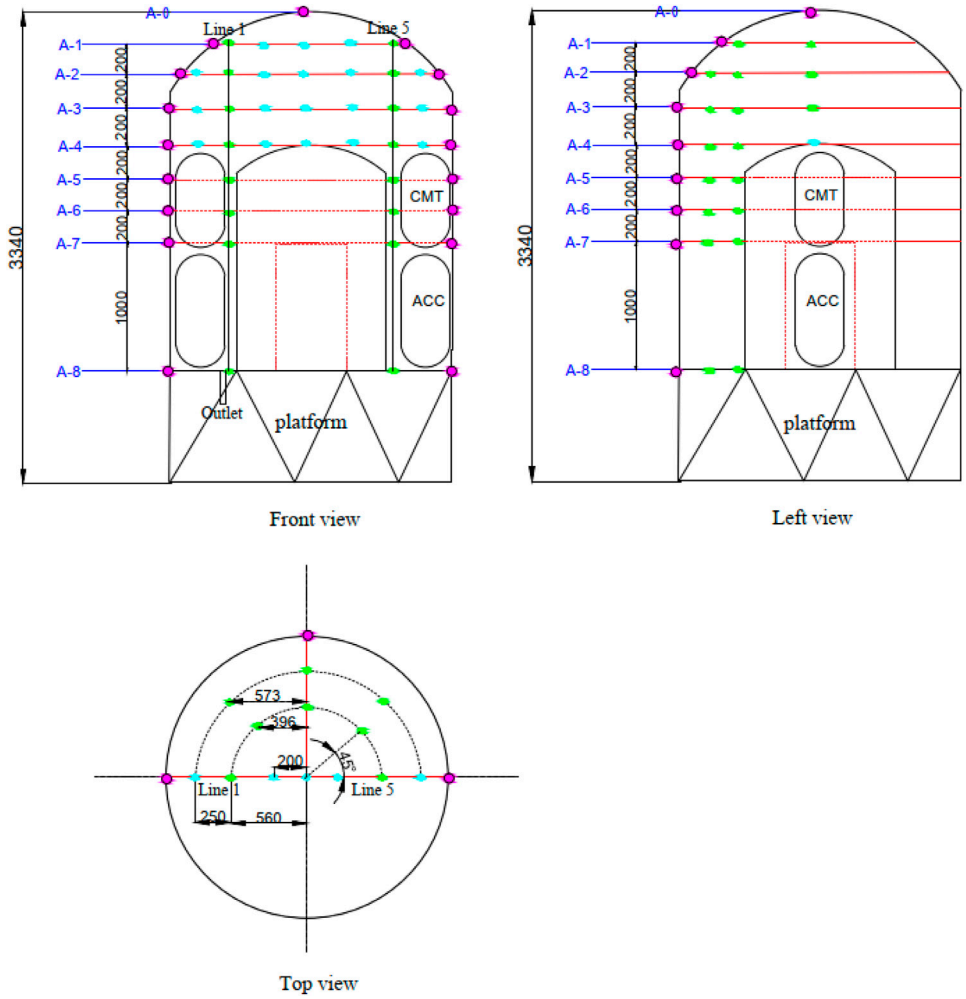

FIGURE 2 | Distribution of thermocouples.

TABLE 2 | Experimental conditions.

No.	Working condition	Jet flow rate (m^3/h)	Jet size (mm)	Jet horizontal location (°)	Jet temperature (°C)	Room temperature (°C)
1	Fundamental case	15.44	25	0	100.5	15
2	Jet horizontal location experiment	15.27	25	45	100.1	14.8
3		15.62	25	90	100.3	14.7
4	Jet size experiment	15.58	15	0	99.8	15.5
5		15.66	50	0	99.6	14.0

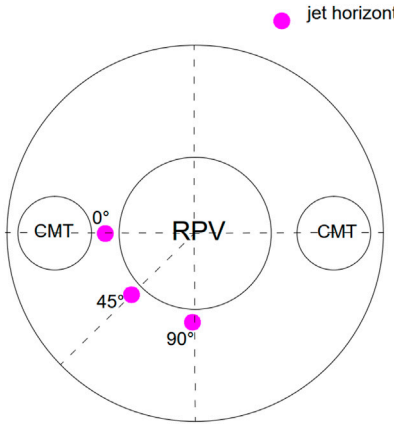

FIGURE 3 | Top view of various jet horizontal locations.

1) The initial temperature of the experiment facility is the room temperature of the laboratory, and the cooling condition is natural convection of air.
2) The airflow rate is adjusted by changing the power of the high-pressure fan; meanwhile, the heater is adjusted so that the temperature of the jet reaches the working temperature.
3) With hot air injected by the jet, the temperature inside the containment increased rapidly. At the same time, the external environment continuously cooled down the wall of the containment by natural convection until stabilization.
4) It takes about 2 h for the temperature field to enter the quasi-steady state. Each experiment lasts for more than 3 h to ensure the accuracy of the experimental results.

EXPERIMENTAL RESULTS AND DISCUSSION

Jet Position

Figure 4 shows the temperature distribution with height at line 1 (L1) and line 5 (L5) under different jet positions. It can be seen from **Figure 4** that the temperature distribution at L1 and L5 at case 2 and case 3 is similar, while the upper temperature of L1 at case 1 is higher than that of the other two cases because the injected hot air directly reaches the position of L5. Then, hot air went through the dome of the containment and downward along the L1. The reason why the bottom temperature (x = 0.0 m) of case 2 and case 3 at L5 is higher than that of x = 1.0 m is that the jet pipe penetrates through the containment from the bottom near L5 in the experimental facility. Although there is insulation outside the jet pipe, the temperature of the air near the jet pipe is a little higher. It can be seen from **Figure 4B** that the temperature of case 1 is generally higher than that of the other two cases, because in case 1, the jet flow is located near L5, and the temperature measuring point at the lower space of the jet is affected by the jet pipe heat dissipation, while x = 1.5 m is the highest because of the jet core region.

Figure 5 illustrates radial temperature distribution at H = 1.8 m and H = 2.2 m. The temperature of case 1 is generally higher than that of the other two working conditions when H = 1.8 m and H = 2.2 m. This is mainly determined by two factors: The first is that the jet of case 1 is located in a narrow space between the two tanks, which results in the jet in this case being a restricted jet flow, whereas it is a free-developing jet flow in case 2 and case 3. The second is that the measuring point is located in the core region of the jet in case 1, which leads to a peak temperature of x = 0.5 m.

The change of jet position is equivalent to the change of the relative position in the complex space of the containment, thus affecting the flow and heat transfer of the jet.

Jet Size

Figure 6 shows the temperature distribution with height at L1 and L5 under different jet sizes. In the upper space (H ≥ 1.8 m) of the containment, the temperature of case 4 is the lowest, and the temperatures of other cases are similar. The temperature distributions of the 3 cases are similar in the middle space (1.2 m < H < 1.8 m). In the lower space (H ≤ 1.2 m), the temperature of case 4 is the highest, and the temperatures of the other two cases are similar. This is because when the mass

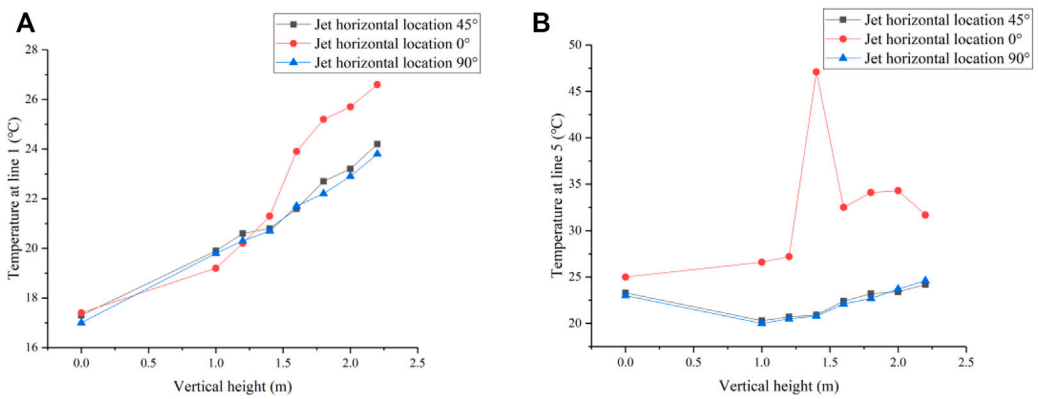

FIGURE 4 | Temperature distribution with height at L1 and L5 under different jet positions. **(A)** L1. **(B)** L5.

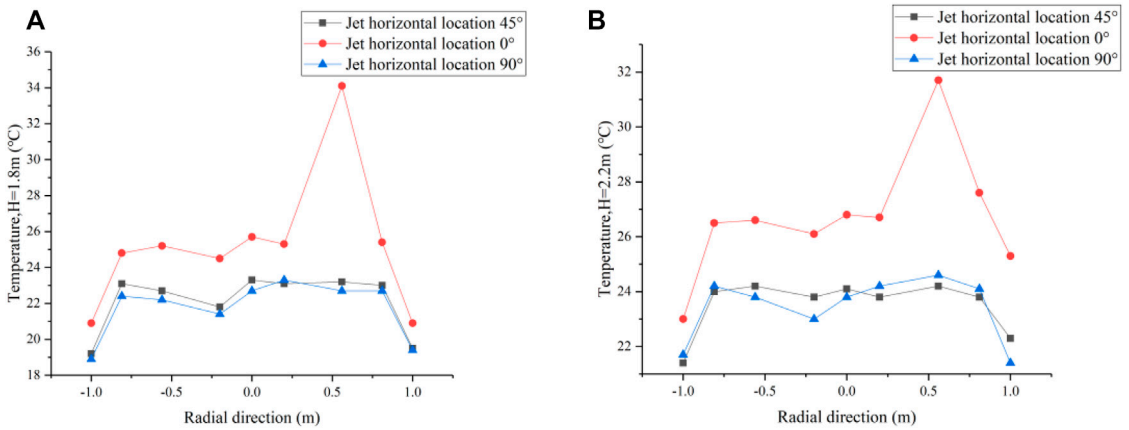

FIGURE 5 | Radial temperature distribution at H = 1.8 m and H = 2.2 m under different jet positions. **(A)** H = 1.8 m. **(B)** H = 2.2 m.

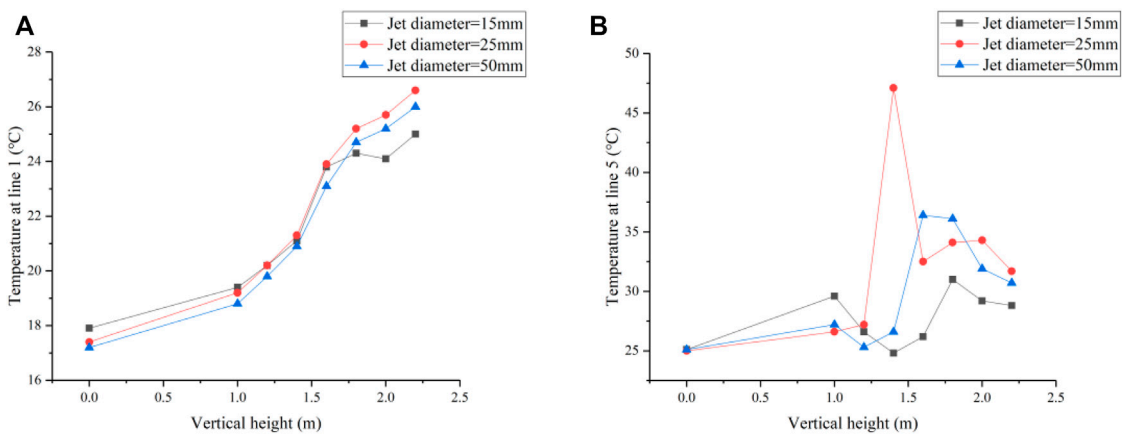

FIGURE 6 | Temperature distribution with height at L1 and L5 under different jet diameters. **(A)** L1. **(B)** L5.

flow rate is the same, the larger the diameter of the jet is, the lower the jet velocity. Case 4, with a higher jet velocity, easily forms a large circulation in the containment, which results in a lower temperature of the upper space and a higher temperature of the lower space than other cases. In **Figure 6B**, only case 1 has a peak temperature. The possible reason for this is that the measuring point (x = 1.4 m) is located in the core region of the jet flow in case 1.

Figure 7 illustrates radial temperature distribution at H = 1.8 m and H = 2.2 m. When H = 1.8 m and x = 0.5 m, the temperature increases with the increase in the jet size. This is because it is close to the jet, and the increase in the jet size leads to a decrease in the velocity, so the temperature is high here. However, when H = 2.2 m, the peak temperature of case 1 is the highest. As the height increases, it needs more kinetics to transfer heat to this position. The smaller the size of the jet, the higher the velocity, and the stronger the heat dissipation around, but at the same time, the cone of the jet core region is also smaller, which leads to decreased heat dissipation, and the final temperature depends on which is the main factor.

When the jet size changes, the most important effect is that the jet velocity changes. A large loop is formed throughout the containment vessel because of the high velocity. It only circulates in the upper space of the containment vessel at a moderate velocity. However, when the jet velocity is lower, the jet's kinetic energy is too small to form a circulation after it reaches the dome of the containment, and the main force is buoyancy.

CFD SIMULATION

Meshing and Independence

Steady simulation using ANSYS CFX was performed based on the experimental conditions. The following experimental model (**Figure 8**) is established, and its mesh quality is shown in **Figure 8**. A jet size of 25 mm was taken as an example to

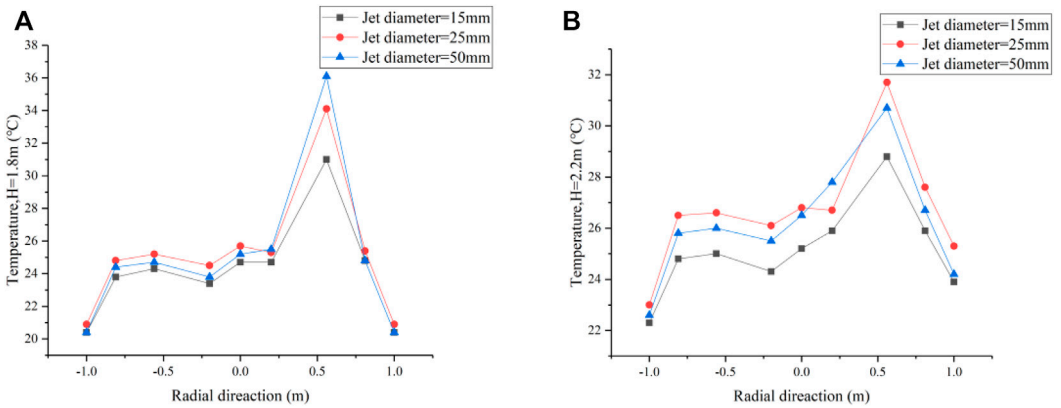

FIGURE 7 | Radial temperature distribution at H = 1.8 m and H = 2.2 m under different jet positions. **(A)** H = 1.8 m. **(B)** H = 2.2 m.

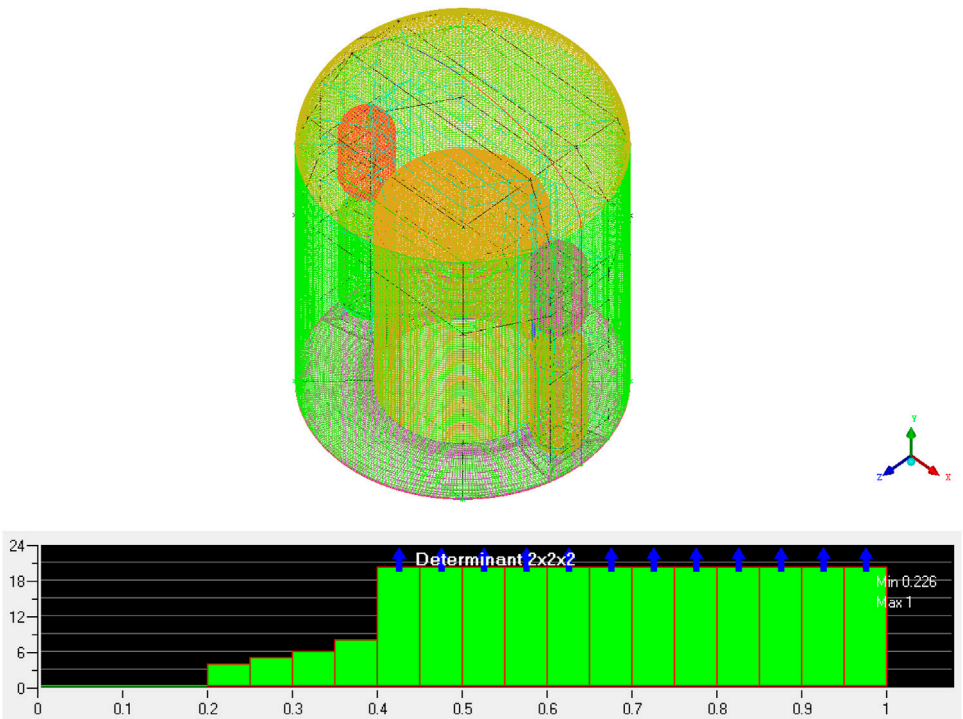

FIGURE 8 | Meshing model and quality.

TABLE 3 | Grid independence test.

Grid number	Temperature, K	Deviation (%)
1000000	299.01	0.121
2000000	298.42	0.077
3000000	298.65	0.000

verify the mesh independence. The total number of grids was selected as 1 million, 2 million, and 3 million, respectively. The temperature of the center in the containment dome (H = 2.0 m) was taken as a reference, and the errors were compared with 3 million grids. As shown in **Tables 2**, **3**, million grids can meet the computing requirements.

Comparison with Experimental Results

In the numerical simulation, the outer wall temperature was set at 15°C. Taking the jet size = 25 mm and jet horizontal location 45° as examples, the experimental results of L1 were compared with the numerical simulation results. According to **Figure 9**, the trend of temperature variation between the experimental results and the numerical simulation results is similar, but the results of the simulation are generally lower than those of the experiment. The

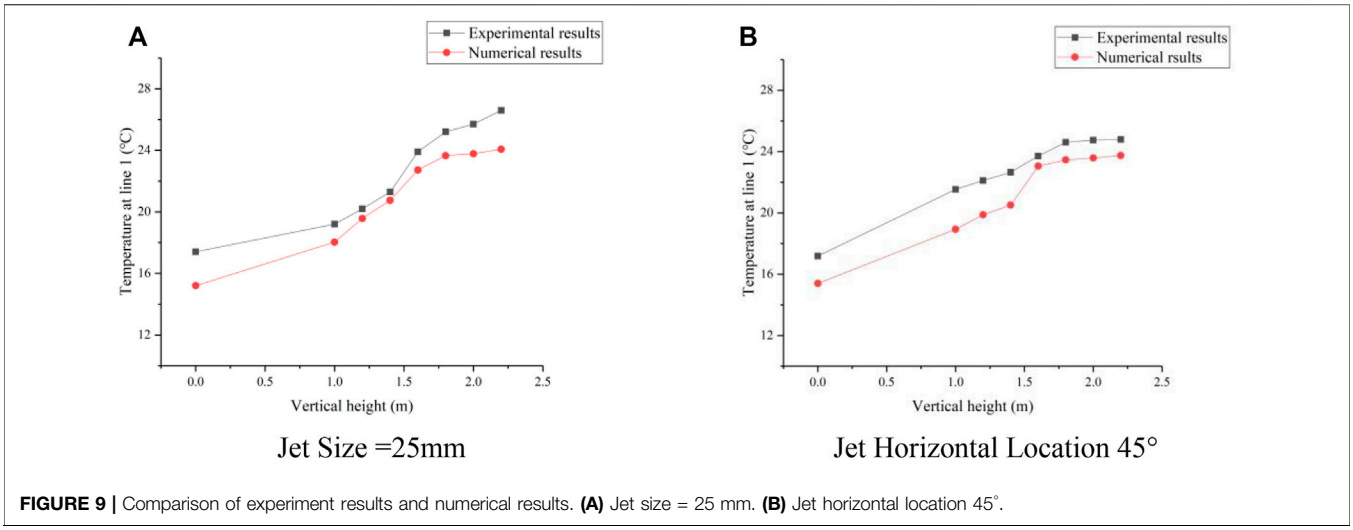

FIGURE 9 | Comparison of experiment results and numerical results. **(A)** Jet size = 25 mm. **(B)** Jet horizontal location 45°.

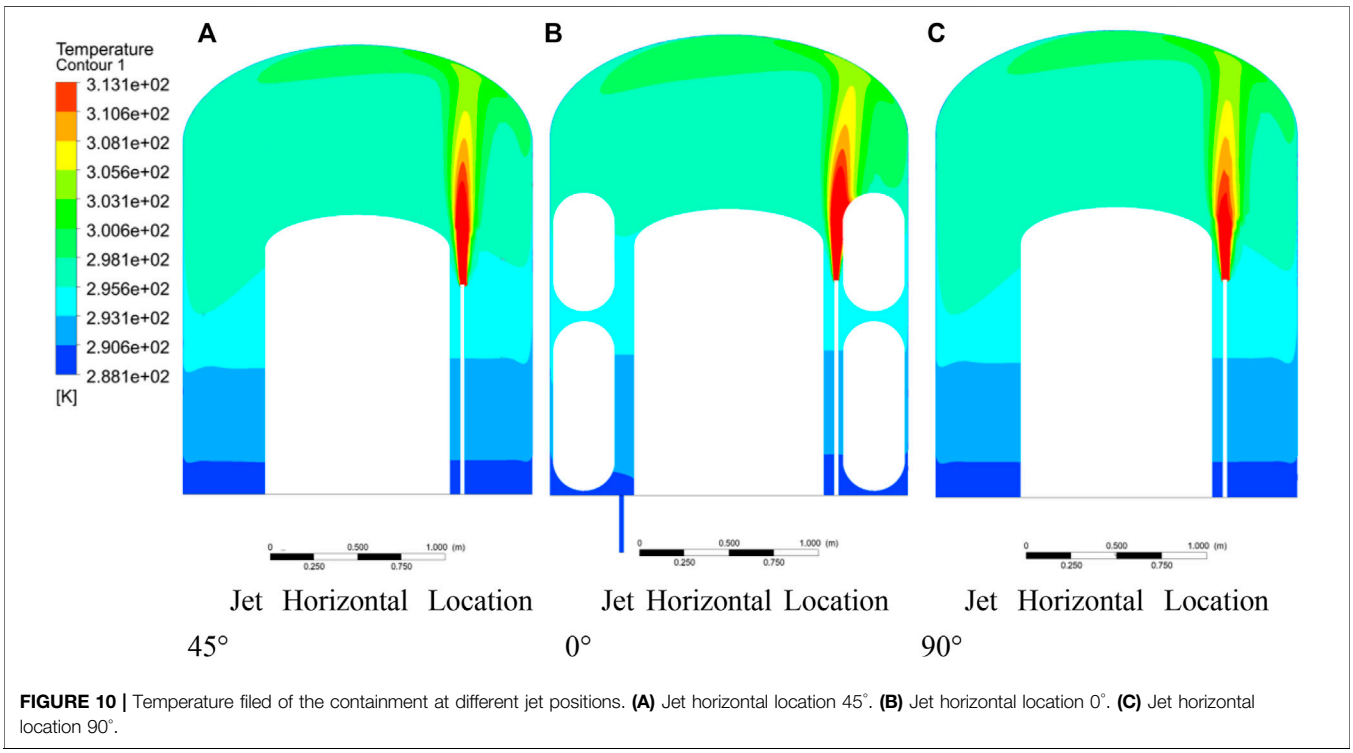

FIGURE 10 | Temperature filed of the containment at different jet positions. **(A)** Jet horizontal location 45°. **(B)** Jet horizontal location 0°. **(C)** Jet horizontal location 90°.

reason is that the simulations used constant wall temperatures, but the temperature of the containment wall increased during the experiment.

Figures 10–13 show the numerical simulation results of jet sections under different jet sizes and jet positions.

It can be seen from **Figure 10** that the temperature fields of the three working conditions at the core region are similar, but there is some difference in the temperature field in the middle of the containment. The temperature in this area in **Figure 10B** is slightly lower than that in the other two working conditions, which indicates that obstacles have an influence on heat transfer and restrain heat transfer in the local area. In addition, the core region in **Figure 10B** is disturbed by obstacles and tends to tilt slightly toward the side with higher obstacles. **Figure 11** shows the velocity vectors in the containment. The velocity distribution is similar between **Figures 11A,C**, and it is different in **Figure 11B** because of the obstacles (4 small tanks). For the length of the core region of the jet, **Figure 11B** is also the largest. This is mainly because the obstacles limited the jet diffused and reduced kinetic dissipation.

It can be seen from **Figure 12** that the temperature difference between the upper and lower spaces of **Figure 12A** is the smallest,

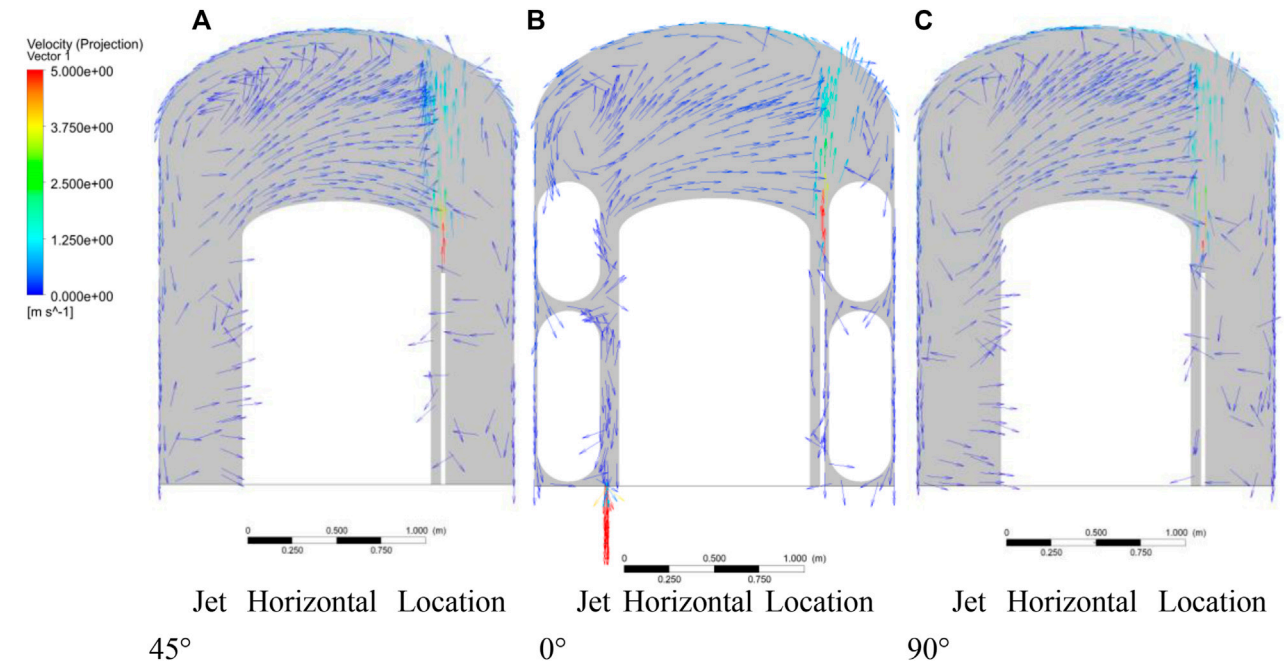

FIGURE 11 | Distribution of velocity vectors in the containment at different jet diameters. **(A)** Jet horizontal location 45°. **(B)** Jet horizontal location 0°. **(C)** Jet horizontal location 90°.

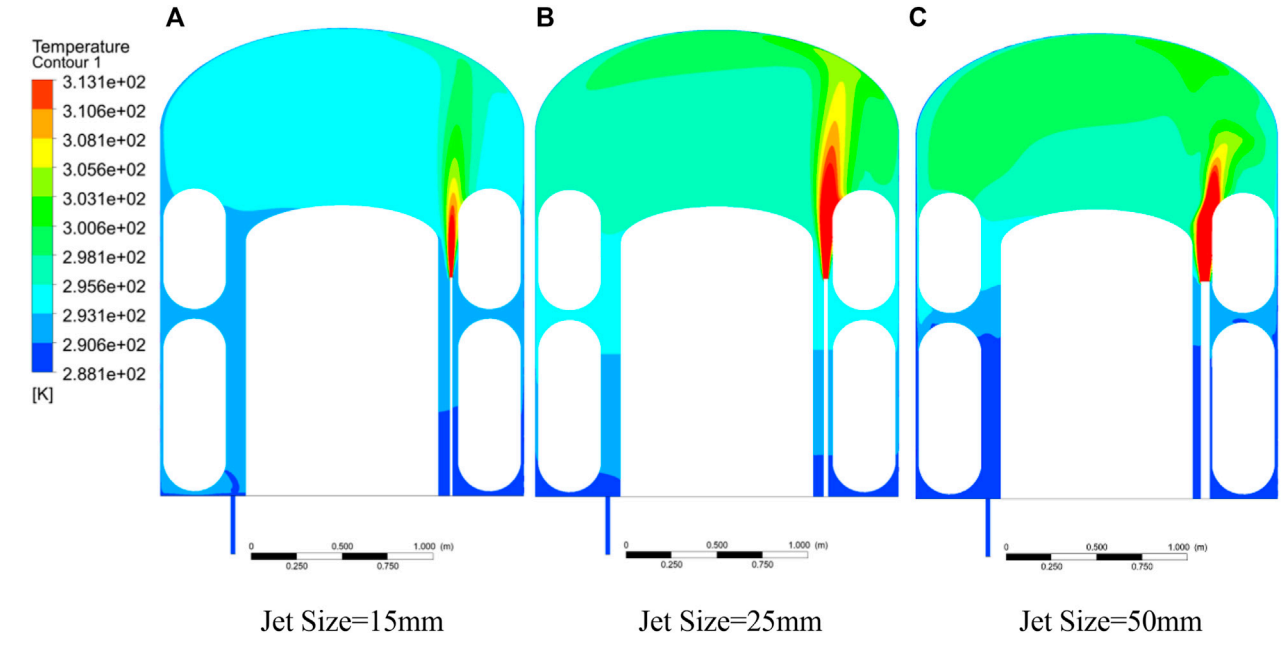

FIGURE 12 | Temperature filed of the containment at different jet diameters. **(A)** Jet size = 15 mm. **(B)** Jet size = 25 mm. **(C)** Jet size = 50 mm.

and the temperature difference between the upper and lower spaces of **Figure 12C** is the largest. Furthermore, the jet flow to the dome of the containment and transform to plume are shown in **Figure 12C**. In addition, both the areas of core regions of temperature in **Figure 12A** and **Figure 12C** are smaller than that of **Figure 12B**. This is because high velocity at the dome surface leads to strong heat exchange with the environment in **Figure 12A**. The core region of **Figure 12C** is small because the velocity is too small to transfer heat far in vertical direction. Obstacles (tanks) on both sides block the development of the jet

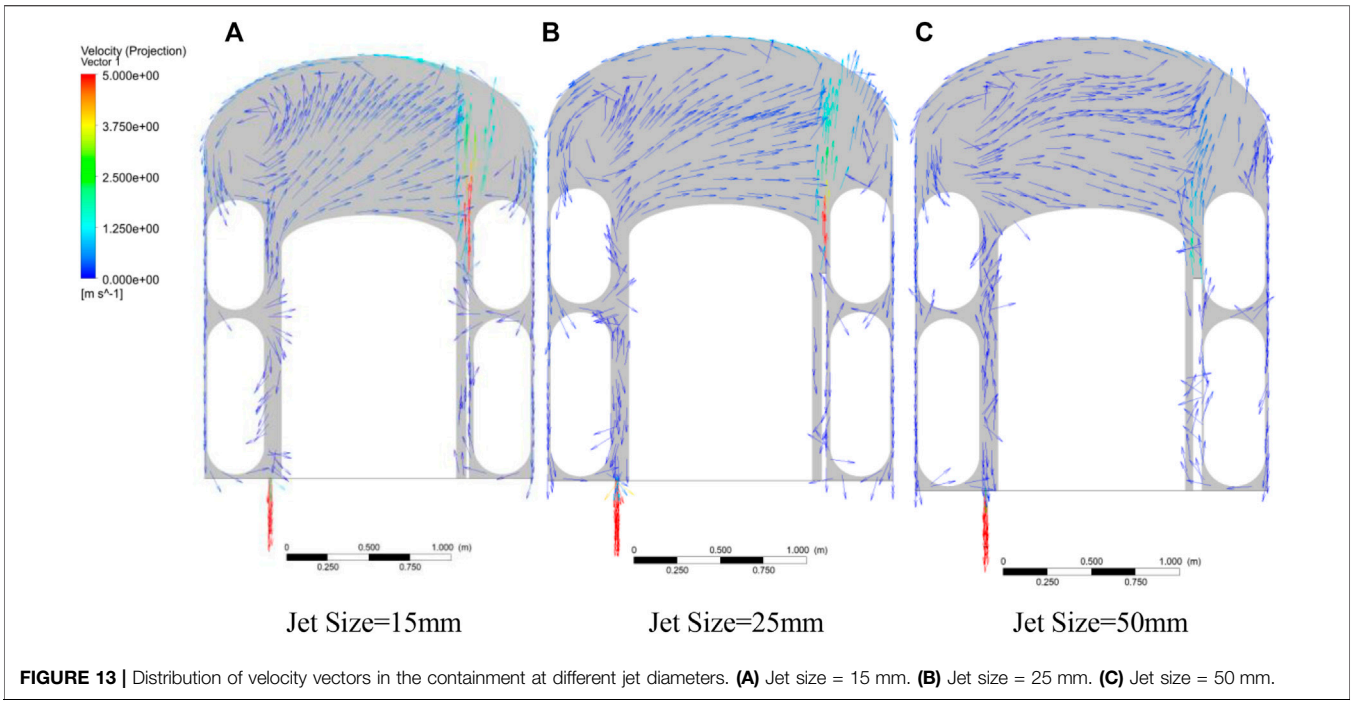

FIGURE 13 | Distribution of velocity vectors in the containment at different jet diameters. **(A)** Jet size = 15 mm. **(B)** Jet size = 25 mm. **(C)** Jet size = 50 mm.

core region. Moreover, the lower the velocity, the easier it is to swerve to the side of the obstacle because of the Coanda effect, which states that a fluid or gas stream will hug a convex contour when directed at a tangent to that surface. It can be seen from **Figure 13** that the smaller the jet size, the larger the core region of velocity. Moreover, the larger the core region of velocity, the more intense the entrainment effect, which leads to a difference of the flow field in the dome of the containment.

CONCLUSION

To study the heat transfer phenomenon in the complex space of small and medium steel containment vessels during jet flow, a series of experiments and numerical simulations were carried out with hot air as the working medium. The diameter and location of the jet are mainly considered, and the following conclusions are drawn:

1) The jet position mainly affects the jet flow pattern by relative position in the complex structure of the containment. When the jet is located in a narrow space, the overall temperature in the containment is higher than the jet located in a large space. When it is close to the obstacle, the core region of the jet will shift slightly toward the obstacle because of the Coanda effect.
2) With the jet sizes changing, the main effect is that the jet velocity changes. The smaller the jet size, the higher the velocity. It is easy to form a circulation in the containment to enhance heat transfer, and the overall temperature is lower. The jet kinetic energy is too small to form a circulation after it reaches the dome of the containment, and the main force is buoyancy.
3) The temperature field inside the small containment vessel is affected by the jet parameters and local structure. In the upper space of the containment, it is mainly affected by the jet parameters, and in the lower space, it is mainly affected by the buoyancy and local structure.

DATA AVAILABILITY STATEMENT

The raw data supporting the conclusion of this article will be made available by the authors, without undue reservation.

AUTHOR CONTRIBUTIONS

WX: writing—original draft, investigation, and formal analysis. YF carried out the experiments and analysis. SL: construction of the facility and analysis. SW: conceptualization, methodology, formal analysis, resources, data curation, writing—editing, and project administration.

FUNDING

This research is supported by the National Key Research Development Project of China (Grant No. 2020YFB1901405), the National Natural Science Foundation of China (No. 11805068), and the Fundamental Research Funds for the Central Universities (2020MS030).

REFERENCES

Albadawi, G., Wang, S., and Cao, X. (2018). Numerical and Experimental Study of Thermal Stratification outside a Small SMR Containment Vessel. *Sustainability* 10 (7), 2332. doi:10.3390/su10072332

Kim, H. T., Song, J. H., and Park, R-J. (2020). Simulation of a Station Blackout Accident for the SMART Using the CINEMA Code. *Front. Energ. Res.* 8. doi:10.3389/fenrg.2020.503918

Lin, S., Wang, S., Niu, F., and Jiang, X. (2021). Experimental Study of Heat Transfer with a Jet Flow in the Complex Space of Small Steel Containment. *Ann. Nucl. Energ.* 154, 108124. doi:10.1016/j.anucene.2020.108124

Liu, X., Meng, Z., Zhang, N., and Sun, Z. (2020). Scaling Design of the Pressure Response Experimental Facility for Pressure Suppression Containment. *Front. Energ. Res.* 8. doi:10.3389/fenrg.2020.524445

Niu, F., Zhuo, W., Cai, J., Su, X., Hu, Y., Zhao, Y., et al. (2016). The Studies of Mixing and thermal Stratification in SMR Containments. *Nucl. Eng. Des.* 298, 14–24. doi:10.1016/j.nucengdes.2015.11.018

Papini, D., Grgić, D., Cammi, A., and Ricotti, M. E. (2011). Analysis of Different Containment Models for IRIS Small Break LOCA, Using Gothic and RELAP5 Codes. *Nucl. Eng. Des.* 241 (4), 1152–1164. doi:10.1016/j.nucengdes.2010.06.016

Wang, S., Wang, Y., Zhuo, W., Niu, F., Yu, Y., Guo, Z., et al. (2017). Experimental Analysis of Steam Mixing and thermal Stratification Phenomena Related to Small Steel Containment Studies. *Ann. Nucl. Energ.* 109, 103–112. doi:10.1016/j.anucene.2017.05.021

Zhang, H., Niu, F., Yu, Y., Zhang, S., Wang, H., and Gang, Z. (2015). Modeling and Experimental Studies on Mixing and Stratification during Natural Convection in Containments. *Ann. Nucl. Energ.* 85, 317–325. doi:10.1016/j.anucene.2015.06.001

Conflict of Interest: Author SL was employed by the company China Nuclear Power Engineering Co., Ltd.

The remaining authors declare that the research was conducted in the absence of any commercial or financial relationships that could be construed as a potential conflict of interest.

frontiers | Frontiers in Energy Research

ORIGINAL RESEARCH
published: 14 April 2022
doi: 10.3389/fenrg.2022.864950

A Conservative Approach for the Fast Deflagration Analysis in the Containment With GASFLOW-MPI

Li Yabing, Lu Xianghui, Chen Peng and Xu Deyang*

China Nuclear Power Technology Research Institute, Shenzhen, China

The nuclear regulation authorities of many countries require that the containment remains its integrity for a local hydrogen risk during any possible accident conditions. Therefore, the combustion consequence should be analyzed to demonstrate that the containment integrity is not being challenged for the hydrogen risk when the flame acceleration risk cannot be safely ruled out. Considering the uncertainties of both the combustion model and severe accident analysis, the criteria and experimentally based combustion (CREBCOM) model is adopted to provide a conservative result for pressure and the thermal load for combustion analyses in this study. Firstly, the CREBCOM is developed in the GASFLOW-MPI code and validated with the RUT experiment. The result shows that the CREBCOM model can provide a reliable overpressure for the choking regime combustion. Then, this model is adopted for the hydrogen safety analysis for the Advanced Pressurized Water Reactor (PWR) 1000. The hydrogen distribution is calculated with the mass and energy release obtained from severe accident analysis, from which, the most unfavorable ignition time and location is selected. The result of the CREBCOM model is compared with that of the turbulent flame closure model, which is a commonly used model for combustion analysis in containment safety. The results show that the CREBCOM model can provide a conservative prediction for the pressure and thermal load of combustion. Therefore, the CREBCOM model with the sonic flame assumption is applicable for the FA risk analysis in a local compartment for nuclear containments where a sonic deflagration cannot be safely excluded and manages to obtain a conservative pressure and thermal load for further evaluation on the containment integrity.

Keywords: local hydrogen risk, fast deflagration, CREBCOM model, containment safety analysis, CFD

OPEN ACCESS

Edited by:
Yapei Zhang,
Xi'an Jiaotong University, China

Reviewed by:
Jianjun Xiao,
Karlsruhe Institute of Technology (KIT), Germany
Hans Pasman,
Texas A&M University, United States

****Correspondence:***
Li Yabing
liyabing2@cgnpc.com

Specialty section:
This article was submitted to Nuclear Energy, a section of the journal Frontiers in Energy Research

Received: *29 January 2022*
Accepted: *22 February 2022*
Published: *14 April 2022*

Citation:
Yabing L, Xianghui L, Peng C and Deyang X (2022) A Conservative Approach for the Fast Deflagration Analysis in the Containment With GASFLOW-MPI. Front. Energy Res. 10:864950. doi: 10.3389/fenrg.2022.864950

INTRODUCTION

Hydrogen can be released and accumulate in some local compartments of the containment, leading to local hydrogen risk due to its geometric complexity. The nuclear regulation authorities of many countries require that the containment integrity should not be challenged by local hydrogen risk during any possible accident conditions (NEA, 2014). The main objective of this analysis consists of two parts: the combustion (pressure and thermal) loads from combustion do not challenge the

Abbreviations: ACC, accumulator; CREBCOM, criteria and experimentally based combustion; DES, detached eddy simulation; PAR, passive automatic recombination; TFC, turbulent flame closure; AICC, adiabatic isochoric complete combustion; DDT, deflagration–detonation–transient; FA, flame acceleration; PZR, pressurizer; SG, steam generator.

containment integrity, and the combustion load does not damage the capability for severe accident analysis (NRC, 2020). In order to meet this regulation, it must be demonstrated that deflagration–detonation–transient (DDT) or flame acceleration (FA) can be safety excluded for any accident sequence or, if not, will not challenge the containment integrity. A commonly adopted method for this issue is 3D CFD analysis including hydrogen release, dispersion, and combustion, by either modeling the whole containment (Dimmelmeier et al., 2012; Kang et al., 2020; Wang and Cao, 2017) or isolating the target compartment (Zhao et al., 2022; Qiang and Yaodong, 2012; Zhang et al., 2018).

A proper FA analysis should include the process of flame acceleration to determine if the combustion reaches the choking regime with isobaric sound speed flame and, if so, calculate the overpressure to impact the influence on the containment integrity. This requires that a calculation covers the combustion region, transiting from the subsonic flame regime to choking regime (Breitung et al., 2000). Lots of efforts are conducted to simulate this whole process, requiring a rather refined mesh and detailed combustion and turbulence models (Goulier et al., 2017; Sathiah et al., 2012; Halouane and Dehbi, 2017) and mainly aiming at experimental facilities with small scales. The combustion models including turbulent flame closure (TFC) models with different flame speed correlations, the eddy breakup model (Yuen et al., 2022), and eddy dispassion model are commonly adopted in the combustion analysis related to nuclear safety (Sathiah et al., 2012; IAEA/CSNI, 2011) The validity of theoretical models depends greatly on the Borghi diagram regime and corresponding flame front structure (Breitung et al., 2000). However, the flame speed, developing from a subsonic to isobaric sound speed, covers different regimes on the Borghi diagram, depending on the gas mixture compositions and boundary conditions like obstacle structures, indicating that it would be difficult to simulate the whole process with a certain combustion model. The capabilities of the combustion model for flame acceleration/deceleration have to be enhanced to a level providing reliable forecast (Zhao, 2017).

Another problem for FA analysis in nuclear safety is its complexity in both spatial and temporal. The obstacles in containment have length scales in a wide range; hence, the obstacles would be simplified in the geometry model for numerical simulations. The complex geometry of the compartment makes it difficult to estimate the block ratio in this area; hence it is quite impractical to estimate the flame acceleration rate for a given set of conditions (Breitung et al., 2000). Moreover, the complexity of the severe accident phenomena, including the accident process, location, and rate of the hydrogen release (Bentaib et al., 2015), also make it impossible to conduct a large number of scenario analyses and build the accident spectrum like what is done in the possibility safety analysis. This means that assessments and evaluations are conducted based on a few analyses for engineering applications, while the questions regarding its reliability and uncertainty are always raised by the nuclear regulation authorities in this situation.

However, it is the thermal and pressure load that really matters for the hydrogen safety analysis for a containment rather than the detailed process of the deflagration (Sathiah et al., 2012). The detailed behavior of the flame accelerating to the choking regime, which cannot be well predicted with many combustion models (IAEA/CSNI, 2011), is less relevant for the hydrogen safety analysis of the containment. More importantly, the choking regime combustion can cause high overpressure that can damage the containment structures. For instance, research presents an analysis on the pressure load of the fast deflagration of hydrogen, indicating that the pressure load of fast hydrogen deflagration can also lead to the structural failure (Yabez et al., 2015). Since a sonic speed flame cannot be safely excluded, the combustion can be assumed as the choking regime obtains a conservative combustion load for the FA risk analysis, thus evaluating the impact of FA on the containment integrity. This is the main idea of the criteria and experimentally based combustion (CREBCOM) model (Efimenko and Dorofeev, 2001).

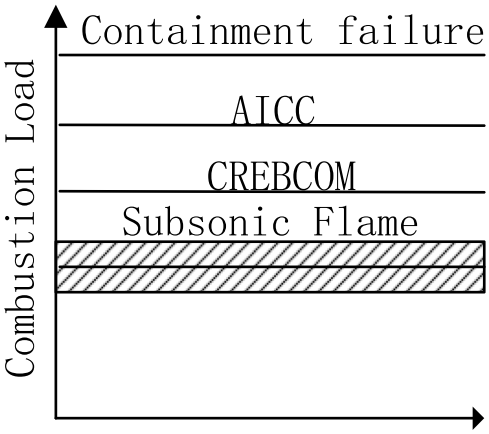

FIGURE 1 | Diagram of safety margins for different combustion analysis methods.

In this study, the CREBCOM model is introduced for hydrogen safety analysis to predict the conservative estimation of loads from hydrogen combustion. The major assumption of this model is to assume the flame speed as the sonic speed for the FA risk situation, neglecting the flame acceleration, thereby obtaining a conservative combustion load. By doing so, the uncertainties of the combustion analysis can be enveloped by conservative loads, thereby reducing the impact of the uncertainties for the combustion assessment of engineering applications, as illustrated in **Figure 1**.

This paper is constructed as follows: the CREBCOM model is introduced and validated at Chapter 2; the geometry and physical model and the initial and boundary of the combustion calculation are introduced in Chapter 3; three combustion cases are analyzed and discussed in Chapter 4; and the main conclusions are summarized in Chapter 5.

METHODOLOGY

The GASFLOW-MPI is a well validated and widely used parallel 3-Dimensional Computational Fluid Dynamics (3D CFD) code for the containment safety analysis (Xiao et al., 2016a). It solves the

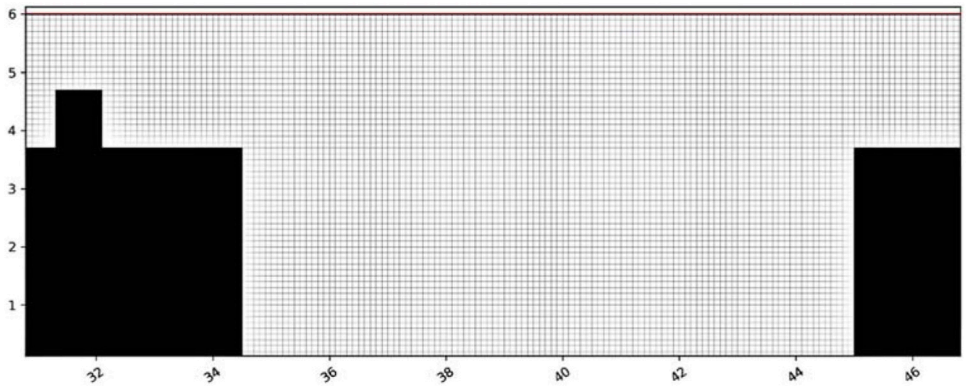

FIGURE 2 | Geometry model and mesh of the RUT facility.

compressible Navier–Stokes equations for three-dimensional volumes in Cartesian or cylindrical coordinates. The relevant phenomena including the release, transportation, and deflagration of the hydrogen are validated in plenty of international projects, for instance, the Thermal Hydraulics, Aerosols and Iodine facility (THAI) (HM-1 and 2) (Royl et al., 2006), MISTRA (ISP47) (NEA, 2007), and THAI HD-23 (Xiao et al., 2017a).

The transport equation for the combustion model of GASFLOW-MPI is given in **Eq. 1**. Two combustion models discussed in this study, i.e., the CREBCOM model and TFC, are with the same formation of the transport equation but different in the source term of the equation, as listed below. The latter one is originated by Zimont in late 1990 (Zimont et al., 1998) and is a widely adopted combustion model in nuclear safety analysis (Sathiah et al., 2012; IAEA/CSNI, 2011). It solves the transport equations of the progress variable, which is suitable for premixed combustion simulation at $\mathrm{Re} \gg 1$, $Da \gg 1$ 1, and $u^{'} \gg S_t$, as given in **Eqs 1**, **2**. The detailed information TFC model of GASFLOW-MPI is presented in Xiao et al. 2016a; Xiao et al., 2017a; Xiao et al., 2017b), and has been well validated with experiment facilities such as THAI facility, hence is not elaborated in this study. Only the CREBCOM model is introduced and validated in the following section:

$$\frac{d}{dt}\int \rho\xi dV = \oint\left[-\rho\vec{u}\xi + \left(\frac{\mu}{Sc} + \frac{\mu_t}{Sc_t}\right)\nabla\xi\right]dS + \int \rho_{un}|\nabla\xi|S_t dV \tag{1}$$

$$TFC\ \text{model}:\ S_t = 0.52\,u' Da^{0.25} \tag{2}$$

where ξ is the process variable of combustion, $\xi = 0$, indicating an unburnt gas mixture, $\xi = 1$, indicating a burnt gas mixture; ρ, μ, $\vec{u}$, and Sc is the density, viscosity and Schmidt number for gas mixtures, respectively. The subscript t indicates the turbulence value, and the subscript un indicates the unburnt value. S_t is the turbulent flame speed. Da is the Damköhler number. u' is the fluctuation velocity.

CREBCOM Model

The main objective of the CREBCOM model is to give a conservative estimation of the loads from hydrogen combustion by adopting a conservative flame speed for different combustion regimes (Efimenko and Dorofeev, 2001). It should be pointed out that this model aims to provide conservative pressure and thermal load rather than reproduce the real physical phenomena. The development of the flame is neglected; instead, a specific combustion model is selected for each combustion regime based on different criteria, as listed in **Table 1**. As for the combustion analysis in the containment, the DDT risk is excluded during the containment design, and the analysis of the slow deflagration can usually be bounded by the adiabatic isochoric complete combustion analysis (NEA, 2014). Hence, this study focuses on the fast deflagration in local compartments. In this situation, the CREBCOM model is implemented in the GASFLOW-MPI as follows: determining the combustion regimes with σ criteria firstly, then applying sonic speed for the flame to calculate the combustion rate for the case that exceeds the σ criteria, as given in **Table 1**. The model is conservative because the flame does not necessarily reach the sonic speed, even for the case that exceeds the σ criteria, and the flame acceleration process is neglected.

TABLE 1 | Structure of CREBCOM model.

Combustion regime	Criteria	Combustion model
Slow deflagration	Flammability	$S_t = f(S_L)$ [18]
Fast deflagration	σ criteria	$S_t = S_{sonic}$
Detonation	λ criteria	Kinetic models

Here, the S_{sonic} refers to the local sonic speed behind the burning front, which depends on the mixture quality and gas temperature. The flame speed in the choking regime is the isobaric sonic speed ranging from 600 to 800 m/s based on the experimental data in Breitung et al. (2000).

Validation of CREBCOM Model

The RUT facility is a large-scale test facility for hydrogen deflagration and detonation at Kurchatov Institute, Russia (Efimenko and Dorofeev, 2001). The RUT test sth6 is used to validate the CREBCOM model. The initial gas mixture is 29.6% H_2 in dry air plus 45 vol% H_2O (Efimenko and Dorofeev, 2001)

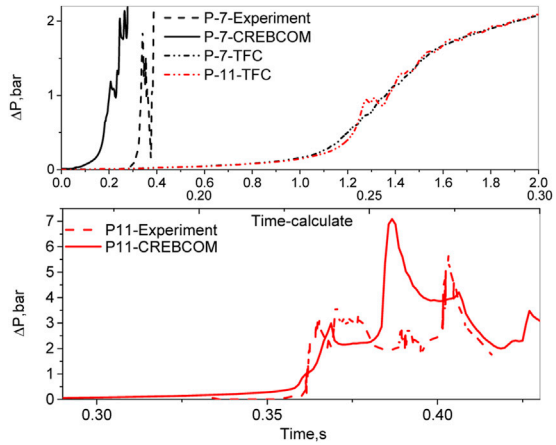

FIGURE 3 | Pressure of P7 and P11 of RUT test sth6—Experiment vs. CREBCOM and TFC model (Efimenko and Dorofeev, 2001; Studer et al., 2013).

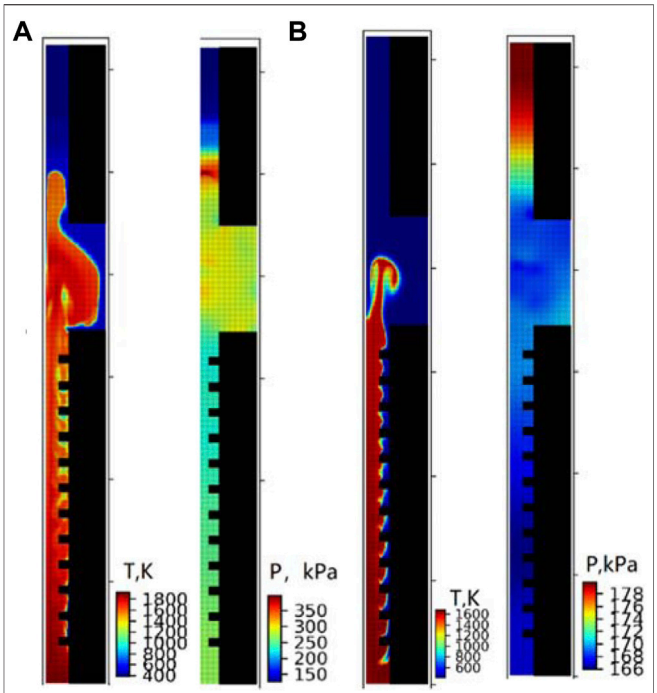

FIGURE 4 | X-Z view of temperature and pressure of RUT calculation. **(A)** S_t = 770*m*/*s*-0.23. **(B)** TFCmodel-1.25s.

with initial temperature at 363 K and pressure at 1 bar. The experiment facility consists of three parts: a channel of 2.5 m × 2.3 m cross-section and 34.6 m long; a canyon 2.5 m × 6 m cross-section and 10.5 m long; a channel of 2.5 m × 2.3 m cross-section and 20 m long. The computational region is meshed uniformly with mesh size equal to 0.1 m (Efimenko and Dorofeev, 2001), with a total mesh number of 1,015,560 as shown in **Figure 2**. The detached eddy simulation (DES) model is adopted for the turbulence model. The heat transfer model is neglected in the simulation because of the short simulation time. The CREBCOM model is adopted with the flame speed 770 m/s as measured in the experiment, which is the choking regime according to Breitung et al. (2000), and another calculation is conducted with the TFC model as a comparison.

In the experiment, the flame accelerates to the choking regime, leading to the first pressure peak (**Figure 3**), which is reproduced by the CREBCOM model. The X-Z view of temperature and pressure are given in **Figure 4**. The results show that the CREBCOM simulation has the similar trend compared with the experiment data (Efimenko and Dorofeev, 2001; Studer et al., 2013), while the TFC simulation underestimates the pressure load of the combustion. This is because the adequate combustion regime of the TFC model is within the Damköhler's limit; however, the Damköhler number is lower than the unit for the choking regime according to the Borghi diagram [9–11]. As a result, the TFC model is insufficient for the combustion analysis for the containment where the FA risk cannot be excluded. Therefore, the CREBCOM model manages to have a reasonable prediction on the overpressure for choking regime combustion and is thereby adequate for the FA analysis of containment.

MODELING

Geometry Model and Mesh

The containment of Advanced Pressurized Water Reactor (PWR) 1000 has an inner radius of 22.5 m and height of 66.4 m. The geometry model is built in cylindrical coordination, with the computational region ranging from −7 m ~ 9.9 5 m at axial direction and 0–23 m in radial direction. The computational region is divided into 26 grids in the radius direction, 72 grids in the peripheral direction, and 70 grids in the axial direction for the hydrogen distribution analysis, and the mesh is refined twice in both the radius and axial direction for the combustion analysis, with a total mesh number of 524,160. A mesh sensitivity is conducted with grids divided by 26 × 72 × 70, 26 × 72 × 140, and 52 × 72 × 140; the results show a similar tendency for these three cases, indicating the grid independence.

The containment has a rather complex inner geometry; hence, it is unrealistic to model all the details inside the containment and a certain simplification must be made. The major structures of the compartments and major manufactures of the primary loop are included in the geometry model, while the small parts below the grid resolution are neglected. Moreover, the geometry is modified, adapting to the orthogonal grid adopted in GASFLOW-MPI. The model includes floors, ceilings, and walls for major compartments [steam generator (SG) compartments, pump compartments, cavity, pressurizer (PZR) compartment, and accumulator (ACC) compartment] shown in **Figures 5**, **6**. The neglected steel parts are modeled as distributed heat sink, which is simplified as a one-side heat transfer surface with the same mass and area as the real geometry. Both conductive and convection heat transfer are calculated for the distributed heat sink.

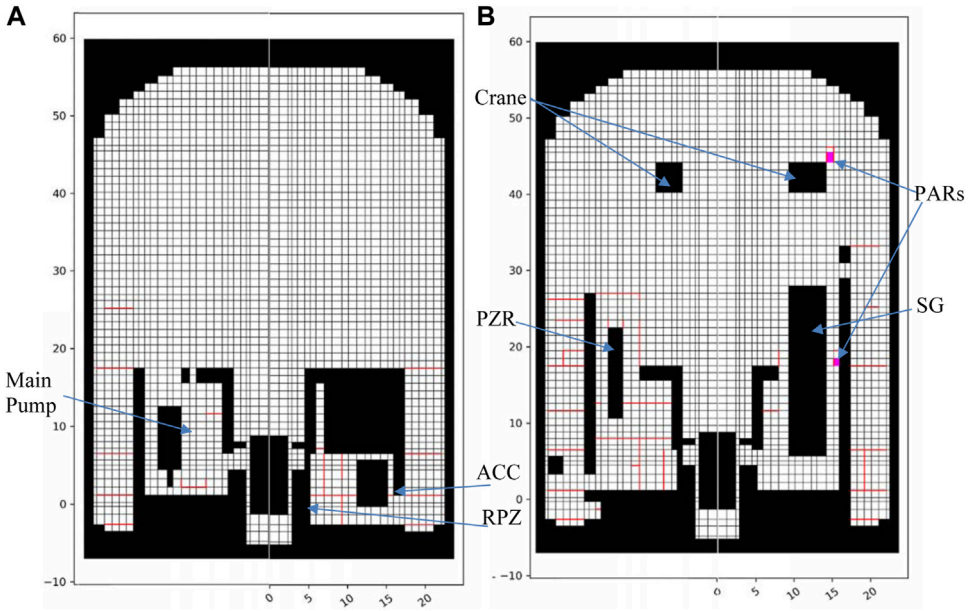

FIGURE 5 | R-Z view of the containment geometry model-case0. **(A)** 0° and 180°. **(B)** SG and PZR compartment.

TABLE 2 | Summary of physical model and initial and boundary conditions.

Models	Mesh	Turbulence model	Heat transfer model	PAR model	Combustion model	Initial condition	Boundary condition
Case 0	26 × 72 × 70	DES model	Convection: Reynold analogy Condensation: Chilton–Chilburn analogy radiation heat transfer	Siemens model	--	1 bar, 318 K	Lumped parameter code calculation
Case 1	52 × 72 × 140			--	TFC model	Flow field from case 0	Ignition in the sigma cloud
Case 2					S_{turb} = 800 m/s		
Case 3					S_{turb} = 600 m/s		

The passive automatic recombination (PAR) is equated in the containment of Advanced PWR 1000 to mitigate the hydrogen risk during severe accidents. The PAR is modeled as a rectangle chimney with suction at the bottom and a vent at the upper part of the side wall, as shown in **Figure 5B**. The recombination rate of the PAR is calculated with the empirical correlation of the Siemens model (Xiao et al., 2016a). Please note that the PAR recombination is neglected during the combustion because the hydrogen-consuming rate for the combustion is far greater than that of the PAR.

Initial and Boundary Condition

For the hydrogen risk analysis for the containment, the mass and energy release are obtained from the lumped parameter code, as well as the initial condition of the containment. **Table 2** summarizes the physical model adopted in the analysis. The DES model is adopted in this analysis, whose detailed information and validation are included in Zhang et al. (2018). For the geometry structures, convective, condensation, and radiant heat transfer are included. Three combustion cases are analyzed: two cases with the CREBCOM model with different flame speeds and one case with the TFC model as a comparison. The flame speed refers to the range of the isobaric sonic speed based on experimental data.

Initial Condition for Combustion Analysis

The hydrogen distribution is calculated with the mass and energy release from a postulated accident with a break at the top of the pressurizer. The hydrogen is released at the top of the pressurizer and is blocked by the compartment ceiling, leading to local hydrogen accumulation below the ceiling. The hydrogen distribution is calculated with GASFLOW-MPI, and the hydrogen risk of FA and DDT are evaluated with the σ criterion (Xiao et al., 2016a) and the λ criterion, respectively. Based on this, the ignition timing and location are selected.

FA and DDT Risk Analysis

Firstly, the DDT risk is analyzed with the λ criterion criteria (Dorofeev et al., 2000). The λ criterion is defined as the ratio of the characteristic size of the flammable gases L and 7 times the detonation cell size λ as given below, with detailed information found in Dorofeev et al. (2000)' and Xiao et al. (2016b).

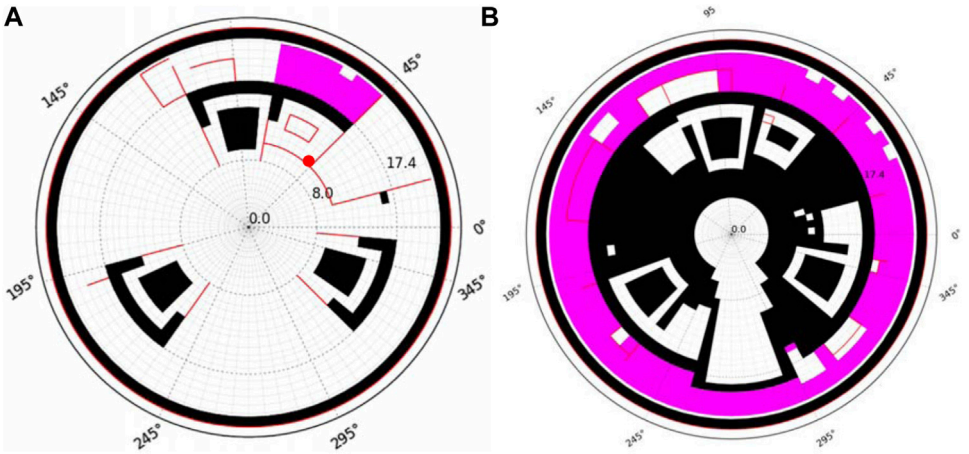

FIGURE 6 | Cross-section view of the containment geometry model-case0. **(A)** Cross-section at the height of the injection (red point: igniting point). **(B)** Cross-section at the 17.5 m.

$$\lambda \text{ criterion} = L/7\lambda \quad (3)$$

The DDT can occur only if the λ criterion is higher than a unit. The DDT risk analysis shows that the λ criterion for a gas cloud with a hydrogen concentration higher than 4 vol% in the containment is far lower than the unit (as shown in **Figure 7**), indicating that the DDT is unlikely to occur. The DDT risk could be safely excluded during the whole accident process, complying with the requirement of safety regulations.

Then, the σ criterion is adopted to evaluate the risk of FA. Once the FA risk cannot be excluded, the combustion analysis should be conducted. The ignition time and location should be selected to have the most punishing result for the combustion. A certain amount of σ cloud (gas cloud over the σ criterion) exists near the hydrogen injection as shown in **Figure 8B**, although it will soon be diminished by the following steam injection. Since the risk of FA cannot be safely excluded during the accident based on the analysis of the σ criterion, it must be demonstrated that the containment integrity will not be challenged after a postulated ignition even at an unfavorable time or location in the containment.

Selection of Ignition Timing and Location

The selection of the ignition time aims at resulting in a more penalizing pressure load in the containment; therefore, the ignition time is selected at the maximum inventory of the σ cloud (gas cloud with $\sigma > 1$), which is 10,000 s after the accident initiated, as shown in **Figure 9**. **Table 3** summarizes the atmosphere conditions of the PZR compartment as well as global containment, and the distributions of the hydrogen, σ criterion, and turbulent kinetic energy are presented in **Figures 8A–C**, respectively. The σ cloud mainly accumulates under the ceiling of the PZR compartment with a total volume of 115 m^3. The ignition location is selected to yield a long run-up distance for the flame propagation, which is the diagonal under the diagonal point of the ceiling, as shown in **Figure 6A**.

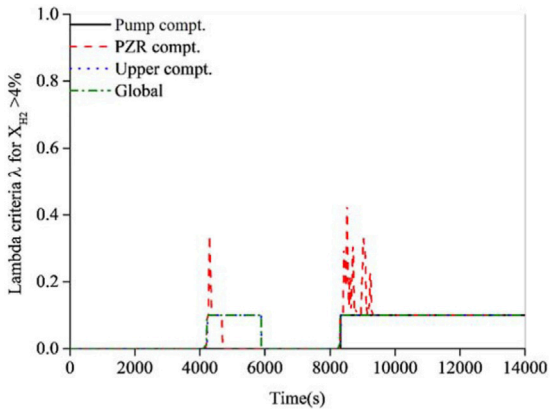

FIGURE 7 | The λ criteria for hydrogen cloud (X_{H2}>4 vol%) in major compartments.

COMBUSTION ANALYSIS

In this section, the three cases with detailed information listed in **Table 2** are analyzed and discussed for the fast deflagration analysis.

Global Combustion Characteristics

The three combustion cases are analyzed with the initial and boundary conditions listed in **Table 2**. The global hydrogen consumption rate is shown in **Figure 10**. The peak combustion rate for the CREBCOM model is 4.3 and 6.7 times higher than that of the TFC model. The distribution of temperature at different time points is presented in **Figure 11** to demonstrate the propagation of the flame for the three cases. By the time of ignition, the average mole fraction of the containment is 6.30%, indicating a global flammable gas mixture; hence, the combustion spreads to the global containment after being ignited in the

TABLE 3 | Atmosphere conditions at ignition times.

Parameters	Pressure (Pa)	Tave (K)	$\varphi_{H2O\text{-}ave}$ (vol %)	$\varphi_{H2\text{-}ave}$ (vol %)	M_{H2} (kg)	σ Cloud volume (m^3)	M_{H2} in σ cloud (kg)	4 vol% cloud volume (m^3)	M_{H2} in 4 vol% cloud (kg)
Global	1.96E+05	384	38	6.30	580	314	5.18	67,454	573
PZR Comp		422	40	8.34	5	115	2.14	538	4.86

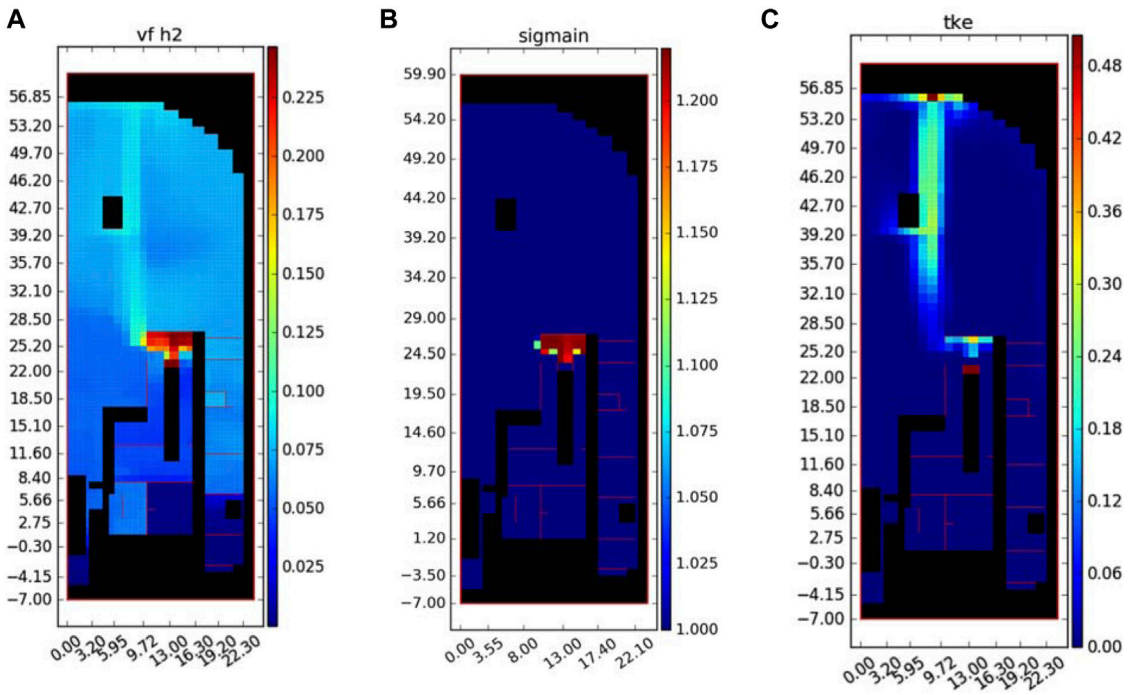

FIGURE 8 | Initial flow field for the combustion analysis. **(A)** Hydrogen concentration. **(B)** σ Criterion. **(C)** Turbulent kinetic energy.

PZR compartment. For case 1, the combustion of the gas mixture with a high hydrogen concentration in the PZR compartment creates a horizontal flame at the junction of the PZR compartment.

Meanwhile, the flame propagates along the hydrogen plume near the junction, forming a vertical flame; both a horizontal and a vertical flame are observed at the outlet of the PZR, as shown in **Figure 11A**. The flame mainly propagates horizontally and upwards, not downwards. In this calculation, the flame only propagates downwards after the rest of the gas mixture above is already being ignited. The situation is quite different for the CREBCOM model. The source term of the combustion transportation equation is given as a constant rather than the calculated flame speed; the calculated flame propagates nearly isotropically, upwards and downwards at the same time, as shown in **Figures 11B,C**. This is physically unrealistic because the flammable limitation to propagate downwards is about 8% (KUMAR et al., 1983) while the hydrogen concentration below the elevation of the injection is about 6%. The flame of case 3 propagates with a similar behavior but with a lower rate compared with case 2. The result of three combustion analyses is summarized in **Table 4**.

The pressure and thermal load

The analysis for both pressure and thermal load is restricted to the sigma cloud where the FA can occur. The transient results with the maximum overpressure for the three cases are given in **Figure 12**. The result shows that the sonic flame speed leads to higher overpressure in the sigma cloud. The peak values for the three cases are 0.098, 0.930, and 0.839 bar, respectively. Note that the peak pressure for case 3 is nearly 2.45 times higher than that of case 2, although the global overpressure of these two cases is similar. This means that the overpressure can reach about 0.930 bar if the flame accelerates toward sonic speed in the sigma cloud. The transient pressure loading can be used to evaluate the response of the containment structures to assess its impact on the integrity of the containment.

Figure 13 shows the maximum surface temperature on the containment structures for each time. The peak values for the two

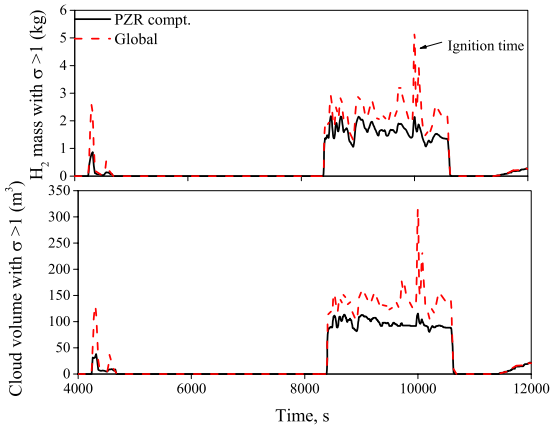

FIGURE 9 | Volume and hydrogen inventory of σ cloud.

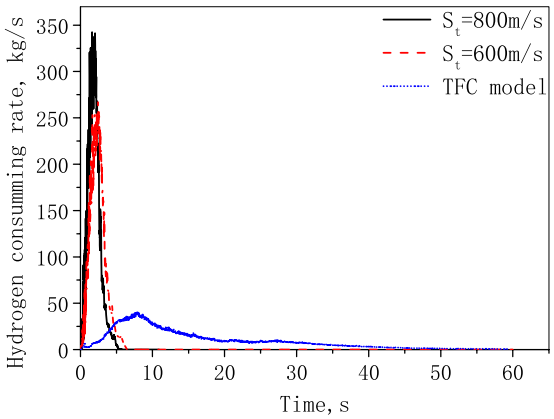

FIGURE 10 | Hydrogen consumption rate.

CREBCOM cases are 8 and 15 K higher than that of the TFC model, respectively. The peak temperature is not necessarily proportional to the flame speed, comparing the two CREBCOM cases. This may be caused by the thermal inertia of the structures. The combustion duration of the case of S_{turb} = 600 m/s, allows the structure heated by the flame for a longer time, leading to a higher peak temperature, compared to the case of S_{turb} = 800 m/s. This temperature can be used to evaluate the survivability of the containment equipment and structures.

DISCUSSION

The results show that the CREBCOM model with isobaric sound flame speed can provide both conservative pressure and thermal load for the combustion consequence analysis compared to the TFC model. While it is not necessary to imply that the model is universally applicable for combustion analysis in the containment, based on the main assumption, the sonic speed assumption should only be applied for the situation where a sonic deflagration cannot be safely excluded. This indicates two restrictions: the first one is FA risk, which is measured with the sigma criterion. The second one is that

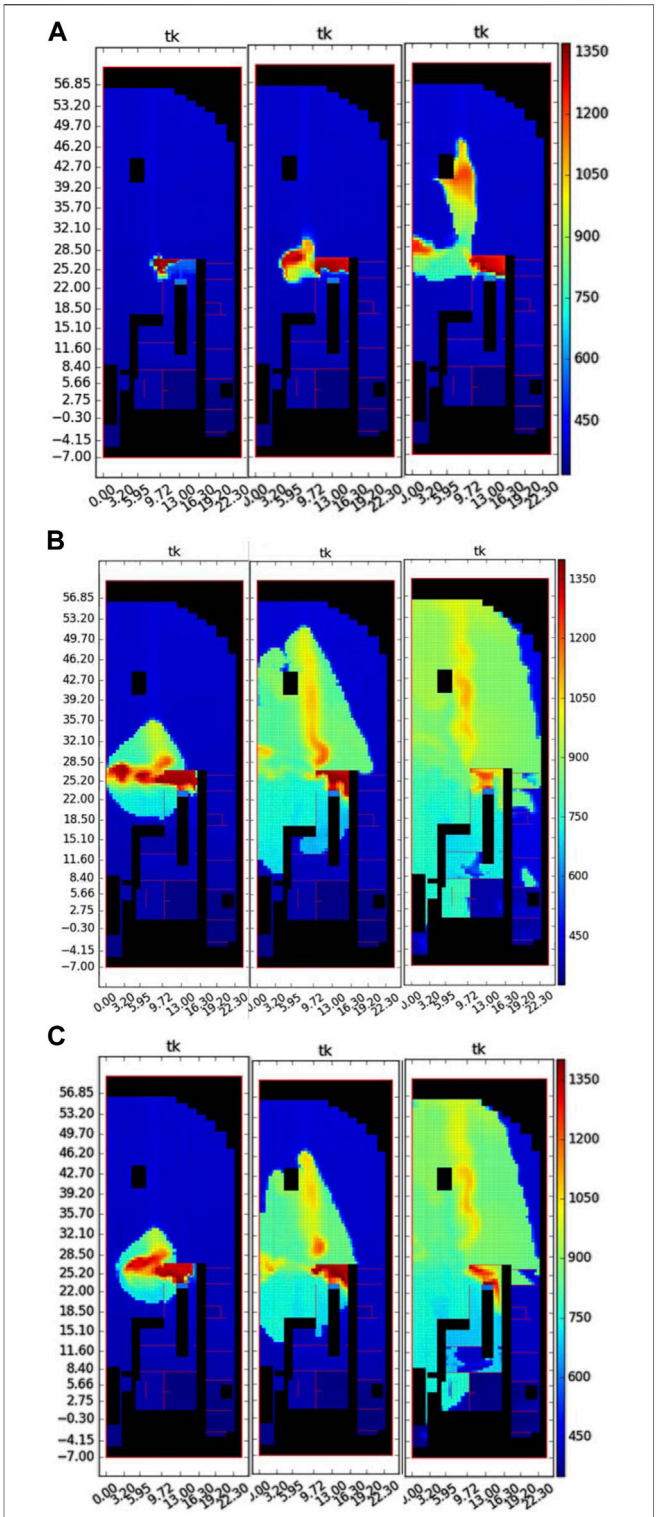

FIGURE 11 | R-Z view of the temperature at the PZR compartment slide (0.5 s – 1 s–2 s after ignition). **(A)** TFC model. **(B)** S_{turb} = 800m/s. **(C)** S_{turb} = 600m/s.

TABLE 4 | Summary of global combustion characteristics.

case number	P_{AICC},bar	Peak P_{gas}, bar	T_{AICC},K	T_{Max},K		Combustion duration, s	Peak $\dot{M}_{H2}$, kg/s	M_{H2} burnt	Max ΔP, bar	Max T_{flame}, K
				Gas	Surface					
Case 1	5.56	3.66	1,102	716	643	55	40.1	555	0.098	1,431
Case 2		4.16		807	651	5.3	175	580	0.930	1,505
Case 3		4.15		811	658	7.1	269	580	0.839	1,471

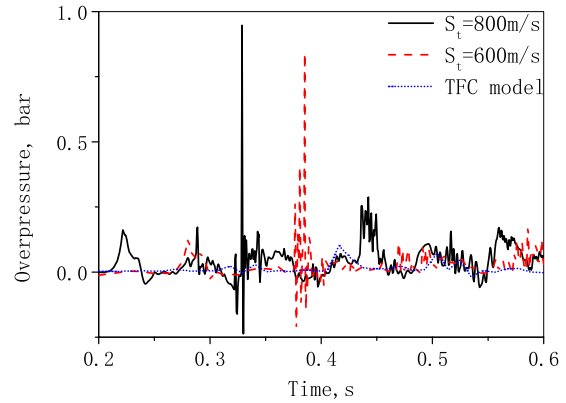

FIGURE 12 | Pressure difference between the two sides of the PZR compt. ceiling.

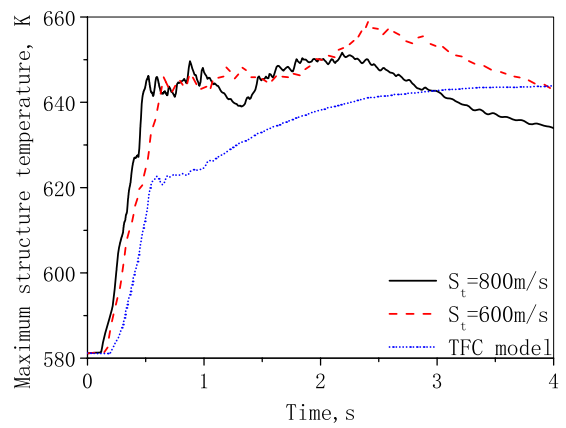

FIGURE 13 | Maximum temperature on the containment structure surface.

the flame can be accelerated toward sonic speed, which is difficult to be analyzed quantitatively. The flame needs a certain length in order to accelerate toward sonic speed; however, there is no criterion associated with the geometry scaling that can determine the FA rate. Based on current knowledge (Breitung et al., 2000), conclusions can be drawn qualitatively that large overpressure is likely to occur at a confined space with obstacles, rather than with large free volume where the flame can be well propagated in the situation of the hydrogen safety analysis for large dry containment of PWRs. Because the gas mixture in the containment is with lean hydrogen and high concentration of steam, and the DDT risk is rule out during the containment design procedure under this situation. For the containment analysis, this means that it is likely to occur at a local compartment where hydrogen cannot be well dispersed rather than the large free volume beneath the containment dome. Therefore, the CREBCOM model is applicable for the FA risk analysis in the local compartment for nuclear containments and manages to obtain a conservative pressure and thermal load for further evaluation on the containment integrity.

CONCLUSION

In this study, the CREBCOM model is introduced, validated, and adopted to evaluate the combustion consequences for local compartments. The main works and conclusions are listed as follows:

1. The CREBCOM model is implemented in the GASFLOW-MPI and validated with the RUT test sth6. The result shows that the CREBCOM model can provide a reliable prediction for choking regime combustion.
2. The combustion analysis is conducted with two combustion models and three cases. Detailed combustion characteristics are compared and discussed. The results show that the CREBCOM model can provide both conservative pressure and thermal load for the containment.

Based on this study, the CREBCOM model with the sonic flame assumption is applicable for the FA risk analysis in the local compartment for nuclear containments where a sonic deflagration cannot be safely excluded and manages to obtain a conservative pressure and thermal load for further evaluation on the containment integrity.

DATA AVAILABILITY STATEMENT

The original contributions presented in the study are included in the article/Supplementary Material, further inquiries can be directed to the corresponding author.

AUTHOR CONTRIBUTIONS

LY: investigation, formal analysis, and writing–original and draft, review, and editing. LX: methodology, investigation, and writing–review and editing. CP: conceptualization, methodology and supervision. XD: boundary condition preparation.

REFERENCES

Bentaib, A., Meynet, N., and Bleyer, A. (2015). Overview on Hydrogen Risk Research and Development Activities: Methodology and Open Issues. *Nucl. Eng. Tech.* 47, 26–32. doi:10.1016/j.net.2014.12.001

Breitung, W., Chan, C., and Dorofeev, S. (2000). *State-of-the-Art Report on Flame Acceleration and Deflagration-To-Detonation Transition in Nuclear Safety*. OECD Nuclear Energy Agency. NEA/CSNI/R.

Dimmelmeier, H., Eyink, J., and Movahed, M.-A. (2012). Computational Validation of the EPR Combustible Gas Control System. *Nucl. Eng. Des.* 249, 118–124. doi:10.1016/j.nucengdes.2011.08.053

Dorofeev, S. B., Sidorov, V. P., Kuznetsov, M. S., Matsukov, I. D., and Alekseev, V. I. (2000). Effect of Scale on the Onset of Detonations. *Shock Waves* 10 (2), 137–149. doi:10.1007/s001930050187

Efimenko, A. A., and Dorofeev, S. B. (2001). CREBCOM Code System for Description of Gaseous Combustion. *J. Loss Prev. Process Industries* 14, 575–581. doi:10.1016/s0950-4230(01)00049-3

Goulier, J., Chaumeix, N., Halter, F., Meynet, N., and Bentaïb, A. (2017). Experimental Study of Laminar and Turbulent Flame Speed of a Spherical Flame in a Fan-Stirred Closed Vessel for Hydrogen Safety Application. *Nucl. Eng. Des.* 312, 214–227. doi:10.1016/j.nucengdes.2016.07.007

Halouane, Y., and Dehbi, A. (2017). CFD Simulations of Premixed Hydrogen Combustion Using the Eddy Dissipation and the Turbulent Flame Closure Models. *Int. J. Hydrogen Energ.* 42, 21990–22004. doi:10.1016/j.ijhydene.2017.07.075

IAEA/CSNI (2012). *ISP-49 on Hydrogen Combustion. Nuclear Energy Agency*. Nuclear Energy Agency Committee on the Safety of Nuclear Installations.

Kang, H. S., Kim, J., Hong, S. W., and Kim, S. B. (2020). Numerical Analysis for Hydrogen Flame Acceleration during a Severe Accident in the APR1400 Containment Using a Multi-Dimensional Hydrogen Analysis System. *Energies* 13, 6151. doi:10.3390/en13226151

Kumar, R. K., Tamm, H., and Harrison, W. C. (1983). Combustion of Hydrogen-Steam-Air Mixtures Near Lower Flammability Limits. *Combustion Sci. Tech.* 33, 167–178. doi:10.1080/00102208308923673

NEA (2007). *International Standard Problem ISP-47 on Containment Thermalhydraulics, Final Report*. Nuclear Energy Agency. NEA/CSNI/R, 10.

NEA (2014). *Status Report on Hydrogen Management and Related Computer Codes*. Nuclear Energy Agency, 8. NEA/CSNI/R.

Nrc, C. F. R. (2020). *CFR 50.44 Combustible Gas Control for Nuclear Power Plant*. Nuclear Regulatory Commission. CFR-2020-title10-vol1.

Qiang, G., and Yaodong, C. (2012). Hydrogen Concentration Distribution Simulation during Severe Accident in Pressurizer Relief Tank Compartment of NPP Containment. *At Energ. Sci Technol* 4, 32–36.

Royl, P., Lee, U. J., Travis, J. R., Breitung, W., and Karlsruhe, D. (2006). "Benchmarking of the 3D CFD Code GASFLOW II with Containment thermal Hydraulic Tests from HDR and Thai," in *CFD4NRS Conference*, München, September 5–7, 685–702.

Sathiah, P., Komen, E., and Roekaerts, D. (2012). The Role of CFD Combustion Modeling in Hydrogen Safety Management-Part I: Validation Based on Small Scale Experiments. *Nucl. Eng. Des.* 248, 93–107. doi:10.1016/j.nucengdes.2012.03.047

Studer, E., Beccantini, A., and Kudriakov, S. (2013). "Hydrogen Combus.Tion Modelling in Large Scale Geometries," in Proceedings of the 21st ICONE, Chengdu, China, July 29–August 2.

Wang, D., and Cao, X. (2017). Numerical Analysis of Different Break Direction Effect on Hydrogen Behavior in Containment during a Hypothetical LOCA. *Ann. Nucl. Energ.* 110, 856–864. doi:10.1016/j.anucene.2017.06.054

Xiao, J., Travis, J. R., and Jordan, T. (2016). *GASFLOW-MPI: A Scalable Computational Fluid Dynamics Code for Gases, Aerosols and Combustion Band 1*, 1. Karlsruhe: KIT Scientific Publishing.

Xiao, J., Breitung, W., Kuznetsov, M., and Zhang, H. (2017). "Numerical Investigations of Turbulent Slow Deflagration of Premixed H2-Air-H2o Mixture in Thai Test HD-22 Using CFD Code GASFLOW-MPI," in The 17th International Topical Meeting on Nuclear Reactor Thermal Hydraulics (NURETH-17), September 3–8, 2017. Xi'an: Qujiang Int'l Conference Center.

Xiao, J., Breitung, W., Kuznetsov, M., Zhang, H., Travis, J. R., Redlinger, R., et al. (2017). GASFLOW-MPI: A New 3-D Parallel All-SpeedCFD Code for Turbulent Dispersion and Combustion Simulations Part II: First Analysis of the Hydrogen Explosion in Fukushima Daiichi Unit 1. *Int. J. Hydrogen Energ.* 42, 8369–8381. doi:10.1016/j.ijhydene.2017.01.219

Xiao, J., Royl, P., and Travis, J. (2016). *GASFLOW-MPI : A Scalable Computational Fluid Dynamics Code for Gases, Aerosols and Combustion in Users' Manual (Revision 1.0)* (Karlsrhule: KIT Scientific Publishing), Vol. 2. doi:10.5445/KSP/1000050393

Yabez, J., Kuznetsov, M., and Souto-Iglesias, A. (2015). An Analysis of the Hydrogen Explosion in the Fukushima-Daiichi Accident. *Int. J. Hydrogen Energ.* 40, 8261–8280.

Yuen, A. C. Y., De Cachinho Cordeiro, I. M., Chen, T. B. Y., Chen, Q., Liu, H., and Yeoh, G. H. (2022). Multiphase CFD Modelling for Enclosure Fires-A Review on Past Studies and Future Perspectives. *Exp. Comput. Multiph. Flow* 4, 1–25. doi:10.1007/s42757-021-0116-4

Zhang, H., Li, Y., Xiao, J., and Jordan, T. (2018). Detached Eddy Simulation of Hydrogen Turbulent Dispersion in Nuclear Containment Compartment Using GASFLOW-MPI. *Int. J. Hydrogen Energ.* 43, 13659–13675. doi:10.1016/j.ijhydene.2018.05.077

Zhao, H., Luo, X., and Zhang, R. (2022). Analysis on Hydrogen Risk under LOCA in marine Nuclear Reactor. *Exp. Comput. Multiphase Flow* 4, 39. doi:10.1007/s42757-020-0077-2

Zhao, Y. (2017). *Investigation on the Mechanism of Flame Acceleration and Deflagration to Detonation Transition of Combustible Gases*. Doctor Thesis. Beijing Institute of Technology.

Zimont, V., Polifke, W., Bettelini, M., and Weisenstein, W. (1998). An Efficient Computational Model for Premixed Turbulent Combustion at High Reynolds Numbers Based on a Turbulent Flame Speed Closure. *J. Gas Turbines Power* 120, 526–532. doi:10.1115/1.2818178

Conflict of Interest: The remaining authors declare that the research was conducted in the absence of any commercial or financial relationships that could be construed as a potential conflict of interest.

The authors LY, LX, CP, XD employed by China Nuclear Power Technology Research Institute Co., Ltd.

frontiers | Frontiers in Energy Research

ORIGINAL RESEARCH
published: 25 April 2022
doi: 10.3389/fenrg.2022.872452

Development, Validation, and Application of the Turbulent Combustion Model for 3D CFD Code CYCAS

Li Yabing[1], *Chen Peng*[1]*, *Lin Chubin*[2] *and Chen Meilan*[1]

[1]China Nuclear Power Research Institute, Shenzhen Science and Technology Building, Shenzhen, China, [2]College of Physics and Optoelectronic Engineering, Shenzhen University, Shenzen, China

The CYCAS code is a 3D CFD code developed independently by the China Nuclear Power Research Institute, aiming at hydrogen safety analysis in containments. In order to equip the CYCAS code with the capability of combustion analysis, a combustion model is screened and developed, and validated with two cases from International Standard Problems. Then a combustion analysis is conducted with a containment to demonstrate the capability of CYCAS to evaluate the pressure and thermal load of combustion. Firstly, the mature and widely-used combustion model, i.e., the Burning Velocity Model (BVM) with Zimont correlation is developed for the CYCAS code in this study. Thereafter, the lamiar flame speed correlation for CYCAS is screened based on the containment atmospheric condition during the accidents. Then, two cases from the THAI facility are calculated to validate the model. The results show that the combustion model in CYCAS manages to have reasonable prediction on the slow deflagration for the gas mixture both with and without steam. Finally, a containment combustion analysis is conducted with the initial hydrogen distribution calculated from a postulated accident. The analysis shows that the CYCAS manages to calculate the pressure and thermal load of the combustion to evaluate the influence of the combustion on the containment integrity and equipment survivability.

Keywords: turbulent combustion, hydrogen risk, containment safety, slow deflagration, CFD

OPEN ACCESS

Edited by:
Yapei Zhang,
Xi'an Jiaotong University, China

Reviewed by:
Han Z,
Tsinghua University, China
Sanjeev Gupta,
Becker Technologies, Germany

****Correspondence:***
Chen Peng
chpeng@cgnpc.com.cn

Specialty section:
This article was submitted to Nuclear Energy, a section of the journal Frontiers in Energy Research

Received: *09 February 2022*
Accepted: *22 March 2022*
Published: *25 April 2022*

Citation:
Yabing L, Peng C, Chubin L and Meilan C (2022) Development, Validation, and Application of the Turbulent Combustion Model for 3D CFD Code CYCAS. Front. Energy Res. 10:872452. doi: 10.3389/fenrg.2022.872452

1 INTRODUCTION

Hydrogen is generated by coolant-cladding interaction during severe accident of nuclear reactors, then it is released to the containment through breaks or valves leading to the flammable gas mixture in containments that may challenge the containment integrity (NEA, 2014). Hence, the combustion analysis should be conducted to demonstrate that the containment integrity is maintained during sever accidents for the containment safety analysis (Dimmelmeier et al., 2012). In the early safety analysis, the combustion analysis of the containment was conducted by one-dimensional lumped parameter codes, whose limitations were gradually recognized with the deepening of the research. Combustion analysis in the containment with the CFD method was gradually applied to the safety analysis for different nuclear power plants (Dimmelmeier et al., 2012; Xiao et al., 2017; Kang et al., 2020; Zhao et al., 2022).

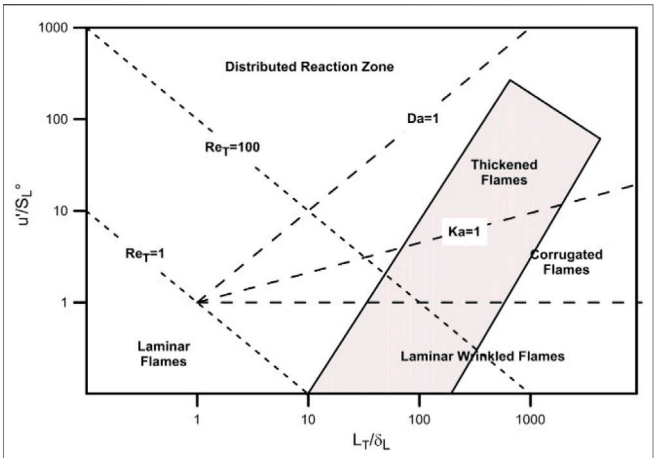

FIGURE 1 | Combustion regime for typical PWRs (light gray).

The CYCAS code is a three-dimensional (3D) CFD code developed independently by the China Nuclear Power Research Institute (Chen et al., 2016). The main objective of this code is to conduct analysis related to the hydrogen safety issues of the containment, namely, release, dispersion, and mitigation. While the combustion model is not included in the previous version of the CYCAS model, in order to equip the CYCAS code with the ability of combustion analysis, the combustion model is screened and developed for the CYCAS code in this study. The combustion model is screened based on the typical combustion regime and the typical atmospheric conditions in the containment during an accident. Goulier et al. (2016) has identified the combustion regime for the typical pressurized water reactor (PWR) as shown in **Figure 1**. The typical atmospheric condition in the containment during an accident includes the following characteristics:

(1) There is a large amount of steam due to the loss of coolant at high pressure and temperature;
(2) the gas mixture is heated and pressurized by several bars due to the previous reason; and
(3) lean hydrogen: the global hydrogen concentration in the containment should not exceed 10 vol% for large dry containment for PWRs according to the safety regulations.

Hydrogen combustion in the containment has drawn the attention of researchers and scholars in the world for decades, especially after the hydrogen explosion in the Fukushima accident in 2011. Experimental and numerical research has been conducted extensively focusing on different combustion regimes, namely, deflagration (NEA, 2011; Yuen et al., 2022), flame acceleration (Studer et al., 2013), and detonation (Kuznetsov et al., 2015), for the last decades. The research of International Standard Problem 49 (ISP-49) on the hydrogen combustion project has conducted validations for many codes and models for hydrogen combustion both openly and blindly and shows that the combustion models with the burning velocity model (BVM) demonstrate reasonable performance (NEA, 2011). Sathiah et al. (2012) developed a BVM with Zimont correlation and validated it using several experiments with the frame of commercial code Ansys Fluent and achieved reasonable predictions. Furthermore, the validation diagram for the BVM with Zimont correlation (Zimont, 2000a) can envelop the typical combustion regime shown in **Figure 1**. Therefore, the BVM with Zimont correlation, which is a mature and widely used combustion model, is adopted in CYCAS code for the safety analysis of containment.

Laminar flame speed is required in the basic formation of the Zimont correlation, which is calculated with the empirical correlations associated with atmospheric parameters, such as the stoichiometric ratio, steam concentration, temperature, and pressure. Many codes (NEA, 2011) for nuclear safety analysis use the Koroll correlation (Liu and Macfarlane, 1983) and Liu correlation (Koroll et al., 1993). However, the lower validation limits of the hydrogen concentration for these two correlation equations are 9 vol% (Liu and Macfarlane, 1983) and 18 vol% (Koroll et al., 1993), respectively. This means that these two correlation equations will have large uncertainties for the lean hydrogen combustion calculations in the range of hydrogen concentrations concerned with the containment safety analysis. In a more recent research, Szabó et al. (2012) presented a group of data from the INSFLA code which are validated for a stoichiometric ratio lower than 0.1252, equivalent to 4.96 vol% H_2 for dry air. In another study, Hu et al. (2009) conducted an empirical correlation for laminar flame speed at different formations through experimental studies. The lamiar speed correlation for CYCAS is screened based on the range of the containment atmosphere during accidents.

In this study, the BVM with Zimont correlation is developed for the CYCAS code and is validated with two experimental tests from the ISP report. Then a containment combustion analysis is conducted with the initial hydrogen distribution calculated from a postulated accident. Both pressure and thermal load of the combustion is calculated to evaluate the influence on the containment integrity and equipment survivability. This study is conducted as follows: **Section 2** introduces the CYCAS code briefly; **Section 3** gives the combustion model and its validation; in **Section 4**, the combustion analysis for a containment is presented such as the modeling and combustion calculation; and the main conclusions are drawn in **Section 5**.

2 CYCAS

2.1 Transport Equations

The CYCAS code solves transient 3D Navier–Stokes (N-S) equations. The conservation equations are listed below:

$$\text{Volume equation: } \frac{\partial V}{\partial t} = \nabla V \cdot \left(-\vec{u}\right), \tag{1}$$

$$\text{Mass equation: } \frac{\partial \rho}{\partial t} = \nabla \cdot \left[-\rho \vec{u}\right] + S_\rho, \tag{2}$$

TABLE 1 | Validation table for CYCAS.

Phenomenon	Validation tests
Turbulent mixing, buoyancy plume	OECD SETH Test 9 (**Figures 2A,B**), Test 9bis, ISP-23
Turbulent mixing, momentum plume	PANDA OECD/SETH Test 4, Test 4bis, Test 5, Test 7, Test 25, HyJet
Convective heat transfer, condensation, non-condensable gas	THAI Th-13
	COPAIN
Containment spray	TOSQAN 101
Turbulent mixing	PANDA HYMERES (**Figures 2C,D**)
PAR mitigation	H2PAR(**Figures 2E,F**), Tests E2bis, Test E19

$$\text{Momentum equation: } \frac{\partial\left(\rho\vec{u}\right)}{\partial t} = \nabla\cdot\left[-\rho\vec{u}\left(\vec{u}\right)\right] - \nabla p - \nabla\cdot\vec{\sigma} + \rho\vec{g} + S_m, \tag{3}$$

$$\text{Internal energy: } \frac{\partial(\rho I)}{\partial t} = \nabla\cdot\left[-\rho I\left(\vec{u}\right)\right] - p\nabla\cdot u - \nabla\cdot\vec{q} + S_I, \tag{4}$$

where $\vec{u}$ is the fluid velocity vector, V is the discretized fluid control volume, I is the internal energy, and p, $\vec{\sigma}$, and $\vec{g}$ are the fluid pressure, viscous stress tensor, and gravity acceleration, respectively. S_ρ, S_m, and S_I are the external source terms for each equation caused by phase change, chemical reaction, and so on.

The secondary order accuracy discrete scheme, i.e., van Leer MUSCL algorithm is adopted. The all-speed implicit method, i.e., Implicit Continuous Eulerian–Arbitrary Lagrangian Eulerian (Hirt et al., 1997), is adopted to solve the transport equations. The detailed information on the transport equations of CYCAS can be found in Chen et al. (2016).

2.2 Physical Models

2.2.1 Convective Heat Transfer Model

The convective heat transfer model in CYCAS is the Reynold analogy extended by Colburn for a wider application range of the *Pr* number, and the heat transfer coefficient of convection is given in **Eq. 5**:

$$h_w = \frac{\rho c_p u^*}{u^+}\mathrm{Pr}^{-\frac{2}{3}}, \tag{5}$$

where ρ is the fluid density; c_p is the specific heat of the fluid; u_* is the wall shear velocity $u_* = (\tau_s/\rho)^{1/2}$; τ_s is wall shear stress; u^+ is the dimensionless velocity, $u^+ = u_c/u_*$; and u_c is the cell-center fluid velocity. u^+ is calculated with a velocity profile of the boundary layer based on the boundary layer theory (Ghiaasiaan, 2011).

2.2.2 Passive Automatic Recombination Model

The Passive Automatic Recombination (PAR) is equated in the containment to mitigate the hydrogen risk during a severe accident. The calculation of the recombination rate and chemical heat is modeled in CYCAS with the empirical correlation of the Siemens model (Kotouc, 2011) (**Eq. 6**). Please note that the PAR is neglected during combustion because the hydrogen-consuming rate for the combustion is far greater than for the PAR.

$$\begin{aligned} &H_2 + O_2 \xrightarrow{catalyst} H_2O + Q_{\mathrm{Chem}}\dot{m}_{H2} \\ &= coeff\cdot conref\cdot\left(k_1P + k_2\right)\cdot\tanh\left(conref - 0.5\right)conref \\ &= \min\left(C_{H2}, 2C_{O2}, 8\%\right)coeff = \begin{cases} 1, C_{H2} < 1.2C_{O2} \\ 0.6, C_{H2} \geq 1.2C_{O2} \end{cases}, \end{aligned} \tag{6}$$

where $\dot{m}_{H2}$ is the hydrogen recombination rate; C_{H2} and C_{O2} are the mole fractions of hydrogen and oxygen, respectively; k_1 and k_2 are empirical constants related to the type of PAR.

2.3 Code Validation

The models for the phenomenon that are relevant to hydrogen safety in the containment are validated with both domestic and international projects, namely the turbulence, convection, and condensation model, as listed in **Table 1**. Two validation cases, the HyJet test on the BMC facility and the ISP-23 test on the HDR facility are presented in Chen et al. (2016). The other tests are included in the internal reports. **Figure 2** gives the geometry models and comparison between the experimental data of the three cases, i.e., OECD SETH Test 9, PANDA HYMERES, and H2PAR, the experimental details of which can be found in Auban et al. (2007), Mimouni et al. (2011), and Paladino et al. (2014), respectively.

3 COMBUSTION MODEL AND VALIDATION

3.1 Burning Velocity Model

The BVM describes the development of the flame with the combustion process variable ξ by solving the transportation equation for ξ, as shown in **Eq. 7**. The second-order accuracy scheme is adopted in the spatial domain, while the first order in the time domain. The combustion source term $\int \rho_{un} S_\xi dV$ is described as a function of the turbulence flame speed, as shown in **Eq. 8**. The Zimont model is selected for the turbulence flame speed model, as given in **Eq. 9** (Zimont and Lipatnikov, 1995; Zimont, 2000b). The turbulence flame speed S_t takes the higher value between the laminar flame speed S_l and the Zimont correlation, which means that the flame is laminar for low turbulence intensity.

$$\frac{d}{dt}\int\rho\xi dV = \oint\left[-\rho\vec{u}\xi + \left(\frac{\mu}{Sc} + \frac{\mu_t}{Sc_t}\right)\nabla\xi\right]dS + \int\rho_{un}S_\xi dV, \tag{7}$$

$$\int\rho_{un}S_\xi dV = \rho_{un}|\nabla\xi|S_t, \tag{8}$$

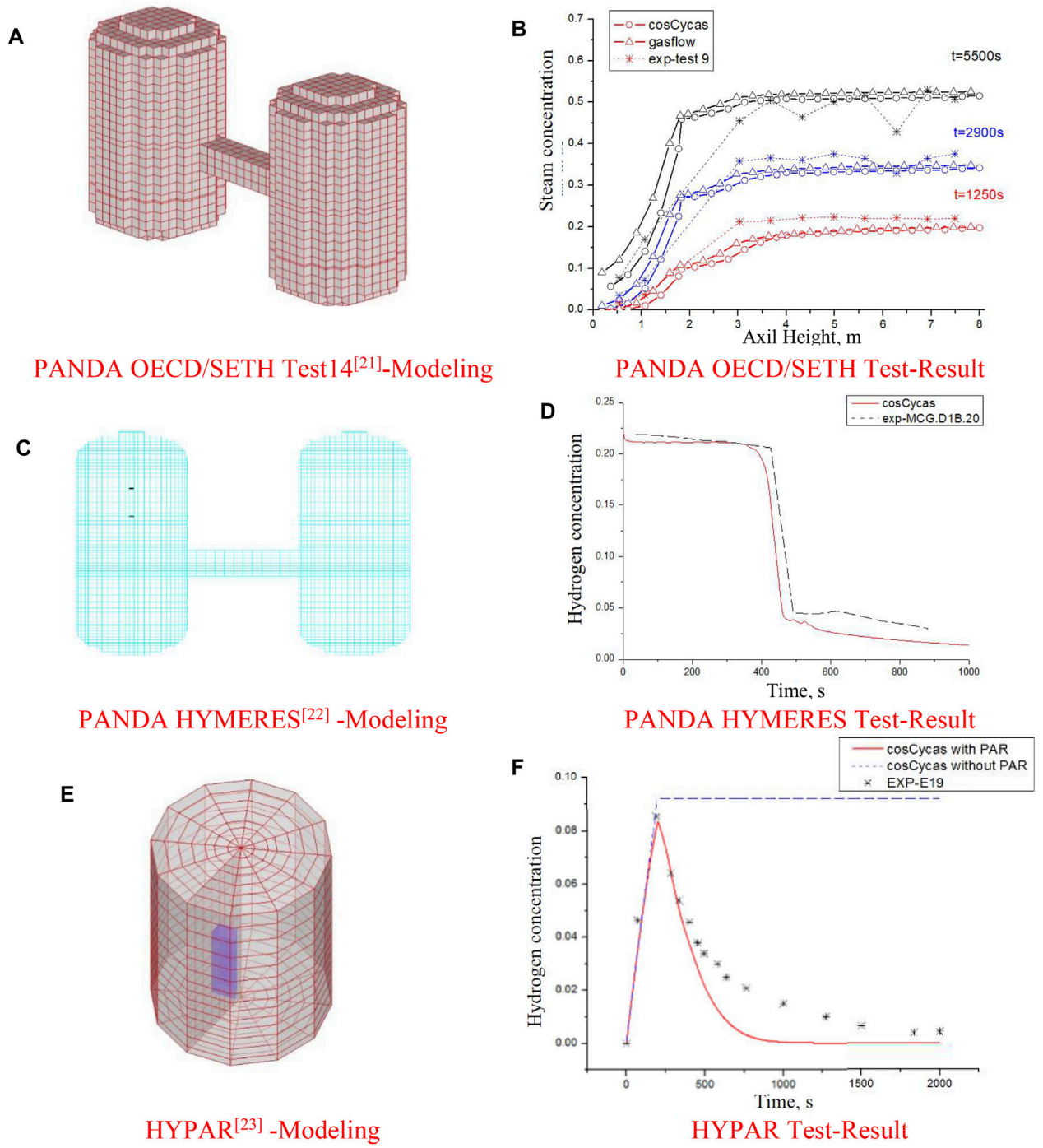

FIGURE 2 | Validation cases of CYCAS. **(A)** PANDA OECD/SETH Test 14 (Auban et al., 2007) modeling. **(B)** PANDA OECD/SETH Test result. **(C)** PANDA HYMERES (Paladino et al., 2014) modeling. **(D)** PANDA HYMERES Test result. **(E)** HYPAR (Mimouni et al., 2011) -modeling. **(F)** HYPAR Test result.

$$S_t = 0.52\, u' Da^{0.25}, \tag{9}$$

where ξ is the combustion process variable: $\xi = 0$, indicating the unburnt gas mixture and $\xi = 1$, indicating the completely burnt gas. μ is the viscosity and Sc is the Schmidt number; the subscript t indicates the turbulence value. ρ_{un} is the density for the unburnt gas mixture and S_t is the turbulence flame speed. Da is the Damköhler number, of which the definition equation is shown in **Eq. 10**.

$$\mathrm{Da} = \frac{(l/u')}{(l_f/S_l)}, \tag{10}$$

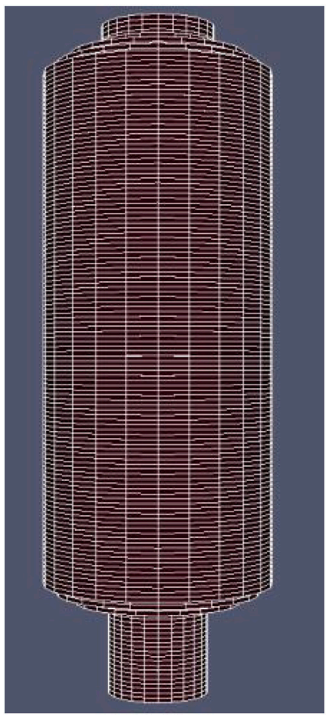

FIGURE 3 | THAI facility and modeling.

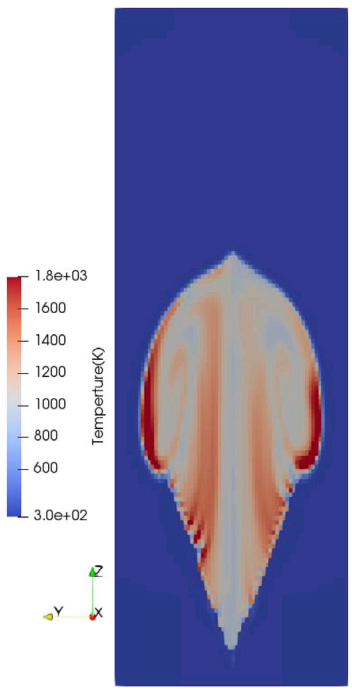

FIGURE 4 | Development of the flame (800 K iso-surface) THAI HD-12 CYCAS calculation.

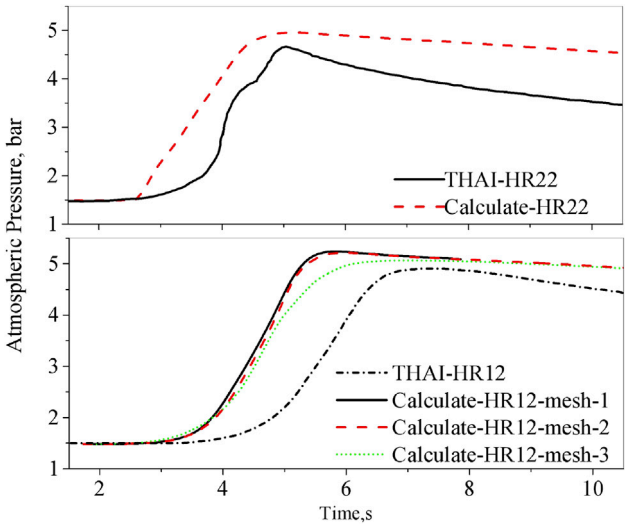

FIGURE 5 | Atmospheric pressure calculation vs. experiment.

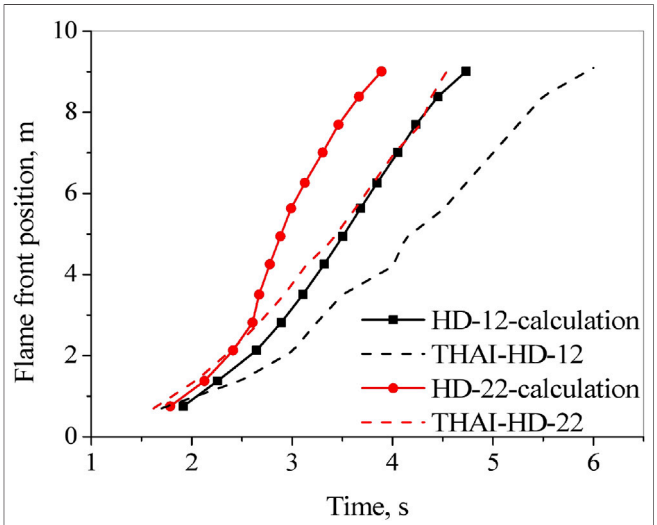

FIGURE 6 | Flame position calculation vs. experiment.

where l is the integral turbulence length, u' is the fluctuation velocity, l_f is the flame thickness, and S_l is the laminar flame speed, with the formation as shown in **Eq. 11**.

$$S_l(T, x_{H_2O}) = S_l(300)F(T)F(x_{h2o})F(P). \tag{11}$$

The terms of $S_l(300)$ is taken from Szabó et al. (2012), the terms $F(T)$ and $F(x_{h2o})$ are from Koroll et al. (1993), and the term of $F(P)$ is from Hu et al. (2009). By doing so, the validation range of **Eq. 11** can envelop the atmospheric condition during the accident conditions, as listed below:

Stoichiometric ratio [0.1252, 6.5];
Temperature [300 K, 523 K];

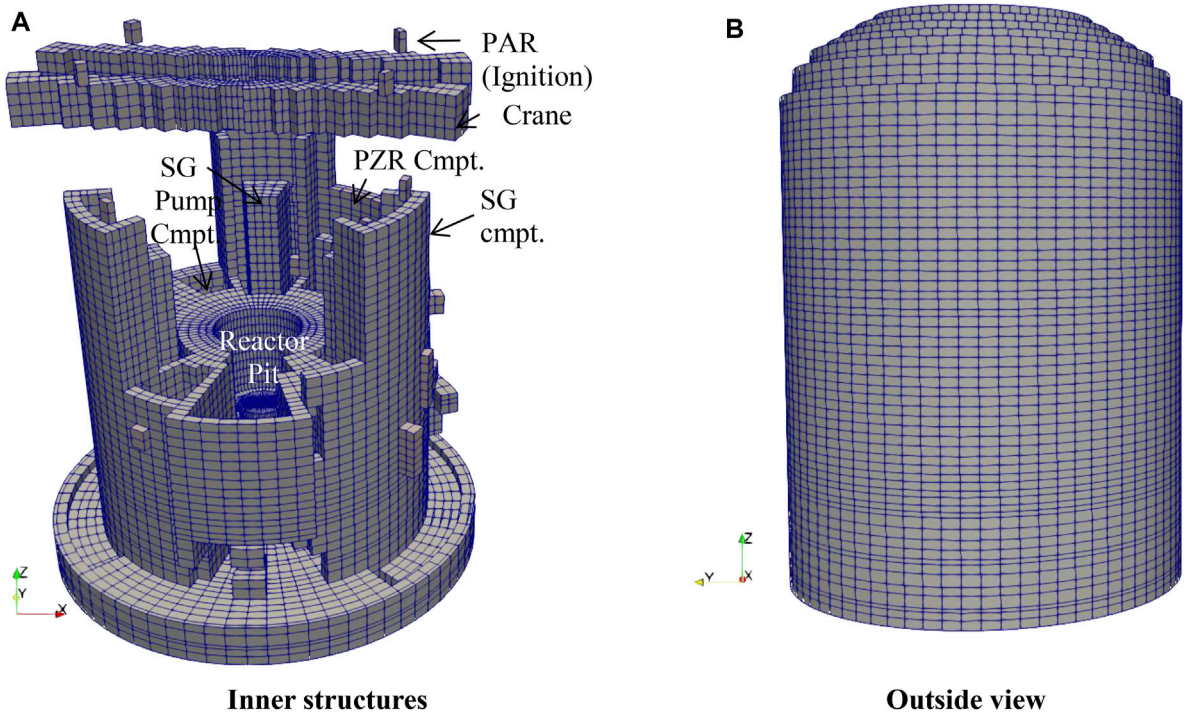

FIGURE 7 | Containment geometry modeling. **(A)** Inner structures. **(B)** Outside view.

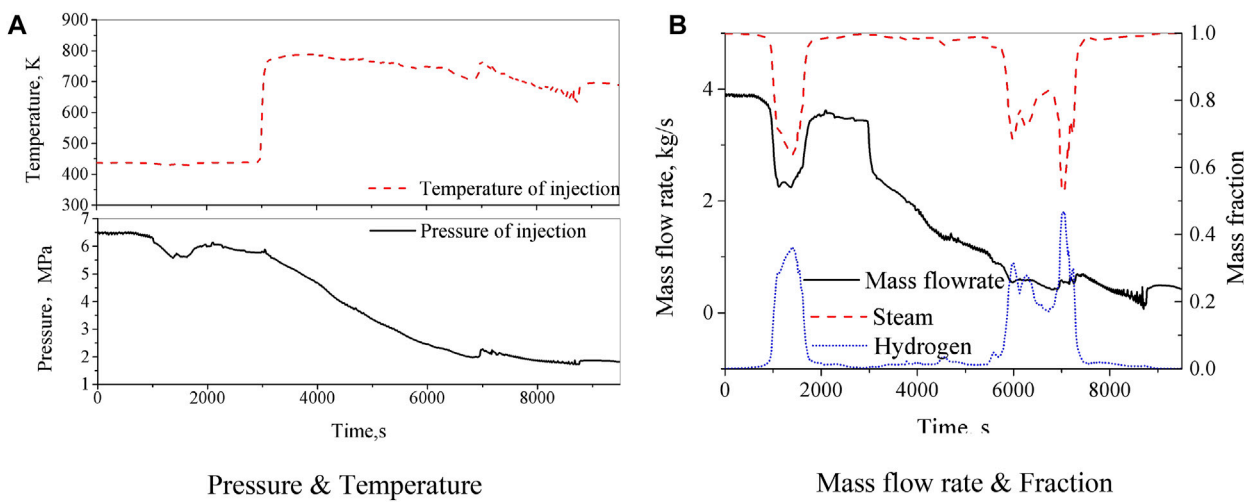

FIGURE 8 | Mass and energy release of the injection. **(A)** Pressure and temperature. **(B)** Mass flow rate and fraction.

Steam concentration [0, steam inerting); and
Pressure (0.1~8 MPa).

The spark ignition is modeled as an external source term to the transport equation of ξ, as shown below (Zimont and Lipatnikov, 1995). The source term indicates that the gas mixture in the ignition cell is ignited by a pulse of spark. Moreover, the quasi-laminar flame is assumed during the ignition stage according to Zimont and Lipatnikov (1995).

$$\frac{d}{dt}\int \rho\xi dV = \rho_{un} W_{ign} = \rho_{un} \exp\left\{-\left[\left(\frac{t-t_0}{\sigma_t}\right)^2\right]\right\}(1-\xi), \quad (12)$$

where t_0 is the time duration of one spark ignition, $\sigma_t = t_0/5$.

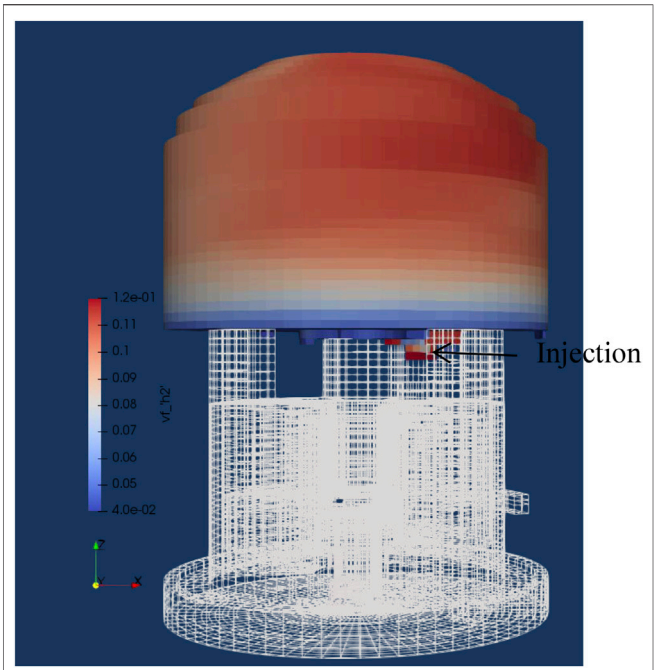

FIGURE 9 | Hydrogen distribution before ignition.

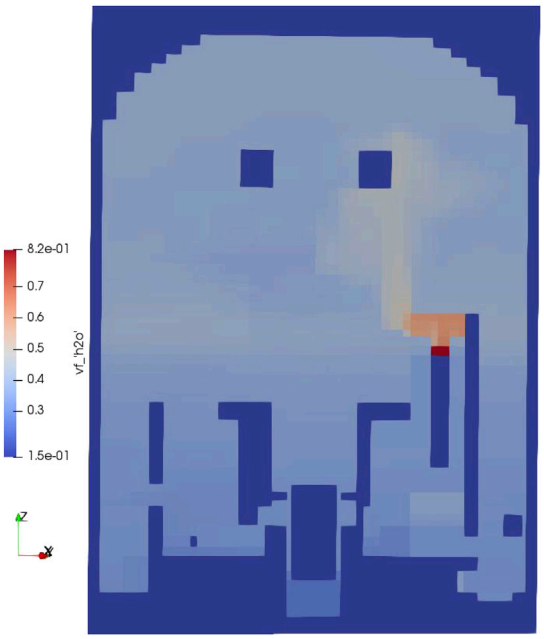

FIGURE 10 | Steam distribution before ignition.

3.2 ISP-49 THAI HD-12 and HD-22

The geometry model of the THAI facility is built in cylindrical coordination, with the computational region radius of 1.6 m and height of 9.2 m, as shown in **Figure 3**. The structure is modeled with four layers with different materials for each layer according to NEA (2011). The models of convective, condensation, and radiation heat transfers are calculated for the heat loss on the structure surface. Two cases from the THAI facility (NEA, 2011) are calculated, one is the HD-12 test without steam, and the other is the HD-22 test with steam.

The initial conditions are listed as follows (NEA, 2011):

HD-12: atmospheric pressure at 1.485 bar, gas temperature at 291 K, hydrogen at 7.98 vol%.
HD-22: atmospheric pressure at 1.487 bar, gas temperature at 365 K, hydrogen at 9.90 vol%, steam at 25.3 vol%.

The ignition is located at 0.7 m from the bottom of the facility. The initial turbulence condition is set as $k_o = 1.5e-4m^2/s^2$ and $\varepsilon_o = 4.8e-4m^2/s^3$, based on Sathiah et al. (2016). Both the convective and radioactive heat transfers to the structures are considered in this calculation.

Firstly, a mesh sensitivity analysis is conducted with three cases with meshes of $35 \times 24 \times 292$, $35 \times 24 \times 146$, and $16 \times 24 \times 73$ grids. The result shows that the first two cases are in accord with each other, while the third case underestimates the peak pressure when compared with the first two cases as shown in **Figure 5**. Therefore, the second mesh, which is $35 \times 24 \times 146$ grids in radial, peripheral, and axial directions, respectively, with a total mesh number of 122,640 is used for the next HD-22 analysis.

The r-z view of the temperature at 2 s after the ignition is shown in **Figure 4** The pressure and flame position are compared with the experimental data as shown in **Figures 5**, **6**. **Figure 5** shows that the peak pressure is overestimated in the CYCAS calculation. The pressure decreases at a smaller slope after the peak, indicating that the heat loss of the structure is underestimated. This could be the reason of the overestimation of the peak pressure. The combustion model in CYCAS overestimates the flame speed in both cases: it takes about 5.8 s to reach the ceiling in the experiment, while the time duration is 4.73 s in the CYCAS calculation for the HD-12 calculation. It takes about 3.9 s to reach the ceiling in the experiment, while the time duration is 4.56 s in the CYCAS calculation for the HD-22 calculation. The same overestimates also occur in the FLUENT calculation for HD-12 in the study by Sathiah et al. (2016), as well as the calculation for HD-22 in NEA (2011). This is mainly due to the model limitation on the flame development from the laminar flame to turbulent flame (NEA, 2011). Despite this limitation, the combustion model in CYCAS manages to have reasonable prediction on the slow deflagration for gas mixture, both with and without steam.

4 SLOW DEFLAGRATION ANALYSIS FOR CONTAINMENT

The model is adopted for a slow deflagration analysis in a containment as engineering application. The main objective of the combustion analysis for the containment includes two parts: the pressure load evaluation from combustion for the containment integrity and the thermal load evaluation for the

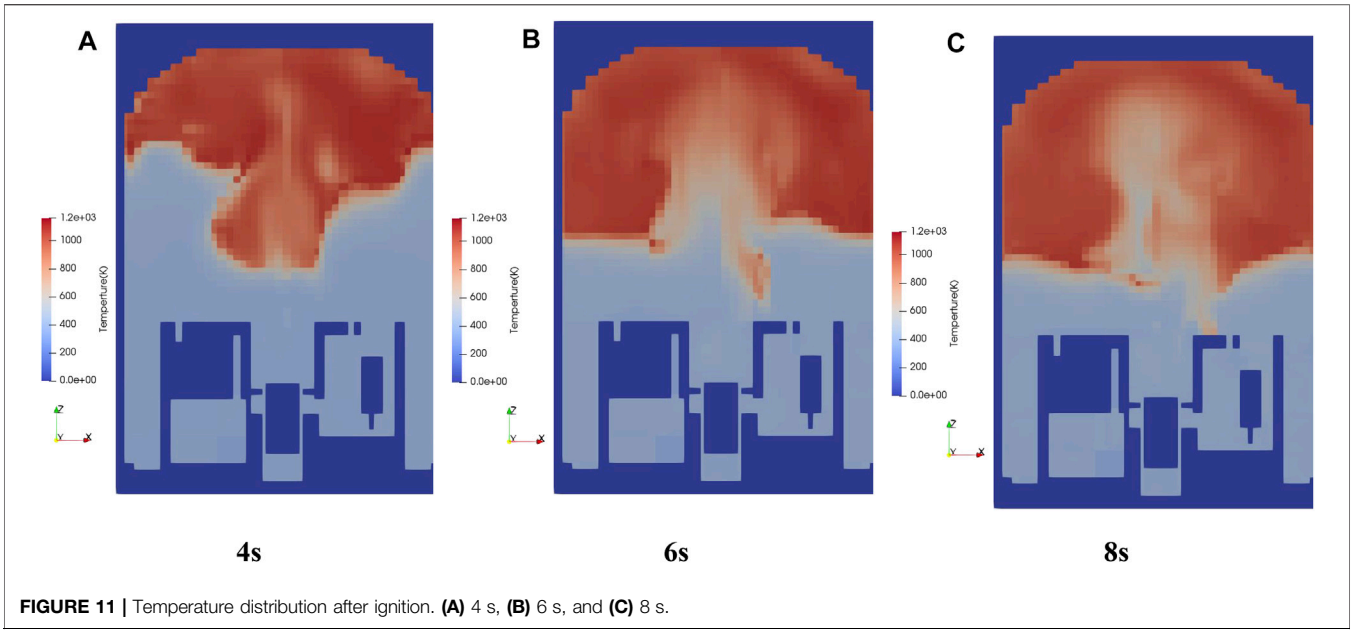

FIGURE 11 | Temperature distribution after ignition. **(A)** 4 s, **(B)** 6 s, and **(C)** 8 s.

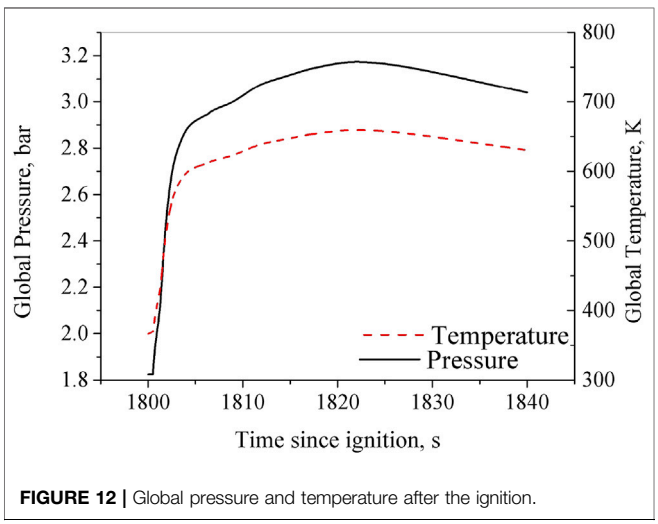

FIGURE 12 | Global pressure and temperature after the ignition.

surrounding structures for equipment survivability. The analysis in this section focuses on these two objectives.

4.1 Modeling

4.1.1 Geometry Modeling

The containment of the reference reactor has an inner radius of 22.5 m and height of 66.4 m. The geometry model is built under cylindrical coordination, namely the major equipment and floors, ceilings, and walls for the compartments, while small objects below the grid resolution are neglected. The geometry model is divided into 26 × 72 × 70 in the radial, peripheral, and axial directions, respectively, with a total mesh number of 524,160. The diagram of the geometry model is shown in **Figures 7A,B**. The mesh sensitivity analysis has been done to demonstrate the grid independence of this containment model.

4.1.2 Initial and Boundary Condition

The initial condition of the gas mixture is calculated by CYCAS with the mass and energy release obtained from the lumped parameter code (given in **Figure 8**). The standard k-ε model is adopted in this analysis. For the geometry structures, the convective, condensation, and radiant heat transfers are included. PARs are included to recombine hydrogen during the hydrogen distribution calculation.

Figures 9, **10** gives the initial hydrogen and steam distribution at the time of ignition. The injection in the calculated postulated accident located at the top of the pressurizer, approximately 22 m in the containment, leading to a hydrogen stratification near the elevation of the injection, is shown in **Figure 9**.

The selection of the timing and location of the ignition aims at the most punishing combustion consequence. The time point at the maximum hydrogen inventory is chosen for the combustion analysis. The combustion is assumed to be ignited by the hot exhaust gas from the PAR located at the crane (shown in **Figure 7A**) for two reasons. First, it is the high hydrogen concentration at the dome of the containment, and the gas mixture is more likely to be ignited by the hot exhaust gas from the PAR. The second is that the combustion near the containment structure can result in high thermal load. The initial condition of the gas mixture is summarized as follows:

Atmosphere: pressure at 1.83 bar; temperature at 366.5 K, and average H_2O concentration at 38 vol%.
Hydrogen: H_2 mass at 503 kg and average H_2 concentration at 10.5 vol%.

4.2 Combustion Analysis

4.2.1 Global Thermal Hydraulics of the Containment

The temperature distribution at different time points is given to illustrate the flame propagation, as shown in **Figure 11**. The

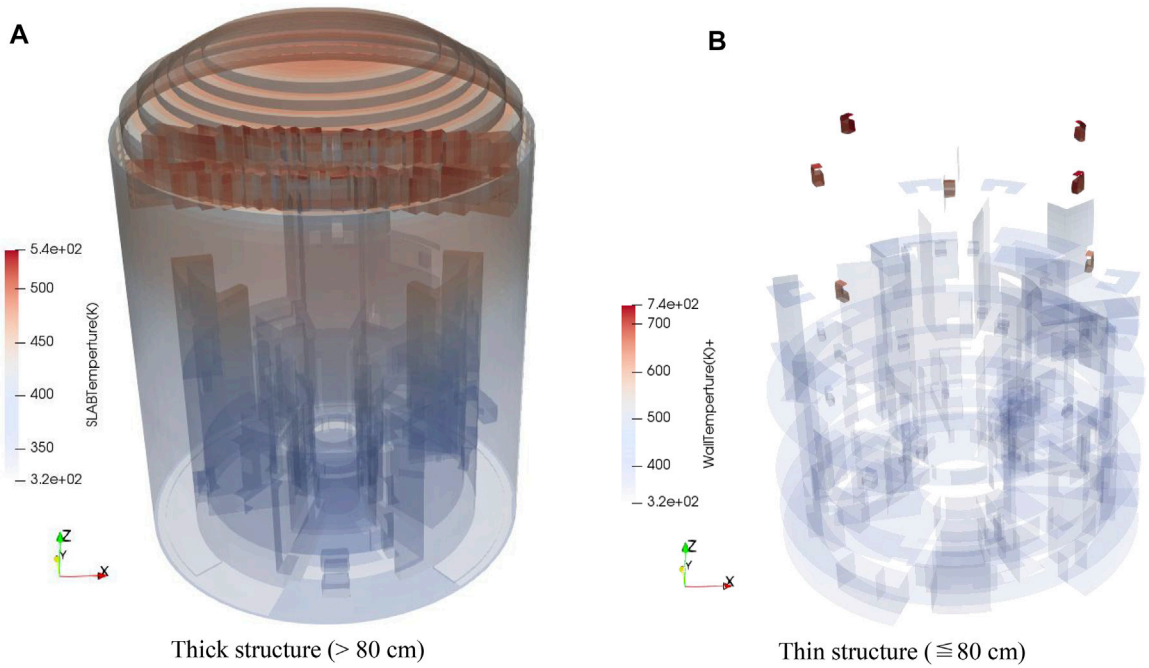

FIGURE 13 | Thermal load to structures. **(A)** Thick structure (>80 cm). **(B)** Thin structure (≦80 cm).

global atmospheric pressure and temperature are given in **Figure 12**. The global pressure and temperature rise fast in the first 2 s, then the growth rate decreases. This is because the flame propagates upward at the first 2 s after being ignited, and then propagates downward with lower speed after being blocked by the containment ceiling. The combustion lasts about 24 s with 439 kg of H_2 consumed. The peak values of pressure and temperature are achieved at 21 s after ignition, with values of 3.17 bar and 659 K, respectively. As a comparison, the pressure and temperature of Adiabatic Isochoric Complete Combustion are 4.97 bar and 1035 K, respectively. The peak pressure is within the range that the containment can withstand, such that the integrity of the containment will not be challenged, while the peak gas temperature is higher than the design temperature of the containment. This does not indicate the thermal load that challenges the containment integrity because the combustion duration is short and the thermal response needs time to build up. The thermal load of containment structures is presented in the following section.

In this calculation, the turbulence is at a low level because hydrogen is released from breaks to the local compartment first, then disperses into the large space of the containment through junctions on the structures. There are also few complex geometries but large free volumes in the flammable gas mixtures. The combustion can be more intense if occurring at local compartments with complex geometries or with higher turbulence intensity, for instance, turbulence induced by a spray. Moreover, the spray can also condense the steam thereby increasing the hydrogen concentration, which can also lead to more intense combustion. Currently, the CYCAS code is not capable of modeling the interaction between the flame and spray droplets. Further research is needed in order to address this issue.

4.2.2 Thermal Load of the Containment Structure

The containment structures are modeled with two methods: the structures with thickness higher than 80 cm are modeled as structures filling in the grids, while others are modeled as walls on the grid surface. The material and its heat transfer material data for each structure are modeled based on the actual engineering data. One thing should be pointed out: only one-dimensional heat conduction in the normal direction of the surface facing the flow field is calculated in CYCAS. This assumption is conservative for local thermal load.

Figure 13 gives the temperature of the structure surface in the containment, both thin walls and thick structures, to evaluate the thermal load of the combustion to structures. The structure temperature rises at the upper part of the containment where the combustion presents, while the temperature at the lower part remains low. The peak temperature of 535 K is reached at the top of the containment dome (given in **Figure 13A**), 40 s after the ignition, which is lower than the atmospheric temperature and also lower than the containment design temperature, indicating that the containment integrity is not challenged despite the high atmospheric temperature of combustion. **Figure 13B** shows a high temperature on the walls of the PARs with a peak temperature of 739 K. Because these walls are initially heated by the chemical heat of the hydrogen recombination with temperatures around 450–500 K, these are then further heated by the burnt gas mixture. The equipment survivability should be

evaluated with the thermal load and survivable temperature for each equipment.

5 CONCLUSION

In this study, a turbulent combustion model is developed for the in-house CFD code CYCAS for the capability of hydrogen combustion analysis for the containment. The model is validated with two tests from the THAI facility, and then a containment analysis is presented to demonstrate the code capability. The following conclusions can be drawn:

(1) The validation with the THAI facility indicates that the combustion model in CYCAS manages to have reasonable prediction on the slow deflagration for gas mixture both with and without steam.
(2) The combustion analysis shows that the combustion model in CYCAS manages to calculate the pressure and thermal load of the combustion to evaluate the influence of the combustion on the containment integrity and equipment survivability.

DATA AVAILABILITY STATEMENT

The original contributions presented in the study are included in the article/Supplementary Material, and further inquiries can be directed to the corresponding author.

AUTHOR CONTRIBUTIONS

LY: Investigation, formal analysis, and writing–original and draft, review and editing. CP: Methodology, investigation and writing—review and editing. LC: Contribution to code validation. CM: Conceptualization, methodology and supervision.

REFERENCES

Auban, O., Zboray, R., and Paladino, D. (2007). Investigation of Large-Scale Gas Mixing and Stratification Phenomena Related to LWR Containment Studies in the PANDA Facility. *Nucl. Eng. Des.* 237 (4), 409–419. doi:10.1016/j.nucengdes.2006.07.011

Chen, M., Lin, J., and Bai, W. (2016). Development and Preliminary Validation of Hydrogen Safety Analysis Code CYCAS. *At. Energ. Sci. Techno.* 50 (2), 295–300.

Dimmelmeier, H., Eyink, J., and Movahed, M.-A. (2012). Computational Validation of the EPR Combustible Gas Control System. *Nucl. Eng. Des.* 249, 118–124. doi:10.1016/j.nucengdes.2011.08.053

Ghiaasiaan, S. M. (2011). *Convective Heat and Mass Transfer*. New York, USA: Cambridge University Press.

Goulier, J., Chaumeixa, N., Haltera, F., Meynet, N., and Bentaï, A. (2016). Experimental Study of Laminar and Turbulent Flame Speed of a Spherical Flame in a Fan-Stirred Closed Vessel for Hydrogen Safety Application. *Nucl. Eng. Des.* 312, 214–227. doi:10.1016/j.nucengdes.2016.07.007

Hirt, C. W., Amsden, A. A., and Cook, J. L. (1997). An Arbitrary Lagrangian-Eulerian Computing Method for All Flow Speeds. *J. Comput. Phys.* 135 (2), 203–216. doi:10.1006/jcph.1997.5702

Hu, E., Huang, Z., He, J., and Miao, H. (2009). Experimental and Numerical Study on Laminar Burning Velocities and Flame Instabilities of Hydrogen-Air Mixtures at Elevated Pressures and Temperatures. *Int. J. Hydrogen Energ.* 34, 8741–8755. doi:10.1016/j.ijhydene.2009.08.044

Kang, H. S., Kim, J., Hong, S. W., and Kim, S. B. (2020). Numerical Analysis for Hydrogen Flame Acceleration during a Severe Accident in the APR1400 Containment Using a Multi-Dimensional Hydrogen Analysis System. *Energies* 13, 6151. doi:10.3390/en13226151

Koroll, G., Kumar, R., and Bowles, E. (1993). Burning Velocities of Hydrogen-Air Mixtures. *Combustion and Flame* 94, 330–340. doi:10.1016/0010-2180(93)90078-h

Kotouc, M. (2011). "Numerical Analysis of the Influence of PAR Unit Elevation with a Vessel on its Performance," in Proceedings of the 19th ICONE, Chiba, Japan, May 16-19, 2011.

Kuznetsov, M., Yanez, J., Grune, J., Friedrich, A., and Jordan, T. (2015). Hydrogen Combustion in a Flat Semi-confined Layer with Respect to the Fukushima Daiichi Accident. *Nucl. Eng. Des.* 286, 36–48. doi:10.1016/j.nucengdes.2015.01.016

Liu, D. D. S., and Macfarlane, R. (1983). Laminar Burning Velocities of Hydrogen-Air and Hydrogen-Airsteam Flames. *Combustion and Flame* 49, 59–71. doi:10.1016/0010-2180(83)90151-7

Mimouni, S., Mechitoua, N., and Ouraou, M. (2011). CFD Recombiner Modelling and Validation on the H2-Par and Kali-H2Experiments. *Sci. Technology Nucl. Installations* 2011, 1–13. doi:10.1155/2011/574514

NEA (2011). *ISP-49 on Hydrogen Combustion"*. Washington, D.C., United States: NEA. NEA/CSNI/R(2011)9.

NEA (2014). Washington, D.C., United States: NEA. NEA/CSNI/R(2014)8.Status Report on Hydrogen Management and Related Computer Codes

Paladino, D., Mignot, G., Kapulla, R., Paranjape, S., Andreani, M., Studer, E., et al. (2014). "OECD/NEA HYMERES Project: For the Analysis and Mitigation of a Severe Accident Leading to Hydrogen Release into a Nuclear Plant Containment," in Proceedings of the ICAPP 2014, Charlotte, USA, April 6-9, 2014. Paper 14322.

Sathiah, P., Komen, E. M. J., Roekearts, D. J. E. M., Holler, T., and Kljenak, I. (2016). The Role of CFD Combustion Modeling in Hydrogen Safety Management–V: Validation for Slow Deflagrations in Homogeneous Hydrogen-Air Experiments. *Nucl. Eng. Des.* 310 (DEC), 289–302. doi:10.1016/j.nucengdes.2016.06.030

Sathiah, P., Komen, E., and Roekaerts, D. (2012). The Role of CFD Combustion Modeling in Hydrogen Safety Management-Part I: Validation Based on Small Scale Experiments. *Nucl. Eng. Des.* 248, 93–107. doi:10.1016/j.nucengdes.2012.03.047

Studer, E., Beccantini, A., Kudriakov, S., and Velikorodny, A. (2013). "Hydrogen Combustion Modelling in Large Scale Geometries," in Proceedings of the 21st ICONE, Chengdu, China, July 29-August 2, 2013.

Szabó, T., Yáñez, J., Kotchourko, A., Kuznetsov, M., and Jordan, T. (2012). Parameterization of Laminar Burning Velocity Dependence on Pressure and Temperature in Hydrogen/Air/Steam Mixtures. *Combust. Sci. Technol.* 184 (10-11), 1427–1444. doi:10.1080/00102202.2012.690253

Xiao, J., Breitung, W., Kuznetsov, M., Zhang, H., Travis, J. R., Redlinger, R., et al. (2017). GASFLOW-MPI: A New 3-D Parallel All-Speed CFD Code for Turbulent Dispersion and Combustion Simulations Part II: First Analysis of the Hydrogen Explosion in Fukushima Daiichi Unit 1. *Int. J. Hydrogen Energ.* 42, 8369–8381. doi:10.1016/j.ijhydene.2017.01.219

Yuen, A. C. Y., De Cachinho Cordeiro, I. M., Chen, T. B. Y., Chen, Q., Liu, H., and Yeoh, G. H. (2022). Multiphase CFD Modelling for Enclosure Fires-A Review on Past Studies and Future Perspectives. *Exp. Comput. Multiph. Flow* 4, 1–25. doi:10.1007/s42757-021-0116-4

Zhao, H., Luo, X., Zhang, R., Lyu, X., Yin, H., and Kang, Z. (2022). Analysis on Hydrogen Risk under LOCA in marine Nuclear Reactor. *Exp. Comput. Multiph. Flow* 4, 39–44. doi:10.1007/s42757-020-0077-2

Zimont, V. L. (2000). Gas Premixed Combustion at High Turbulence. Turbulent Flame Closure Combustion Model. *Exp. Therm. Fluid Sci.* 21, 179±186. doi:10.1016/s0894-1777(99)00069-2

Zimont, V. L., and Lipatnikov, A. N. (1995). A Numerical Model of Premixed Turbulent Combustion of Gases. *Chem. Phys. Rep.* 14 (7), 993–1025.
Zimont, V. L. (2000). Gas Premixed Combustion at High Turbulence. Turbulent Flame Closure Combustion Model. *Exp. Therm. Fluid Sci.* 21, 179–186. doi:10.1016/s0894-1777(99)00069-2

Conflict of Interest: Author LY, CP, CM is employed by China Nuclear Power Technology Research Institute Co. ltd. Author LC is a student of Shenzhen University.

The remaining authors declare that the research was conducted in the absence of any commercial or financial relationships that could be construed as a potential conflict of interest.

Publisher's Note: All claims expressed in this article are solely those of the authors and do not necessarily represent those of their affiliated organizations, or those of the publisher, the editors, and the reviewers. Any product that may be evaluated in this article, or claim that may be made by its manufacturer, is not guaranteed or endorsed by the publisher.

frontiers | Frontiers in Energy Research

ORIGINAL RESEARCH
published: 29 April 2022
doi: 10.3389/fenrg.2022.881728

Investigating the Use of C/SiC Ceramic Composites in an Innovative Light-Water Reactor Core Grouping Catcher

Xu Han[1,2], Litong Zhang[1], Ji Xing[2]*, Weimin Ma[2], Yidan Yuan[2], Haoxuan Wang[3], Yiguang Wang[4] and Xiao Zeng[2]*

[1]Science and Technology on Thermostructural Composite Materials Laboratory, Northwestern Polytechnical University, Xi'an, China, [2]China Nuclear Power Engineering Co Ltd, Beijing, China, [3]Beijing Institute of Long March Aerospace Vehicles, Beijing, China, [4]Institute of Advanced Structure Technology, Beijing Institute of Technology, Beijing, China

China Nuclear Power Engineering, Northwestern Polytechnical University, and Beijing Institute of Technology have undertaken a joint research work with the goal of developing corium retention containers for use in an innovative light-water reactor core grouping catcher (CGC). In Serious Accidents (SAs), the corium will be retained in the C/SiC ceramic composite spherical shell container and thrown into the pool for passive cooling. In order to investigate the capability of the C/SiC ceramic composites to withstand the high temperature of 1800°C and the huge thermal shock at the initial stage of cooling, in this work, the high-temperature performance of these composites is studied. Furthermore, the compatibility of these composites with corium is investigated, and a retention container design prototype is proposed. The thermal conductivity, thermal expansion coefficient, high-temperature tensile strength, and thermal shock resistance of the candidate C/SiC specimens to be used in the manufacturing of the detention container are measured. The FactSage software package is used for the chemical compatibility study and product composition analysis of the composite SiC deposition layer and corium. The corrosion process of the SiC deposition layer of the composite material caused by corium is investigated through high-temperature corrosion tests and the electron microscopy analysis of the SiC specimen with the incorporation of CeO_2. The results show that the C/SiC ceramic composite can meet the design criteria of the CGC corium retention container, and it is impossible to cause a carbon reaction disaster through the failure of the composite SiC deposition layer.

Keywords: hualong one, severe accident, corium retention, core catcher, core grouping catcher

OPEN ACCESS

Edited by:
Yapei Zhang,
Xi'an Jiaotong University, China

Reviewed by:
Xiaojing Liu,
Shanghai Jiao Tong University, China
Guang Ran,
Xiamen University, China

****Correspondence:***
Xu Han
doc_hanxu@163.com
Ji Xing
zhanglt@nwpu.edu.cn

Specialty section:
This article was submitted to Nuclear Energy, a section of the journal Frontiers in Energy Research

Received: *23 February 2022*
Accepted: *07 April 2022*
Published: *29 April 2022*

Citation:
Han X, Zhang L, Xing J, Ma W, Yuan Y, Wang H, Wang Y and Zeng X (2022) Investigating the Use of C/SiC Ceramic Composites in an Innovative Light-Water Reactor Core Grouping Catcher. Front. Energy Res. 10:881728. doi: 10.3389/fenrg.2022.881728

1 INTRODUCTION

China Nuclear Power Engineering, Northwestern Polytechnical University, and Beijing Institute of Technology have recently investigated the application of C/SiC ceramic composites in the design of the light-water reactor (LWR) core catcher. The goal of the project is to develop corium retention containers for use in an innovative LWR core grouping catcher (CGC) (Han et al., 2018). Due to its innovative scheme, the CGC can reduce the direct contact between corium and water, increase the heat transfer area for cooling, and considerably simplify the final disposal of SAs.

TABLE 1 | Comparison of the functions of the WWER and EPR core catchers.

Level		Object/Target	WWER	EPR
Basic functions	Substance control	Corium	Corium packing basket (crucible)	Spreading room
		Gas	Gas is released to containment	Gas is released to containment
	Energy removal	Direct immersion	Top of crucible immersed directly i	Spreading room flooding
		Indirect cooling	Wall of crucible is cooled by coils	Cooling from floor of Spreading room
	Critical safety	Corium	Neutron poison	Sacrificial dilution
Complete functions	Redundant sets	Container and Cooling	NaN	NaN
	Derivative problems	Safety risks	Insufficient cooling	Steam explosion
	Maintenance	Accessibility and tools	Normal	Normal
Additional functions	Mutual supports	Water source and Heat removal	FAK	IRWST

Owing to their unique high-temperature properties (Katoh et al., 2012; Zinkle et al., 2014; Angelici Avincola et al., 2015), small neutron absorption cross sections, high oxidation resistance, chemical inertness, high melting point, low irradiation growth, and stabilization in nuclear waste, SiC ceramic composites have attracted significant interest for various nuclear applications. For example, these composites have been used in accident tolerant fuel (ATF) cladding for a pressurized water reactor (PWR) (Qiu et al., 2020), a wrapper tube for a sodium-cooled fast reactor (Braun et al., 2021), and a SiC-coated fuel particle capsule for a PWR (Lippmann et al., 2001). Compared with C/SiC composites, SiC/SiC composites have the advantages of a small neutron absorption cross section, high thermal conductivity, unified interfacial materials, and high chemical stability. Therefore, SiC/SiC composites are more suitable for ATF applications. However, for serious accidents that are extremely unlikely to occur and for low requirements on the material irradiation performance, C/SiC composites are more suitable than SiC/SiC composites as their technology is more mature and economical. In this study, the high-temperature performance of C/SiC ceramic composites was investigated, and the compatibility of these composites with the core melt was studied. Our results demonstrate the application feasibility of C/SiC composites as the structural material for core melt retention containers.

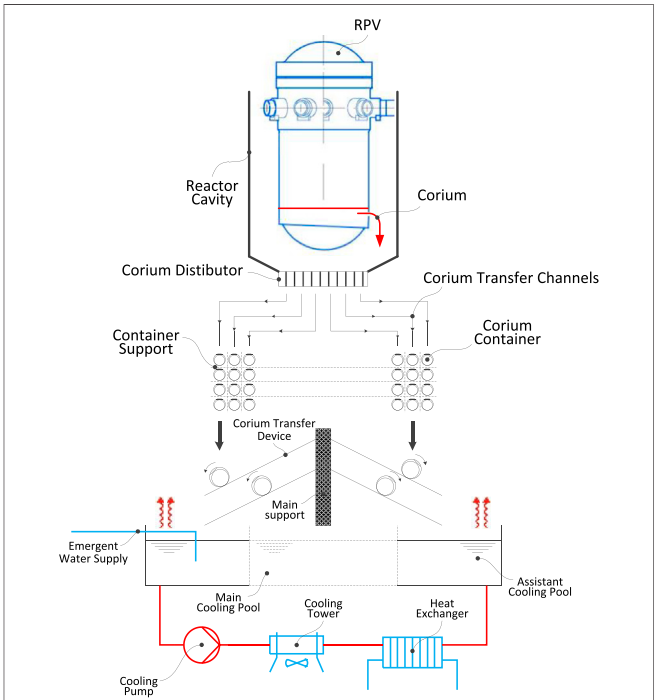

FIGURE 1 | Schematic diagram of the CGC principle.

2 CONCEPTUAL DESIGN OF THE CGC

2.1 Typical Core Catcher Design

Since the concept of the core catcher was first put forward, many schemes have been proposed. The most important among these schemes is the in-vessel corium retention (IVR) combined with the passive cooling of the external vessel surface, such as the core catchers of the VVER-440&640, AP1000, and BWR-1000 reactors (Khabensky et al., 2009). Another important scheme is the ex-vessel corium retention (EVR). In the EVR approach, the molten core is released into the under-reactor cavity of a concrete pit filled with water. Two typical EVR core catchers have been fully developed: 1) a crucible-type catcher developed for Russian NPPs with a VVER-1000 reactor (Kolev, 2001; Kukhtevich et al., 2001) and 2) a core catcher with melt spreading developed for the European EPR reactor (Sidorov et al., 2001; Fischer, 2004). As shown in **Table 1**, regardless of whether the IVR or EVR schemes are considered with crucible or spreading catchers, the functions of the core catcher design can be divided into three levels: 1) "Basic functions", which depend on the system targets; 2) "Complete functions", which are used to solve the derivative problems introduced by the establishment of the system; 3) "Additional functions", which are related to the mutual support with other systems. This table compares and analyzes the core catcher function settings of the WWER and EPR reactors.

At the basic functional level, the corium mass is the most important factor in the core catcher design; the shape of the retention container, sacrificial material (SM) amount, neutron poison choice, and cooling mode depend on this factor. At the

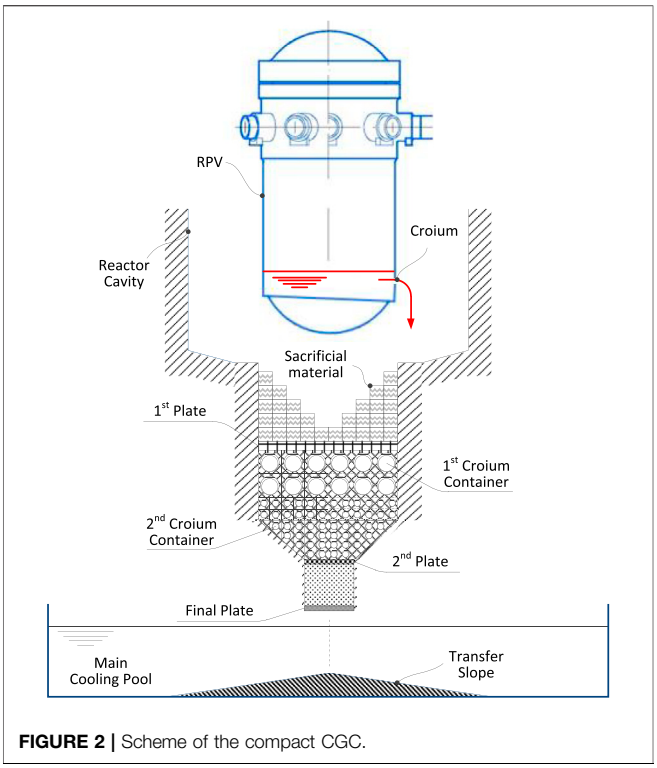

FIGURE 2 | Scheme of the compact CGC.

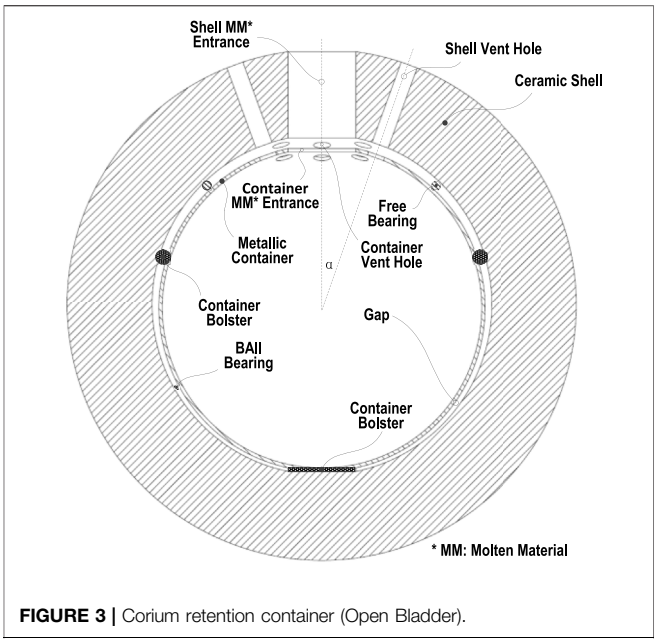

FIGURE 3 | Corium retention container (Open Bladder).

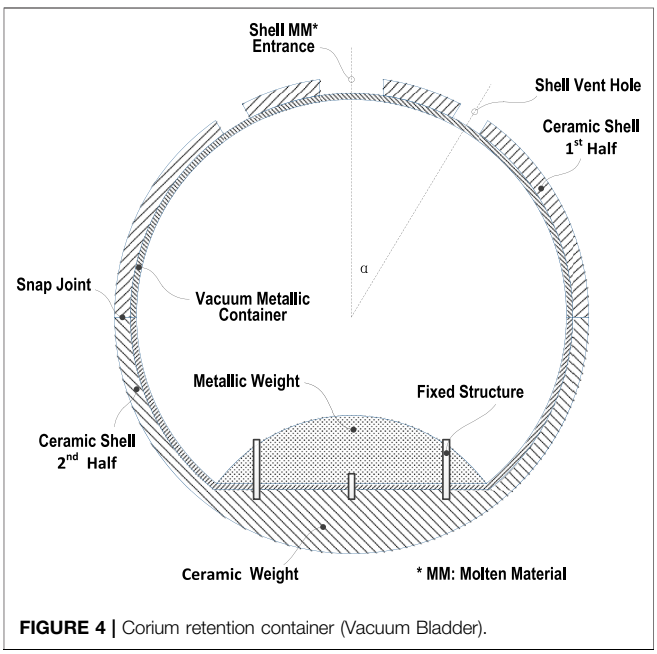

FIGURE 4 | Corium retention container (Vacuum Bladder).

complete functional level, redundancy is not considered in the current design of the core catcher. Direct water contact for cooling introduces the risk of steam explosion. At an additional functional level, the cooling water required by the core catcher can be provided by other systems; this is an approach that meets the low-cost requirements of the core catcher design.

The current core catcher design does not take into account the final disposal of SAs. After the Fukushima nuclear accident, the melted core cannot be transferred, and has been continuously cooled for 10 years. Only the radioactive wastewater accumulated from unit 2 has reached almost one million cubic meters and is still being produced. Therefore, the future core catcher should have the following characteristics: 1) A good transportability to meet the final disposal requirements of the corium; 2) A high redundancy for the detention and cooling functions; 3) A good level of isolation to avoid the risk of steam explosion; 4) A high degree of compactness for minimizing the use of sacrificed materials and reducing the total amount of corium; 5) Passive features for a more reliable cooling.

2.2 CGC

In the innovative CGC scheme, corium will be retained in the C/SiC ceramic composite spherical shell container and thrown into the pool for passive cooling.

Figure 1 shows a schematic diagram of the CGC principle. After the reactor pressure vessel (RPV) failure, corium will undergo four processes, namely distribution, perfusion, transfer, and cooling, to achieve a long-term retention. The scheme of a compact CGC is shown in **Figure 2**. After the RPV failure, the molten core does not spread into the catcher immediately; corium will first flow into a premix chamber containing the SM of fusible oxides so that its temperature can be reduced to 1800°C. The presence of the SM and premix chamber ensures corium retention for a period exceeding the time of the melt relocation from the vessel. During this period, the decay heat of the corium and relocated molten core is exploited for the SM melting and dissolution. The SM can immobilize the corium in the premix chamber temporarily for around 1 h. The melt will then penetrate through the bottom plate (first Plate) of the premix chamber and flow into the perfusion chamber. Spherical corium retention containers were piled in the

TABLE 2 | Tensile strengths of the C/SiC composites before and after the thermal shock tests.

After Thermal Shock Tests			As Received Samples			Strength Retention(%)
samples	Tensile strength (MPa)	Average (MPa)	samples	Tensile strength(MPa)	Average(MPa)	
TS1	269.26	273.38	AS1	325.06	315.74	86.6
TS2	272.12		AS2	320.27		
TS3	281.98		AS3	307.19		
TS4	274.42		AS4	322.71		
TS5	269.11		AS5	303.47		

perfusion chamber, and the gaps between the containers were filled with the SM. The diameter of the retention containers is larger in the upper region of the perfusion chamber and decreases toward the bottom region. The SM in the perfusion chamber can protect the surface of the retention containers and increase the fluidity of corium. As shown in **Figures 3**, **4**, the corium retention container consists of a ceramic shell and an inner metal bladder. When the metal bladder is prevacuumized melted, corium will be transferred into the retention container. Similar to the process in the premix chamber, corium will be immobilized in the perfusion chamber for a sufficient amount of time to complete the perfusion process and cool down further. The containers and residual melt will then penetrate through the bottom plate (second Plate) of the perfusion chamber and pour into the lubrication chamber. The SM in the lubrication chamber serves a lubricant. After a short stagnation period, the containers and residual corium will melt through the bottom of the lubrication chamber (Final Plate) and fall into the main cooling pool.

The most important aspects of the core grouping catcher are the designs of the corium retention container and functional SM. In this work, the high-temperature performance of the C/SiC ceramic composites was investigated, and their compatibility with the core melt was studied. Our findings prove the application feasibility of C/SiC composites as the structural material for core melt retention containers.

3 THERMAL SHOCK PROPERTIES OF THE C/SIC COMPOSITES

The thermal shock resistance of the C/SiC composites is an important parameter that should be considered for their application in the detention container. As the temperature of corium is in the range of 1800–2000°C, the thermal shock properties of the C/SiC composites were investigated in a simulated process as follows: the C/SiC composites were heated using an oxyacetylene flame for 30 s to stabilize the temperature, which was measured to be 1850–2000°C using an infrared thermometer. The flame temperature was controlled by adjusting the ratio of oxygen gas to acetylene gas. The heated C/SiC composites were then dropped in distilled water to cool down within seconds. The tensile strengths of the thermally shocked C/SiC composites were measured and compared with those of the as-received samples. The results are presented in **Table 2**.

The damage caused to the C/SiC composites during the thermal shock process is due to the two following reasons. One cause of damage is the high-temperature flame, which damages the fiber and matrix through oxidation and consequently affects the tensile strength of the composites. This type of damage should also occur when corium fills the C/SiC containers in real application environments. The second cause of damage is the internal stress that is induced due to the rapid temperature change from 1800°C to 2000°C to room temperature. Owing to the difference in the coefficients of thermal expansion (CTEs) between the SiC matrix and the carbon fiber, SiC experiences a compressive stress at high temperatures followed by a tensile stress at room temperature, which results in cracks in the matrix and a reduction in the strength of the composites. After the thermal shock, the C/SiC composites still retained 86.6% of their original strength, which satisfies the strength requirement for the corium container. The weak interface in the C/SiC composites is beneficial to deflect the propagation of cracks in the matrix, which contributes to partially release the internal stress, thus leading to the high strength retention observed during the thermal shock.

4 CORROSION OF SIC DUE TO CORIUM

The main components of corium are listed in **Table 3**.

As the spherical C/SiC container has an inner radius of 100 mm with 0.1-mm-thick SiC coatings, the molar ratios of SiC to the elements in the mixture composed of RPV material, UO_2, and steel should be SiC:Fe:Cr:Ni:Zr:UO_2 = 0.25:47.98:12.33:5.44:2.81:0.75. Under the same assumptions, the ratios of SiC to the elements in the molten oxide mixture should be SiC:UO_2:ZrO_2:Zr = 0.25:14.24:3.75:6.75.

4.1 Thermodynamic Analysis of the Corrosion of SiC due to Corium

Based on the aforementioned ratios of SiC to the molten oxide mixture and of SiC to the mixture of RPV, UO_2, and steel, the reaction products can be calculated using the FactSage software package. It is noted that, due to the reactions of SiC with the molten oxide mixture and the mixture of RPV, UO_2, and steel, the newly formed condensed phases are ZrC and $SiZr_2$ in the temperature range of 1800–2500°C and ZrC

TABLE 3 | Main components of corium.

The Temperature of Inject Steel mixture: 2000°C		The Temperature of Inject Oxide mixture: 2600°C	
The Mixture of Zirconium at the Bottom of RPV, UO2 and Steel		**The Mixture of Oxides**	
Fe (73%)	52.3 tons	UO2 (78%)	75 tons
Cr (18%)	12.5 tons	ZrO2 (9%)	9 tons
Ni(9%)	6.2 tons	Zr (13%)	12 tons
Zr	5 tons	—	—
UO_2	4 tons	—	—

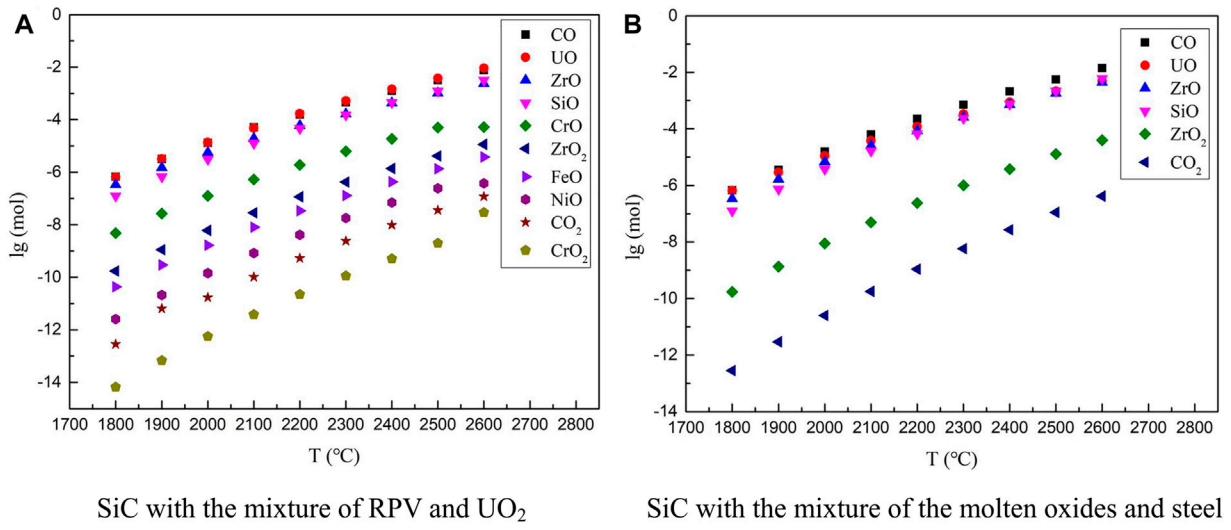

FIGURE 5 | Gaseous products in the reactions of SiC with corium.

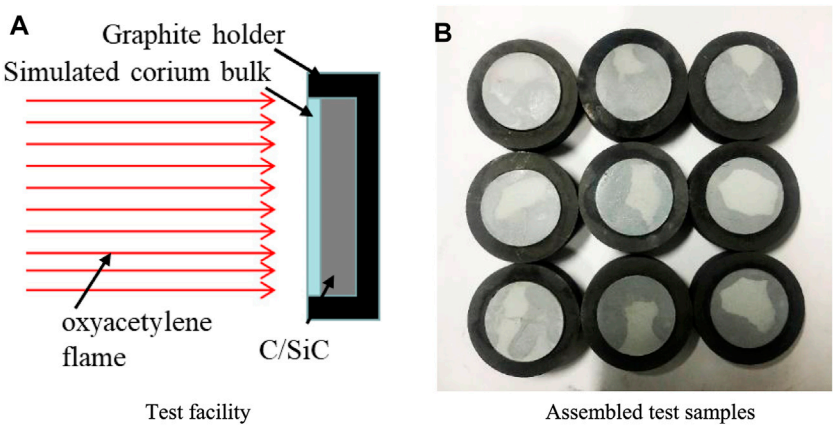

FIGURE 6 | Schematic assembly of the corium and C/SiC composites for the kinetic corrosion test.

and Si_3Zr_5 at 2600°C. The other condensed phases are not involved in the reactions. The gaseous products are summarized and depicted in **Figure 5**.

According to the Calculation Results, the Possible Reactions Between SiC and Corium Are Listed Below

$$SiC(s)+2UO_2(l) = SiO(g) + CO(g) + 2UO(g) \quad (1)$$

$$SiC(s)+3UO_2(l) = SiO(g)+CO_2(g) + 3UO(g) \quad (2)$$

$$2Zr(l)+3UO_2(l) = ZrO(g)+ZrO_2((g) + 3UO(g) \quad (3)$$

$$2Cr(l)+3UO_2(l) = CrO(g)+CrO_2(g) + 3UO(g) \quad (4)$$

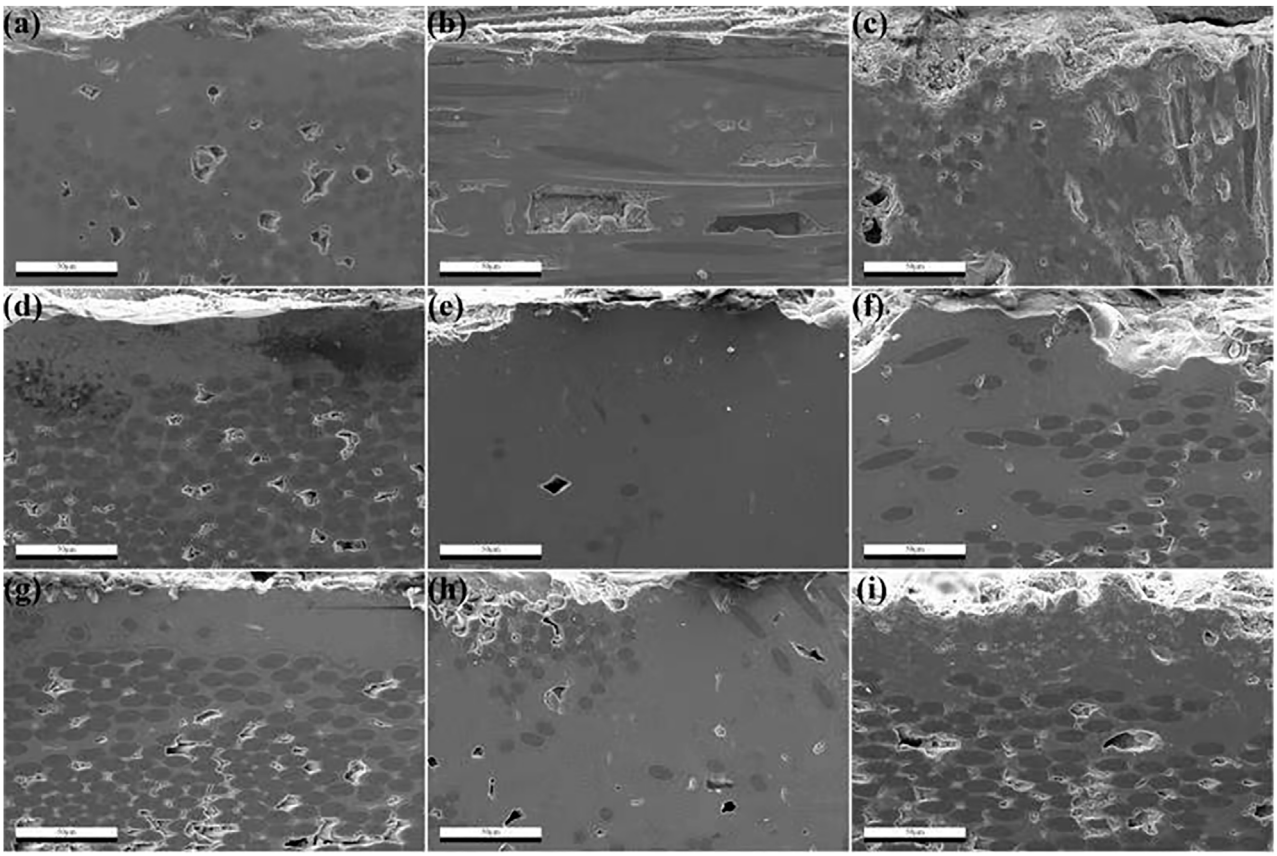

FIGURE 7 | Typical cross-sectional morphology image of the corroded C/SiC samples.

$$(\mathrm{Fe} \sim \mathrm{Ni})\,(\mathrm{l}) + 2\mathrm{UO_2}\,(\mathrm{l}) = \mathrm{FeO}\,(\mathrm{g}) + \mathrm{NiO}\,(\mathrm{g}) + 2\mathrm{UO}\,(\mathrm{g}) \quad (5)$$

$$\mathrm{SiC}\,(\mathrm{s}) + 3\mathrm{Zr}\,(\mathrm{l}) = \mathrm{ZrC}\,(\mathrm{s}) + \mathrm{SiZr_2}\,(\mathrm{s}) \quad (6)$$

$$3\mathrm{SiC}\,(\mathrm{s}) + 8\mathrm{Zr}\,(\mathrm{l}) = 3\mathrm{ZrC}\,(\mathrm{s}) + \mathrm{Si_3Zr_5}\,(\mathrm{s}) \quad (7)$$

$$\mathrm{SiC}\,(\mathrm{s}) + 2\mathrm{ZrO_2}\,(\mathrm{s}) = \mathrm{SiO}\,(\mathrm{g}) + \mathrm{CO}\,(\mathrm{g}) + 2\mathrm{ZrO}\,(\mathrm{g}) \quad (8)$$

As can be seen from **Figure 6**, the concentrations of all the gaseous products increase with the increase in the reaction temperature. This indicates that all the metals and oxides can corrode the SiC coatings at high temperatures. However, the concentration of all the gaseous products is low, indicating that this high-temperature corrosion of SiC due to corium is not pronounced. The concentration of hazardous gas, such as explosive CO, is too low to be omitted. A lower concentration of gaseous products is obtained for the reaction between SiC and the mixture of the oxide melt compared with that obtained for the reaction between SiC and the mixture of RPV, UO_2, and steel; this indicates that the oxide melt causes less corrosion to the SiC coating.

The above results were obtained based on the assumption that all the SiC coatings would fully react with corium. In a real situation, corium only corrodes the SiC coatings on the contacted interfaces. The formation of ZrC and Si_2Zr (or Si_3Zr_5 at 2600°C) during the corrosion at the interface would hinder the further corrosion of SiC. Therefore, the corrosion of the C/SiC container due to corium is limited, and the concentration of the generated gaseous products is suitable from a safety perspective.

4.2 Kinetics of the Corrosion of C/SiC due to Corium

The kinetics of two types of corium (listed in **Table 3**) were studied in the temperature range of 1,400–2000°C. In nuclear material research, CeO_2 is often used as a surrogate for UO_2 for its similar physical and chemical properties (Patnaik et al., 2021). So UO_2 oxide was replaced with the simulated CeO_2. A high-temperature oxyacetylene flame was achieved by adjusting the ratio between acetylene gas and oxygen gas. The bulk with a corium ratio as shown in **Figure 6** (with UO_2 substituted by CeO_2) was pasted on the surface of the C/SiC composites. The oxyacetylene flame was oriented perpendicular to the surface of the composites. The schematic of the process is shown in **Figure 6**.

At each corrosion temperature, the reaction was allowed to proceed for three different durations, namely 150, 300, and 450 s. After the corrosion test, the cross sections of the corroded samples were observed via scanning electron microscopy (SEM), and the corrosion thickness was measured by

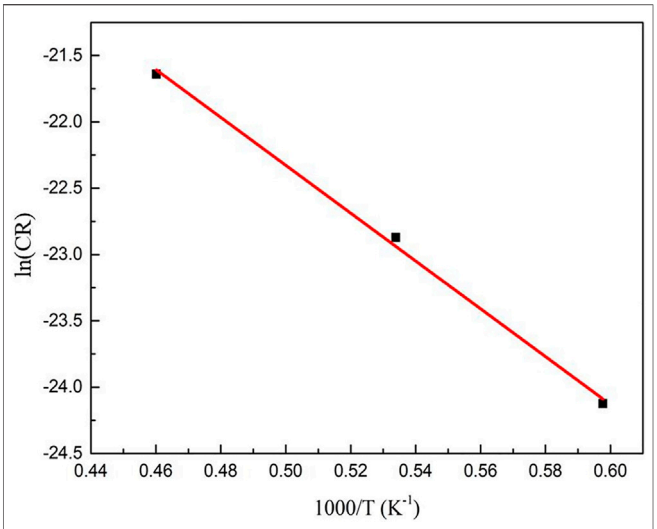

FIGURE 8 | Logarithm of the corrosion rates of SiC due to oxide corium.

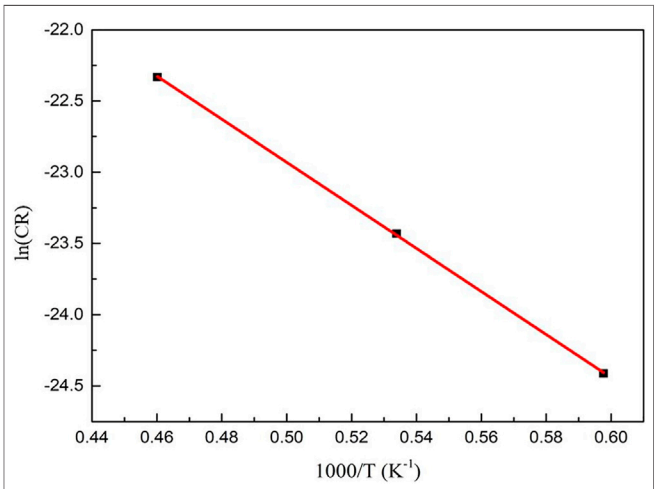

FIGURE 9 | Logarithm of the corrosion rates of SiC due to the mixture of UO_2 and steel. The data is fitted by a straight line. The corrosion activation energy and the value of *A* were calculated to be 150 kJ/mol and 1.66 × 10–^{6}, respectively.

comparing the corroded central area and the unreacted area at the rim of the C/SiC composites. A typical cross-sectional morphology image of the corroded samples is shown in **Figure 7**.

As for the oxide corium, the corrosion temperatures measured using the infrared pyrometer were 1,400°C, 1,600°C, and 1900°C. The corresponding corrosion rates were found to be 0.0015, 0.004, and 0.012 μm/s, respectively.

Usually, a thermally activated reaction process obeys the Arrhenius equation, which is written as:

$$CR = A\exp\left(-\frac{E}{RT}\right) \tag{9}$$

where *CR* is the corrosion rate, *A* is a constant, *E* is the activation energy for the corium corrosion, *T* is the temperature, and *R* is the universal gas constant.

By taking the logarithm of both sides of **Eq. 9**, the following equation is obtained:

$$\mathrm{In}CR = \mathrm{In}A - \frac{E}{RT} \tag{10}$$

The logarithm of the corrosion rates of SiC due to oxide corium as a function of the reciprocal of the temperature is plotted in **Figure 8**. The data is well fitted by a straight line, and the corrosion activation energy was calculated to be 126 kJ/mol from the slope of this line based on **Eq. 10**. The value of *A* was calculated to be 2.11 × 10–^{7}.

By substituting the values of *E* and *A* into **Eq. 9**, the corrosion rates at various temperatures can be predicted; the obtained results are listed in **Table 4**.

Based on the thermodynamic results and corrosion kinetics, the corrosion of SiC due to oxide corium is limited. Even at a temperature as high as 2600°C, the SiC thickness (*t*) that is corroded within 1,000 s is only 66 μm, which is less than the thickness of the C/SiC coatings. Although, according to the thermodynamic analysis, CO and SiO gases are produced during the corrosion, the kinetic results indicate that the corrosion reactions occur only on the contact areas. The amount of the gaseous products is less than 0.01 mol, and they can thus be omitted.

The corrosion kinetics of SiC due to the mixture of RPV, UO_2, and steel was also studied. The measured corrosion temperatures were adjusted to 1,400°C, 1,600°C, and 1900°C. The corresponding corrosion rates were 0.002, 0.007, and 0.024 μm/s, respectively. The corrosion rates were measured using the aforementioned method for the corrosion of SiC due oxide corium. The corrosion rates and corresponding temperatures are plotted in **Figure 9** according to **Eq. 10**

TABLE 4 | Predicted corrosion rates of SiC due to oxide corium in the temperature range of 1,400–2600°C.

Temperature (°C)	*CR* (μm/s)	t_{1000s} (μm)	Temperature (°C)	*CR* (μm/s)	t_{1000s} (μm)
1,400	0.0015 (measured)	1.5	2100	0.021	21
1,500	0.0025	2.5	2200	0.028	28
1,600	0.004 (measured)	4	2300	0.035	35
1700	0.006	6	2400	0.044	44
1800	0.009	9	2500	0.054	54
1900	0.012 (measured)	12	2600	0.066	66
2000	0.016	16	—	—	—

TABLE 5 | Predicted corrosion rate of SiC due to the mixture of UO_2 and steel in the temperature range of 1,400–2600°C.

Temperature (°C)	*CR* (μm/s)	t_{1000s} (μm)	Temperature (°C)	*CR* (μm/s)	t_{1000s} (μm)
1400	0.002 (measured)	2	2100	0.050	50
1500	0.004	4	2200	0.068	68
1600	0.007 (measured)	7	2300	0.090	90
1700	0.011	11	2400	0.117	117
1800	0.017	17	2500	0.149	149
1900	0.024 (measured)	24	2600	0.187	187
2000	0.036	36	—	—	—

By substituting the values of *E* and *A* into **Eq. 9**, the corrosion rates of SiC due to the mixture of RPV, UO_2, and steel in the temperature range of 1,400–2600°C can be predicted; the calculated results are listed in **Table 5**.

Compared with the corrosion of SiC due to oxide corium, the corrosion of SiC due to the mixture of RPV, UO_2, and steel is more significant. However, the molten mixture of RPV, UO_2, and steel usually has a temperature lower than 2000°C in a real situation. Thus, the corroded thickness of SiC due to the melt at 2000°C within 1,000 s is only 36 μm, which is still less than the thickness of the C/SiC coatings.

5 Prototype Design of the Corium Retention Container

If the retention containers were filled with corium in case of an accident, they would be quickly dropped into water. The thermal shock resistance of the retention container material is an important parameter for real applications. Based on the results presented in **Section 3**, the C/SiC composite exhibits a good thermal shock resistance. The C/SiC composite retains a high strength after the thermal shock, which ensures that it can withstand the posttreatment, separation, and transportation processes after cooling.

The C/SiC composite has a thermal conductivity of 11–20 W/mK in the range from room temperature to 1800°C; thus, it can continuously conduct the corium internal heat to the cooling medium. However, the thermal conductivity of the C/SiC composite is still lower than that of most metals. Thus, the thickness of the C/SiC container should be appropriately reduced to be within 3 mm, which can effectively promote the heat transfer. In addition, the size of the C/SiC container can be reduced in order to effectively increase the heat transfer area. It is suggested that the diameter of the C/SiC spherical container should be ~100 mm. This size would not only benefit the heat conduction but also reduce the costs related to the fabrication of C/SiC containers.

The failure of the C/SiC material caused by the corrosion due to corium at high temperatures is the most concerning issue. Through this study, it can be seen that C/SiC has a good corrosion resistance to corium at high temperatures. SiC usually only reacts with Zr in corium to form Zr_2Si and ZrC condensed products, which can effectively prevent the further reaction between corium and SiC. The formation of CO from the reaction between carbide and the melt was initially thought to be an issue. However, the thermodynamic analysis and kinetic investigations show that the amount of CO formed in the system can be ignored. A large amount of C in the carbides is consumed by Zr to form stable ZrC, preventing the formation of CO.

SiC coatings play a key role in the application of C/SiC composites to detention containers. Crack-free and pore-free SiC coatings not only can ensure the thermochemical stability of the composite but are also beneficial to the mechanical and thermal conductivity of C/SiC. According to the kinetic results, a 100–150-μm-thick coating can meet the corrosion resistance requirements. This thickness is the most commonly adopted thickness for C/SiC composite coatings. It is recommended to add SiC whiskers or nanowires in the preparation process to improve the crack resistance of the SiC coating and avoid coating cracking during usage.

6 CONCLUSION

The results show that the C/SiC ceramic composite can meet the design criteria of the CGC corium retention container, and it is impossible to cause a carbon reaction disaster through the failure of the composite SiC deposition layer.

DATA AVAILABILITY STATEMENT

The datasets presented in this article are not readily available because; The data came from a joint research. Requests to access the datasets should be directed to doc.hanxu@gmail.com.

AUTHOR CONTRIBUTIONS

XH and JX conceived of the presented idea with some key advice from YY and WM. XH and LZ proposed the prototype design of the CGC. XH, HW, XZ and YW carried out the experiment. HW and XZ analyzed the raw experimental data and performed the calculation related.

REFERENCES

Angelici Avincola, V., Grosse, M., Stegmaier, U., Steinbrueck, M., and Seifert, H. J. (2015). Oxidation at High Temperatures in Steam Atmosphere and Quench of Silicon Carbide Composites for Nuclear Application. *Nucl. Eng. Des.* 295, 468–478. doi:10.1016/j.nucengdes.2015.10.002

Braun, J., Sauder, C., Rouillard, F., and Balbaud-Célérier, F. (2021). Mechanical Behavior of SiC/SiC Composites after Exposure in High Temperature Liquid Sodium for Sodium Fast Reactors Applications. *J. Nucl. Mater.* 546, 152743. doi:10.1016/j.jnucmat.2020.152743

Fischer, M. (2004). The Severe Accident Mitigation Concept and the Design Measures for Core Melt Retention of the European Pressurized Reactor (EPR). *Nucl. Eng. Des.* 230 (1), 169–180. doi:10.1016/j.nucengdes.2003.11.034

Han, X., Jing, C., Zhu, C., Wang, Y., Li, J., Yuan, Y., et al. (2018). Research on New Conceptual Design of PWR Core Catcher. *J. Nucl. Power Eng.* 39, 102–105. doi:10.13832/j.jnpe.2018.01.0102

Katoh, Y., Snead, L. L., Szlufarska, I., and Weber, W. J. (2012). Radiation Effects in SiC for Nuclear Structural Applications. *Curr. Opin. Solid State. Mater. Sci.* 16 (3), 143–152. doi:10.1016/j.cossms.2012.03.005

Khabensky, V. B., Granovsky, V. S., Bechta, S. V., and Gusarov, V. V. (2009). Severe Accident Management Concept of the VVER-1000 and the Justification of Corium Retention in a crucible-type Core Catcher. *Nucl. Eng. Tech.* 41 (5), 561–574. doi:10.5516/net.2009.41.5.561

Kolev, N. T. (2001). "SWR 1000 Severe Accident Control the Rough In-Vessel Melt Retention by External Cooling," in Proc. of ICONE9, 9th Int. Conf. on Nucl. Eng, April 2-12, 2001, Nice, France (Nice, France: Framatome Advanced Nuclear Power, NDS1), 8–12.

Kukhtevich, I. V., Bezlepkin, V. V., Rogov, M., Novak, V., and Granovskii, V. (2001). The Concept of Localization of the Corium in the Ex-Vessel Stage of a Severe Accident at a Nuclear Power Station with a VVER-1000 Reactor. *Therm. Eng.* 48 (9), 699–706.

Lippmann, W., Knorr, J., Nöring, R., and Umbreit, M. (2001). Investigation of the Use of Ceramic Materials in Innovative Light Water Reactor – Fuel Rod Concepts. *Nucl. Eng. Des.* 205 (1-2), 13–22. doi:10.1016/s0029-5493(00)00369-1

Patnaik, S., Lopes, D. A., Spencer, B. W., Besmann, T. M., Roberts, E., and Knight, T. W. (2021). Evaluation of Ceria as a Surrogate Material for UO2 in Experiments on Fuel Cracking Driven by Resistive Heating. *Nucl. Eng. Des.* 384, 111482. doi:10.1016/j.nucengdes.2021.111482

Qiu, B., Wang, J., Deng, Y., Wang, M., Wu, Y., and Qiu, S. Z. (2020). A Review on Thermohydraulic and Mechanical-Physical Properties of SiC, FeCrAl and Ti3SiC2 for ATF Cladding. *Nucl. Eng. Tech.* 52 (1), 1–13. doi:10.1016/j.net.2019.07.030

Sidorov, A. S., Nedorezov, A. B., Rogov, M. F., Novak, V. P., and Kukhtevich, I. V. (2001). The Device for Core Melt Localization at the Tyan'van Nuclear Power Station with a VVER-1000 Reactor. *Therm. Eng.* 48 (9), 707–712.

Zinkle, S. J., Terrani, K. A., Gehin, J. C., Ott, L. J., and Snead, L. L. (2014). Accident Tolerant Fuels for LWRs: A Perspective. *J. Nucl. Mater.* 448 (1-3), 374–379. doi:10.1016/j.jnucmat.2013.12.005

Conflict of Interest: Authors XH, JX, WM, YY and XZ were employed by the company China Nuclear Power Engineering Co Ltd.

The remaining author declares that the research was conducted in the absence of any commercial or financial relationships that could be construed as a potential conflict of interest.

frontiers | Frontiers in Energy Research

ORIGINAL RESEARCH
published: 11 May 2022
doi: 10.3389/fenrg.2022.892406

Density Measurement of Molten Drop With Aerodynamic Levitation and Laser Heating

Yaopeng Gong[1,2], *Li Zhang*[2], *Yidan Yuan*[2]*, *Qiang Guo*[2], *Weimin Ma*[3] *and Shanfang Huang*[1]

[1]Department of Engineering Physics, Tsinghua University, Beijing, China, [2]China Nuclear Power Engineering Co., Ltd (CNPE), Beijing, China, [3]Royal Institute of Technology (KTH), Stockholm, Sweden

Thermophysical properties of molten core materials (corium) are necessary input parameters of models and computer codes which predict the severe accident progression in light water reactors. The corium contains the components of UO_2, ZrO_2, Zr and Fe. The measurement of molten corium properties is a very challenging task due to high melting points of corium which can reach 3000 K. This paper presents a density measurement system for a molten drop based on techniques of aerodynamic levitation, laser heating and image processing. A sphere of alumina was firstly levitated by argon gas flow above a conical converging-diverging nozzle. The sphere was then heated up and melted into a liquid drop by a laser beam. The shape of the drop was recorded by a high-speed camera, and the density was calculated from image processing.

Keywords: molten drop, density measurement, aerodynamic levitation, laser heating, image processing

OPEN ACCESS

Edited by:
Yapei Zhang,
Xi'an Jiaotong University, China

Reviewed by:
Yingchun Wu,
Zhejiang University, China
Luteng Zhang,
Chongqing University, China

****Correspondence:***
Yidan Yuan
yidanyuan2010@aliyun.com

Specialty section:
This article was submitted to Nuclear Energy, a section of the journal Frontiers in Energy Research

Received: *09 March 2022*
Accepted: *20 April 2022*
Published: *11 May 2022*

Citation:
Gong Y, Zhang L, Yuan Y, Guo Q, Ma W and Huang S (2022) Density Measurement of Molten Drop With Aerodynamic Levitation and Laser Heating. Front. Energy Res. 10:892406. doi: 10.3389/fenrg.2022.892406

INTRODUCTION

Thermophysical properties of core melt (corium) are basic input parameters for physical models and computer codes which are developed to simulate severe accident phenomena of risk importance in light water reactors (Sehgal, 2011). Thermophysical properties of corium are also needed to assess the effectiveness of mitigation strategies, such as in-vessel (Kymäläinen et al., 1997) and ex-vessel (Fischer, 2004) melt retentions, which are preferred in advanced light water reactors. Due to high temperatures, molten corium properties are scarce, and extrapolation data (even from solid state) of corium have been used so far.

The corium contains the components of UO_2, ZrO_2, Zr and Fe, among which the molten oxides can reach the temperature of around 3000 K. Conventional measurement methods for thermophysical properties of molten oxides include the sessile drop method (Stalder et al., 2010) and the rotating bob method (Abalin et al., 2000), but both are hampered by interactions between sample and substrate at high temperatures. Thus, contactless methods, such as electromagnetic levitation (EML) (Bojarevics and Pericleous, 2003; Etay et al., 2008; Mohr et al., 2019), electrostatic levitation (ESL) (Rhim et al., 1999; Paradis et al., 2004; Paradis and Ishikawa, 2005; Tamaru et al., 2018), acoustic levitation (AL) (Trinh et al., 1988; Bayazitoglu and Mitchell, 1995; Ansari Hosseinzadeh and Holt, 2017; Kremer et al., 2018), gas-film levitation (GFL) (Barbé et al., 1999; Haumesser et al., 2002; Grishchenko and Piluso, 2011), aerodynamic levitation (ADL) (Granier and Heurtault, 1983; Coutures et al., 1994; Glorieux et al., 1999; Millot et al., 2008; Langstaff et al., 2013; Benmore and Weber, 2017; Kondo et al., 2019) and hybrid levitation (Weber et al., 1994; Ishikawa et al., 2006), are developed for measurements of material samples above 1800 K to avoid sample-substrate interactions.

In the EML method, an inhomogeneous electromagnetic field is generated in a coil and the sample with eddy currents is levitated via Lorentz force. Since the electromagnetic field is used for both levitation and heating of the sample, metallic materials with significant electrical conductivities are applicable in this method. This method is generally implemented under microgravity for viscosity measurement and under normal gravity for surface tension measurement since viscosity measurement is more sensitive to gravity (Mohr et al., 2019). The main drawback is that the interactions between the electromagnetic field and induced current in liquid metal disturb the measurements of surface tension and viscosity (Bojarevics and Pericleous, 2003; Etay et al., 2008).

For the ESL method, a charged sample is levitated by an electrostatic field via Coulomb force. Metallic materials are chargeable (Paradis and Ishikawa, 2005) while oxidic materials are impossible to be charged at low temperatures through hot electron effects and very time-consuming through UV photoelectric effects (Paradis et al., 2014). Besides, the charged surface may change the shape of the drop, which complicates the measurements of surface tension and viscosity, even though heating and levitation are separated.

Electric conductivity of a sample is not required for the AL method, and stable suspension of even irregular objects can be achieved in a well-designed acoustic field (Andrade et al., 2018). The acoustic force is used to counteract gravity in gas. However, the axial force is several times greater than the radial force, which results in large deformation of the molten sample. Besides, a high-density sample requires a greater acoustic intensity which may lead to strong surface oscillations causing droplet atomization and fragmentation.

For the GFL method, inert gas flows through a porous membrane to levitate the sample of a fairly large mass (up to 200 g for an oxide sample). The porous membrane with a concave is designed to guarantee levitation stability. Various empirical correlations are used to correct the influence of the large sample deformation, which results in lower measurement accuracy (Grishchenko and Piluso, 2011).

For the ADL method, the sample is levitated by gas in a conical converging-diverging nozzle proposed by Nordine (Nordine and Atkins, 1982) in which Bernouilli force stabilizes the sample to the nozzle axis. The ADL method relaxes the requirements of materials and only volatile materials are inapplicable. Many pioneering works on ADL have been focused on structural studies of liquids and glasses combined with Nuclear Magnetic Resonance and synchrotron radiation techniques (Benmore and Weber, 2017). The ADL method has the potential applied in the studies on thermophysical properties, glass forming and oxidation/reduction reactions due to its convenience, simplicity and low cost. Molten sample motion induced by gas flow has an impact on measurement, which is a technical difficulty needed to solve.

The hybrid levitation method combines two contactless methods such as aero-acoustic levitation (Weber et al., 1994) and electrostatic-aerodynamic levitation (Ishikawa et al., 2006) for better levitation stability. The levitation force is mainly provided by gas flow, and the acoustic or Lorentz force is used for levitation stability and position control. The high stability is obtained at the expenses of complex devices and high costs.

Since the melting points of corium components are so high that the container wall substrate is prone to interact with the molten sample, making the contact methods unsuitable for the property measurements of corium components. Among the contactless methods, EML and ESL are only applicable for metallic materials with good electric conductivity, while AL is difficult to provide both sufficient levitation force and stability at high temperatures. The GFL method has low stability at very high temperatures up to 3000 K. Therefore, the ADL method is selected in the present study to measure the properties of molten corium components due to its low requirements of sample materials, simplicity and low cost.

This paper firstly presents the experimental setup designed to measure the thermophysical properties of corium components. Secondly, the principles of density measurement and the commissioning of the setup are described. Alumina as the simulant of UO_2/ZrO_2 is employed in the commissioning which includes sample preparation, high-speed camera calibration and levitation stabilization. Finally, density measurement results are provided.

EXPERIMENTAL SETUP

The experimental setup, named ALSEE (Aerodynamic Levitation-laSEr hEating installation for melt properties), is illustrated in **Figure 1**. It is designed for the measurements of thermophysical properties of molten corium components (UO_2/ZrO_2/Zr/Fe and their mixtures), including density, surface tension and viscosity. The ALSEE test facility is composed of an aerodynamic levitation system, laser heating system, image recording system, temperature measurement system, acoustic excitation system and data acquisition system (DAS). The first four systems and DAS have been built, which are sufficient for density measurement. The acoustic excitation system under installation is intended for the measurements of surface tension and viscosity.

Aerodynamic Levitation System

The aerodynamic levitation system consists of an aerodynamic levitator, a gas flow controller (KOFLOC EX250SC), and a 2D optical micrometer (Keyence TM-3000). Located in the center of the levitator is a conical converging-diverging nozzle to levitate a sample sphere of 2–3 mm in diameter. The argon gas stored in a high-pressure gas tank is depressurized to about 200 KPa and reaches the nozzle for sample levitation. The gas flow controller enables fine regulations of argon gas flowrate. To monitor and improve the sample levitation stability, a 2D optical micrometer is placed on the horizontal side of the sample sphere to measure the levitation height. The argon gas flowrate can be accordingly adjusted to improve the stability.

Laser Heating System

The laser heating system consists of two CO_2 laser devices (Synrad ti-100HS) and their laser-beam delivery optics. The two 100 W CO_2 laser devices controlled by a laser controller

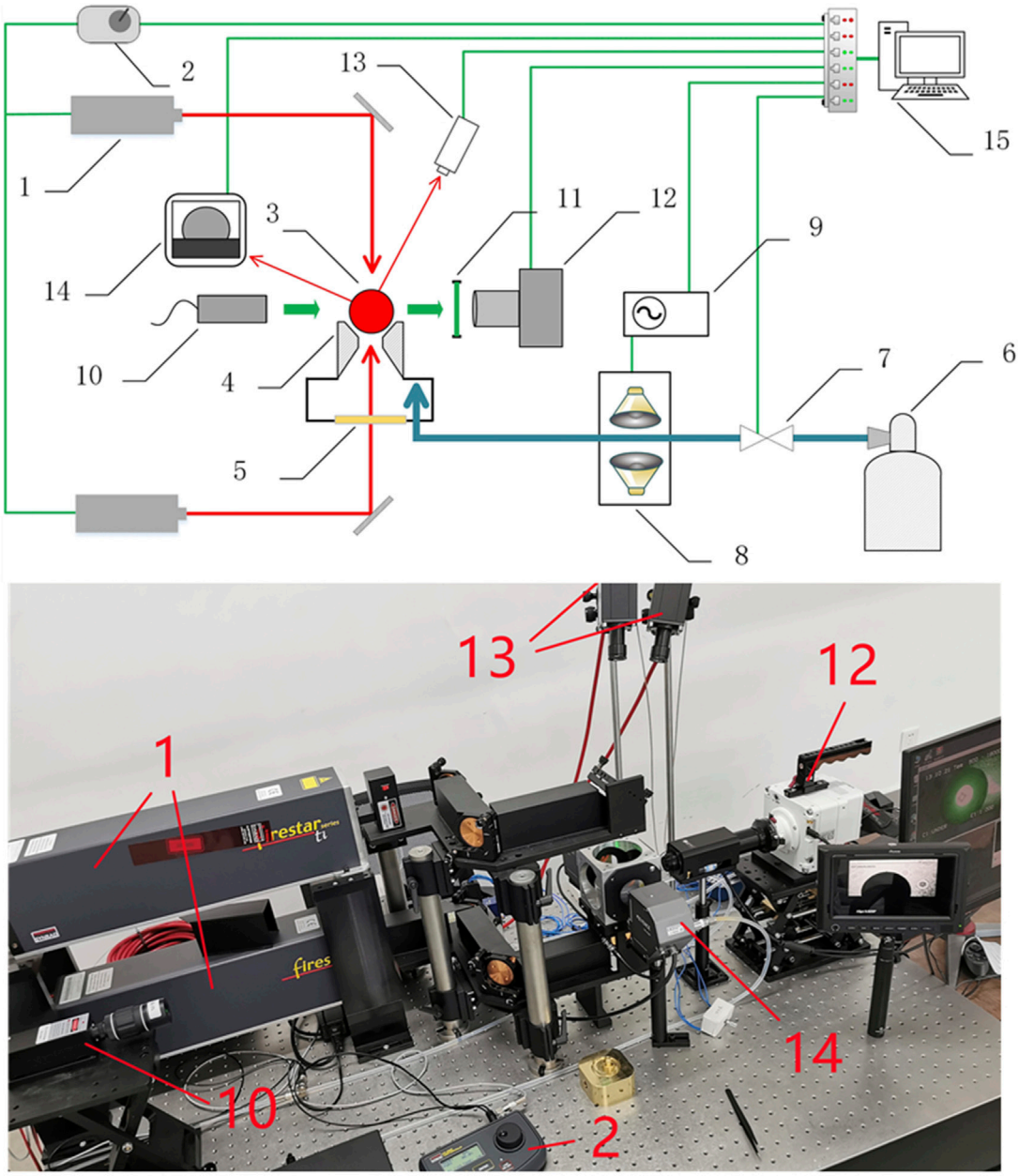

FIGURE 1 | Schematic view and picture of the ALSEE experimental setup: 1- CO_2 laser, 2- laser controller, 3- levitated sample, 4- conical converging-diverging nozzle, 5- ZnSe window, 6- argon gas tank, 7- gas flow controller, 8- loudspeakers, 9- waveform generator, 10- backlighting laser, 11- narrow-band filter, 12- high-speed camera, 13- bichromatic pyrometers, 14- 2D optical micrometer, 15- data acquisition system.

(Synrad UC 2000) are placed as such that they heat both the lower and the upper sides of the sample (see **Figure 1**). Each device emits a laser beam with a wavelength of 10.6 μm and a diameter of 2 mm. Two laser beams are guided to the sample via flat mirrors and focusing lenses. Since the lower laser beam passes through the gas channel, a ZnSe window transparent to the 10.6 μm laser beam is installed under the levitator.

High stability (2%) of the laser output power is necessary to the fine temperature regulations, and the heating efficiency is as high as practically achievable. The laser beam with the wavelength of 10.6 μm is favorable to absorption of oxidic materials. Two waveplates are inserted into the optical paths to convert linearly polarized beams into circularly polarized beams.

Image Recording System

The image recording system consists of a high-speed camera (Phantom VEO440L), a zoom lens (Movetem MAZ12.0×LZ), a backlighting laser (CNI MGL-III-532) and a narrow-band filter.

The high-speed camera equipped with the zoom lens has a magnification of 14 and a working distance of 85 mm, which makes full use of camera pixels.

The backlighting laser is employed in a shadow photography system in which the backlighting laser with a beam expander is positioned on the opposite side of the high-speed camera with the narrow-band filter installed in front of the camera lens. The shutter speed of the camera is therefore independent of temperature of the sample, and sharp edges of the sample can be obtained from the images.

Since the shadow photography system has not been ready yet, the present study uses conventional photography in which the direct images of the incandescent sample at high temperatures are recorded. The higher the temperature, the brighter the sample. This means the shutter speed of the camera has to be adjusted to obtain reasonable images at different temperatures.

Temperature Measurement System

The sample temperature is measured with two bichromatic pyrometers (Sensortherm H311), one with the measuring range of 1173–2073 K (0.75–0.93 μm and 0.93–1.1 μm), and the other 1873–3573 K (0.78 and 0.99 μm) with the measurement uncertainty of 0.5%. A programmable temperature controller (Sensortherm Regulus RD) integrates the temperature ranges of these two pyrometers and is connected to the laser controller, achieving fast temperature measurement and control. When the molten sample is heated by lasers which are indirectly controlled by the temperature controller, the temperature fluctuation is below 10 K. The pyrometers measure the spectral radiance of the sample at two selected wavelengths (signals are collected by two separate channels, respectively) and calculate the ratio. The influence of the argon gas around the sample is negligible since the ratio is almost unchanged even though both the two signals are changed.

Acoustic Excitation System

The acoustic excitation system consists of a waveform generator and a group of loudspeakers. The waveform generator generates sinusoidal voltages of various frequencies which are transmitted to the loudspeakers. The loudspeakers are coupled to the argon gas pipeline. Therefore, the sound wave generated from the loudspeakers can be imposed on the molten sample through the argon gas. The molten sample is excited by the sound wave and the surface begins to vibrate. The resonance frequency can be found by measuring the vibration amplitude of the molten sample at different frequencies, and then the surface tension can be derived. Viscosity is finally calculated from the decay constant when loudspeakers working at the resonance frequency stop and the damped oscillations of the molten sample start. The acoustic excitation system is under installation and intended for measurements of surface tension and viscosity.

DENSITY MEASUREMENT

Measurement Principles

The density is the ratio of mass to volume of the sample. The mass of the sample is measured with an electronic balance and the volume is obtained from the images recorded by the high-speed camera. In the beginning, a sample is levitated above the conical nozzle and heated by the upper laser. Then the sample melts into a liquid drop. The images of the sample are recorded by the camera, and image processing is performed frame by frame with a software program written in MATLAB. The surface profile of the drop is determined through an image edge detection technique. Since the drop appears ellipsoidal, its center as well as semi-major axis and semi-minor axis are determined by an ellipse fitting algorithm. Based on these data, the density is calculated with the following equation:

$$\rho = \frac{3M}{4\pi r_a^2 r_b} \tag{1}$$

where ρ is the sample density, M the sample mass, r_a the semi-major axis, and r_b the semi-minor axis.

Image Edge Detection

Previous studies have shown that the Canny edge detection algorithm generally performs better than other operators such as Sobel, Robert, Prewitt, Laplacian, and Laplace of Gaussian (Maini and Aggarwal, 2009). A common Canny edge detection algorithm includes the following four steps: 1) a Gaussian filter is used to smooth the original image which eliminates the noise; 2) the edges including gradient intensity and gradient direction of the image are calculated by the first-order difference method with the Canny operator; 3) the Non-Maxima Suppression is performed so that only the points with the largest local gradient are retained; and 4) the double threshold algorithm is used to detect and connect the edges. The *edge* function using the Canny operator in MATLAB is preferred because it improves the Canny operator and threshold value.

Ellipse Fitting

In this paper, least-squares fitting based on algebraic distances is performed using the pseudo inverse technique (Zhang, 1997). A 2-D elliptic equation can be described as follows:

$$Q(x, y) = Ax^2 + 2Bxy + Cy^2 + 2Dx + 2Ey + F = 0 \tag{2}$$

A common practice is to minimize the algebraic distance, which means to minimize the following function:

$$\psi = \sum_{i=1}^{n} Q^2(x_i, y_i) \tag{3}$$

When the normalization of $A + C = 1$ is considered, the elliptic equation becomes:

$$Q(x, y) = A(x^2 - y^2) + 2Bxy + 2Dx + 2Ey + F + y^2 = 0 \tag{4}$$

Therefore, the elliptic equation can be described by a vector p:

$$\mathrm{p} = [A, B, D, E, F]^T \tag{5}$$

For a point (x_i, y_i) on the ellipse, the following vectors are constructed:

$$a_i = [x_i^2 - y_i^2, 2x_i y_i, 2x_i, 2y_i, 1]^T \tag{6}$$

$$b_i = -y_i^2 \tag{7}$$

Then, the elliptic equation becomes:

$$Q(x_i, y_i) = a_i^T p - b_i = 0 \tag{8}$$

Given n points, the following matrix yields:

$$M = [a_1, a_2, \ldots .a_n]^T \tag{9}$$

$$q = [b_1, b_2, \ldots .b_n]^T \tag{10}$$

The function to minimize becomes:

$$\psi(p) = (Mp - q)^T (Mp - q) \tag{11}$$

Obtaining its partial derivative with respect to p and setting it to zero yield:

$$2M^T (Mp - q) = 0 \tag{12}$$

The solution is:

$$p = (M^T M)^{-1} M^T q \tag{13}$$

Therefore, elliptical parameters including *A, B, C, D, E,* and *F* are all known. Finally, the semi-major and semi-minor axes are determined as follows:

$$r_a = \sqrt{\frac{2(AE^2 + CD^2 + FB^2 - 2BDE - ACF)}{(B^2 - AC)\left[\sqrt{(A-C)^2 + 4B^2} - (A+C)\right]}} \tag{14}$$

$$r_b = \sqrt{\frac{2(AE^2 + CD^2 + FB^2 - 2BDE - ACF)}{(B^2 - AC)\left[-\sqrt{(A-C)^2 + 4B^2} - (A+C)\right]}} \tag{15}$$

Measurement Accuracy

The measurement uncertainty of density mainly comes from uncertainties of the sample mass and volume according to **Eq. 1**. Mass is determined by the electronic balance which has the uncertainty of 0.05 mg for a sample of 19.69 mg. Since the semi-major and semi-minor axes of the ellipsoidal sample are obtained from image processing of the sample images, the measurement uncertainties of the semi-major and semi-minor axes can be considered, which are about 4.4 pixels within 690 pixels and 3.5 pixels within 670 pixels. According to **Eq. 1**, the accuracy of density measurement is 1.40%.

Some uncertainties in the measurement are not quantifiable such as the distortion of the photography of an incandescent object and the departure from the ellipsoidal assumption. The first influencing factor can be resolved through the shadowgraphy which will be implemented. However, caution must be paid to the possible deviation from an ellipsoidal shape, since the ellipsoidal shape may be affected not only by the joint forces of gravity and argon gas flow, but also by the temperature gradient inside the sample.

EXPERIMENTAL RESULTS AND DISCUSSION

Sample Preparation

Powders or irregular objects can be melted into a nearly spherical sample by laser heating in a device called the laser hearth melter. The laser hearth melter is made of copper and the structure is shown in **Figure 2**. Oxide samples with a diameter of 2–3 mm can be made by the laser hearth melter. According to previous studies, the induced impurities are negligible (Richard Weber et al., 1996).

About 20 mg of alumina (99.9% purity) was put in the concave of the laser hearth melter and was heated into a liquid drop by the upper laser. A nearly spherical shape was formed due to surface tension. After the laser was turned off, the sample was solidified and homogenized by turning it over and remelting it. The alumina samples prepared by the laser hearth melter are also shown in **Figure 2**. When the laser power is gradually reduced to zero, the alumina drop can crystallize to form a transparent bead.

High-Speed Camera Calibration

The sample diameter determined by the image processing is represented by pixels, so it is necessary to convert pixels to standard length units. Standard stainless-steel spheres with diameters of 2.0 and 2.5 mm were used in the calibration where the standard spheres were loaded on the nozzle and photographed by the camera. To improve measurement accuracy, the camera was set up with the maximum resolution of 2,560 × 1,600 pixels. The calibration for the relationship of pixel with micrometer given in **Table 1** is obtained through the comparison of the pixels with accurate diameters of the standard spheres.

Levitation Stability

An alumina sample was firstly placed on the conical nozzle and levitated by argon gas flow. When the argon gas flowrate was about 0.4 L/min, there formed a gap of about 50 μm between the sample and the nozzle wall at ambient temperature without laser heating. The sample position fluctuation was monitored by the 2-D optical micrometer. When the sample was heated to 3333 K, the sample position fluctuation was determined by image processing results of the images recorded by the high-speed camera since the micrometer couldnot work when the sample was highly luminous. It turned out that the sample position fluctuation was below 10 μm at 298 K and 3333 K, as depicted in **Figure 3**. Though levitation instability was found when the sample was heated and melting, levitation stability resumed after the sample was entirely molten, i.e., after the formation of a drop at a prescribed temperature. Compared with the position fluctuations of 100 μm in an ESL experiment (Tamaru et al., 2018) and 40 μm in an ADL experiment (Krishnan et al., 1997), levitation stability in the present study is improved with the optimized nozzle.

At ambient temperature, the levitation is stable since the argon gas flow in the conical nozzle is laminar. When the upper laser is turned on for heating, the sample position fluctuation can reach about 200 μm since the thermal conductivity of the solid-state alumina sample is small, resulting in a large asymmetric temperature gradient. Therefore, the argon temperature field around the sample surface is also asymmetric which deteriorated the levitation stability.

During the melting of an alumina sample as shown in **Figure 4**, the solid and liquid parts coexist. The irregular shape of the melting sample will change the mass center,

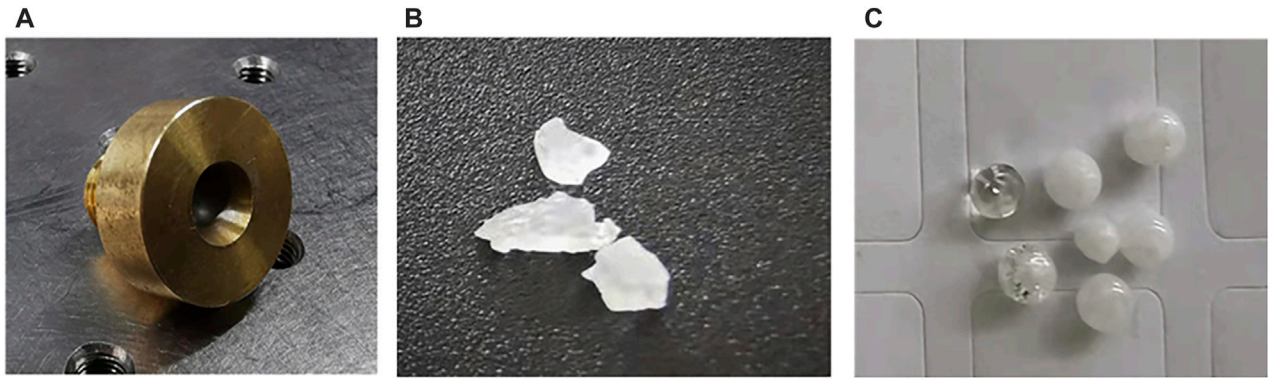

FIGURE 2 | Preparation of alumina samples: **(A)** laser hearth melter. **(B)** irregular alumina objects. **(C)** alumina samples prepared by the laser hearth melter.

TABLE 1 | High-speed camera calibration.

Material	Diameter (mm)	Diameter in pixels (pixel)	Camera calibration (μm/pixel)
Stainless-steel	2.0	1,167.14	1.7136
Stainless-steel	2.0	1,168.34	1.7118
Stainless-steel	2.5	1,458.81	1.7137
Stainless-steel	2.5	1,458.52	1.7141
	Average		1.7133

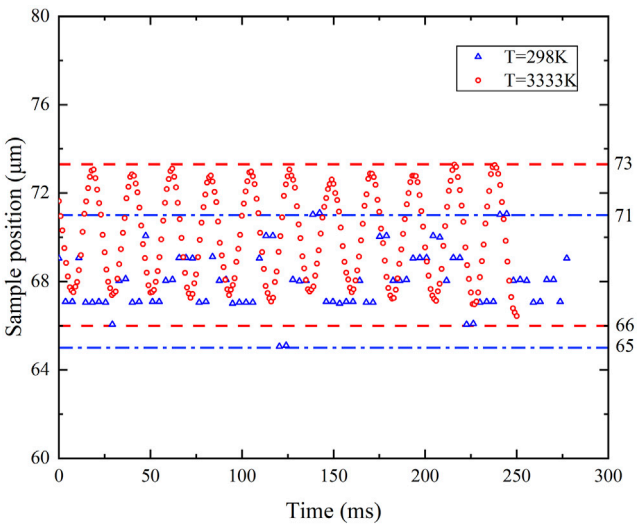

FIGURE 3 | Sample fluctuating upward and downward the equilibrium position in 6 μm at 298 K and 7 μm at 3333 K (the y-axis is offset for zoom-in view).

weakening levitation stability. When the sample starts to melt from the upper part to the lower part, the melting process is potentially stable, since the newly melted liquid part with lower temperature and higher density stays at the solid-liquid interface. If the sample is heated by the lower laser, it will start to melt from the lower part to the upper part, the newly melted liquid part with lower temperature and higher density will move to the bottom. The flow inside the liquid part will deteriorate the stability. Therefore, only the upper laser is used for sample melting to ensure levitation stability.

When an alumina sphere is entirely molten and the temperature is above 2300 K, the levitation of the drop is stable. This can be related to the increase in thermal conductivity and improvement of temperature uniformity. Besides, due to the decrease in density and increase in viscosity of argon gas around the sample, Reynolds number is less than 1/6 of that at ambient temperature which further improves the stability (Paradis et al., 1996).

Density of Alumina

Density measurement was conducted in the cooling process of the alumina sample after the sample was levitated, heated to 3333 K and stabilized for seconds. The cooling process was induced by the sudden shutdown of the heating laser. The camera was set up to record at 1,000 fps with a resolution of 2,560 × 1,600 pixels. The temperature was synchronously recorded by pyrometers.

The temperature history of the cooling process and sample images at different stages are shown in **Figure 5**. A sudden temperature rise is found while the recalescence phenomenon is recorded when the sample solidifies. In the sample images, the ellipse edge, major axis and minor axis determined by image processing are all plotted. The whole morphology of the molten drop is difficult to obtain due to the nozzle shielding. Therefore, it is difficult to evaluate the joint effects of gravity

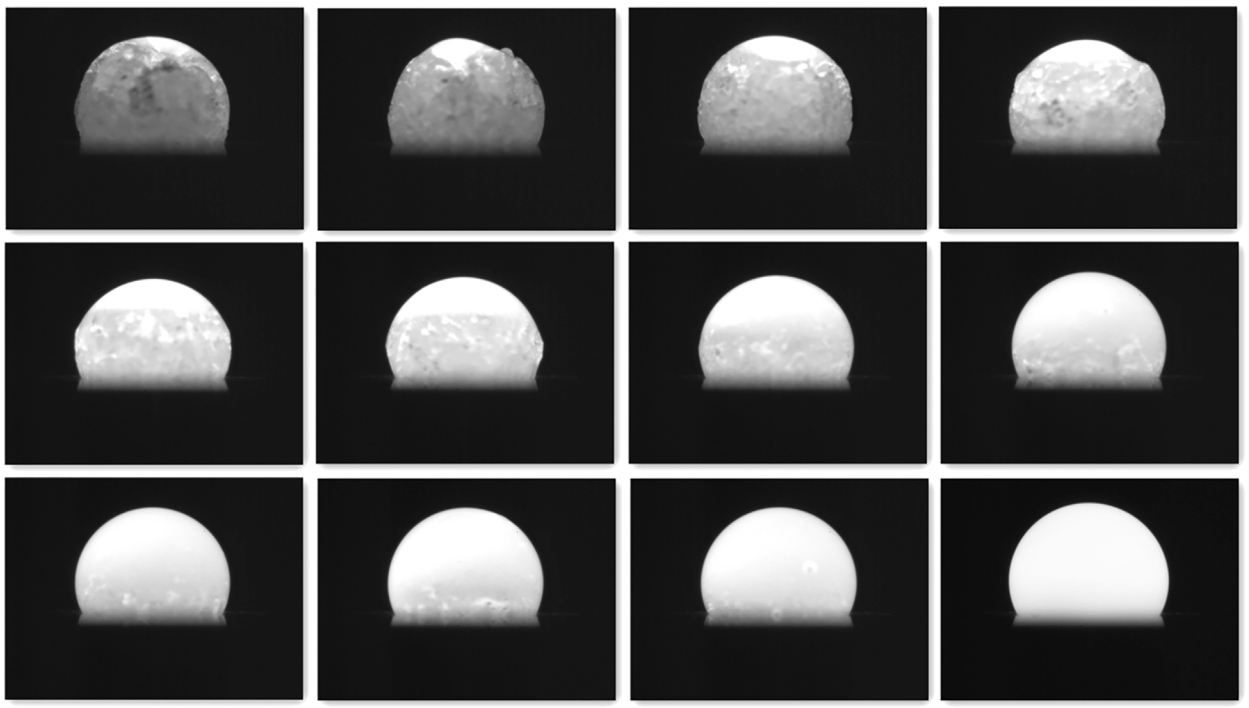

FIGURE 4 | Melting process of the alumina sample heated by the upper laser. Lower part of the sample is hidden by the conical nozzle.

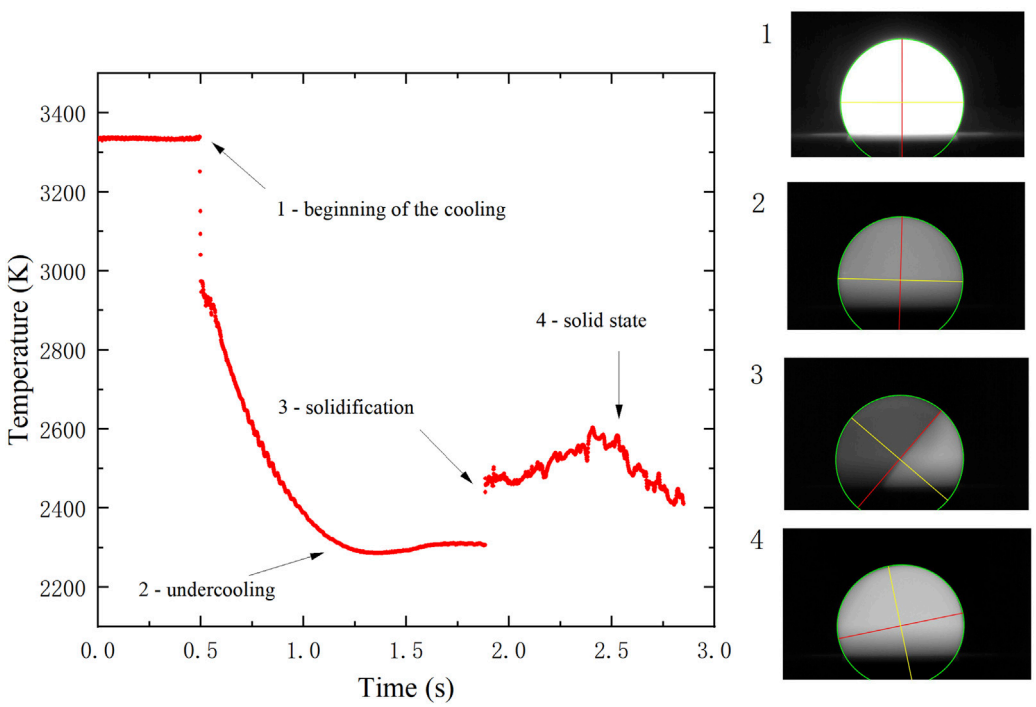

FIGURE 5 | Temperature history and images of an alumina sample during the cooling process induced by shutdown of the heating laser.

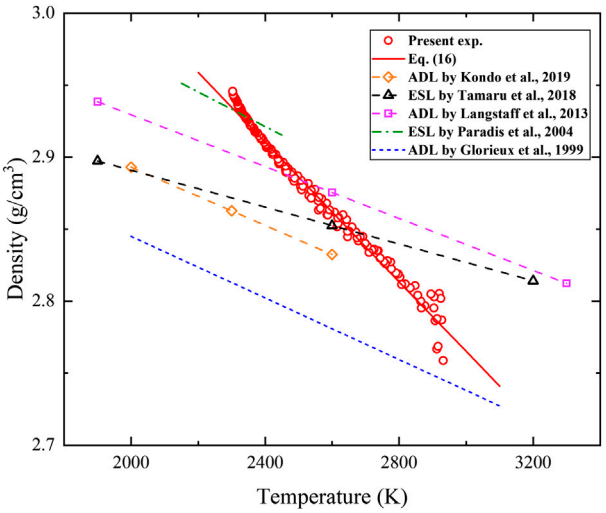

FIGURE 6 | Temperature-dependent density of liquid alumina. Density and temperature data of the present experiment have error bars of 1.40% and 0.5% respectively.

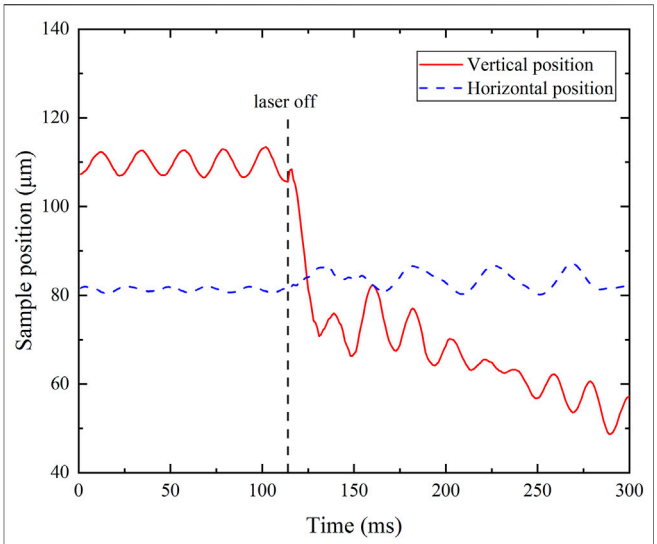

FIGURE 7 | Position change after turning the upper laser off (the y-axis is offset for zoom-in view).

TABLE 2 | Liquid alumina density in literatures.

Density at 2327 K g/cm^3	Temperature coeff. 10–3 g/(cm^3·K)	Temperature K	Measurement technique	References
2.93	−0.242	2,300–3,000	Aerodynamic levitation	Measured in present exp
2.86	−0.101	2000–2,600	Aerodynamic levitation	Kondo et al. (2019)
2.87	−-0.064	1913–3,139	Electrostatic levitation	Tamaru et al. (2018)
2.81	−0.074	1732–2,597	Electrostatic levitation	Tamaru et al. (2018)
2.9	−0.09	1900–3,240	Aerodynamic levitation	Langstaff et al. (2013)
2.93	−0.12	2,175–2,435	Electrostatic levitation	Paradis et al. (2004)
2.81	−0.107	2000–3,100	Aerodynamic levitation	Glorieux et al. (1999)
2.71	−0.0678	2000–3,275	Aerodynamic levitation	Coutures et al. (1994)
2.80	−0.151	2,327–3,210	Aerodynamic levitation	Coutures et al. (1994)
3.06	-	2,327	Max press gas bubble	Ikemiya et al. (1993)
2.72	−0.28	2,323–2,965	Aerodynamic levitation	Granier and Heurtault (1983)
3.06	−0.965	2,323–3,023	Max press gas bubble	Shpilrain and Yakimovich (1973)
2.98	−1.15	2,325–2,775	Max press gas bubble	Elyutin et al. (1973)
3.03	−0.752	2,323–2,673	Pendant drop	Rasmussen (1972)
3.04	−1.15	2,323–2,828	Archimedean	Mitin and Nagabin,(1970)
2.69	−0.79	2,320–3,100	Sessile drop	Zubarev et al. (1969)
3.05	−1.127	2,375–2,625	Pendant drop	Kirshenbaum and Cahill (1960)
3.05	-	2,327	Pendant drop	Kozakevitch (1960)
2.97	-	2,327	Pendant drop	Kingery (1959)
2.55	-	2,327	Pendant drop	Wartenberg et al. (1936)

and argon gas flow shearing on the drop morphology. Nevertheless, the sample images show that the visible part of the liquid drop agrees well with the ellipsoidal assumption. Therefore, it is reliable to calculate the drop volume based on the ellipsoidal assumption.

The sample mass before and after the experiment is measured to be 19.82 and 19.69 mg. This is because the heating of the sample takes a few minutes, and the highest temperature 3333 K has exceeded the boiling point of alumina (3240 K), resulting in large evaporation and mass loss before the cooling process. On the other hand, since the cooling process takes less than 5 s, the mass loss during this period is negligible. Hence, the mass of 19.69 mg is used to calculate the density.

The temperature-dependent density measured in the present study is depicted in **Figure 6**, where the data measured by the ADL and ESL methods (Glorieux et al., 1999; Paradis et al., 2004; Langstaff et al., 2013; Tamaru et al., 2018; Kondo et al., 2019) are also plotted for comparison. More related data measured by various contact and contactless methods are given in **Table 2**. The relationship between density and temperature for the

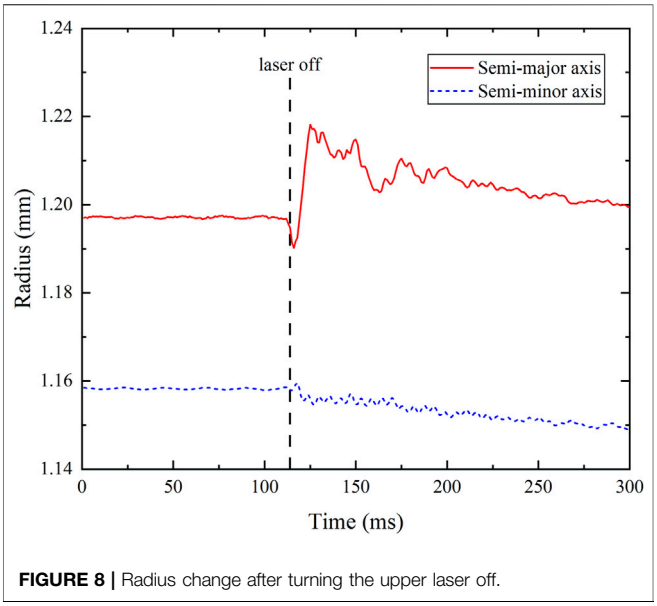

FIGURE 8 | Radius change after turning the upper laser off.

temperature range of 2300 K < T < 3000 K obtained in the present study can be fitted by the following equation:

$$\rho = -(2.421 \pm 0.089) \times 10^{-4} \times T + (3.493 \pm 0.023)\ (g/cm^3) \quad (16)$$

Large fluctuations in the density measurement are found at the beginning of the cooling process. This is because the rapid thermal transient upon the shutdown of the laser results in a sudden position change as shown in **Figure 7**. The sample is positioned well in the horizontal direction, but moves down about 40 μm in 15 ms since the sample volume decreases with reducing temperature. The argon gas flow induced velocity and pressure changes quickly, producing disturbance of the sample surfaces as shown in **Figure 8**. The downward displacement may firstly elongate and then flatten the alumina drop, resulting in the decrease and then increase of the semi-major axis. The disturbance gradually disappears when a stable levitation is successfully re-established. Therefore, measured data between 3000 and 3333 K is not used due to poor accuracy.

When the temperature is lower, alumina density is overestimated with a fixed shutter time of the camera, which is a common phenomenon for the conventional photography of an incandescent object. In the image edge detection code, the edge of the liquid drop is determined by the gradient of gray value in the sample images. A threshold is set in the Canny algorithm to recognize the edge. When the gradient is greater than the threshold, it is considered as the edge. During the cooling process. the lightness of the liquid drop decreases before solidification (see **Figure 5**). The gradient is then smaller overall at lower temperatures. However, the threshold does not change, causing the detected edge moves towards the inside of the sample. Hence, the drop volume is underestimated and the density is overestimated. The edge movement is related to the temperature of the sample and the shutter time of the camera. Therefore, the detected edge movement accounts for the higher temperature coefficient of density in the present study. Besides, results may be different with different shutter times due to this common phenomenon. Shadowgraphy will be implemented to eliminate the effects of image brightness changes in future work. The background will be bright and the liquid drop will be black in sample images when a backlighting laser and a narrow-band filter are used. The brightness of the images is then independent of temperature during the cooling process. Nevertheless, conventional photography is still of great value and permits to visualize both the presence of impurities and the surface conditions, which can be used to investigate the solidification after undercooling.

In addition to the accuracy of the instruments, there are still multiple factors that affect the measurement accuracy. In the present study, the sample top side is heated by a single laser while the bottom side is not heated. Temperature gradient of a few hundred Kelvin is expected and may lead to a density gradient within the sample. The joint effect of gravity and argon gas flow shearing on drop morphology is still hard to estimate since lower part of the sample is hidden by the conical nozzle. The sample volume calculated by image processing of the visible portion based on 2-D ellipse fitting will also be affected. Besides, the pyrometers focus on the top side of the sample, which overestimate the sample temperature.

As shown in **Table 2**, a large density disparity exists between results obtained by contact methods. For example, the density at 2327 K of alumina, is 3.06 g/cm^3 in (Ikemiya et al., 1993) and 2.55 g/cm^3 in (Wartenburg et al., 1936). These contact measurements are quite old and are greatly affected by sample contamination. This may also account for the large disparity between the contact and contactless methods. Among the contactless methods, the density measured by Glorieux et al. (1999) is significantly lower. The reason may be that the sample is imaged from the top and assumed to be spherical, while the liquid alumina is closer to the ellipsoid under gravity and gas flow shearing. For example, the semi-major axis is about 3.4% longer than the semi-minor axis for the alumina drop at 3333 K (see **Figure 8**). Ignoring the influence of asphericity may overestimate the volume and underestimate the density of the sample. The density measured by Paradis et al. (2004) is higher instead. The reason may be the high-vacuum conditions. The liquid drop may become unstable due to sample evaporation. Another reason may be the low camera resolution. Work by Tamaru et al. (2018) is done under microgravity. Voids may form within the sample and are difficult to be removed, which may cause errors. Considering the 1.40% error bar of density (calculated based on mass and radius uncertainties) in the present study, good agreement is found with previously reported data measured by the ADL and ESL methods.

The liquid drop may rotate when levitated by argon gas flow. The higher the flow rate, the faster the rotation speed. When the levitation is well controlled, the deviation of the rotation axis from the vertical direction is small. However, when the temperature is close to the boiling point, or some large disturbance is introduced externally, the levitation becomes less stable and the deviation angle becomes larger. The destruction of flow field symmetry will

lead to large measurement errors. Therefore, when a large deviation angle from the vertical direction during the cooling process occurs, another experiment is suggested for more accurate results. If the drop accidentally sticks to the nozzle wall during the measurement, the experiment needs to be terminated and restarted after cleaning the nozzle.

CONCLUSION

This paper presents an experimental setup (ALSEE) developed at CNPE for measurements of density, surface tension and viscosity of molten corium components based on aerodynamic levitation and laser heating. A conical converging-diverging nozzle is optimized to realize stable levitation at both ambient and high temperatures. The alumina density is measured during the cooling process upon the shutdown of laser heating after the drop is heated to 3333 K. Image processing including image edge detection and ellipse fitting is performed to calculate the volume of the ellipsoidal drop assumed in the present study.

In the present study, the alumina density is 2.929 g/cm^3 at the melting point of 2327 K, with the temperature coefficient of -2.421×10^{-4} g/(cm^3·K) from 2,300 to 3000 K. The uncertainty of density is 1.40%. Good agreement is found with other reported density data. The ellipsoidal assumption of the liquid drop levitated by the conical nozzle is confirmed to be reliable to calculate its volume. Large fluctuations at the beginning of the cooling process can be related to the rapid thermal transient upon the shutdown of the laser. Conventional photography of an incandescent object accounts for the higher temperature coefficient of density. Temperature gradient and deviation from the ellipsoidal shape also contribute to measurement errors.

Future research will focus on reducing measurement uncertainty which is mainly due to the volume overestimation of the sample photography of an incandescent object, the large temperature gradient by laser heating and the ellipsoidal assumption. The shadowgraphy will be used in the future with a backlighting laser and a narrow-band filter. The dual laser heating method will be used to reduce the temperature gradient. Finally, Measurements of density, surface tension and viscosity of corium components will be conducted when the acoustic excitation system is ready.

DATA AVAILABILITY STATEMENT

The raw data supporting the conclusion of this article will be made available by the authors, without undue reservation.

AUTHOR CONTRIBUTIONS

Experiment design and operation are finished by YG and LZ. Many suggestions are provided by QG. The experiment and paper writing is guided by YY, WM, and SH.

FUNDING

This work was supported by National Key R&D Program of China (Grant No. 2018YFB1900100).

REFERENCES

Abalin, S. S., Asmolov, V. G., Daragan, V. D., D'yakov, E. K., Merzlyakov, A. V., and Vishnevsky, V. Y. (2000). Corium Kinematic Viscosity Measurement. *Nucl. Eng. Des.* 200, 107–115. doi:10.1016/s0029-5493(00)00238-7

Andrade, M. A. B., Pérez, N., and Adamowski, J. C. (2018). Review of Progress in Acoustic Levitation. *Braz J. Phys.* 48, 190–213. doi:10.1007/s13538-017-0552-6

Ansari Hosseinzadeh, V., and Holt, R. G. (2017). Finite Amplitude Effects on Drop Levitation for Material Properties Measurement. *J. Appl. Phys.* 121, 174502. doi:10.1063/1.4982908

Barbé, J.-C., Parayre, C., Daniel, M., Papoular, M., and Kernevez, N. (1999). High-Temperature Containerless Viscosity Measurement by Gas-Film Levitation. *Int. J. Thermophys.* 20, 1071–1083. doi:10.1023/a:1022698619162

Bayazitoglu, Y., and Mitchell, G. F. (1995). Experiments in Acoustic Levitation - Surface Tension Measurements of Deformed Droplets. *J. Thermophys. Heat Transf.* 9, 694–701. doi:10.2514/3.726

Benmore, C. J., and Weber, J. K. R. (2017). Aerodynamic Levitation, Supercooled Liquids and Glass Formation. *Adv. Phys. X* 2, 717–736. doi:10.1080/23746149.2017.1357498

Bojarevics, V., and Pericleous, K. (2003). Modelling Electromagnetically Levitated Liquid Droplet Oscillations. *ISIJ Int.* 43, 890–898. doi:10.2355/isijinternational.43.890

Coutures, J., Rifflet, J.-C., Florian, P., and Massiot, D. (1994). A Thermal-Analysis and Very High-Temperature Al-27 NMR-Study of the Solidification Behavior in Contactless Conditions of Liquid Alumina-Alumina–Effects of the Melt Temperature and Oxygen Partial-Pressure. *Revue Int. des Hautes Temp. des Refract.* 29, 123–142.

Elyutin, V., Mitin, B., and Anisimov, Y. S. (1973). Surface Tension and Density of Al 2 O 3-BeO Melts, Izvestiya Akademii Nauk SSSR. *Neorganicheskie Mater.* 9, 1585–1587.

Etay, J., Schetelat, P., Bardet, B., Priede, J., Bojarevics, V., and Pericleous, K. (2008). Modelling of Electromagnetic Levitation - Consequences on Non-contact Physical Properties Measurements. *High Temp. Mater. Process.* 27, 439–448. doi:10.1515/htmp.2008.27.6.439

Fischer, M. (2004). The Severe Accident Mitigation Concept and the Design Measures for Core Melt Retention of the European Pressurized Reactor (EPR). *Nucl. Eng. Des.* 230, 169–180. doi:10.1016/j.nucengdes.2003.11.034

Glorieux, B., Millot, F., Rifflet, J.-C., and Coutures, J.-P. (1999). Density of Superheated and Undercooled Liquid Alumina by a Contactless Method. *Int. J. Thermophys.* 20, 1085–1094. doi:10.1023/a:1022650703233

Granier, B., and Heurtault, S. (1983). Method for Measuring the Density of Liquid Refractories-Aapplications to Alumina and Yttrium Oxide. *Revue Int. des Hautes Temp. des Refract.* 20, 61–67.

Grishchenko, D., and Piluso, P. (2011). Recent Progress in the Gas-Film Levitation as a Method for Thermophysical Properties Measurements: Application to ZrO_2-Al_2O_3 System. *High Temp. High Press* 40, 127–149.

Haumesser, P. H., Garandet, J. P., Bancillon, J., Daniel, M., Campbell, I., and Jackson, P. (2002). High Temperature Viscosity Measurements by the Gas Film Levitation Technique: Application to Various Types of Materials. *Int. J. Thermophys.* 23, 1217–1228. doi:10.1023/a:1019892220523

Ikemiya, N., Umemoto, J., Hara, S., and Ogino, K. (1993). Surface Tensions and Densities of Molten Al2O3, Ti2O3, V2O5 and Nb2O5. *ISIJ Int.* 33, 156–165. doi:10.2355/isijinternational.33.156

Ishikawa, T., Yu, J., and Paradis, P.-F. (2006). Noncontact Surface Tension and Viscosity Measurements of Molten Oxides with a Pressurized Hybrid

Electrostatic-Aerodynamic Levitator. *Rev. Sci. Instrum.* 77, 053901. doi:10.1063/1.2198787

Kingery, W. D. (1959). Surface Tension of Some Liquid Oxides and Their Temperature Coefficients. *J Am. Ceram. Soc.* 42, 6–10. doi:10.1111/j.1151-2916.1959.tb09134.x

Kirshenbaum, A. D., and Cahill, J. A. (1960). The Density of Liquid Aluminium Oxide. *J. Inorg. Nucl. Chem.* 14, 283–287. doi:10.1016/0022-1902(60)80272-2

Kondo, T., Muta, H., Kurosaki, K., Kargl, F., Yamaji, A., Furuya, M., et al. (2019). Density and Viscosity of Liquid ZrO2 Measured by Aerodynamic Levitation Technique. *Heliyon* 5, e02049. doi:10.1016/j.heliyon.2019.e02049

Kozakevitch, P. (1960). Viscosité et éléments structuraux des aluminosilicates fondus : laitiers CaO-AI_2O_3-Sio_2 entre 1 600 et 2 100 °C. *Rev. Mater. Paris* 57, 149–160. doi:10.1051/metal/196057020149

Kremer, J., Kilzer, A., and Petermann, M. (2018). Simultaneous Measurement of Surface Tension and Viscosity Using Freely Decaying Oscillations of Acoustically Levitated Droplets. *Rev. Sci. Instrum.* 89, 015109. doi:10.1063/1.4998796

Krishnan, S., Felten, J. J., Rix, J. E., Weber, J. K. R., Nordine, P. C., Beno, M. A., et al. (1997). Levitation Apparatus for Structural Studies of High Temperature Liquids Using Synchrotron Radiation. *Rev. Sci. Instrum.* 68, 3512–3518. doi:10.1063/1.1148315

Kymäläinen, O., Tuomisto, H., and Theofanous, T. (1997). In-vessel Retention of Corium at the Loviisa Plant. *Nucl. Eng. Des.* 169, 109–130. doi:10.1016/S0029-5493(96)01280-0

Langstaff, D., Gunn, M., Greaves, G. N., Marsing, A., and Kargl, F. (2013). Aerodynamic Levitator Furnace for Measuring Thermophysical Properties of Refractory Liquids. *Rev. Sci. Instrum.* 84, 124901. doi:10.1063/1.4832115

Maini, R., and Aggarwal, H. (2009). Study and Comparison of Various Image Edge Detection Techniques. *Int. J. Image Process.* 3, 1–11.

Millot, F., Sarou-Kanian, V., Rifflet, J.-C., and Vinet, B. (2008). The Surface Tension of Liquid Silicon at High Temperature. *Mater. Sci. Eng. A* 495, 8–13. doi:10.1016/j.msea.2007.10.108

Mitin, B., and Nagibin, Y. A. (1970). Density of Liquid Alumina. *Russ. J. Phys. Chem.* 44, 741–742.

Mohr, M., Wunderlich, R. K., Koch, S., Galenko, P. K., Gangopadhyay, A. K., Kelton, K. F., et al. (2019). Surface Tension and Viscosity of Cu50Zr50 Measured by the Oscillating Drop Technique on Board the International Space Station. *Microgravity Sci. Technol.* 31, 177–184. doi:10.1007/s12217-019-9678-1

Nordine, P. C., and Atkins, R. M. (1982). Aerodynamic Levitation of Laser-heated Solids in Gas Jets. *Rev. Sci. Instrum.* 53, 1456–1464. doi:10.1063/1.1137196

Paradis, P.-F., Ishikawa, T., Lee, G.-W., Holland-Moritz, D., Brillo, J., Rhim, W.-K., et al. (2014). Materials Properties Measurements and Particle Beam Interactions Studies Using Electrostatic Levitation. *Mater. Sci. Eng. R Rep.* 76, 1–53. doi:10.1016/j.mser.2013.12.001

Paradis, P.-F., Ishikawa, T., Saita, Y., and Yoda, S. (2004). Non-contact Thermophysical Property Measurements of Liquid and Undercooled Alumina. *Jpn. J. Appl. Phys.* 43, 1496–1500. doi:10.1143/jjap.43.1496

Paradis, P.-F., and Ishikawa, T. (2005). Surface Tension and Viscosity Measurements of Liquid and Undercooled Alumina by Containerless Techniques. *Jpn. J. Appl. Phys.* 44, 5082–5085. doi:10.1143/jjap.44.5082

Paradis, P. F., Babin, F., and Gagné, J. M. (1996). Study of the Aerodynamic Trap for Containerless Laser Materials Processing in Microgravity. *Rev. Sci. Instrum.* 67, 262–270. doi:10.1063/1.1146581

Rasmussen, J. J. (1972). Surface Tension, Density, and Volume Change on Melting of Al2O3 Systems, Cr2O3, and Sm2O3. *J Am. Ceram. Soc.* 55, 326. doi:10.1111/j.1151-2916.1972.tb11298.x

Rhim, W.-K., Ohsaka, K., Paradis, P.-F., and Spjut, R. E. (1999). Noncontact Technique for Measuring Surface Tension and Viscosity of Molten Materials Using High Temperature Electrostatic Levitation. *Rev. Sci. Instrum.* 70, 2796–2801. doi:10.1063/1.1149797

Richard Weber, J. K., Felten, J. J., and Nordine, P. C. (1996). Laser Hearth Melt Processing of Ceramic Materials. *Rev. Sci. Instrum.* 67, 522–524. doi:10.1063/1.1146631

Sehgal, B. R. (2011). *Nuclear Safety in Light Water Reactors: Severe Accident Phenomenology*. Oxford: Academic Press.

Shpilrain, E., and Yakimovich, K. (1973). Experimental Study of the Density of Liquid Alumina up to 2750 C. *High. Temp.-High Press.* 5, 191–198.

Stalder, A. F., Melchior, T., Müller, M., Sage, D., Blu, T., and Unser, M. (2010). Low-bond Axisymmetric Drop Shape Analysis for Surface Tension and Contact Angle Measurements of Sessile Drops. *Colloids Surfaces A Physicochem. Eng. Aspects* 364, 72–81. doi:10.1016/j.colsurfa.2010.04.040

Tamaru, H., Koyama, C., Saruwatari, H., Nakamura, Y., Ishikawa, T., and Takada, T. (2018). Status of the Electrostatic Levitation Furnace (ELF) in the ISS-KIBO. *Microgravity Sci. Technol.* 30, 643–651. doi:10.1007/s12217-018-9631-8

Trinh, E. H., Marston, P. L., and Robey, J. L. (1988). Acoustic Measurement of the Surface Tension of Levitated Drops. *J. Colloid Interface Sci.* 124, 95–103. doi:10.1016/0021-9797(88)90329-3

Wartenburg, H., Wehner, G., and Saran, E. (1936). The Surface Tension of Molten Al 2 O 3 and La 2 O 3, Nach. *Akad. Wiss. Goettingen* 2, 65–71.

Weber, J. K. R., Hampton, D. S., Merkley, D. R., Rey, C. A., Zatarski, M. M., and Nordine, P. C. (1994). Aero-Acoustic Levitation: A Method for Containerless Liquid-Phase Processing at High Temperatures. *Rev. Sci. Instrum.* 65, 456–465. doi:10.1063/1.1145157

Zhang, Z. (1997). Parameter Estimation Techniques: A Tutorial with Application to Conic Fitting. *Image Vis. Comput.* 15, 59–76. doi:10.1016/s0262-8856(96)01112-2

Zubarev, Y. V., Kostikov, V., Mitin, B., Nagibin, Y. A., and Nishcheta, V. (1969). Some Properties of Liquid Aluminum Oxide, Izvestiya Akademii Nauk SSSR. *Neorganicheskie Mater.* 5, 1563–1565.

Conflict of Interest: Authors YG, LZ, YY, and QG were employed by the company China Nuclear Power Engineering Co., Ltd.

The remaining authors declare that the research was conducted in the absence of any commercial or financial relationships that could be construed as a potential conflict of interest.

This work was commercially supported by China Nuclear Power Engineering Co., Ltd apart from National Key R&D Program of China (Grant No. 2018YFB1900100) and was approved to be published by China Nuclear Power Engineering Co., Ltd without any conflict of interest.

Publisher's Note: All claims expressed in this article are solely those of the authors and do not necessarily represent those of their affiliated organizations or those of the publisher, the editors, and the reviewers. Any product that may be evaluated in this article, or claim that may be made by its manufacturer, is not guaranteed or endorsed by the publisher.

frontiers | Frontiers in Energy Research

ORIGINAL RESEARCH
published: 20 May 2022
doi: 10.3389/fenrg.2022.840503

Experimental and Numerical Study on the Gravitational Deposition and Coagulation of Aerosols

Huiyu Yu, Haifeng Gu, Zhongning Sun, Yanmin Zhou, Junyan Chen and Yingzhi Li*

Nuclear Power Plant Institute, Harbin Engineering University, Harbin, China

The gravitational deposition and coagulation of aerosols were studied experimentally based on the COSTTHES (Containment Source-Term and Thermal Hydraulics Experiment System) facility and numerically investigated based on a continuous general dynamic equation; the experimental and the numerical results were in good agreement. In the present study, the applicability of the zero-dimensional model for deposition and coagulation of aerosols was verified. A considerable distortion can occur due to the coagulation of the aerosol, which significantly influenced the removal rate of the aerosol with a diameter greater than 0.76 μm, and the dynamic shape factor value of the aerosol used in the present experiment was obtained as 4. In the experimental and numerical studies, it was found that the combined effect of the gravitational deposition and coagulation of the aerosol can increase the number density of the aerosol with specific diameters, and the concentration-increment size would increase as settling continued.

Keywords: gravitational deposition, coagulation, COSTTHES, GDE, aerosol

OPEN ACCESS

Edited by:
Jun Wang,
University of Wisconsin-Madison, United States

Reviewed by:
Longchao Yao,
Zhejiang University, China
Guangzong Zheng,
China Institute of Atomic Energy, China

****Correspondence:***
Haifeng Gu
guhaifeng@hrbeu.edu.cn

Specialty section:
This article was submitted to Nuclear Energy, a section of the journal Frontiers in Energy Research

Received: *21 December 2021*
Accepted: *20 April 2022*
Published: *20 May 2022*

Citation:
Yu H, Gu H, Sun Z, Zhou Y, Chen J and Li Y (2022) Experimental and Numerical Study on the Gravitational Deposition and Coagulation of Aerosols. Front. Energy Res. 10:840503. doi: 10.3389/fenrg.2022.840503

INTRODUCTION

Aerosol is one of the matter of concerns in the area of nuclear safety. During the course of a severe accident of a Pressurized Water Reactor (PWR), aerosols might be released from the ruptures of the coolant loop or generated from the Molten Core—Concrete Interaction (MCCI) (Sevón, 2005), and water vapor can be generated in the containment building, which causes the increase in pressure and temperature. Once the containment is breached, the radioactive aerosol will be released, which leads to a severe threat to the environment and the public. The radioactivity and the health hazard of the potential leakage are related to the concentration and size of the aerosol, and the time evolution of the aerosol concentration and the size distribution is influenced by various mechanisms. It is therefore of great importance to investigate the time evolution of the aerosol concentration and the size distribution of the aerosol.

The natural removal mechanisms (gravitational deposition, Brownian diffusion, thermophoresis settling, and diffusiophoresis settling) dominate aerosol size distribution and aerosol concentration in the absence of a spray system (Powers et al., 1996). In addition to the aforementioned settling mechanisms, coagulation affects the behavior of aerosol as well (Kwon and Lee, 2002). Though the coagulation does not result in the change in the mass of the aerosol in the containment, it influences the Particle Size Distribution (PSD) of the aerosol and then influences the overall removal efficiency of the aerosol (Schnell et al., 2006). The zero-dimensional Continuous General Dynamic Equation (Continuous GDE) is the commonly used numerical model to describe the settling and coagulation behavior of the aerosol (Friendlander, 2000). Many methods were developed to solve the GDE: the moment method (Zurita-Gotor and Rosner, 2004; Xie, 2014; Yu et al., 2015), the direct simulation

Monte Carlo (DSMC) method (Sheng and Shen, 2006; Sheng and Shen, 2007), the and sectional treatment method (Hounslow et al., 1988; Lister et al., 1995; Kumar and Ramkrishna, 1996; Geng et al., 2013). The moment method suffers from the shortcoming that a priori knowledge of the mathematical form of the size distribution of the aerosol is required; however, the experimental data provided by the instrument usually deviate more or less from the perfect mathematical form. As to the DSMC, its computation is expensive if the number of aerosol particles is large. In the settling process, the continuous decay of the particle number leads to a decrease in the simulation accuracy of the DSMC (Sheng and Shen, 2006).

Numerical studies related to the gravitational deposition and coagulation of the aerosol were conducted to analyze the behavior of the aerosol settling and coagulation. Lindauer and Castleman (1970) numerically studied the relative importance of Brownian and gravitational coagulation on the transient behavior of aerosol undergoing coagulation and gravitational settling. In his study, the homogeneous dispersed aerosol particles were assumed to be spherical. Powers et al. (1996) established a numerical model in which the settling mechanisms and coagulation mechanisms of aerosol were considered. In their study, it was indicated that the coagulation of the aerosol particles could lead to fantastic distortion from spherical, and the distortion of the aerosol agglomerate was considered by employing the dynamic shape factor. Garcia-Nieto (2006) numerically studied the scavenging efficiencies of aerosol emissions from coal-fired power plants; in the model, the coagulation and settling of aerosol were considered and the aerosol was considered as spherical particles, and it was found that the respirable dust has the lowest scavenging efficiency. Ghosh et al. (2017) developed a numerical model based on a semi-implicit solved GDE method, and it was revealed that the charge could significantly enhance the coagulation process of the aerosol. The model was validated against the results obtained by the experiment which was conducted in a $0.5m^3$ volume vessel. Recently, Narayanam et al. (2021) analyzed the growth and coagulation characteristics of the suspended sodium combustion aerosols in a closed chamber using the HAARM-S code which was based on the moment method; in their evaluation, the maximum error was around 50%.

Kwon and Lee (2002) investigated separately the gravitational deposition and coagulation of aerosol using a horizontal cylinder and vertical cylinder; the experimental facility structure and its scale ensured the homogeneous distribution of the aerosol, that is, the potential stratification of the aerosol concentration was eliminated. The discussion of effective time in this study implied that the stratification of the aerosol concentration could occur under a static condition. The characteristics of the size evolution and the deposition velocity of the aerosol were studied experimentally by Kumar et al. (2015) (Subramanian et al., 2011; Misra et al., 2013; Kumar et al., 2015), and the experiments were conducted based on the ATF facility which had a closed chamber of $1m^3$ volume. Liu et al. (2017) conducted an experimental and numerical study on the decay of aerosol under high-concentration conditions and found that the wall-loss correction was valid when the initial concentration of the aerosol was less than $10^4 cm^{-3}$. The experimental study was conducted based on a stainless-steel cylinder container with a height of $0.55m$ and a volume of $0.54m^3$. In this numerical study, the aerosol was assumed to be a spherical particle and, hence, the dynamic shape factor was not considered. Freitag et al. (2018) investigated experimentally the wash-down of the aerosol due to the condensation of steam on the vertical wall of the containment; the experiment was conducted in the large-scaled THAI facility and the experimental results were compared with the COCOSYS calculations. Tian et al. (2020) investigated the characteristics of the natural deposition of aerosol using an enclosed vessel. The characteristics of the influences of the aerosol concentration and the static electricity on the deposition of the aerosol were investigated experimentally based on a cuboid vessel made of Plexiglass; the vessel had a height of $1.5m$ and a volume of $1.5m^3$. In the above numerical studies, most numerical models did not consider the influence of the dynamic shape factor of the aerosol, and the applicability of the zero-dimensional numerical model was not verified in a large-scaled container under a static condition. In the experimental studies of Liu, Kumar, and Tian, the small-scaled experimental facility minimized the influence of the stratification of aerosol concentration. However, the small scale of the experimental facility might amplify the influence of gas extraction due to sampling, which therefore might introduce additional errors.

FIGURE 1 | Vessel of the COSTTHES facility.

In the present work, the combined effect of aerosol coagulation and gravitational deposition was studied experimentally based on

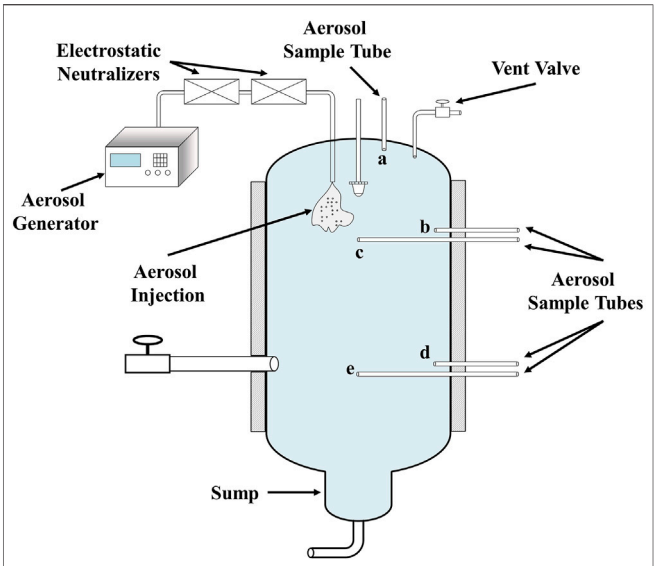

FIGURE 2 | Overview of the COSTTHES facility.

the COSTTHES (Containment Source-Term and Thermal Hydraulics Experiment System) facility. The multisampling configuration (three sampling elevations) and the dimensions of the COSTTHES facility (a vessel with a height of 4.3m and a volume of 13.5m^3) were made for the observation of the stratification of aerosol concentration and weakened the influence of the gas extraction due to sampling. In addition to the experiment, numerical analysis was conducted as well based on the continuous GDE considering the dynamic shape factor. Hence, the applicability of the zero-dimensional numerical model can be investigated under the condition in which the stratification of aerosol concentration can occur and the influence of the dynamic shape factor of the aerosol can be investigated.

EXPERIMENTAL FACILITY AND METHOD

Experimental Facility

The experimental study in the present work was conducted based on the COSTTHES facility. The facility and schematic of COSTTHES are shown in **Figure 1** and **Figure 2**

The COSTTHES facility is composed of a closed cylindrical vessel (13.5m^3 volume, 4.3m high, and 2m internal diameter). The aerosol generated from a PALAS RBG 2000D aerosol generator traveled through two electrostatic neutralizers to minimize the effect of static electricity before being injected into the vessel from the dome. Five sample tubes at different heights and radial positions were employed to obtain the aerosol spatial distribution, and the sampled aerosol was analyzed using a Welas Promo 3000H particle size spectrometer which has high precision, a wide measurement range (0.1–10 μm of aerosol diameter), and is capable of online sampling under high-pressure and high-temperature conditions. The configurations of the sample positions shown in **Figure 2** are listed in **Table 1**.

TABLE 1 | The configuration of the sample positions.

Sample notation	Height (m)	Distance from the wall (m)	Sampling zone
a	3.98	0.32	Up
b	3.09	0.2	Middle
c	3.09	1.0	Middle
d	0.71	0.2	Down
e	0.71	1.0	Down

Experimental Procedure

In the experiment, as dried and filtered air was blown into the vessel to remove the water vapor and environmental aerosols, the humidity in the vessel was close to zero. While the air was transmitted, the vessel permitted the gas discharge to remain at atmospheric pressure; therefore, the pressure in the vessel was $1.01 \times 10^5 Pa$ and the temperature was 25°C. Then, the TiO_2 aerosol particles with an initial geometric mean diameter of $0.41\mu m$ and an initial geometric standard deviation of 1.32 were injected into the vessel. In the process of aerosol injection, the electrostatic neutralizers were kept in operation to ensure that the aerosol was not charged. The aerosol injection continued until the total number density of the aerosol was over $10^4/cm^3$ to manifest the influence of aerosol coagulation (Hussein et al., 2009; Yu et al., 2013; Liu et al., 2017). When the total number density of the aerosol reached the desired level, the aerosol generator was shut down but the feeding gas was still on for a few minutes to mix the aerosol inside the vessel. After the mixing step of the aerosol, the first sampling was carried out for 1 min to obtain the initial distribution of the aerosol; then all the valves of the vessel were shut down for hours to isolate the gas and aerosol inside the vessel from that of the environment. In the sampling process, the aerosol was extracted with the air in the vessel using a particle size spectrometer (Welas Promo 3000H) and the aerosols with different diameters were counted to obtain the size distribution of the aerosol. By switching the connection between the particle size spectrometer and the sample tube, the spatial distribution of the aerosol could be built. Considering the impact of gas extraction due to aerosol sampling, the sample operation was carried out discontinuously. The sampling flow rate at each sample position was controlled at 5L/min and each sampling continued for 1 min, so that every sampling resulted in air extraction less than 25L compared with the COSTTHES vessel volume of 13.5m^3.

An experiment was conducted to investigate the radial distribution of aerosol and the results are presented in **Figure 3**; it can be noted that the size spectra at the same height were adequately close to each before the aerosol was homogenous. Therefore, the experimental data acquired at the sampling positions c and e were employed to represent the size spectra at the corresponding heights. Because the aerosol was injected from the dome of the vessel, when the aerosol injection was just complete the number density at the higher position was much higher than that at the lower position, as shown in **Figure 4**. After 2.3 h of settling and mixing, the aerosol became almost

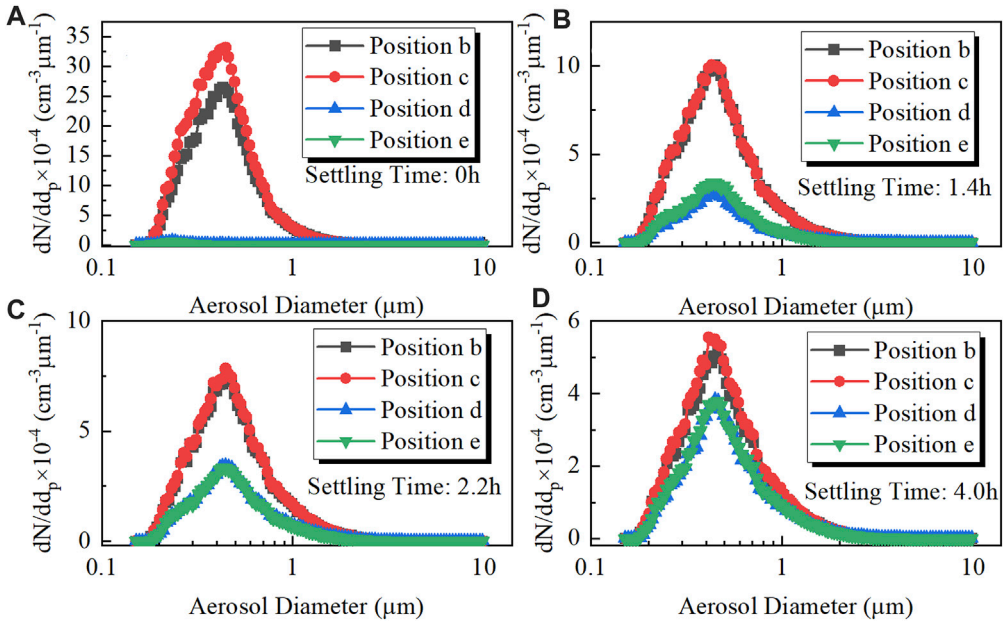

FIGURE 3 | Radial distribution of aerosol: **(A)** 0 h settling, **(B)** 1.4 h settling, **(A)** 2.2 h settling and (D) 4.0 h settling.

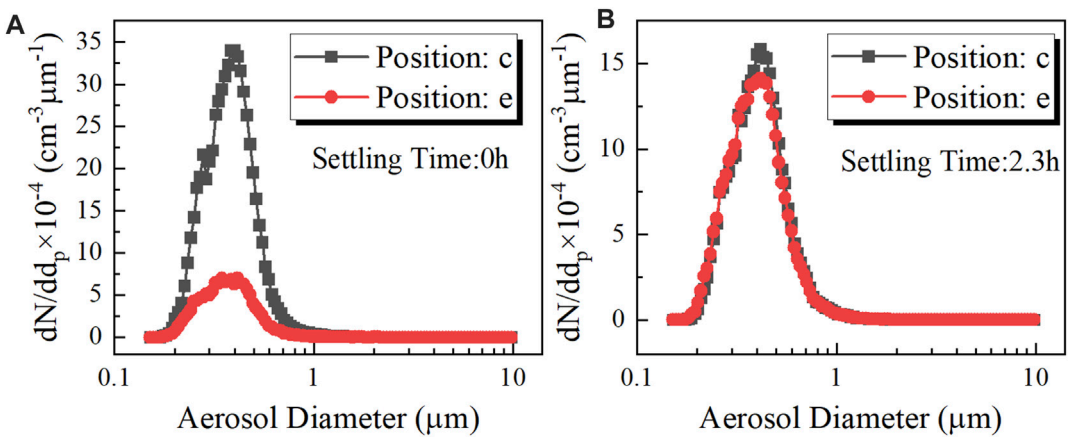

FIGURE 4 | Homogenization of the aerosol: **(A)** 0 h settling, **(B)** 2.3 h settling.

homogeneous in the vessel and the aerosol state at this moment and thereafter was used in the analysis.

COMPUTATION MODEL

General Dynamic Equation

In the present model, the aerosol spatial distribution was assumed to be homogeneous and the gravitational coagulation, Brownian coagulation, and gravitational deposition were considered the influencing mechanisms. Hence, the Continuous General Dynamic Equation (Continuous GDE) that governs the aerosol kinetic behavior can be written in the following form (García-Nieto, 2001; García-Nieto, 2006; Kwon and Lee, 2002):

$$\frac{\partial n(v,t)}{\partial t} = \frac{1}{2}\int_0^v \beta(v-v',v')n(v-v',t)n(v',t)dv' - n(v,t)\int_0^\infty \beta(v,v')n(v',t)dv' - \frac{v_g}{h}n(v,t) \quad (1)$$

where $n(v,t)$ (m^{-6}) is the number density of particles of volume v at a time $t$and represents the number of aerosols in unit spatial volume per unit aerosol volume, $\beta(v,v')$ is the coagulation kernel which is used to predict the coagulation frequency between

particles of volumes v and v', v_g is the gravitational deposition velocity, and h is the height of the vessel.

The first term on the right-hand side (RHS) of **Eq. 1** represents the rate of formation of particles between volumes v and $v+dv$ generated by coagulations between particles of volumes v and $v-v'$. The second term on the RHS stands for the death rate of particles of volumes between v and $v+dv$ due to coagulations with all other particles. The last term on the RHS represents the death rate of particles of volumes between volumes v and $v+dv$ due to gravitational deposition (Gelbard, 1982). The coagulation kernel can be written as (Powers et al., 1996)

$$\beta = \beta_G + \left(1 + 9/8\alpha^{2/3}\right)\beta_B \tag{2}$$

where β_G is the kernel of gravitational coagulation (Kwon and Lee, 2002), β_B is the kernel of Brownian coagulation (Kwon and Lee, 2002), and

$$\alpha = \frac{4\pi}{3kT}\rho_p g v_1^{1/3} v_2^{1/3} \left| v_1^{2/3} - v_2^{2/3} \right| \left(\frac{3}{4\pi}\right)^{4/3} \tag{3}$$

where v_1 and v_2 denote the volumes of particles involved in the coagulation.

$$\beta_G = K_1 \varepsilon \left\{ (r_1 + r_2)^2 \left| r_1^2 - r_2^2 \right| + C_m \lambda (r_1 + r_2)^2 |r_1 - r_2| \right\} \tag{4}$$

where $K_1 = 2\pi\rho_p g/9\mu$, $\varepsilon = 3y_c^2/2(r_1+r_2)^2$, y_c is the minimum between r_1 and r_2, with r_1 and r_2 being the radii of the particles involved in the coagulation, C_m is the Cunningham slip correction factor, $C_m = 1 + \frac{2\lambda}{d_p}(1.257 + 0.4\exp(-1.1 d_p/2\lambda))$, and λ is the mean free path of an air molecule.

$$\beta_B = K_2 (r_1 + r_2) \left\{ \left(\frac{1}{r_1} + \frac{1}{r_2}\right) + C_m \lambda \left(\frac{1}{r_1^2} + \frac{1}{r_2^2}\right) \right\} \tag{5}$$

where $K_2 = 2kT/3\mu$.

Discretization of the General Dynamic Equation

The form of the nonlinear integro-partial-differential equation of the GDE makes the analytical solution rarely tractable. The widely used moment method can be used to determine the solution of the GDE with a low computation time; nevertheless, it does not permit variation in the resolution of the size distribution due to the fixed number of parameters (Lister et al., 1995). Moreover, in the moment method, one needs to assume the form of the initial size distribution of the particle, such as log-normal distribution for aerosols. However, the size distribution of the aerosol obtained with an instrument (e.g., a particle size spectrometer) usually does not perfectly fit the ideal log-normal distribution. Hence, the sectional treatment of the aerosol size distribution introduced by Lister et al. (1995) was used in the present model. In Lister's discretization scheme, the size distribution of the aerosol is divided into a finite number of sections (groups) and the ratio of volumes of two adjacent sections is $2^{1/q}$; therefore,

$$\frac{v_{i+1}}{v_i} = 2^{1/q} \tag{6}$$

where i is the index of the section and q is a positive integer constant.

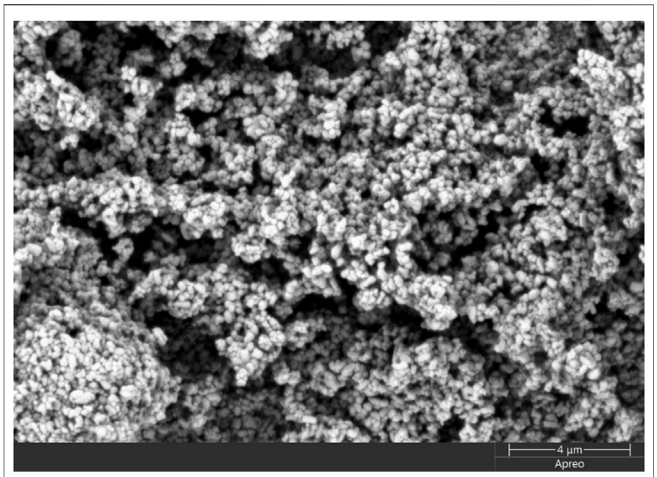

FIGURE 5 | SEM image of the aerosol employed in the present study.

According to Lister's discretization scheme, **Eq. 1** can be transformed into

$$\begin{aligned}
\frac{dN_i}{dt} = & \sum_{j=1}^{i-S(q)-1} \beta_{i-1,j} N_{i-1} N_j \frac{2^{(j-i+1)/q}}{2^{1/q}-1} \\
& + \sum_{k=2}^{q} \sum_{j=i-S(q-k+1)-k}^{i-S(q-k+2)-k+1} \beta_{i-k,j} N_{i-k} N_j \frac{2^{(j-i+1)/q} - 1 + 2^{-(k-1)/q}}{2^{1/q}-1} \\
& + \frac{1}{2}\beta_{i-q,i-q} N_{i-q}^2 \\
& + \sum_{k=2}^{q} \sum_{j=i-S(q-k+1)-k+1}^{i-S(q-k+2)-k+2} \beta_{i-k+1,j} N_{i-k+1} N_j \frac{-2^{(j-i)/q} + 2^{1/q} - 2^{-(k-1)/q}}{2^{1/q}-1} \\
& - \sum_{j=1}^{i-S(q)} \beta_{i,j} N_i N_j \frac{2^{(j-i)/q}}{2^{1/q}-1} - \sum_{j=i-S(q)+1}^{\infty} \beta_{i,j} N_i N_j - \frac{v_g}{h} N_i
\end{aligned} \tag{7}$$

where $N_i = \int_{v_i}^{v_{i+1}} n(v,t)dv$, $S(q) = \sum_{p=1}^{q} p$, and

$$v_g = \rho_p d_p^2 g C_m \big/ 18\mu_g \chi \tag{8}$$

where χ is the dynamic shape factor of the aerosol.

The accuracy and the resolution of the discretized size distribution of the aerosol increase with the increasing value of q. When $q = 6$, **Eq. 7** can be sufficiently precisely solved (Lister et al., 1995). **Equation 7** is a first-order linear ordinary differential equation and was solved using the finite-difference method in the present model.

EXPERIMENTAL RESULTS AND ANALYSIS

Dynamic Shape Factor

The sedimentation velocity of the aerosol particle is related to the dynamic shape factor of the aerosol, the diameter of the

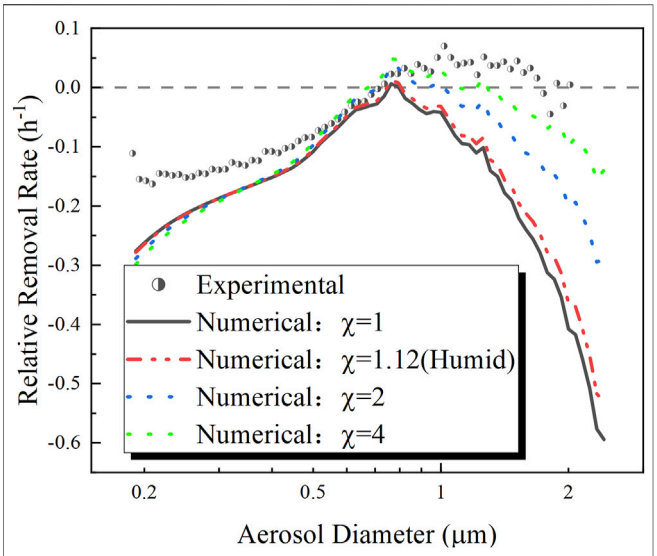

FIGURE 6 | Distributions of the relative removal rate of the experimental result and the numerical result.

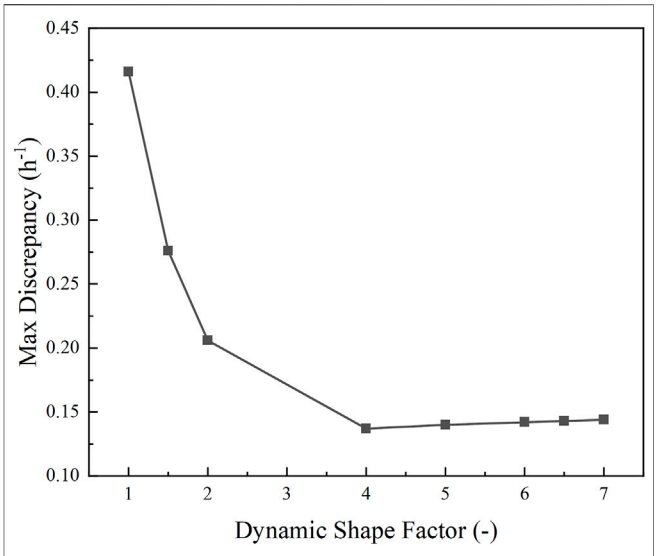

FIGURE 7 | Max discrepancy between the relative removal rate of the experimental result and the numerical result.

aerosol, the viscosity of air, and the density of the aerosol. The dynamic shape factor χ is defined as the ratio of the drag force experienced by a non-spherical particle to that experienced by a volume-equivalent spherical particle traveling at the same velocity in the same medium (Lau and Chuah, 2013). Hence, the dynamic shape factor is one of the important parameters influencing the sedimentation velocity of the aerosol of the non-spherical aerosol particle or coagulation that occurred. The primary particle of the aerosol employed in the present experiment was nearly spherical, as shown in **Figure 5**. However, the coagulation can generate significant distortions from spherical, which makes the dynamic shape factor greater than 1. In a humid environment such as the containment under a severe reactor accident, the surface tension effects produced by vapor condensation can reduce the dynamic shape factor (Powers et al., 1996). The dynamic shape factor in the humid environment can be calculated by $\chi = [\epsilon\rho_p + (1-\epsilon)\rho_w]/\rho_p$, where ϵ is the packing fraction and is suggested to be 0.63 (Powers et al., 1996); then, the value of the dynamic shape factor was 1.12 for the aerosol material of TiO_2. Since the present experiment was conducted under dry air conditions, the dynamic shape factor was believed to be greater than 1.12 (humid conditions).

The removal constant defined by **Eq. 9** was usually used to evaluate the settling process of the aerosol. However, when the deposition is combined with coagulation of the aerosol, the removal constant might not be a constant throughout the settling process. Hence, in the present study, the relative removal rate was defined by **Eq. 10** and employed to analyze the settling process of the aerosol.

$$\lambda_i = \frac{dN_i}{N_i dt} \tag{9}$$

$$\bar{\lambda}_i = \frac{\int_0^{T_{sett}} \lambda_i(t)dt}{T_{sett}} \tag{10}$$

where T_{sett} is the settling time in the experiment.

The comparison between the relative removal rate of the experimental result and that of the numerical result is shown in **Figure 6**. It can be noticed that the numerical relative removal rate was approaching the experimental one for the aerosol with a diameter greater than 0.76 μm as the dynamic shape factor of the aerosol increased. According to **Eq. 8**, the gravitational deposition velocity of the aerosol particle decreases with increasing dynamic shape factor. Therefore, the gravitational deposition dominates the removal rate of TiO_2, an aerosol particle with a diameter greater than 0.76 μm.

The max discrepancies between the experimental distribution of the relative removal rate and the numerical ones with different dynamic shape factors are shown in **Figure 7** which indicates that the value of the dynamic shape factor is 4 in the present experiment.

Stratification of Aerosol Concentration

In the light of the above analysis, the dynamic shape factor in the present numerical study was set to 4, and the size distribution of the aerosol of the experimental result and that of the numerical result are compared in **Figure 8**. The comparison indicated that the experimental result and the numerical prediction were in good agreement.

Under the action of the gravitational deposition, the number density of the aerosol continuously decreased, as shown in **Figure 9** and **Figure 10**. As shown in **Figure 10**, the total number density of the aerosol increased with decreasing height; in other words, the stratification of the

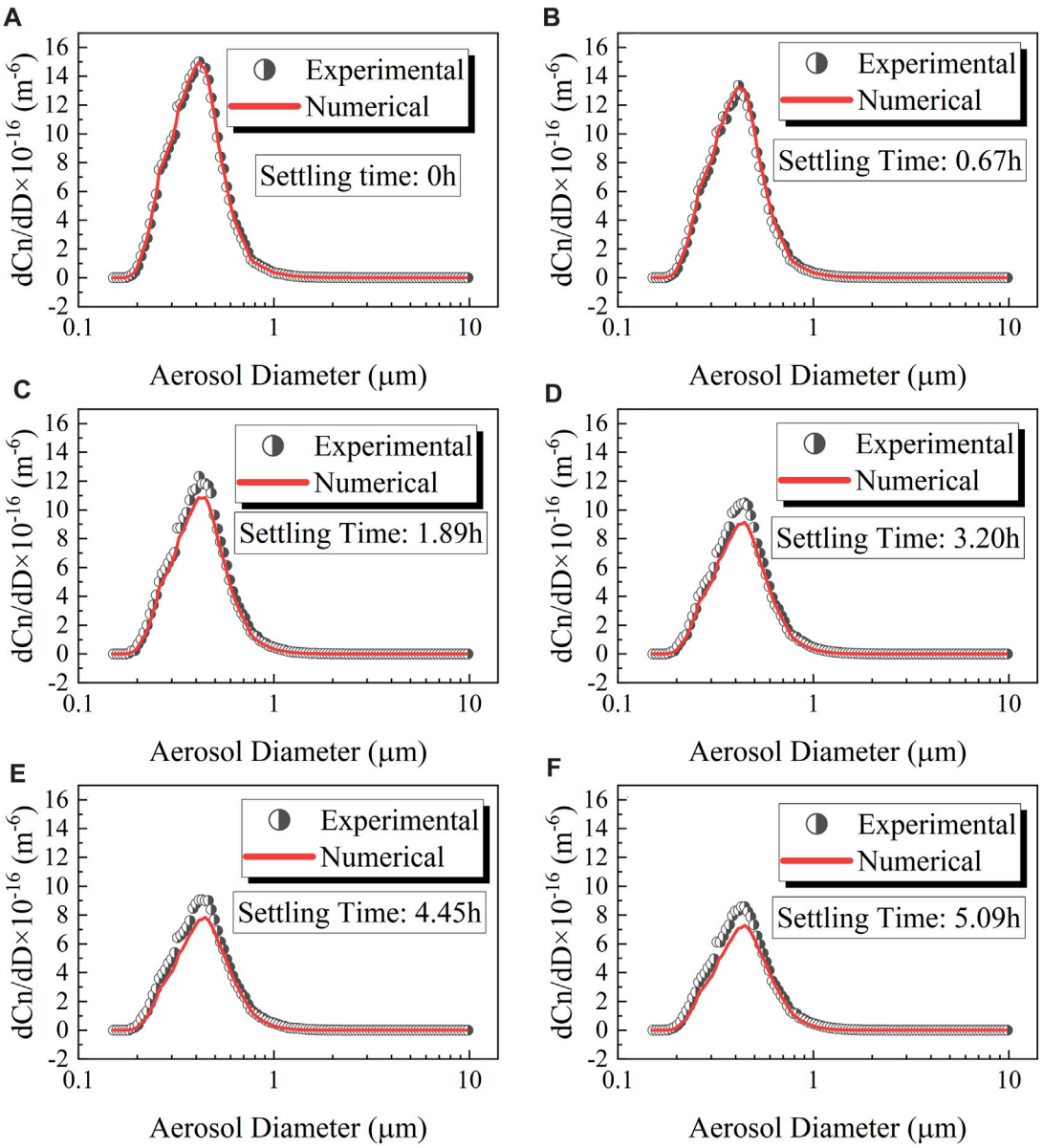

FIGURE 8 | Comparison of the experimental and numerical size distribution of the aerosol at different time, the dynamic shape factor x = 4: **(A)** 0 h, **(B)** 0.67 h, **(C)** 1.89 h, **(D)** 3.20 h, **(E)** 4.45 h and **(F)** 5.09 h.

aerosol concentration could be observed. However, in **Figure 9**, the median diameter of the aerosol did not appear stratified like the number density. As shown in **Figure 10**, the largest difference in the total number density of the aerosol in the Up Zone and the Down Zone was observed to be 9.5% at 3.2 h, and the largest prediction error with respect to the average total number density of the aerosol was 8.4% at 3.8 h. Hence, in 5.1 h of aerosol settling the stratification did not significantly affect the applicability of the zero-dimensional numerical model (GDE).

In the coagulation process, small particles aggregate into larger particles, which leads to an increase in the number density of the large particles. Nevertheless, the deposition of the large particle is much stronger than that of the small particles, which, on the contrary, results in a decrease in the number density of the large particles. In the present experiment, the median diameter of the aerosol particles increased throughout the duration of aerosol settling, as shown in **Figure 11**, which indicated that the coagulation mechanism is stronger than the deposition mechanism in the total number density range of the present experiment ($3.0 \times 10^4/cm^3$–$4.7 \times 10^4/cm^3$). In the settling of the aerosol, though the median diameter of the aerosol kept increasing, the growth trend was slowing down, which indicated that the coagulation mechanism was weakening compared with the gravitational deposition.

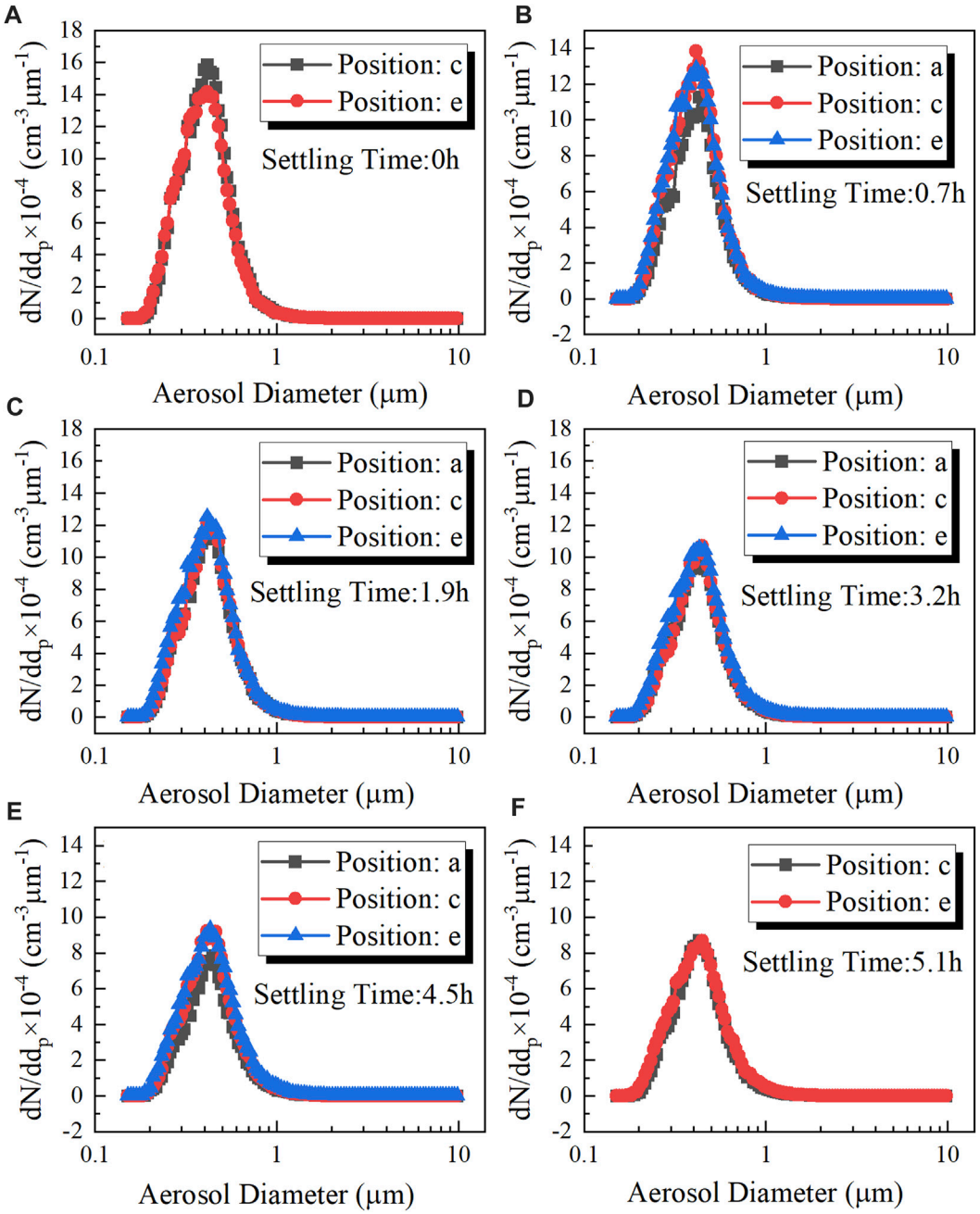

FIGURE 9 | Evolution of the size distribution of the aerosol at different elevations: **(A)** 0 h, **(B)** 0.7 h, **(C)** 1.9 h, **(D)** 3.2 h, **(E)** 4.5 h, and **(F)** 5.1 h.

Concentration-Increment Size

In order to analyze separately the influences of different mechanisms considered in the numerical model, the relative removal rate due to coagulation and gravitational deposition was calculated and is shown in **Figure 12**. According to **Eq. 7**, **Eq. 8**, and **Eq. 10**, the gravitational deposition is not affected by the number density of the aerosol, and the relative removal rate due to gravitational deposition did not vary with the settling time. However, the absolute value of the relative removal rate due to coagulation of the aerosol decreased with settling time, which is attributed to the decreasing collision frequency due to the decreasing number density of the aerosol.

In the experimental result (**Figure 6**) and numerical result (**Figure 12**), a concentration increment phenomenon was observed. For the tiny aerosol (diameter below 0.6 μm), the relative removal rate was negative because of the predominant coagulation mechanism. For the large aerosol (diameter above 1.1 μm), the relative removal rate was negative as well because of the predominant gravitational deposition mechanism. However, the two aforementioned mechanisms were both weak for the medium

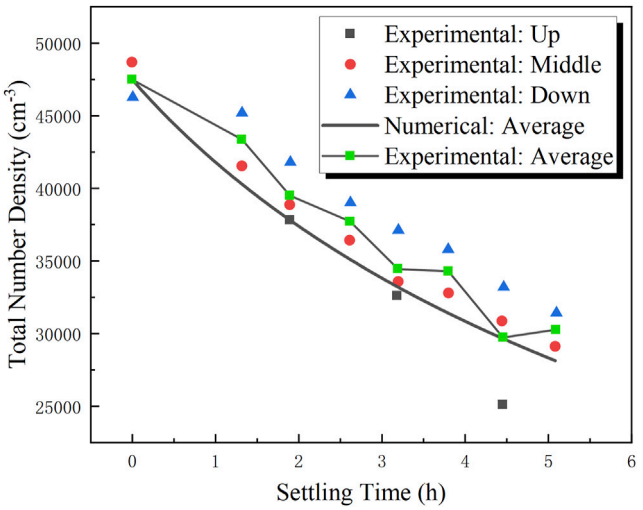

FIGURE 10 | Evolution of the total number density of the aerosol.

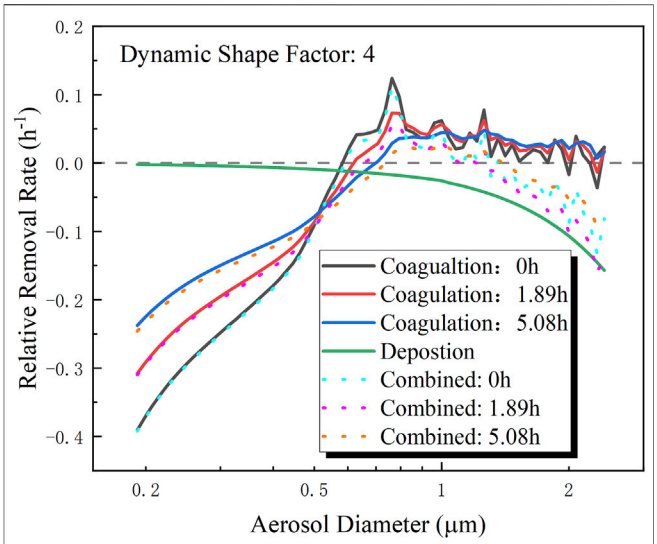

FIGURE 12 | Size distribution of the relative removal rate due to gravitational deposition and coagulation.

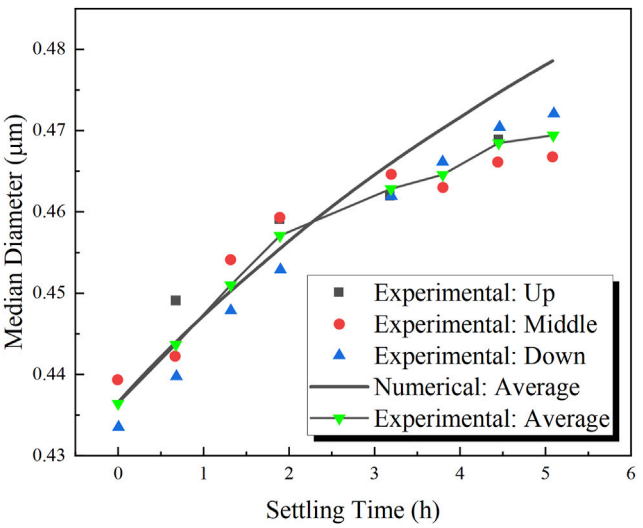

FIGURE 11 | Evolution of the median size of the aerosol.

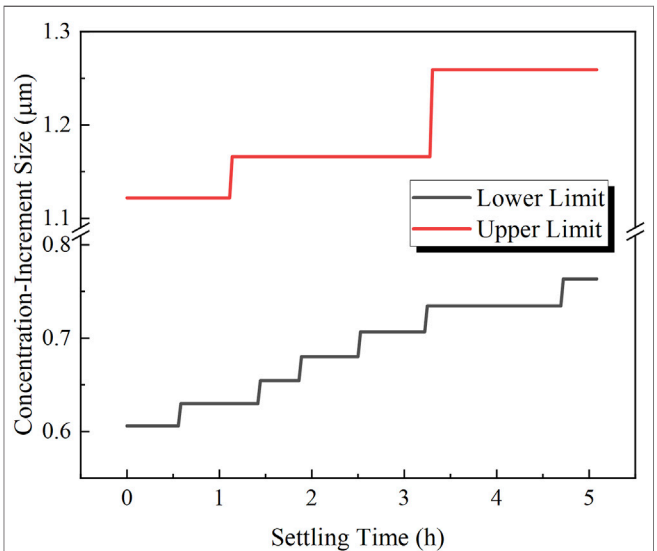

FIGURE 13 | Time evolution of the concentration-increment size.

size aerosol (diameter between 0.6 and 1.1 μm), which led to a positive relative removal rate (that is, the number density increased in a period). The time evolution of the concentration-increment size range is shown in **Figure 13**, within 5.1 h of settling; the lower limit of the concentration-increment size range was increased from 0.61 to 0.76 μm and the upper limit increased from 1.12 to 1.26 μm. Hence, as the gravitational deposition and coagulation continued, the concentration-increment size increased.

CONCLUSION

The gravitational deposition and coagulation are significant phenomena for the aerosol in the severe reactor accident. In this study, the gravitational deposition and coagulation were studied experimentally based on the COSTTHES facility and numerically with the population balance method. According to the present experimental and numerical studies, we draw the following conclusions: 1) The comparison between the experimental results and the numerical results showed that the present numerical model could predict the deposition and coagulation behavior of the aerosol with a satisfying agreement. 2) The experimental results and the numerical predictions showed that the behavior of the aerosol with a diameter greater than 0.76 μm was dominated by the gravitational deposition

mechanism, which was influenced significantly by the dynamic shape factor, and, in the present experiment, the dynamic shape factor was inferred to be 4. 3) The stratification of aerosol concentration was observed in the experiment; the largest difference in the total number density of the aerosol at different elevations was observed to be 9.5%, and the largest prediction error was 8.4%. Hence, the zero-dimensional numerical model was still applicable within 5.1 h of settling though the aerosol concentration stratification existed. 4) In the present experiment, the median diameter of the aerosol kept growing within 5.1 h of settling, which indicated that gravitational deposition was the predominant mechanism compared with coagulation. The slowing down growth trend of the median diameter of the aerosol indicated the weakening coagulation mechanism due to the decreasing number density of the aerosol. 5) A concentration increment phenomenon was observed in the experiment and predicted by the numerical model during aerosol settling, and it was found that as the gravitational deposition and coagulation continued the concentration increment size increased.

DATA AVAILABILITY STATEMENT

The original contributions presented in the study are included in the article/Supplementary Material; further inquiries can be directed to the corresponding author.

AUTHOR CONTRIBUTIONS

YH contributed to the conception and design and data analysis of the study. GH, SZ, and ZY provided guidance and suggestions for the study. CJ and LY assisted in the experiment.

FUNDING

This work was supported by the National Key R&D Program of China under Grant (number 2020YFB1901401).

REFERENCES

Friendlander, S. K. (2000). *Smoke, Dust and Haze: Fundamentals of Aerosol Dynamics*. New York, USA: Oxford University Press. 38-2208-38-2208. doi:10.5860/choice.38-2208

Freitag, M., Gupta, S., Beck, S., and Sonnenkalb, M. (2018). Experimental and Analytical Investigations of Aerosol Processes—Wash-Out and Wash-Down. *Nucl. Sci. Eng.* 193, 198–210. doi:10.1080/00295639.2018.1479091

García-Nieto, P. J. (2001). Parametric Study of Selective Removal of Atmospheric Aerosol by Coagulation, Condensation and Gravitational Settling. *Int. J. Environ. Health Res.* 11, 149–160. doi:10.1080/09603120020047528

García-Nieto, P. J. (2006). Study of the Evolution of Aerosol Emissions from Coal-Fired Power Plants Due to Coagulation, Condensation, and Gravitational Settling and Health Impact. *J. Environ. Manag.* 79, 372–382. doi:10.1016/j.jenvman.2005.08.006

Gelbard, F. (1982). *MAEROS User manual.[LMFBR]*. Albuquerque, NM (USA): Sandia National Labs.

Geng, J., Park, H., and Sajo, E. (2013). Simulation of Aerosol Coagulation and Deposition under Multiple Flow Regimes with Arbitrary Computational Precision. *Aerosol Sci. Technol.* 47, 530–542. doi:10.1080/02786826.2013.770126

Ghosh, K., Tripathi, S. N., Joshi, M., Mayya, Y. S., Khan, A., and Sapra, B. K. (2017). Modeling Studies on Coagulation of Charged Particles and Comparison with Experiments. *J. Aerosol Sci.* 105, 35–47. doi:10.1016/j.jaerosci.2016.11.019

Hounslow, M. J., Ryall, R. L., and Marshall, V. R. (1988). A Discretized Population Balance for Nucleation, Growth, and Aggregation. *AIChE J.* 34, 1821–1832. doi:10.1002/aic.690341108

Hussein, T., Hruška, A., Dohányosová, P., Džumbová, L., Hemerka, J., Kulmala, M., et al. (2009). Deposition Rates on Smooth Surfaces and Coagulation of Aerosol Particles inside a Test Chamber. *Atmos. Environ.* 43, 905–914. doi:10.1016/j.atmosenv.2008.10.059

Kumar, A., Subramanian, V., Baskaran, R., and Venkatraman, B. (2015). Size Evolution of Sodium Combustion Aerosol with Various Rh. *Aerosol Air Qual. Res.* 15, 2270–2276. doi:10.4209/aaqr.2015.03.0150

Kumar, S., and Ramkrishna, D. (1996). On the Solution of Population Balance Equations by Discretization-I. A Fixed Pivot Technique. *Chem. Eng. Sci.* 51, 1311–1332. doi:10.1016/0009-2509(96)88489-2

Kwon, S. B., and Lee, K. W. (2002). Experimental and Numerical Study of Aerosol Coagulation by Gravitation. *Part. Part. Syst. Charact.* 19, 103–110. doi:10.1002/1521-4117(200205)19:2<103::AID-PPSC103>3.0.CO;2-I

Lau, R., and Chuah, H. K. L. (2013). Dynamic Shape Factor for Particles of Various Shapes in the Intermediate Settling Regime. *Adv. Powder Technol.* 24, 306–310. doi:10.1016/j.apt.2012.08.001

Lindauer, G. C., and Castleman, A. W. (1970). The Importance of Gravitational Coagulation on the Settling of High-Mass Density Aerosols. *Nucl. Sci. Eng.* 42, 58–63. doi:10.13182/nse70-a19327

Lister, J. D., Smit, D. J., and Hounslow, M. J. (1995). Adjustable Discretized Population Balance for Growth and Aggregation. *AIChE J.* 41, 591–603. doi:10.1002/aic.690410317

Liu, L., Zhang, Z., Wu, Y., Yang, W., Wu, S., and Zhang, L. (2017). Decay of High-Concentration Aerosol in a Chamber. *Aerosol Sci. Eng.* 1, 155–159. doi:10.1007/s41810-017-0015-z

Misra, J., Subramanian, V., Kumar, A., Baskaran, R., and Venkatraman, B. (2013). Investigation of Aerosol Mass and Number Deposition Velocity in a Closed Chamber. *Aerosol Air Qual. Res.* 13, 680–688. doi:10.4209/aaqr.2012.06.0159

Narayanam, S. P., Kumar, A., Pujala, U., Subramanian, V., Srinivas, C. V., Venkatesan, R., et al. (2021). Theoretical Simulation on Evolution of Suspended Sodium Combustion Aerosols Characteristics in a Closed Chamber. *Nucl. Eng. Technol.* 0–6. doi:10.1016/j.net.2021.12.029

Powers, D. A., Washington, K. E., Burson, S. B., and Sprung, J. L. (1996). *A Simplified Model of Aerosol Removal by Natural Processes in Reactor Containment*. U.S. Nucl. Regul. Comm. Albuquerque USA: (NRC), NUREG-CR-6173.

Schnell, M., Cheung, C. S., and Leung, C. W. (2006). Investigation on the Coagulation and Deposition of Combustion Particles in an Enclosed Chamber with and without Stirring. *J. Aerosol Sci.* 37, 1581–1595. doi:10.1016/j.jaerosci.2006.06.001

Sevón, T. (2005). *Molten Core-Concrete Interactions in Nuclear Accidents: Theory and Design of an Experimental Facility*. Helsinki, Finland: VTT Technical Research Centre of Finland.

Sheng, C., and Shen, X. (2006). Modelling of Acoustic Agglomeration Processes Using the Direct Simulation Monte Carlo Method. *J. Aerosol Sci.* 37, 16–36. doi:10.1016/j.jaerosci.2005.03.004

Sheng, C., and Shen, X. (2007). Simulation of Acoustic Agglomeration Processes of Poly-Disperse Solid Particles. *Aerosol Sci. Technol.* 41, 1–13. doi:10.1080/02786820601009704

Subramanian, V., Baskaran, R., Misra, J., and Indira, R. (2011). Experimental Study on the Behavior of Suspended Aerosols of Sodium and Nonradioactive Fission Products (SrO2and CeO2) in a Closed Vessel. *Nucl. Technol.* 176, 83–92. doi:10.13182/NT11-A12544

Tian, L. T., Gu, H., Yu, H., and Chen, J. (2020). Experimental Study on the Natural Deposition Characteristics of Erosols in Containment. *Front. Energy Res.* 8, 345. doi:10.3389/fenrg.2020.527598

Xie, M.-L. (2014). Asymptotic Behavior of TEMOM Model for Particle Population Balance Equation over the Entire Particle Size Regimes. *J. Aerosol Sci.* 67, 157–165. doi:10.1016/j.jaerosci.2013.10.001

Yu, M., Koivisto, A. J., Hämeri, K., Seipenbusch, M., and Hämeri, K. (2013). Size Dependence of the Ratio of Aerosol Coagulation to Deposition Rates

for Indoor Aerosols. *Aerosol Sci. Technol.* 47, 427–434. doi:10.1080/02786826.2012.759640

Yu, M., Liu, Y., Lin, J., and Seipenbusch, M. (2015). Generalized TEMOM Scheme for Solving the Population Balance Equation. *Aerosol Sci. Technol.* 49, 1021–1036. doi:10.1080/02786826.2015.1093598

Zurita-Gotor, M., and Rosner, D. E. (2004). Aggregate Size Distribution Evolution for Brownian Coagulation-Sensitivity to an Improved Rate Constant. *J. Colloid Interface Sci.* 274, 502–514. doi:10.1016/j.jcis.2004.02.065

Conflict of Interest: The authors declare that the research was conducted in the absence of any commercial or financial relationships that could be construed as a potential conflict of interest.

Publisher's Note: All claims expressed in this article are solely those of the authors and do not necessarily represent those of their affiliated organizations, or those of the publisher, the editors, and the reviewers. Any product that may be evaluated in this article, or claim that may be made by its manufacturer, is not guaranteed or endorsed by the publisher.

frontiers | Frontiers in Energy Research

ORIGINAL RESEARCH
published: 26 May 2022
doi: 10.3389/fenrg.2022.883972

High-Temperature Characterization of Melted Nuclear Core Materials: Investigating Corium Properties Through the Case Studies of In-Vessel and Ex-Vessel Retention

Jules Delacroix, Christophe Journeau and Pascal Piluso*

CEA, DES, IRESNE, DTN, Saint-Paul-Lez-Durance, France

OPEN ACCESS

Edited by:
Yapei Zhang,
Xi'an Jiaotong University, China

Reviewed by:
Huandong Chen,
Sun Yat-sen University, Zhuhai Campus, China
Luteng Zhang,
Chongqing University, China

****Correspondence:***
Jules Delacroix
jules.delacroix@cea.fr

Specialty section:
This article was submitted to Nuclear Energy, a section of the journal Frontiers in Energy Research

Received: *25 February 2022*
Accepted: *20 April 2022*
Published: *26 May 2022*

Citation:
Delacroix J, Journeau C and Piluso P (2022) High-Temperature Characterization of Melted Nuclear Core Materials: Investigating Corium Properties Through the Case Studies of In-Vessel and Ex-Vessel Retention. Front. Energy Res. 10:883972. doi: 10.3389/fenrg.2022.883972

During a severe accident in a nuclear reactor, the molten core—or corium—may be relocated into the reactor vessel's lower plenum in case of core support plate failure. The severe accident management strategy for In-Vessel Retention—or IVR—consists in stabilizing the corium within the reactor pressure vessel by external cooling of the vessel's lower head. If now, the vessel fails due to excessive thermal loading on its walls, the Ex-Vessel Retention—or EVR—strategy is adopted. In this case, the core melt stabilization can be achieved by effective corium spreading, either in the reactor vessel cavity or in a dedicated "core-catcher", and cooling by water. The success of both strategies highly depends on the corium behavior at high temperatures, conditioning vessel's integrity for IVR, and promotion for the spreading of the EVR. This involves a variety of fundamental mechanisms closely related to heat and mass transfer regimes prevailing at the system scale, which requires further analytical and experimental insight to determine the primary mechanisms and feed the modeling tools, allowing the numerical simulations of severe accident scenarios.

Within the framework of corium characterization at high temperatures, the present study aims at filling the lack of such fundamental data as density, surface tension, liquidus and solidus temperatures, and viscosity. In order to accurately measure these properties at high temperatures, the VITI facility is designed with various configurations. Concerning IVR, the influence of density and surface tension is particularly highlighted through VITI-SD and VITI-MBP configurations, and practical applications of experimental results are finally discussed, in link with the focusing effect issue at the thin upper metallic layer of the corium pool. Concerning EVR, the properties of interest are solidus/liquidus temperature and dynamic viscosity, and typical experimental results obtained through VITI-VPA and VITI-GFL configurations are discussed in view of characterizing corium spreading.

Keywords: corium, severe accident, high temperature, physical properties, in-vessel retention, ex-vessel retention, VITI experiment

1 INTRODUCTION

Following the Fukushima Daiichi accident, safety studies have been performed: families of initiators have been re-evaluated, and several assessment analyses have been performed, including response to severe accident conditions, mitigation tools, and coping time (Baek, et al., 2017; Song, 2021). International programs have been devoted to the understanding and modeling of the Fukushima Daiichi severe accident (Nakayoshi, et al., 2020; Pellegrini, et al., 2020).

Even if the overall severe accident phenomenology is relatively well-known, the complex coupling of physical mechanisms and their modeling involving corium progression can generate discrepancies for severe accident calculation assessment. As an example, let us mention the various calculations of the Fukushima Daiichi accident as predicted by different severe accident integral codes (Pellegrini, et al., 2016). Such discrepancies have been recently reduced by taking the same physical properties in all participating codes (Pellegrini, et al., 2022).

The lack of reliable knowledge of corium properties is certainly one of the major sources of uncertainties. This issue can be highlighted through the case study of the mitigation approaches called the In-vessel retention (IVR) (Bakuta, et al., 2015; Fichot, et al., 2020) and ex-vessel retention (EVR) (Journeau, et al., 2005) strategies. Specific severe accident phenomena such as fuel coolant interaction and steam explosion could damage the containment building and lead to fission product release. Accurate knowledge of corium properties has been identified as a major issue, which must be addressed to ensure reliable nuclear safety for pressurized water reactors (Piluso, et al., 2017).

During a severe accident in a nuclear reactor, the molten core—or corium—may be relocated into the reactor vessel's lower plenum in case of core support plate failure. Different Severe Accident Management (SAM) strategies have been proposed for the current fleet and new-built reactors in which the molten core retention is to be achieved either in-vessel or ex-vessel (Fischer, et al., 2016; Amidu, et al., 2022). The severe accident management strategy for IVR consists in stabilizing the corium within the Reactor Pressure Vessel (RPV) by external cooling of the vessel's lower head (Ma, et al., 2016). The success of the IVR strategy highly depends on corium behavior at the lower head scale. This behavior involves a variety of mechanisms in link with heat and mass transfer at the pool scale. Such phenomena may lead to the stratification of the corium pool, as observed in MASCA (Tsurikov, 2007) and RASPLAV (Asmolov and Tsurikov, 2000) experiments, performed in the framework of OECD projects, and CORDEB (Fichot, et al., 2022), an EU project. In particular, the formation of a "thin" light metal layer on top of the stratified corium pool, in direct contact with the vessel wall, may deeply alter corium pool topology. As shown hereafter, the so-called "focusing effect" (concentration of the heat flux in a thermally conductive metallic layer) is of primary interest regarding vessel integrity and requires further analytical and experimental insight to determine the fundamental mechanisms. A recent benchmark exercise (Carénini, et al., 2017) involving integral code-based sensitivity analyses has demonstrated the major impact of light metal layer properties. In this configuration, the sign of surface tension temperature coefficient $d\sigma/dT$ will play an important role in the Bénard–Marangoni current at the free surface atop the thin layer, impacting thus convection patterns, as shown hereafter.

In case IVR cannot be guaranteed, EVR is adopted. In the case of EVR through the Concrete Cavity [EVRCC, (Amidu, et al., 2022)], there are two options depending whether the cavity is filled or not by water at the time of the vessel melt-through. In the case of a wet cavity (Fischer, et al., 2016), the corium jet fragments, a process largely controlled by surface tension (Thakre, 2015), and forms a debris bed that will be cooled by the surrounding water. In addition, surface tension will also play an important role, for example, in oxide-metal ex-vessel configurations (stratification and emulsion). If water cooling is revealed to be impossible, the concrete basemat will be ablated because of continuing Molten Core Concrete Interaction (MCCI) (Farmer, et al., 2016). In case of an initially dry cavity, the MCCI starts and water flooding is activated with the goal of arresting concrete ablation (Bonnet, et al., 2017). For other types of nuclear reactors based on a so-called "core-catcher" approach, for example, the European Pressurized Reactor (EPR), the core melt stabilization is achieved by designing a core-catcher in a dedicated lateral compartment (Fischer, 2004). The melt discharge from the RV cavity to the core-catcher requires effective corium spreading before flooding to reduce the heat flux due to the corium decay heat. Spreading is controlled by the coupling of melt solidification with hydrodynamics through the evolution of its rheology (Journeau, 2006). It is, thus, of prime interest to determine the evolution of viscosity as a function of melt temperature and composition and characterizing accurately the different phase transitions experienced by corium mixtures.

Consequently, the previous observations enhance the necessity to access reliable measurements of density, surface tension, liquidus and solidus temperatures, and viscosity for achieving a consistent modeling of the actual corium flow topology. These issues are addressed in this study in order to bridge the gap between numerical simulations and actual corium thermal-hydraulics.

In the recent years, the VIscometer Temperature Installation (VITI) experimental facility of the CEA Cadarache PLINIUS prototypic corium platform (Journeau, et al., 2022) has been upgraded, conferring it the status of a versatile apparatus, dedicated to the investigation of fundamental phenomena linked to severe accident issues. Among other topics, this upgrade has made possible the high-temperature characterization of the corium properties of interest, each linked to a specific configuration of VITI. In this article, the unique capabilities of VITI are highlighted within the scope of both IVR and EVR. On the one hand, in **Section 2**, the focus is placed on the measurements of the surface tension and density of liquid metals at high temperatures for IVR through the VITI-SD and VITI-MBP configurations, respectively. The typical results that can be obtained are then discussed through the prism of the focusing effect issue. On the other hand, in **Section 3**, the case study of corium spreading is investigated for EVR, involving rather the solidus/liquidus temperatures and dynamic viscosity of

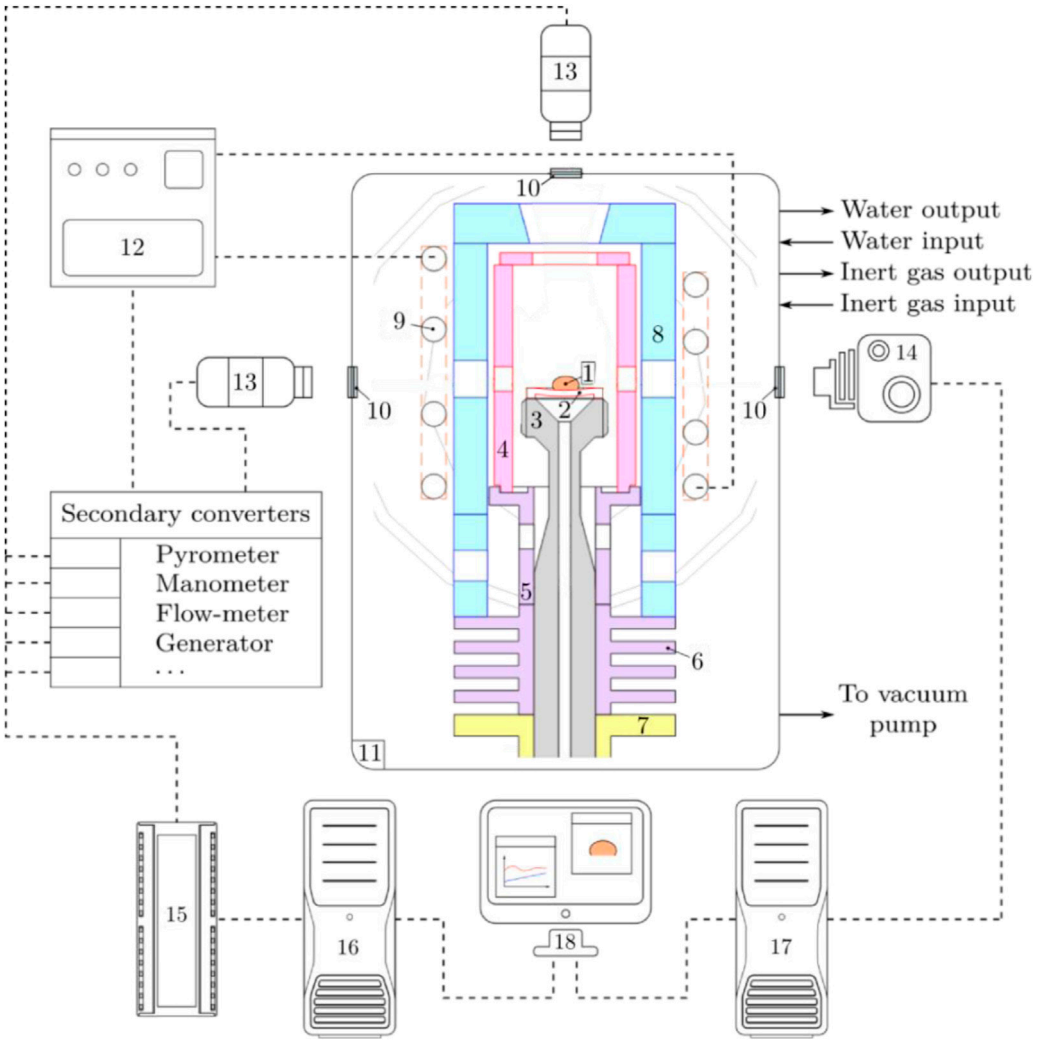

FIGURE 1 | Overall layout of VITI-SD configuration (Chikhi, et al., 2019). 1: liquid droplet; 2: substrate; 3: substrate support; 4: susceptor; 5: susceptor support; 6: fins; 7: global support; 8: thermal shield; 9: inductor; 10: windows; 11: confinement vessel; 12: generator; 13: pyrometers; 14: camera; 15: data bus; 16: acquisition PC; 17: imaging PC; 18: monitoring.

oxide mixtures that are measured through the VITI-VPA and VITI-GFL configurations, respectively.

2 MEASURING THE SURFACE TENSION AND DENSITY OF LIQUID METALS AT HIGH TEMPERATURES FOR IN-VESSEL RETENTION: THE VITI-SD AND VITI-MBP EXPERIMENTS

As previously introduced, in order to properly describe the thermal-hydraulics of the upper layer, there is a need for experimental data about the density and surface tension of liquid steels at high temperatures. In French PWR, the vessel is made of 304L austenitic stainless steel and 16MND5 (A508) ferritic steel, while the internal structure of the core is made of 316 and 304L austenitic stainless steel. Concerning surface tension, a review of the existing literature (Dubberstein, et al., 2015; Brooks, et al., 2005; Egry and Brillo, 2009; Matsumoto, et al., 2005) underlines a significant dispersion of surface tension measurements from both qualitative and quantitative viewpoints, in link with experimental uncertainties on σ, T, and the sample's composition. Concerning the latter, the major impact of such minor components as sulfur must be taken into account, given their potential influence on the evolution of $\sigma(T)$ (Mills, and Brooks, 1994). Moreover, to our knowledge, there seems to be no available data above the temperature of 1800°C, in link with the significant vaporization of steel occurring around this threshold temperature. Finally, for 16MND5-grade, the data are missing for both density and surface tension.

The VITI facility is used to provide such new data at high temperatures for the density and surface tension of the liquid

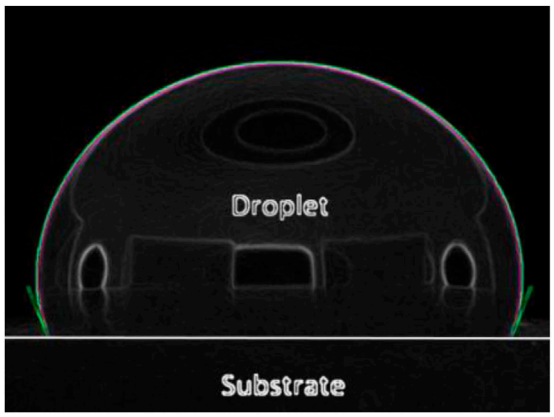

FIGURE 2 | Contour fitting—green line—of liquid steel sessile droplet.

steels of interest. On the one hand, the Sessile Droplet—SD—technique is used for the measurement of density ρ, and on the other hand, the Maximum Bubble Pressure—MBP—is used for the proper estimation of σ.

2.1 VITI-SD Configuration and Density Measurements

2.1.1 Experimental Layout

The VITI-SD general layout is displayed in **Figure 1**. The liquid droplet 1) rests on a dedicated plane substrate 2), made of yttria-stabilized zirconia, chosen for its chemical inertia with liquid steel at high temperature, and the drop-substrate system bears on the substrate support 3).

The whole system is heated by the so-called indirect induction method: the water-cooled inductor 9), connected to the power generator 12), is electromagnetically coupled with the so-called susceptor 4), which is supported by 5). The susceptor heats the sample up to the target temperature by radiative heat transfer. The thermal shield 8) is placed around the susceptor in order to decrease thermal losses and minimize temperature gradients at sample scale in the High-Temperature Chamber—HTC. The whole assembly lies upon thermal fins 6) for heat dissipation and, finally, on the global support 7). The experiments are carried out within the water-cooled confinement vessel 14) in an inert atmosphere of argon, in slight overpressure. The bichromatic video pyrometer 13) and the camera 14) allow for droplet imaging through adequate windows 10) and holes designed in the HTC. Finally, the whole acquisition data are collected by the data bus 15) and sent to the data acquisition computer 16), in parallel to the imaging computer 17), for sample monitoring 18).

2.1.2 Experimental Procedure, Measurement Principle, and Uncertainties

The original samples consist of specifically machined cylindrical pellets, whose both typical diameter and height are around 5 mm. Then, samples are mechanically polished, exposed to a chemical attack, and stored in acetone to avoid adverse oxidation prior to experimental tests. The average chemical compositions of the two studied alloys are measured before (as received) and after VITI-SD measurements (as tested). Spark spectrometers are used for general analysis of chemical composition by ICP-AES. Carbon, oxygen, sulfur, and nitrogen are measured with elementary combustion analyzers. Then, the initial atmosphere in the VITI confinement vessel is removed after several vacuum pumping/argon cleaning and monitored with a dedicated oximeter prior to the test. The induction heating is then started, and the sample is gradually heated with a 50°C/min temperature ramp until it reaches a liquid state, typically after a few dozen minutes (**Figure 2**).

At a given temperature of the aforementioned liquidus, the imaging system allows to take high-resolution pictures of the sessile droplet, as shown **Erreur ! Source du renvoi introuvable.** The sample is weighed before and after the test to ensure its mass m remains constant. By means of classical contour fitting techniques (Hoorfar, and Neumann, 2006), the droplet volume V can be determined, and thus density can be easily estimated: by definition, $\rho = m/V$. Then, other temperatures can be investigated to determine $\rho(T)$, up to the threshold of significant evaporation, and if required, beyond this threshold by extrapolation.

The sources of systematic uncertainty for density measurements at high temperatures are scaling uncertainty—linked to the resolution of the imaging system—leading to an error in volume estimation and temperature uncertainty. Mass uncertainty is negligible, given the weighing accuracy. Following JCGM 100 (2008), and according to Delacroix, et al. (2022), the relative systematic uncertainty associated with VITI-SD density measurements is about 1% when the experimental setup is carefully prepared.

2.1.3 Experimental Results

The measurements corresponding to six experimental tests are shown in **Figure 3**. The results clearly indicate a linear decrease of density with temperature following a linear tendency, as expected. There is no significant difference between 304LP1 and 304LP4 grades, which are almost identical in composition (except in minor elements). The density of ferritic steel 16MND5 is slightly higher than that of austenitic steel, given the larger iron content. The reproducibility between different samples is quite satisfying within experimental uncertainty. Additional details—such as original correlations $\rho(T)$—can be found in Chikhi, et al. (2019); Korobeinikov, et al. (2021); Delacroix, et al. (2022), in the framework of welding pool modeling.

2.2 VITI-MBP Configuration and Surface Tension Measurements

2.2.1 Experimental Layout

The VITI-MBP general layout is shown in **Figure 4**. Let us only introduce the main differences with VITI-SD. Here, the sample consists of a liquid steel pool 1) placed in a crucible 2). A zirconia-made capillary tube 3) of radius r is placed above the crucible and connected with the micrometer translation stage 12), which allows for the control of capillary immersion depth h into the liquid pool. A flow meter 13) regulates the argon gas flow in the capillary at a low gas flow rate. A pressure sensor 14) finally enables the measurement of pressure difference p between the capillary tip immersed in the pool and the surrounding atmosphere.

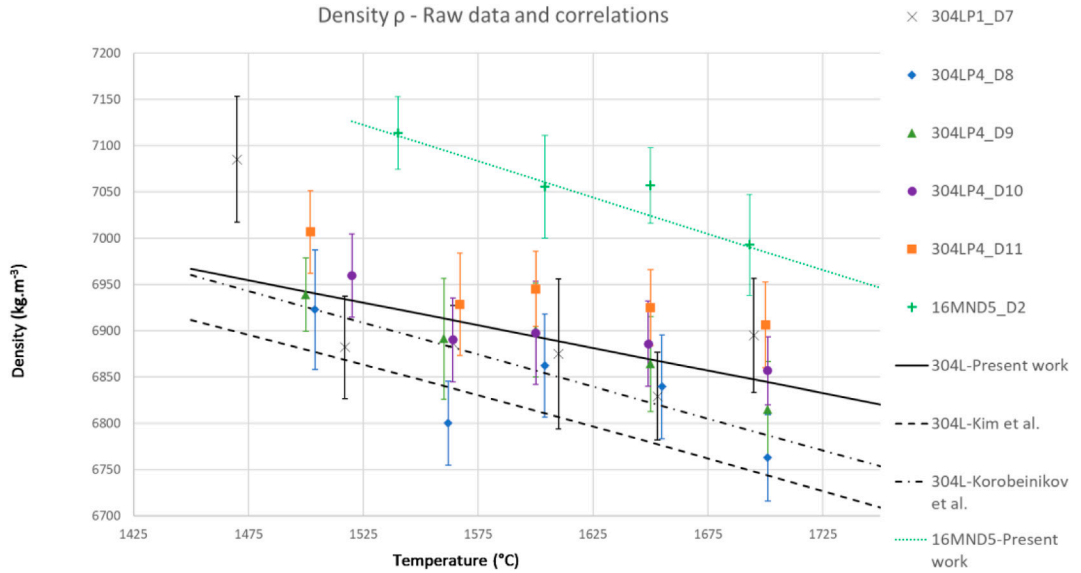

FIGURE 3 | VITI-SD density measurements and comparison with literature for 304L (Korobeinikov, et al., 2021; Kim, 1975).

2.2.2 Experimental Procedure, Measurement Principle, and Uncertainties

The experimental procedure for MBP tests is similar to the procedure for SD tests. The difference is that for MBP tests, slices of raw steel rods are directly used, constituting cylindrical loads whose typical diameter and height are around 30 and 45 mm, respectively. After atmosphere preparation and starting of induction heating, once the melting point is reached, the sample melts into a liquid pool, into which the capillary tube is immersed. The latter is carefully machined with high mechanical accuracy to allow for controlled bubbling inside liquid corium. The tip of the capillary tube is accurately controlled by means of a dedicated optical test bench: the surface roughness is assessed, and its inner diameter is determined with 10 µm accuracy, by edge detection after optical calibration.

As detailed in Dubberstein and Heller, (2013), at a given immersion depth h, typical pressure oscillations p are shown in the left-hand part of **Figure 5**. At the very beginning of the bubble growth process, the curvature radius r_b of the new bubble is much larger than the capillary radius: $r_b \gg r$. Consequently, a local pressure minimum is observed, representative from the hydrostatic pressure inside the pool. Then, the gas bubble begins to grow at the tip of the capillary tube. The pressure continuously grows up to a local maximum, for which $r = r_b$, corresponding to a growth duration t_{life}. At this local maximum, it is thus possible to derive the Laplace–Young equation as follows:

$$p = \frac{2\sigma}{r} + \rho g h,$$

thus giving access to surface tension σ, provided density ρ is known. Afterward, further immersion of the capillary tube into the molten pool allows achieving satisfying statistics, prior to the investigation of other temperatures. The quality of measurement results in a linear dependence $p(h)$, as shown in the right-hand part of **Figure 5**.

According to the Young–Laplace equilibrium, the main sources of systematic uncertainty for surface tension measurements at different temperatures are linked to geometry—capillary radius r and immersion depth h, pressure p, density ρ, and temperature T. Once again, following JCGM 100 (2008), and according to Delacroix, et al. (2022), the relative systematic uncertainty associated with VITI-MBP surface tension measurements is about 2.5%.

2.2.3 Experimental Results

The results corresponding to six experimental tests are reviewed in **Figure 6**. They tend to indicate that the surface tension of all vessel steel grades under consideration follow a concave parabolic evolution as a function of temperature. However, the peak of the parabola differs between grades with low sulfur content [S]—304LP1 and 16MND5—and the grade with high [S], namely, 304LP4. Moreover, the surface tensions of the three studied steels are ordered as follows: $\sigma_{304LP4} < \sigma_{304LP1} < \sigma_{16MND5}$.

Elemental analyses—that are not detailed here—confirm the impact of impurities. Recent articles (Korobeinikov, et al., 2021; Delacroix, et al., 2022) highlight the decisive role played by both sulfur and oxygen, acting similarly to surface active agents or surfactants. They tend to favor the decrease of surface tension values and may also influence the sign of $d\sigma/dT$ at a given temperature T. Additional details—such as original correlations $\sigma(T)$-- can be found in Korobeinikov, et al., (2021); Delacroix, et al., (2022) as well.

2.3 Discussion About the Influence on In-Vessel Corium Stratification and the Particular Issue of Focusing Effect

As previously mentioned, the IVR strategy is a mitigation strategy where corium is to be retained in the vessel by ex-vessel reactor vessel cooling by water to avoid vessel-wall melt-through. The

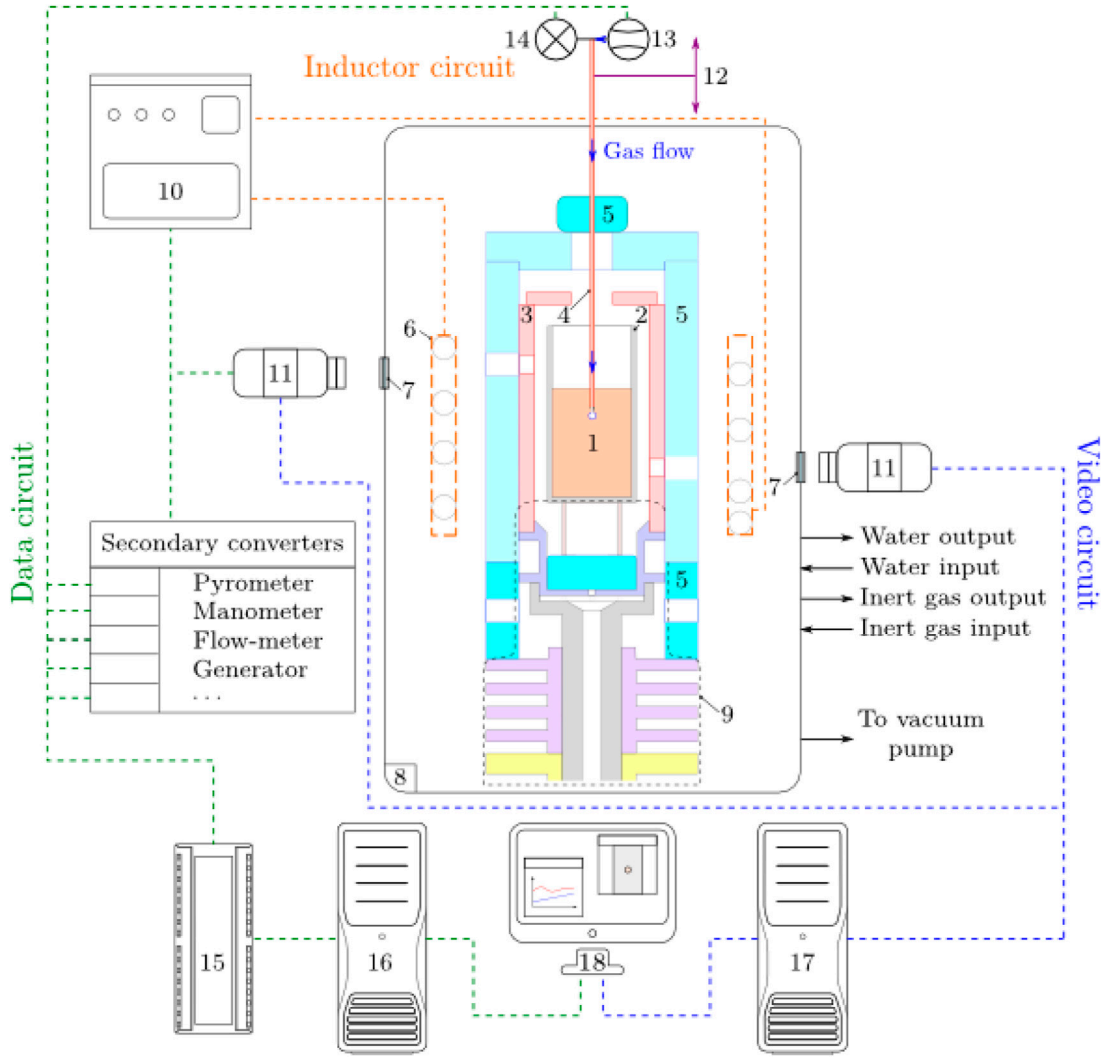

FIGURE 4 | Overall layout of VITI-MBP configuration (Delacroix, et al., 2022). 1: liquid pool; 2: crucible; 3: susceptor support; 4: capillary tube; 5: thermal shield; 6: inductor; 7: windows; 8: confinement vessel; 9: supporting system; 10: generator; 11: pyrometers; 12: µm translation stage; 13: µ-flow meter; 14: µ-pressure sensor; 15: data bus; 16: acquisition PC; 17: imaging PC; 18: monitoring.

success of the strategy mainly depends on the heat flux distribution at the corium pool interface compared to the Critical Heat Flux (CHF), above which vessel integrity is not ensured.

As shown on the left part of **Figure 7**, the corium pool configuration is rather complex, in link with the existence of miscibility gaps between the oxide (*e.g.*, UO_2-ZrO_2) and the metallic (*e.g.* light: steel—mainly Fe; heavy: Zr-U) phases. Three main areas may be roughly distinguished: the molten oxide pool, possibly surrounded by a solid crust; the heavy metal layer, at the very bottom of the vessel; and the light metal layer, on top of the oxide pool.

The presence of this thin upper metallic layer is a major issue. The heat produced by the decay of fission products in the oxide pool can be preferentially transferred to the upper metallic layer, which in turn transfers it to the vessel wall. Assuming high thermal conductivity of liquid metal compared to the oxide pool, the main part of the thermal load on the vessel may be concentrated in the metallic layer, leading to the so-called "focusing effect" phenomenon.

Historically, stationary IVR studies have been performed to quantify the thermal load from the molten pool to the vessel wall (Rempe, et al., 1997; Esmaili and Khatib-Rahbar, 2005; Theofanous, et al., 1997). More recently, a transient approach to the stratified corium pool (Seiler, et al., 2007; Zhang, et al., 2011; Le Tellier, et al., 2015) and a benchmark between different severe accident scenario codes (Sangiorgi, 2015) pointed out that the use of conservative assumptions may result in heat fluxes exceeding the CHF, in link with the focusing effect. If now, we focus on the thermal-hydraulics of the upper metallic layer, recent Computational Fluid Dynamics (CFD) simulations showed that bulk convection is mainly driven by the Rayleigh–Bénard instability and lateral recirculation along the cooled vessel wall

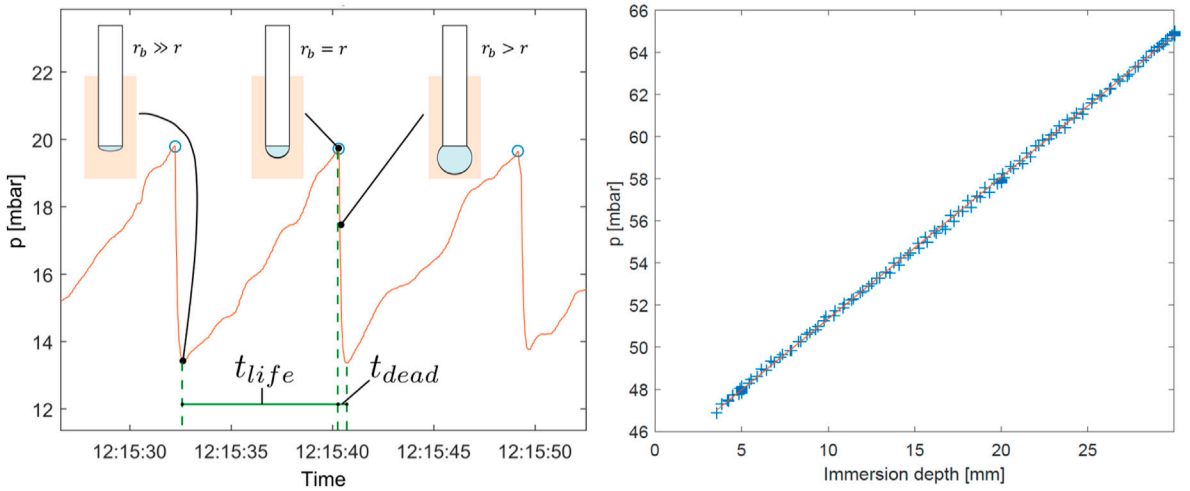

FIGURE 5 | Principle of VITI-MBP measurements at given temperature T. Left: pressure p peak detection at given immersion depth h. Right: linear correlation $p(h)$.

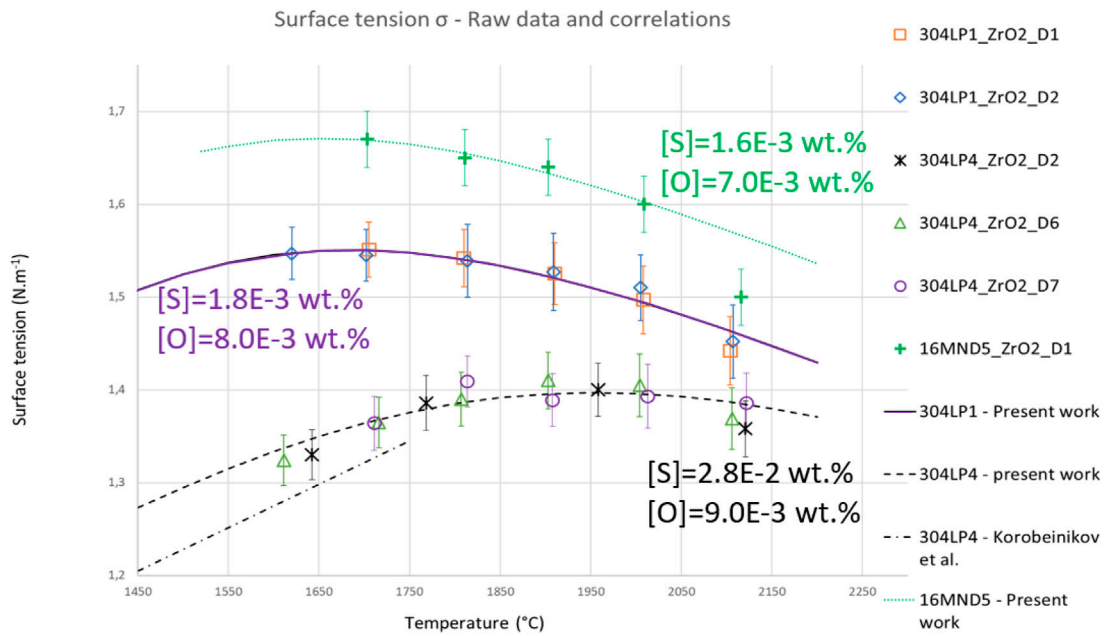

FIGURE 6 | VITI-MBP surface tension measurements and comparison with literature at "low" temperatures for 304L (Korobeinikov, et al., 2021; Delacroix, et al., 2022). The mass fraction of sulfur [S] and oxygen [O] related to each grade is also indicated.

(Saas, et al., 2017), for which the evolution of density ρ with temperature T plays a significant role, along with viscosity as well. For thin enough metallic layers, the Bénard–Marangoni effect may also significantly influence the flow topology. As shown in **Figure 7**(right), depending on the dependence of surface tension σ on temperature, the surface flow could either promote or impede the Rayleigh–Bénard convection. In particular, if σ decreases with T, the co-current surface and bulk flows will favor heat extraction at the free surface, thus reducing the thermal load on the vessel wall (Dang, et al., 2021).

Concerning density, the measurements performed with VITI-SD shown in **Figure 3** can be directly used to feed CFD simulations of the Rayleigh–Bénard convection patterns governing the thermal-hydraulics of the upper metallic layer. The linear decrease with temperature confirms the predicted orientation of Rayleigh–Bénard cells, with a slight difference in magnitude expected between the different steel grades according to the change in temperature coefficients.

Concerning surface tension, in the light of the results shown in **Figure 6**, the level of surface tension at the free surface of the top

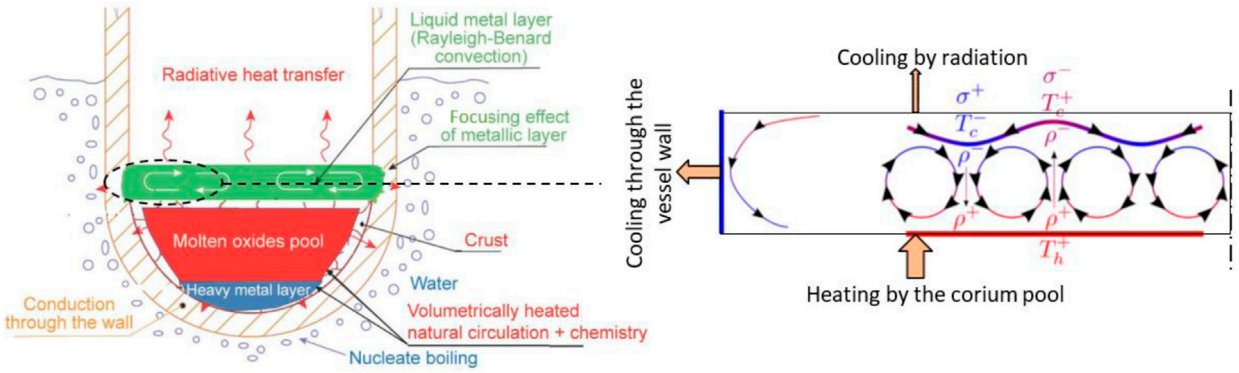

FIGURE 7 | Typical IVR configuration. Left: stratified corium pool and typical transfer phenomena (Ma, et al., 2016). Right: zoom on the Bénard-Marangoni flow at the surface of the thin upper metallic layer, according to surface tension evolution with temperature (courtesy from R. Le Tellier).

metallic layer may significantly vary according to local composition. As the Bénard–Marangoni surface flow directly depends on the temperature coefficient of surface tension $d\sigma/dT$, the surface flow could alternatively promote or impede the Rayleigh–Bénard convection depending on temperature range and actual melt composition. This means that whether in transient regime and/or if the free surface experiences significant thermal (and/or compositional) gradients, the resulting inflection in the surface tension profile could lead to complicated flow topologies in the metallic layer stemming from local surface tension gradient. This amends the conclusion of Chikhi, et al. (2019) to some extent, where the case $d\sigma/dT > 0$ seemed the most probable considering preliminary results.

3 MEASURING THE SOLIDUS/LIQUIDUS TEMPERATURES AND THE VISCOSITY OF LIQUID OXIDES AT HIGH TEMPERATURES FOR EX-VESSEL RETENTION: THE VITI-VPA AND VITI-GFL CONFIGURATION

Let us now turn to the investigation corium spreading in link with the EVR strategy. In this case, the VITI facility is used to gain physical insight about ex-vessel corium phase transitions and rheology, especially for oxides in the present article. On the one hand, the Visual Polythermal Analysis—VPA—technique is used for the measurement of solidus and liquidus temperatures T_{sol} and T_{liq}, respectively. On the other hand, the Gas Film Levitation—GFL—technique is implemented to give a first estimate of dynamic viscosity η.

3.1 VITI-VPA Configuration and Solidus/Liquidus Temperatures

3.1.1 Experimental Layout

The VITI-VPA general layout is shown in **Figure 8**. The single difference with VITI-SD configuration is the supporting system, which defines a field-of-view more convenient for phase transition detections by the camera focusing on the (originally) solid corium pellet.

3.1.2 Experimental Procedure, Measurement Principle, and Uncertainties

The experimental procedure for VPA tests is exactly the same as for SD tests, except that the solid oxide pellets of corium are specifically machined in a glove box before transferring them into the VITI confinement vessel in controlled conditions. Before reaching high temperatures, the pellets are subjected to heat treatment for a dozen minutes far below theoretical solidus (around 500°C) to eliminate residual organic pollution. Once melted, both high-definition (HD) camera and video-pyrometers constitute the polythermal imaging system for the VITI-SD tests, whose typical configuration is shown in **Figure 9**. Video-pyrometer 1 focuses on the top of the melting sample, thus measuring the temperature T_{sample}, while video-pyrometer 2 focuses on the substrate, thus giving the temperature $T_{substrate}$. The HD camera allows for sharp imaging of the substrate/sample system.

The methodology applied for VITI-VPA experiments derived from the approach proposed in Bechta (2007) is depicted in **Figure 10**. The high-resolution camera allows for a visual online detection of both solidus and liquidus points, in correlation with temperature measurements, by scrutinizing the first—respectively last—evidence of a liquid—respectively solid—phase at the surface of the sample. This allows us to define a first "solidus interval" $[T^-_{sol,vid}, T^+_{sol,vid}]$ – respectively "liquidus interval" $[T^-_{liq,vid}, T^+_{liq,vid}]$ – based on imaging interpretation.

In parallel, the posttreatment of temperature data supplied by the pyrometers alone, or polythermal analysis, is used as a complementary measurement procedure. The quantity corresponding to the temperature difference $\Delta T = T_{sample} - T_{substrate}$ can be defined from video-pyrometers alone. As shown in **Figure 10**, close to both solidus and liquidus temperatures, the evolution of ΔT shows noticeable inflection points due to swift changes of surface radiative properties and the enthalpy difference caused by phase transition. This polythermal

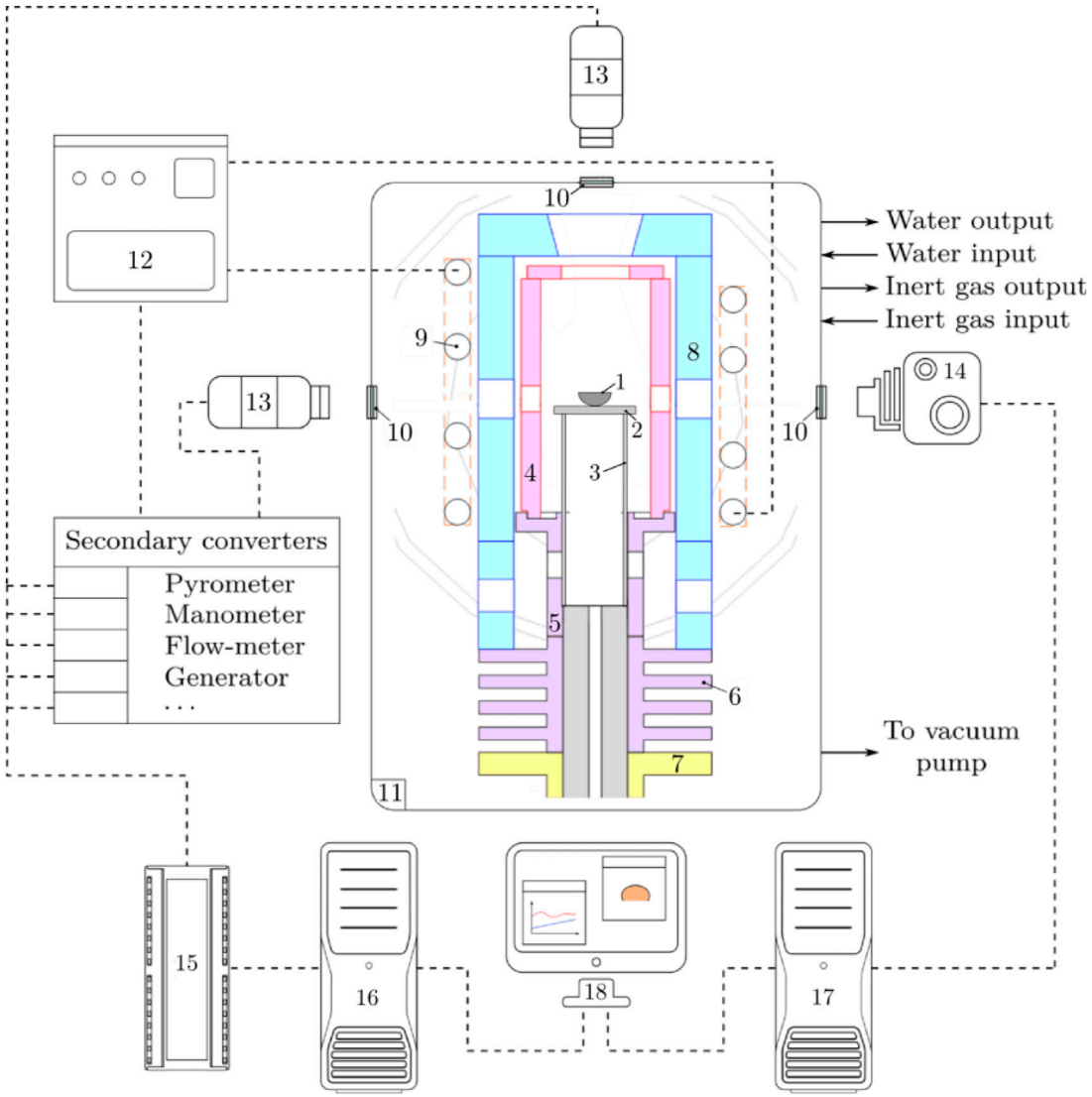

FIGURE 8 | Overall layout of VITI-VPA configuration (Delacroix, et al., 2019). 1: corium sample; 2: substrate; 3: substrate support; 4: susceptor; 5: susceptor support; 6: fins; 7: global support; 8: thermal shield; 9: inductor; 10: windows; 11: confinement vessel; 12: generator; 13: pyrometers; 14: camera; 15: data bus; 16: acquisition PC; 17: imaging PC; 18: monitoring.

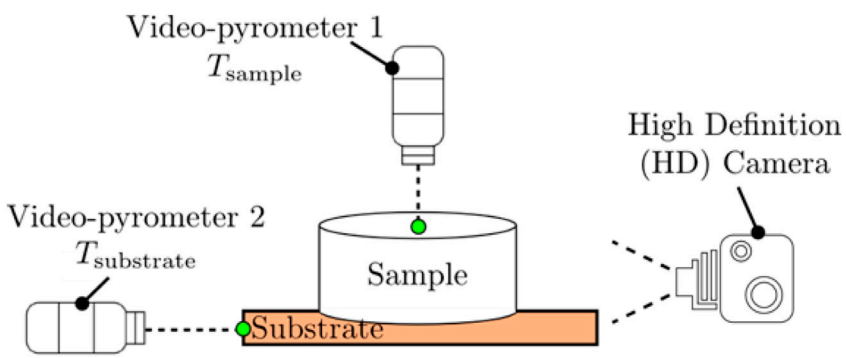

FIGURE 9 | Visual Polythermal Analysis (VPA) imaging system of VITI.

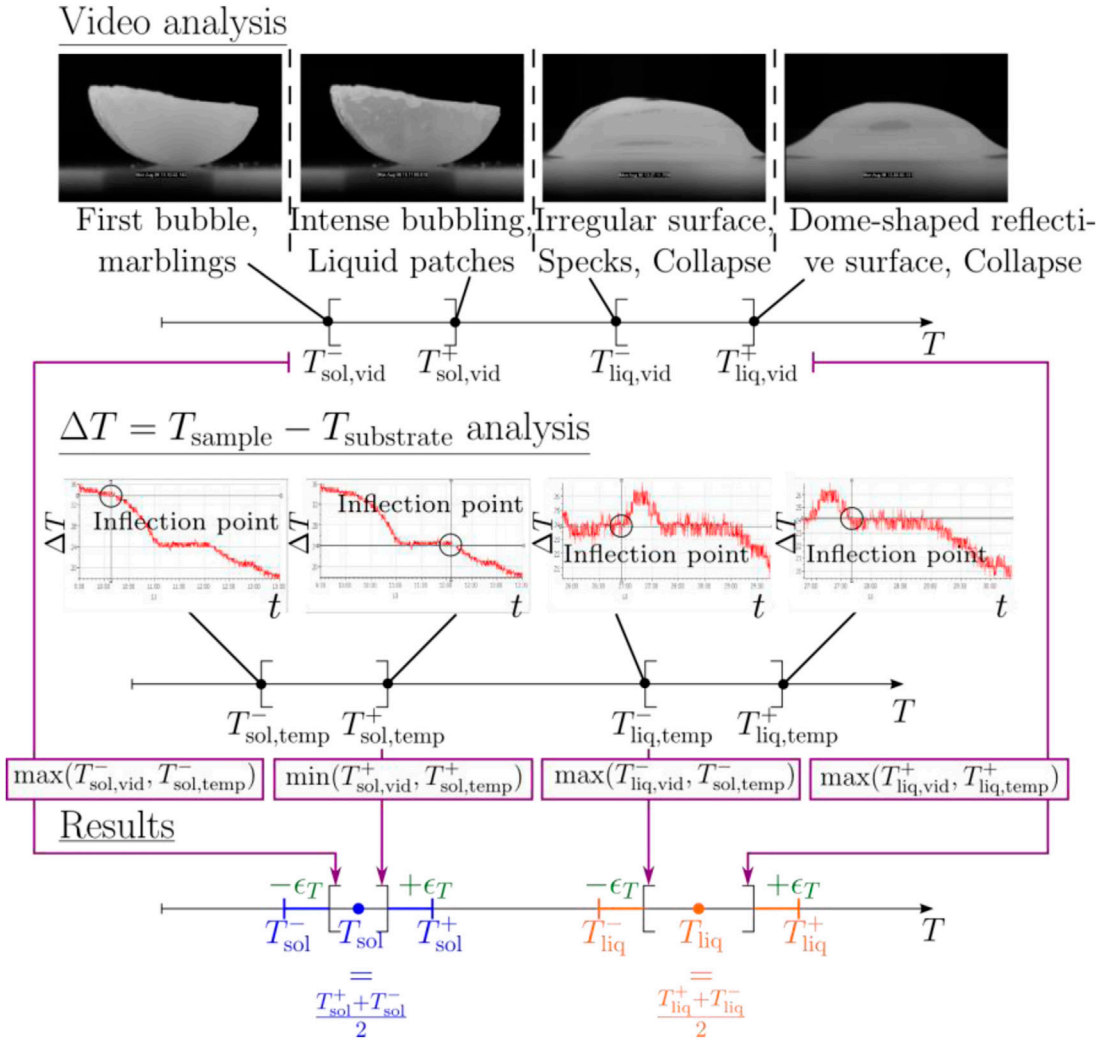

FIGURE 10 | Principle of visual polythermal analysis.

analysis leads to the definition of other temperature intervals, both for solidus $[T^-_{sol,temp}, T^+_{sol,temp}]$ and liquidus $[T^-_{liq,temp}, T^+_{liq,temp}]$.

The two approaches are then merged through VPA, leading to the definition of best-estimated intervals for both T_{sol} and T_{liq}. The main sources of systematic uncertainty for solidus/liquidus measurements are obviously linked to camera resolution for visual detection and to pyrometer accuracy. According to Delacroix, et al. (2019), the relative systematic uncertainty associated with VITI-VPA solidus and liquidus temperature measurements amounts typically to 3%.

3.1.3 Experimental Results

Let us give an application in link with corium spreading by discussing the results originally presented in Delacroix, et al. (2019) and shown **Figure 11**. The solidus and liquidus temperatures of various CSM mixtures (confidential composition) are measured according to the mass fraction of the corium. Obviously, the addition of sacrificial material to corium significantly lowers liquidus temperatures and solidus temperatures to a lesser extent. The reader may find additional details in Delacroix, et al. (2019), including comparisons with thermodynamic calculations.

3.2 VITI-GFL Configuration and Viscosity Measurements

3.2.1 Experimental Layout

The VITI-GFL general layout is shown in **Figure 12**. Let us only introduce the main differences with VITI-SD. Here, the liquid drop 1) is levitated on the lower diffuser 2) made of porous graphite, avoiding contact with the substrate by means of a thin gas film. The upper diffuser 5) can be vertically translated and constitutes the mobile actuator enabling droplet

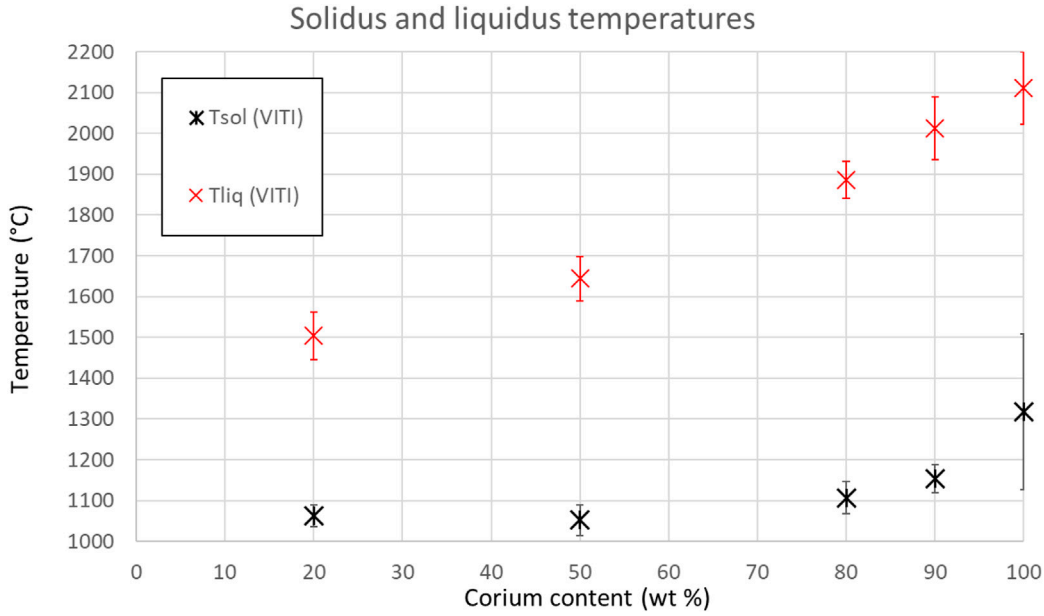

FIGURE 11 | VITI-VPA solidus and liquidus temperature measurements, according to corium content in Corium-Sacrificial Material (CSM) mixtures (Delacroix, et al., 2019).

relaxation for measuring dynamic viscosity η. This configuration minimizes the potential chemical interaction between the melt and its environment (substrate or crucible in other configurations).

3.2.2 Experimental Procedure, Measurements Principle, and Uncertainties

The experimental procedure for GFL tests is almost the same as for SD tests. The main challenge is to ensure the correct levitation of the sample, which is specifically machined to assess its stability at a solid state over the thin gas film and when moving the upper actuator before heating.

The principle of VITI-GFL measurement is based on the analysis of droplet relaxation. As shown in **Figure 13**, the liquid droplet is initially "at rest", levitating on the thin gas film generated by the lower diffuser. Then, the upper diffuser is drawn closer to the droplet. Once again, a thin gas film avoids any direct contact between the droplet and the diffuser. The upper diffuser is translated further downward so that the liquid droplet apex is subjected to an initial slight deformation of Δh_0 from its initial position h_0. The upper diffuser is then instantly moved upward, and the droplet experiences free oscillations. The time-evolution of droplet apex position h is tracked by means of a high-speed camera.

Droplet oscillations are governed by the values of the Ohnesorge number, defined by $\mathrm{Oh} = \eta/\sqrt{\sigma\rho R_S}$, where R_S is the radius of the equivalent sphere with the same volume as the liquid droplet. If $\mathrm{Oh} > 1$, the aperiodic mode prevails, while if $\mathrm{Oh} < 1$, the pseudo-periodic mode prevails—see **Figure 13**.

In this article, let us only focus on the pseudo-periodic mode. In this case, the time evolution of droplet apex position h can be written as follows:

$$h(t) = h_0 + \Delta h_0 \exp\left(-\frac{t}{\tau_p}\right)\cos(\omega t + \varphi),$$

where τ_p, ω, and φ correspond to damping time, angular frequency, and phase. In practice, this equation is fitted on the experimental profile. The fitted parameter of interest is τ_p because it can be linked to viscosity owing to a variational approach based on the analogy with damped mechanical harmonic oscillators (Haumesser, et al., 2002) deriving from Chandrasekhar formalism (Chandrasekhar, 1970). In fact, $\tau_p = f(\text{geometry}, \rho, \sigma, \eta)$. Density and surface tension being determined apart, for example, by VITI-SD and VITI-MBP experiments, it is thus possible to estimate the dynamic viscosity of the liquid sample.

As for VITI-SD, the main sources of systematic uncertainty for viscosity measurements at high temperatures are scaling uncertainty—linked to the resolution of the imaging system—leading to an error in apex location detection limit and temperature uncertainty. According to Grishchenko and Piluso (2011), the relative systematic uncertainty associated with VITI-GFL density measurements can amount to 10%; given the difficulty to properly track the exact position of the droplet apex, the magnitude of the initial deformation being restricted in order to apply the model based on the underlying linear perturbation theory.

3.2.3 Experimental Results

An application of VITI-GFL measurements is given in **Figure 14**, where prospective results are obtained for pure alumina Al_2O_3 and for the zirconia–alumina eutectic composition ZrO_2 (42.5 wt%)-Al_2O_3. First, the addition of zirconia to alumina at eutectic composition allows decreasing

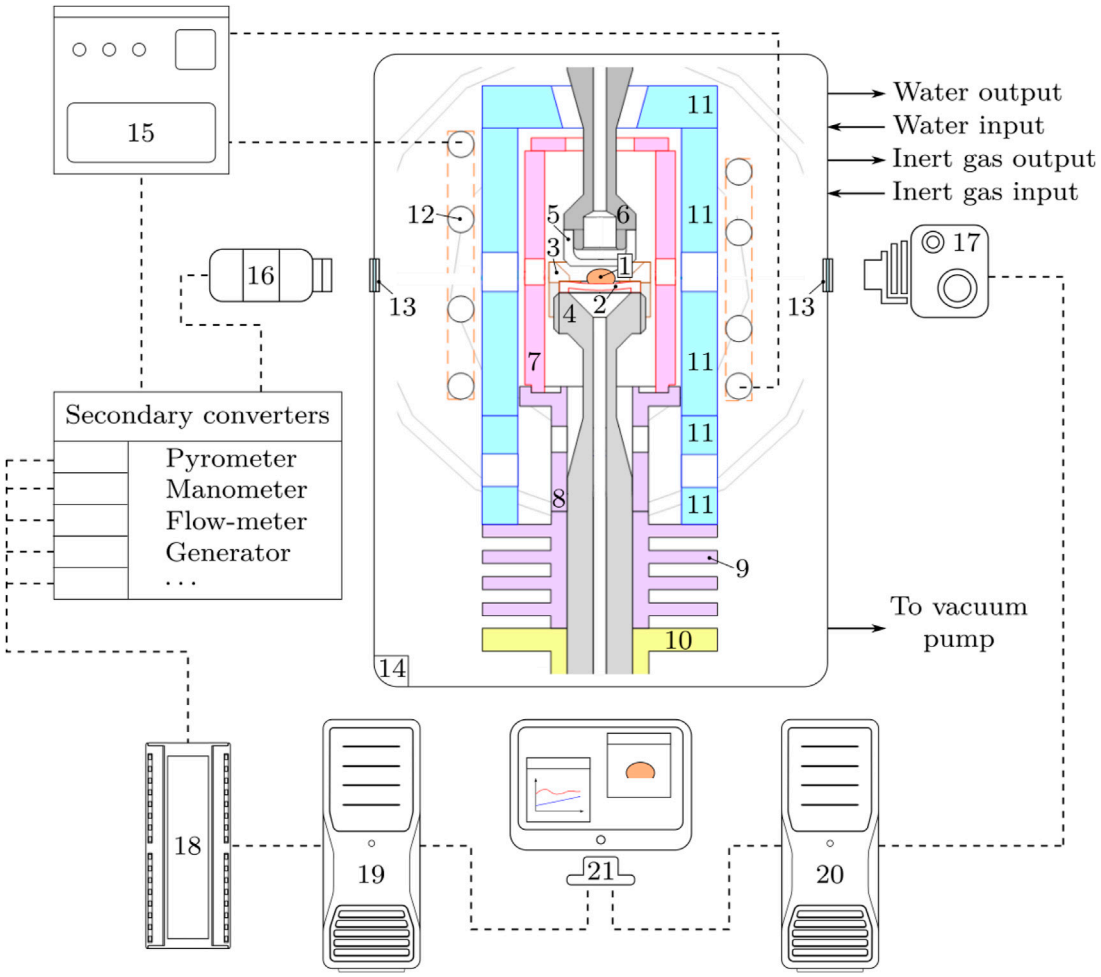

FIGURE 12 | Overall layout of VITI-GFL configuration (Grishchenko and Piluso, 2011). 1: drop; 2: lower diffuser; 3: screwing system; 4: lower diffuser holder; 5: upper diffuser; 6: upper diffuser holder; 7: susceptor; 8: susceptor holder; 9: fins; 10: global support; 11: thermal shield; 12: inductor; 13: windows; 14: VITI confinement vessel; 15: generator; 16: pyrometer; 17: high-speed camera; 18: data bus; 19: data acquisition computer; 20: imaging computer; 21: monitoring.

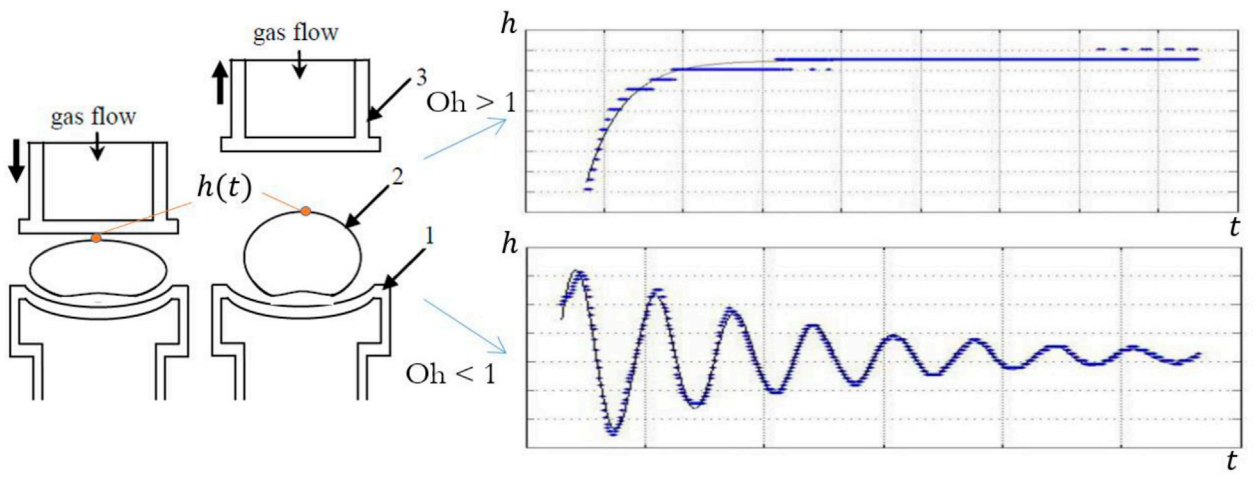

FIGURE 13 | Estimation of dynamic viscosity by droplet apex tracking with VITI-GFL.

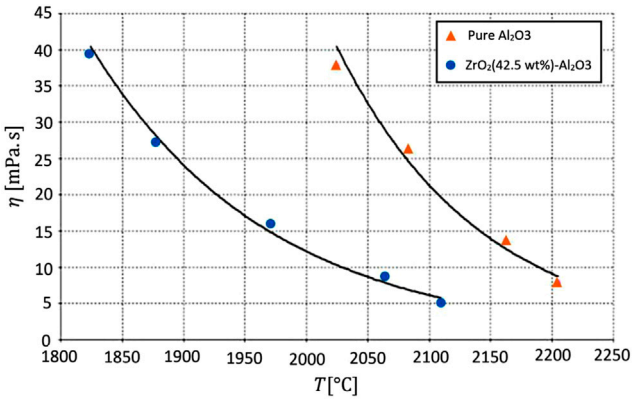

FIGURE 14 | VITI-GFL viscosity measurements of alumina and zirconia-alumina eutectic, from Grishchenko and Piluso (2011).

the liquidus temperature—from 2025°C to 1825°. Then, the viscosity of pure alumina is found significantly larger than the viscosity of the eutectic composition at a given temperature for which both are at liquid state.

3.3 Discussion About the Influence on Ex-Vessel Retention Strategy and the Particular Issue of Corium Spreading

In the EVR strategy, the surface-to-volume ratio of corium must be maximized to increase coolability. In the EPR core catcher concept (Fischer, et al., 2016), and as a backfit for some Gen 2 reactors (Bonnet, et al., 2016), spreading is a means to reduce the melt thickness and thus the average heat fluxes to concrete, as shown **Figure 15**. Spreading is, indeed, controlled by the melt properties, mainly kinematic viscosity (Journeau, et al., 2003). For additional safety improvements in both central and lateral approaches, sacrificial materials can be used to improve molten core coolability by effectively spreading the molten core on the concrete basemat to form a thin layer. The addition of such sacrificial materials into the melt aims, indeed, at lowering the viscosity of the resulting Corium-Sacrificial Material (CSM) mixture and lowering its liquidus temperature compared to that of mere corium. The influence of liquidus (and solidus) temperatures—related to phase transitions—and viscosity and their measurements are also discussed in this article.

As shown in **Figure 11**, the VITI-VPA measurements clearly demonstrate that the addition of judicious sacrificial material to corium significantly lowers liquidus temperatures. The decrease of liquidus temperature obviously promotes corium spreading: the longer corium remains at a liquid state, the further it will spread. At the reactor scale, this validates the choice of the sacrificial material under consideration as it will be gradually incorporated into the melt while interacting with corium, thus delaying its freezing and favoring spreading.

Now, concerning viscosity, and by analogy with the CSM issue, considering in **Figure 14** that alumina stands for corium and zirconia for sacrificial material, one could conclude that the

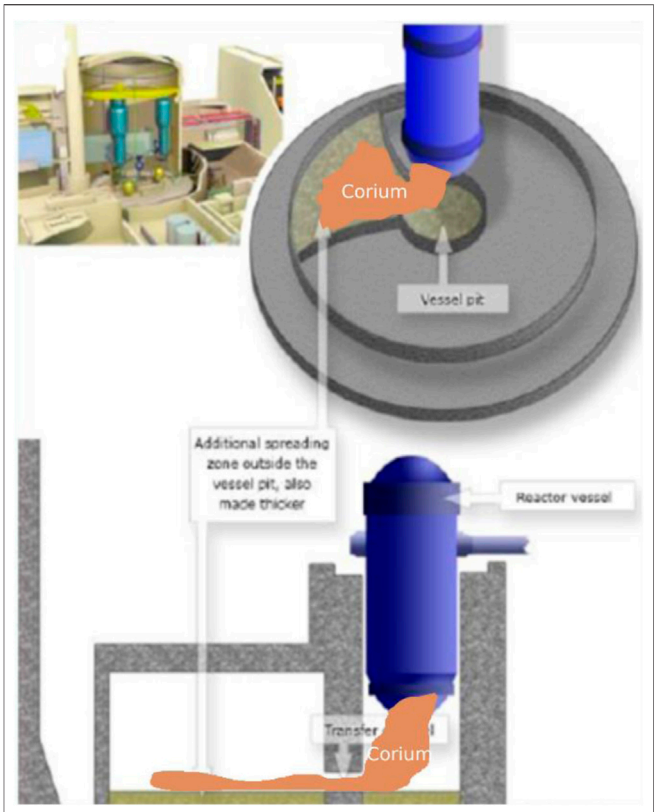

FIGURE 15 | Ex-Vessel Retention Strategy and corium spreading over a large surface, as adapted from Bonnet, et al. (2016).

addition of relevant materials into the melt may not only succeed in altering phase transitions but may also deeply influence corium rheology. A first simplified approach could assume the following statement: if dynamic viscosity follows the same trend as solidus/liquidus temperatures, then it is a two-fold positive effect for corium spreading. If not, then a competition shall occur between the thermodynamic and thermophysical properties.

4 CONCLUSION

Within the framework of corium characterization at high temperatures, a consistent approach has been proposed in the present article in order to fill the lack of such fundamental data as density, surface tension, liquidus and solidus temperatures, and viscosity. The discussion highlights the prominent role played by such properties in the physical mechanisms governing the behavior of corium, when applied to In-Vessel Retention—IVR—and Ex-Vessel Retention—EVR—strategies. Concerning the IVR mitigation strategy, in link with the focusing effect issue at the thin upper metallic layer, the influence of density and surface tension has been discussed. Concerning the EVR mitigation strategy, the impact of solidus/liquidus temperatures and dynamic viscosity on corium spreading has been pointed out

for oxide samples. The unique capacities of the VITI facility have been highlighted: indeed, VITI has been declined into various configurations, enabling access to the original experimental measurements for the properties of interest at high temperatures.

The different configurations of the VITI facility can be applied to a variety of oxide and metallic corium compositions representative of nuclear reactor severe accidents. For instance, if in the present article only metallic compositions are discussed for the VITI-MBP experimental setup, the MBP technique has also been applied to oxide corium compositions, giving access to original data for both in-vessel (Chikhi, et al., 2021) and ex-vessel (Delacroix, et al., 2020) corium compositions.

Corium thermophysical property measurements at high temperatures constitute an experimental issue that is now addressed by the VITI facility through its different configurations. The potential high variability of such properties with temperature prevents from adopting a classical parametric approach as far as numerical simulations are concerned. For instance, the viscosity may vary by several orders of magnitude, depending on the working temperature, especially considering the large solidification intervals often associated with such multicomponent systems as corium. It is most likely that large parts of the domain (composition, temperature, and pressure) shall remain inaccessible to the experimental approach. A relevant example is found when considering the stratified corium pool in the IVR strategy: the liquid/liquid interfacial tension between the oxide layer and the metallic layer may be required to compute corium pool thermal hydraulics (Zanella, et al., 2021), but the MBP approach gives only access to liquid/gas surface tensions. As proposed, for example, in Gajavalli and Le Tellier (2022), a modeling approach allowing to deduce liquid/liquid interfacial tension from separate surface tension measurements could provide further physical insight into corium pool topology.

In order to enhance severe accident code simulation reliability for various nuclear reactor types (PWRs, BWRs, and CANDU), reliable corium properties both in composition and in temperature are absolutely needed. Acquiring experimental thermophysical property data on key properties and corium compositions should be the first step. The general modeling of thermophysical properties should be the second step. The final step would be the building of thermophysical property databases coupled with severe accident codes. Such kind of approach is under construction in the frame of national and international projects.

DATA AVAILABILITY STATEMENT

The data analyzed in this study is subject to the following licenses/restrictions: Restricted access due to organization policy. Requests to access these datasets should be directed to the corresponding author.

AUTHOR CONTRIBUTIONS

JD, CJ, and PP carried out the experiments and related analytical work and wrote this article in a collegial manner.

ACKNOWLEDGMENTS

The authors would like to express their special thanks to Dr. Romain Le Tellier for many insightful discussions and to Dr. Christophe Suteau for his constant support.

REFERENCES

Amidu, M. A., Olatubosun, S. A., Ayodeji, A., and Addad, Y. (2022). Severe Accident in High-Power Light Water Reactors: Mitigating Strategies, Assessment Methods and Research Opportunities. *Prog. Nucl. Energy* 143, 104062. - ISSN: 0149-1970. doi:10.1016/j.pnucene.2021.104062

Asmolov, V., and Tsurikov, D. (2000). "RASPLAV Project : Major Activities and Results [Conference]," in Proceeding of the OECD/NEA RASPLAV Seminar, Munich, Germany.

Baek, W.-P., Yang, J.-E., Ball, J., Glown, G., Bisconti, G., Peko, D., et al. (2017). Safety Research Opportunities Post-Fukushima. Initial Report of the Senior Expert Group. Boulogne-Billancourt: Organisation for Economic Co-Operation and Development, NEA-OECD.

Bakuta, N., Le Tellier, R., and Saas, L. (2015). "Assessment of Advanced Corium-In-Lower-Head Models in MAAP and PROCOR Codes," in Proc. ERMSAR 2015, 7th Eur. Rev. Mtg. Sev. Acc. Res., Marseille, France. [Conference].

Bechta, S. V., Krushinov, E. V., Almjashev, V. I., Vitol, S. A., Mezentseva, L. P., Petrov, Y. B., et al. (2007). Phase Diagram of the UO2-FeO1+x System. *J. Nucl. Mater.* 362, 46–52. - ISSN: 0022-3115. doi:10.1016/j.jnucmat.2006.11.004

Bonnet, J. M., Robledo, F., Farmer, M. T., Cranga, M., Spengler, C., Vola, D., et al. (2017). State of the Art Report on Molten Core Concrete Interaction and Ex-Vessel Molten Core Coolability, NEA-OECD.

Bonnet, J. M., Raimond, E., Cenerino, G., Vola, D., and Fichot, F. (2016). "Strategy for the Corium Stabilisation in Case of a Severe Accident for the French PWRs," in IAEA Technical Meeting on Phenomenology and Technologies Relevant to In-Vessel Melt Retention and Ex-Vessel Corium Cooling, Shanghai, China, October 2016. [Report] : Tech. rep.

Brooks, R. F., Dinsdale, A. T., and Quested, P. N. (2005). The Measurement of Viscosity of Alloys—A Review of Methods, Data and Models [Journal]. *Meas. Sci. Technol.* 16, 354–362. doi:10.1088/0957-0233/16/2/005

Carénini, L., Fichot, F., and Seignour, N. (2017). Modelling Issues Related to Molten Pool Behaviour in Case of In-Vessel Retention Strategy. *Ann. Nucl. Energy* 118, 363–374. doi:10.1016/j.anucene.2018.04.032

Chandrasekhar, S. (1970). *Hydrodynamic and Hydromagnetic Stability [Book]. - [s.l.]*. Dover publications.

Chikhi, N., Delacroix, J., Fouquart, P., and Turquais, B. (2021). Measurement of Corium Surface Tension Using the Maximum Bubble Pressure. *Nucl. Eng. Des.* 379, 111266. doi:10.1016/j.nucengdes.2021.111266

Chikhi, N., Fouquart, P., Delacroix, J., and Piluso, P. (2019). Measurement of Type 304L Stainless Steel and 16MND5 Ferritic Steel Density and Surface Tension: Possible Impact for Stratified Molten Pool. *Nucl. Technol.* 205, 200–212. doi:10.1080/00295450.2018.1486160

Dang, C., Peybernes, M., Le Tellier, R., and Saas, L. (2021). Numerical Simulations of the Rayleigh-Bénard-Marangoni Convections in a Thin Metallic Layer [Journal]. *Ann. Nucl. Energy* 150, 107848. doi:10.1016/j.anucene.2020.107848

Delacroix, J., Chikhi, N., Fouquart, P., Journeau, C., Tatsahura, K., Tsukamoto, T., et al. (2019). "Solidus and Liquidus Temperatures of Corium-Sacrificial

Material Mixtures: Experimental Results and Thermodynamic Calculations [Conference]," in Proceedings of FDR2019, International Topical Workshop on Fukushima Decommissioning Research.

Delacroix, J., Journeau, C., Chikhi, N., Fouquart, P., and Zhan, D. (2020). Measurements of In-Vessel and Ex-Vessel Liquid Corium Surface Tension and Density in the VITI-MBP Test Bench within ALISA Euro-Chinese Project. *Mech. Eng. J.* 7, 611. doi:10.1299/mej.19-00611

Delacroix, J., Piluso, P., Chikhi, N., Asserin, O., Borel, D., Brosse, A., et al. (2022). Measurements of Liquid AISI 304L Steel Density and Surface Tension, and Influence of Surface-Active Elements at High Temperatures. *Steel Res. Int.* 2100624. doi:10.1002/srin.202100624

Dubberstein, T., Heller, H.-P., Klostermann, J., Schwarze, R., and Brillo, J. (2015). Surface Tension and Density Data for Fe-Cr-Mo, Fe-Cr-Ni, and Fe-Cr-Mn-Ni Steels. *J. Mater Sci.* 11 0150, 7227–7237. doi:10.1007/s10853-015-9277-5

Dubberstein, T., and Heller, H.-P. (2013). The Thermophysical Properties of Liquid TRIP/TWIP-Steel Alloys Using the Maximum Bubble Pressure Method. *Adv. Eng. Mat.* 15, 583–589. doi:10.1002/adem.201200310

Egry, I., and Brillo, J. (2009). Surface Tension and Density of Liquid Metallic Alloys Measured by Electromagnetic Levitation. *J. Chem. Eng. Data* 54, 2347–2352. doi:10.1021/je900119n

Esmaili, H., and Khatib-Rahbar, M. (2005). Analysis of Likelihood of Lower Head Failure and Ex-Vessel Fuel Coolant Interaction Energetics for AP1000. *Nucl. Eng. Des.* 235, 1583–1605. doi:10.1016/j.nucengdes.2005.02.003

Farmer, M. T., Gerardi, C., Bremer, N., and Basu, S. (2016). Key Findings and Remaining Questions in the Areas of Core-Concrete Interaction and Debris Coolability. *Nucl. Technol.* 196, 10. doi:10.13182/nt16-43

Fichot, F., Carénini, L., Bakouta, N., Esmaili, H., Humphries, L., Laato, T., et al. (2020). Elaboration of a Phenomena Identification Ranking Table (PIRT) for the Modelling of In-Vessel Retention [Journal]. *Ann. Nucl. Energy* 146, 107617. doi:10.1016/j.anucene.2020.107617

Fichot, F., Michel, B., Almjashev, V., Le Guennic, C., Bakouta, N., Le Tellier, R., et al. (2022). Chemical Interactions of Molten Steel with (U-Zr-O) Corium: Main Outcomes of the CORDEB Program. *Nucl. Eng. Des.* 388, 111588. doi:10.1016/j.nucengdes.2021.111588

Fischer, M., Bechta, S. V., Bezlepkin, V. V., Hamazaki, R., and Miassoedov, A. (2016). Core Melt Stabilization Concepts for Existing and Future LWRs and Associated Research and Development Needs. *Nucl. Technol.* 196, 524–537. doi:10.13182/nt16-19

Fischer, M. (2004). The Severe Accident Mitigation Concept and the Design Measures for Core Melt Retention of the European Pressurized Reactor (EPR). *Nucl. Eng. Des.* 230, 169–180. - 11th International Conference on Nuclear Energy. - ISSN: 0029-5493. doi:10.1016/j.nucengdes.2003.11.034

Gajavalli, K., and Le Tellier, R. (2022). Butler-based Thermodynamic Modelling of Interfacial Energies for In-Vessel Corium Systems. *J. Nucl. Mater.*. (submitted).

Grishchenko, D., and Piluso, P. (2011). Recent Progress in the Gas-Film Levitation as a Method for Thermophysical Properties Measurements: Application to ZrO2-Al 2O3 System [Journal]. *High. Temperatures-High Press.* 40, 127–149.

Haumesser, P.-H., Bancillon, J., Daniel, M., Perez, M., and Garandet, J.-P. (2002). High-temperature Contactless Viscosity Measurements by the Gas-Film Levitation Technique: Application to Oxide and Metallic Glasses. *Rev. Sci. Instrum.* 73, 3275–3285. doi:10.1063/1.1499756

Hoorfar, M., and W. Neumann, A. (2006). Recent Progress in Axisymmetric Drop Shape Analysis (ADSA). *Adv. Colloid Interface Sci.* 121, 25–49. doi:10.1016/j.cis.2006.06.001

JCGM 100 (2008). *Evaluation of Measurement Data - Guide to the Expression of Uncertainty in Measurement [Report]*.

Journeau, C. (2006). *L'étalement du corium: Hydrodynamique, Rhéologie et Solidification d'un bain d'oxydes à hautes températures [Report]*. Ph.D. dissertation. France: University of Orléans.

Journeau, C., Boccaccio, E., Brayer, C., Cognet, G., Haquet, J.-F., Jégou, C., et al. (2003). Ex-vessel Corium Spreading: Results from the VULCANO Spreading Tests. *Nucl. Eng. Des.* 223, 75–102. doi:10.1016/s0029-5493(02)00397-7

Journeau, C., Bouyer, V., Charollais, F., Chikhi, N., Delacroix, J., Denoix, A., et al. (2022). Upgrading the PLINIUS Platform toward Smarter Prototypic-Corium Experimental R&D. *Nucl. Eng. Des.* 386, 111511. doi:10.1016/j.nucengdes.2021.111511

Journeau, C., Brayer, C., and Piluso, P. (2005). "Uncertainties on Thermodynamic and Physical Properties DataBases for Severe Accidents and Their Consequences on Safety Calculations [Report]," in *Tech. Rep. / OECD Workshop on Evaluation of Uncertainties in Relation to Severe Accidents and Level 2 PSA* (Aix en Provence, France.

Kim, C. S. (1975). Thermophysical Properties of Stainless Steels. Argonne National Lab, United States, ANL-75-55.

Korobeinikov, I., Chikhi, N., Fouquart, P., Turquais, B., Delacroix, J., Seetharaman, S., et al. (2021). Surface Tension and Density of Cr–Mn–Ni Steels with Transformation Induced Plasticity Effect [Journal]. *Steel Res. Int.* 92, 2000260.

Le Tellier, R., Saas, L., and Bajard, S. (2015). Transient Stratification Modelling of a Corium Pool in a LWR Vessel Lower Head. *Nucl. Eng. Des.* 287, 68–77. doi:10.1016/j.nucengdes.2015.02.009

Ma, W., Yuan, Y., and Sehgal, B. R. (2016). In-Vessel Melt Retention of Pressurized Water Reactors: Historical Review and Future Research Needs. *Engineering* 2, 103–111. - ISSN: 2095-8099. doi:10.1016/j.eng.2016.01.019

Matsumoto, T., Misono, T., Fujii, H., and Nogi, K. (2005). Surface Tension of Molten Stainless Steels under Plasma Conditions. *J. Mater Sci.* 40, 2197–2200. doi:10.1007/s10853-005-1932-9

Mills, K. C., and Brooks, R. F. (1994). Measurements of Thermophysical Properties in High Temperature Melts. *Mater. Sci. Eng. A* 178, 77–81. doi:10.1016/0921-5093(94)90522-3

Nakayoshi, A., Rempe, J. L., Barrachin, M., Bottomley, D., Jacquemain, D., Journeau, C., et al. (2020). Review of Fukushima Daiichi Nuclear Power Station Debris Endstate Location in OECD/NEA Preparatory Study on Analysis of Fuel Debris (PreADES) Project. *Nucl. Eng. Des.* 369, 110857. - ISSN: 0029-5493. doi:10.1016/j.nucengdes.2020.110857

Pellegrini, M., Dolganov, K., Herranz, L. E., Bonneville, H., Luxat, D., Sonnenkalb, M., et al. (2016). Benchmark Study of the Accident at the Fukushima Daiichi NPS: Best-Estimate Case Comparison. *Nucl. Technol.* 196, 198–210. doi:10.13182/nt16-63

Pellegrini, M., Herranz, L., Sonnenkalb, M., Lind, T., Maruyama, Y., Gauntt, R., et al. (2020). Main Findings, Remaining Uncertainties and Lessons Learned from the OECD/NEA BSAF Project. *Nucl. Technol.* 206, 1449–1463. doi:10.1080/00295450.2020.1724731

Pellegrini, M., Journeau, C., Seiler, N., Herranz, L. E., Bocanegra, R., Spengler, C., et al. (2022). "Analytical Benchmark on the Long Term Interaction of Molten Core and Dry Concrete at Fukushima Daiichi Unit 1 [Conference]," in Accepted by Nureth-19 Int. Top. Mtg. Nucl. React., Brussels (Brussels: Thermal Hydraulics).

Piluso, P., Adorni, M., Azarian, G., Bang, K.-H., Basu, S., Buck, M., et al. (2017). Status Report on Ex-Vessel Steam Explosion: EVSE, NEA-OECD.

Rempe, J. L., Knudson, D. L., Allison, C. M., Thinnes, G. L., and Atwood, C. L. (1997). Potential for AP600 In-Vessel Retention Through Ex-Vessel Flooding. Idaho National Engineering and Environmental Laboratory, Technical Evolution Report, INEEL/EXT-97-00779.

Saas, L., Tellier, R. L., and Skrzypek, E. (2017). "Rayleigh-Bénard and Bénard-Marangoni Convection in a Thin Metallic Layer on Top of Corium Pool," in The 8th European Review Meeting on Severe Accident Research – ERMSAR-2017, Warsaw, Poland.

Sangiorgi, M. (2015). In-Vessel Melt Retention (IVMR) Analyses of a VVER-1000 NPP. 6th ASTEC User's Club/2nd CESAM Workshop.

Seiler, J. M., Tourniaire, B., Defoort, F., and Froment, K. (2007). Consequences of Material Effects on In-Vessel Retention. *Nucl. Eng. Des.* 237, 1752–1758. doi:10.1016/j.nucengdes.2007.03.007

Song, J. (2021). Perspectives on a Severe Accident Consequences-10 Years after the Fukushima Accident. *J. Nucl. Eng.* 2, 398–411. doi:10.3390/jne2040030

Thakre, S. (2015). *On Fuel Coolant Interactions and Debris Coolability in Light Water Reactors [Report*. Ph.D. dissertation. Stockholm, Sweden: KTH.

Theofanous, T. G., Liu, C., Additon, S., Angelini, S., Kymäläinen, O., and Salmassi, T. (1997). In-vessel Coolability and Retention of a Core Melt. *Nucl. Eng. Des.* 169, 1–48. doi:10.1016/s0029-5493(97)00009-5

Tsurikov, D. (2007). *MASCA2 Project: Major Activities and Results [Report]*. Cadarache, France: Tech. rep. / Material scaling seminar.

Zanella, R., Tellier, R. L., Plapp, M., Tegze, G., and Henry, H. (2021). Three-dimensional Numerical Simulation of Droplet Formation by Rayleigh-Taylor Instability in Multiphase Corium. *Nucl. Eng. Des.* 379, 111177. doi:10.1016/j.nucengdes.2021.111177

Zhang, Y. P., Qiu, S. Z., Su, G. H., and Tian, W. X. (2011). A Simple Novel Analysis Procedure for IVR Calculation in Core-Molten Severe Accident. *Nucl. Eng. Des.* 241, 4634–4642. - The18th International Conference on Nuclear Engineering (ICONE-18). - ISSN: 0029-5493. doi:10.1016/j.nucengdes.2011.03.055

Conflict of Interest: The authors declare that the research was conducted in the absence of any commercial or financial relationships that could be construed as a potential conflict of interest.

Publisher's Note: All claims expressed in this article are solely those of the authors and do not necessarily represent those of their affiliated organizations, or those of the publisher, the editors, and the reviewers. Any product that may be evaluated in this article, or claim that may be made by its manufacturer, is not guaranteed or endorsed by the publisher.

frontiers | Frontiers in Energy Research

ORIGINAL RESEARCH
published: 30 May 2022
doi: 10.3389/fenrg.2022.899405

Study on Thermal Shock Failure Characteristics of RPV During IVR System Start-Up for Typical Advanced PWR

*Dahuan Zhu *, Hongping Sun, Bin Zheng, Tao Huang, Jian Deng *, Youyou Xu and Yuejian Luo*

Key Laboratory of Nuclear Reactor System Design Technology, Nuclear Power Institute of China, Chengdu, China

When the large pressurized water reactor in-vessel retention (IVR) system is put into operation, the outer wall of the reactor pressure vessel (RPV) will experience severe temperature fluctuations and be subjected to high internal pressure loads at the same time. In order to ensure the structural integrity of the RPV under such conditions, first, through the severe accident system program, the case that has the greatest impact on the pressure-bearing thermal shock of the outer wall of the reactor pressure vessel was selected under the station blackout (SBO) accident. Then, based on this case, the fracture mechanics finite element method was used to calculate and evaluate the pressure thermal shock (PTS) of the RPV, and the final crack size at the end of the life of the core barrel and the lower head was obtained by fatigue crack expansion calculation. The maximum ratio of the stress intensity factor correction value and corresponding limit value under the PTS transient load is about 0.874, which meets the requirements of RCC-M specification. The results of the study indicate that the RPV will not experience fracture failure when the IVR system is put into service during the station blackout accident for the HPR1000 nuclear power plant.

Keywords: in-vessel retention system, pressure vessel, pressurized thermal shock, fracture mechanics, advanced PWR

OPEN ACCESS

Edited by:
Yapei Zhang,
Xi'an Jiaotong University, China

Reviewed by:
Yandong Hou,
Northeast Electric Power University, China
Xiaojing Liu,
Shanghai Jiao Tong University, China

****Correspondence:***
Dahuan Zhu
dahuan_zhu@sina.com
Jian Deng
dengjian_npic@163.com

Specialty section:
This article was submitted to Nuclear Energy, a section of the journal Frontiers in Energy Research

Received: *18 March 2022*
Accepted: *11 April 2022*
Published: *30 May 2022*

Citation:
Zhu D, Sun H, Zheng B, Huang T, Deng J, Xu Y and Luo Y (2022) Study on Thermal Shock Failure Characteristics of RPV During IVR System Start-Up for Typical Advanced PWR. Front. Energy Res. 10:899405. doi: 10.3389/fenrg.2022.899405

INTRODUCTION

The in-vessel retention system is one of the key mitigation measures for the HPR1000 nuclear power plant in the event of a severe accident (Zeng et al., 2016). During the severe accident, the core loses cooling, and most of the reactor's melt debris that could threaten containment integrity is prevented by injecting sufficient water to cool the outside of the reactor pressure vessel (RPV) and acting simultaneously with the other safety features (e.g., first-loop depressurization) to ensure the structural integrity of the RPV, thereby trapping the core melt debris in the RPV. External phenomena (direct containment heating and melt-concrete reaction) greatly reduce the possibility of containment failure (Emad et al., 2021). When the IVR is commissioned, the outer wall of the RPV will experience severe temperature fluctuations, while at the same time the inner wall of the vessel is subjected to high pressure loads (Thamaraiselvi and Vishnuvardhan, 2020). To ensure that the RPV structure is not at a risk of rapid fracture failure under such severe loads and to ensure the structural integrity of the RPV, a pressure-bearing thermal shock (PTS) analysis study of the RPV is required for the safety analysis of the HPR1000 nuclear power plant.

Most of the previous PTS studies have focused on the effect of PTS transients on the barrel material and structural integrity under the loss of coolant accident (LOCA) condition of the RPV inner wall (Bass et al., 2001). The reactor pressure vessel subjected to pressurized thermal shock was modeled under the loss-of-coolant accident (LOCA) transient using the 3D-XFEM code (Mora et al., 2019). The results show that medium LOCA is more severe than large LOCA, resulting in meandering of the cooling plume causing oscillation of the stress intensity factor values. Chen et al. studied the structural integrity of the reactor pressure vessel under the thermal shock loading (Chen et al., 2014). The results show that the crack depth, crack type, plastic effect, and cladding thickness change the safety margin (SM) significantly, and the SM at the deepest point of the crack is not always smaller than that of the surface point, indicating that both the deepest and surface points of the crack front should be considered. The deterministic structural integrity assessment of the reactor pressure vessels was carried out by Chen under pressurized thermal shock loading (Chen et al., 2015). The results have shown that the critical part along the crack front is always the clad-based metal interface point rather than the deepest point for either the crack initiation assessment or the crack arrest assessment under the thermal load. The pressure vessel integrity under the pressurized thermal shock condition was carried out for safety analysis (Stahlkopf, 1984). The action taken by utilities to mitigate the effects of PTS on the reactor vessels was obtained from the results. For the AP1000 pressurized thermal shock (Wang et al., 2017), the thermal hydraulic and stress coupling analysis was studied under the SBLOCA scenario. The results show that the most critical zone was located in the direct vessel injection nozzle chamfering under accident transient. The probabilistic analysis in integrity assessments of the reactor pressure vessels was researched under the pressurized thermal shock conditions (Pugh et al., 2007). The stress intensity factors for the underclad and through clad defects were studied in a reactor pressure vessel subjected to a pressurized thermal shock (Marie et al., 2005). There are also many key impact studies on the PTS, including elastic and elastoplastic fracture analyses (Sun et al., 2017), constraint effect analysis (Kim et al., 2003), and structural reliability evaluation (Chou and Huang, 2014). Therefore, it is necessary to carry out thermal shock research for the HPR1000 nuclear power plant in order to study the safety assessment of the PTS of the RPV.

After comparison, the thermal stress in the lower head of the reactor pressure vessel is slightly larger than that in the core section barrel, but the stress generated by the pressure and the amount of fast neutron injection is much larger in the core section barrel than in the lower head, so only the core barrel is analyzed for fast fracture. In addition, in order to ensure that the reactor pressure vessel does not have the risk of fast fracture failure throughout the life cycle, IVR misinjection is considered by the end of 60 annual life cycles. Unlike previous studies on the effect of PTS on the inner wall of the RPV, the PTS analysis at the time of IVR commissioning investigates the effect of rapid cooling transients on the structural integrity of the outer wall of the RPV in terms of fracture failure. Compared with the PTS transient of the RPV inner wall, the IVR-injected PTS transient loads tend to be more severe for the following reasons: 1) the convective heat transfer coefficient between the IVR-injected coolant and the RPV base material surface is higher than the equivalent heat transfer coefficient of the PTS transient of the RPV inner wall containing the buffered overlay layer. 2) The temperature change of the injected coolant after the IVR injection is more drastic. Thus, the study of thermal shock behavior of the pressure vessel is of great significance for the IVR design of the HPR1000 nuclear power plant.

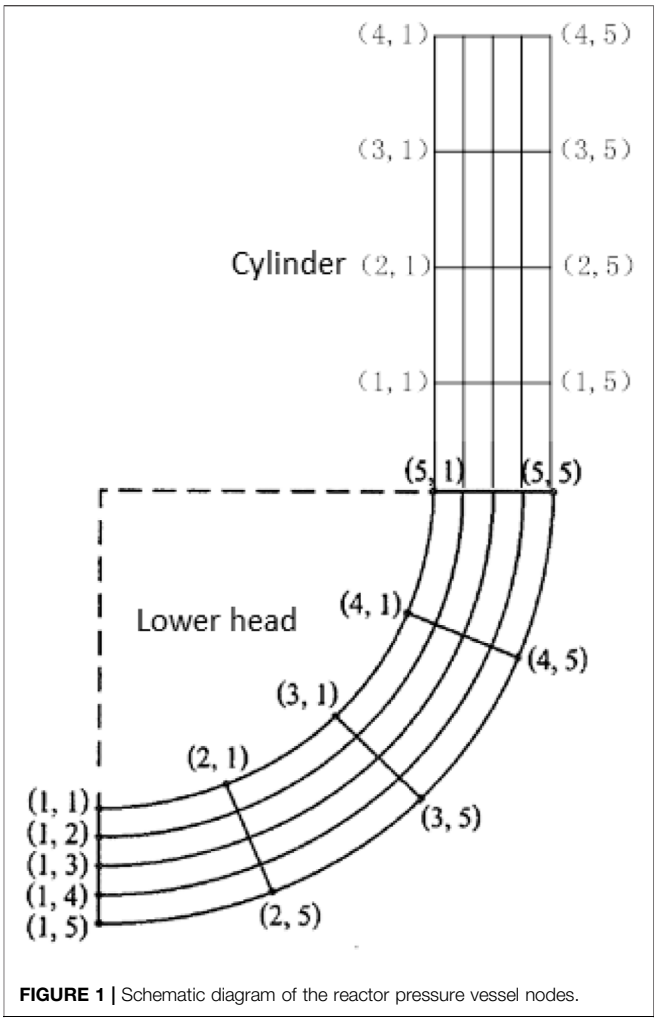

FIGURE 1 | Schematic diagram of the reactor pressure vessel nodes.

METHODS AND MATHEMATICAL MODELS

In this work, the autonomous severe accident analysis software is used for thermal calculations, and the ANSYS program is used for finite element calculations. The fatigue crack extension and rapid fracture are calculated and evaluated by the RCC-M specification (Chen et al., 2016) and the RSE-M method (Faidy, 2011), and the evaluation criteria in this work are considered according to accident conditions.

Crack Extension Calculation Method

The calculation of fatigue crack expansion for hypothetical crack service life growth includes three parts: calculation of the temperature field and stress, stress intensity factor, and crack expansion.

TABLE 1 | Comparison of the steady-state calculation results.

Event	SBO accident(s)
Emergency stop stack	0.0
The core of the reactor becomes exposed.	6,360
Annotation box is inserted	--
Emptying of the injection box	--
Core exit temperature reaches 650°C	7,260
Starting of water injection into the pile cavity	10,560
Pressure regulator quick pressure relief valve unloading	14,160
Core melt migration begins	--
Lower head dried-up	--
Calculation termination	12,800

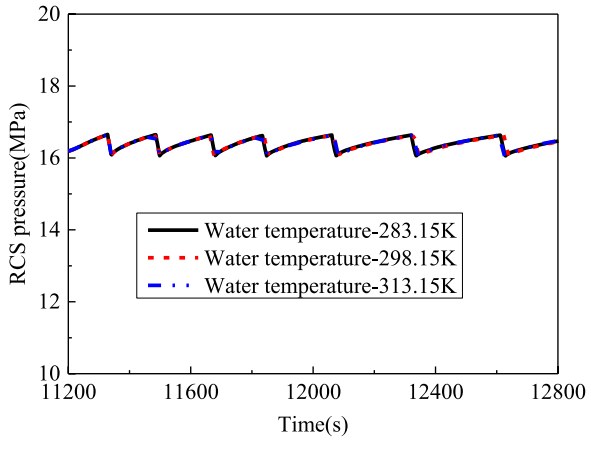

FIGURE 2 | RCS pressure with different IVR water temperatures.

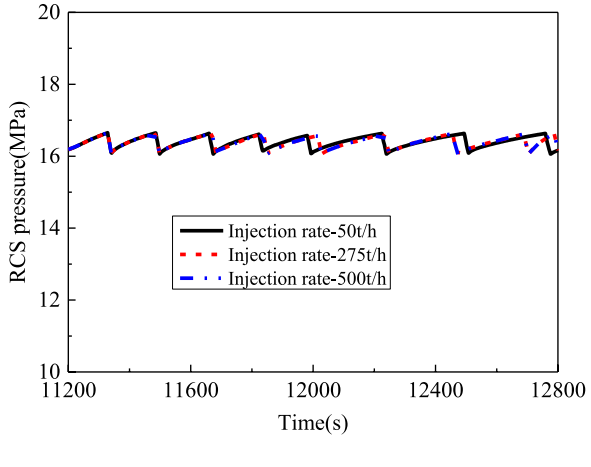

FIGURE 3 | RCS pressure with different IVR injection rates.

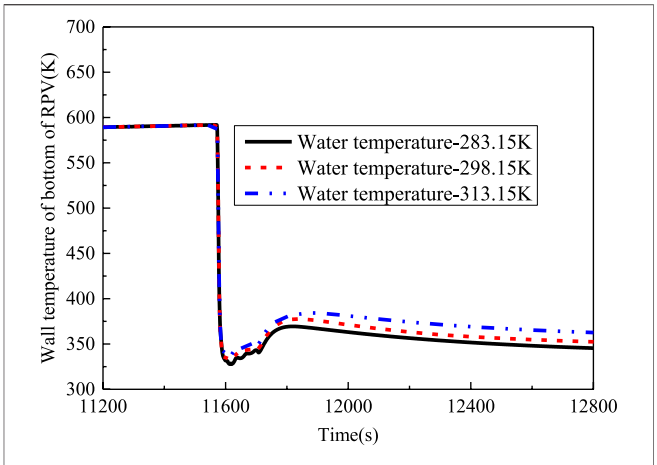

FIGURE 4 | Wall temperature of the bottom of the RPV.

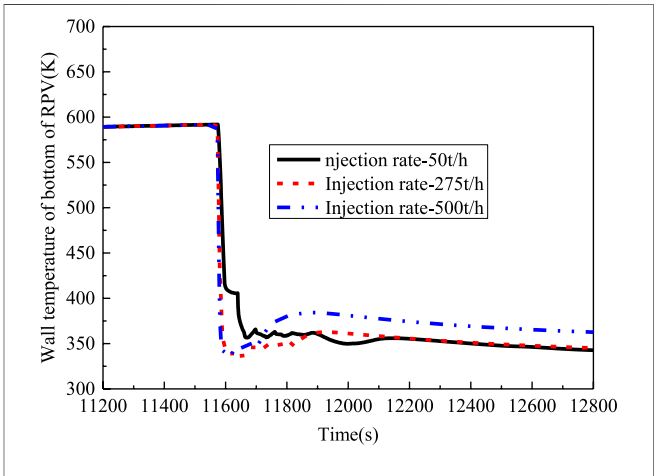

FIGURE 5 | Wall temperature of the bottom of the RPV.

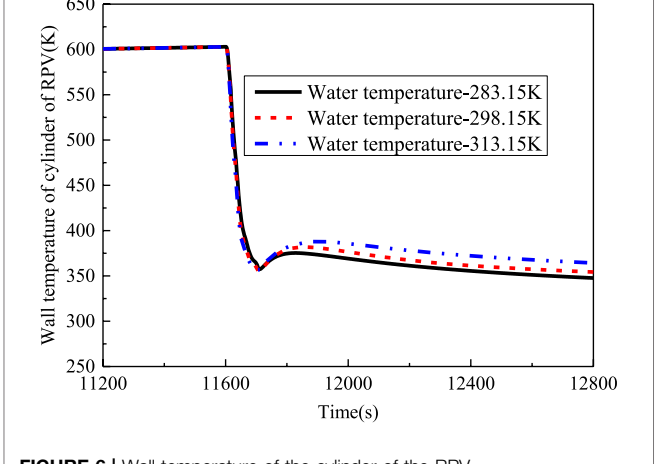

FIGURE 6 | Wall temperature of the cylinder of the RPV.

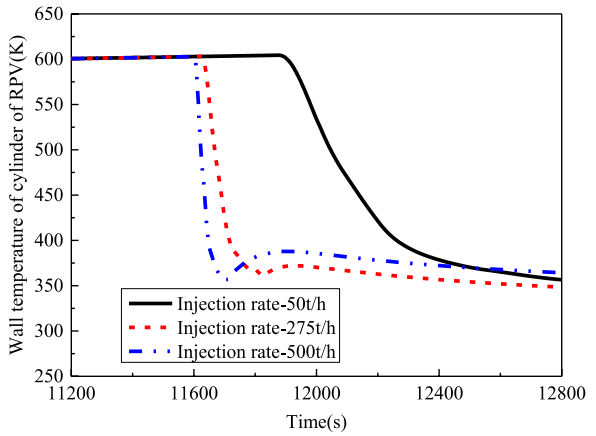

FIGURE 7 | Wall temperature of the cylinder of the RPV.

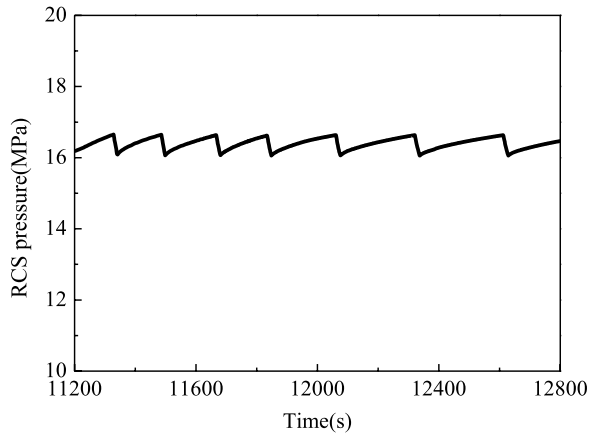

FIGURE 8 | RCS pressure.

1) Temperature field and stress calculation: The ANSYS program is used to calculate the temperature field and stress of all transients under the action of temperature and pressure transient load, line by line.
2) Calculation of the stress intensity factor: The normal stress is extracted at each transient at each load step at the defect, and according to the RCC-M specification, the normal stress distributed along the wall thickness is fitted with the four subpolynomials.

$$\sigma = \sigma_0 + \sigma_1\left(\frac{x}{L}\right) + \sigma_2\left(\frac{x}{L}\right)^2 + \sigma_3\left(\frac{x}{L}\right)^3 + \sigma_4\left(\frac{x}{L}\right)^4, \quad (1)$$

where x is the distance of the data point from the inner surface; σ is the normal stress of the crack surface.

The stress intensity factor K_I is then calculated as

$$K_I = \left[i_0\sigma_0 + i_1\sigma_1\left(\frac{a}{L}\right) + i_2\sigma_2\left(\frac{a}{L}\right)^2 + i_3\sigma_3\left(\frac{a}{L}\right)^3\right]\sqrt{\pi a}, \quad (2)$$

where i_j (j = 0,1,2,3) is the influence factor. Considering that the area near the crack tip has entered plasticity, the plastic correction is required, *KI*, from which the stress intensity factor *KCP* of the plastic correction is obtained.

$$K_{CP} = \alpha K_I\sqrt{\frac{a + r_y}{a}}, \quad (3)$$

$$\alpha = \begin{cases} 1 & r_y \le 0.05z \\ 1 + 0.15\left(\dfrac{r_y - 0.05z}{0.035z}\right) & 0.05z < r_y \le 0.12z \\ 1.6 & r_y > 0.12z \end{cases}, \quad (4)$$

where r_y is the radius of the plastic zone; S_y is the yield strength of the material at the crack tip temperature; and t is the wall thickness.

3) Calculation of crack growth: Transient combination is conducted, and ΔK_I is calculated; then, according to ΔK_{CP} and $\Delta K_{CP}R\frac{K_{CP,min}}{K_{CP,max}}$, different formulas are selected to calculate $\frac{da}{dN}$; the crack length $a' = a_0 + \int\frac{da}{dN}dN$ is updated (a_0 is the initial crack length; N is the number of transient occurrences), and steps (2) and (3) are repeated until the final crack size is obtained at the end of service life. Among them, the fatigue crack growth rate parameter adopts the growth rate parameter in the air environment in the specification.

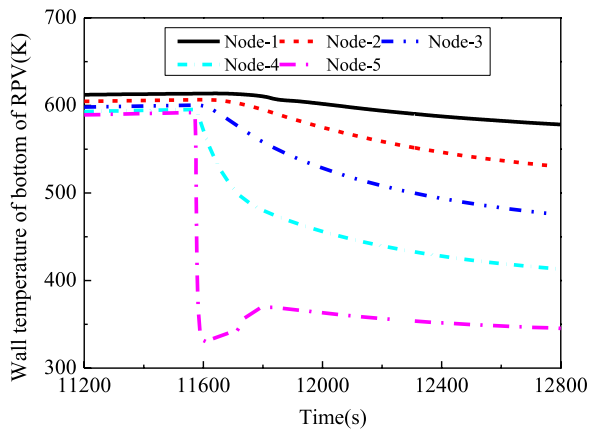

FIGURE 9 | Wall temperature of the bottom of the RPV.

PTS Analysis Evaluation Guidelines

The mechanical analysis specification for the HPR1000 RPV design is mainly the RCC-M specification. However, the PTS event is not clearly defined in the RCC-M code, and its related rapid fracture analysis and evaluation are not mandatory. According to the pressure vessel PTS assessment guidelines in China's energy industry standards and US 10CFR50.61 (EricksonKirk et al., 2005), a PTS is strictly defined as an event or transient in a pressurized water reactor that causes sudden cooling (i.e., thermal shock) within the RPV, accompanied by the significant internal pressure. According to this definition, the PTS transient is not limited to the LOCA transient in the RPV interior. In 1978, a PTS event of a non–water

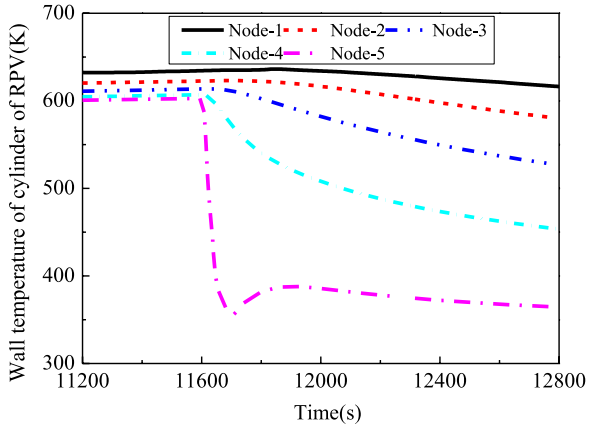

FIGURE 10 | Wall temperature of the cylinder of the RPV.

loss type accident occurred at the Rancho Seco nuclear power plant in California (Li and Modarres, 2005). For the PTS analysis, the Russian WWER reactor PTS guidelines are more specific and list a series of initial event groups that require PTS analysis, which, in addition to LOCA, also explicitly include events such as cavity flooding that result in external cooling of the RPV (Server and Nanstad, 2015). According to the pressure vessel PTS assessment guidelines in China's energy industry standards, the key elements of the PTS event or transient definition include: 1) for the reactor pressure vessels in pressurized water reactors only; 2) thermal shock stress caused by sudden cooling when the coolant flows through the wall; and 3) mechanical load stress caused by the superimposed possible high pressure. The drastic temperature changes experienced by the RPV at the time of IVR commissioning in HPR1000 and the possible concurrent internal high pressure transient loads are consistent with the key characteristics of a PTS event. However, for PTS events, the PTS codes of most countries, including China, except for a few countries such as Russia mainly impose restrictions on the fracture toughness of the RPV materials and lack more adequate analytical arguments such as quantitative stress intensity factor calculation and evaluation under the PTS transient events. Therefore, in this work, quantitative stress intensity factor calculation and evaluation under the PTS transient events after the IVR system is carried out for the HPR1000 RPV. The quantitative crack extension calculation, fracture calculation, and evaluation are based on the rapid fracture analysis and evaluation guidelines required by the nonmandatory RCC-M design mechanical analysis code for the HPR1000 RPV. The specific fracture evaluation guidelines are as follows.

When crack tip temperature $T \le T_{R,NDT} + 60^{\circ}C$,

$$K_{cp} \le K_{IC}/1.2, \tag{5}$$

$$K_{IC} = 40 + 0.09\left(T - T_{R,NDT}\right) + 20\exp\left[0.038\left(T - T_{R,NDT}\right)\right]. \tag{6}$$

When crack tip temperature $T > T_{R,NDT} + 60^{\circ}C$,

$$K_{cp} \le K_{JC}/1.0, \tag{7}$$

$$K_{JC} = \begin{cases} 245 & T \le 50^{\circ}C, \\ 200 & T \ge 200^{\circ}C, \end{cases} \tag{8}$$

where K_{cp} is the stress intensity factor after plastic correction; K_{IC} is the critical fracture toughness of the material; K_{JC} is the fracture toughness of ductile tearing of the material; $T_{R,NDT}$ is the reference nonductile transition temperature; T is the temperature between 50–200°C, which is calculated by the linear interpolation of temperature.

According to the RCC-M specification, the radiation effect, thermal aging effect, and strain aging effect is considered in the calculation of $T_{R,NDT}$. The core barrel is subjected to large fast neutron irradiation during the life of the reactor. Due to the increase in $T_{R,NDT}$ caused by irradiation, the fracture toughness of the material is reduced. The influence of the irradiation effect of $T_{R,NDT}$ is calculated as follows:

$$T_{R,NDT} = T_{R,NDT\,(\text{initial})} + \Delta T_{R,NDT}, \tag{9}$$

$$T_{R,NDT} = \left[22 + 556\left(C_{Cu} - 0.08\right) + 2778\left(C_p - 0.008\right)\right]\left(10^{-19} f\right)^{0.5}, \tag{10}$$

where $T_{R,NDT\,(\text{initial})}$ is the initial nonductile transition temperature; C_{Cu} is the mass percentage of copper; when it is

TABLE 2 | Calculation results of the hypothetical crack propagation of the core barrel and lower head.

Service time/a	Core barrel		Lower head	
	Crack depth/mm	Crack length/mm	Crack depth/mm	Crack length/mm
0	4.500	27.000	4.500	27.000
5	4.551	27.038	4.513	27.010
10	4.602	27.076	4.526	27.020
15	4.653	27.115	4.540	27.030
20	4.706	27.155	4.553	27.040
25	4.758	27.196	4.566	27.050
30	4.812	27.237	4.580	27.060
35	4.866	27.279	4.593	27.070
40	4.921	27.322	4.607	27.080
45	4.976	27.365	4.620	27.091
50	5.032	27.409	4.634	27.101
55	5.0889	27.454	4.647	27.111
60	5.146	27.500	4.661	27.122

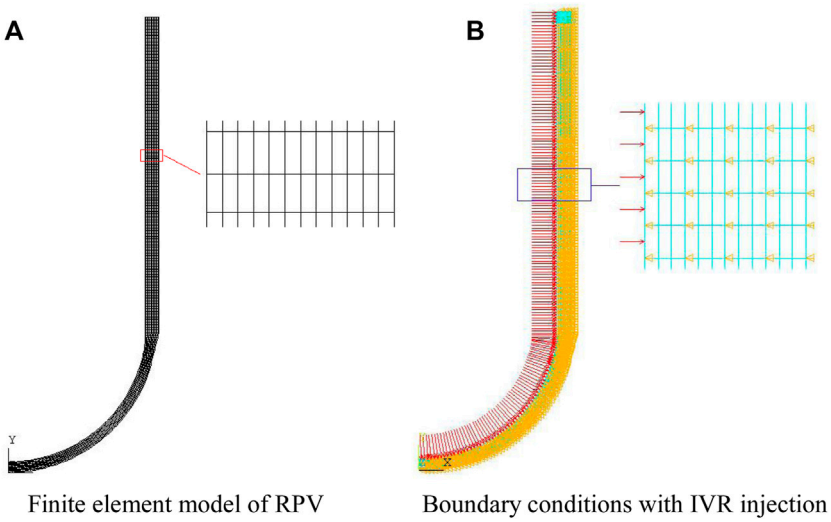

FIGURE 11 | Schematic diagram of boundary conditions of the finite element model with IVR injection. **(A)** Finite element model of the RPV **(B)** Boundary conditions with the IVR injection.

less than 0.08%, 0.08% is considered; C_p is the mass percentage of phosphorus; when it is less than 0.008%, 0.008% is considered; and f is the fast neutron fluence rate, 10^{19}cm^{-2}.

The design initial brittle transition temperature of the RPV base metal core barrel section is less than or equal to -23.3°C. The design of initial brittle transition temperature of the RPV lower head forging is less than or equal to - 20°C. The C_{Cu} of the core barrel is not more than 0.05%, and the C_p of the core barrel is not more than 0.008%. The C_{Cu} of the lower head forgings should not be greater than 0.08%, and the C_p of the lower head forgings is less than or equal to 0.008%. The peak value of fast neutron fluence at 3/4 wall thickness of the pressure vessel at the end of reactor life (the load factor is considered as 100%) is 4.17×10^{18}cm^{-2}. Therefore, after considering the neutron irradiation, the calculation result of $T_{R,NDT}$ at the end of the life of the core barrel is −9.1°C. In addition, the fast neutron fluence rate in the lower head area is significantly lower than that in the core barrel area. The calculation conservatively adopts the fast neutron fluence rate in the core barrel area, so the calculation result of $T_{R,NDT}$ at the end of the lower head life is −5.8°C.

Considering the effect of thermal aging, the nonductile transition temperature of base metal $T_{BM,NDT,aged}$ is as follows:

$$T_{BM,NDT,aged} = T_{BM,NDT(initial)} + \Delta T_{BM,NDT,aged}, \quad (11)$$

where $T_{BM,NDT(initial)}$ is the initial nonductile transition temperature of the base metal, considering that the service life of the reactor is 60 a, and the temperature is conservatively considered as 350°C; the calculated result of $T_{BM,NDT,aged}$ is −5.3°C.

Considering the effect of strain aging, the nonductile transition temperature of base metal $T_{BM,NDT,strain}$ is as follows:

$$T_{BM,NDT,strain} = T_{BM,NDT(initial)} + \Delta T_{BM,NDT,strain}, \quad (12)$$

where the value of $T_{BM,NDT(initial)}$ is 15°C; the calculated result of $T_{BM,NDT,strain}$ is −8.3°C.

According to the RCC-M specification, the superposition effects of the irradiation effect, thermal aging effect, and strain aging effect on the nonductile transition temperature are not considered. Therefore, the temperature of the core barrel and lower head materials at the end of life is −5.3°C.

THERMAL ANALYSIS

In order to evaluate whether there is a risk of mechanical failure of the pressure vessel structure under such temperature changes and pressure loads and whether the structural integrity of the pressure vessel can be ensured, it is first necessary to perform the pressure and temperature transient analysis of the pressure vessel after IVR activation to provide input for the pressure-bearing thermal shock analysis of the pressure vessel. In this article, the pressure vessel pressure and temperature transients are analyzed for the IVR late injection condition. The late injection condition is the maximum delay time considered for the input of the reactor's cavity water injection cooling system. The program used is the autonomous severe accident software.

Initial Conditions and Assumptions

HPR1000 is an advanced million kilowatt pressurized water reactor, which belongs to the third-generation nuclear power technology. The initial power of the core is 100% nominal power, and the average reactor coolant temperature is taken as a nominal value. The pressure of the regulator is taken as a nominal value. The water level of the regulator is the full power operating water level. The steam generator water level is the full power operating level. The reactor's coolant flow rate is the best estimated flow rate. It is assumed that the core outlet coolant temperature reaches 650°C when the delayed 55 min is implemented to the in-vessel retention system, with a water injection flow rate of 500 t/h. The range of water temperatures in the fire-fighting pool

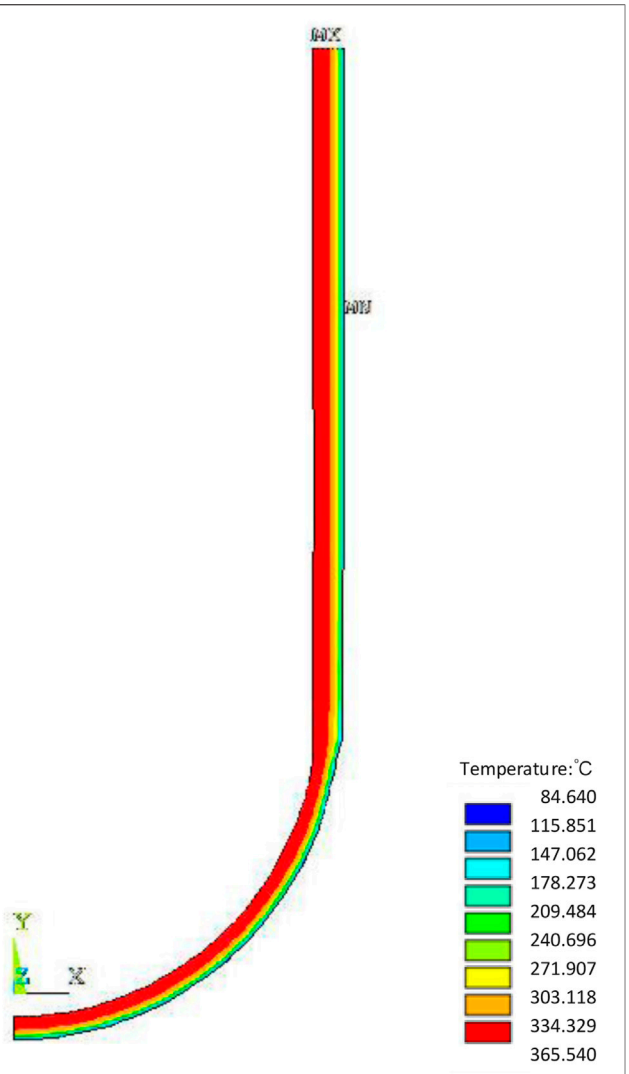

FIGURE 12 | Temperature distribution at the most dangerous time of the IVR-delayed injection.

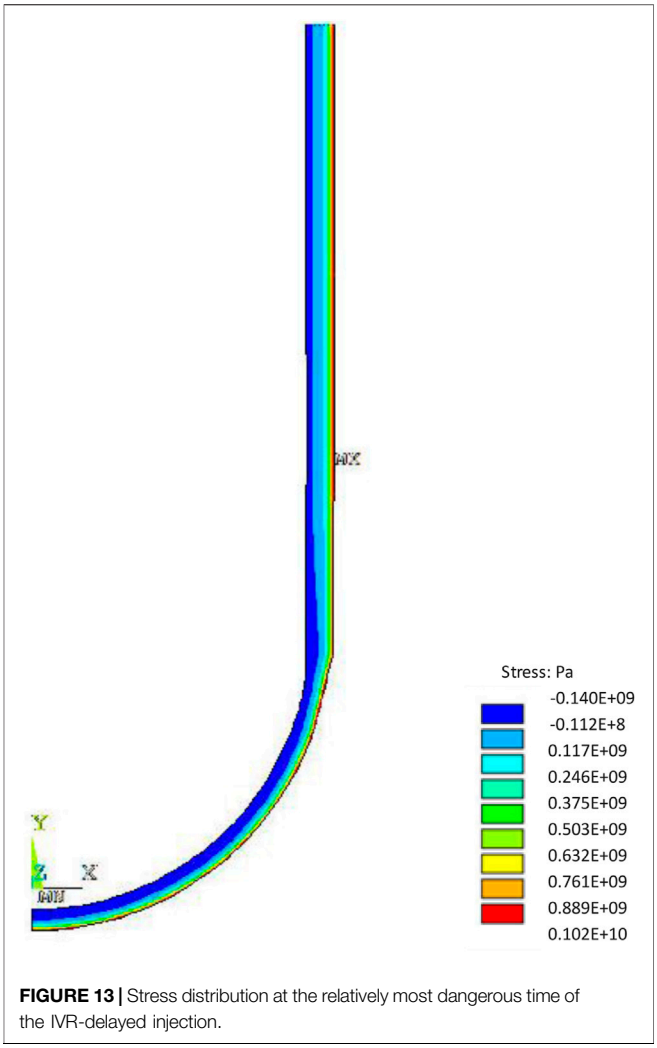

FIGURE 13 | Stress distribution at the relatively most dangerous time of the IVR-delayed injection.

is considered, and conservatively, a lower injection water temperature of 10°C is selected for the temperature transient analysis. The insulation layer is arranged outside the lower head of the pressure vessel and the wall of the cylinder with a gap of 150 mm. In this work, sensitivity analysis is performed for the two key parameters during IVR injection, including the temperature of IVR injection water and the injection flow rate, which are the most concerned parameters in the IVR system. The temperatures of the injection water are considered as 10, 25, and 40°C, and the injection flow rates are considered as 50 t/h, 275 t/h, and 500 t/h, respectively.

Analysis of Calculation Results

The schematic diagram of the pressure vessel wall nodes is shown in **Figure 1**. The lower head of the pressure vessel is axially divided into five nodes, the wall surface of the pressure vessel cylinder is axially divided into four nodes, and the wall thickness of the lower head of the pressure vessel and the cylinder is divided into five nodes. The event sequence is shown in **Table 1**. The pressure on the inner wall surface of the pressure vessel is shown in **Figure 2** From **Figure 3**, it can be seen that the pressure vessel's lower head and cylinder are subjected to cooling its inner wall surface to maintain a high pressure state; the pressure is maintained at 16.3 MPa, with a small range of fluctuations. The wall temperature changes from node 1 to node 5 of the lower head of the pressure vessel are shown in **Figures 4**, **5**, respectively, and the wall temperature changes from node 1 to node 4 of the straight cylinder of the pressure vessel are shown in **Figures 6**, **7**, respectively. It can be seen that after the IVR is put into operation, the temperature of each node of the lower head

TABLE 3 | Calculation results of the hypothetical crack propagation of the core barrel and lower head.

Part	K_{CP}/MPa · $\sqrt{m}$	Limit value/MPa · $\sqrt{m}$	Ratio
Core barrel	197.985	226.587	0.874
Lower head	173.126	233.131	0.743

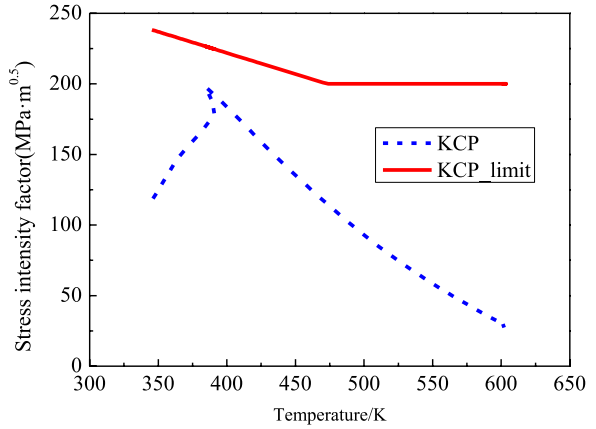

FIGURE 14 | Evaluation results of the RPV cylinder under the late SBO injection condition.

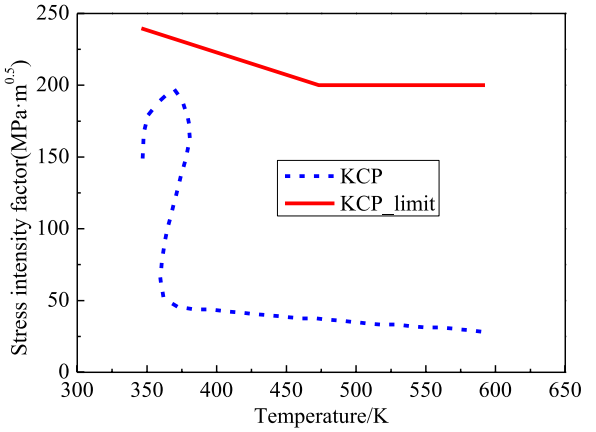

FIGURE 15 | Evaluation results of the RPV lower head under the late SBO injection condition.

and cylinder of the pressure vessel decreases, the temperature of the outer surface decreases sharply, and the temperature of the inner surface decreases slowly. In general, as the IVR water temperature decreases and the injection flow rate increases, the thermal shock on the outer surface of the reactor pressure vessel also increases.

Based on the above mentioned analysis, with the different water temperatures and injection flow rates, the time and degree of thermal shock experienced by the wall of the pressure vessel are obviously different. The lower the IVR water temperature and the higher the injection flow, the faster the cooling rate of the outer surface of the reactor pressure vessel is. Therefore, it can be seen that in this analysis, the thermal impact on the outer surface of the reactor pressure vessel is greater, when the IVR water temperature is 283.15 K, and the water injection rate is 500 t/h.

RPV WALL STRUCTURAL INTEGRITY ANALYSIS

Selection of Working Conditions and Determination of Hypothetical Cracks

In the abovementioned analysis, it is known that the case with a water temperature of 283.15 K and injection rate of 500 t/h is the most ambient for the pressure vessel wall; thus, this condition was chosen for the structural integrity analysis of the pressure vessel wall. Since the IVR is put in, the outer surface is subjected to tensile stress, while the inner surface is subjected to compressive stress, and usually the value of normal stress (circumferential stress) for the axial cracks is higher, so only the axial cracks on the outer surface are considered. Since the PTS crack size is not specified in the RCC-M code, the reference available is the hypothetical crack provision in the Russian PTS analysis guidelines for the WWER reactors. According to the Russian PTS analysis guidelines, the hypothetical crack depth is 1/4 wall thickness or a smaller depth based on the NDT capability, and the ratio of crack depth to half-length a/c is 0.3–0.7. Engineering calculations show that if the hypothetical crack depth is taken as 1/4 wall thickness in the Russian PTS guidelines, the fracture mechanics analysis results of the IVR transient action will significantly exceed the code's fracture limits. Therefore, by referring to the Russian PTS guidelines for determining the depth of smaller hypothetical cracks, the hypothetical crack situation was determined by considering the NDT method of the HPR1000 RPV cylinder and the uncertainty of the corresponding NDT method:1) axial semielliptical crack on the outer surface; 2) core cylinder and lower head area, the initial hypothetical crack depth and length are 4.5 and 27 mm, respectively; 3) based on the initial hypothetical crack, the crack size of the RPV at the end of 60a service life was obtained by the fatigue crack expansion calculation as the hypothetical crack size for PTS analysis of the HPR1000 IVR transients.

The input data involved in PTS analysis of the RPV under the late IVR injection conditions mainly include the following: transient load under normal operation and disturbance conditions, hydrostatic test load, severe temperature fluctuation, and the corresponding internal pressure load suffered by the RPV wall under the late IVR injection conditions of typical accidents. The severe temperature and pressure fluctuation data of the RPV wall after the late IVR operation of the typical SBO accident obtained by the severe accident system analysis program are shown in **Figures 8–10**.

Crack Extension Analysis

Among them, the fatigue crack expansion rate parameters are adopted from the specification for the air environment. The main results of the fatigue crack expansion calculation are shown in **Table 2**. At the end of life, the final crack depth in the cylinder area of the reactor pressure vessel is 5.118 mm, and the final crack length is 27.478 mm. The final crack depth in the lower head area is 4.661 mm, and the final crack length is 27.122 mm. It can be clearly seen that in the whole life, the area with the larger crack depth and length of the reactor pressure vessel is the cylinder, that is, there is a great risk of failure in this area under accident conditions. Therefore, the

fracture failure of the reactor pressure vessel will be evaluated based on the results of the fatigue crack growth analysis.

PTS Fracture Calculation and Evaluation

In this work, the finite element model of the lower head and cylinder of the reactor pressure vessel and the boundary conditions when the IVR is enabled are shown in **Figure 11**. The temperature and stress at the most dangerous time of SBO-delayed injection calculated based on the model are shown in **Figure 12** and **Figure 13**, respectively. It can be seen that under the SBO accident, the maximum temperature of the inner wall of the reactor pressure vessel during the IVR injection is about 638.7 K, and its temperature gradually decreases from inside to outside. When the IVR is put into use, the maximum stress on the outer wall of the reactor pressure vessel is about 1.02e9 Pa, and the stress decreases gradually from outside to inside. Based on the final hypothetical crack size obtained from the fatigue crack expansion calculation and the input load, the main calculation results of the PTS strike analysis evaluation after the IVR input are shown in **Table 3**, according to the evaluation guidelines in Chapter 2, where the ratio of the maximum stress intensity factor correction value to the corresponding limit value is 0.874 approximately, which is at the cylinder of the reactor pressure vessel. **Figures 14**, **15**, respectively, show the stress intensity factor evaluation results of the cylinder and lower head of the reactor pressure vessel during IVR injection. The difference between the two figures is mainly due to the inconsistent degree of the thermal shock experienced at different positions of the outer wall of the pressure vessel. The calculated stress intensity factors of the lower head and cylinder under different temperatures are lower than the limit value of the stress intensity factor. Therefore, it shows that during the SBO accident, the reactor pressure vessel can bear the pressure and resist the thermal shock without fracture failure.

CONCLUSION

During the development of IVR for the HPR1000 nuclear power plant, in order to ensure the structural integrity of the RPV under the combined effect of a sudden cold shock load on the external surface and a high internal pressure load caused by IVR commissioning, the sensitivity of the two key parameters of IVR in the pressure thermal shock was analyzed. The results show that with the decrease in IVR water temperature and the increase in the injection flow rate, the more intense will be the change in the wall temperature of the reactor pressure vessel after IVR is put into operation, indicating that the thermal shock is greater. Then, based on the case with the maximum thermal impact on the wall of the reactor pressure vessel, quantitative fracture mechanics calculation and evaluation of RPV were carried out by the PTS analysis method, and the fatigue crack expansion calculations were used to obtain the fracture mechanics of the RPV core barrel and lower head area at the end of life. The results show that the area with large crack depth and length is the cylinder area of the reactor pressure vessel; in other words, there is a great risk of failure in this area under accident conditions. Based on the results of fatigue crack growth analysis, the fracture failure of the reactor pressure vessel was evaluated. The results of the PTS analysis after the IVR input are that the ratio of the maximum stress intensity factor correction value to the corresponding limit value in the RPV structure is about 0.874, which satisfies the fracture mechanics limit value of the RCC-M code. The results of the study in this work indicate that the HPR1000 RPV will not experience fracture failure when the IVR is put into operation.

DATA AVAILABILITY STATEMENT

The original contributions presented in the study are included in the article/Supplementary Material, further inquiries can be directed to the corresponding author.

AUTHOR CONTRIBUTIONS

DZ: conceptualization, software, and writing—original draft preparation. HS: methodology and data curation. BZ and TH: reviewing and editing. JD: visualization. YX: investigation and reviewing and editing. YL: supervision and project administration.

FUNDING

The authors appreciate the financial support from the National Key R&D Program of China (No. 2019YFB1900703).

REFERENCES

Bass, B. R., Pugh, C. E., Sievers, J., and Schulz, H. (2001). Overview of the International Comparative Assessment Study of Pressurized Thermal-Shock in Reactor Pressure Vessels (RPV PTS ICAS). *Int. J. Press. Vessel. Pip.* 78 (2-3), 197–211. doi:10.1016/s0308-0161(01)00030-8

Chen, M., Lu, F., Wang, R., Huang, P., Liu, X., Zhang, G., et al. (2015). The Deterministic Structural Integrity Assessment of Reactor Pressure Vessels under Pressurized thermal Shock Loading. *Nucl. Eng. Des.* 288, 130–140. doi:10.1016/j.nucengdes.2015.03.008

Chen, M., Lu, F., Wang, R., and Ren, A. (2014). Structural Integrity Assessment of the Reactor Pressure Vessel under the Pressurized Thermal Shock Loading. *Nucl. Eng. Des.* 272, 84–91. doi:10.1016/j.nucengdes.2014.01.021

Chen, M., Qian, G., Shi, J., Wang, R., Yu, W., Lu, F., et al. (2016). Application of the French Codes to the Pressurized Thermal Shocks Assessment. *Nucl. Eng. Technol.* 48 (6), 1423–1432. doi:10.1016/j.net.2016.06.009

Chou, H., and Huang, C. (2014). "Structural Reliability Evaluation on the Pressurized Water Reactor Pressure Vessel under Pressurized thermal Shock Events," in Pressure Vessels and Piping Conference, Anaheim, CA, July 20–24, 2014.

Emad, M. S., Mohamed, M. A., and Mohammed, A. (2021). A Comprehensive Review on Pressurized thermal Shock: Predictive, Preventive and Safety Issues. *J. Therm. Anal. Calorim.* 146, 525–544. doi:10.1007/s10973-020-10030-4

EricksonKirk, M., Chokshi, N., Woods, R., Junge, M., Malik, S., and Bessette, D. (2005). "Technical Basis for Revision of the Pressurized thermal Shock (PTS) Screening Limit in the PTS Rule (10 CFR50.61)," in 18th International Conference on Structural Mechanics in Reactor Technology, Beijing, China, August 7-12, 2005.

Faidy, C. (2011). "RCC-M, RSE-M and RCC-MRx: A Consistent Set of Mechanical Components Codes and Standards," in Pressure Vessels and Piping Conference, Baltimore, MA, July 17–21, 2011.

Kim, J.-S., Choi, J.-B., Kim, Y.-J., and Park, Y.-W. (2003). Investigation on Constraint Effect of Reactor Pressure Vessel under Pressurized thermal Shock. *Nucl. Eng. Des.* 219 (3), 197–206. doi:10.1016/s0029-5493(02)00282-0

Li, F., and Modarres, M. (2005). Probabilistic Modeling for Fracture Mechanic Studies of Reactor Vessels with Characterization of Uncertainties. *Nucl. Eng. Des.* 235 (1), 1–19. doi:10.1016/j.nucengdes.2004.09.004

Marie, S., Ménager, Y., and Chapuliot, S. (2005). Stress Intensity Factors for Underclad and through Clad Defects in a Reactor Pressure Vessel Submitted to a Pressurised Thermal Shock. *Int. J. Press. Vessel. Pip.* 82 (10), 746–760. doi:10.1016/j.ijpvp.2005.06.001

Mora, D. F., Niffenegger, M., Qian, G., Jaros, M., and Niceno, B. (2019). Modelling of Reactor Pressure Vessel Subjected to Pressurized thermal Shock Using 3D-XFEM. *Nucl. Eng. Des.* 353, 110237. doi:10.1016/j.nucengdes.2019.110237

Pugh, C. E., Bass, B. R., and Dickson, T. L. (2007). Role of Probabilistic Analysis in Integrity Assessments of Reactor Pressure Vessels Exposed to Pressurized Thermal-Shock Conditions. *Eng. Fail. Anal.* 14 (3), 501–517. doi:10.1016/j.engfailanal.2005.08.006

Server, W. L., and Nanstad, R. K. (2015). *6-Integrity and Embrittlement Management of Reactor Pressure vessels(RPVs) in Light-Water Reactors*. Cambridge: Woodhead Publishing Series in Energy, 132–155. doi:10.1533/9780857096470.2.132

Stahlkopf, K. E. (1984). Pressure Vessel Integrity under Pressurized Thermal Shock Conditions. *Nucl. Eng. Des.* 80, 171–180. doi:10.1016/0029-5493(84)90165-1

Sun, X., Chai, G., and Bao, Y. (2017). Elastic and Elastoplastic Fracture Analysis of a Reactor Pressure Vessel under Pressurized thermal Shock Loading. *Eur. J. Mech. - A/Solids* 66, 69–78. doi:10.1016/j.euromechsol.2017.06.008

Thamaraiselvi, K., and Vishnuvardhan, S. (2020). Fracture Studies on Reactor Pressure Vessel Subjected to Pressurised thermal Shock: A Review. *Nucl. Eng. Des.* 360, 110471. doi:10.1016/j.nucengdes.2019.110471

Wang, M., Bai, L., Wang, L., Qiu, S., Tian, W., and Su, G. H. (2017). Thermal Hydraulic and Stress Coupling Analysis for AP1000 Pressurized thermal Shock (PTS) Study under SBLOCA Scenario. *Appl. Therm. Eng.* 122, 158–170. doi:10.1016/j.applthermaleng.2017.04.106

Zeng, M., Wang, S., Duan, J., Sun, J., Zhong, P., and Zhang, Y. (2016). Review of Nuclear Power Development in China: Environment Analysis, Historical Stages, Development Status, Problems and Countermeasures. *Renew. Sustain. Energ. Rev.* 59, 1369–1383. doi:10.1016/j.rser.2016.01.045

Conflict of Interest: The authors declare that the research was conducted in the absence of any commercial or financial relationships that could be construed as a potential conflict of interest.

Publisher's Note: All claims expressed in this article are solely those of the authors and do not necessarily represent those of their affiliated organizations, or those of the publisher, the editors, and the reviewers. Any product that may be evaluated in this article, or claim that may be made by its manufacturer, is not guaranteed or endorsed by the publisher.

frontiers | Frontiers in Energy Research

ORIGINAL RESEARCH
published: 13 June 2022
doi: 10.3389/fenrg.2022.915450

Coupled Analysis of Heat Transfer in a Molten Pool With Three-Layer Configuration

Jian Deng, Dahuan Zhu, Yuejian Luo, Hongping Sun, Ming Zhang, Lili Liu, Qingan Xiang, Xiaoli Wu, Youyou Xu and Qingwen Xiong*

Science and Technology on Reactor System Design Technology Laboratory, Nuclear Power Institute of China, Chengdu, China

Understanding a reliable description of the heat transfer in the molten pool with three-layer configuration is inevitable for the design of severe accident mitigation measures in research reactors, such as IVR-ERVC. However, investigations on a thick lower metallic layer are scarce. Thus, further studies on heat transfer in a molten pool with a thick lower metallic layer are highly required, based on previous severe accident studies in light water reactors. This study conducts a numerical simulation of heat transfer in the molten pool with a thick lower metallic layer during a severe accident, combining model development, code verification, and code application. First, the MPCAP code has been developed, based on the coupled simulation of natural convection inside the molten pool, two-dimensional heat conduction in the RPV lower head, and convection outside the reactor vessel wall. Then, a verification case has been conducted using three-layer configuration in AP1000. The AP1000 verification case indicates that the MPCAP code predicts important parameters in the molten pool well.

Keywords: IVR-ERVC, thick metallic layer, heat transfer in molten pool, numerical simulation, coupled analysis

OPEN ACCESS

Edited by:
Yapei Zhang,
Xi'an Jiaotong University, China

Reviewed by:
Hongyang Wei,
Harbin Engineering University, China
Xiaojing Liu,
Shanghai Jiao Tong University, China

****Correspondence:***
Yuejian Luo
luo_yuejian@163.com

Specialty section:
This article was submitted to Nuclear Energy, a section of the journal Frontiers in Energy Research

Received: *08 April 2022*
Accepted: *02 May 2022*
Published: *13 June 2022*

Citation:
Deng J, Zhu D, Luo Y, Sun H, Zhang M, Liu L, Xiang Q, Wu X, Xu Y and Xiong Q (2022) Coupled Analysis of Heat Transfer in a Molten Pool With Three-Layer Configuration. Front. Energy Res. 10:915450. doi: 10.3389/fenrg.2022.915450

1 INTRODUCTION

At present, the proportion of nuclear energy is low. Nuclear energy, a clean energy with a large space for development, is an important component of sustainable energy structure. In the process of development of nuclear energy science, research reactors which are used for scientific research, operational training, and technological development play an important role in many fields, such as physics, chemistry, biology, medicine, and agriculture, . According to the latest statistics from the International Atomic Energy Agency (IAEA), there are 258 operational research reactors in 56 countries and territories worldwide (RRDB, 2020).

Nuclear safety has been the focus of public attention since the beginning of the development of nuclear energy, and safety analysis has always been the focus of nuclear energy scientific research. Since the Three Mile Island accident and the Chernobyl accident, the severe accident of nuclear reactor has received wide attention in the international community, and the IAEA has explicitly required that severe accident and their mitigation measures must be taken into account in the design of nuclear power plants (Gilbert, 1979). The National Nuclear Safety Administration of China issued the Regulations on the Design and Safety of Nuclear Power Plants (HAF102-2016) which also requires additional safety facilities for the design of nuclear power plants, the expansion of safety system capabilities, the prevention of severe accidents, and the mitigation of the consequences of a severe accident. The IAEA Research Reactor Safety also states that the potentially serious consequences of all foreseeable events must be taken into account in the design of the research

reactor and that safety facilities can prevent severe accidents and mitigate the consequences of severe accidents (Safety of Research Reactors, 2016).

It is an important part of severe accident research to formulate measures to relieve severe accident mitigation and reduce the serious consequences of core melting. How to deal with core melting is a key point in the mitigation measures of a severe accident, and the significant mitigation measure adopted by advanced nuclear power plants includes in-vessel retention (IVR) and ex-vessel retention (EVR). In reactors with a semi-sphere shape pressure vessel, the external reactor vessel cooling (ERVC) is used to remove the decay heat from the lower head of the pressure vessel and maintains the integrity of the lower head. Some research reactors also have a semi-sphere shape pressure vessel, which is a foundation of IVR-ERVC implementation. On the basis of the application of IVR-ERVC for commercial light water reactors, the IVR-ERVC measure could be adopted in research reactors, which is conducive to the formulation of mitigation measures for a severe accident.

By research studies on pressure vessels with molten materials in the Three Miles Island nuclear accident, it is presented that the core molten materials will be relocated to the pressure vessel's lower plenum, and eventually form a molten pool. In spite of decay heat, the pressure vessel can still maintain integrity. On this basis, a retention strategy for molten material in the lower plenum is proposed for reactors with a semi-sphere shape lower head. At first, IVR-ERVC has been used in the VVER-440 unit in Loviisa nuclear power plant (Kymäläinen et al., 1997), and gradually adopted as a key technology for the retention strategy for molten materials in reactor lower plenum, such as AP1000, ACP1000, CPR1000, CAP1400, APR1400 (Rempe et al., 1997; Theofanous et al., 1997; Cummins et al., 2003; Esmaili And Khatib-Rahbar, 2004; Oh And Kim, 2005; Wang et al., 2010; Li et al., 2015).

In commercial light water reactors, a steady-state molten pool, which is considered to be formed under an enveloped condition, generally consists of two- and three layers, as shown in **Figure 1**. The two-layer molten pool includes a lower oxide layer and an upper metallic layer. The oxide layer with an internal heat source has uranium dioxide, zirconium dioxide, and other oxides, and the metallic layer has stainless steel, and zirconium alloy, generally believed to have no internal heat source. The three-layer molten pool includes a lower heavy metallic layer, intermediate oxide layer, and upper light metallic layer. The heavy metallic layer with an internal heat source has metal uranium, stainless steel, and zirconium alloy. The decay heat in the oxide layer heats the heavy metallic layer and the light metallic layer. The light metallic layer is similar to the two-layer molten pool. It is generally believed that the precipitation of heavy metal uranium is less, and the heavy metallic layer is thinner. In addition, the heat transfer performance of heavy metal uranium is well, the heat in the heavy metallic layer is only conducted through the inner wall of the pressure vessel. Because of the high melting point of oxide molten materials, there is a crust around the oxide molten pool, and the inner temperature of the crust is the melting point of oxide molten materials. The configuration of the molten pool is closely related to molten components, the core melting process, and especially the relocation of molten materials to the lower head.

Under the effect of the temperature difference and density difference, natural convection occurs inside a steady-state molten pool, and the heat transfer along the angle can be determined by empirical heat transfer correlations. On the one hand, the heat in a metallic layer is removed through upper radiation and conduction in the pressure vessel's inner wall surface. The thinner metallic layer leads to higher heat flux in the inner surface wall of the pressure vessel, which is easy to exceed the critical heat flux (CHF), resulting in the failure of the pressure vessel wall because of thermal load. This phenomenon is a focusing effect, which needs to be paid attention to. On the other hand, the power density of the heavy metallic layer is related to the quality of light metals such as dissolved zirconium alloy and stainless steel in heavy metal uranium. When the amount of desolvation is less, the heavy metallic layer is thinner and the power density is larger, which is easy to form a focusing effect in the lower heavy metallic layer. The focusing effect in the lower heavy mental layer is similar to that of the upper light metallic layer. Especially the CHF value decreases with angles, and thermal failure could occur near a heavy metallic layer located at the bottom of the pressure vessel.

In research reactors with U-Al alloy fuels, the molten materials include uranium dioxide, alumina, U-Al alloy, aluminum alloy. Oxide molten pool is mainly alumina-based, all obtained by high-temperature oxidation reaction. The molten metallic layer is mainly U-Al alloys, and less metallic aluminum alloys are extracted. The density of U-Al alloy is greater than alumina, forming a molten pool configuration with a lower thick metallic layer with U-Al alloy, a middle thinner oxide layer, and an upper thinner metallic layer. The internal heat source is concentrated in the lower molten pool and tends to conduct to the pressure vessel wall, which could make the middle oxide layer and upper metallic layer solidify, forming a three-layer molten pool configuration, as shown in **Figure 2**. Whether the oxide layer and metallic layer solidify is closely related to the heat source in the oxide layer and the upward heat transfer from the lower heavy metallic layer.

At present, all heat transfer methods in the molten pool are focusing on the molten pool configuration of the light water reactor, and don't apply to reactors with a thicker lower heavy metallic layer mentioned above. It needs to be studied based on the current heat transfer method in the molten pool. This method could include the determination of molten pool configuration, and heat transfer from the molten pool to the outer surface wall of the pressure vessel. Most heat transfer method in the molten pool is based on lumped parameter method, which has been studied by many researchers. Cao et al. have studied the two-dimensional conduction inside the lower headwall and heat convection outside the lower headwall (Cao et al., 2015). In addition, Liu et el. havefocused on the effects of heat transfer inside and outside molten pools by coupled analysis, which could decrease the focusing effects (Liu et al., 2018; Luo et al., 2018; Luo et al.,

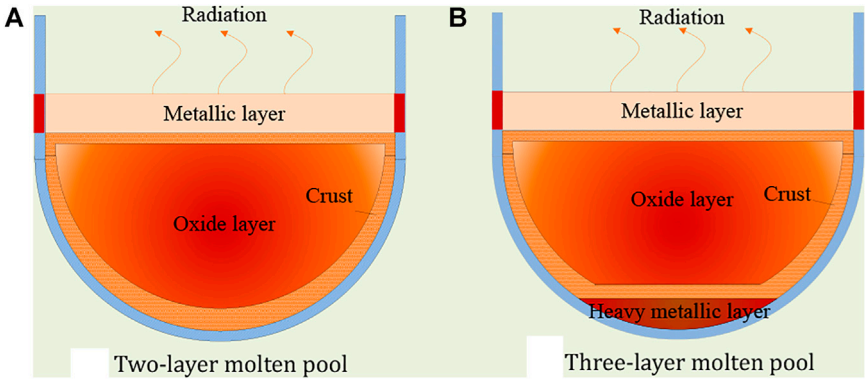

FIGURE 1 | Schematic diagram of molten pool configuration. **(A)** Two-layer molten pool. **(B)** Three-layer molten pool.

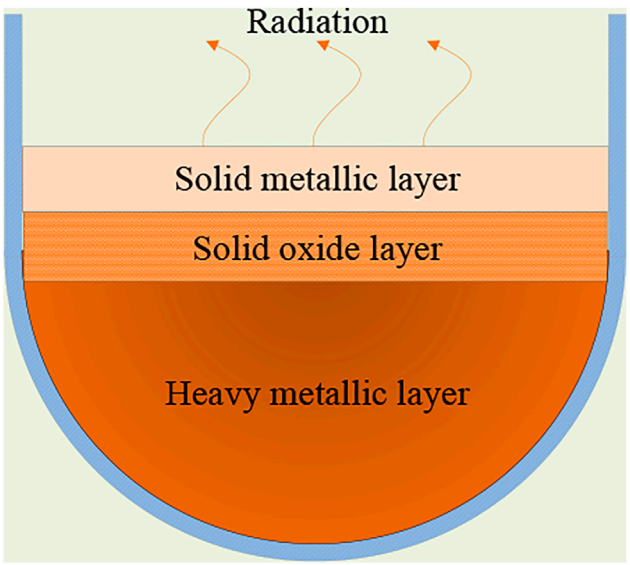

FIGURE 2 | Schematic diagram of molten pool configuration with a lower heavy metallic layer.

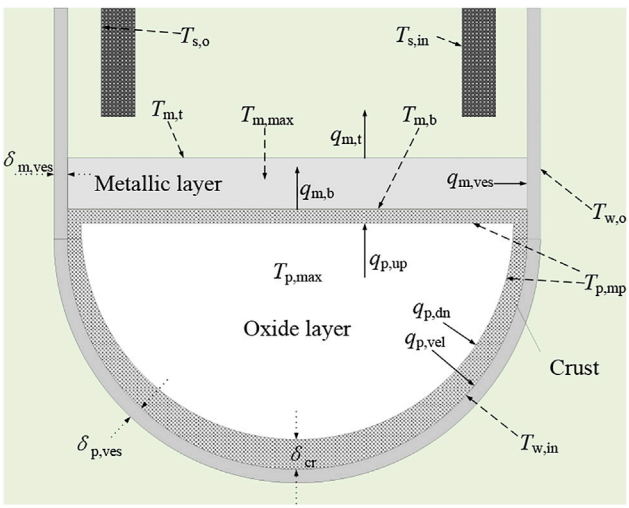

FIGURE 3 | Schematic diagram of two-layer molten pool with parameters.

2019). These researches are important and significant for engineering assignment for large-scale nuclear power plants, especially decreasing the focusing effects, and also helpful in this study.

In this study, a new heat transfer method in the molten pool for a reactor with a thicker lower heavy metallic layer has been presented. Firstly, a molten pool configuration determination has been developed to solve whether a solidified middle oxide layer or upper metallic layer exists based on an improved lumped parameter method. Secondly, a comprehensive analysis has been adopted to solve the heat transfer in the molten pool based on previous coupled analysis, considering natural convection inside the molten pool, two-dimensional conduction inside the lower headwall, and convection outside the lower headwall. Then, an MPCAP (Molten Pool Coupled Analysis Program) code has been developed, and a verification calculation with AP1000 has been conducted.

2 METHODOLOGY

This chapter develops a coupled analysis code MPCAP for heat transfer in the molten pool with a thick lower heavy metallic layer, on the basis of coupled analysis method using the improving lumped parameter method and detailed heat transfer from inside molten pool to the outside lower headwall.

2.1 The Traditional Lumped Parameter Method

In lumped parameter method, the molten pool is calculated as a whole using average parameter values, as shown in **Figures 3–5**.

The traditional lumped parameter method indicates that the ratio of heat transfer up and down in the oxide layer is fixed and determined by the ratio of Nusselt number, which is obtained by the empirical correlation (Theofanous et al., 1997; Liu et al., 2018):

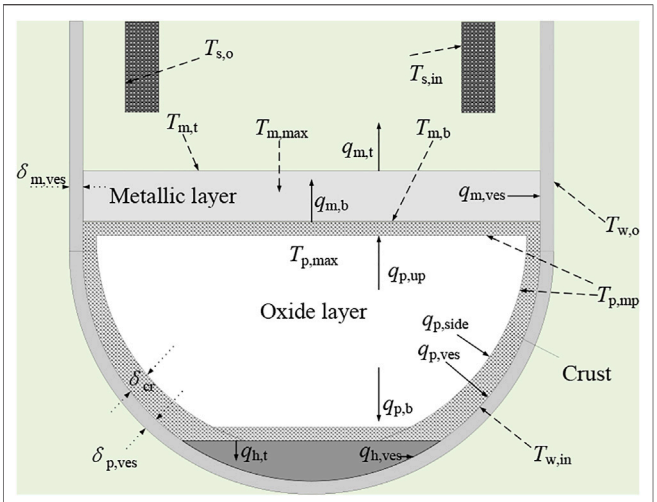

FIGURE 4 | Schematic diagram of three-layer molten pool with parameters.

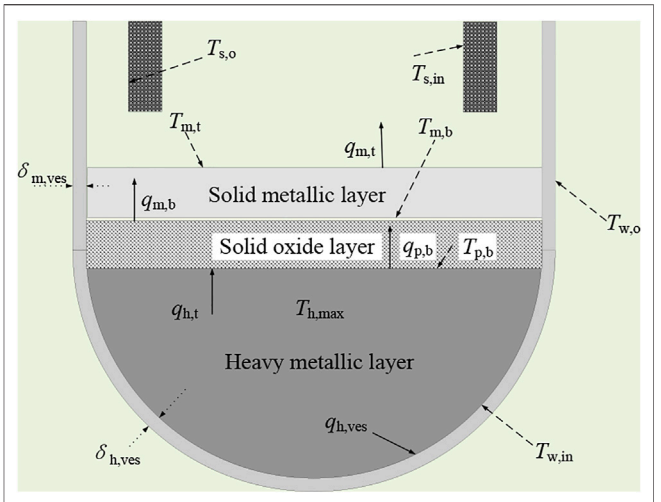

FIGURE 5 | Schematic diagram of thick heavy metallic layers with parameters.

$$R = \frac{\mathrm{Nu}_{p,up}}{\mathrm{Nu}_{p,dn}}. \tag{1}$$

Using a heat balance relationship,

$$Q_p V_p = q_{p,up} s_{p,up} + q_{p,dn} s_{p,dn}. \tag{2}$$

We get

$$q_{p,dn} = \frac{Q_p V_p}{s_{p,dn} + R s_{p,up}}, \tag{3}$$

$$q_{p,up} = \frac{Q_p V_p R}{s_{p,dn} + R s_{p,up}}, \tag{4}$$

$$q_{p,dn}(\theta) = q_{p,dn} \frac{\mathrm{Nu}_{p,dn}(\theta)}{\overline{\mathrm{Nu}_{p,dn}}}. \tag{5}$$

Using the heat flux obtained by the abovementioned formulae, the total parameters in the oxide layer and metallic layer are calculated respectively, and the main parameters are obtained including the distribution of heat flux along the lower headwall, the thickness of crust, and the thickness of the lower headwall of the pressure vessel. In this calculation process, only one-dimensional conduction is considered, and the outer surface wall of the lower head is a fixed temperature or a fixed heat transfer coefficient.

This thickness of pressure vessel in commercial light water reactor is generally more than 15 cm, which is obvious two-dimensional conduction. Two-dimensional conduction can transmit heat from a higher temperature area axially to a lower temperature area, redistributing the temperature field inside the lower head, which has a protective effect on the focusing effect near the metallic layer. In the numerical simulation, the simple and conservative use of one-dimensional conduction will significantly overestimate the phenomenon of the focusing effect and cannot obtain accurate prediction results, making the evaluation results of IVR-ERVC conservative.

In the lower headwall of a pressure vessel, two-dimensional conduction and external convection had a significant impact on the heat transfer of the molten pool, and ultimately affect the heat flux distribution in the outer surface wall of the lower head. The traditional lumped parameter method above simply determines the up and down heat transfer by the ratio of Nusselt number, which is not consistent with the actual situation and couldn't apply to molten pool configuration with a thicker lower heavy metallic layer. Later in this section, we will focus on the heat transfer in the molten pool based on the improved lumped parameter method and briefly introduce two-dimensional conduction and external vessel heat transfer.

2.2 Heat Transfer in Molten Pool

This section is based on a three-layer molten pool configuration, including a lower heavy metallic layer, central oxide layer, and upper light metallic layer. When the power density of the heat source in the oxide layer is low, the heat in a heavy metallic layer may be transferred to the oxide layer, affecting the oxide layer and metallic layer. This section first discusses the configuration of the molten pool on the basis of heat transfer in the heavy metallic layer and determines the formation of the oxide layer and metallic layer in the molten pool. On the basis of judging the configuration of the molten pool, the heat transfer in the oxide layer and metallic layer are discussed. The main parameters are shown in **Figure 4**, at which the temperature of the oxide layer is highest and the heat is transferred from the oxide layer to the metallic layer and heavy metallic layer, respectively.

2.2.1 Heat Transfer in the Heavy Metallic Layer and Determination of Molten Pool Configuration

Different internal heat sources and heat transfer capability may cause different molten pool configurations. In the actual reactor molten pool, the decay power density in the heavy metallic layer is high, where the capacity of heat transfer is strong. In addition, the melting point of the lower heavy metallic layer is smaller,

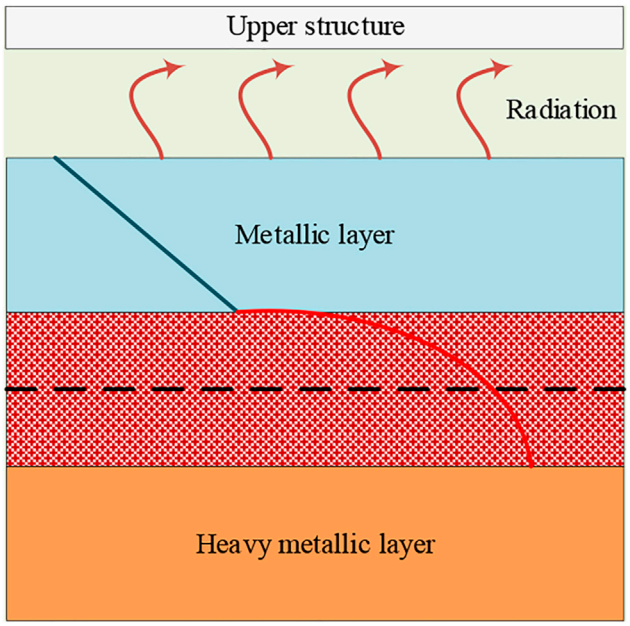

FIGURE 6 | Schematic diagram of temperature gradient in the solid oxide layer.

indicating that there is a molten state. The lower heavy metallic layer is cooled through the pressure vessel wall. Since the lower heavy metallic layer is thin, convection is not obvious, and conduction prevails. We can simply get heat flux to form a heavy metallic layer on the inner wall surface of the pressure vessel:

$$q_{\mathrm{h,ves}} = \frac{q_{\mathrm{p,b}} s_{\mathrm{p,b}} + Q_{\mathrm{h}} V_{\mathrm{h}}}{s_{\mathrm{h,b}}}. \tag{6}$$

When the lower heavy metallic layer is thick, the natural convection is similar to the oxide layer, and the distribution of heat flux on the side of the lower heavy metallic layer can be obtained by using the Nusselt number distributed along angle:

$$q_{\mathrm{h,ves}}(\theta) = \left(T_{\mathrm{h,max}} - T_{\mathrm{w,in}}\right) \frac{\mathrm{Nu}_{\mathrm{h,dn}}(\theta) \cdot k_{\mathrm{h}}}{h_{\mathrm{h}}}. \tag{7}$$

$$q_{\mathrm{p,b}} s_{\mathrm{p,b}} + Q_{\mathrm{h}} V_{\mathrm{h}} = \int_0^{\theta_h} q_{\mathrm{h,ves}}(\theta) \cdot 2\pi r_{\mathrm{in}} \sin\theta \cdot r_{\mathrm{in}} \mathrm{d}\theta. \tag{8}$$

The state of the oxide layer is related to the internal heat source of the oxide layer and the heat transfer between the heavy metallic layer and the oxide layer. When there is a sufficient internal heat source in the oxide layer, the heat is transmitted from the oxide layer to the metallic layer and heavy metallic layer, and the maximum temperature of the oxide layer is inside the oxide layer. When the maximum temperature is higher than the melting point of the oxide layer, a molten oxide layer is formed with crust. When there is an insufficient heat source in the oxide layer, the heat in the heavy metallic layer is transmitted to the oxide layer, and the maximum temperature of the oxide layer is at the bottom of the oxide layer. The solidification of the metallic layer is related to the internal heat source and upward heat transfer from the oxide layer to the metallic layer, and it is generally believed that the internal heat source in the metallic layer is low, and the solidification of the metallic layer is mainly related to the upward heat transfer from oxide layer.

For the molten pool with a thicker heavy metallic layer, there is an obvious internal heat source in the lower heavy metallic layer. The solidification of the oxide layer is the key to molten pool configuration. For a thinner solidified oxide layer and metallic layer, it is considered that there is only conduction like an infinite plate. The temperature distribution in the oxide layer and metallic layer is shown in **Figure 6**. The oxide layer is parabolic and the metallic layer is linear based on whether there is an internal heat source. When heat is transferred from a heavy metallic layer to an oxide layer, the maximum temperature of the oxide layer is in contact with the oxide layer, but it is not the vertex of the parabola. When heat is transferred from the oxide layer to the heavy metallic layer, the maximum temperature of the oxide layer is inside the oxide layer, which is the vertex of the parabola.

To judge the heat transfer between the heavy metallic layer and oxide layer, it can be assumed that there is no heat transfer between those two layers, and then the temperature between the heavy metallic layer and oxide layer is distributed as a parabola type. In this situation, the maximum temperature of the heavy metallic layer is equal to the temperature at the top of the heavy metallic layer, and the temperature of the top of the oxide layer is equal to the temperature of the bottom of the metallic layer:

$$T_{\mathrm{m,b}} = T_{\mathrm{p,t}} = \frac{Q_{\mathrm{p}} h_{\mathrm{p}}^2}{k_{\mathrm{p}}} + T_{\mathrm{h,t}} = \frac{Q_{\mathrm{p}} h_{\mathrm{p}}^2}{k_{\mathrm{p}}} + T_{\mathrm{h,max}}. \tag{9}$$

At the same time, the temperature at the bottom of the metallic layer:

$$T_{\mathrm{m,b}} = T_{\mathrm{m,t}} + \frac{q_{\mathrm{m,t}} h_{\mathrm{m}}}{k_{\mathrm{m}}}. \tag{10}$$

Also,

$$q_{\mathrm{m,t}} = q_{\mathrm{m,b}} = q_{\mathrm{p,t}}, = Q_{\mathrm{p}} h_{\mathrm{p}}.$$

The heat is radiated from the metallic layer to the upper space of the reactor core, mainly consisting of two parts: one is between the top surface of the metallic layer and the inner surface of the inner component of the pressure vessel reactor, and another is between the outer surface of the component of pressure vessel reactor and the upper inner surface of the pressure vessel. The inner component of the pressure vessel reactor includes upper structures, which don't relocate to the lower head during severe accidents. Ignoring radiation between the top surface of the metallic layer and the pressure vessel, and simplifying the geometry of components inside the core as a flat rectangular, we can calculate the heat transfer in the upper space of the metallic layer. Radiation from the top surface of the metallic layer:

$$q_{m,s} = \frac{\sigma\left(T_{m,t}^4 - T_{s,in}^4\right)}{\frac{1}{\varepsilon_{m,t}} + \frac{1-\varepsilon_s}{\varepsilon_s} \cdot \frac{s_{m,t}}{s_s}}. \quad (12)$$

The internal conduction of components inside the core is approximated as one-dimensional conduction:

$$q_s = \frac{k_s\left(T_{s,in} - T_{s,o}\right)}{\delta_s}. \quad (13)$$

The outer surface of the reactor component is approximately equal to the upper inner surface area of the pressure vessel, and if the emission rate is the same, then the radiation is

$$q_{s,ves} = \varepsilon_s \sigma\left(T_{s,o}^4 - T_{ves,in}^4\right). \quad (14)$$

Approximately, one-dimensional conduction in the upper-pressure vessel wall is

$$q_{ves} = \frac{k_{ves}\left(T_{ves,in} - T_{ves,o}\right)}{\delta_{ves}}. \quad (15)$$

Obviously, in the abovementioned several heat transfer processes, the quantity of heat transfer is equal; then,

$$q_{m,t}s_{m,t}, = q_{m,s}s_{m,t} = q_s s_s, = q_{s,ves}s_{ves}, = q_{ves}s_{ves}.$$

The bottom temperature of the metallic layer could be obtained above **Eqs 10–16** or **Eqs 7–9**, which could be compared. If the former value is larger, then the heat is transferred from the oxide layer to the heavy metallic layer. On the contrary, the heat is transferred from the heavy metallic layer to the oxide layer. It is discussed, respectively, in the following part.

2.2.2.1 Heat Is Transferred From the Oxide Layer to the Heavy Metallic Layer

When heat is transferred from the oxide layer to the heavy metallic layer, at first, we assume that there is a parameter indicating the ratio of heat transfer from the oxide layer to the heavy metallic layer, and we set it as f_{ph}, equaling 0~1. Then, **Eq. 8** is written as

$$f_{ph}Q_pV_p + Q_hV_h = \int_0^{\theta_h} q_{h,ves}(\theta) \cdot 2\pi r_{in} \sin\theta \cdot r_{in} d\theta. \quad (17)$$

Also, **Eq. 11** is written as

$$q_{m,t} = q_{m,b} = q_{p,t} = \left(1 - f_{ph}\right)Q_p h_p. \quad (18)$$

The temperature at the bottom of the oxide layer is equal to the temperature at the top of the heavy metallic layer:

$$T_{p,b} = T_{h,t} = T_{h,max} + \frac{f_{ph}Q_pV_p}{s_{h,t}} \Big/ \frac{Nu_{h,up}k_h}{h_h}. \quad (19)$$

By **Eqs 7**, **17–19**, the temperature at the bottom of the oxide layer is obtained.

There is a symmetrical point in the temperature distribution of the oxide layer, as shown in **Figure 7**. When the maximum temperature is on the right, the symmetry temperature T_{sym} is equal to the temperature at the bottom of the oxide layer, which is $T_{p,b}$. When the maximum temperature is on the left, the symmetry temperature T_{sym} is equal to the temperature at the top of the oxide layer, which is $T_{p,t}$.

When the maximum temperature is on the right, meaning that $f_{ph} < 0.5$, and the temperature at the bottom of the metallic layer is

$$h_{sym,t} = \left(1 - 2f_{ph}\right)h_p, \quad (20)$$

$$T_{m,b} = T_{p,t} = T_{sym} - \left(\frac{Q_p h_{sym,t}^2}{2k_p} + \frac{f_{ph}Q_p h_p}{k_p}\right) = T_{p,b} - \left(\frac{Q_p h_{sym,t}^2}{2k_p} + \frac{f_{ph}Q_p h_p}{k_p}\right). \quad (21)$$

When the maximum temperature is on the left, meaning that $f_{ph} > 0.5$, the temperature at the bottom of the metallic layer is

$$h_{sym,b} = \left(2f_{ph} - 1\right)h_p, \quad (22)$$

$$T_{m,b} = T_{p,t} = T_{sym} = T_{p,b} + \left(\frac{Q_p h_{sym,b}^2}{2k_p} + \frac{\left(1 - f_{ph}\right)Q_p h_p}{k_p}\right). \quad (23)$$

The temperature at the bottom of the metallic layer obtained above is $T_{m,b}$, and also the temperature at the bottom of the metallic layer could be obtained by **Eqs 10**, **12–16**, **18**. For comparison, we adjust f_{ph} and repeat the above steps until the convergence limit is reached, and finally determine the ratio of heat transfer from the oxide layer to the heavy metallic layer.

2.2.2.2 Heat Is Transferred From the Heavy Metallic Layer to the Oxide Layer

When heat is transferred from the heavy metallic layer to the oxide layer, at first we assume that there is a parameter indicating the ratio of heat transfer from heavy metallic layer to the oxide layer, and we set it as f_{hp}, equaling 0~1. Then, **Eq. 8** is written as

$$\left(1 - f_{fp}\right)Q_hV_h = \int_0^{\theta_h} q_{h,ves}(\theta) \cdot 2\pi r_{in} \sin\theta \cdot r_{in} d\theta. \quad (24)$$

Also, **Eq. 11** is written as

$$q_{m,t} = q_{m,b} = q_{p,t} = Q_p h_p + f_{hp}Q_hV_h \big/ s_{h,t}. \quad (25)$$

Equation 19 is written as

$$T_{m,b} = T_{h,t} = T_{h,max} - \frac{f_{hp}Q_hV_h}{s_{h,t}} \Big/ \frac{Nu_{h,up}k_h}{h_h}. \quad (26)$$

The temperature at the bottom of the metallic layer is equal to the temperature at the top of the oxide layer:

$$T_{m,b} = T_{p,t} = T_{h,t} - \left(\frac{Q_p h_h^2}{2k_p} + f_{hp}\frac{Q_hV_h}{s_{h,t}}\frac{h_p}{k_p}\right). \quad (27)$$

The temperature at the bottom of the metallic layer obtained above is $T_{m,b}$, and also, the temperature at the bottom of the metallic layer could be obtained by **Eqs 10**, **12–16**, **18**. For

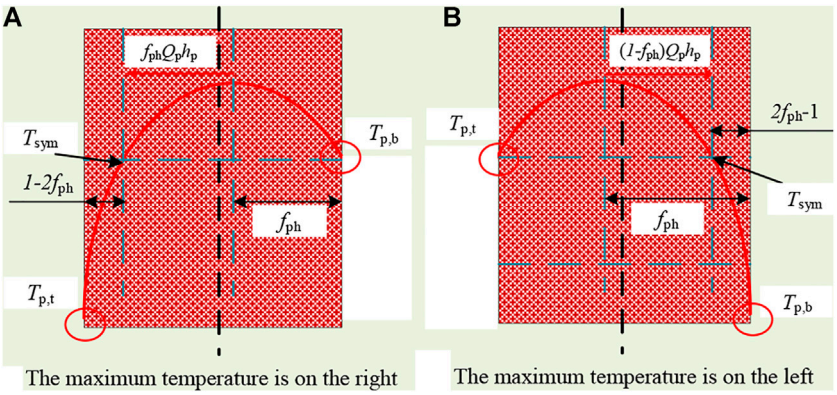

FIGURE 7 | Schematic diagram of temperature symmetry in the solid oxide layer. **(A)** The maximum temperature is on the right. **(B)** The maximum temperature is on the left.

comparison, we adjust f_{hp} and repeat the above steps until the convergence limit is reached, and finally determine the ratio of heat transfer from the oxide layer to the heavy metallic layer.

On the basis of obtaining the heat transfer between the oxide layer and heavy metallic layer, the heat in the oxide layer and metallic layer can be obtained to determine whether it is a molten pool. The highest temperature of the metallic layer occurs at the bottom surface and the lowest temperature occurs at the top surface. When heat is transferred from a heavy metallic layer to an oxide layer, the maximum temperature in the oxide layer is in contact with the heavy metallic layer. When heat is transferred from the oxide layer to the heavy metallic layer, the maximum temperature is inside the oxide layer, which may exceed the melting points of the oxide layer to form a molten pool, where the maximum temperature of the oxide layer is

$$T_{p,max} = T_{h,t} + \frac{Q_p\left(f_{ph}h_p\right)}{2k_p}. \tag{28}$$

When the maximum temperature of the oxide layer exceeds the melting point of the oxide layer, the heat transfer calculation in the molten pool will be carried out.

2.2.2 Code MACAP Development

In the above section, an improving lumped method has been presented to determine the molten pool configuration. Also, there is coupled effect of heat transfer among natural convection inside a molten pool, two-dimensional conduction in the lower headwall, and convection outside the lower headwall, which has been studied using a coupled analysis method. Based on the above study, code MACAP has been developed for a thicker lower heavy metallic layer in this section. In code MACAP, the flow chart is shown in **Figure 8**.

At first, we assume that there is a known temperature in the pressure vessel inner wall surface, and then determine the heat transfer between the heavy metallic layer and oxide layer. When the maximum temperature of the oxide layer exceeds the melting point of the oxide layer, the heat transfer calculation in the molten oxide layer should be carried out. After obtaining the heat flux of the inner wall of the pressure vessel, it is used as an input parameter for two-dimensional conduction in the lower head, considering convection outside the vessel wall. Then the temperature of the inner wall surface of the pressure vessel is re-obtained. The convergence is judged and the calculation is repeated until the convergence limit is reached. Finally, the main parameters including the heat flux of the outer surface wall of the pressure vessel are obtained.

3 AP1000 THREE-LAYER MOLTEN POOL CONFIGURATION VERIFICATION

As an extension of AP600, AP1000 has a high degree of similarity to AP600 in all respects, with only the outer pressure vessel wall surface being closer to the cavity than AP600 in terms of IVR-ERVC effectiveness assessment. Both INEEL (Rempe et al., 1997) and ERI (Esmaili And Khatib-Rahbar, 2004) have carried out the studies on three-layer molten pool configuration. However, no calculation results are available for point estimation calculation. This section uses the input parameters in the ERI study to carry out a point estimation calculation for a three-layer molten pool configuration in AP1000 calculates the average heat flux at the bottom of the heavy metallic layer, also compares the calculation results of code MPCAP with those of Zhang et al. (2010).

3.1 AP1000 Three-Layer Molten Pool Configuration Verification Preparation

The study of ERI and the study of Zhang et al. have used different heat transfer correlations for molten pools in AP1000. The study of ERI does not consider heat transfer from the oxide layer to the heavy metallic layer, while the study of Zhang et al. considers heat transfer from the oxide layer to the heavy metallic layer.

In this verification calculation, the code MPCAP uses the same heat transfer correlations as the study of ERI to calculate

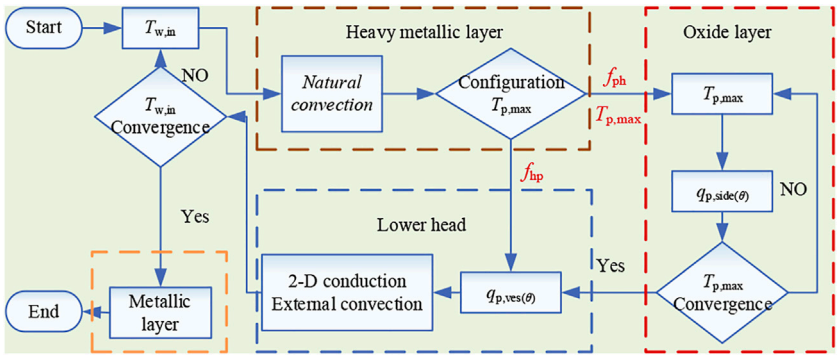

FIGURE 8 | Flow chart of the coupled analysis method in MPCAP code.

TABLE 1 | Main input parameters in AP1000 verification calculation.

Molten pool		External flow channel	
Mass of UO_2 (t)	62.3	Radius of the vessel (m)	4.0
Mass of stainless steel (t)	37.4	Thickness of the vessel (m)	0.15
Mass of zircaloy (t)	13.7	Width of the vessel (m)	0.15
Oxidation fraction of zircaloy (%)	0.28	Inlet temperature (K)	323.15
Decay heat power (MW)	27.1	Flow rate (kg/s)	200.0

the heat transfer from the oxide layer to the metallic layer and the heat transfer from the oxide layer to the heavy metallic layer. The other main input parameters are shown in **Table 1**.

3.2 AP1000 Three-Layer Molten Pool Configuration Verification Results

The results of the AP1000 three-layer molten pool configuration verification focused on heat flux in the outer surface wall of the pressure vessel wall, comparing the values calculated by code MPCAP with those calculated by the study of Zhang et al. The heat flux through pressure vessel wall is shown in **Figure 9**. When the heat transfer from the oxide layer to the heavy metallic layer is not considered, meaning that there is no heat transfer between the oxide layer and heavy metallic layer, the calculated values of code MPCAP in the inner wall surface is close to the results of the study of Zhang et al. When the heat transfer from oxide layer to heavy metallic layer is considered, the heat flux in the bottom region is higher. Due to a low CHF value in the bottom region, the heavy metallic layer shows an obvious focusing effect. In addition, the phenomenon of the focusing effect cannot be alleviated even by considering the effect of two-dimensional conduction.

The results of the AP1000 three-layer molten pool configuration verification show that code MPCAP is able to predict the heat flux distribution. The heat transfer from the oxide layer to the heavy metallic layer exacerbates the focusing effect in the heavy metallic layer but reduces the heat flux in the metallic layer. The CHF value in the bottom area of the heavy metallic layer is low, and therefore, there is a risk of failure. The heat transfer from the oxide layer to the heavy metallic layer needs to be considered in the effectiveness assessment of IVR-ERVC.

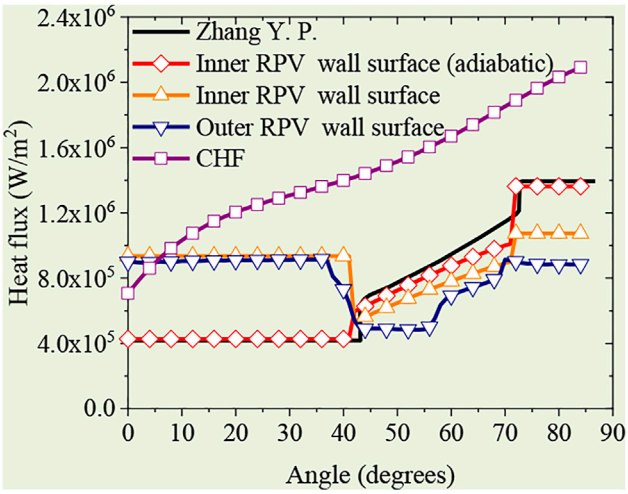

FIGURE 9 | Heat flux of inner RPV wall surface in AP1000 verification calculation.

4 CONCLUSION

Investigations on heat transfer in the thick lower heavy metallic layer are scarce, which have been conducted in this study for the IVR-ERVC adopted in research reactors. The main conclusions are presented as follows:

(1) The heat transfer in the molten pool has obvious influences on molten pool configuration. In this study, an improving lumped parameter method has been used to judge molten pool configuration. On this basis, a coupled analysis code MPCAP has been developed, which is based on the coupled simulation of natural convection inside a molten pool, two-dimensional conduction in the lower headwall, and convection outside the reactor vessel wall.

(2) The AP1000 three-layer molten pool configuration verification shows that code MPCAP is generally able to

give reasonable predictions for the heat transfer in the molten pool.

DATA AVAILABILITY STATEMENT

The original contributions presented in the study are included in the article/Supplementary Material; further inquiries can be directed to the corresponding author.

AUTHOR CONTRIBUTIONS

JD and other authors have made all contributions to this manuscript.

FUNDING

This work in this paper was supported by the National Key R&D Program of China (Grant number: 2018YFB1900100).

REFERENCES

Cao, Z., Liu, X., and Cheng, X. (2015). A Two Dimensional Approach for Temperature Distribution in Reactor Lower Head During Severe Accident. *Ann. Nucl. Energy* 85, 467–480. doi:10.1016/j.anucene.2015.04.042

Cummins, W. E., Corletti, M., and Schulz, T. (2003). Westinghouse AP1000 Advanced Passive Plant[C]. *Proc. ICAPP*, 4–7.

RRDB. *Database[EB/OL]*. 2020, Available at: https://nucleus.iaea.org/RRDB/Reports/CategoryList.

Esmaili, H., and Khatib-Rahbar, M. (2004). *Analysis of In-Vessel Retention and Ex-Vessel Fuel Coolant Interaction for AP1000[R]. US Nuclear Regulatory Commission*. Washington, DC: Office of Nuclear Regulatory Research.

Gilbert, C. (1979). *Nuclear Reactor Safety-A Review of the Rasmussen Report (WASH-1400)*: Sydney. Australian Nuclear Science and Technology Organisation.

Kymäläinen, O., Tuomisto, H., and Theofanous, T. (1997). In-Vessel Retention of Corium at the Loviisa Plant[J]. *Nucl. Eng. Des.* 169 (1-3), 109–130.

Li, Y. B., Tong, L. L., Cao, X. W., and Guo, D. Q. (2015). In-Vessel Retention Coolability Evaluation for Chinese Improved 1000 MWe PWR. *Ann. Nucl. Energy* 76, 343–349. doi:10.1016/j.anucene.2014.09.035

Liu, X., Luo, Y., Zhen, C., Guo, R., and Cheng, X. (2018). Safety Research of IVR-ERVC for Advanced Water Cooled Reactor. *Energy* 156 (AUG.1), 458–467. doi:10.1016/j.energy.2018.05.123

Luo, Y., Liu, X., and Cheng, X. (2018). In- and Ex-Vessel Coupled Analysis for In-Vessel Retention. *Prog. Nucl. Energy* 109 (NOV), 74–82. doi:10.1016/j.pnucene.2018.07.013

Luo, Y., Liu, X., and Cheng, X. (2019). IVR-ERVC Study of 1700 MW Class PWR Based on MAAP Simulation and Coupled Analysis. *Ann. Nucl. Energy* 126 (APR), 1–9. doi:10.1016/j.anucene.2018.11.003

Oh, S., and Kim, H. (2005). *Proceedings: Evaluation of Uncertainties in Relation to Severe Accidents and Level-2 Probabilistic Safety Analysis*, 7–9. Effectiveness of External Reactor Vessel Cooling (ERVC) Strategy for APR1400 and Issues of Phenomenological Uncertainties[C]//Workshop.

Rempe, J., Knudson, D., Allison, C., Thinnes, G. L., and Atwood, C. L. (1997). *Potential for AP600 In-Vessel Retention Through Ex-Vessel flooding*. Idaho: Lockheed Idaho Technologies Co., Idaho National Engineering.

Safety of Research Reactors (2016). *Safety of Research Reactors[M]*. Vienna, Austria: International Atomic Energy Agency.

Theofanous, T., Liu, C., Additon, S., Angelini, S., Kymäläinen, O., and Salmassi, T. (1997). In-Vessel Coolability and Retention of a Core Melt[J]. *Nucl. Eng. Des.* 169 (1-3), 1–48. doi:10.1016/s0029-5493(97)00009-5

Wang, J., Chang, H., Zheng, W., and Zhou, Z. (2010). *In-Vessel Retention of Molten Core Debris for CAP1400[C]//18th International Conference on Nuclear Engineering*. Two Park Avenue New York NY, USA: American Society of Mechanical Engineers Digital Collection, 569–575. doi:10.13182/NT08-A3924

Zhang, Y. P., Qiu, S. Z., Su, G. H., and Tian, W. X. (2010). Analysis of Safety Margin of In-Vessel Retention for AP1000. *Nucl. Eng. Des.* 240 (8), 2023–2033. doi:10.1016/j.nucengdes.2010.04.020

Conflict of Interest: The authors declare that the research was conducted in the absence of any commercial or financial relationships that could be construed as a potential conflict of interest.

Publisher's Note: All claims expressed in this article are solely those of the authors and do not necessarily represent those of their affiliated organizations, or those of the publisher, the editors, and the reviewers. Any product that may be evaluated in this article, or claim that may be made by its manufacturer, is not guaranteed or endorsed by the publisher.

NOMENCLATURE

k Thermal conductivity, W/(m·K)

Q Volume power density, W/m^3

r Radius, m

s Area, m^2Structure

ε Emissivity

σ Stefban–Boltzmann, W/(m^2·K^4)

Subscript

b Bottom

dn Downward

in Inside

max Maximum

o Outside

side Sideward

up Upward

w Wall

Nu Nusselt number

q Heat flux, W/m^2

T Temperature, K

δ Thickness, m

θ Angle, degree

V Volume, m^3

cr Crust

h Heavy metallic layer

m Light metallic layer

mp Melting point

p Oxide pool

t Top

ves Vessel

s Structure

frontiers | Frontiers in Energy Research

ORIGINAL RESEARCH
published: 17 June 2022
doi: 10.3389/fenrg.2022.907374

Shear Performance of Zirconium Alloy Welds Under Different Strain Rates

Haoyu Wang[1], Tianfei Zhao[2], Shuanghui Cao[2], Quan-yao Ren[1], Menglong Liu[1], Jibin Zhang[1], Yong Zheng[3], Yuanming Li[1] and Lianfeng Wei[3]**

[1]Science and Technology on Reactor System Design Technology Laboratory, Nuclear Power Institute of China, Chengdu, China, [2]School of Aeronautics, Northwestern Polytechnical University, Xi'an, China, [3]Science and Technology on Reactor Fuel and Materials Laboratory, Nuclear Power Institute of China, Chengdu, China

Welding is one of the important connection methods for zirconium alloy, and the shear failure under the dynamic load is a typical failure mode of the weld. Aiming at clarifying the shear failure of zirconium alloy welds, three kinds of double-notched shear weld specimens with welding sizes of 2, 4, and 6 mm were designed, respectively; the shear performance of specimens under quasi-static and dynamic loading was tested by tensile testing machine and split Hopkinson pressure bar (SHPB). The stress–strain curves and shear strength were determined for the weld under quasi-static and dynamic loading. It was demonstrated that 1) an obvious strain rate strengthening effect was observed for the shear strength performance of zirconium alloy weld; 2) the shear performance of zirconium alloy weld was not sensitive to its length, but the tolerance to micro defects in the weld was improved with the increase of the weld length, which gave rise to a small increment of shear strength; 3) the failure mode of zirconium alloy welds under quasi-static loading was the typical lamellar tearing failure, and the angle between the fracture and base metal was about 17°; however, the shear failure mode showed obvious brittle characteristics under dynamic loading and the angle between fracture and base metal was almost parallel to the loading direction.

Keywords: zirconium alloy, weld, shear, strain rate, dynamic load

OPEN ACCESS

Edited by:
Luteng Zhang,
Chongqing University, China

Reviewed by:
Kui Zhang,
Xi'an Jiaotong University, China
Jacek Janiszewski,
Military University of Technology in Warsaw, Poland
Yan Xiang,
Royal Institute of Technology, Sweden

***Correspondence:**
Yuanming Li
Lym_npic@126.com
Lianfeng Wei
252044665@qq.com

Specialty section:
This article was submitted to Nuclear Energy, a section of the journal Frontiers in Energy Research

Received: *30 March 2022*
Accepted: *09 May 2022*
Published: *17 June 2022*

Citation:
Wang H, Zhao T, Cao S, Ren Q-y, Liu M, Zhang J, Zheng Y, Li Y and Wei L (2022) Shear Performance of Zirconium Alloy Welds Under Different Strain Rates. Front. Energy Res. 10:907374. doi: 10.3389/fenrg.2022.907374

HIGHLIGHTS

1) The quasi-static and dynamic shear performances of zirconium alloy welds with different sizes were determined.
2) The shear performance of zirconium alloy welds showed an obvious strain rate strengthening effect.
3) The dynamic shear failure of zirconium alloy welds was because of the micro holes generated in the electron beam welding process.

1 INTRODUCTION

Zirconium alloy has been widely used as a structural material in the nuclear industry for its low thermal neutron absorption cross-section, excellent corrosion resistance, good irradiation stability, and mechanical properties (Adamson et al., 2019; Kalavathi and Kumar Bhuyan, 2019). As a credible connection method, welding has been applied in different zirconium alloy devices (Slobodyan M., 2021; Slobodyan M. S., 2021), such as nuclear fuel assemblies. Zirconium alloy cladding tube was

welded with the end plugs, which served as the first barrier to nuclear reactor safety, and the spacer grid consisted of zirconium alloy strips, which were welded together with welding spots and lines. The fuel element with a rectangular cross-section was formed by the long welding line in the reactor transient test facility (TREAT) of Argonne National Laboratory (Vandegrift et al., 2019; Parga et al., 2017). Moreover, due to the good corrosion resistance, zirconium alloy was also utilized as a structural material in the dissolver equipment in the post-treatment device of the fast breeder reactor, a heat exchanger (Bandi et al., 2018), and pressure vessel (Tomie et al., 1990) in the chemical process industry, where the connection was also made by welding.

As an important structure in the above-mentioned fuel assemblies and other pieces of equipment, zirconium alloy welds should have sufficient mechanical strength so as not to be damaged during operation. Song et al. (2012) used zirconium alloy plate welds as specimens and determined mechanical properties (such as yield strength and tensile strength) of the base metal zone, heat-affected zone, and weld zone based on the instrumented indentation method. Then, a numerical simulation was carried out on the spacer grid crush strength with different weld properties (Song and Lee, 2012), which demonstrated that the crush strength decreased by about 30% when the zirconium alloy base metal properties were replaced by the weld material properties. However, Parga et al. (2017) found that the zirconium alloy base metal and weld zone by electron beam welding presented equivalent mechanical properties, but the hardness of the heat-affected zone was slightly higher. Considering the large influence of porosity on the mechanical properties and corrosion performance of zirconium alloy welds, X-ray tomography was used to conduct the three-dimensional visualization and quantitative measurement of the porosity of Zr-4 plate welding joints by the electron beam under different welding parameters (Bandi et al., 2018). Tao et al. (2013) developed a pulsed laser spot welding technology for the junction connection of Zr-4 sheets with a thickness of 0.457 mm and studied the effect of shot numbers, pulse width, and peak power on the size, mechanical properties, and the microstructure of the weld zones. Sakamiti et al. (2019) compared the mechanical properties, microstructure, and corrosion of zirconium alloy welds between resistance welding and laser beam welding. Sakamiti et al. (2019) found that the tensile strength of resistance welding welds (8,700 ± 100 N) was much larger than that of pulse laser welding welds (3,500 ± 200 N) because the fit gaps between welds were compensated by the electrode load during resistance welding and reduced to zero nearly in resistance welding technology.

In the above-mentioned studies on the mechanical properties of zirconium alloy welds, the static tensile strength was mainly focused and so were the effects of welding methods on the mechanical properties of welds. However, studies on the shear strength of zirconium alloy welds were scarce, especially for that under dynamic loads at different strain rates. Shear failure is a typical and common mode of weld failure, which needs much attention in the related design of welds. For example, when the fuel assembly dropped in the transportation (Kim et al., 2019) or underwent an earthquake shock (Pellissetti et al., 2021), strong shear loads would be exposed to the zirconium structure. Thus, it is of great significance to study the shear performance of zirconium alloy welds under dynamic and static loadings. Recently, the double-notched shearing technique was developed and widely applied to study the shear failure of some metals (Xu et al., 2018; Zhou et al., 2019). For the designed double-notched specimen, the compression load can be transformed into the local shear load with good uniformity, and the shear deformation of the specimen surface can also be observed clearly. In the present study, the double-notched shear weld specimens were designed to study the shear performance of zirconium alloy welds, and the electronic tensile testing machine and the split Hopkinson pressure bar (SHPB) device were used to carry out the shear tests under quasi-static and dynamic loads. In addition, the effects of strain rate and weld length on the shear performance are discussed, which could provide fundamental information for the design and failure analysis of zirconium alloy welds.

2 SPECIMENS AND EXPERIMENTS

2.1 Double-Notched Shear Specimen and its Fixture

The double-shear specimens were made from three Zr–Sn–Nb alloy plates using the vacuum electron beam scanning welding method for both sides, whose chemical composition is shown in **Table. 1**. The weld specimen for the double-notched shear test is shown in **Figure 1B** while the welding plate after sampling is shown in **Figure 1A**. It should be noted that the welding zone is marked by the red dotted line and the heat affecting zone is marked by a green rectangular box. The design of weld specimens kept the shear failure appearing in the welding zone. Moreover, to ensure the geometrical accuracy of the specimen, the high-precision slow-feeding wire cutting machine was used to cut the specimens with a cutting accuracy of 0.1 mm.

As shown in **Figure 1C**, the double-notched shear specimen was composed of two supporting ends and one loading end. There were two welding zones for the shear test between the supporting end and the loading end. To study the influence of welding length on the shear performance, three kinds of specimens were made with welding lengths of 2, 4, and 6 mm. Moreover, the fillet with a radius of 1.5 mm was set at the corner of the shear area to prevent stress concentration in this area during the shearing tests.

As shown in **Figure 2A**, the fixture consisting of a restraint end and a connecting end was designed to apply load on the shear zone of weld specimens uniformly. The assembly relationship between the fixture and specimen is shown in **Figure 2B**. During the test, the restraint end and the connecting end were connected by bolts. The slots were designed in the restraint part to prevent toppling and transverse displacement of the specimen. Moreover, the observation window was considered in the restraint end for observing the real-time deformation process of the specimen by high-speed photography.

TABLE 1 | Chemical composition (wt%) of the Zr–Sn–Nb alloy plate.

Sn	Nb	Fe	Cr	O	Zr
0.8%–1.2%	0.25%–0.35%	0.3%–0.4%	0.05%–0.10%	0.09–0.12%	rest

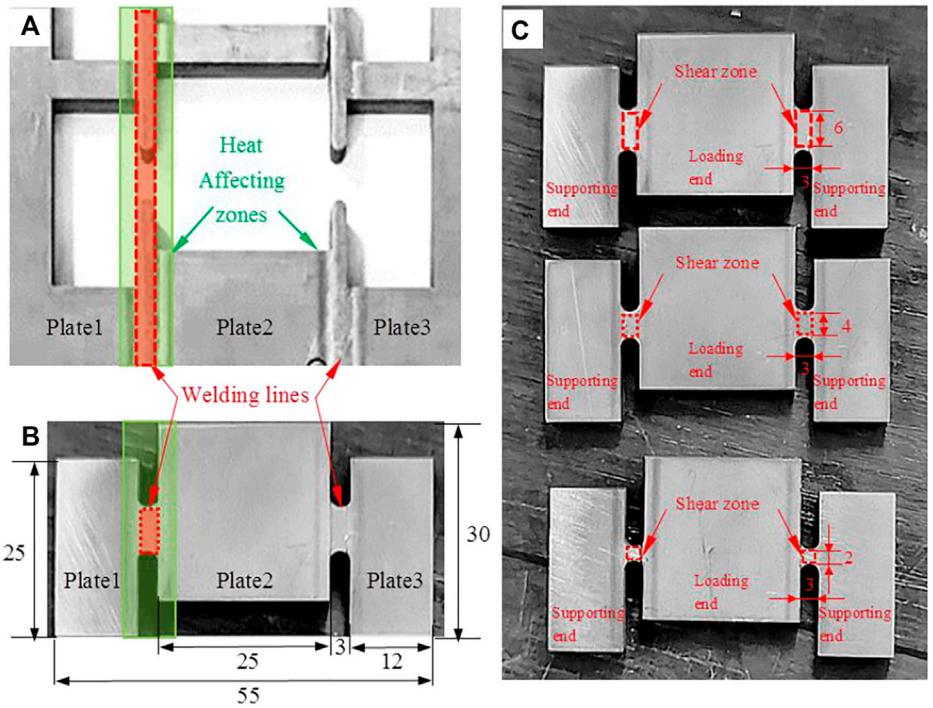

FIGURE 1 | Specimens design: **(A)** welding plate after sampling, **(B)** welding specimen with a welding length of 6 mm, and **(C)** three kinds of weld specimens with different lengths.

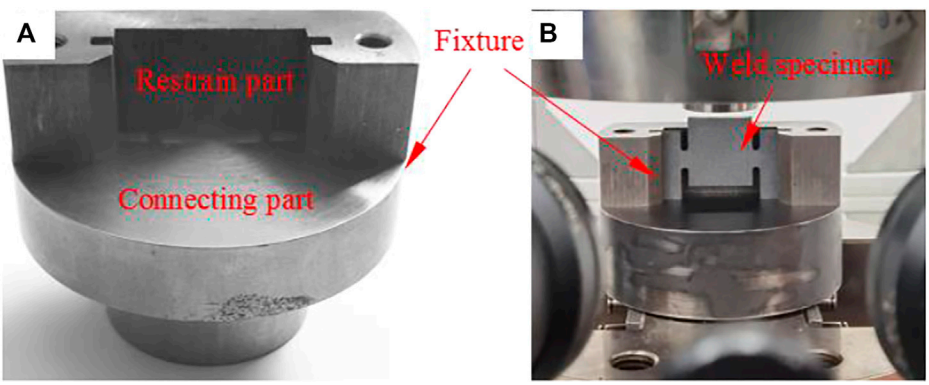

FIGURE 2 | Fixture design: **(A)** fixture and **(B)** clamping relationship between the weld specimen and fixture.

2.2 Quasi-Static Shear Test

As shown in **Figure 3A**, the quasi-static shear test was carried out by the MTS 10-ton tensile and torsional fatigue testing machine. Moreover, Aramis optical non-contact full-field strain measurement system provided by the German GOM Company was used to measure the shear strain of the specimen in real time. The system captured the randomly distributed spots on the specimen surfaces by two cameras and converted them into digital data by CCD (charge-coupled device), and processed the digital data into the required strain data with its built-in software

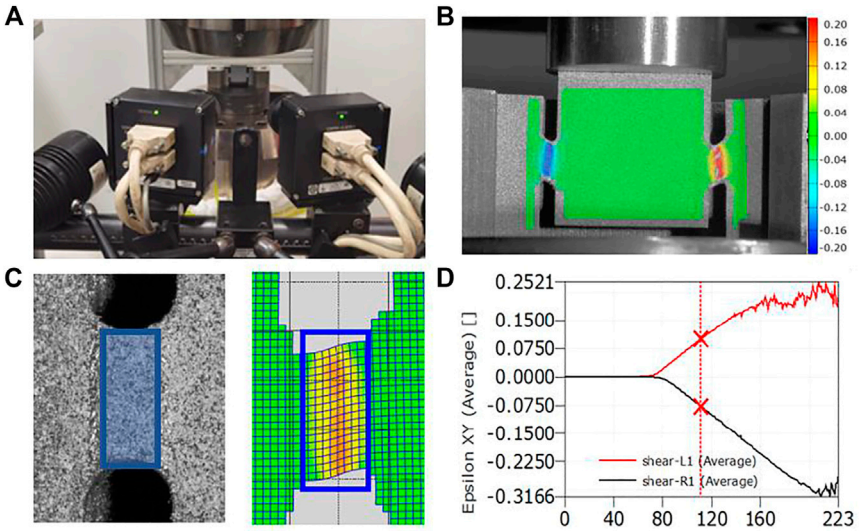

FIGURE 3 | Quasi-static shear test: **(A)** Aramis optical full-field strain measurement system, **(B)** shear strain field on the specimen surface, **(C)** average shear strain selection zone, and **(D)** average shear strain curves at left and right weld shear zones.

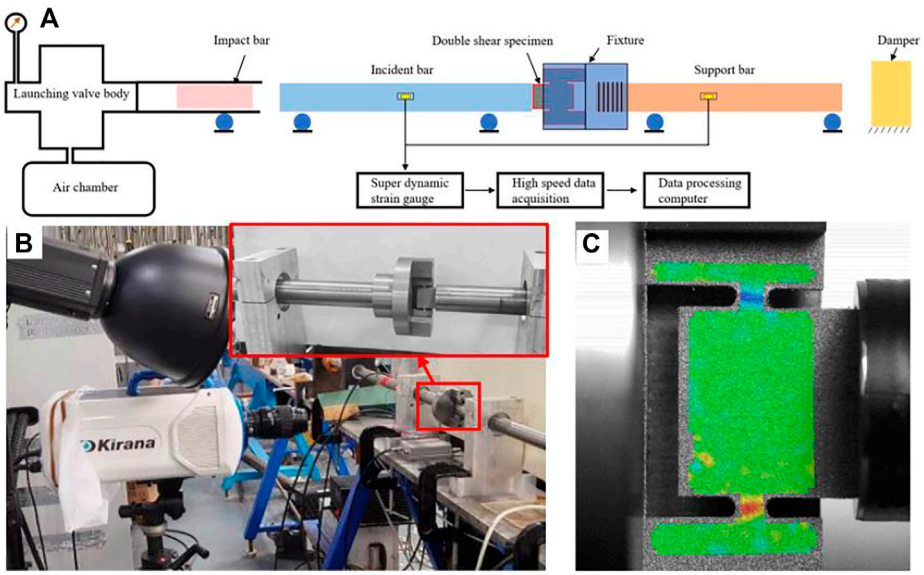

FIGURE 4 | SHPB test device: **(A)** SHPB schematic diagram, **(B)** ultra-high-speed camera recording system, and **(C)** shear strain field on the specimen surface.

with an accuracy of 0.001. A typical full-field shear strain field is shown in **Figure 3B**, which shows that the shear deformation of the specimen was mainly concentrated in the weld zone, and almost no deformation occurred in the other zones.

It should be noted that the shear strain was not uniform in the welding zone as shown in **Figure 3C**. Therefore, the selected zone to calculate the averaged shear strain had a large influence on the averaged strain value, which must remove the heat-affecting zone. In addition, the shear strain would be too large if the selected zone were too narrow. After several shear tests, it was observed that the obvious strain features appeared in the zone with a width of 2 mm for all specimens with three different welding lengths. Thus, the zone with a width of 2 mm, as shown in **Figure 3C**, was selected to calculate the average shear strain value. Moreover, the absolute values of the average shear strain in the left and right shear zones gradually increased with the shear load, as shown in **Figure 3D**. The average shear strain in the right shear zone was negative because the coordinate origin was established on the centerline of the specimen.

The averaged shear stress was calculated as

$$\tau_s = \frac{F}{2h_s l_s}, \tag{1}$$

TABLE 2 | Dynamic shear test conditions.

Welding length (mm)	Strain rate (s^{-1})	Broken/Unbroken
2	1,000	Unbroken
	1,500	Unbroken
	1700	Unbroken
	2000	Broken
	3,000	Broken
	4,000	Broken
4	2,200	Unbroken
	2,400	Unbroken
	2,700	Unbroken
	3,000	Broken
	4,000	Broken
6	2,800	Unbroken
	3,200	Unbroken
	3,800	Unbroken
	4,000	Broken

where h_s is the thickness of the specimen (5 mm); l_s is the length of the shear zone (2, 4, and 6 mm for different specimens); F is the loading force measured by the sensors of the testing machine (in N).

2.3 Dynamic Shear Test

As shown in **Figure 4**, the split Hopkinson pressure bar (SHPB) experimental technique was used to measure the dynamic shear properties of welds of different sizes under a high strain rate. SHPB devices mainly consisted of an impact bar, incident bar, and support bar, and these bars were made of titanium alloy rods with a diameter of ϕ 32 mm and lengths of 120, 1,500, and 1,200 mm, respectively. As shown in **Figure 4A**, the double-notched shear specimen was placed in the restraint part of the fixture while the fixture was connected with the support bar by threads, and the loading end of the specimen was in contact with the incident bar in the center.

In the dynamic shear test, the incident bar was hit by the impact bar by the release of air pressure in the chamber, which produced the compression strain pulse signal that acted on the loading end of the specimen. When the incident strain pulse reached the contact interface between the incident bar and the specimen, it was reflected and transmitted due to the differences between the wave impedance of the incident bar and specimen. All the three strain pulse signals were measured by the strain gauge attached to the rod. Moreover, the deformation process and real-time strain field were recorded with a Kirana high-speed camera, and Aramis optical measurement system was applied to calculate the strain as shown in **Figures 4B,C**. The speckle dots on the surface of the specimen were obtained by the fine spray paint.

It was difficult to achieve a constant strain rate during the sample deformation for the high strain hardening behavior. Aiming at showing the strain rate level, the average strain rate during the loading process was calculated, and the test conditions are listed in **Table. 2**. It should be noted that the definition of broken specimens and unbroken specimens will be explained in detail in **Section 3.2**.

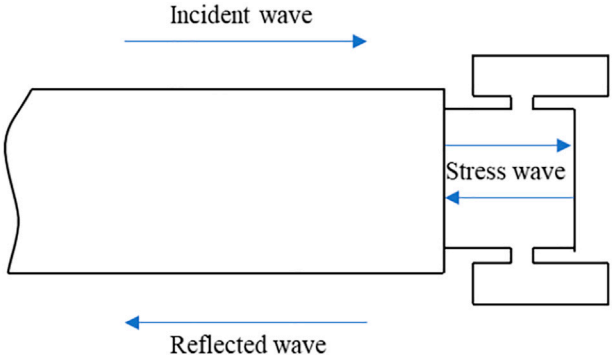

FIGURE 5 | Loading end of SHPB.

Based on the one-dimensional stress wave theory, the dynamic shear stress can be calculated by the three stress wave signals on the incident and support bars ($\varepsilon_T/\varepsilon_I/\varepsilon_R$), which are expressed as follows:

$$\begin{aligned}\dot{\gamma}_s &= -\frac{C_0}{w_s}(\varepsilon_T - \varepsilon_I + \varepsilon_R)\\ \gamma_s &= -\frac{C_0}{w_s}\int_0^t (\varepsilon_T - \varepsilon_I + \varepsilon_R)dt.\\ \tau_s &= \frac{EA_{bar}}{4h_s l_s}(\varepsilon_T + \varepsilon_I + \varepsilon_R)\end{aligned} \tag{2}$$

Based on the study of Zhou et al. (2019), since the transmitted wave was reflected and transmitted many times at the contact interfaces between the specimen and the fixture as well as between the fixture and the support rod, the transmitted strain wave signal that recorded on the support rod was seriously dispersed and was not suitable for the calculation of the dynamic shear stress. But if the incident bar and the loading end of the specimen were treated as a mini-system (as shown in **Figure 5**), the equilibrium state could be achieved in the loading end of the specimen. With the analogy to the quasi-static loading system, the stress and strain of the specimen can be obtained using the incident bar. A similar system and data processing method were adopted by Zhou et al. (2019) and Xu et al. (2018).

Due to the mini-system equilibrium relation of SHPB, the transmitted wave strain is the sum of incident wave strain and reflected wave strain as shown in **Eq. 3**. Thus, the dynamic shear stress can be calculated as in **Eq. 4**.

$$\varepsilon_I + \varepsilon_R = \varepsilon_T, \tag{3}$$

$$\begin{aligned}\dot{\gamma}_s &= -\frac{2C_0}{w_s}\varepsilon_R\\ \gamma_s &= -\frac{2C_0}{w_s}\int_0^t \varepsilon_R dt.\\ \tau_s &= \frac{EA_{bar}}{2h_s l_s}(\varepsilon_I + \varepsilon_R)\end{aligned} \tag{4}$$

In **Equations 2–4**, $\dot{\gamma}_s$ is the average shear strain rate in the shear zone, mm/(mm s); γ_s is the average shear strain in the shear

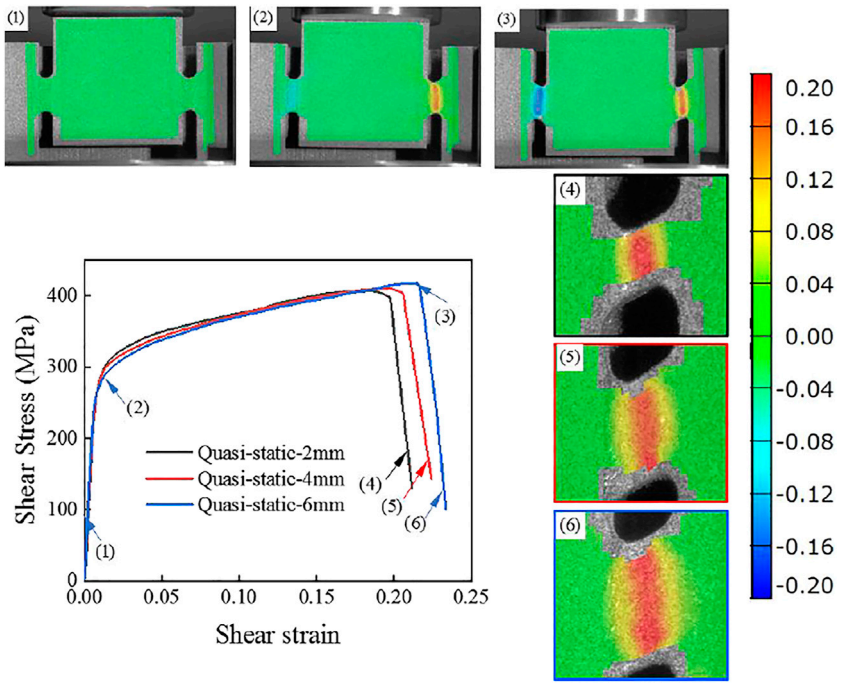

FIGURE 6 | Quasi-static shear stress–strain curves and the corresponding shear strain field.

TABLE. 3 | Shear test data of zirconium alloy welds with different welding lengths.

Welding length (mm)	Shear yield strength (MPa)	Maximum shear strength (MPa)	Maximum shear strain
2	311	407	0.21
4	317	416	0.22
6	325	424	0.23

zone, mm/mm; τ_s is the average shear stress in the shear zone, MPa; ε_R, ε_T, and ε_I are the strains of the reflected wave, transmitted wave, and incident wave, mm/mm; h_s is the thickness of the specimen (=5 mm); w_s is the width of the selected welding zone (=3 mm); l_s is the length of the selected welding zone, mm; C_0 is the elastic wave velocity in the incident bar(= 4.97×10^6 mm/s); E is the elastic modulus of the incident bar (=1.10×10^5 MPa); and A_{bar} is the cross-sectional area (=804 mm^2).

3 EXPERIMENTAL RESULTS AND DISCUSSIONS

3.1 Quasi-Static Shear Performance

The shear stress–strain curves of different specimens in the quasi-static shear test are shown in **Figure 6** while the values of the shear yield strength and maximum shear strength are listed in **Table. 3**. The shear stress–strain curves almost coincided in the elastic zone. The shear yield strengths of the specimens with lengths of 2, 4, and 6 mm were about 310, 317, and 325 MPa, respectively, while the maximum shear strengths were about 407, 416, and 424 MPa, respectively. Therefore, the shear strength increased slightly with the increase in the welding length, and the deviations of the shear yield strength and maximum shear strength for the specimens with three welding lengths were less than 5%.

The shear strain fields for the specimen with a welding length of 6 mm at the initial loading condition, yield condition, and maximum shear strength condition are shown in **Figures 6(1), (2), and (3)**, respectively. At the initial loading condition, the uniform deformation appeared on welding zones on both sides; the shear strain increased rapidly when the welding zone reached the plastic deformation zone; at last, with the load increasing, larger deformation occurred and then the shear failure occurred.

When the welds were almost broken, the shear strain fields of the weld with lengths of 2, 4, and 6 mm are shown in **Figures 6(4), (5), and (6)**, respectively. As can be seen, with the length of the weld increasing, the surrounding region bearing the shear deformation also gradually increased, which gave rise to the larger maximum shear strength. It was considered that the

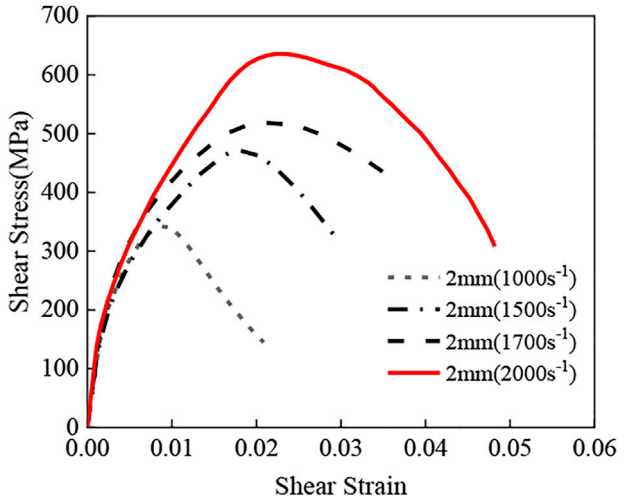

FIGURE 7 | Dynamic shear stress–strain curves of specimens with 2 mm welding length.

weld with a larger length improved the resistance to the local micro deflects. To sum up, the shear yield strength and maximum shear strength increased with the welding length increasing for the larger average shear strain in the welding zone.

3.2 Dynamic Shear Performance

For clarifying the influences of shear strain rate and welding length on the shear strength, SHPB tests on the specimens of the same size were conducted under different strain rates. The dynamic shear stress–strain curves of the specimen with a welding length of 2 mm under different strain rates are shown in **Figure 7**, while their final deformation shapes are shown in **Figure 8**. As can be seen, the strain rate had a great influence on the shear stress–strain curves and the final deformation shape.

As shown in **Figure 8**, the weld specimens did not break under the strain rates of 1,000, 1,500, and 1,700 s^{-1}, and these specimens are called "unbroken" ones. Thus, the shear stress peak values under these three strain rates in **Figure 7** were at the initial unloading conditions, which were not the maximum shear strength values of welds. Moreover, although no fracture occurred, the shear stress increased with the strain rate due to a larger impact load.

As shown in **Figure 8D**, the shear failure appeared on the weld specimens with a length of 2 mm when the strain rate reached 2,000 s^{-1}, and this kind of specimen is called a "broken" specimen. Thus, the shear stress peak value with a strain rate of 2,000 s^{-1} was recognized as the maximum shear strength of the weld specimens. Moreover, it can be observed that the lower welding zone (in the black line) had larger shear deformation than the upper welding zone (in the red line). In this test, it was deduced that: the shear fracture first appeared in the upper welding zone due to nonuniformly distributed micro defects;

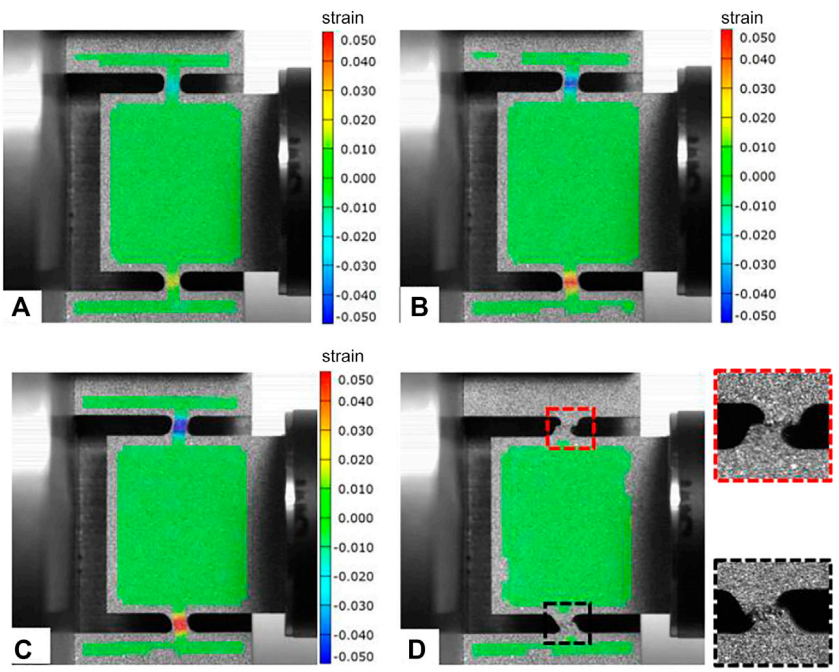

FIGURE 8 | Failure morphology of specimens with 2 mm welding length: **(A)** 1000 s^{-1}, **(B)** 1500 s^{-1}, **(C)** 1700 s^{-1} and **(D)** 2000 s^{-1}.

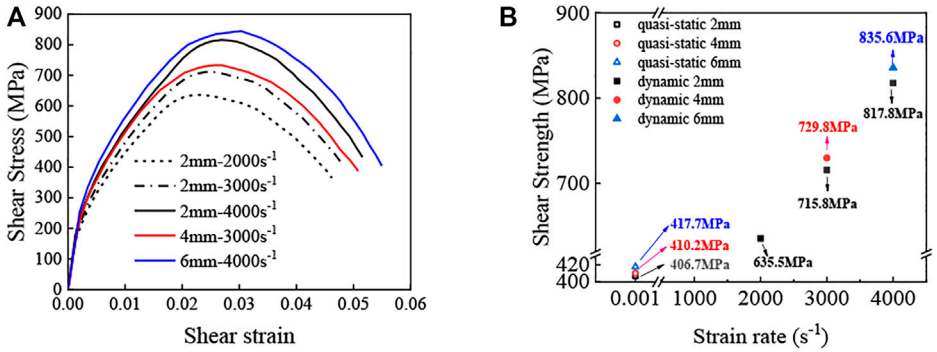

FIGURE 9 | Shear performance comparison with different welding lengths under different strain rates: **(A)** dynamic shear stress–strain curves and **(B)** shear strengths.

then, the lower welding zone bear the load by itself and an obvious shear deformation occurred.

With the emitting pressure on the impact bar increasing gradually, the shear stress–strain curves of zirconium alloy weld specimens with lengths of 4 and 6 mm had similar rules, and the failed strain rates were 3,000 and 4,000 s^{-1}, respectively. To study the influence of welding lengths, the tests on the weld specimens with lengths of 4 and 6 mm were also conducted under strain rates of 3,000 and 4,000 s^{-1}.

As shown in **Figure 9**, with the strain rate increasing from 2,000 to 4,000 s^{-1} under the quasi-static conditions, the maximum shear strength of the weld specimen with a length of 2 mm increased obviously. The maximum shear strength values were 407, 636, 716, and 818 MPa at strain rates of 2,000, 3,000, and 4,000 s^{-1} under quasi-static conditions, respectively. Compared with the maximum shear strength values under the quasi-static test, the maximum shear strength values at strain rates of 2,000, 3,000, and 4,000 s^{-1} increased by about 56, 76, and 101%, respectively. Therefore, the zirconium alloy weld had a typical strain rate strengthening effect.

As shown in **Figure 9B**, under the quasi-static conditions, the maximum shear strengths of 4 and 6 mm weld specimens were 0.9 and 2.7% larger than that of the 2 mm weld specimen. When the strain rate was 3,000 and 4,000 s^{-1}, the maximum shear strengths of 4 and 6 mm weld specimens were 2.0 and 2.2% larger than that of 2 mm weld specimens, respectively. These phenomena demonstrated that the larger welding length gave rise to a larger shear strength but with a small increment.

3.3 Fracture Analysis

Aiming at studying the fracture mechanisms of zirconium alloy weld shear failure under different strain rates, focused ion/electron double beam microscopy was used to observe the microstructures of fractures.

The macro morphology of the weld fracture under quasi-static shear test conditions is shown in **Figures 10A–C**, which shows typical shear failure features. The obvious shear deformation appeared at the weld, while the angle between the loading direction and the fracture on the side broken earlier was about 17°.

As shown in the fracture SEM pictures of the 2 mm weld specimen, many tearing ridges were observed, whose direction was almost parallel to the direction of shear loading. By enlarging the zone in the black line of the SEM picture, some tearing steps appeared on both sides of the tearing ridges, and most micro cracks were located near the tearing steps. Moreover, some micro holes that did not form the micro cracks were also found. Based on the above-mentioned phenomena, the lamellar tearing was inferred to be the main mechanism of micro cracks formation. By enlarging the zone in the blue line of the SEM picture, a few dimples were found, which indicated that the ductile fracture appeared in some local zone. It should be noted that the dimple shape did not show the ductile fracture morphology of the metal, but presented layered distribution and was stretched along the loading direction. Thus, it can be concluded that the slight ductile deformation occurred in this zone first and then the micro holes appeared; further this zone was torn in the loading process.

By comparison among the SEM pictures of the fracture of 2, 4, and 6 mm weld specimens, it was found that, with the increase in the welding length, the number of tearing ridges decreased obviously and the fracture tended to be smoother. Micro cracks derived from tearing steps could be still seen but dimples were not observed for the fracture SEM picture of 4 and 6 mm welds, which might result because the larger welding length led to a more uniform load on the shear face and weakened the stress concentration and the plastic flow in the local zone. Moreover, the number of cracks also decreased with the increase in the welding length, which was attributed to the full propagation of micro cracks into the fracture.

Therefore, the transition from the brittle fracture accompanied by a few local ductile fractures in the 2 mm weld specimen to the brittle fracture in the 6 mm weld specimen was the main reason for the increment of shear strength.

The SEM pictures of the fracture under a dynamic load are shown in **Figure 11**. The dynamic shear fracture was almost parallel to the loading direction, which is distinct from that of the quasi-static shear fracture, as shown in **Figure 10**, and indicated

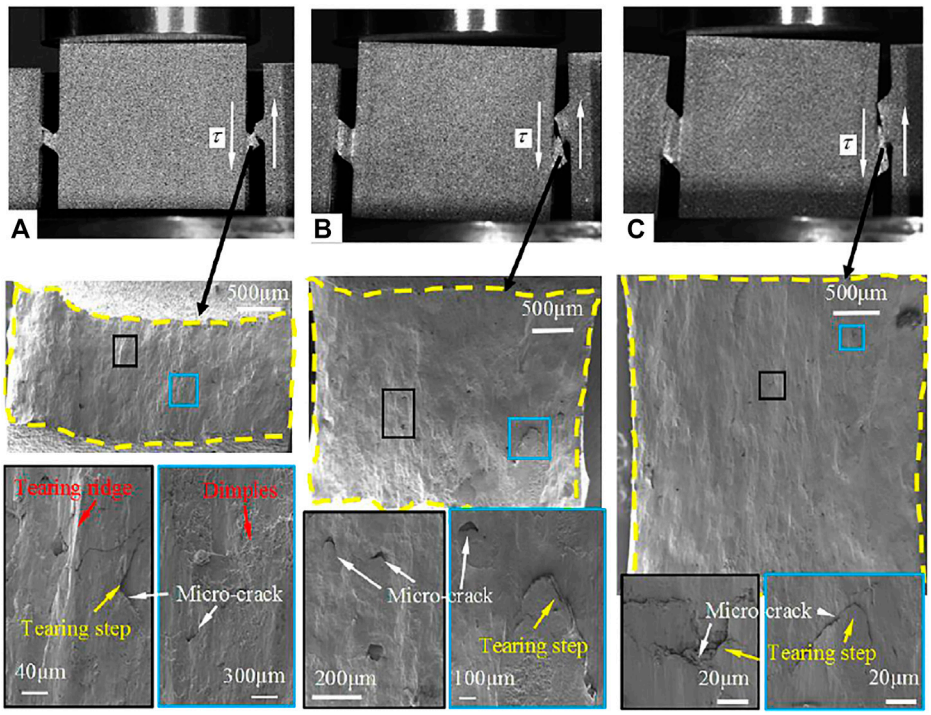

FIGURE 10 | SEM images of the fracture surface of weld specimens with different welding lengths under quasi-static tests with a shear strain rate of about 0.001 s^{-1}: **(A)** 2 mm weld specimen, **(B)** 4 mm weld specimen, and **(C)** 6 mm weld specimen.

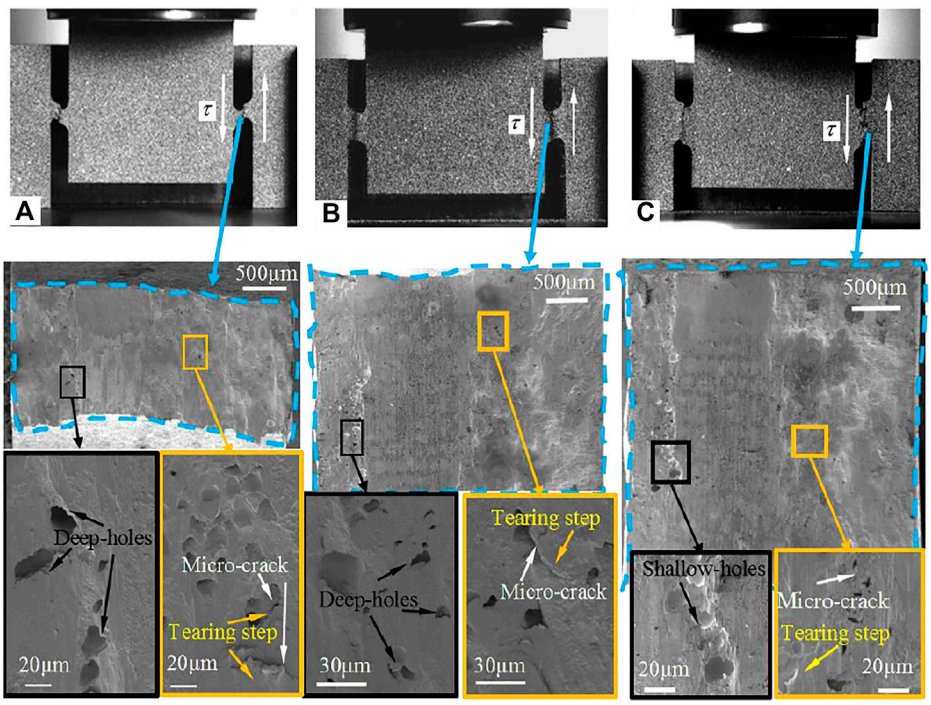

FIGURE 11 | SEM images of the fracture surface of weld specimens with different welding lengths under dynamic test conditions: **(A)** 2 mm weld specimen (2000 s^{-1}), **(B)** 4 mm weld specimen (3000 s^{-1}), and **(C)** 6 mm weld specimen (4000 s^{-1}).

the typical brittle fracture characteristics. Moreover, the dynamic shear fracture surface was smoother compared with the quasi-static shear fracture surface, and the lamellar tearing zone was located on the right side of the fracture. However, the lamellar tearing zone was very small and the obvious tearing steps were nearly not observed, and the number of micro cracks was also small. Instead, the nearly circular deep holes were found in the zone in black lines of SEM pictures.

When the attention was paid to these deep micro holes, some interesting phenomena were found: all the deep micro holes in the SEM pictures of three different weld specimens were located in the zone which was several millimeters from the welding surface. It was speculated that in the electron beam welding process, the temperature gradient appeared due to the large melting temperature of zirconium alloy; when the electron beam bombarded the welding zone, the melt zirconium alloy froze at a larger rate at the surface than that at the bottom of the molten pool, and the metal steam might be hard to be released; thus, the linear porosity and nail tip defects might arise (Liang et al., 2019) and continuous micro gas holes might appear (Liu and He, 2016) at the bottom of the molten pool. The double-side electron beam welding method was adopted in the weld specimens in this study; therefore, the micro holes appeared near both sides of the weld specimens.

Because micro holes were located near the weld surface, micro cracks appear in the zone near the welding surface first and propagated to the macro cracks; then, the macro cracks propagated to the other side rapidly and the smooth fracture formed in the middle zone. As shown in **Figure 11**, because a few lamellar tearing steps appeared on the right sides of the fractures (the zone in the yellow lines), the cracks of all weld specimens propagated from the left side to the right side. Moreover, it should be noted that no dimples were observed in the SEM pictures and they showed typical shear brittle fracture features. Thus, the dynamic shear failure of the zirconium alloy welding specimen was deduced to result from the micro hole defects generated in the electron beam welding process; in dynamic loading, the micro holes and micro cracks propagated rapidly and formed fractures due to the stress concentration near the micro holes defects.

4 CONCLUSION

Aiming at studying the influences of strain rate and welding length on the zirconium alloy welding strength, double-notched shear specimens with welding lengths of 2, 4, and 6 mm were made by electron beam welding and a slow-feeding wire cutting machine. Based on the specimens, the quasi-static and dynamic shear tests were conducted. The following conclusions can be reached:

1) The shear performance of zirconium alloy welds showed an obvious strain rate strengthening effect: the maximum shear strengths of 2 mm weld at strain rates of 2,000, 3,000, and 4,000 s^{-1} were about 56, 76, and 101% larger than those under quasi-static conditions.
2) For present specimens, with the increase in the welding length, all the maximum shear strength of the zirconium alloy weld under quasi-static and dynamic shear tests increased with a small amplitude, which might result from the larger tolerance for the micro defects and need more experimental data to verify.
3) The failure mode of zirconium alloy welds under quasi-static loading was the typical lamellar tearing failure, and the angle between the fracture and base metal was about 17°. The shear failure mode showed obvious brittle characteristics under dynamic loading, and the fracture was almost parallel to the loading direction. The dynamic shear failure of zirconium alloy weld was due to the micro gas holes generated in the electron beam welding process.

DATA AVAILABILITY STATEMENT

The original contributions presented in the study are included in the article/supplementary material; further inquiries can be directed to the corresponding authors.

AUTHOR CONTRIBUTIONS

HW: conception and design of the study, analysis of data, drafted the manuscript; TZ: experimental design, experimental execution; SC: experimental execution, data processing; Q-YR: analysis of data, drafting the manuscript; ML: investigation; JZ, LW: made samples; YZ, YL: analysis of data.

FUNDING

The authors are grateful for the support from the National Key R&D Program of China (Grant No. 2018YFE0116100) and the Natural Science Foundation of China (Grant Nos: 12105273).

REFERENCES

Adamson, R. B., Coleman, C. E., and Griffiths, M. (2019). Irradiation Creep and Growth of Zirconium Alloys: A Critical Review. *J. Nucl. Mater.* 521, 167–244. doi:10.1016/j.jnucmat.2019.04.021

Bandi, B., Dinda, S. K., Kar, J., Roy, G. G., and Srirangam, P. (2018). Effect of Weld Parameters on Porosity Formation in Electron Beam Welded Zircaloy-4 Joints: X-Ray Tomography Study. *Vacuum* 158, 172–179. doi:10.1016/j.vacuum.2018.09.060

Kalavathi, V., and Kumar Bhuyan, R. (2019). A Detailed Study on Zirconium and its Applications in Manufacturing Process with Combinations of Other Metals, Oxides and Alloys - A Review. *Mater. Today Proc.* 19, 781–786. doi:10.1016/j.matpr.2019.08.130

Kim, H.-J., Yim, J.-S., Tahk, Y.-W., Oh, J.-Y., and Kong, E.-H. (2019). Drop Behaviors of a Plate-type Fuel Assembly Used in Research Reactor for a Drop Accident. *Prog. Nucl. Energy* 113, 255–262. doi:10.1016/j.pnucene.2019.01.020

Liang, L., Hu, R., Wang, J., Luo, M., Huang, A., Wu, B., et al. (2019). A CFD-FEM Model of Residual Stress for Electron Beam Welding Including the Weld

Imperfection Effect. *Metall Mat Trans A* 50 (5), 2246–2258. doi:10.1007/s11661-019-05154-8

Liu, C., and He, J. (2016). Numerical Analysis of Fluid Transport Phenomena and Spiking Defect Formation during Vacuum Electron Beam Welding of 2219 Aluminium Alloy Plate. *Vacuum* 132, 70–81. doi:10.1016/j.vacuum.2016.07.033

Parga, C. J., van Rooyen, I. J., Coryell, B. D., Lloyd, W. R., Valenti, L. N., and Usman, H. (2017). Room Temperature Mechanical Properties of Electron Beam Welded Zircaloy-4 Sheet. *J. Mater. Process. Technol.* 241, 73–85. doi:10.1016/j.jmatprotec.2016.11.001

Pellissetti, M., Kessler, H., Schmidl, J., Nykyforchyn, A., and Akcay, S. S. .(2021). Seismic Performance of Fuel Assemblies and Impact Force Correlations with Intensity-Compatible Sets of Recorded Ground Motion Time Histories. *Nucl. Eng. Des.* 375 (2021), 111052. doi:10.1016/j.nucengdes.2021.111052

Sakamiti, G. P., Siqueira, R. H. M. d., Carvalho, S. M. d., Meireles, J. B., and Lima, M. S. F. d. (2019). Weldability of a Zirconium Alloy Comparing Resistance and Pulsed Laser Methods. *Nucl. Mater. Energy* 20, 100693. doi:10.1016/j.nme.2019.100693

Slobodyan, M. (2021). Resistance, Electron- and Laser-Beam Welding of Zirconium Alloys for Nuclear Applications: A Review. *Nucl. Eng. Technol.* 53 (4), 1049–1078. doi:10.1016/j.net.2020.10.005

Slobodyan, M. S. (2021). Arc Welding of Zirconium and its Alloys: A Review. *Prog. Nucl. Energy* 133, 103630. doi:10.1016/j.pnucene.2021.103630

Song, K.-n., Hong, S.-d., Lee, S.-h., and Park, H.-y. (2012). Effect of Mechanical Properties in the Weld Zone on the Structural Analysis Results of a Plate-type Heat Exchanger Prototype and Pressurized Water Reactor Spacer Grid. *J. Nucl. Sci. Technol.* 49 (9), 947–960. doi:10.1080/00223131.2012.713571

Song, K.-n., and Lee, S.-h. (2012). Effect of Weld Properties on the Crush Strength of the PWR Spacer Grid. *Sci. Technol. Nucl. Installations* 2012, 1–12. doi:10.1155/2012/540285

Tao, W., Cai, C., Li, L., Chena, Y., and Wanga, Y. L. (2013). Pulsed Laser Spot Welding of Intersection Points for Zircaloy-4 Spacer Grid Assembly. *Mater. Des.* 52, 487–494. doi:10.1016/j.matdes.2013.05.037

Tomie, M., Abe, N., and Hano, M. (1990). Electron Beam Welding of Zirconium Plate. *Trans. JWRI* 19 (1), 149–150.

Vandegrift, J., Parga, C. J., Coryell, B., Butt, D. P., and Jaques, B. J. (2019). Oxidation Behavior of Welded Zry-3, Zry-4, and Zr-1Nb Tubes. *Nucl. Mater. Energy* 21, 100714. doi:10.1016/j.nme.2019.100714

Xu, Z., Liu, Y., Sun, Z., Hu, H., and Huang, F. (2018). On Shear Failure Behaviors of an Armor Steel over a Large Range of Strain Rates. *Int. J. Impact Eng.* 118, 24–38. doi:10.1016/j.ijimpeng.2018.04.003

Zhou, D., Zhao, X., Li, B., Hou, N., Ma, Z., Sun, T., et al. (2019). Shear-band-to-crack Transition in Bulk Metallic Glasses under Quasi-Static and Dynamic Shearing. *J. Non-Crystalline Solids* 521, 119484. doi:10.1016/j.jnoncrysol.2019.119484

Conflict of Interest: The authors declare that the research was conducted in the absence of any commercial or financial relationships that could be construed as a potential conflict of interest.

Publisher's Note: All claims expressed in this article are solely those of the authors and do not necessarily represent those of their affiliated organizations, or those of the publisher, the editors, and the reviewers. Any product that may be evaluated in this article, or claim that may be made by its manufacturer, is not guaranteed or endorsed by the publisher.

frontiers | Frontiers in Energy Research

ORIGINAL RESEARCH
published: 12 July 2022
doi: 10.3389/fenrg.2022.927497

Influence of Jet on Aerosol Retention by Pool Scrubbing Under Multihole Injector

*Yuxiang Li, Yan Wu and Xuewu Cao**

School of Mechanical Engineering, Shanghai Jiao Tong University, Shanghai, China

In severe nuclear power plant accidents, when the containment is in a serious challenging state, the gas mixture in the containment can be injected into the spent fuel pool through the multihole injector by the containment depressurization measure, to reduce the risk of containment overpressure failure and the release of radioactivity to the environment. The pool scrubbing efficiency of aerosol under the jet regime is studied on the small-scale aerosol pool scrubbing facility, focusing on the influence of mass flux, steam fraction, submergence, particle diameter, and pool initial temperature on the aerosol decontamination factor (DF). The results show that under the jet regime, the DF value is significantly greater than that in the bubble regime and the effect of jet flow on the mechanism of steam condensation and aerosol removal of the rising zone is weak under the conditions explored. DF increases with the increase of mass flux owing to the droplet interception and inertial collision aerosol removal mechanisms. Because the high pool temperature weakens the aerosol removal by steam condensation, DF decreases with the increase of initial pool temperature under the conditions explored. Based on the experimental data and the analysis of the removal mechanism under the jet regime, an empirical model of aerosol DF considering mass flux, steam fraction, pool temperature, submergence, and particle size is established and verified by the international experiments. The proposed model can be used to calculate DF in the process of containment overpressure discharge.

Keywords: aerosol retention, decontamination factor, jet regime, bubble regime, empirical model

OPEN ACCESS

Edited by:
Luteng Zhang,
Chongqing University, China

Reviewed by:
Thomas Gelain,
Institut de Radioprotection et de Sûreté Nucléaire, France
Tomohisa Yuasa,
Central Research Institute of Electric Power Industry (CRIEPI), Japan

****Correspondence:***
Xuewu Cao
caoxuewu@sjtu.edu.cn

Specialty section:
This article was submitted to Nuclear Energy, a section of the journal Frontiers in Energy Research

Received: *24 April 2022*
Accepted: *02 June 2022*
Published: *12 July 2022*

Citation:
Li Y, Wu Y and Cao X (2022) Influence of Jet on Aerosol Retention by Pool Scrubbing Under Multihole Injector. Front. Energy Res. 10:927497. doi: 10.3389/fenrg.2022.927497

INTRODUCTION

For the Chinese Advanced Passive Pressurized Water Reactor, containment overpressure venting is activated when the containment pressure continues to rise owing to the failure of the PCCS and other pressure relief measures in severe accidents. The gas mixture containing aerosols from containment is planned to be discharged into the spent fuel pool (SPF) through the multihole injector to reduce the risk of radioactive release to the environment (Gao et al., 2017; Gao et al., 2022). In the process of containment overpressure venting, the steam volume fraction gas exceeds 90%, the discharge mass flow rate can reach 7 kg/s, and the injector has 300 holes with a diameter of 1 cm (Gao et al., 2017). In this case, the aerosol-laden gas mixture is injected into the pool in the form of a jet regime at high speed and hits the water body to produce broken droplets, which are entrained in the gas and collide with the aerosol particles so that the aerosol is retained in the pool.

Lebel et al. (2022) conducted a review of different pool scrubbing experiments in 2022. A summary of the experimental study of pool scrubbing under the jet regime is given in **Table 1**. The LACE-Espana

TABLE 1 | Summary of experimental study of pool scrubbing under the jet injection regime.

Experimental program	Aerosol	Carrier gas	AMMD[a] (μm)	Steam mass fraction X_m	Submerged depth (m)	Pool temperature (°C)	Pool pressure (bar)	Jet mass flux (kg/m^{2}s)
LACE-Espana 1994	CsI	N_2+steam	1.7, 5.6	0.1	2.5	110	2	70
RCA 1995	Ni	Air	3.3–3.9	0	0.25–2.5	114–119	2.3–2.5	92
POSEIDON-II 2003	SnO_2	N_2+steam	0.29–0.54	0–0.72	0.3–4	80–94	1	77–134
ARTIST-II 2009–2012	SiO_2	N_2	1.4, 3.7	0	0.3	25–30	1	63, 780
RSE 2013–2016	SiO_2	Air	0.4, 1	0	1.0	20	1	64, 85
PSP 2018	SiO_2	Air + steam	0.72–0.96	0–0.1	0.3	23–35	1	74–152
HARBIN 2020	TiO_2	Air	0.94	0	0.3	20	1	>200
This study 2022	TiO_2	N_2+ Air + steam	1.0–4.0	0–0.90	0.7–2.5	20–99	1–2.15	40–212

[a]*AMMD, aerodynamic mass median diameter; MMD, mass median diameter; AMMD, MMD×$(\rho_p/1000)^{0.5}$, where ρ_p is aerosol density in kg/m^3.*

project was completed by Centro de Investigaciones Energéticas MedioAmbientales y Tecnológicas (CIEMAT) (Marcos et al., 1994). The main objectives were to analyze the pool scrubbing dependence on steam mass fraction and particle diameter under a single-hole injector and the bubble regime. Just two experiments were in the jet regime, but the steam mass fraction is only 0.1, and the retention capacity is slightly enhanced. In 1995, RCA experiments were also conducted by CIEMAT (Peyres et al., 1995), and the effect of different submerged depths (0.25–2.5 m) on pool scrubbing under the jet regime was studied. The POSEIDON-II program carried out 17 experiments at the Paul Scherrer Institute (PSI) (Dehbi et al., 1997; Dehbi et al., 2001). They analyzed pool scrubbing dependence on steam mass fraction (0–72%), mass flow rate (87–153 kg/h), submergence (0.3–4 m), and pool temperature (80°C–94°C) under a single-hole injector. In 2011, a continuation project ARTIST-II was initiated to address issues raised in the aerosol trapping in the steam generator (ARTIST) project by PSI (Lind et al., 2011). The effect of pool scrubbing under two different mass fluxes (63 and 780 kg/m^{2}s) and particle sizes in four sets of experiments with nitrogen as the carrier gas was investigated. The RSE experiments were completed within the framework of the EU-PASSAM project of Italy to study the effect of pool scrubbing in natural water and seawater and in the presence of additives under the air jet regime (Albiol et al., 2018; Herranz et al., 2018b). PSP experiments were carried out by CIEMAT within the framework of the EU-PASSAM project (Herranz et al., 2018a) to study the effect of pool scrubbing under a single-hole injector at steam mass fraction lower than 10% and mass fluxes in the range of 74–152 kg/m^{2}s. In recent years, more and more institutions have also paid attention to the pool scrubbing process again. Sun et al. (2019) studied the dependence of decontamination factor (DF) on aerosol concentration in pool scrubbing with a single-hole injector. The results showed that DF increased monotonically with decreasing particle number concentration, but the correlation was weak when the particle concentration is greater than 10^{11} P/m^3 in the water submergence higher than 1.6 m. Diao et al. (2020) conducted HARBIN experiments, which mainly studied the effect of nozzle inlet pressure and gas injection direction on noncondensing gas jet flow, showing that the aerosol removal efficiency increases as the inlet pressure increases (from 0.12 to 0.4 MPa). The SAAB experiments were carried out at Research Center Juelich. This is a large-scale facility with the ability to perform a great variation of experiments, and the first test series with soluble particles including cesium iodide (CsI) had been reported by Vennemann et al. (2022).

Most of the earlier experiments on aerosol pool scrubbing were carried out under the conditions of low mass flow rate and single-hole injector. In contrast, the research on aerosol pool scrubbing in the jet regime was carried out only under the conditions of lower steam fraction shown in **Table 1**, which failed to reflect the high steam fraction characteristics of the gas mixture discharged from the containment and the multihole structure of the discharge device. Therefore, the effects of steam fraction, pool depth, mass flux, and pool temperature on the pool scrubbing effect under the multihole and jet regime should be investigated.

For the model of pool scrubbing DF, Wassel et al. (1985) introduced the aerosol scrubbing model, which has been the basis of several pool scrubbing analysis codes, such as SUPRA, BUSCA, and SPARC codes (Owczarski et al., 1985). However, because of droplet–particle interaction in the jet region, these tools are not suitable for high-velocity conditions. Berna et al. (2016) introduced the collision interception between aerosol particles and droplets generated by gas impact in the case of noncondensable gas jet injection, and the SPARC90-Jet code is developed, which enhanced the simulation of pool scrubbing in the jet regime of noncondensable gas. Yan et al. (2020) considered the deposition mechanism from fluctuation interface and entrainment droplets simultaneously, improving the simulation of pool scrubbing under the jet regime of noncondensable gas.

In this paper, an empirical model of aerosol DF is proposed considering mass flux, steam fraction, pool temperature, submergence, and particle size based on the experimental data and the mechanisms of interception and inertial impact in the jet regime and is validated by other tests.

MATERIALS AND METHODS

Experimental Facility and Test Conditions

The experiment was carried out at a small-scale aerosol pool scrubbing facility (SAPOS) (Li et al., 2021), mainly including a

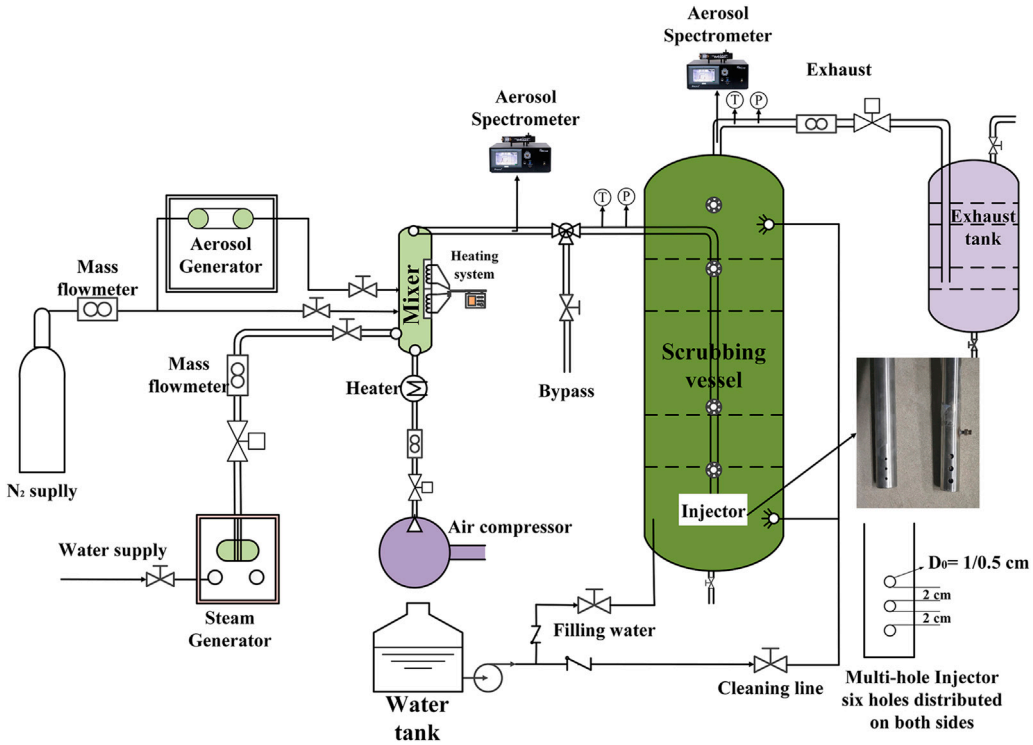

FIGURE 1 | Schematic of small-scale aerosol pool scrubbing facility.

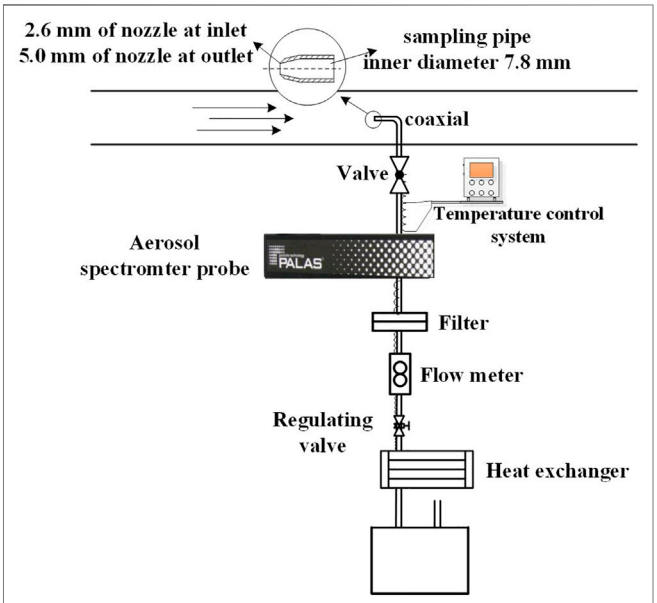

FIGURE 2 | Schematic of the aerosol concentration measurement system.

test vessel, a gas supply system, a data acquisition system, aerosol supply, and measurement systems (**Figure 1**). The test vessel is a vertical cylinder with upper and lower ellipsoidal heads, 5.0 m in height and 1.0 m in diameter. The gas supply system mainly includes the air compressor, steam generator, and nitrogen cylinder. The air compressor can provide a maximum mass flow rate of 90 kg/h, the steam generator can provide 150 kg/h, and the nitrogen is mainly used for the aerosol generator with a maximum flow rate of 40 kg/h. Electric heat tracing is arranged on the steam and air pipe to prevent steam condensation. The titanium dioxide (TiO_2) aerosols are generated using pure nitrogen as the carrier gas. Pressures, temperatures in the pipe and vessel, and fluid mass flow rates are measured and collected using the data acquisition system.

The study focuses on the influence of thermal parameters on the effect of aerosol scrubbing pool with the typical structure of a multihole injector. Two downward vertical injectors with different apertures of the injector are used with the hole diameters (D_0) of 1 and 0.5 cm. Both injectors have six holes and are divided on either side of the injector. The bottom of the multihole injector is 50 cm above the bottom of the vessel.

As shown in **Figure 2**, the aerosol concentration measurement system comprises a thin-wall sampling nozzle, temperature control system, aerosol spectrometer system, filter membrane (>0.1 μm), flow meter, regulating valve, and heat exchanger. The inner diameter of the thin-wall sampling nozzle is 2.6 and 5.0 mm at the inlet and outlet pipes, respectively. **Figure 3** shows the aerosol particle size distribution at a mass median diameter (MMD) of 0.5 μm, which is an approximately standard normal distribution with a geometric standard deviation (GSD) of 1.26. **Table 2** shows the experimental parameters and their ranges. The experiments were performed while changing only one parameter to clarify the influence of other parameters.

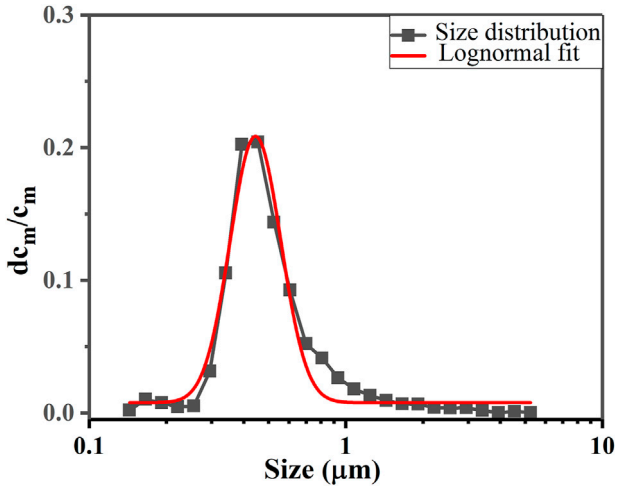

FIGURE 3 | Aerosol size distribution of TiO_2 with mass median diameter 0.50 μm.

Uncertainty Analysis

The DF is defined as the ratio of the inlet aerosol mass flow rate to the outlet aerosol mass flow rate, as shown in **Eq. 1**:

$$DF = \frac{W_{a-in}}{W_{a-out}} \approx \frac{Q_{in}C_{m-in}}{Q_{out}C_{m-out}} \tag{1}$$

where $W_{a\text{-}in}$ and $W_{a\text{-}out}$ are the aerosol mass flow rates in and out of the test vessel, respectively, mg/s; $C_{m\text{-}in}$ and $C_{m\text{-}out}$ denote the inlet and outlet aerosol mass concentrations, respectively (mg/m^3); and Q_{in} and Q_{out} represent the inlet and outlet volume flow rates, respectively, m^3/s.

Aerosol concentration is affected by many factors, mainly including aspiration efficiency, aerosol deposition in the sampling pipe, and the measurement error of the aerosol particle size spectrometer. The efficiency of making a particle enter the sampling pipe is called aspiration efficiency. The thin-wall sampling nozzle and coaxial sampling method are used in this experiment, as shown in **Figure 2**, and the aspiration efficiency can be calculated using **Eqs 2** and **3** (Liu et al., 1989; Zhang and Liu, 1989). The flow velocity at the inlet pipe and the *Stk* number at the sampling nozzle is in the range of 4–20 m/s and 0.01–0.4, respectively, and the sampling velocity is 15.7 m/s. The flow velocity at the outlet pipe is in the range of 4–13 m/s, the *Stk* number is lower than 0.02, and the sampling velocity is 4.3 m/s. Therefore, the aspiration efficiency of the inlet and outlet ranges from 0.95 to 1.05.

$$\begin{cases} \eta_{\text{asp}} = 1 + \dfrac{\dfrac{U_0}{U} - 1}{1 + \dfrac{0.418}{Stk}} & \cdots\cdots \dfrac{U_0}{U} > 1 \\ \eta_{\text{asp}} = 1 + \dfrac{\dfrac{U_0}{U} - 1}{1 + \dfrac{0.506\sqrt{U_0/U}}{Stk}} & \cdots\cdots \dfrac{U_0}{U} < 1 \end{cases} \tag{2}$$

$$Stk = \frac{\rho_p d_p^2 U_0}{18\mu D} \tag{3}$$

where η_{asp} is the aspiration efficiency; U_0 is the ambient gas stream velocity, m/s; U is the sampling velocity, m/s; *Stk* is the dimensionless stokes number; ρ_p is the particle density, kg/m^3; d_p is the particle diameter, m; μ is the dynamic viscosity of ambient gas steam, Pa·s; D is the nozzle diameter of sampling pipe, m.

Aerosol deposition in a pipe is mainly caused by the inertial collision in the bend pipe, and the deposition velocity is written as **Eq. 4** (Chatzidakis, 2018). Moreover, the fractional penetration is calculated by using **Eq. 5** (Sehmel, 1968; Benjamin and Jugal, 1974). The *Stk* numbers of the inlet and outlet sampling pipeline range from 0.003 to 0.1, and the penetration rate of the sampling pipeline is greater than 95%.

$$V_i = U \cdot Stk \cdot d_0 \cdot \pi / L_c \tag{4}$$

$$P_s = e^{-\left(\frac{V_i \cdot \pi \cdot d_0 \cdot L_c}{Q_s}\right)} \tag{5}$$

TABLE 2 | Small-scale aerosol pool scrubbing experimental test conditions.

Parameter	Standard value	Range
Nozzle diameters (cm)	0.5	0.5, 1.0
Pool depth (m)	1.2	1.2–4.0
Initial water temperature (°C)	50	50–100
Pressure above pool (kPa)	150	100–215[a]
Gas mass flow rate (kg/h)	70	70
Gas temperature (°C)	170	170
Gas pressure (kPa)	175	110–240
Steam mass fraction (%)	64	0–90
The inlet aerosol mass concentrations (mg/m^3)	15–30	15–30, 50, 120
The inlet aerosol mass concentrations (P/m^3)	1×10^{11}	1×10^{11}–5×10^{11}
Aerosol mass median diameter (MMD) (μm)	0.50	0.50, 1.44, 1.64, 2.00
Geometric standard deviation (GSD)	1.26	1.26, 2.42, 1.81, 2.02

[a]*Different pressures above the pool in the different steam mass fraction experiments (0%–103 kPa, 50%–170 kPa, 64%–150 kPa, 80%–130 kPa, and 90%–120 kPa) and the different initial water temperature experiments (50°C–150 kPa, 75°C–170 kPa, and 100°C–215 kPa).*

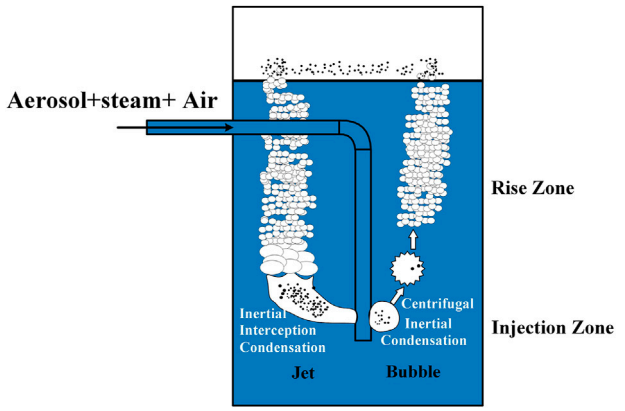

FIGURE 4 | Schematic diagram of the pool scrubbing process.

where V_i is the deposition velocity, m/s; P_s is the fractional penetration through the bend pipe; L_c is the elbow arc length, m; Q_s is the volume flow rate of sampling, m^3/s; and d_0 is the diameter of sampling pipe, m.

The maximum deviation of the aerosol concentration measurement system is 20% after calibration using the filter sampling method with different aerosol concentrations, which considers aspiration efficiency, aerosol deposition in the sampling pipe, and the measurement error of the aerosol particle size spectrometer. The volume flow at the inlet and outlet can be calculated using the ideal gas equation of $Q = WRT/Mp$, where Q is the volume flow rate of the carrier gas, m^3/s; W is the mass flow rate of the carrier gas measured by the flowmeter with an accuracy of 1%, g/s; T and p denote the temperature and pressure of the carrier gas measured using the sensor with an error of ±1 K and ±1.0% full scale, respectively, K and Pa; M is the molecular weight, g/mol; and R is an ideal gas constant, 8.314 J/(mol·K).

The error transfer formula proposed by Kline and McClintock (1953) is used to estimate the error of indirect measurement parameters, shown as **Eq. 6**. The detailed relative error calculation for the DF is expressed in **Eqs 7** and **8**, and the maximum error is 29%.

$$\sigma_Y = \sqrt{\left(\frac{\delta Y}{\delta x_1}\right)^2 \sigma_{x_1}^2 + \left(\frac{\delta Y}{\delta x_2}\right)^2 \sigma_{x_2}^2 + \ldots + \left(\frac{\delta Y}{\delta x_n}\right)^2 \sigma_{x_n}^2} \quad (6)$$

$$\frac{\sigma_{DF}}{DF} = \sqrt{\left(\frac{\sigma_{Q_{in}}}{Q_{in}}\right)^2 + \left(\frac{\sigma_{C_{m-in}}}{C_{m-in}}\right)^2 + \left(\frac{\sigma_{Q_{out}}}{Q_{out}}\right)^2 + \left(\frac{\sigma_{C_{m-out}}}{C_{m-out}}\right)^2} \quad (7)$$

$$\frac{\sigma_Q}{Q} = \sqrt{\left(\frac{\sigma_W}{W}\right)^2 + \left(\frac{\sigma_T}{T}\right)^2 + \left(\frac{\sigma_p}{P}\right)^2} \quad (8)$$

where Y is calculated from the measured quantities x_1, x_2, ..., x_n with errors σ_{x1}, σ_{x2}, ..., σ_{xn}. In this study, the measured quantities mainly include $C_{m\text{-}in}$, $C_{m\text{-}out}$, W, T, and p, and the indirect calculations include DF and Q.

RESULTS AND DISCUSSION

Influence of Jet Regime of Decontamination Factor

According to the different characteristics of gas–liquid hydrodynamic behavior, the pool scrubbing process can be divided into two central regions, as shown in **Figure 4**, including injection and rise zone. The injection zone is characterized by the formation of the unstable vapor globule or jet column, which subsequently breaks up into bubble swarm. At last, the bubble swarm quickly rises to the surface of the pool and escapes in a very short period time.

In the injection zone, with the flow rate increase, the gas injection form changes from bubble to jet regime. To study the effect of different flow regimes on aerosol DFs, experiments are carried out with different injectors with hole diameters of 1 and 0.5 cm under the same gas mass flow rate (70 kg/h). The flow regime at a mass flux of 41 kg/m^2s is given in **Figure 5**, indicating that large unstable bubbles are generated and gradually broken up into small bubbles, and finally rise to the pool surface, which is a typical bubble flow regime. The flow regime at a mass flux of 164 kg/m^2s is given in **Figure 6**, indicating that the gas core flows along the horizontal jet direction, and the size of gas core continues to increase away from the nozzle. At the end of the horizontal gas core, numerous small bubbles disperse and move upwards gradually under the action of buoyancy.

The DFs versus different steam mass fractions at flow regimes are shown in **Figure 7**. The higher steam fraction results in an enhanced of steam condensation mechanism, and an increased aerosol retention effect. The steam condensation mechanism can be described as **Eq. 9** (Owczarski and Burk, 1991), ln(S) and ln(DF) show a linear relationship as shown in **Figure 8**. Their growth slopes are almost the same in the two different flow regimes, but the DF value is significantly higher in the jet regime.

$$\begin{cases} S = \dfrac{1 - X_{s,eq}}{1 - X_s} \\ X_{s,eq} = \dfrac{p_s}{p_0 + \rho_l g H} \end{cases} \quad (9)$$

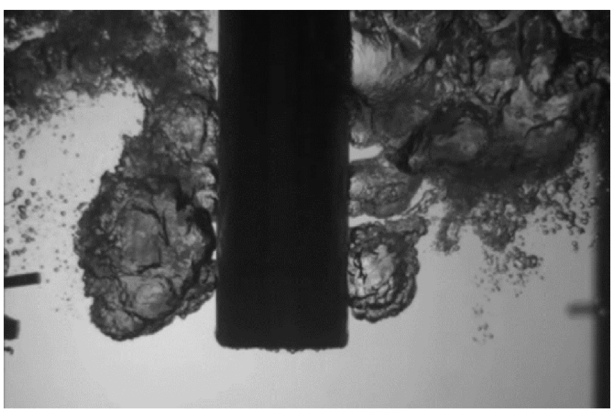

FIGURE 5 | Bubble flow image at 41 kg/m^2 s (D_0=1 cm, X_m=0.64).

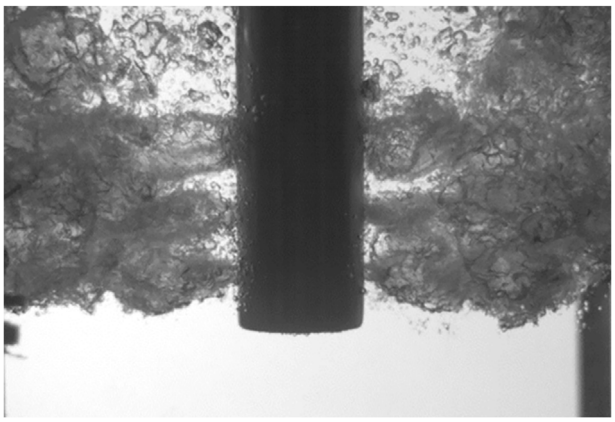

FIGURE 6 | Jet flow image at 164 kg/m^2 s (D_0=0.5 cm, X_m=0.64).

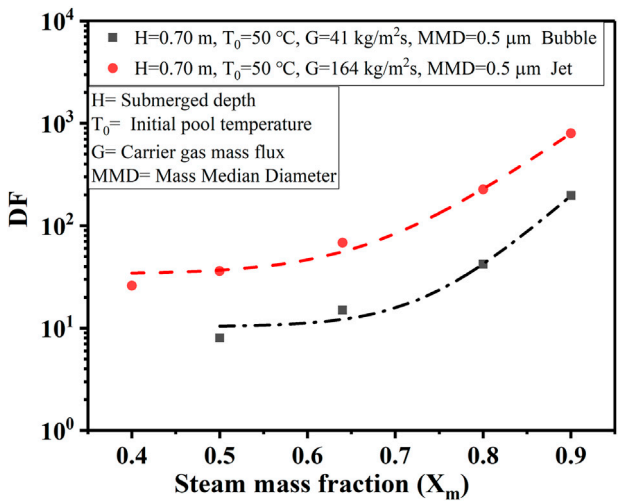

FIGURE 7 | Steam mass fraction effect on decontamination factor (DF).

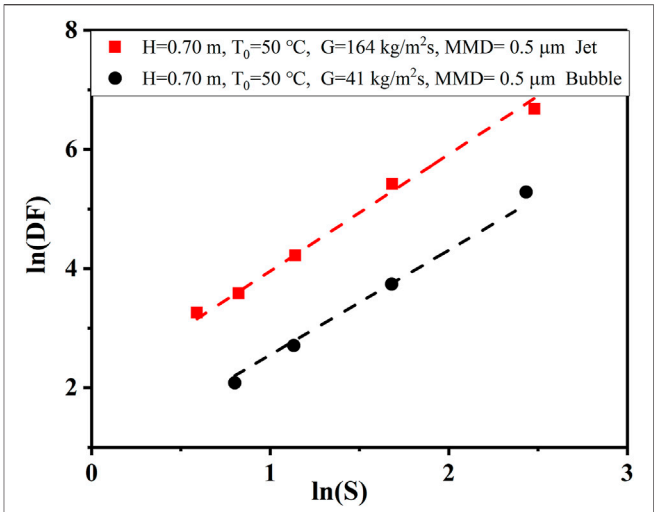

FIGURE 8 | Correlation between ln(DF) and ln(S) under different flow regimes.

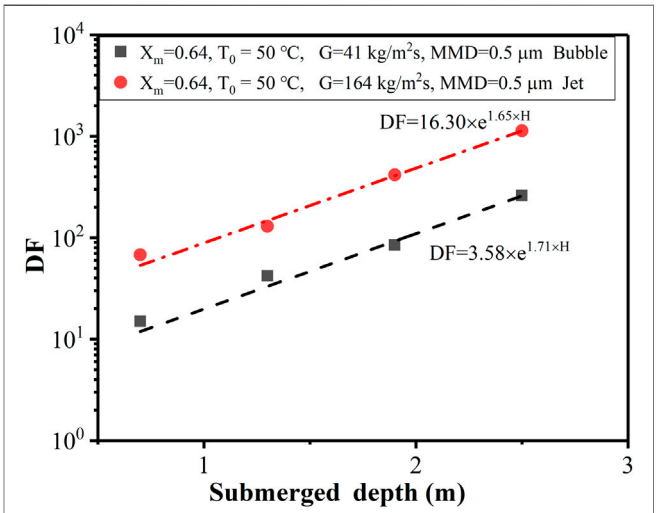

FIGURE 9 | Effect of submerged depth on DF.

where S is the fractional loss in gas volume caused by condensation; X_s is the mole fraction of steam in inlet gas mixture; $X_{s,eq}$ is the mole fraction of steam after it attains thermal and steam equilibrium in the pool at the inlet depth. p_s is the saturated steam pressure at pool temperature, Pa; p_0 is the pressure above the pool, Pa; ρ_l is the density of pool water, kg/m^3; H is submerged depth, m. Condensation will occur if 1-$X_{s,eq}$ is greater than 1-X_s, otherwise evaporation will occur and this retard particle motion toward the interface. For 1-$X_{s,eq}$<1-X_s, it is assumed that DF = 1.

Figure 9 shows the DFs of different flow regimes at different submerged depths. DF increases exponentially with the increase of submergence depth. The increase in submerged depth leads to an increase in the rising distance of bubbles, making the action time of the aerosol removal mechanism (gravity deposition, centrifugal deposition, Brownian diffusion) longer, which also makes the aerosol removal more efficient. The same growth trend of DF at different flow regimes indicates that jet flow mainly affects aerosol retention at the injection region. At the same time, **Figures 8** and **9** also illustrates that jet regime contributes to the aerosol retention in pool within the range of experimental conditions.

Influence of Mass Flux on Decontamination Factor in Jet Regime

The effect of different mass fluxes on DF under the jet regime is studied with pure air as the carrier gas. According to the dimensionless Weber number (We), the inlet gas regime is judged as the jet regime (We ≥ 10^5) and the bubble regime (We < 10^5) (Herranz et al., 2018b). The mass fluxes range from 50 to 170 kg/m^{2}s, and We as shown in **Eq. 10** ranges from 10^5 to 10^6 in this experiment.

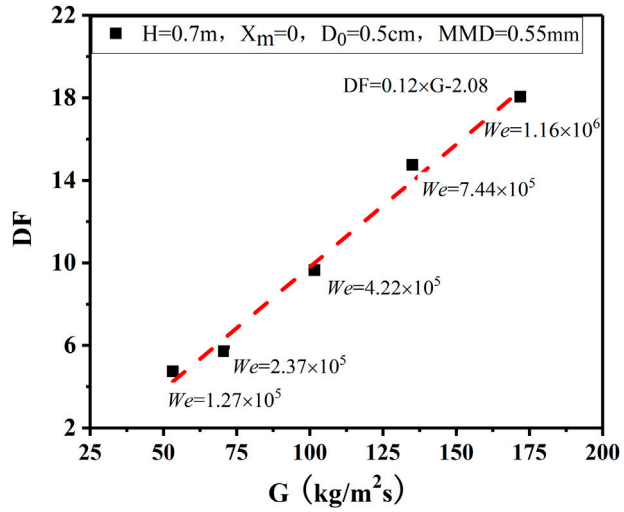

FIGURE 10 | Influence of mass flux on DF with incondensable gas under the jet regime.

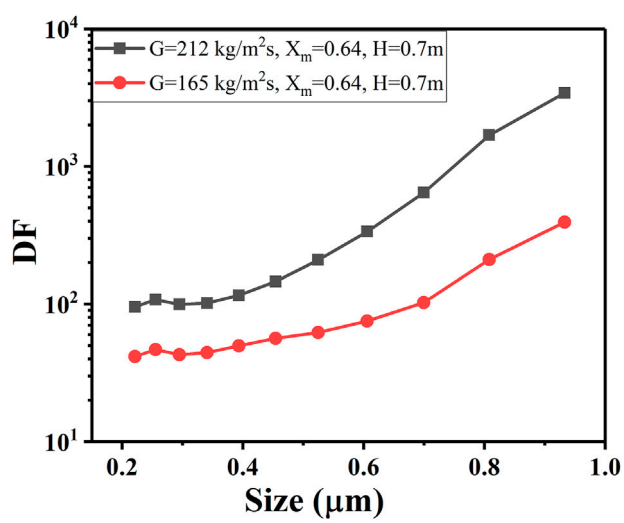

FIGURE 11 | Influence of mass flux on DF with the presence of steam under the jet regime.

$$\mathrm{We} = \frac{\rho_l D_{inj} v_{inj}^2}{\sigma} \tag{10}$$

where ρ_l is the density of pool water, kg/m^3; D_{inj} is the hole diameter of the injector, m; v_{inj} is the gas velocity at the outlet, m/s; and σ is the surface tension of pool liquid, N·m.

Figure 10 shows that the mass flux greatly influences the retention of aerosols in the pool, and DF increases approximately linearly with the increase of mass flux. **Figure 11** also implies that DF increases with the increase of injection mass flux and particle size with the same steam mass fraction of 64%. This is mainly because, in the injection zone, the high-speed gas interacts with the water and causes water entrainment in the form of droplets. Then the aerosol is removed by droplet interception, inertial collision, and diffusion. As the jet mass flux increases, the jet length and entrained droplet fraction increase, as shown in **Eqs 11** and **12** (Berna et al., 2016). Therefore, the droplet interception and inertial collision effects are enhanced, resulting in an increase in DF.

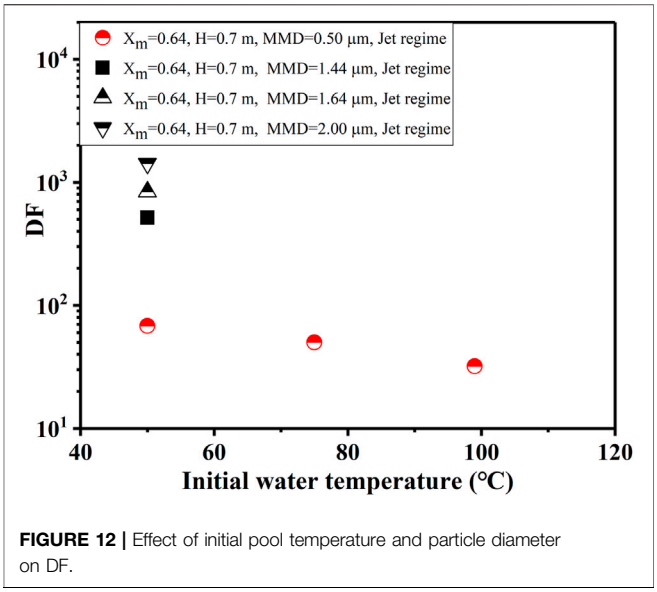

FIGURE 12 | Effect of initial pool temperature and particle diameter on DF.

$$\frac{L}{D_0} = 10.7 Fr^{0.46} \left(\frac{\rho_g}{\rho_l}\right)^{0.35} \quad Fr = \frac{\rho_g u_0^2}{(\rho_l - \rho_g) g D_0} \tag{11}$$

$$\frac{E}{1-E} = 5.51 \times 10^{-7} \cdot We_g^{2.68} Re_g^{-2.62} Re_l^{0.34} \left(\frac{\rho_g}{\rho_l}\right)^{-0.37} \left(\frac{\mu_g}{\mu_l}\right)^{-3.71} c_w^{4.24} \tag{12}$$

where L is the length of the jet, m; D_o is the pore size of the injector, m; u_0 is the velocity of gas, m/s; ρ_g is the density of gas, kg/m^3; ρ_l is the density of pool water, kg/m^3; μ_g is the dynamic viscosity of gas, Pa·s; μ_l is the dynamic viscosity of liquid, Pa·s; We_g is the Weber number of gas; Re_g is the Reynold number of gas; Re_l is the Reynold number of liquid; E is the entrained droplet fraction; and c_w is a factor used to illustrate the effect of surface tension.

Influence of Pool Temperature and Particle Diameter on Decontamination Factor

Experiments on three pool initial temperatures with 50°C, 73°C, and 97°C are carried out to reveal the influence of pool temperature on DF. The DF decreases with the initial temperature increase, shown in **Figure 12**. The main reason is that as the pool temperature increases, the mole fraction of steam after it attains thermal and steam equilibrium in the pool at the inlet depth is higher. As a result, the steam condensation is weakened, which can be described as **Eq. 9**. At the same time, the increase in pool temperature accelerates the rise of stable bubbles, which is also unfavorable to the aerosol scrubbing.

Figure 12 also shows the DFs of different particle mass median diameters (0.50, 1.44, 1.64, and 2.00 μm). It is expected that DF strongly depends on the particle diameter and shows an order of magnitude increase with the particle diameter due to inertial impaction, gravity settling, and Brownian diffusion during the injection and rise regions. It can also be seen from **Figure 11** that the DF hardly changes for a particle diameter smaller than 0.50 μm, while for a particle diameter greater than 0.50 μm, the DF increases rapidly. This reveals that the influence of inertial impaction on the DF is dominant for large particles.

TABLE 3 | Aerosol deposition velocity in the rise zone.

Parameter	Model
Gravity settling	$V_g = \frac{\rho_p g d_p^2 C_c}{18\mu_g}$
Centrifugal deposition	$v_C = \frac{v_s^2 v_g}{r_{cg}}$
Brownian diffusion	$v_{dl} = \xi\sqrt{\frac{D}{\pi t_e}} D = \frac{kTC_c}{3\pi\mu_g d_p}$

Here, v_g is gravity setting velocity; v_s is the tangential velocity of bubble surface, which is closely related to the shape of the bubble and the relative velocity of the rising bubble; r_c is the radius of the surface curvature of the bubble; k is Boltzmann's constant; T is the diffusion ambient temperature gas; and t_e is the exposure time of the moving surface.

SCRUBBING MODEL

In the case of the jet regime, the gas can enter the pool through an injector and form a jet column at the outlet due to high flow velocity, followed by the rupture of the column to form small bubbles that rise rapidly to the surface of the pool and eventually escape. The following describes the establishment of empirical equations for DF calculation under the jet regime.

Decontamination Factor of Injection Zone

In the injection zone, the form of gas–liquid interaction affects the process of pool scrubbing, where the gas injection velocity and composition are key variables. When the injection zone is in the jet regime, steam condenses at the injector outlet at first, and ln(DF) is proportional to ln(S), as shown in **Figure 8**. Then the remaining gas interacts with water, and a fraction of the liquid film contacting the gas can enter the gas core in the form of droplets, which capture the aerosol particles. At this point, the main removal mechanisms include droplet interception and inertial impaction. This is mainly related to droplet diameter, gas velocity, and particle size, among which droplet diameter and gas velocity are affected by the mass flux of the remaining gas (G_n). It can be seen from **Figure 10** that DF is in a linear relationship with G. DF is approximately proportional to the square of the particle diameter by nonlinear fitting of the experimental data in **Figure 12**. Therefore, the DF value in the injection region is simplified into **Eq. 13**.

$$DF_{in} = \left(\frac{1 - X_{s,eq}}{1 - X_s}\right)^n \left(AG_n \cdot d_p^2 + B\right) \tag{13}$$

where DF_{in} is the DF value in the injection region; G_n is the mass flux of the uncondensed gas, $G_n = G(1–X_m)/(1–X_{m,eq})$, $X_{m,eq}$ is the mass fraction of steam after it attains thermal and steam equilibriumin the pool at the inlet depth. d_p is the aerosol particle diameter, m; and n, A, and B are constants.

Decontamination Factor of Rise Zone

In the rise zone, the aerosol is gradually transferred from the bubble to the water due to gravity settling, centrifugal deposition, and Brownian diffusion, shown in **Table 3** (Owczarski et al., 1985; Li et al., 2020). The DF of the rise zone for pool scrubbing is expressed as **Eq. 14**.

$$\begin{cases} DF_{rise} = \exp\left(\lambda \times \dfrac{H}{v_{sw}}\right) \\ \lambda = \dfrac{1}{V_B}\int\left(v_c + v_d + v_g\right)dA \end{cases} \tag{14}$$

where λ is the retention efficiency coefficient of particles in the bubble, s^{-1}; v_{sw} is the average rising velocity of the bubble group, m/s; V_B is the stable bubble volume, m^3; and A is the bubble surface area for particle deposition, m^2.

The bubble diameter and its rising velocity are assumed to be constant. **Eq. 14** can be simplified as a function of the particle diameter (m) and the submerged depth (m), shown as **Eq. 15**, where C and D are constants.

$$DF_{rise} = e^{\left(Cd_p^2 + Dd_p^{-0.5}\right)\times H} \tag{15}$$

Empirical Model of Decontamination Factor Calculation

The product of DFs calculated by different mechanisms is the final cumulative DF. Therefore, the overall DF may be written as $DF = DF_{in} \times DF_{rise}$ as **Eq. 16**.

$$DF = \left(\frac{1 - X_{s,eq}}{1 - X_s}\right)^n \left(AG_n \cdot d_p^2 + B\right)e^{\left(Cd_p^2 + Dd_p^{-0.5}\right)H} \tag{16}$$

The best fit of all these experiment data used is achieved by the following **Eq. 17** under the conditions explored. Moreover, this correlation should only be used for multihole injector systems in an open pool with steam mass fractions from 0 to 90%, particle diameters from 0.2 to 2 μm, submerged depths from 0.7 to 2.5 m, and G_n from 20 to 212 kg/m^2s.

$$DF = \left(\frac{1 - X_{s,eq}}{1 - X_s}\right)^{1.9} \left(0.130 \cdot 10^{12} \cdot G_n \cdot d_p^2 + 0.774\right)e^{\left(0.311 \cdot 10^{12} \cdot d_p^2 + \mathbf{0}.862 \cdot 10^{-3} \cdot d_p^{-0.5}\right)H} \tag{17}$$

The proposed empirical model is validated with the RAC, ACE, ARTIST, and RSE experimental data, shown in **Figure 13**. To evaluate the effectiveness of the empirical model quantitatively, the under-prediction factor (UF) is adopted,

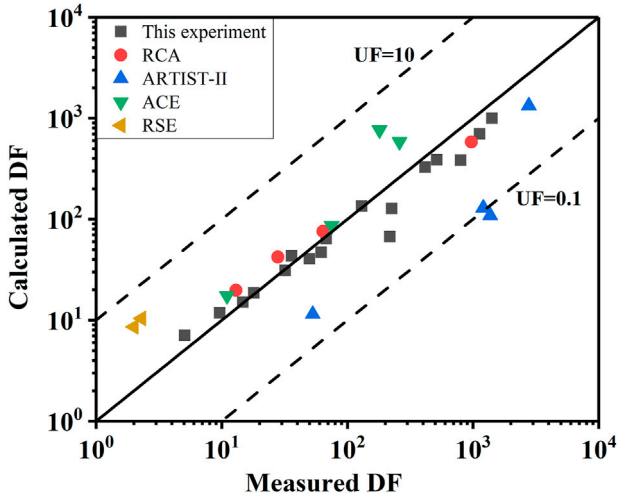

FIGURE 13 | Comparison between the calculated DF and the experimental data.

defined as **Eq. 18** (Humphries et al., 2015; He et al., 2021). The UF in the range of 0.1–10 is usually considered acceptable. The closer the UF is to 1, the better the consistency containment.

$$\begin{cases} \mathrm{UF} = \lg^{-1}(\mathrm{MD}) \\ \mathrm{MD} = \dfrac{\sum_{j=1}^{J}\left(\lg \mathrm{DF_m} - \lg \mathrm{DF_c}\right)_j}{J} \end{cases} \tag{18}$$

where MD is the mean difference of DF, $\mathrm{DF_m}$ is the experimental DF, and $\mathrm{DF_c}$ is the calculated DF.

The predicted DF result is in good agreement with the experimental result with the UF in the range of 0.1–10, except ARTIST. The calculated DF of ARTIST text has a large discrepancy from the experimental values owing to the complex geometry (tube bundle) in the steam generator tube rupture accident. Further study will be to expand the test mass flux to extend the applicability of the empirical model. In summary, this empirical model can be used to calculate the DF during containment overpressure discharge.

CONCLUSION

A study of the aerosol retention efficiency under jet regime conditions was carried out at the SAPOS facility. The flow regime gradually changes from bubble regime to jet regime With the increase of mass flux. When the carrier gas is a non-condensing gas, the flow regime is judged as the jet regime ($We \geq 10^5$) and the bubble regime ($We < 10^5$). When the carrier gas contains steam, the flow regime at the two mass fluxes of 41 and 164 kg/m^{2}s are bubble and jet regimes, respectively. With the increase of steam fraction and submerged depth, the trend of DF growth is approximately the same under different flow regimes, but the DF value is significantly higher in the jet regime in the conditions explored. The influence of mass flux and pool initial temperature on the DF is also investigated, and the results show that the DF increases with increasing mass flux due to the enhanced droplet interception and inertial collision aerosol removal mechanism, and because the high-water temperature weakens the aerosol removal by steam condensation, DF decreases with the increase of initial pool temperature.

In addition, an empirical model of aerosol DF considering mass flux, steam fraction, pool temperature, submerged depth, and particle size is established for the jet regime and verified by the international experiments under the conditions explored. The proposed model can be used to calculate DF in the process of containment overpressure discharge.

DATA AVAILABILITY STATEMENT

The original contributions presented in the study are included in the article/Supplementary Material, and further inquiries can be directed to the corresponding author.

AUTHOR CONTRIBUTIONS

YL: performed the experiment, formal analysis, writing—original and draft. YW: methodology, investigation, writing—review and editing, and supervision. XC: conceptualization, methodology, and supervision.

REFERENCES

Albiol, T., Herranz, L., Riera, E., Dalibart, C., Lind, T., Del Corno, A., et al. (2018). Main Results of the European PASSAM Project on Severe Accident Source Term Mitigation. *Ann. Nucl. Energy* 116, 42–56. doi:10.1016/j.anucene.2018.02.024

Benjamin, Y. H. L., and Jugal, K. A. (1974). Experimental Observation of Aerosol Deposition in Turbulent Flow. *J. Aerosol. Sci.* 5, 148–155. doi:10.1016/0021-8502(74)90046-9

Berna, C., Escrivá, A., Muñoz-Cobo, J. L., and Herranz, L. E. (2016). Enhancement of the SPARC90 Code to Pool Scrubbing Events under Jet Injection Regime. *Nucl. Eng. Des.* 300, 563–577. doi:10.1016/j.nucengdes.2016.02.027

Berna, C., Escrivá, A., Muñoz-Cobo, J. L., and Herranz, L. E. (2015). Review of Droplet Entrainment in Annular Flow: Characterization of the Entrained Droplets. *Prog. Nucl. Energy* 79, 64–86. doi:10.1016/j.pnucene.2014.11.011

Chatzidakis, S. (2018). *SCC Aerosol Transport Model Summary Report*. United States: Oak Ridge National Lab. doi:10.2172/1492159

Dehbi, A., Suckow, D., and Guentay, S. (2001). Aerosol Retention in Low-Subcooling Pools under Realistic Accident Conditions. *Nucl. Eng. Des.* 203, 229–241. doi:10.1016/S0029-5493(00)00343-5

Dehbi, A., Suckow, D., and Guentay, S. (1997). The Effect of Liquid Temperature on Pool Scrubbing of Aerosols. *J. Aerosol Sci.* 28, S707–S708. doi:10.1016/S0021-8502(97)85352-9

Diao, H., Zhou, Y., Gu, H., Li, Y., and Yan, C. (2020). Experimental Study on the Scrubbing Efficiency of Aerosols Contained in Horizontal and Vertically

Downward Submerged Gas Jet. *Prog. Nucl. Energy* 126, 103406. doi:10.1016/j.pnucene.2020.103406

Gao, S., Fu, Y., Sun, D., Mei, Q., Pan, N., Zhang, S., et al. (2017). Comparison Research on Different Aerosol Pool Scrubbing Models. In Proceedings of the 2017 25th International Conference on Nuclear Engineering. Shanghai, China: Nuclear Engineering Division. doi:10.1115/ICONE25-66540

Gao, Z. C., Qiu, Z. F., Tong, L. L., and Cao, X. W. (2022). Aerosol Pool Scrubbing Phenomena during the Containment Depressurization Venting. Part I: Scaling Analysis. *Ann. Nucl. Energy* 165, 108764. doi:10.1016/j.anucene.2021.108764

He, L. W., Li, Y. X., Zhou, Y., Chen, S., Tong, L. L., and Cao, X. W. (2021). Investigation on Aerosol Pool Scrubbing Model during Severe Accidents. *Front. Energy Res.* 9, 691419. doi:10.3389/fenrg.2021.691419

Herranz, L. E., Iglesias, R., and Fontanet, J. (2018b). Mitigation of Source Term in Suppression Pools: Large Uncertainties in Predictability. *Ann. Nucl. Energy* 120, 509–515. doi:10.1016/j.anucene.2018.06.010

Herranz, L. E., Lopez, C., and Penalva, J. (2018a). Investigation on Jet Scrubbing in Nuclear Reactor Accidents: from Experimental Data to an Empirical Correlation. *Prog. Nucl. Energy* 107, 72–82. doi:10.1016/j.pnucene.2018.04.019

Humphries, L. L., Louie, D. L. Y., Figueroa, V. G., Young, M. F., Weber, S., Ross, K., et al. (2015). *MELCOR Computer Code Manuals Vol.3: MELCOR Assessment Problems Version 2.1.7347 2015*. USA: Sandia National Laboratories.

Jung, C. H., and Lee, K. W. (1998). Filtration of Fine Particles by Multiple Liquid Droplet and Gas Bubble Systems. *Aerosol Sci. Technol.* 29, 389–401. doi:10.1080/02786829808965578

Kline, S. J., and McClintock, F. A. (1953). Describing Uncertainties in Single Sample Experiments. *Mech. Eng.* 75, 3–8.

Lebel, L. S., Morreale, A. C., Freitag, M., Gupta, S., Allelein, H. J., Klauck, M., et al. (2022). "Aerosol Experiments and Measurement Techniques on Pool Scrubbing-Related Source Term Issues," in The 19th International Topical Meeting on Nuclear Reactor Hydraulics (NURETH-19) Brussels, Belgium.

Li, Y., Tong, L., and Cao, X. (2021). Experimental Study on Influencing Factors of Aerosol Retention by Pool Scrubbing. *Front. Energy Res.* 9, 675841. doi:10.3389/fenrg.2021.675841

Lind, T., Dehbi, A., and Güntay, S. (2011). Aerosol Retention in the Flooded Steam Generator Bundle during SGTR. *Nucl. Eng. Des.* 241, 357–365. doi:10.1016/j.nucengdes.2010.10.025

Liu, B. Y. H., Zhang, Z. Q., and Kuehn, T. H. (1989). A Numerical Study of Inertial Errors in Anisokinetic Sampling. *J. Aerosol Sci.* 20, 367–380. doi:10.1016/0021-8502(89)90012-8

Marcos, C., Gomez, M., Melches, S., Martin Espigares, M., and Lopez Jimenez, J. (1994). *Lace-Espana Experimental Programme on the Retention of Aerosols in Water Pools*. Spain: CIEMAT.

Owczarski, P. C., and Burk, K. W. (1991). *SPARC-90: A Code for Calculating Fission Product Capture in Suppression Pools*. Richland, Washington, USA: Pacific Northwest Laboratory. doi:10.2172/6120360

Owczarski, P. C., Schreck, R. I., and Postma, A. K. (1985). Technical Bases and User's Manual for the Prototype of a Suppression Pool Aerosol Removal Code (SPARC). *U. S. Nucl. Regul. Comm.* doi:10.2172/5797428

Peyres, V., Espigares, M. M., Polo, J., Escudero, M. J., Herranz, L. E., and Lopez Jimenez, J. (1995). *Pool Scrubbing and Hydrodynamic Experiments on Jet Injection Regime*. Spain: CIEMAT.

Sehmel, G. A. (1968). *Aerosol Deposition from Turbulent Airstreams in Vertical Conduits*. Richland, Washington, USA: Pacific Northwest Laboratory. doi:10.2172/4549565

Slinn, W. G. N. (1983). *Atmospheric Sciences and Power Production-Precipitation Scavenging*. Oak Ridge, Tennessee: Div. of Biomedical and Environmental Research, U.S. Dept. of Energy. (Chap 11).

Sun, H., Sibamoto, Y., Okagaki, Y., and Yonomoto, T. (2019). Experimental Investigation of Decontamination Factor Dependence on Aerosol Concentration in Pool Scrubbing. *Sci. Technol. Nucl. Installations* 2019, 1–15. doi:10.1155/2019/1743982

Vennemann, R., Klauck, M., and Allelein, H.-J. (2022). Experimental Investigation on the Retention of Soluble Particles by Pool Scrubbing. *J. Nucl. Eng. Radiat. Sci.* 8, 044502-1–044502-5. doi:10.1115/1.4051250

Wassel, A. T., Mills, A. F., Bugby, D. C., and Oehlberg, R. N. (1985). Analysis of Radionuclide Retention in Water Pools. *Nucl. Eng. Des.* 90, 87–104. doi:10.1016/0029-5493(85)90033-0

Yan, X., Zhou, Y., Diao, H., Gu, H., and Li, Y. (2020). Development of Mathematical Model for Aerosol Deposition under Jet Condition. *Ann. Nucl. Energy* 142, 107394. doi:10.1016/j.anucene.2020.10710.1016/j.anucene.2020.107394

Zhang, Z. Q., and Liu, B. Y. H. (1989). On the Empirical Fitting Equations for Aspiration Coefficients for Thin-Walled Sampling Probes. *J. Aerosol Sci.* 20, 713–720. doi:10.1016/0021-8502(89)90060-8

Conflict of Interest: The authors declare that the research was conducted in the absence of any commercial or financial relationships that could be construed as a potential conflict of interest.

frontiers | Frontiers in Energy Research

TYPE Original Research
PUBLISHED 26 September 2022
DOI 10.3389/fenrg.2022.892592

OPEN ACCESS

EDITED BY
Luteng Zhang,
Chongqing University, China

REVIEWED BY
Yapei Zhang,
Xi'an Jiaotong University, China
Yacine Addad,
Khalifa University, United Arab Emirates

*CORRESPONDENCE
Yidan Yuan,
yidanyuan2010@aliyun.com

SPECIALTY SECTION
This article was submitted to Nuclear Energy,
a section of the journal
Frontiers in Energy Research

RECEIVED 09 March 2022
ACCEPTED 25 August 2022
PUBLISHED 26 September 2022

CITATION
Zhang L, Guo P, Yuan Y, Liang Y, Guo Y, Li W, Guo Q and Ma W (2022), Numerical simulation of natural convection and heat transfer in a molten pool with embedded cooling tubes. *Front. Energy Res.* 10:892592. doi: 10.3389/fenrg.2022.892592

Numerical simulation of natural convection and heat transfer in a molten pool with embedded cooling tubes

Li Zhang[1], Pengya Guo[1], Yidan Yuan[1]*, Yangyang Liang[1], Yong Guo[1], Wei Li[1], Qiang Guo[1] and Weimin Ma[2]

[1]China Nuclear Power Engineering Co, LTD, Beijing, China, [2]Royal Institute of Technology (KTH), Stockholm, Sweden

This study described the natural circulation and heat transfer of a molten pool in a specifically designed core catcher conceived for a pressurized water reactor. In addition to external cooling, the core catcher features internal cooling tubes embedded in the molten pool. To investigate the coolability in such a configuration, first, a full-scale core catcher simulation is conducted to give a preliminary study under a real SA situation. Results illustrated that cooling efficiency can be remarkably enhanced due to the inner tubes. Then a test facility of the 2D slice with the geometrical scaled factor of 1:4 has been developed, and molten salt ($NaNO_3$–KNO_3) experiments will be implemented in the near future. This study also performed a pre-test simulation using molten $NaNO_3$–KNO_3 as a stimulant to study the heat transfer and flow characteristics of the salt pool. The melt convection in the test section was represented by a two-dimensional mesh with a WMLES turbulence model using the FLUENT code. The simulation captured the heat transfer enhancement by the cooling tubes as expected, and the results would help decide the proper test matrix and improvement of instrumentation required to obtain the necessary data for code validation.

KEYWORDS

severe accident, molten pool, coolability, core catcher, simulation

Introduction

During the course of a severe accident in NPPs, the reactor core may be melted down by the decay heat and transferred to the lower head of the reactor pressure vessel (RPV). The RPV may be melted through and relocated to the reactor cavity, resulting in basement melt penetration without countermeasures to mitigate the progress. Therefore, arresting the melted core in a controlled way in RPV or in the containment is of great importance, which leads to the in-vessel melt retention (IVR) or ex-vessel melt retention (EVR) strategy, respectively.

For high-power reactors like VVER-1000/1,200 and EPR, the EVR strategy is preferred to terminate the accident and mitigate the consequences in case of

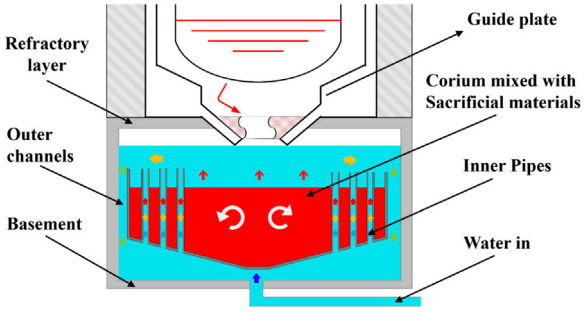

FIGURE 1
Sketch of the conceptual ex-vessel coolability enhancement.

containment melting through (Ha et al., 2011) despite the IVR being simpler and costless. The VVER-1000/1,200 reactors (Asmolov, 2005) are equipped with core catchers installed under the RPV, while the EPR (Fischer, 2004) reactors are using the large spreading room for enhancement of ex-vessel cooling of the corium. For these two typical types of advanced reactors with an ex-vessel melt retention strategy, the key issue is ensuring that the corium flows into the designated area and cools down as expected. For these purposes, various measures such as the addition of sacrificial material (Khabensky et al., 2009) and multiple cooling methods have been adopted to deal with corium conditioning and to enhance heat transfer between the corium and coolant (Fischer et al., 2005).

To analyze the safety margin of in-vessel retention for AP1000, Zhang et al. (2010) developed a point estimate procedure IVRASA (IVR analysis code in a severe accident) for modeling the two-layer configuration and postulated three-layer steady-state core melt configurations. Their results indicated that for the two-layer configuration, the overall heat flux remains below the critical heat flux (CHF), while for the postulated three-layer configuration, due to the portioning of partial metal into the bottom layer, the heat flux in the light metal layer could surpass CHF. COPRA (Zhang et al., 2016a; Zhang et al., 2016b) (Corium Pool Research Apparatus) experiments on the in-vessel melt pool behavior had been extensively conducted in Xi'an Jiaotong University with a 2D 1/4 circular slice of full-scale (1:1) lower plenum of RPV for the Chinese large-scale advanced PWR, where simulant material $NaNO_3$–KNO_3 were chosen as working fluid with eutectic (50 mol% $NaNO_3$–50 mol % KNO_3) and non-eutectic (20 mol% $NaNO_3$–80 mol% KNO_3) composition. Experimental results showed that the downward heat transfer toward the vessel wall of the COPRA test was lower than that from other previous experiments and correlations with the relevant range of Rayleigh numbers (10^{15} ~ 10^{17}). With the COPRA experimental results, Luo et al. (2018) and Luo et al. (2019) numerically investigated the behavior of internally heated melt pool with eutectic salt, using the algebraic Wall Modeled LES (WMLES) model for the turbulence modeling, and found power changing will not affect the sideward heat flux significantly, while it had intensive impacts on the crust growth on the curved sidewall with a polar angle below 30°. Ge et al. (2019) numerically studied the effects of stratified interface instability on the thermal focusing effect in a two-layer corium pool, and relevant results can provide a reference for reactor IVR safety analysis and optimization design.

Motivated by the improvement of the cooling limit, the present study introduces a conceptual Ex-Vessel Retention design with a set of perforated tubes penetrating through a crucible which is filled with sacrificial materials under the RPV (see Figure 1). The whole device is kept dry during normal operation, while in case of severe accidents, water will be injected into the pit through the bottom of the basement until almost near the top of those tubes. Once the corium is pouring out from the RPV, the melt flow will be restricted to the center of the device by a refractory guide plate so that those tubes located along the outer circle wound not be damaged. When almost all the core melt is captured and its mixing with the sacrificial material comes to the state of layer reversion, the cooling water

TABLE 1 Geometry of the full size device and 1:4 scaled model.

Parameters	Full size	1:4 scaled model
Inner crucible diameter/mm	4,210	1,052.5
Inclination angle of the inner crucible/°	12	12
Total height of the inner crucible straight section/mm	3,500	875
Inner crucible melt height/mm	2000	500
Number of cooling heat transfer tubes/piece	72	6
Outer diameter of the cooling heat transfer tube/mm	100	25
Wall thickness of the cooling heat transfer tube/mm	16	3
Space between the cooling heat transfer tubes/mm	500	125
Slice thickness of the experiment section/mm	500	125
Total volume of the slice experiment section/L	-	119.90
melt volume of the slice experiment section/L	-	71.67

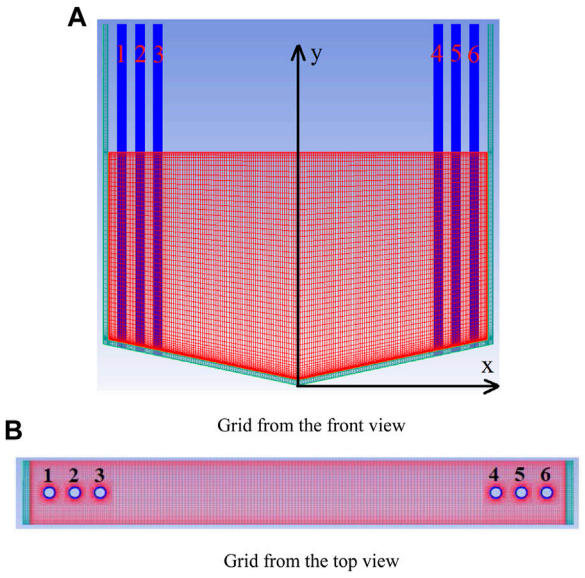

FIGURE 2
Schematic diagram of the 2D half-round slice. **(A)** Grid from the front view. **(B)** Grid from the top view.

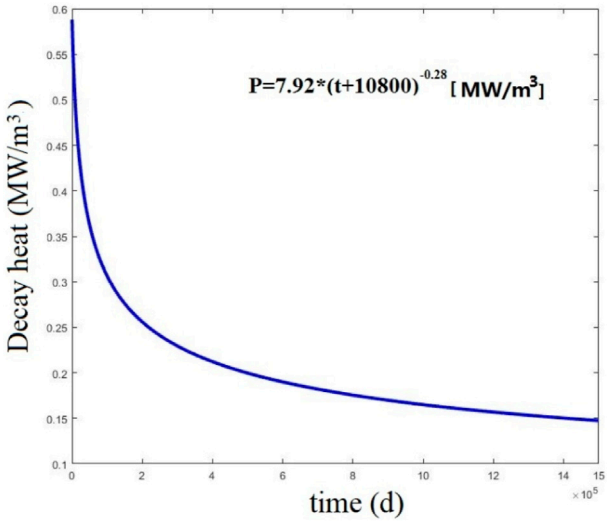

FIGURE 3
Typical decay heat of the reactor after severe accident.

will be injected again until the whole pit is flooded and all the melt is surrounded by water. The internal flow of the coolant will be driven by natural circulation as well as the molten pool itself. The decay heat will finally be released by water evaporation and the mixture of the melt and sacrificial material will finally be solidified in the device. In order to analyze the efficacy in coolability enhancement of this design, a full-scale simulation

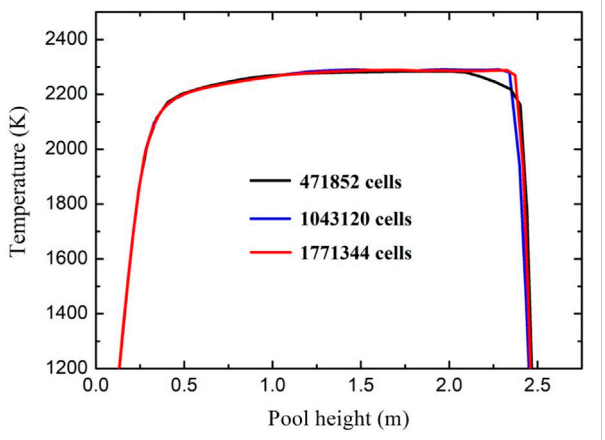

FIGURE 4
Central temperature vs. pool height at 10000s.

with code FLUENT is conducted to give a preliminary study in the real situation. Actually, a slice test facility with a geometrical scaled factor of 1:4 is proposed meanwhile, and a pre-test simulation is carried out using non-eutectic molten salt which is 20–80% mixture of $NaNO_3$ and KNO_3 based on the test facility in the near future.

Modeling

Model and grid

Similar to the in-vessel molten pool, computation analysis is a complementary way to investigate the mechanism of heat transfer and pool behavior for the conceptual ex-vessel retention design. As to a similar problem, lots of simulation methods or models done by previous researchers could be referred to. The ECM and PECM methods performed by C.T. Tran (Tran and Dinh, 2009) were applied to predict thermal loads imposed on the vessel wall and control rod guide tubes (CRGTs) during core debris heatup and melting in a boiling water reactor (BWR) lower plenum. Buck et al. (2010) used ASTEC and ATHLET-CD as well as CFD code CONV in developing the post-test calculations compared with the FSt4 LIVE test. In addition, Zhang et al. (2013) developed a two-dimensional numerical model with the SIMPLE algorithm in investigating the LIVE-L4 molten pool heat transfer characteristics too. Andrej Horvat (Horvat and Mavko, 2004) performed a numerical analysis of natural convection with the SST model of CFX 5.7 fluid dynamic software according to Asfia experiments. In addition, the fixed interface model has been successfully employed to describe the heat transfer in the system of the immiscible fluids numerically compared to data measured in the SIMECO experiments (Gubaidullin and Sehgal, 2004).

TABLE 2 Physical properties for real melt and non-eutectic mixture of $NaNO_3$–KNO_3 (20–80%).

Physical properties [unit]	Prototype melt	$NaNO_3$–KNO_3
Density [kg/m^3] (Boussinesq)	7,200	1866
Heat capacity [J/(kg·K)]	525	cp = -32.96 + 5.13*T-5.89E-3*T^2+1.97E-6*T^3
Conductivity [W/(m·K)]	4	T < 497.15 K, λ = 0.5
		497.15 K ≤ T < 557.15 K, λ = 0.6
		557.15 K ≤ T < 653.15 K, λ = 0.422
Viscosity [kg/(m·s)]	0.005	T < 497.15 K, μ = 10
		497.15 K ≤ T < 673.15 K μ = 0.01132*1.4E-5*T
		T ≥ 673.15 K, μ = 0.001928
Volume expansion coefficient [K^{-1}]	1E-4	0.000381
Latent heat of melting [J/kg]	332,420	161,960
Solidus temperature [K]	1800	497.15
Liquidus temperature [K]	2,400	557.15

TABLE 3 Physical properties for stainless steel.

Physical properties [unit]	Value
Density [kg/m^3]	7,850
Heat capacity [J/(kg·K)]	490
Conductivity [W/(m·K)]	15.4

Zhang et al. (2018) and Zhang et al. (1000) launched a numerical simulation by Fluent 17.1 based on the wall-modeled large eddy simulation (WMLES) method and the VOF model, as well as the phase change model, to obtain the corium pool heat transfer characteristic which agreed well with COPRA experimental data.

The numerical work in this study is a 2D half-round slice compared to the whole lower head which includes a molten pool, crucible, and cooling tubes, as shown in Figure 2. The red part is the molten pool (mixture of core melt and sacrificial material), the green part is the crucible, and the blue part is the cooling tubes. The prototype case calculation was launched corresponding to the full size listed in Table 1. The decay heat under the real situation is input as $P = 7.92 \cdot (t + 10800)^{-0.28}$ [MW/m^3] considering that the reactor should be shut down after 3 h during the severe accident (see Figure 3). Here P is a conservative value computed from $P = \frac{Q_d}{V}$, where Q_d is the decay heat expression for melt pool $Q_d = 0.125 f_d P_0 t^{-0.28}$ (Gaus-Liu and Miassoedov, 2013), f_d is the auxiliary value considering heat carried by a fusion product (1 as conservative consideration), P_0 is the initial power of HPR1000 (about 3050 MW), and V is the total volume of the mixture of core melt and sacrificial material (about 50 m^3) in the conceptually designed core catcher. In order to have a 0.5 MW/m^3 volumetric heat generation identical to the prototype case aforementioned, the volumetrical heat generation in the salt melt

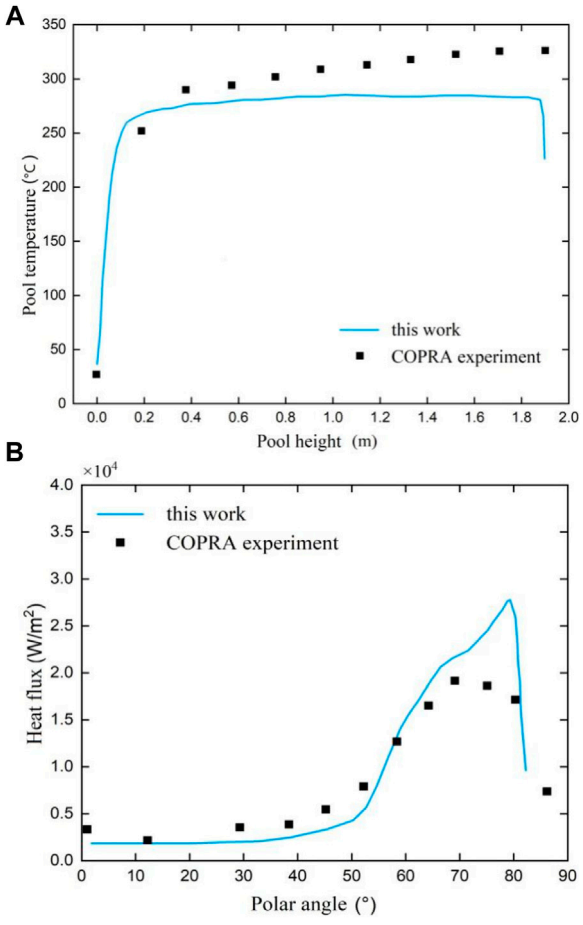

FIGURE 5
Verification of the model according to COPRA molten salt experiment. **(A)** Temperature profile vs. pool height. **(B)** Flux distribution along with the polar angle.

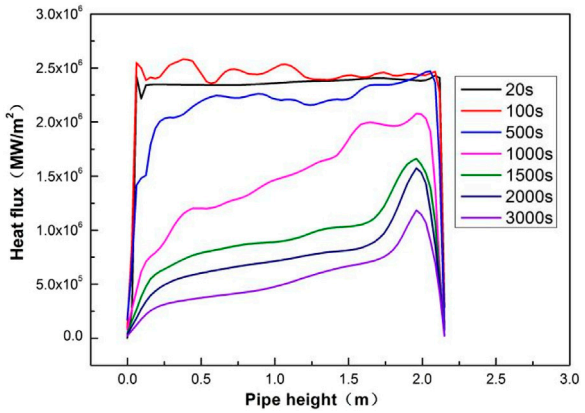

FIGURE 6
Heat flux vs. the height of the inner tube at the beginning.

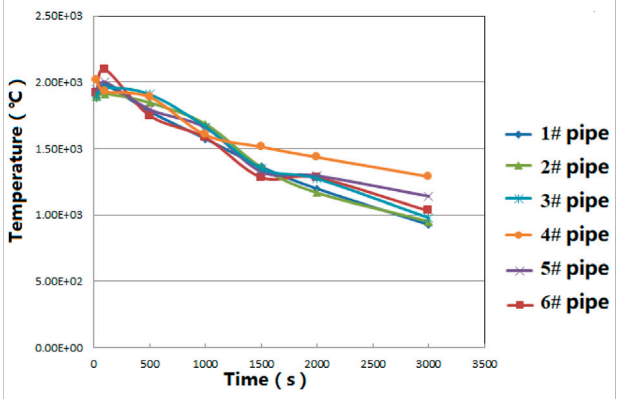

FIGURE 7
Maximum temperature along the tubes vs. time.

test is given as 50 kW/m^3 to induce strong natural turbulent convection in the melt pool, considering about 20% of heat loss. In addition, the salt mixture would probably decompose above 653K, so the heat release is limited.

The wall-modeled large eddy simulation is selected as the turbulence model so as to the solidification–melting phase transition model. Large temperature gradients are likely to occur near the wall of the cooling tubes and the wall of the crucible, so the grid needs to be heavily refined. Among them, a double O-block division is adopted near the cooling tube to achieve mesh densification and quality improvement. Tran et al. (2010) recommended that the boundary layer mesh size should satisfy $\Delta x < H/1{,}500$ in calculating the molten pool whose Ra' ($Ra' = \frac{g\beta q_v H^5}{\alpha\nu\lambda}$) is between 10^{14}~10^{15} (same level with the designed test in this study), where q_v is the volumetric heat rate and H is the molten pool height. H in the simulation model is set as 520 mm, so the boundary grid size should be less than 0.35 mm, and the actual size is taken as 0.3 mm in this study for the salt test simulation. To evaluate the rationality of mesh size for LES, the integral length scale (Addad et al., 2008) can be defined as

$$L_o^{RANS} = \left(\frac{k^{3/2}}{\varepsilon}\right)_{RANS} = \left(\frac{k^{1/2}}{C_\mu \omega}\right)_{RANS}.$$

where k is the turbulent kinetic energy, ε is the turbulent dissipation rate, and ω is the turbulence specific dissipation rate. Tests based on the 1,043,120 cells' mesh shows the LRV in most region of the molten pool is above 10. So the mesh size used in the study is enough in our point of view. Time steps are adopted between 0.01 and 0.5s, while the cell convective Courant number during LES calculation is always below 1. The central vertical temperature profile at 10000s for the prototype melt case is derived from simulation (see Figure 4). The figure shows that a grid with 1,043,120 cells is enough to get relatively acceptable results of heat transfer and natural convection in the molten pool. For the prototype melt case, transient results are acquired because how long will the melt be cooled down is much more cared about and a smaller time step is set at the first beginning thinking of quick decline of decay heat. However, the salt melt test simulation is almost a steady-state problem according to the test condition in future, specifically for the steady volumetrical heat generation and isothermal outer cooling through the boundaries.

Physical properties

The physical properties of the prototype melt and non-eutectic mixture of $NaNO_3$–KNO_3 (20–80%) are shown in Table 2. Among them, the physical properties of prototype melt are set as constant, while heat capacity, conductivity, and viscosity data for $NaNO_3$–KNO_3 are changing with temperature. The Boussinesq approximation is assigned to the density for both to produce the volume force. In addition, stainless steel is used as the vessel wall both in prototype condition and simulant experiment. Its physical properties are listed in Table 3.

Boundary condition

For the prototype melt case, the outer wall of the molten pool on the side of the cooling water and the inner wall of the cooling tube are both set to a constant temperature 100°C. The top boundary of the molten pool is also set as 100°C, considering that the water around is saturated and it is conservative in coolability evaluation. The front and back walls are set as adiabatic boundaries.

For the experiment of $NaNO_3$–KNO_3, since the water is injected from the bottom then into the tubes, the outer wall of the molten pool on the side and the inner wall of the cooling tubes are

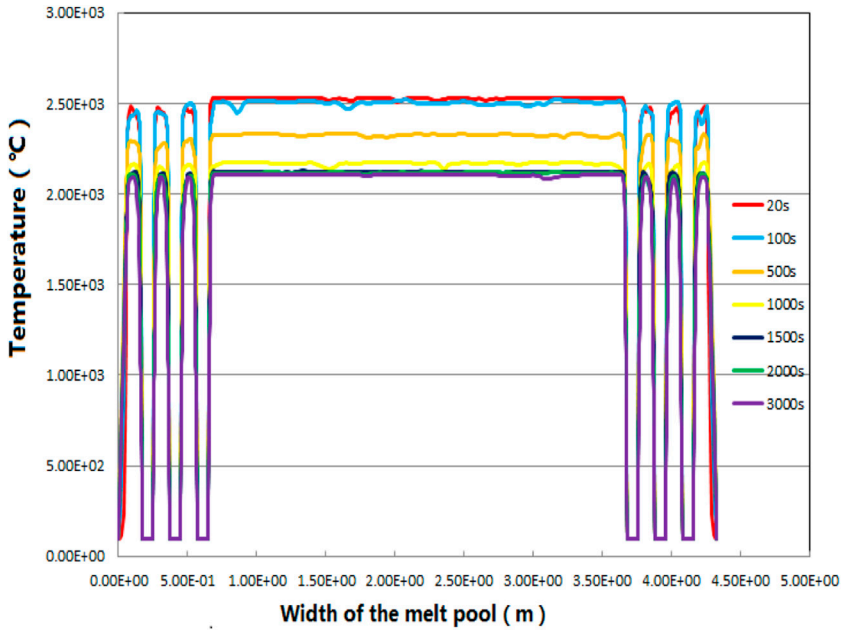

FIGURE 8
Temperature evolution at 0.2 m beneath the melt surface.

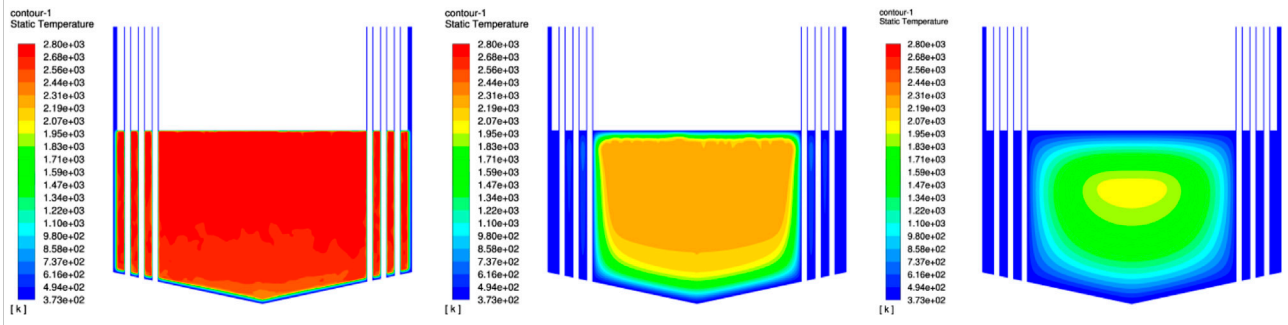

FIGURE 9
Thermal profile of the molten pool vs. time: 1) within 1000s; 2) several days; 3) several months.

both set to 25°C, thinking that the cooling water in the experiment is under room temperature. The top of the molten pool is set as convection boundary and the convection coefficient for $NaNO_3$–KNO_3 is set as 11.2 W/(m^2·K). The front and back walls are set as adiabatic boundaries too. The inner wall of the molten pool and the outer wall of the cooling tube above the liquid level are set as the radiation boundary, and the outside zone temperature is set to 25°C with the surface emissivity 0.6. In addition, boundary temperature of top and bottom sections of the cooling tube as well as the top of the side wall of the molten pool is also 25°C.

Verification of the model

The model was verified according to the experimental results of COPRA (Ge et al., 2019). The temperature profile vs. pool height (Figure 5) and heat flux distribution along with the polar angle had a good agreement according to the case of $NaNO_3$–KNO_3 (20–80%) molten salt experiment data. So it was indicated that the WMLES method is capable of illustrating the heat transfer and flow feature in a high-Rayleigh-number molten pool.

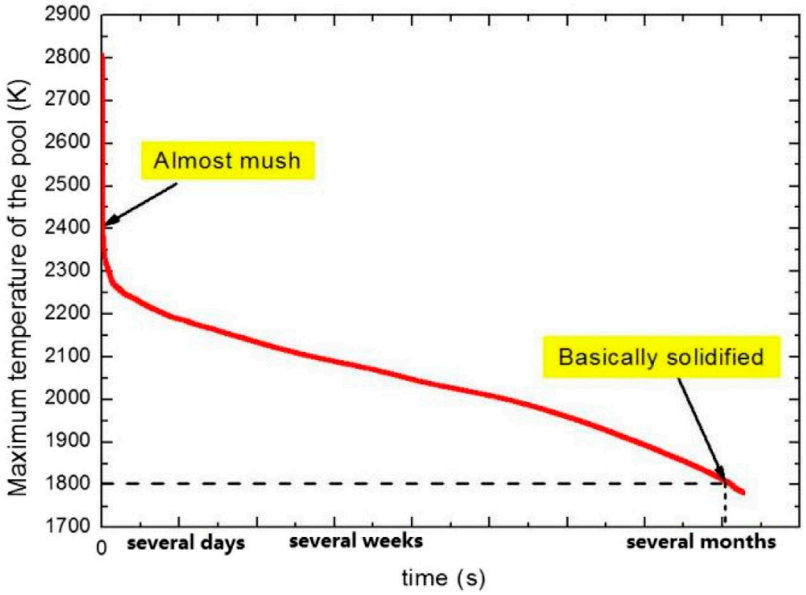

FIGURE 10
Solidification of the molten pool: T_{max} vs. time.

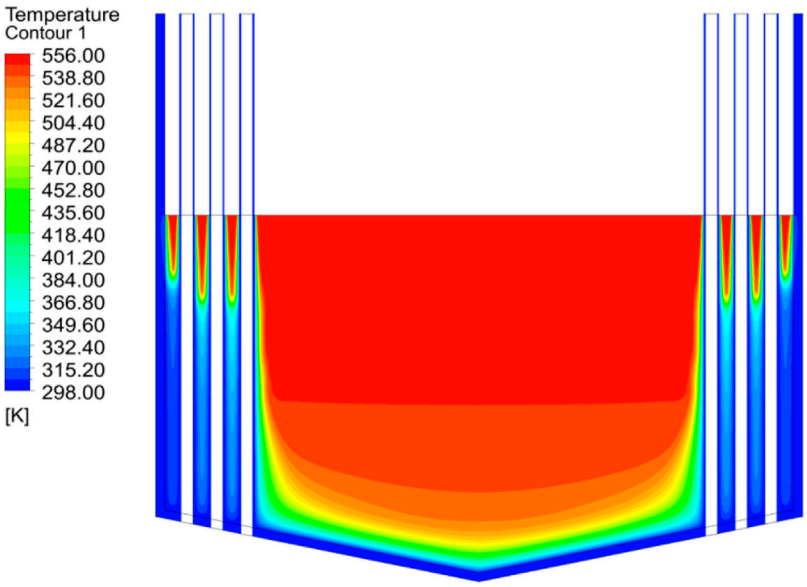

FIGURE 11
Temperature distribution of molten pool ($NaNO_3$–KNO_3).

Results and discussion

Coolability evaluation in the real situation

The most important question for this ex-vessel conceptual design is whether those cooling tubes would survive and keep functional. So the thermal load along the tubes is calculated in the prototype model as revealed by Figure 6. The heat flux is as high as 2.5 MW/m^2 at the first 100s and would quickly drop to 1 MW/m^2 during a few thousand seconds. With almost 72 tubes in the pool, the cooling surface is enlarged, which will greatly enhance the coolability of the device. The largest heat flux is located in 0.2 m beneath the

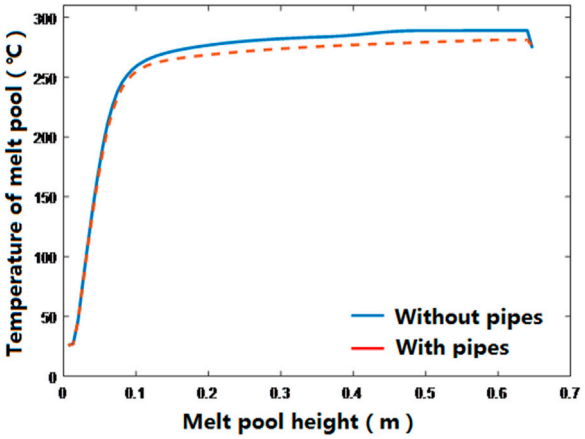

FIGURE 12
Temperature profile in the center of the molten pool ($NaNO_3$–KNO_3).

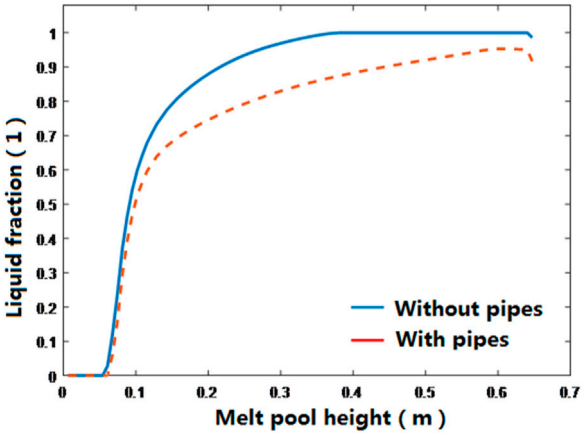

FIGURE 14
Distribution of liquid phase fraction in the center of the molten pool ($NaNO_3$–KNO_3).

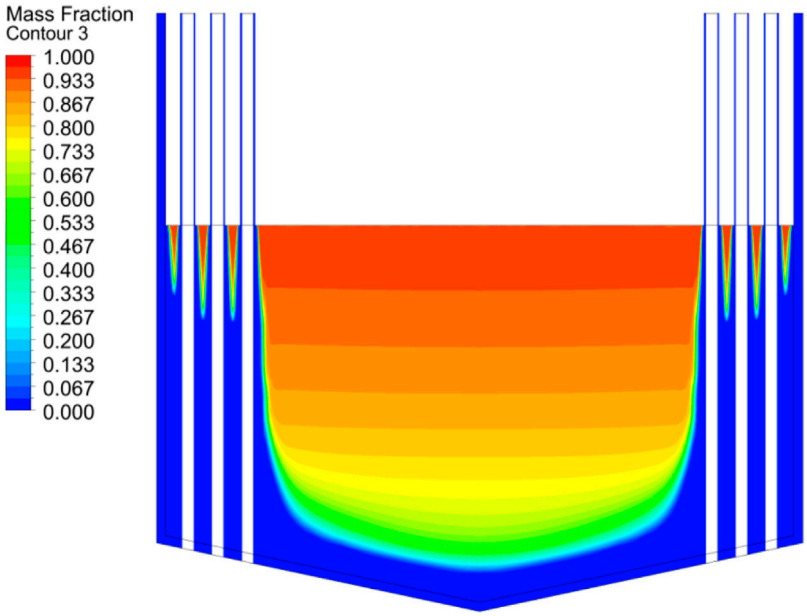

FIGURE 13
Distribution of liquid phase fraction in molten pool ($NaNO_3$–KNO_3).

melt surface. Maybe this is a dangerous situation for the tubes to be destroyed because CHF of the vertical stainless steel tube could be exceeded. According to the maximum temperature along the tubes (Figure 7), mostly the tubes would bear as high as 2000°C in the first 1000s including the left and right walls. But in fact, the refractory crust solidified by the coolant water may work as the proof from heat around the tubes; its conductivity is quite lower. So those tubes could still possibly survive in the authors' opinion. But this needs to be proved by experiment or more detailed modeling. As revealed in Figure 6, the heat flux in the lower part of the tube is much smaller than that in the top part near the melt surface, thanks to the weak convection and lower heat transfer along the inclined bottom part.

The initial temperature for the prototype melt case is assumed as 2800 K in the calculation. It is conservative because the reaction

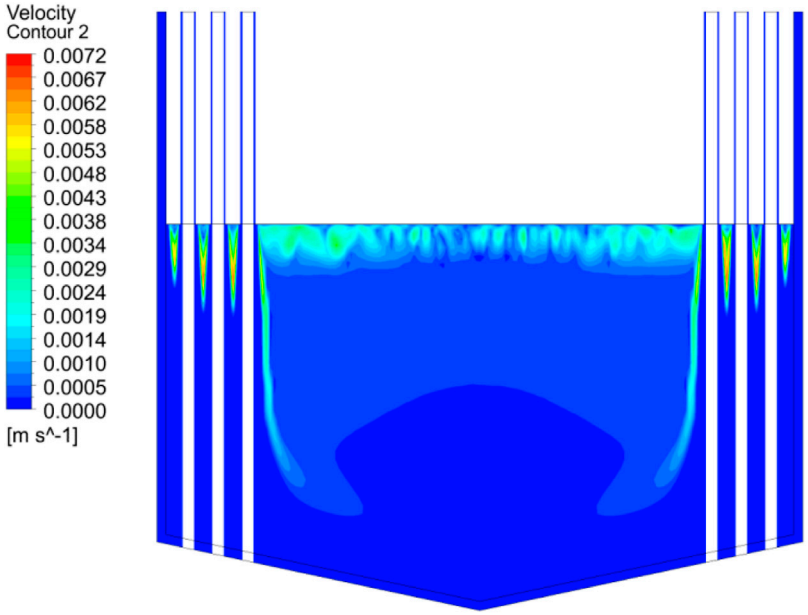

FIGURE 15
Velocity contour diagram of molten pool ($NaNO_3$–KNO_3).

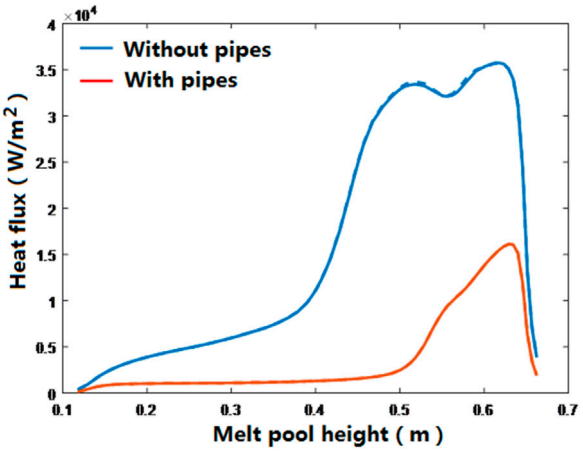

FIGURE 16
Heat flux distribution on the side wall of the molten pool ($NaNO_3$–KNO_3).

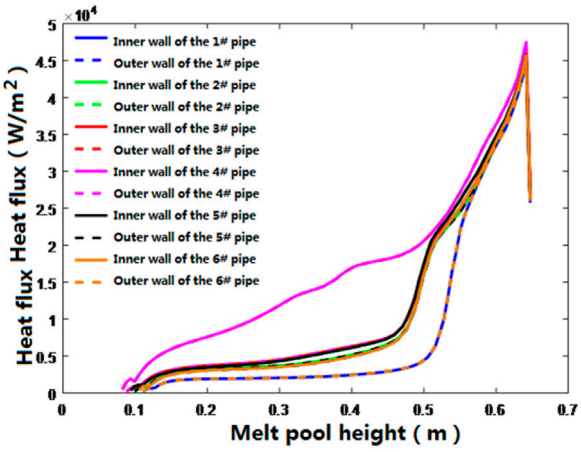

FIGURE 17
Heat flux distribution along the cooling tubes ($NaNO_3$–KNO_3).

between the core melt and sacrificial material is endothermic. Figure 8 indicates that the largest temperature along 1.8 m pool level will decline from 2800 to 2400 K during the first 3000s. The temperature near those tubes would dramatically drop to a very low value within the space between the tubes. Specific heat and latent heat of the melt must be the main heat source at the first thousands of seconds, while during long time cooling, decay heat may act as the important role.

From the results of the simulation, it will take several months (no more than 10) for almost all the melt cooling down to temperature of 1800K, as shown by Figures 9, 10. Melt near the tubes, inclined bottom, and the top surface which directly

TABLE 4 Statistics of total heat flow in the molten pool.

	Input power [W]	Top flow [W]	Side wall flow [W]	Bottom flow [W]	Tube flow [W]
Without tubes	4,400	1,094	2,192	458	0
With tubes	4,400	357	588	337	2,474

contacts with water will quickly be solidified, while the center of the pool is still a mushy zone after several months.

Molten salt test simulation

The initial temperature for the molten salt of the test simulation is assumed as 298.15 K and a steady state solver is launched. Results show the temperature profile at the bottom of the molten pool rises more rapidly as the height increases no more than 0.1 m (see Figures 11, 12) in the center of the molten pool. Then temperature seems steady as high as 280°C afterward. The upper center part of the molten pool is the hottest with or without tubes. But the temperature difference between the two is insignificant. Due to the heat loss by convection on the top, temperature near the pool surface decreases within a thin layer. The brim of the pool, mainly near the lower part of the tubes, is easily and quickly cooled down.

Similar to Figures 11, 12, temperature near the bottom of the molten pool, the side walls, and the cooling tube is lower than the solidus temperature, so it seems to be encrusted (see Figures 13, 14). Only a small area near the upper part of the cooling tube is still liquid. The distribution of the liquid phase in the main body of the molten pool is consistent with the temperature distribution. As the height increases, the liquid phase fraction rises more rapidly, and as the height rises further, the rising rate slows down. The liquid phase fraction profile in the center with tubes shows great reduction compared to case without tubes.

The fluid is likely to move obviously between the upper part of the cooling tubes, and velocity may reach 0.0055–0.0072 m/s (see Figure 15). The convection under the melt surface is also relatively tense. In the case with tubes, the vector and flow stream lines inside the molten pool are more regular. It can be seen that the strong heat exchange of the cooling tubes also strengthens the regularity of the flow inside the molten pool.

As shown in Figure 16, since the bottom molten pool might be crusted, heat flux gradually increases with the pool height on the side wall of the molten pool. There may be great growth at the height 0.4–0.6 m until the peak value is reached near the molten pool surface. The maximum heat flux is 16.14 kW/m^2 in the case with tubes, about one half of the one without tubes. Due to the effect of convection at the melt surface, the heat flux drops rapidly to some extent. The average heat flux on the side wall is 3.74 kW/m^2. Moreover, the ratio of heat flux peak to the average value is 4.32.

As revealed by Figure 17,

1) For the inner walls of cooling tubes 3 and 4, the heat flux is basically larger than that of others when the height of the molten pool is less than 0.45 m, probably because they are very close to the center of the hot pool. Above 0.5 m, thermal load seems the same for all the tubes since there are almost no differences for the melt around. The peak appears below the molten pool surface, which is about 44.75–47.48 kW/m^2.
2) The addition of the cooling tubes can reduce the peak and average heat flux of the side wall to 45.1 and 23.1%, respectively, which is a great enhancement of coolability.

The total heat flow statistics are shown in Table 4. It can be seen that without tubes, the heat flow on the side wall of the molten pool is much greater than that on the bottom wall, and the former is about 4.79 times that of the latter. After adding the cooling tubes, the heat flow exported from the cooling tube is much larger than that imposed on the side wall and bottom wall, and the ratio of the three is about 7.34:1.74:1. Therefore, the cooling tubes can transmit most of the heat out of the molten pool, which will greatly reduce thermal loads of the catcher brim, thereby reducing the risk of integrality breach by real high-temperature core melt.

Conclusion

According to the prototype melt numerical results, it seems that 1) cooling efficiency can be remarkably enhanced due to the inner tubes. The maximum temperature of the molten pool drops rapidly during the first several days and the cooling rate is relatively smooth until the melt basically solidifies after several months; 2) thermal loads of the tubes reach a peak of 2.5 MW·m^{-2} during the first hundred seconds, and the most dangerous part is located on the top of the molten pool.

As to the 1:4 scaled pre-test simulation with molten salt ($NaNO_3$–KNO_3) as simulant of the corium, it can be concluded that1) the adaption of the cooling tubes can greatly reduce the peak and average heat flux of the side wall, which seems a great enhancement of coolability under the steady state and a good protector

for the catcher side walls; 2) with the incensement of pool height, the heat flux gradually increases until reaches the peak value near the molten pool surface, which is the same as the prototype melt case.

In the future, a 1:4 scaled heat transfer experiment of the molten pool will be conducted. Apart from the declining and vertical walls, thermal loads on inner tubes can also be investigated; till then scaled analysis work and test results shall be compared with the numerical calculations.

Data availability statement

The original contributions presented in the study are included in the article/Supplementary Material; further inquiries can be directed to the corresponding author.

Author contributions

LZ, PG, and YL were contributors to the simulation work and the model interpretation; YG, WL, and QG were contributors to the experiment facility and scaling work related which was important for the numerical caculation. YY was the corresponding author and WM was the technical advisor.

Funding

This work was supported by the National Key R&D Program of China (Grant No. 2018YFB1900100).

Conflict of interest

Authors LZ, PG, YY, YL, YG, WL, and QG were employed by the company China Nuclear Power Engineering Co, LTD.

The remaining author declares that the research was conducted in the absence of any commercial or financial relationships that could be construed as a potential conflict of interest.

Publisher's note

References

Addad, Y., Gaitonde, U., and Laurence, D. (2008). Optimal unstructured meshing for large eddy simulations" book chapter in quality and reliability of large-eddy simulations. *ERCOFTAC Ser.* 12, 93–103. doi:10.1007/978-1-4020-8578-9_8 (ISBN: 978-1-4020-8577-2)

Asmolov, V. G. (2005). "Crucible-type core catcher for VVER-1000 reactor," in *Proceedings of ICAPP'05* (Seoul: Korea, May), 15–19.

Buck, M., Burger, M., Miassoedov, A., Gaus-Liu, X., Palagin, A., Godin-Jacqmin, L., et al. (2010). The LIVE program – results of test L1 and joint analyses on transient molten pool thermal hydraulics. *Prog. Nucl. Energy* 52, 46–60. doi:10.1016/j.pnucene.2009.09.007

Fischer, M. (2004). The severe accident mitigation concept and the design measures for core melt retention of the European Pressurized Reactor (EPR). *Nucl. Eng. Des.* 230, 169–180. doi:10.1016/j.nucengdes.2003.11.034

Fischer, M., Herbst, O., and Schmidt, H. (2005). Demonstration of the heat removing capabilities of the EPR core catcher. *Nucl. Eng. Des.* 235, 1189–1200. doi:10.1016/j.nucengdes.2005.02.022

Gaus-Liu, X., and Miassoedov, A. LIVE experimental results of melt pool behaviour in the PWR lower head with insulated upper lid and external cooling [C]. The 21st International Conference on Nuclear Engineering (ICONE-21), Chengdu, China, October 2013 12

Ge, K., Zhang, Y., Tian, W., Su, G., and Qiu, S. (2019). Effect of stratified interface instability on thermal focusing effect in two-layer corium pool. *Int. J. Heat Mass Transf.* 133, 359–370. doi:10.1016/j.ijheatmasstransfer.2018.12.117

Gubaidullin, A. A., and Sehgal, B. R. (2004). Numerical analysis of natural convection and mixing in two-fluid stratified pools with internal heat sources. *J. Heat. Transf.* 126, 600–610. doi:10.1115/1.1777578

Ha, K. S., Yeol Kim, H., Kim, J., and Park, J. H. (2011). An evaluation of a direct cooling method for the ex-vessel corium stabilization. *Nucl. Eng. Des.* 241, 4737–4744. doi:10.1016/j.nucengdes.2011.03.033

Horvat, A., and Mavko, B. Numerical investigation of natural convection heat transfer in volumetrically heated spherical segments. International Conference Nuclear Energy for New Europe 2004, Portorož ,Slovenia, 2004 September 6-9.

Khabensky, V. B., Granovsky, V. S., Bechta, S. V., and Gusarov, V. V. (2009). Etc. Severe accident management concept of the VVER-1000 and the justification of corium retention in a crucible-type core catcher. *Nucl. Eng. Technol.* 41, 561–574. doi:10.5516/net.2009.41.5.561

Luo, S., Zhang, Y., Zhang, D., Su, G., and Qiu, S. (2019). Numerical analysis of simulant effect on natural convection characteristics in corium pools. *Appl. Therm. Eng.* 156, 730–740. doi:10.1016/j.applthermaleng.2019.04.101

Luo, S., Zhang, Y., Zhou, Y., Tian, W., Su, G., and Qiu, S. (2018). COPRA experiment and numerical research on the behavior of internally-heated melt pool with eutectic salt. *Appl. Therm. Eng.* 140, 313–324. doi:10.1016/j.applthermaleng.2018.05.041

Tran, C. T., and Dinh, T. N. (2009). The effective convectivity model for simulation of melt pool heat transfer in a light water reactor pressure vessel lower head. Part I: Physical processes, modeling and model implementation. *Prog. Nucl. Energy* 51, 849–859. doi:10.1016/j.pnucene.2009.06.007

Tran, C. T., Kudinov, P., and Dinh, T-N. (2010). An approach to numerical simulation and analysis of molten corium coolability in a boiling water reactor lower head. *Nucl. Eng. Des.* 240 (9), 2148–2159. doi:10.1016/j.nucengdes.2009.11.029

Zhang, L., Luo, S., Zhang, Y., Wenxi, G. H., Su, G., and Qiu, S. (2018). Large eddy simulation on turbulent heat transfer in reactor vessel lower head corium pools. *Ann. Nucl. Energy* 111, 293–302. doi:10.1016/j.anucene.2017.08.055

Zhang, L., Zhang, Y., Su, G. H., Ma, Z., Bu, S., Sun, W., et al. Numerical simulation for the heat transfer in two-layer corium pool in HPR1000 reactor. 12th International Topical Meeting on Nuclear Reactor Thermal-Hydraulics, Operation and Safety (NUTHOS-12) Qingdao, China, October 14-18, 2018

Zhang, Y. P., Qiu, S., Su, G., and Tian, W. (2010). Analysis of safety margin of in-vessel retention for AP1000. *Nucl. Eng. Des.* 240, 2023–2033. doi:10.1016/j.nucengdes.2010.04.020

Zhang, Y. P., Su, G. H., Qiu, S. Z., Tian, W. X., Gaus-Liu, X., Kretzschmar, F., et al. (2013). A simple novel and fast computational model for the LIVE-L4. *Prog. Nucl. Energy* 68, 20–30. doi:10.1016/j.pnucene.2013.04.009

Zhang, Y. P., Zhang, L., Zhou, Y., Tian, W., Qiu, S., Su, G., et al. (2016). Natural convection heat transfer test for in-vessel retention at prototypic Rayleigh numbers – results of COPRA experiments. *Prog. Nucl. Energy* 86, 80–86. doi:10.1016/j.pnucene.2015.10.014

Zhang, Y. P., Zhang, L., Zhou, Y., Tian, W., Qiu, S., Su, G., et al. (2016). The COPRA experiments on the in-vessel melt pool behavior in the RPV lower head. *Ann. Nucl. Energy* 89, 19–27. doi:10.1016/j.anucene.2015.11.013

Frontiers in
Energy Research

Advances and innovation in sustainable, reliable and affordable energy Explores sustainable and environmental developments in energy. It focuses on technological advances supporting Sustainable Development Goal 7: access to affordable, reliable, sustainable and modern energy for all.

Discover the latest Research Topics

See more →

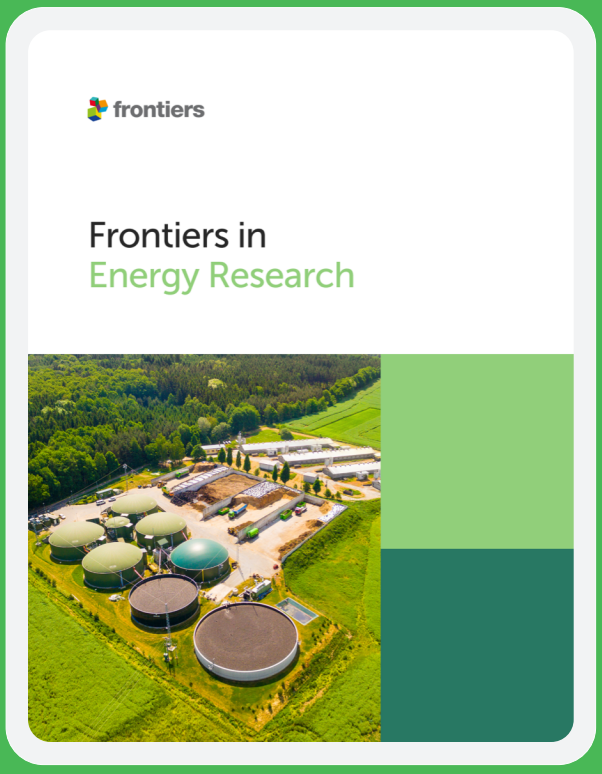

Frontiers

Avenue du Tribunal-Fédéral 34
1005 Lausanne, Switzerland
frontiersin.org

Contact us

+41 (0)21 510 17 00
frontiersin.org/about/contact